



University
of Glasgow

Cappelluti, Mauro Davide (2018) *Nanostructured materials for water purification: synthesis, insights and performance evaluation*. PhD thesis.

<https://theses.gla.ac.uk/9100/>

Copyright and moral rights for this work are retained by the author

A copy can be downloaded for personal non-commercial research or study, without prior permission or charge

This work cannot be reproduced or quoted extensively from without first obtaining permission in writing from the author

The content must not be changed in any way or sold commercially in any format or medium without the formal permission of the author

When referring to this work, full bibliographic details including the author, title, awarding institution and date of the thesis must be given

Enlighten: Theses

<https://theses.gla.ac.uk/>
research-enlighten@glasgow.ac.uk



University
of Glasgow

**Nanostructured Materials for
Water Purification: Synthesis,
Insights and Performance
Evaluation**

Mauro Davide Cappelluti

Submitted in fulfilment of the requirements for the
Degree of Doctor of Philosophy

School of Engineering
College of Science and Engineering

University of Glasgow
(May 2018)

Abstract

Membrane filtration and Advanced Oxidative Processes (AOPs) are among the most efficient and cost-effective methods employed in water purification. A system to integrate the two methods using photoactive colloidal particles was studied in this thesis, with the final purpose of overcoming membrane fouling, one of the main issues occurring in filtration processes. The production of nanostructured TiO₂ microparticles through a simple and extremely rapid synthesis and an easy method to assemble a multifunctional coating integrating inorganic particles on filtration membranes were targeted as the most promising solutions from the technological and environmental point of view.

The control of microwave-assisted heating applied to hydrothermal treatments, a relatively recent synthetic method, allowed the production of nanostructured mesoporous spherical TiO₂ particles, bringing the synthesis to the minute scale, extremely rapid compared with conventional heating, and achieving products otherwise difficult to obtain without the help of surfactants or templating agent. The as-synthesised particles showed photoactivity under visible light, with rate of specific reactions (selective de-ethylation) 4 times higher compared with commercial photocatalysts. Furthermore, the particles were modified to extend the limited intrinsic absorbance of TiO₂ in the visible light, with promising results given by formation of stoichiometric defects (in particular oxygen vacancies) through annealing under vacuum. This treatment allowed the achievement of comparable or even higher performance in photocatalytic degradation of rhodamine B with respect to commercial TiO₂ photocatalysts, including Aeroxide P25, with degradation rate towards organic molecules (rhodamine B) of even 60-70% after 1 hours, compared to the 25% of P25.

The production of a multifunctional coating for water treatment by integration of colloidal and nanometric TiO₂ particles has been also studied. A simple technique to integrate TiO₂ nanoparticles onto different substrate, in particular filtration membranes, was produced by simple electrostatic interactions involving the use of polyelectrolytes, water-soluble charged polymer forming organised layers when assembled in a macromolecular structure defined as polyelectrolyte multilayers (PEMs). Electrostatic assembly was applied as an environmentally friendly technique to anchor nanoparticles (P25) on different surfaces, transferring their properties to these. In particular, the application of TiO₂ particles conferred

hydrophilic and superhydrophilic to a relatively hydrophobic surface (Mylar) by controlling the multilayer assembly conditions, in particular the ionic strength of the polyelectrolyte solutions.

Chapter 1 is dedicated to the description of the research background and the problematics aimed to be solved, with in-depth description of ultrafiltration and Advanced Oxidation Processes (AOPs) for water purification, microwave heating for inorganic nanoparticle synthesis and the antibacterial action of active nanoparticles through photocatalytic processes. Polyelectrolyte multilayers (PEMs) are also introduced as efficient method for surface functionalisation and integration of nanoparticles. The synthesis procedures and methodological analysis for characterisation, properties and performance assessment are detailed in **chapter 2**.

The application of Flash-Microwave Synthesis (FMH), which associates the principle of acid digestion with the application of a constant power microwave irradiation, was used for the synthesis of nanostructured mesoporous TiO₂ microparticles. The minute-scale reaction allowed the production of controlled spherical particles with tunable size (200 nm to several microns), adopting a template and surfactant-free approach relatively environmentally friendly from the point of view of the reactants and the energy demand. Details of the synthesis and full characterisation of the particles are given in **chapter 3**. In **chapter 4**, several methods for extending the limited photocatalytic response of TiO₂ to the visible light are presented, with successful modification of the previously synthesised particle through annealing under vacuum, outperforming commercial standards due to the reduced band gap (1.9-2.7 eV), presence of oxygen vacancy defect and high adsorbing power towards organic molecules in solution. Photodegradation mechanisms and structural insights of the visible-light activity have been also investigated.

Finally, the results of the integration of commercial TiO₂ nanoparticles onto ultrafiltration membranes and other surfaces by using polyelectrolyte multilayers are reported in **chapter 5**. The achievement of superhydrophilic behaviour on the treated surface, with contact angles below 15° on Mylar surfaces, and the possibility of removing fouled active layer from a membrane replacing it with a newly generated one can be both implemented as potential antifouling strategies for water treatment.

Table of Contents

Abstract.....	I
Table of Contents.....	III
List of Tables.....	IX
List of Figures	XIII
Acknowledgement.....	XXVII
Conference Contributions and Presentations	XXIX
Publications.....	XXIX
Declaration.....	XXX

List of Abbreviations used in Chapter 1	1
-----------------------------------------------	---

Chapter 1 : Photoactive nanoparticles and multifunctional coatings in membrane filtration processes

1.1 Introduction	3
1.2 Membrane separation processes	4
1.2.1 Low-pressure filtration process: MF and UF	5
1.2.2 Polymer membranes	6
1.3 Membrane Fouling	8
1.4 Antifouling strategies.....	9
1.4.1 Antibacterial and sterilisation processes	11
1.5 Photocatalysis as a purification process	12
1.5.1 Photocatalytic materials	14
1.6 Nanoparticles for environmental applications.....	16
1.7 Titanium dioxide (TiO ₂)	18
1.7.1 Photocatalytic activity	19
1.7.2 Photo-induced hydrophilicity	21
1.7.3 Visible light active TiO ₂	22
1.7.4 Toxicity and antibacterial properties of TiO ₂	24
1.7.5 TiO ₂ in water treatment and membranes.....	25
1.8 Microwave-assisted hydrothermal synthesis.....	27
1.8.1 Hydrothermal/solvothermal methods	27
1.8.2 Microwave chemistry.....	28
1.8.3 MW-assisted hydrothermal/solvothermal synthesis.....	30
1.9 Polyelectrolyte multilayers (PEMs).....	32
1.9.1 Polyelectrolytes	33

1.9.2 Parameters influencing PEM structures	34
1.9.3 PEM on filtration membranes	37
1.9.4 PEM in antifouling and antimicrobial strategies	38
1.10 Nanocomposite coating by LbL technique	39
1.11 Aim of the project	41
1.12 References	42
List of Abbreviations used in Chapter 2	52

Chapter 2 : Materials, methods and models

2.1 Materials	54
2.2 TiO ₂ particles synthesis	55
2.2.1 Flash Microwave-assisted synthesis.....	55
2.2.2 Post-synthesis thermal treatments	56
2.3 PEM-modified surfaces	57
2.3.1 Coating technique	57
2.3.2 Surface preparation	58
2.4 Powder X-ray Diffraction	59
2.4.1 Principles of the technique	59
2.4.2 Data collection and analysis	60
2.4.3 Rietveld refinement.....	62
2.4.4 Particle Size and Strain Analysis	64
2.4.5 Whole Powder Pattern Modelling (WPPM)	65
2.5 Spectroscopic technique for structural and physical characterisation.....	66
2.5.1 FT-Infrared spectroscopy.....	66
2.5.2 Raman spectroscopy	67
2.5.3 UV-Vis spectroscopy.....	70
2.5.4 Diffuse Reflectance UV-Vis (DR-UV-Vis) spectroscopy.....	71
2.5.5 X-ray photoelectron spectroscopy (XPS).....	73
2.5.6 Electronic paramagnetic resonance (EPR)	74
2.6 Elemental analysis (C, N, H).....	75
2.7 Specific surface area determination	76
2.7.1 Pore size distribution.....	77
2.8 Thermal analysis	78
2.8.1 Simultaneous thermogravimetric analysis (STA:TG-DTA).....	78
2.8.2 Mass spectrometry (MS)	79
2.9 Colloidal dispersion stability.....	80
2.9.1 Dynamic Light Scattering (DLS)	80
2.9.2 Zeta-potential	81

2.10 Coating and thin film characterisation	82
2.10.1 Contact angle measurement	82
2.10.2 Atomic Force Microscopy (AFM).....	83
2.10.3 Multi parametric Surface Plasmon Resonance (MP-SPR)	84
2.11 Electron microscopy	86
2.11.1 Scanning Electron Microscopy (SEM).....	86
2.11.2 Energy-dispersive X-Ray spectroscopy (EDX).....	87
2.11.3 Transmission Electron Microscopy (TEM)	88
2.12 Photocatalytic degradation	89
2.12.1 Organic dyes as pollutant model.....	89
2.12.2 Degradation experiment	92
2.13 Total Organic Carbon (TOC) determination	93
2.14 Hydraulic characterisation of membranes	94
2.14.1 Dead-end filtration	96
2.14.2 Fouling	97
2.15 References	99
 List of Abbreviations used in Chapter 3	 102

Chapter 3 : Flash microwave-assisted hydro/solvothermal synthesis of TiO₂ submicroparticles

3.1 Introduction.....	104
3.2 Aims.....	106
3.3 Synthesis of mesoporous TiO ₂ sub-microparticles.....	106
3.3.1 Synthesis conditions	106
3.4 Characterisation of the as-synthesised sub-microparticles	108
3.4.1 Crystalline structure	108
3.4.2 Morphology	114
3.4.3 Surface area and pore size	128
3.5 Spectroscopic characterisation	136
3.5.1 Raman spectroscopy	136
3.5.2 Optical properties.....	141
3.5.3 Size determination by optical spectroscopy.....	148
3.6 Examples of comparative analysis	153
3.6.1 Effect of treatment time	153
3.6.2 MW pulsed regime	155
3.6.3 Influence of the solvent	158
3.7 Surface analysis, composition and impurities	161
3.7.1 XPS analysis	161

3.7.2 Thermal analysis	163
3.7.3 FT-IR and Raman analysis of the impurities	167
3.8 Discussion	172
3.8.1 Hydrothermal conditions under microwave heating	172
3.8.2 Theoretical calculations	173
3.8.3 <i>In-situ</i> measurement	176
3.8.4 Principles of the reaction	180
3.8.5 Kinetic mechanism of microsphere formation	183
3.8.6 Precursor concentration	186
3.8.7 Treatment time and MW power	187
3.8.8 Acid mediator	188
3.8.9 Effect of the solvent	191
3.8.10 Impurities	192
3.9 Conclusion	194
3.10 References	196
List of Abbreviation used in Chapter 4	203

Chapter 4 : Towards active visible-light photocatalysis: reducing treatment and vacuum activation

4.1 Introduction	204
4.1.2 Aims	205
4.2 Synthesis and treatments	205
4.2.1 Calcination	205
4.2.2 Post-synthesis thermal treatment under specific atmosphere	206
4.3 Overview of commercial photocatalysts	207
4.3.1 Aeroxide® P25	207
4.3.2 Kronos7000	209
4.4 Effect of the oxidative calcination of FMH-TiO ₂	212
4.4.1 Crystallite growth and phase transition	212
4.4.2 Optical properties	216
4.4.3 Surface area and pore size	217
4.4.4 Effects of the treatment time	218
4.4.5 Inert gas calcination of FMH-TiO ₂ materials	222
4.5 Nitrogen doping by ammonolysis treatment	225
4.5.1 Ammonolysis	225
4.5.2 Structural analysis	227
4.5.3 Optical properties	229
4.5.4 Efficacy of doping	232

4.5.5 Thermal analysis	233
4.6 Vacuum activation.....	237
4.6.1 Structural and physical modifications	238
4.6.2 Optical properties.....	241
4.6.3 Thermal stability	243
4.7 Efficacy of the reducing treatment	245
4.7.1 XPS analysis	245
4.7.2 EPR analysis.....	248
4.7.3 Comparison with reverse oxidation reaction	250
4.8 Other reductive thermal treatments	252
4.8.1 Hydrogen atmosphere	252
4.8.2 Microwave heating	253
4.9 Photocatalytic properties	255
4.9.1 Untreated particles	257
4.9.2 Effect of the thermal treatment.....	261
4.9.3 Effect of reductive treatments.....	262
4.10 Discussion	268
4.10.1 Calcination	268
4.10.2 Reducing treatments	270
4.10.3 Efficacy of the reducing treatments.....	272
4.10.4 Degradation performance.....	275
4.11 Conclusions.....	280
4.12 References	283

List of Abbreviations used in Chapter 5	288
-----------------------------------------------	-----

Chapter 5 : TiO₂-Polyelectrolyte Multilayers (PEMs) composites for membrane filtration

5.1 Introduction.....	289
5.1.1 Aims	290
5.2 Polyelectrolyte multilayers (PEMs) for environmental applications	291
5.2.1 Selection of polyelectrolytes and conditions	291
5.2.2 Adhesion mechanism and kinetics	294
5.2.3 Surface characterisation of PEM-modified surfaces	301
5.3 Polyelectrolyte-TiO ₂ composites.....	304
5.3.1 Dispersion of TiO ₂ particles in aqueous solution	304
5.3.2 Integration of TiO ₂ nanoparticles into PEMs	306
5.3.3 Stabilising effect of polyelectrolytes	314
5.4 PEM-modified membranes.....	317

5.4.1 Ultrafiltration (UF) membranes	317
5.4.2 Morphology	318
5.4.3 Swelling and water content	321
5.4.4 Porosimetry	323
5.4.5 Spectroscopic characterisation	326
5.4.6 Contact angle measurements	330
5.4.7 Permeability	333
5.5 TiO ₂ -PEM composite membranes.....	339
5.6 Improvement of PEM deposition conditions	345
5.6.1 TiO ₂ -PEM composite coating	346
5.7 Fouling test and coating resistance	352
5.8 Discussion	358
5.8.1 PEM deposition	358
5.8.2 TiO ₂ stability and integration with polyelectrolytes	362
5.8.3 Further improvement of PEM coating on particles and surfaces	364
5.8.4 Development of an integrated system	365
5.9 Conclusions	367
5.10 References	370

Chapter 6 : Conclusion and future work

6.1 Conclusions	375
6.2 Future works	379

Appendices

Appendix A: Figures and tables for Chapter 3	384
Appendix B: Figures and tables for Chapter 4	398
Appendix C: Figures and tables for Chapter 5	407

List of Tables

Table 1.1: Basic characteristic of membranes for low-pressure filtration processes	5
Table 1.2: Common polymers used in filtration processes..	8
Table 2.1: Statistical reliability factor for the structural refinement	63
Table 2.2: Correlation exponential term for the Tauc expression	72
Table 3.1: Summary of the synthesis parameters for the FMH-TiO ₂ particles.....	107
Table 3.2: Results of the WPPM refinement and size analysis compared with the Scherrer calculation.	111
Table 3.3: Surface area values for representative samples of the NE series (prepared using 2 M and 1 M HNO ₃) using different calculation methods	132
Table 3.4: Surface area and pore size distribution data for some selected FMH-TiO ₂ samples, compared with the crystalline size (calculated by Scherrer equation) and the secondary particle distribution	135
Table 3.5: Band positions and relative intensity for the Raman spectra of commercial anatase (Sigma, 99.9%) and Aeroxide®	139
Table 3.6: Results of the band gap calculation for TiO ₂ commercial anatase and rutile.....	142
Table 3.7: Optical band gap (indirect and direct) and Urbach energy (minimum and maximum values estimated from other synthesis conditions, e.g. treatment time) for FMH-TiO ₂ particles, classified according to the synthesis conditions (type of acid and solvent), acid and precursor concentration.....	144
Table 3.8: Effect of the treatment time on selected characteristics of the FMH-TiO ₂ particles, CW series (TTIP conc. 164 mM, HCl 2 M solution).....	154
Table 3.9: Selected characteristics of particles prepared by MW-pulsed treatment (1 min reaction per cycle).....	156
Table 3.10: Selected characteristics for particles produced using different ratios of ethanol and water (HNO ₃ -mediated synthesis).....	161
Table 3.11: XPS integrated signal for the selected NE series sample using Casa® software.	162
Table 3.12: CHN combustion microanalysis results for some representative FMH-TiO ₂ samples	164
Table 3.13: List of the IR bands observed for the FMH-TiO ₂ particles, with their assignment.	171
Table 4.1 Result of the Rietveld refinement for Aeroxide P25, with the estimated relative concentration of the two polymorphs	209
Table 4.2: Principal characteristics and properties of pure anatase, Aeroxide P25 and Kronos7000	211
Table 4.3: Band gap and Urbach energy calculations for some representative FMH-TiO ₂ samples (acid and precursor concentrations indicated respectively) calcined at different temperature .	217

Table 4.4: BET and BJH calculations for the nitrogen adsorption/desorption isotherms of the representative sample belonging to the <i>NE</i> series (2 M HNO ₃ in ethanol, 162 mM precursor concentration, 1 min MW treatment) before and after calcination (573 - 773 K), which isotherms and BJH porosity are shown in Figure 4.8.	218
Table 4.5: Influence of the heating time on the microstructural parameters of particles calcined at 773 K.....	222
Table 4.6: Summary of the optical band gap and Urbach energy values of P25 and anatase after ammonolysis treatment at different temperatures.....	231
Table 4.7: Summary of the optical band gap and Urbach energy values of FMH-TiO ₂ (<i>NE</i> series, 2 M HNO ₃) after ammonolysis treatment at different temperatures	231
Table 4.8: Elemental analysis results on anatase and P25 under thermal ammonolysis treatment at different temperature.	233
Table 4.9: Optical properties of the selected ammonolysed FMH-TiO ₂ samples, before and after STA analysis, compared to P25 underwent the same treatment.	236
Table 4.10: Collection of selected structural data and Raman spectral features for FMH-TiO ₂ samples annealed under dynamic vacuum at different temperature and duration.	240
Table 4.11: Combustion CHN microanalysis for some representative vacuum heated FMH-TiO ₂ samples	241
Table 4.12: Results from DR-UV-Vis analysis for the <i>NE</i> samples heated under static vacuum ..	242
Table 4.13: Results of the optical analysis for the samples produced under dynamic vacuum conditions	243
Table 4.14: Results of the optical analysis for selected samples produced under dynamic vacuum conditions at constant temperature (673 K) for different times. The results include also the re-oxidation experiment performed on the sample heated under dynamic vacuum for 7 hours and then calcined in air at the same temperature for 3 hours.....	245
Table 4.15: List of samples analysed by XPS, with the peak position and the atomic concentration, calculated from the integrated intensity of the signal, for Ti, O and C (no N was detected). <i>NE</i> (2 M HNO ₃ , 162 mM prec. Concentration, 1 min MW treatment) was selected as representative sample for the different thermal treatments.	245
Table 4.16: List of the sample selected for the EPR analysis with their corresponding g values	249
Table 4.17: Phase composition and optical properties of commercial anatase MW-heated under vacuum as a function of the treatment time..	254
Table 4.18: Results of degradation test for the reference materials, using different concentration of photocatalyst in Rhodamine aqueous solution	256
Table 4.19: List of the untreated FMH-TiO ₂ sample, with degradation performance under UVA and visible light.....	257
Table 4.20: Structural characteristics and degradation performance of the samples tested (Figure 4.45).....	262
Table 4.21: Degradation performance of commercial TiO ₂ photocatalyst ammonolysed at different temperature	263
Table 4.22: Description of the FMH-TiO ₂ vacuum heated samples reported in Table 4.23.....	266

Table 4.23: Optical-electronic characteristics of the vacuum heated samples with the corresponding photocatalytic performance observed in the rhodamine degradation experiments.....	267
Table 5.1: Characteristic of the polyelectrolyte species investigated in this project.	292
Table 5.2: effect of the concentration of polyelectrolyte on the solution conductivity for strong polyelectrolytes.	293
Table 5.3: List of the commercial membranes used in the thesis project.	318
Table 5.4: AFM roughness values calculated for the selected membranes. R_a indicates the average roughness, R_q indicates the root-mean squared roughness of the surface	321
Table 5.5: BET surface area and pore size distribution analysis for the commercial UF membranes	325
Table 5.6: BET surface area and pore size distribution analysis for the PEM-coated SM ultrafiltration membranes.....	325
Table 5.7: General properties of the PSS/PDDA multilayer (K series) on SM membranes.	335
Table 5.8: SM-B membrane series, (PDDA-PSS) _n multilayer on SM-UF membranes, varying the ionic strength of the polyelectrolyte solution and the rinsing method.	337
Table 5.9: Relevant properties of PES UF membranes (SM type) coated with a composite (PDDA/PSS) multilayer with integration of TiO ₂ (Aeroxide P25, 1 g/L). PDDA composed the outermost layer in all membranes.	339
Table 5.10: Characteristics of selected PEM-coated membrane produced using the improved deposition method.....	346
Table 5.11: List of the sample of Mylar foil coated with the TiO ₂ - composite multilayer by using the improved deposition method..	348
Table 5.12: List of the membrane coated with TiO ₂ -composite PEMs and their properties..	351
Table 5.13: Permeate flux during the different stage of the fouling experiment for TiO ₂ -PEM coating on SM membrane, applied by using immersion coating.	354
Table 5.14: Permeate flux during the different stage of the fouling experiment for TiO ₂ -PEM coating on SM membrane, applied by using the “improved” deposition method.	356
Table A.1: Error calculation estimated for the optical band gap measurement of commercial materials	388
Table A.2: Comparison among the different values of surface area, pore volume and average pore size in the recent literature for Aeroxide® P25.....	389
Table A.3: Coefficient for the exciton quantum confinement equation for the Raman peak broadening and redshift.	391
Table A.4: relative intensity of the mass spectrometer signal of the lighter molecules containing carbon and nitrogen atoms (from reference [1]).....	391
Table A.5: Description and comparison of the DFT kernel for Carbon and SiO ₂ for N ₂ adsorption at 77 K of Aeroxide P25.	395
Table A.6: Thermodynamic parameters for the solvent used in this thesis.....	396

Table A.7: List of the characteristics of the acids used for the particle preparation. The acids were used without further purification.	396
Table A.8: pH measurement of the acidic solution used for the FMH synthesis.	397
Table A.9: Conductivity of the acidic solution used for the FMH synthesis.	397
Table A.10: pH and conductivity of mixed solution of water and ethanol.	397
Table A.11: CHN microanalysis of the FMH-TiO ₂ particles after oxidative calcination (thermal annealing in air) at 773 K in function of the treatment time	400
Table A.12: Optical properties, surface area and pore size analysis of the FMH-TiO ₂ samples (NE, 2 M, 164 mM) calcined under N ₂	400
Table A.13: Crystallographic data for Ti/Ti-N phases observed after ammonolysis at high temperature (data from ICSD database).	402
Table A.14: XPS signal integration for the N-doped P25 and the N-doped FMH-TiO ₂ representative sample, both treated by ammonolysis at 773 K (3 hrs).	404
Table A.15: Band gap values and Urbach energies of the Ti ₂ O ₃ sample calcined in air at different temperatures.	406
Table A.16: Band gap values and Urbach energies of the TiN sample calcined in air at different temperatures.	406
Table A.17: Initial model used for the thickness determination from the SPR curves, provided by the instrument company (Bionavis).....	407
Table A.18: Z-average, zeta potential and conductivity measurement relative to P25 basic system stabilised by the addition of polycations	408
Table A.19: Z-average, zeta potential and conductivity measurement relative to P25 acid system stabilised by the addition of polyanions.	408
Table A.20: Zeta potential measurement for anatase, P25 and Kronos (100 mg/L suspension) at different pH values.	409

List of Figures

Figure 1.1: Classification scheme of different Advance Oxidation Processes (AOP) based on wastewater treatment technologies	14
Figure 1.2: Band gap values and band-edge positions with respect to the vacuum level and NHE for selected semiconductors. Red bars represent the conduction-band edges, the green ones indicate the valence-band edges. The band energies are compared to the water redox reaction potentials.....	16
Figure 1.3: Structural representation using planar Ti_3O building-block model (upper images) and TiO_6 polyhedrals (lower images) for the three main TiO_2 polymorphic phases	19
Figure 1.4: Mechanism of electron- hole pair formation in TiO_2 particle irradiated by photons with energy comparable with the material band gap. Example of reactions in the presence of pollutants (indicated with P) in water	21
Figure 1.5: Schematic representation of the mechanism of reversible wettability of TiO_2 surface exposed to UV light irradiation and under dark.	22
Figure 1.6: Scheme of a typical Layer-by-Layer (LbL) dip coating with immersion in oppositely charged polyelectrolyte solution.....	33
Figure 2.1: (a) Comparison between a conventional stainless steel autoclave for hydrothermal treatment and a MW-transparent autoclave; (b) schematic diagram of the structure of the MW-transparent autoclave.....	56
Figure 2.2: Schematic representation of the Bragg's law conditions for constructive interference of X-ray beams from atomic planes in a crystal	60
Figure 2.3: (a) schematic representation of the Bragg-Brentano geometry; (b) picture and (c) schematic diagram of the PANalytical X'Pert PRO MPD diffractometer, with numbers indicating the corresponding components.....	61
Figure 2.4: Schematic diagram of IR and Raman transition mechanisms, compared to Rayleigh (elastic) scattering and IR absorption.	69
Figure 2.5: (a) Integrating sphere device, with $BaSO_4$ support and sample prepared for the measurement and (b) geometry of the integrating sphere (from Shimadzu).	71
Figure 2.6: IUPAC classification of the adsorption/desorption isotherm for different materials.	76
Figure 2.7: (a) Section view and (b) schematic diagram of the electron optical component of a scanning electron microscope (SEM)	87
Figure 2.8: Examples of common organic dyes used in photodegradation evaluation tests	89
Figure 2.9: (a) picture of rhodamine solutions (10^{-3} M on the left and ca. $5 \cdot 10^{-5}$ M on the right) and (b) absorbance spectrum of rhodamine B in aqueous solution.	92
Figure 2.10: Picture of the degradation setup during operations using UVA light..	93
Figure 2.11: (a) schematic of the dead-end filtration system for membrane characterisation and fouling experiments.	96
Figure 3.1: Representative PXD patterns for the principal synthesis series as compared with crystalline anatase.....	109

Figure 3.2: Profile fitting of a sample from the <i>NE</i> series of FMH-TiO ₂ particles using the PM2K software	110
Figure 3.3: Example of log-normal distribution of the grain size diameter estimated using the WPPM method for FMH-TiO ₂ , <i>NE</i> sample (2 M HNO ₃ , 162 mM precursor concentration, 1 min MW treatment).	111
Figure 3.4: PXD patterns of TiO ₂ samples synthesised using different acids of the same concentration (nominally 1 M) in ethanol. Crystalline anatase is also shown as a reference. ...	112
Figure 3.5: PXD patterns as a function of the acid concentration (HCl) in <i>CE</i> series samples (164 mM precursor concentration; treatment time 1 min at 750W MW power).	113
Figure 3.6: PXD patterns of samples prepared using 2 M HCl solution (if not otherwise indicated) as a function of different synthesis conditions: (a) 1.5 M acid concentration, 164 mM TTIP, 90 s MW synthesis; (b) 60 s MW synthesis, 164 mM TTIP; (c) 30 s MW synthesis, 164 mM TTIP; (d) 60 s synthesis in H ₂ O, 82 mM TTIP; (e) 90 s synthesis, 164 mM TTIP; (f) 60 s synthesis, 82 mM TTIP. ...	114
Figure 3.7: SEM images of selected FMH-TiO ₂ samples (<i>NE</i> series) produced using different precursor and acidity concentrations. (a) 1M acid, 648 mM precursor; (b) 2 M acid, 648 mM precursor; (c) 2 M acid, 324 mM prec.; (d) 0.5 M acid, 324 mM prec.; (e) 2 M acid, 80 mM prec.; (f) 1 M acid, 80 mM prec.; (g) 1M acid, 40 mM prec; (h) 1 M acid, 20 mM prec.	115
Figure 3.8: (a),(b) SEM images and (c) particle size distribution of FMH TiO ₂ particles from the <i>CE</i> sample series (HCl as an acid mediator in ethanol solution). Each of the samples was produced using the same MW treatment time (1 min) at full power (700 W). Acid concentration and precursor concentration in volume are indicated in the graph respectively.	116
Figure 3.9: Particle size distribution of FMH-TiO ₂ particles, <i>NE</i> series produced using 2 M HNO ₃ solution and a precursor concentration of (a) 656 mM, (b) 328 mM, (c) 164 mM, (d) 82 mM, (e) 40 mM.	118
Figure 3.10: SEM size distribution of FMH-TiO ₂ particles, <i>NE</i> series produced using 1 M HNO ₃ solution and a precursor concentration of (a) 656 mM, (b) 328 mM, (c) 164 mM, (d) 82 mM, (e) 40 mM and (f) 20 mM.	119
Figure 3.11: SEM images of the FMH-TiO ₂ particles at high magnification. (a) The roughness of the particle surface is due to the gold sputtered for during the specimen preparation for the SEM analysis. (b) Polydisperse sample with fusing phenomena between sub-micron particles.	120
Figure 3.12: Examples of (a) the multimodal size distribution and (b) cracks present in the sub-micron spheres.	121
Figure 3.13: TEM analysis of TiO ₂ microspheres, <i>CE</i> sample series (synthesised using a solution of 1M HCl in absolute ethanol, 1 min MW treatment at full power-700W). (a) bright field and (b) dark field image of a cluster of particles, (c) magnified details of the crystalline grains that comprise the particle.	122
Figure 3.14: TEM analysis of TiO ₂ microspheres from the <i>NE</i> series (synthesised using a solution of 2 M HNO ₃ in absolute ethanol, 1 min MW treatment at full power-700W). (a) bright field and (b) dark field images; (c) high magnification of the detail of a particle edge and (d) a cluster of primary nanoparticles dissociated from the microsphere after calcination treatment (773 K, 3 h in air).	123
Figure 3.15: (a and b) Higher magnification (300k X) of the representative sample from the <i>NE</i> series (synthesised using a solution of 2 M HNO ₃ in absolute ethanol, 1 min MW treatment at full power-700W), with primary crystallites observable at the edges marked with red arrows.	123
Figure 3.16: TEM analysis of particles synthesised using a solution of HCl 37% v/v in absolute ethanol (2 M HCl, 1 min MW treatment at full power). (a) Bright field and (b) dark field images of a cluster of particles; (c) magnified details of the primary nano-crystals that constitute the secondary particles and (d) detail of the nano-sized acicular structures.	124

Figure 3.17: SAED analysis of the TiO ₂ particles synthesised using ethanol as solvent. (a) CE series (2 M HCl in ethanol); (b) CE series (1 M HCl in ethanol); (c) NE series (2 M HNO ₃ in ethanol). The rings are indexed and the crystalline phase is reported next to the sample label.....	125
Figure 3.18: Size distribution analysis for the spherical microspheres of the NE series as a function of acid concentration, with (a) average particle diameter and (b) width of the size distribution calculated from the SEM images.	126
Figure 3.19: Particle size distribution, calculated by SEM image analysis, of NE series particles (1 M HNO ₃ , 1 min MW treatment at full power) as a function of the precursor concentration.	127
Figure 3.20: (a) Average particle size and (b) size distribution FWHM for particles in the NE series as a function of the precursor concentration, when varying the acid concentration.	127
Figure 3.21: Nitrogen adsorption/desorption isotherms for as-synthesised materials. Following acids and solvents were used: (a) HCl (2 M) in ethanol (CE series); (b) HCl (2 M) in water (CW); (c) HNO ₃ in ethanol (NE); (d) HNO ₃ in water (NW)	128
Figure 3.22: N ₂ adsorption/desorption isotherms for some selected FMH-TiO ₂ sample synthesised using (a) 2 M and (b) 1 M HNO ₃ solution respectively	129
Figure 3.23: N ₂ adsorption/desorption isotherms for the NE series, at different HNO ₃ concentration.....	130
Figure 3.24: Pore size distribution of a representative sample of the NE series (2 M HNO ₃ , 162 mM, 1 min MW treatment) calculated by using (a) the adsorption isotherm and (b) the desorption or both isotherms, via BJH equation or DFT calculation.	131
Figure 3.25: Plot of surface area against particle diameter for rutile and anatase according to equation 3.10. The range of experimentally determined BET surface areas and sphere diameters (from SEM) are shown for comparison. Typical surface areas for anatase and Aeroxide P25 particles are indicated for reference.	133
Figure 3.26: Distribution of surface area values as a function of acid and precursor concentration (indicated in volume proportion).	134
Figure 3.27: Schematic showing the active vibrational modes in (a) the anatase and (b) rutile lattice.	136
Figure 3.28: (a) Curve fitting of E _{g,1} mode of a selected FMH-TiO ₂ sample (NE series, 1 M HNO ₃ , 162 mM precursor, 1 min MW treatment) using Gaussian and Lorentzian curves; (b) fitting of the same data using Pseudo-Voigt and split Pseudo-Voigt curves.	137
Figure 3.29: Raman spectra of (a) anatase, (b) Aeroxide P25 and (c) rutile (The spectra were collected, normalised and corrected with an appropriate scale factor).....	138
Figure 3.30: Detail of the E _{g,1} mode in the Raman spectra of NE particles (2 M HNO ₃ , 162 mM TTIP concentration, 1 min MW synthesis) compared to anatase. The Roman numerals indicate the order of sampling points on the specimen.	139
Figure 3.31: Raman spectra of the FMH-TiO ₂ particles, NE series, as a function of the precursor concentration. The spectra were normalised using the E _{g,1} mode peak intensity as the maximum value.	140
Figure 3.32: (a) Absorbance and (b) reflectance spectra for TiO ₂ rutile and anatase.....	141
Figure 3.33: Band gap calculation for TiO ₂ polymorphs; calculation of the Kubelka-Munk functions for (a) indirect and (b) direct band gap.	141

Figure 3.34: Reflectance spectra (obtained by DR-UV-Vis spectroscopy) of different FMH-TiO ₂ samples compared with reflectance of commercial anatase (dashed line). All samples were synthesised using 2 M of acid (HNO ₃ for NE, NW and HCl for CE, CW) and 162 mM of TTIP precursor.	143
Figure 3.35: (a) Indirect and (b) direct band gap calculation of the selected FMH-TiO ₂ samples using the Kubelka-Munk functions. The functions for anatase are represented with dashed lines.	143
Figure 3.36: Effect of the precursor concentration on the indirect optical band gap of the TiO ₂ particles in the NE series with varying acid concentration.	145
Figure 3.37: Effect of the acid concentration on the optical band gap for the NE series. The dotted lines indicate the precursor concentration in volume (1:10, 1:20 and 1:40 indicate 328 mM, 164 mM and 82 mM respectively).	146
Figure 3.38: (a) Urbach energy calculation for representative FMH-TiO ₂ samples for each type of synthesis.	147
Figure 3.39: Blue-shift and broadening of the E _{gl} peak in nanocrystalline TiO ₂ anatase, calculated according to the model proposed by Xue <i>et al.</i> and Zhu <i>et al.</i> , modifying the calculation using a different initial peak position (ω_0) and profile line (Γ_0), according to the variation of these values reported in literature.	149
Figure 3.40: Comparison of the different model for the evaluation of the quantum-size effect developing the Brus equation in function of (a) the reduced mass μ and (b) the dielectric constant of the material.	151
Figure 3.41: Raman spectra for the CW series of FMH-TiO ₂ particles (TTIP conc. 164 mM, HCl 2 M solution) as a function of the MW treatment time.	154
Figure 3.42: (a) Raman spectra, (b) SEM particle size distribution and (c) band gap analysis of samples prepared by pulsed MW synthesis using 1 min cycle (1, 2 and 5 cycles are shown respectively).	156
Figure 3.43: (a) N ₂ adsorption/desorption isotherms for the MW-pulsed FMH-TiO ₂ samples and (b) pore size distribution using BJH calculation for the adsorption and desorption branches of the isotherms.	157
Figure 3.44: Examples of particles and agglomerates from (a, b) the CW series (2 M HCl, 162 mM precursor, 90 s MW treatment) and (c, d) the NW series (1 M HNO ₃ , 162 mM precursor, 90 s MW treatment).	158
Figure 3.45: PXD patterns for samples produced with pure ethanol (NE series), pure water (NW series) and at various water:ethanol ratios: (a) pure ethanol; (b) 1:3; (c) 1:1; (d) pure water. .	159
Figure 3.46: SEM images of TiO ₂ particles synthesised using different hydrolysis ratios (the relative concentration of water in ethanol is indicated in the images: (a) 20%; (b) 40%; (c) 50%; (d) 60%; (e) 70%; (f) 80%).	160
Figure 3.47: (a) N ₂ adsorption-desorption isotherms and (b) BJH pore size distribution analysis for different samples of ethanol-water ratios in the HNO ₃ -mediated synthesis	160
Figure 3.48: XPS of the selected NE series sample (2 M HNO ₃ , 162 mM TTIP, 1 min MW treatment), showing the peak fitting for (a) the Ti _{2p} and (b) O _{1s} signals.	162
Figure 3.49: XPS peak fitting for the C 1s signals of (a) NE series FMH-TiO ₂ submicroparticles and (b) Aeroxide P25.	163
Figure 3.50: Thermogravimetric (TG) analysis of selected TiO ₂ samples produced under different synthetic conditions.	164

Figure 3.51: Differential thermal analysis (DTA) of a representative FMH-TiO ₂ sample (NE series, 2 M, 324 mM) using different heating ramps.	166
Figure 3.52: Evolved gas MS analysis of the signal presumably associated to N ₂ O (MW: 44) and NO (MW: 30) for the FMH-TiO ₂ sample (NE series, 2 M, 324 mM)	166
Figure 3.53: IR spectra of typical samples from each series. The spectra are displaced on the intensity scale for better visualisation. The IR vibrations typical of the hydroxyl groups are marked in blue, the spectral region in which the signals not related to TiO ₂ occur are marked in red... ..	168
Figure 3.54: IR spectra of MW-synthesised particles (1:20 TTIP, HNO ₃ 2 M, 1min) before and after thermal treatment under oxidizing atmosphere at different temperatures.	169
Figure 3.55: IR spectra of different FMH-TiO ₂ particles belonging to the NE, NW and BE series, (where BE uses titanium tetrabutoxide instead of TTIP), in the spectral region 1800-900 cm ⁻¹ . The most relevant IR modes are marked with dashed lines and labelled.	170
Figure 3.56: Raman spectra of some samples from the NE series in the lower frequency region in which N and C-based impurities generally occur.	172
Figure 3.57: (a) Kennedy-Rabenau pressure-temperature diagram for hydrothermal conditions ^[96] and (b) Rajamathi-Seshadri application of the Peng-Robertson equation for the estimation of the molar volume of toluene inside a pressurised vessel	174
Figure 3.58: Calculation of the molar volume for (a) water and (b) ethanol using the Peng-Robertson equation to give isobaric curves as a function of temperature.	175
Figure 3.59: (a) Pressure-temperature diagram at equilibrium conditions and (b) estimated volume expansion in a sealed vessel for different solvents.	176
Figure 3.60: (a) Temperature profiles and (b) maximum values for temperature and pressure as a function of MW power for deionised water (filling factor 30%) using the single-mode reactor... ..	177
Figure 3.61: Temperature profiles for MW heating of absolute ethanol (3 mL) at different applied MW power. Incomplete temperature profiles have been fit and extrapolated by using Gompertz sigmoidal functions.	178
Figure 3.62: Pressure profiles for MW heating of absolute ethanol (3 mL) at different applied MW power.	179
Figure 3.63: Schematic mechanism of acid-mediated synthesis of anatase or rutile in sol-gel and hydrothermal processes. Adapted from Li <i>et al.</i> ^[113]	182
Figure 3.64: Mechanism of formation of primary, secondary and tertiary particles in alcohol-mediated synthesis of TiO ₂ nanoparticles.....	186
Figure 3.65: Pseudo-Hoffmeister series for the tendency of acid anions to form anatase or rutile in acid-mediated sol-gel or hydrothermal syntheses.	188
Figure 3.66: Time-temperature-precipitation diagram for acid-mediated sol-gel synthesis of crystalline TiO ₂ in the presence of HNO ₃	189
Figure 3.67: N ₂ adsorption/desorption isotherms for the CE/CW series, with different concentrations of HCl.	190
Figure 4.1: Rietveld refinement against PXD data for Aeroxide P25: experimental pattern (red), calculated pattern (green) difference profile (purple) and tick marks for anatase (blue) and rutile (red) phases.....	208
Figure 4.2: (a) Absorbance spectra and (b) Kubelka-Munk function transformation for the optical indirect band gap for pure anatase, rutile, Aeroxide® P25 and Kronos7000.	210

Figure 4.3: Thermal evolution of the crystalline structure of the as-synthesised FMH-TiO ₂ particles (series NE, 2 M HNO ₃ concentration, 162 mM (1:20 in volume) precursor concentration, 1 min treatment at full MW power) under an oxidative atmosphere. The intensity values of the PXD patterns were all normalised to simplify the visual comparison.	213
Figure 4.4: Calculation of the average grain size of (a) representative FMH-TiO ₂ samples calcined at different temperatures (773, 823 and 873 K) and (b) calcined under constant flow of argon during <i>in situ</i> variable temperature measurement (heating ramp 5 K/min).	214
Figure 4.5: Calculation of phase fraction of rutile calculated by integrated intensity from the <i>in situ</i> temperature PXD measurement of different samples.	214
Figure 4.6: Differential thermal analysis (DTA) of commercial anatase, Aeroxide P25 and two representative FMH-TiO ₂ samples (NE series, 1 M and 2 M acid concentration, both synthesised using 162 mM of precursor concentration).	215
Figure 4.7: Kubelka-Munk functions for (a) direct and (b) indirect band gap calculations of the sample reported in Figure 4.3 as a function of the calcination temperature.	216
Figure 4.8: (a) Nitrogen adsorption/desorption isotherms and (b) BJH pore size distribution (calculated from the desorption isotherms) for a representative sample belonging to the NE series (2 M HNO ₃ in ethanol, 162 mM precursor concentration, 1 min MW treatment) before and after calcination (573 - 773 K).	218
Figure 4.9: PXD patterns for the study of the duration of the calcination for a representative sample of FMH-TiO ₂ microparticles. (a) untreated sample and calcined at 773 K for (b) 1h, (c) 2h and (d) 3h.	219
Figure 4.10: (a) Average crystallite size of the particles and (b) relative content of anatase as a function of the treatment time for Aeroxide P25 and FMH-TiO ₂ samples.	220
Figure 4.11: (a) N ₂ adsorption/desorption isotherms and (b) pore size distribution of FMH-TiO ₂ (3 M HNO ₃ , 162 mM TTIP, 1 min MW treatment) calcined at 773 K for 1, 2 and 3 hours respectively.	221
Figure 4.12: Kubelka-Munk functions for the determination of (a) the direct optical band gap and (b) Urbach localised states for the samples calcined in air at constant temperature for different time.	221
Figure 4.13: Comparison of PXD patterns of representative samples of FMH-TiO ₂ particles (2M HNO ₃ , 162 Mm TTIP, 1 min MW treatment, the same described in the previous section) calcined under different conditions (air, N ₂ or dynamic vacuum) at (a) 773 K and (b) 873 K.	223
Figure 4.14: Surface area values (a) and N ₂ adsorption-desorption isotherms (b) of the FMH-TiO ₂ particles in function of the temperature and the atmosphere of the annealing treatment	224
Figure 4.15: Effect of sintering under N ₂ on the optical properties of the FMH-TiO ₂ particles, through the observation of the Kubelka-Munk functions for (a) indirect band gap and (b) Urbach localised states.	224
Figure 4.16: PXD patterns of (a) commercial anatase, (b) Aeroxide P25, FMH-TiO ₂ particles (NE series, 2 M HNO ₃ , with (c) 648 mM and (d) 162 mM precursor (TTIP) concentration after ammonolysis (constant flow NH ₃ , 3 hrs, heating rate 10 K/min) at different temperature. (A indicates anatase, R rutile, N (bold) TiN and * the unidentified peaks).	228
Figure 4.17: Absorbance spectra of ammonolysed anatase at different temperatures.	229
Figure 4.18: Kubelka-Munk function transformations for the indirect band gap of (a) commercial anatase, (b) P25, NE series, 2 M HNO ₃ , with (c) 648 mM and (d) 162 mM precursor (TTIP) concentration, after ammonolysis at different temperatures.	230

Figure 4.19: PXD patterns of the P25 treated under ammonolysis at 873 K before and after the TG-DTA analysis (heating program: 1173 K under Ar, heating ramp 5 K/min).....	234
Figure 4.20: DTA profiles of ammonolysed P25 and FMH-TiO ₂ particles (NE series, 2 M, 648 mM, ammonolysed at 773 K for 3 hrs). the thermal program consisted of a 5 K/min heating ramp up to 1173 K under constant argon flow.	235
Figure 4.21: MS evolved gas analysis of the nitrogen doped samples (P25 treated under NH ₃ constant flux, 873 K for 3 hours and NE - 1M HNO ₃ , 648 mM TTIP ammonolysed at 773 K for 3 hours. (a) analysis of released N ₂ (MW:28) and (b) N ₂ O (MW:44).	235
Figure 4.22: (a) Absorbance spectra and (b) Kubelka-Munk functions for the calculation of the indirect band gap of ammonolysed samples before and after STA.	236
Figure 4.23: Examples of specimens of vacuum-activated FMH-TiO ₂ (series NE; 2 M HNO ₃ , 162 mM precursor concentration) after heating for 3 h under dynamic vacuum at (a) 373K, (b) 473 K, (c) 573 K, (d) 673 K and (e) 773 K or at 773 K for (f) 30 min and (g) 1 hr); (h) was produced under static vacuum conditions (static pressure around 2 kPa, 3hr thermal treatment at 773 K).....	238
Figure 4.24: PXD patterns of FMH-TiO ₂ particles (series NE, 2 M HNO ₃ , 162 mM precursor concentration) annealed under dynamic vacuum at different temperatures (R and A signifying rutile and anatase peaks respectively).	239
Figure 4.25: Raman bands of the FMH-TiO ₂ particles annealed under dynamic vacuum at different temperature and treatment duration. The individuation of the principal modes (relative to TiO ₂ anatase) are indicated.	239
Figure 4.26: IR spectra of NE (2 M, 162 mM) FMH-TiO ₂ particles calcined under dynamic vacuum at different temperatures.	241
Figure 4.27: (a) Diffuse reflectance spectra and (b) Kubelka-Munk plots for to the indirect band gap for the NE series (2 M HNO ₃ , 162 mM (1:20 volume) prec. conc.) after heating under static vacuum.	242
Figure 4.28: (a) DR-UV-Vis spectra and (b) Kubelka-Munk function for the indirect band gap for dynamic vacuum annealed FMH-TiO ₂ samples at different annealing temperatures and times (3 hrs when not indicated).	243
Figure 4.29: (a) Reflectance spectra and (b) Kubelka-Munk transformations for indirect band gap (b) for NE series (2M HNO ₃ , 1:5 precursor concentration) samples previously heated at 673 K under dynamic vacuum.	244
Figure 4.30: XPS spectra in the Ti 2 <i>p</i> and O 1 <i>s</i> regions respectively for (a,b) N-doped Aeroxide P25 (commercial TiO ₂ photocatalyst) and (c,d) the N-doped FMH-TiO ₂ particles (NE series, 2 M HNO ₃ , 162 mM precursor concentration, 1 min MW treatment).	246
Figure 4.31: XPS analysis of the Ti 2 <i>p</i> and O 1 <i>s</i> signals for vacuum annealed FMH-TiO ₂ (series NE, 2 M, 1:20 v/v precursor concentration, vacuum treatment 773 K, static conditions, 3 hrs).	247
Figure 4.32: XPS analysis of the Ti 2 <i>p</i> and O 1 <i>s</i> signals for FMH-TiO ₂ (series NE, 2 M, 1:20 v/v precursor concentration) annealed under Ar atmosphere (673 K, 3 hrs).	247
Figure 4.33: EPR spectra of (a) ammoniated P25 and (b) of ammoniated FHM-TiO ₂ compared to ammoniated P25.	248
Figure 4.34: EPR spectra of FMH-TiO ₂ particles calcined (a) under static vacuum and (b) under dynamic vacuum conditions. The EPR of (a) was collected at different temperatures indicated in the graph.	249
Figure 4.35: Colour of samples as commercial Ti ₂ O ₃ (Johnson-Matthey) is oxidised at different temperatures (3 hours thermal treatment, heating rate 10 K/min).....	250

Figure 4.36: Colours of the samples of commercial TiN (Aldrich, 99%) after heating in air at different temperatures (3 hours thermal treatment, heating rate 10 K/min).....	251
Figure 4.37: Absorbance spectra of (a) TiN and (b) Ti ₂ O ₃ after progressive oxidation at different temperature.	251
Figure 4.38: (a) Absorbance spectra and (b) Kubelka-Munk transformation for the indirect band gap for the hydrogenated FMH-TiO ₂ particles	253
Figure 4.39: (a) PXD patterns and (b) Kubelka-Munk function for indirect band gap (b) of commercial anatase heated in a MW cavity for 0.5 - 4 min. “A” denotes anatase peaks, “R” denotes rutile peaks.	254
Figure 4.40: Results of the degradation experiment for different concentration of Aeroxide P25 (a) under UVA and (b) under visible light irradiation; comparison between degradation experiment of the reference materials (commercial anatase, P25 and Kronos7000, 1 g/L in Rhodamine solution) performed (c) under UVA and (d) under visible light irradiation.	256
Figure 4.41: (a) degradation curve and (b) apparent degradation rate for selected FMH-TiO ₂ particles under visible light (P25 is included as a comparison).....	258
Figure 4.42: Rhodamine UV-Vis spectra using (a) P25 and (b) FMH-TiO ₂ as a catalyst for its degradation under visible light. The dashed trend line indicates the maximum value for each spectrum.	259
Figure 4.43: Image of the rhodamine solution collected after degradation under visible light in presence of FMH-TiO ₂ particles ((a) NE, 0.5 M, 162 mM and (b) NE, 1 M, 40 mM)	259
Figure 4.44: Degradation curves for the 5 degrees of N-ethylation of the Rhodamine molecule (RhB contains 4, Rh110 none) for (a) P25 and (b) FMH-TiO ₂ particles (b) under visible light irradiation.....	260
Figure 4.45: Degradation curves for selected FMH-TiO ₂ samples calcined in air (synthesis conditions and calcination temperature are reported in Table 4.20, all samples treated for 3 hrs using a heating ramp of 10 K/min), under (a) UVA and (b) visible light	261
Figure 4.46: Degradation curves of P25 and Kronos ammonolysed at 773 K (N773), mixed in solution with RhB (dye concentration 1.5 10 ⁻⁵ mol/L, catalyst concentration 500 mg/L) under (a) UVA and (b) visible light.	264
Figure 4.47: Comparison of degradation curves for rhodamine B using P25 and vacuum annealed FMH-TiO ₂ samples under (a) UVA light and (b) visible light..	265
Figure 4.48: Comparison between the XPS analysis of the N 1s signal performed (a) on the N-doped P25 and (b) the data reported by Irie <i>et al.</i>	273
Figure 4.49: Proposed mechanism of degradation of rhodamine B	276
Figure 4.50: (a) Initial adsorption and (b) degradation rate under visible light after 1 hour for some of the untreated FMH-TiO ₂ samples	278
Figure 5.1: SPR sensogram for the minimum resonance angle of a (PDDA/PSS) multilayer, deposited on gold coated surface exposing it to the polyelectrolyte solutions (both 10 mM concentration and pH 10) for 5 min using a flow rate of 20 μL/min. Rinsing step <i>ca.</i> 5 min at 50 μL/min flow rate.....	295
Figure 5.2: Adsorption profiles of the different layers of (a) PDDA and (b) PSS in the PDDA/PSS multilayer reported on the same scale.	296
Figure 5.3: SPR Kinetic mode measurement of the <i>in-situ</i> deposition of PAH/PAA multilayer at pH 3 and PAH/PSS at pH 9 (excitation laser wavelength 670 nm, deposition time 10 minutes, flow rate 10 μL/min, rinsing time 5 minutes at 50 μL/min, deposition on Au coated chip).....	296

Figure 5.4: SPR curves (resonance angle) for deposition of PDDA-PSS multilayer (10 mM concentration, pH 10) at different ionic strength (adjusted with NaCl); flow rate 20 $\mu\text{L}/\text{min}$, rinsing time 5 minutes at 50 $\mu\text{L}/\text{min}$, deposition on Au coated chip.	298
Figure 5.5: SPR curves (resonance angle) for deposition of PDDA-PSS multilayer (10 mM concentration, pH 10, $I_s = 100 \text{ mM NaCl}$) using deionised water at neutral pH and pH 10 (adjusted with 1 M NaOH solution). Flow rate 20 $\mu\text{L}/\text{min}$, rinsing time 5 minutes at 50 $\mu\text{L}/\text{min}$, deposition on Au coated chip).	298
Figure 5.6: SPR curves (resonance angle) for the deposition of a PDDA/PSS multilayer (10 mM concentration, pH 10, $I_s = 100 \text{ mM NaCl}$) using different injection times. Flow rate 20 $\mu\text{L}/\text{min}$, rinsing time 5 minutes at 50 $\mu\text{L}/\text{min}$, deposition on Au coated chip.	299
Figure 5.7: (a) maximum intensity during deposition step and (b) shift values observed during the rinsing step approximately 1 min before the deposition of the following layer as a function of the number of layers, calculated from the SPR curve in Figure 5.6.	300
Figure 5.8: (a) UV-Vis transmittance measurements on PEM-coated microscope glass slides. Different PEMs were used: (a) uncoated slide; (b) (PAH-PAA) ₅ , 5 min/ly; (c) (PAH-PAA) ₅ , 10 min/ly; (d) (PAH-PAA) ₅ , 10 min/ly; (e) (PAH-PAA)(CHI-PAA) ₃ (PAH-PAA), 10 min/ly.	302
Figure 5.9: Contact angle measurement on microscope glass slide coated using different PEM under different deposition conditions (time of immersion, outermost layer). Statistical analysis is reported in Table A.18 in the Appendix.	303
Figure 5.10: Zeta potential measurement for anatase, P25 and Kronos (100 mg/L suspension) at different pH values. For each pH value, the measurement was repeated 4 times.	305
Figure 5.11: (a) DLS Z-average particle diameter and (b) zeta potential measurement of TiO ₂ P25 nanoparticles suspension (100 mg/L) in presence of different concentration of NaCl.	305
Figure 5.12: Schematic of the composite TiO ₂ -PEM multilayer assembly: (a) deposition of the polyelectrolytes on the substrate with priming function; (b) exposure of the substrate in a colloidal suspension of negatively charged TiO ₂ particles; (c) exposure of the coated surface to other polyelectrolyte solution and TiO ₂ particle suspension.	307
Figure 5.13: Deposition of TiO ₂ -composite PEM on Mylar sheets; (a) (PDDA-PSS) ₃ (PDDA-TiO ₂) ₃ , with TiO ₂ exposed, (b) (PDDA-PSS) ₃ (PDDA-TiO ₂) _{3.5} , with PDDA exposed, all layer deposited with an immersion time of 10 min. (c) (PDDA-PSS) ₃ (PDDA-TiO ₂) ₃ and (d) (PDDA-PSS) ₃ (PDDA-TiO ₂) _{3.5} , with immersion time of 10 min for the polyelectrolytes and 20 min for TiO ₂	308
Figure 5.14: SPR resonance angle curves for (PDDA-PSS) multilayer integrated with TiO ₂ suspensions at different concentration as anionic layer (ionic strength 0, pH 10.5)	310
Figure 5.15: SPR resonance angle curves of a (PDDA-PSS) multilayer compared to the same structure integrated with TiO ₂ particles (P25, 150 mg/L, pH 10.5).	311
Figure 5.16: Transmittance spectra of glass slides coated with TiO ₂ composite (PAH-PAA) multilayers, with different combination of TiO ₂ and polyelectrolyte layers or different deposition time (10 min when not indicated).	312
Figure 5.17: Contact angle measurement on glass slide coated with different configuration of TiO ₂ integrated composite multilayer (PDDA-PSS).	313
Figure 5.18: Contact angle of glass slides modified with (a) different concentration of TiO ₂ nanoparticle suspension integrated in a (PAH/PAA) _n multilayer and (b) different combinations of PEI on a TiO ₂ modified (PDDA-PSS) _n multilayer.	314
Figure 5.19: Zeta potential of the TiO ₂ suspension (100 mg/L) with addition of (a) polycations and (b) polyanions.	316
Figure 5.20: Hydrodynamic diameter of TiO ₂ particles functionalised with using different concentrations of polyelectrolytes.	316

Figure 5.21: AFM image of the SM-UF membrane; top view of (a) 2 μm^2 section and a (b) 5 μm^2 section of the membrane surface, with relative chromatic scale bar for the profile depth.	319
Figure 5.22: AFM images of portion of modified SM-UF membranes using different PEM systems under different conditions; (a) (PDDA-PSS) _{3.5} , 5 min deposition; (b) (PDDA-PSS) _{3.5} , 10 min deposition; (c) (PDDA-PSS) _{3.5} , 5 min deposition, 150 mM NaCl; (d) (PDDA-PSS) _{3.5} , 5 min deposition, 500 mM NaCl; (e) (PAH-PAA) _{4.5} , 5 min deposition (f) (PAH-PSS) _{4.5} , 5 min deposition.	320
Figure 5.23: Water uptake measurement for the original untreated commercial membranes ..	322
Figure 5.24: N ₂ isotherm adsorption-desorption curves for UF membranes, with active layer made of (a) PAN and (b) PES. The rejection capacity of the membranes is indicated in the legend. ..	324
Figure 5.25: (a) N ₂ isotherm adsorption-desorption curves for PEM-coated UF membranes and (b) pore size distribution of the commercial UF membranes.....	325
Figure 5.26: (a) FT-IR and (b) Raman spectra for the commercial UF membranes.	326
Figure 5.27: UV-Vis Absorbance spectra for the commercial membranes compared with the textile support.....	328
Figure 5.28: (a) UV-Vis absorption spectra of UF-SM membranes coated with different number of (PDDA-PSS) layers and (b) the same spectra normalised for the value of maximum intensity. The outermost polyelectrolyte and the number of layers are indicated in the legend.	329
Figure 5.29: Wide angle XRD pattern for different UF membrane compared with their bare support and after modification with PEM coating.	330
Figure 5.30: Contact angle variation on SM-UF membrane active surface after deposition of different polyelectrolyte multilayer systems: (a) (PDDA-PSS) _n ; (b) (PAH-PSS) _n ; (c) (PAH-PAA) _n ..	332
Figure 5.31: Contact angle of (PDDA-PSS) _{3.5} multilayer on different surfaces.	332
Figure 5.32: (a) effect of the PEI primer layer on the contact angle of different multilayers on SM-UF membranes; sessile drop images of (b) (PAH-PSS) _{4.5} , (c) (PEI-PSS)(PAH-PSS) _{3.5} , (d) (PAH-PAA) _{4.5} , (e) (PEI-PAA)(PAH-PAA) _{3.5} multilayers.	333
Figure 5.33: Permeability curve for an SM-UF PES membrane. The membrane was not previously compacted.	334
Figure 5.34: Effect of different rinsing conditions or presence of support on PEM-modified SM-UF membrane ((PDDA-PSS) _{2.5} , 2 min deposition).	336
Figure 5.35: Permeation curve for the PES UF-membranes modified with PEM-coating under the same deposition conditions (2 min immersion, 5.5 bilayers): (a) unmodified PES; (b) (PDDA-PSS) _{5.5} modified PES; (c) (PEI-PSS)(PDDA-PSS) _{4.5} modified PES.	338
Figure 5.36: SEM images of TiO ₂ -PEM composite multilayer on SM membranes, prepared by immersion coating deposition. The composite multilayer consists of (PDDA-PSS)(PDDA-TiO ₂) _{3.5} , prepared using different concentration of TiO ₂ in suspension: (a) and (d) were prepared using a 250 mg/L suspension, (b) and (e) 500 mg/L and (c) and (f) 1 g/L.	341
Figure 5.37: Effect of the insertion of TiO ₂ nanoparticles in (PDDA-PSS) multilayer deposited on SM-UF membranes on (a) water uptake and (b) contact angle measurement.	342
Figure 5.38: (a) contact angle of the TiO ₂ -PEM composite multilayer ((PDDA-PSS)(PDDA-TiO ₂) _{3.5}) on SM membranes with different concentration of TiO ₂ and (b) dispersion of the contact angle values.	343
Figure 5.39: (a) contact angle values of (PAH-PSS) ₂ (PAH-TiO ₂) _{3.5} multilayer with the surface immersed in TiO ₂ suspension for 5, 10 and 20 min as shown in (b), (c) and (d) respectively, with increase of the hydrophilic behaviour..	344
Figure 5.40: SEM images of TiO ₂ -PEM composite coating on Mylar foil.....	346

- Figure 5.41:** Pictures of Mylar samples coated with nanocomposite TiO₂-PEMs ((PDDA-PSS)₂(PDDA-TiO₂)_{3.5}) under different conditions; (a) 5 min immersion for the polyelectrolytes, 10 min for TiO₂; (b) 10 min immersion for all layers; (c) 5 min immersion for the polyelectrolytes, 20 min for TiO₂; (d) 5 min immersion, application of a protective (PDDA-PSS) layer at the end of the deposition process. 347
- Figure 5.42:** Contact angle for different sample of TiO₂-composite PEM coating on Mylar foils. The characteristics and the preparation conditions of the coating are listed in Table 5.11.. 349
- Figure 5.43:** SEM images of SM membrane coated with a TiO₂-PEM composite multilayer by using the improved deposition method. 349
- Figure 5.44:** Permeability curves of SM-UF membranes coated with two different system of multilayers using the “oscillating box” method. The curves are compared with similar system with presence of an alternate layer of TiO₂ replacing the polyanion in the multilayer coating. 350
- Figure 5.45:** Fouling test using alginate solution (20 mg/L, 20 mM NaCl, pH 7.5) on PES UF membrane (SM-01) using the dead-end filtration cell..... 352
- Figure 5.46:** Fouling experiment of SM-UF membrane, performed at 1 bar (0.1 MPa) using a 50 mM alginate solution with 20 mM NaCl. (a) equilibration with salt solution only; (b) fouling with alginate; (c) pure water filtration after membrane physical cleaning. 353
- Figure 5.47:** Fouling experiments on different UF membranes coated with a (PDDA-PSS) multilayer. Specifically, SM-UF membrane with (a) no coating. (b) (PDDA-PSS)_{3.5}, 2 min/ly, (c) (PDDA-PSS)_{2.5}, 10 min/ly, (d) (PDDA-PSS)_{5.5}, 2 min/ly, rinsed with deionise water at pH 10, (e) (PDDA-PSS)_{5.5}, 5 min/ly. 355
- Figure 5.48:** Fouling experiments on different UF membranes coated with a (PDDA-PSS) multilayer using the improved procedure. Specifically, SM-UF membrane with (a) (PAH-PSS)_{5.5}, 5 min/ly (b) (PAH-PSS)₂(PAH-TiO₂)_{3.5}, 5 min/ly, (c) (PDDA-PSS)₂(PDDA-TiO₂)₂(PDDA-PSS)_{1.5}, 5 min/ly, (d) (PDDA-PSS)₂(PDDA-TiO₂)_{3.5}, 5 min/ly, polyelectrolyte solution with 500 mM NaCl.. 357
- Figure 5.49:** Schematic of (a) the effect of pH on polymer conformation of PAA (up) and PAH (down) and (b) schematic representation of the internal structure of (PAH/PAA)_n multilayer assembled at different pH conditions. 359
- Figure 5.50:** (a) image of the experimental setup (realized on August 2014 at Johns Hopkins University, Dept. of Geography)(b) schematic diagram of the system..... 366
- Figure A.1:** PXD pattern of LaB₆ (Aldrich, 99%) using different instrumental conditions, specifically the step size (“s”) and the divergence slit (“d”), both in angular values. 384
- Figure A.2:** (a) Particle size counting method by using the ImageJ software and (b) comparison between particle diameter distribution using the approximating the particle to perfect spheres compared with the Feret’s diameter..... 384
- Figure A.3:** Particle size distribution of FMH-TiO₂ particles, NE series produced using 0.5 M HNO₃ solution and a precursor concentration of (a) 328 mM, (b) 164 mM and (c) 80 mM. 385
- Figure A.4:** SEM images of particles from the CW series (2 M HCl in water, 162 mM precursor concentration, 90 s MW treatment) at different magnification: (a) 50k X; (b) 100k X and (c) 300k X. 386
- Figure A.5:** Example of Raman spectra baseline subtraction using the 8-degree polynomial fit. (sample from the NE series, 1 M HNO₃, 162 mM precursor, 1 min MW treatment)..... 387
- Figure A.6:** Example of Raman spectra normalisation procedure. The sample (NE series, 1 M HNO₃, 162 mM precursor, 1 min MW treatment) was collected using different acquisition time (A: 5 s; B: 10 s). (a) represents the spectra as they were collected; in (b) the spectra are normalised without baseline subtraction; in (c) baseline subtraction is applied to the two spectra and finally in (d) the spectra of (c) are normalised for the maximum of the most intense peak (E_{g,1} mode). 387

Figure A.7: Comparison among the different values reported for the surface area and the pore volume of Aeroxide® P25, with the estimated average pore size reported in brackets (when reported)	388
Figure A.8: Classification of the hysteresis loop in mesoporous material, in which capillary condensation occurs, according to Thommes <i>et al.</i> □	390
Figure A.9: PXD patterns for the CW series of FMH-TiO ₂ particles (TTIP conc. 164 mM, HCl 2 M solution) as a function of the MW treatment time: (a) 30 s; (b) 60 s; (c) 90 s; (d) 120 s; (e) 150 s.	390
Figure A.10: (a) reflectance spectra and (b) Kubelka-Munk function for the calculation of the indirect band gap of FMH-TiO ₂ particles (CE series, 2 M HCl in ethanol, 164 mM TTIP concentration) for different MW treatment time, compared with reflectance and Kubelka-Munk functions of bulk anatase and rutile. The calculated value of band gaps are reported in Table 3.8.....	391
Figure A.11: Absolute values (in pressure) of the different signal detected during the MS analysis of the evolved gas by heating the FMH-TiO ₂ particles	392
Figure A.12: Evolved gas MS for the signal relative to (a) N ₂ and N and (b) to molecular O ₂ and atomic O for the selected FMH-TiO ₂ sample (NE series, 2 M, 324 mM).	392
Figure A.13: Differential DTA of the sample NE series, 2 M, 324 mM (shown in Figure 3.51) with the peak (a) relative to the release of gaseous impurities and the peak (b) probably indicating the phase transition.	393
Figure A.14: Detail of (a) peak (a) and (b) peak (b) reported in Figure A.13	393
Figure A.15: SEM images of the products of the flash MW-assisted reactions performed using 50 mM (a) and 200 mM (b) of HCl in ethanol (164 mM precursor concentration, 90 s MW treatment at full power)	393
Figure A.16: Comparison between different DFT model with the BJH calculation (considering both the adsorption and the desorption branches of the isotherm)	394
Figure A.17: Complete XPS spectrum for the untreated FMH-TiO ₂ particles (series NE, precursor concentration 1:20, 2 M HNO ₃ , 1 min MW treatment at full power) with all the signals relative to Ti, O, C and N.	396
Figure A.18: Temperature-Pressure profile for water at low MW power, measured using a single-mode MW cavity (CEM Discovery®).....	398
Figure A.19: PXD patterns of commercial anatase (Aldrich), Aeroxide® P25 and Krono7000. The patterns were normalised in intensity.	398
Figure A.20: SEM images of Kronos (Kronoclean 7000) sample.	399
Figure A.21: In situ variable temperature measurement of the sample CE (1 M, 162 mM prec. concentration). PXD pattern collected at (a) 573 K, (b) 673 K, (c) 773 K, (d) 873 K and (e) 973 K.	399
Figure A.22: In situ variable temperature measurement of the sample CE (2 M, 162 mM prec. concentration). PXD pattern collected at (a) 573 K, (b) 623 K, (c) 673 K, (d) 723 K and (e) 773 K.	400
Figure A.23: Band gap calculation (indirect Kubelka-Munk function transformation) in case of non-zero absorption at wavelength higher than the optical band gap, due to reduction treatments (ammonolysis, vacuum heating, etc.).	401
Figure A.24: TG of ammonolysed samples after STA.	401

Figure A.25: PXD pattern of the selected ammonolysed FMH-TiO ₂ sample (NE, 2 M, 648 mM) before and after the STA analysis.....	402
Figure A.26: PXD patterns of representative FMH-TiO ₂ samples heated under static and dynamic vacuum (treatment temperature 773 K when not indicated)	403
Figure A.27: PXD patterns of a representative FMH-TiO ₂ sample (NE series, 2 M HNO ₃ , 648 mM precursor concentration, 1 min MW treatment) annealed under static vacuum at 673 K for different times: (a) 3 hrs, (b) 5 hrs, (c) 7 hrs, (d) 9 hrs. (e) PXD of the sample annealed under vacuum for 7 hrs and successively calcined in air for additional 3 hrs at 673 K.	403
Figure A.28: (a) EPR spectra of FMH-TiO ₂ sample calcined under argon constant flow at 673 K and (b) comparison of the EPR signal of all the selected samples.	404
Figure A.29: PXD pattern relative to the thermal oxidation under air of Ti ₂ O ₃ in function of the temperature (thermal treatment performed for 3 hrs, heating rate 10 K/min)	405
Figure A.30: PXD pattern relative to the thermal oxidation under air of TiN in function of the temperature (thermal treatment performed for 3 hrs, heating rate 10 K/min)	405
Figure A.31: Comparison of the photoactivity of MW heated anatase with untreated anatase under (a) UVA and (b) visible light irradiation.....	406
Figure A.32: DR-UV-Vis transmittance of microscope glass slides coated using different combination of (a) (PAH-PAA) and (b) (PDDA-PSS) multilayers.	407
Figure A.33: Example of texture calculated from AFM images from selected PEM-modified UF membranes, measured using Gwyddion software. (a) untreated SM membrane; (b) (PDDA-PSS) _{5,5} ; (c) (PDDA-PSS) _{3,5} ; (d) (PDDA-PSS) _{3,5} (immersion time 10 min/ly); (e) (PDDA-PSS) _{3,5} (Ionic strength 100 mM); (f) (PDDA-PSS) _{3,5} (Ionic strength 500 mM); (g) (PAH-PSS) _{4,5} ; (h) (PAH-PAA) _{4,5}	409
Figure A.34: Statistical analysis for the roughness calculated by AFM measurement on UF membranes. The full data are reported in Table 5.4. (a) R _a values, indicating the average roughness and (b) R _q values, indicating the root-mean squared roughness of the surface.	410
Figure A.35: Water uptake values for UF-SM membranes coated with different PEMs.	411
Figure A.36: Statistical analysis for the water uptake measurement on SM membrane coated with different number of layers of a (PAH-PAA) coating, reported in Figure A.35.	411
Figure A.37: N ₂ adsorption-desorption isotherms for nanofiltration (NF) membranes and textile support of the commercial UF membranes analysed in chapter 5.	412
Figure A.38: Statistical analysis of the effect of different multilayers on contact angle measurement on SM membrane surface reported in Figure 5.30.	413
Figure A.39: Statistical analysis of contact angle measurements on (PDDA-PSS) multilayers on different surfaces (Mylar sheet, PAN and PES membranes) showed in Figure 5.31. The numbers in the graph indicate 1: Mylar foil; 2: PAN membrane and 3: PES membrane.	414
Figure A.40: Statistical analysis on the effect of different multilayers on contact angle measurements on SM membranes (Table 5.7).	414
Figure A.41: Statistical analysis of (a) contact angle and (b) water uptake measurements on the SM-B membrane series, (PDDA-PSS) _n multilayer on SM-UF membranes, varying the ionic strength of the polyelectrolyte solution and the rinsing method (Table 5.8).	415
Figure A.42: Statistical analysis for the water uptake measurements on the SM membranes coated with a composite (PDDA/PSS) multilayer with integration of TiO ₂ (Aeroxide P25, 1 g/L), reported in Table 5.9..	416

Figure A.43: Statistical analysis of the contact angle measurement results reported in Table 5.10. The letters in the graph indicate *A*: (PDDA-PSS)_{2.5}, 2 min immersion; *B*: (PDDA-PSS)_{5.5}, 1 min immersion; *C*: (PDDA-PSS)_{5.5}, 5 min immersion; *D*: (PDDA-PSS)_{5.5}, 2 min immersion; *E*: (PDDA-PSS)_{2.5}, 1 min immersion; *F*: (PAH-PSS)_{5.5}, 5 min immersion.416

Figure A.44: Statistical analysis of the contact angle measurements reported in Table 5.12. The letters in the graph indicate *A*: (PDDA-PSS)₂(PDDA-TiO₂)₂(PDDA-PSS)_{1.5}; *B*: (PDDA-PSS)₂(PDDA-TiO₂)_{3.5} with TiO₂ concentration of 1 g/L; *C*: same as *B* using TiO₂ concentration of 500 mg/L; *D*: same as *B* using an ionic strength of 100 mM (NaCl) for the deposition process; *E*: (PEI-TiO₂)_{5.5}; *F*: (PAH-PSS)₂(PAH-TiO₂)_{3.5}.417

Acknowledgement

I would like to thank my supervisors, Professor William Sloan, for all the assistance and support provided, and Professor Duncan H. Gregory, for offering me the possibility to work in his group, having the opportunity to improve my knowledge and my skills and most of all for all the professional and personal support received in these years.

I would also like to thank my previous supervisor, Dr. Xue Jin, for having offered me the possibility of this PhD and the precious opportunity to visit Johns Hopkins University. I would like to acknowledge Dr. Kai Loon Chen from this last institution for the opportunity of working with his group, a learning experience from the scientific, cultural and personal point of view. At Johns Hopkins I had the occasion to meet brilliant academics and students, in particular Mike, Dano, Li, Xitong and Steven among the others.

I would like to acknowledge my collaborators, thanks to which some part of this thesis would have never been completed. Thanks to Dr. Christoph Busche for the EPR analysis, to Dr. Emina Hadzifejzovic (University of Oxford) for the XPS analysis, Dr. Susan Gannon for the assistance with the SPR and to Fengyuan Liu, William Taube and Dr. Carlos Garcia Nunez for the access to the James Watt Nanofabrication Centre facilities, in particular for the AFM measurements.

A special thank goes to Dr. Sina Saremi, who guided me at the very beginning of my project and prepared me how to manage every kind of issue in a chemistry laboratory: your dedication to work and your knowledge have been a source of inspiration. I would also like to thank Dr. Michele Cariello for all the help, support and friendship given during all these years. I could not be more blessed to have people like you and Stefania as friend. Thanks to my family, especially my mother, who “bothered” and supported me with her company thorough all these years. Her resilience always gave me strength to overcome all the worst. Thanks also to my father and my brother Andrea, far from here but close with their feelings.

A huge thanks to my colleagues, starting Simon and Mimmo, both much more than simple colleagues, always there when I needed the most. Thanks also to all the other past and present “inhabitants” of the C3-13, Irene, Giulia, Sebastian, Iwona, Tina, James, Guang, Hallam, Eleni, Mark, Tom, Dr. Xiao, the silent company of Jay, the noisy presence of Joachim, the temporary but nonetheless cheerful presence of Brenna, Nikos, Yengling and Sofia and the new arrivals Jan, Zhen and Manmeet. I will never forget unforgettable moments like the (in)famous Christmas dinner and having added a tiny bit of something to this life experience, making more enjoyable spending time in the lab. Laura, you need a special mention for sharing probably the stressful period of our life, between overnight experiment and writing up.

Thanks to all my official and “unofficial” students; I hope to have passed you something more than simple knowledge (or angry Italian swearing). You made me angry, you almost made me crazy, we spent amazing and awful time, nights out and nights awake. Thanks Connor, Haroon, Paul, Shanlong (you are just great!), Yu (a sort of younger brother) and Ayesha (good luck for everything!).

My sincere gratitude goes also to the people from Engineering. I have always been a sort of alien over there, but for the relative little time I have spent with them I had occasion to meet other brilliant researchers and, first of all, people. Thanks to Mathieu, Keira, Steph, Aoife, Yiannis, Eri, Jill, Alex, Kevin, Giulia and Simon. A very special thank goes to the two person I probably bother the most during this years: Anne McGarrity and Julie Russell, who both tried to contain my invasion of mess around the lab.

In rapid succession, I would like to thank all the other amazing people I have met in these years, starting from the people in Chemistry, especially Sarah, Jake, Francois, Isa, Alex, MJ, Moya, Mike, Tom, Giacomo, Roberta, Albane, Jessica, Laura and Kiko, Kike, Alexandra, Angelos, Carolina, Anamari and all the others; the "coffee group" of the lab next door, especially Stephan, John, Liam, Cosma, Alan and Nor; the friends from Strathclyde, Ines, Nuno, Ivan, Paula, Ana, Andreia, Miguel, Florimond and Thomas (I hope for all of you the best of luck for your future and your career); my flatmates here and in US, Sean, Nate, Miles, Arthur and Jakob. The technical staff: Stuart Mackay, Arlene Sloan, Andy Monaghan, Jim Gallagher, Dr. Claire Wilson, Michael Beglan, Jim Mclwer, Tim Motngomery. Elaine McNamara and Heather Lambie for all the help with the administrative organisation. Karen Mclachlan and her smile, the janitors Jim and Gordon, Ted, Bruce and Paul from the store. It has been a pleasure to break the daily routine with a brief chat with all of you. A lot of other people and entities are worth of a mention, from the random people leaving food on the office table during the writing up, the night security, the staff from Tesco in Byres Road, several brands of coffee and energy drinks, but this thesis is already long enough.

It has been a literally a war, a daily-based struggle. I came here with a totally different mindset and for totally different reasons; I grew up, evolved, aged and suffered. It doesn't matter where we were, but where we are and where (and mostly how) we are going. A cycle is ending, waiting for a new beginning.

Conference Contributions and Presentations

- **34th RSC Solid State Group Christmas Meeting,**
Glasgow (18-19 December 2014)
“Microwave-assisted hydrothermal synthesis of TiO₂ particles for environmental processes” (poster contribution)
- **6th EuChemS,**
Seville (Spain) (11-15 September 2016)
“Nano-composite coating for water purification” (poster contribution)
- **36th RSC Solid State Group Christmas Meeting,**
Loughborough (20-21 December 2016)
“Microwave-assisted synthesis of nanostructured TiO₂ for photocatalytic water treatment” (poster contribution)

Several oral presentations in research group meetings (Inorganic Solid State Chemistry and Water & Environmental Engineering) and section meetings (Inorganic and Nanomaterial Chemistry section, School of Chemistry)

Publications

M.D. Cappelluti, E. Hadzifejzovic, X. Jin, D.H. Gregory, *Flash microwave hydrothermal (FMH) synthesis of nanostructured sub-micrometric TiO₂ particles for environmental applications* (in preparation).

M.D. Cappelluti, E. Hadzifejzovic, C. Busche, X. Jin, D.H. Gregory, *Simple Vacuum Activation of mesoporous TiO₂ microparticles for visible light photocatalysis* (in preparation).

M.D. Cappelluti, S. Gannon, D.H. Gregory, *In-situ SPR analysis of TiO₂-polyelectrolyte multilayer composite coatings for ultrafiltration applications* (in preparation).

Declaration

The work presented in this thesis is the original work of the author except where specific reference is made to other sources. It has not been submitted, in whole or in part, for any other degree at this or any other institution.

Mauro Davide Cappelluti

January 2018

List of Abbreviations used in Chapter 1

ATP: Adenosine Triphosphate

AOC: Assimilable Organic Carbon

AOP: Advanced Oxidation Process

BOD: Biochemical Oxygen Demand

COD: Chemical Oxygen Demand

DIPS: Diffusion Induced Phase Separation

DMO: Domestic Microwave Oven

DNA: Deoxyribonucleic Acid

DSSC: Dye-Sensitised Solar Cell

DSSP: Decomposition of Single-Source Precursor (*Hydrothermal classification*)

ED: Electrodialysis

EPS: Extracellular Polymeric Substance

ESA: Electrostatic Self-Assembly

FRO: Forward Reverse Osmosis

IEM: Ion-Exchange Membrane

HA: Hyaluronic Acid

IPS: Induced Phase Separation

ISAM: Ionic Self-Assembly Monolayer

ISRS: Indirect-Supply Reaction Source (*Hydrothermal classification*)

LbL: Layer-by-Layer

LSPR: Localised Surface Plasmon Resonance

MF: Microfiltration

MW: Microwaves

MWCO: Molecular Weight Cut-Off

NF: Nanofiltration

NHE: Normal Hydrogen Electrode

NOM: Natural Organic Matter

NP: Nanoparticle

PAA: Poly(acrylic acid)

PAN: Polyacrylonitrile

PAH: Poly(allylamine hydrochloride)

PDDA: Poly(diallyldimethylammonium chloride)

PE: Polyelectrolyte
PEEK: Poly(etheretherketone)
PEG: Polyethylene glycol
PEI: Polyethyleneimine
PEM: Polyelectrolyte Multilayer
PES: Poly(ethersulfone)
PS: Polysulfone
PSS: Poly(sodium 4-styrenesulfonate)
PTFE: Polytetrafluoroethylene
PV: Pervaporation
RBM: Reshaping Bulk Materials (*Hydrothermal classification*)
RMP: Recrystallisation of Metastable Precursors (*Hydrothermal classification*)
RO: Reverse Osmosis
SA: Sodium Alginate
SRNF: Solvent Resistant Nanofiltration
TMP: Transmembrane Pressure
UF: Ultrafiltration
US: Ultrasound
UV: Ultraviolet (radiation)
UVA: Ultraviolet A (radiation)
WHO: World Health Organisation

Chapter 1

Photoactive nanoparticles and multifunctional coatings in membrane filtration processes

1.1 Introduction

Environmental pollution is one of the most prominent problem of this century, unequivocally related to other important issues such as scarcity and exhaustion of natural resources and an increasing global consumption of energy. This last factor is related to the fast population growth and the progressive development of deprived countries. In this respect, one of the most worrying issues is the fate of the global water resources.

The global demand in drinking water is one of the major challenges for mankind in this century; more than other energetic resources, such as oil or combustion gas, the increase in the global population increases also the need for easy access to fresh water, since already more than 40% of the world inhabitants are living in regions with prominent water scarcity. A great portion of the global population have no access to clean water or sanitation. Around 800 million people have no access to safe drinking water and more than one third of the global population live below the standard for acceptable sanitary conditions, according to a recent report from the World Health Organisation (WHO).^[1] On the other hand, industrial and domestic overuse and pollution are causes of concern in the regions where access to water and sanitary conditions is better, lowering the quality of the water resources, contaminating the soil and introducing pollutants into the food chain. The global demand for water in the last century has increased seven times, while in the same period the global population has only increased four-fold.^[2] Water purification processes are therefore essential for the resolution of the water crisis and the preservation of water reserves. The development of cost-effective and environmentally friendly novel technologies for removal of pollutants and reuse of waste water is a key point in water purification research.

In this thesis the application of solar (light) energy in water purification processes has been studied, considering simple, environmentally safe and relatively

inexpensive techniques, in order to provide or at least to demonstrate the feasibility of a novel approach to the manufacture of filtration devices with promising potential commercial and industrial applications.

1.2 Membrane separation processes

Membrane separation processes have become essential in water purification. High process efficiency together with the low energy consumption and the possibility of scaling-up are key factors to take into account for efficiency and reliability in purification treatments, making this kind of processes indispensable. [3]

Membrane separation is based on the presence of a selective surface, the membrane, which allows the filtration of certain components (in some cases only the solvent molecules) blocking the others. The movement of matter through the membrane is generally favoured by the application of an external pressure. These pressure-driven processes are very important in water purification for the removal of colloidal size objects, microorganisms and in some cases electrolytes. The four most important pressure-driven processes in water filtration are microfiltration (MF), ultrafiltration (UF), nanofiltration (NF) and reverse osmosis (RO), whose basic characteristics and applications are reported in Table 1.1. The different processes are classified according to the pressure developed on the membrane surface (transmembrane pressure, TMP) and the rejection capacity (measured as molecular weight cut-off, MWCO), which constitute the defining properties of a membrane, useful for the selection of a specific application in purification processes. Apart from the pressure-driven filtration, other membrane-based processes involving different filtration mechanisms are employed for several technological applications. Electrodialysis (ED), pervaporation (PV), gas separation and forward reverse osmosis (FRO) are the most relevant examples of these processes.

Filtration processes are classified on the basis of the direction of the flux with respect to the membrane surface. When the flux is perpendicular to the surface, the configuration is referred to as dead-end; whereas when the flux is tangential to the surface, the configuration is defined as cross-flow. Cross-flow filtration is preferred in wastewater treatment and industrial processes, since this configuration prevents the accumulation of matter and objects on the membrane surface minimising the time of contact with the membrane surface and hence

increasing the operative lifetime of the membrane. ^[4] In a dead-end configuration, the membrane is rapidly covered with filtered matter, reducing progressively the performance of the process. Dead-end configuration is used for solution concentration or small-scale colloidal object removal.

Table 1.1: Basic characteristic of membranes for low-pressure filtration processes.^[5]

	Pore Size (nm)	TMP (bar)	MWCO (kDa)	Main purposes
Microfiltration (MF)	100-5000	1-10		Microorganisms removal (sterilisation, water treatment), petrol refining ^[6]
Ultrafiltration (UF)	1-100	1-10	500-10 ⁵	Purification of biological solutions, pre-treatment filter before the desalination ^[7]
Nanofiltration (NF)	0.5-10	10-30	100-500	Purification of biological solutions, water softening, colour removal, COD and BOD reduction ^[8] , pharmaceutical and biochemical industrial processes
Reverse Osmosis (RO)	< 0.5	35-100		Desalination, wastewater treatment in industrial, agricultural, drinking water production applications ^[9]

Two main configurations of membrane are used in water purification processes: flat sheet and fibre. The vessel hosting the membranes is referred as to a “pressure vessel” or module. Flat sheets are usually wrapped inside the module, whereas fibres are bundled in groups of several thousand, enrobed in resin. The water flows through the module, passing tangentially to the sheet surface or inside the fibres. The permeate is free to pass through the membranes and is collected from the module side, whereas the retentate exits the module. In industrial processes, fibre configuration is generally preferred given the higher surface area exposed to the feed flow.

1.2.1 Low-pressure filtration process: MF and UF

Filtration processes requiring relatively low-pressure are employed for the removal of solid particles of colloidal size and large molecules as a stand-alone process or often used as a preliminary treatment for further advanced purification processes, such as electrolyte removal or water softening by nanofiltration (NF) or reverse osmosis (RO). Low-pressure processes are generally classified according to their sieving capacity, determined by the size of the pore of the membrane.

The two main low-pressure processes are microfiltration (MF) and ultrafiltration (UF), both based on size-exclusion principles and generally employed for the removal of colloidal object from the treated sample. In ultrafiltration (UF), solutes of molecular weight from 3000 to 50000 Da ^[10] are rejected by the membrane allowing the solvent to pass through. UF is generally employed for the removal of oils, particulates, bacteria, proteins and other large macromolecules. Ultrafiltration is important in food processing, such as juice and wine clarification, egg white pre-concentration and cheese whey treatment. A feature of the UF membrane is the porous skin layer.^[11]

1.2.2 Polymer membranes

The introduction of polymeric materials for industrial and commercial filtration purposes began relatively recently (1980's). The development of polymers with particularly high mechanical resistance, thermal and chemical stability, allowed the substitution of more expensive ceramic membranes to be replaced for water treatment processes, with applicability also to particularly harsh environmental conditions, case in which inorganic membranes are usually preferred.^[12, 13]

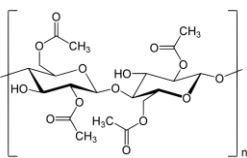
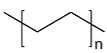
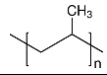
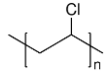
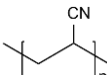
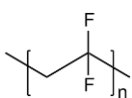
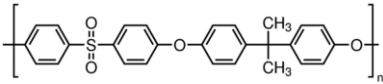
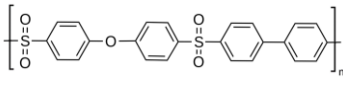
The biggest advantage of the use of a polymeric membrane is the extremely easy and highly controllable production of hierarchical porosity. Usually, a commercial polymeric membrane consists of a reinforcing fabric support (cellulose or cotton) to provide mechanical resistance and a porous layer. The surface of the porous layer is composed of a thin film known as an active layer. This is the interface for the separation of the membrane, through which the water molecules are able to filter, while other objects contained in the feed are retained.

UF requires higher thermal, chemical, biological and mechanical stability compared with the other filtration processes. For this reason, the typical materials employed for the fabrication of UF membranes include thermally resistant polymers; for their good chemical and mechanical resistance, materials such as polysulfone (PS), poly(ethersulfone) (PES), poly(etheretherketone) (PEEK), polyacrylonitrile (PAN) are among the most important in fabrication for UF membranes, as shown in Table 1.2. Almost all the polymers used for UF membranes have a glass transition temperature above 145 °C.^[14]

The most common process for the fabrication of polymer membranes is the phase inversion method or induced phase separation (IPS). Following this methodology,

the polymer is dissolved in a solvent, producing a generally viscous solution, defined as a dope or casting solution, that is then cast on a surface using different techniques (blade coating, spin coating). This surface is later exposed to a coagulating agent, which causes the rapid solidification of the polymer layer. Depending on the nature of coagulating agent, the IPS technique is classified according to the phase separation process. For instance, the process is caused by a change in temperature (Thermal IPS), by a chemical reaction (Reactive IPS) or by physical diffusion (DIPS) of the coagulating agent, generally a solvent in which the polymer is not soluble. The molecular diffusive exchange in the biphasic system of the dope solution and the coagulation bath is the driving force for the phase separation. This last technique is the most widespread, mostly because of the use of a water immersion bath, which makes the process very easy and inexpensive to perform. Production of polymer hollow fibres occurs generally via an extrusion process.

Table 1.2: Common polymers used in filtration processes. ^[15, 16]

Material	Structure	Properties
Cellulose Acetate (CA)		Hydrophilic, high level of crystallinity, stability over a very narrow pH range between 4 and 6.5, poor resistance to microbial attack
Polyethylene (PE)		Low cost, poor mechanical strength
Polypropylene (PP)		Low cost, poor mechanical strength
Polyvinyl chloride (PVC)		Low cost, High chemical stability
Polyacrylonitrile (PAN)		High mechanical strength, high durability, superior resistance to hydrolysis and oxidation, hydrophobic
Polyvinylidene fluoride (PVDF)		High mechanical strength, high durability, hydrophilic, chemical and oxidation resistance, good physical and thermal stability in a wide range of pH
Polysulfone (PS)		High mechanical strength, high durability, hydrophobicity ^[17]
Polyether sulfone (PES)		High mechanical strength, high durability, excellent thermal and chemical stability, hydrophilic, amorphous, low tolerance of aromatic hydrocarbons or ketones

1.3 Membrane Fouling

According to the IUPAC definition,^[18] membrane fouling is a process causing the decline of the membrane general performance, caused by the progressive deposition of suspended or dissolved solid matter on the outer surface of the membrane, in its pores or affecting both of these.

During an industrial process or water filtration operation, a wide range of colloidal sized objects could be responsible for fouling. A general classification of the foulants comprises:

- Colloidal foulants, such as clays or flocs
- Biological foulants, including microorganisms, bacteria, fungi and other
- Organic foulants, such as oils, polyelectrolytes and humics
- Inorganic or “scaling” foulants, for example mineral precipitates

Also known as membrane contamination, the accumulation of solids on the membrane surfaces is the main cause of the decline in permeate flux and consequently the decline of the overall filtration performance. Higher pressure is required to maintain the same filtration efficiency, increasing the energy consumption of the process. Membrane fouling is particularly heinous for polymeric membranes, limiting their application and operative lifetime. Apart from the limited application of the conventional cleaning procedures which are potentially damaging the membrane structure, the surface of polymeric membranes is intrinsically hydrophobic. Surface with low affinity for water are known to favour the adsorption and deposition of organic and biological foulant via nonspecific interactions.^[19, 20]

A critical degree of fouling totally compromises the membrane workability; especially in long-term filtration process where productivity constantly declines, and selectivity is altered by the change in pore size caused by the progressive filling or covering of the membrane by solid matter. Finally, the overall operational life-time of the membrane is irremediably shortened, because of frequent back-flushing operations and harsh chemical cleaning, damaging the structure of the active layer and making the replacement of the membrane or the whole filtration module unavoidable.

Among the fouling causes, more than 45% of all cases can be attributed to biological factors, more than any other single cause.^[21] Biofouling is defined as the accumulation and establishment of living organisms (microorganisms, plants, algae, animals) on a wetted or liquid exposed surface. Biofouling can be considered as a biotic form of organic fouling. On the other hand, organic matter derived from microbial cellular debris can be ascribed as an abiotic form of biofouling.^[22]

Microorganisms are symbiotic with the surface, living or inanimate, onto which they attach and develop. When the microorganism attaches irreversibly onto a surface, it starts producing extracellular polymeric substances (EPSs), highly hydrated polysaccharides, which strongly bind to the surface composing the matrix of the biofilm. The biofilm constitutes to make a comfortable environment for the attachment of other microorganisms and their growth, providing essential nutrients, oxygen and entrapping other useful components for the microorganism development.^[23] Contamination by biofouling is a relevant issue in several fields, especially in healthcare, for surgical equipment and medical implants, but also for food packaging^[24] and storage,^[25] marine and industrial equipment and of course, in water purification systems.^[26, 27]

1.4 Antifouling strategies

Each process of removing and preventing the accumulation of solid matter from forming on a surface is defined as an anti-fouling treatment. Three main different approaches can be employed to fight against fouling: (1) pre-treatments, which involve preliminary removal of foulants in process such as flocculation, coagulation and sedimentation. These always occur in water treatment facilities because of their cost-effectiveness; (2) Post-treatments, which are performed once the membrane is fouled, including all chemical or physical cleaning processes;^[28] (3) Most intriguingly, the modification of the surface to prevent, delay or destroy the cause of fouling. Limiting the discussion to the membrane field, the cleaning process can seldom be performed *in situ* and often requires removing the modules from their working environment. Such treatments can be detrimental for the membrane integrity. For example, compounds for chemical cleaning can corrode the polymer.^[29] By contrast, membrane modification allows the design of a functionalised material with inherent antifouling properties. The

modification can be limited to the surface only, with coating processes that do not affect the overall structure of the membrane. The efficacy of membrane modification can potentially reduce the influence and the intervention of the other two antifouling approaches.

Antifouling or low-fouling surfaces are not only important in water treatment processes but also in biomedical applications, providing surfaces resistant to bacterial or protein adhesion and enhancing the immuno-"camouflage" of body-implanted tissue, minimising the risk of immune rejection.^[30] The classic antifouling strategies in surface modification consist of: **(1)** increasing the surface hydrophilicity and negative charge distribution on the surface, **(2)** preventing the most common interactions between foulants and membrane surface, such as hydrophobic interactions, or **(3)** imparting electrostatic repulsion properties against negatively charged particles.^[31] The improvement of the hydrophilicity and the increase of negative charge on the membrane surface have been reported to reduce the interaction with foulants and to increase membrane lifetime.^[32, 33] Organic matter, proteins and bacteria generally attach to surface via nonspecific interactions, especially in the case of most of the polymers employed in filtration technology. In biology, nonspecific interactions identify all the type of interactions not occurring between specific molecules and characterised by low interaction activity.^[34]

For this reason, one of the most common surface modifications is performed by grafting hydrophilic moieties, by surface coating with specific thin film or by blending the membrane matrix during the membrane synthesis process, using particular adjuvants such as amphiphilic macromolecules (polyethylene glycol),^[35] highly hydrated zwitterions^[36] or hydrophilic nanoparticles (generally oxides). Modification of the surface wettability has been widely exploited, testing superhydrophilic, superhydrophobic^[37] or mixed behaviour surfaces through amphiphilic coatings. Other approaches have concentrated on the other factors influencing fouling, such as the morphological characteristics of the surface. Original strategies have been developed to design surface patterns and topography inspired by natural biomimetic surfaces, such as mollusc shells or marine fish and mammals that show natural antifouling behaviour.^[38]

1.4.1 Antibacterial and sterilisation processes

Disinfection and sterilisation processes aim to remove microorganisms from water and are effective in making water safe for drinking. However, these processes only delay the establishment of the biofilm, since even a single surviving unit can trigger the biofilm establishment. The most common process involves the use of biocides, with chlorine and its derivatives, such as chloramines and chlorine dioxide among the most popular. Despite the efficiency of chlorinate as a disinfectant, polymer materials are sensitive to chlorine and chlorinated by-products, especially in case of RO membranes. The inability of the biocide to reach the membrane surface reduces the efficacy of the method. Biocide activity would be more effective on the membrane surface, where microorganisms find a suitable platform for their multiplication. The main concern about chlorine use is the environmental issue related with the formation of harmful by-products, such as trihalomethanes, haloacetic acids and N-nitrosodimethylamine, which are reported as carcinogenic compounds. Another drawback is represented by the increase of assimilable organic carbon (AOC) due to the oxidation of organic substances in biodegradable components, providing further nourishment for microorganisms.

Due to the high resistance of the biofilm to the cleaning processes, the only approach considered valuable for the preservation of the membrane surface is the prevention of the biofilm formation, hindering the initial adhesion of the microorganisms and their consequent reproduction and proliferation. ^[39] Different material surface characteristics have been proposed to have an influence on the first stage of bacterial adhesion: surface roughness, charge, hydrophobicity, Lewis acid-base reactions and hydrogen-bonding capacity. The modification of these parameters can potentially disrupt the adhesion of microorganisms on the membrane surface. ^[40]

One of the general approaches for the investigation of adhesion-resistance surfaces is to make a comparison with protein adhesion mechanisms. According to some theories, bacteria use a layer of protein to anchor themselves to the surface; for this reason, a resistance to protein should lead to a corresponding resistance to bacterial attachment. ^[41] From the mechanistic point of view, the process of adhesion of microorganisms to a surface is driven mainly by hydrophobic and electrostatic interactions, *via* emission of proteins or by using outer organs (fibrils

or other extracellular appendages). Similarly, as for the general antifouling approach, improving the hydrophilicity of the surface has been considered as an effective method to prevent bacterial adhesion. [42] A highly hydrophilic surface presents a strong affinity with water in aqueous environment, making the adhesion of microorganisms unfavourable.

Another interesting approach involves the production of a surface with a sufficient density of mobile cationic charges. Cationic amphiphilic molecules show antimicrobial properties due to the strong electrostatic interaction between the molecules and the negative sites of the lipid bilayer composing the outer membrane of cellular organisms. Van der Waals interactions between the hydrophobic parts of the antimicrobial molecules and the phospholipids in the membrane contribute to the disruption of the bacterial cell membranes, leading to the death of the microorganism due to the leakage of the cytoplasmic components. [43] The cationic-killing action would prevent adhesion killing the microorganisms directly.

1.5 Photocatalysis as a purification process

Photocatalysis is considered as a promising solution for the removal of environmental contaminants. The process is triggered by a source of light, which implies a requirement for the efficient exploitation of solar energy. The photocatalytic reaction leads to the generation of radical species from photo-generated charge carriers and solvent or air molecules. Photocatalytic processes generally follow a common mechanistic path: irradiating energy excites electrons in the valence band (the highest occupied electronic energy level in the material) causing the generation of an electron and consequently a hole (a positive vacancy in the original band). The pair of charged carriers diffuses towards the surface, where they are trapped. Holes and electrons in this state represent a very high oxidizing and reducing activity respectively; their reaction with water or oxygen in the air leads to the generation of very reactive species, such as hydroxyl radicals ($\cdot\text{OH}$) and superoxide anions (O^{2-}). Photocatalysis can be classified as an Advance Oxidation Process (AOP). A scheme of the most common AOPs is represented in Figure 1.1. The main advantage of AOPs is the almost complete mineralisation of organic compounds into harmless molecules, avoiding the formation of unwanted harmful by-products such as in chlorination processes. AOC formation is prevented

offering a clear advantage in purification or sanitation processes. However, the oxidation of high molecular weight organic compounds such as Natural Organic Matter (NOM) has been reported to release intermediate products such as aldehydes and ketones.^[44]

AOPs include irradiation with UV, ozonisation, use of hydrogen peroxide as in the Fenton process and also ultra-sonication. AOPs find their principal application in removal of organic contaminants. A vast range of hydrocarbons, from petroleum to chlorinated compounds used as industrial solvents and cleaners (and which sometimes could be resistant to biodegradation), easily oxidised organic molecules, for example alkenes (and relevant pollutants such as trichloroethylene, perchloroethylene and vinyl chloride), or simple aromatic compounds (toluene, benzene, xylene, phenol) undergo complete mineralisation when treated with AOPs. Ozone is used as a disinfectant in water and wastewater treatment and it exhibits strong oxidative deactivation and neutralisation towards a vast range of microorganisms (bacteria, viruses, protozoa and endospores). Unfortunately, ozone is not stable, demanding on-site production, and could lead to the formation of harmful by-products, such as brominated compounds and residual AOC.

The first photocatalytic AOP was reported in the late 1970's with the decomposition of cyanide in aqueous TiO₂ suspension.^[45] Since then, photocatalytic process have been applied to environmental remediation of a vast range of pollutants such as dyes, pesticides, pharmaceutical products and endocrine disrupting compounds, generally using transition metal oxides with semiconducting properties as catalyst but also sulphides and in some cases halides.^[46] A more detailed description of these materials is provided in the following section.

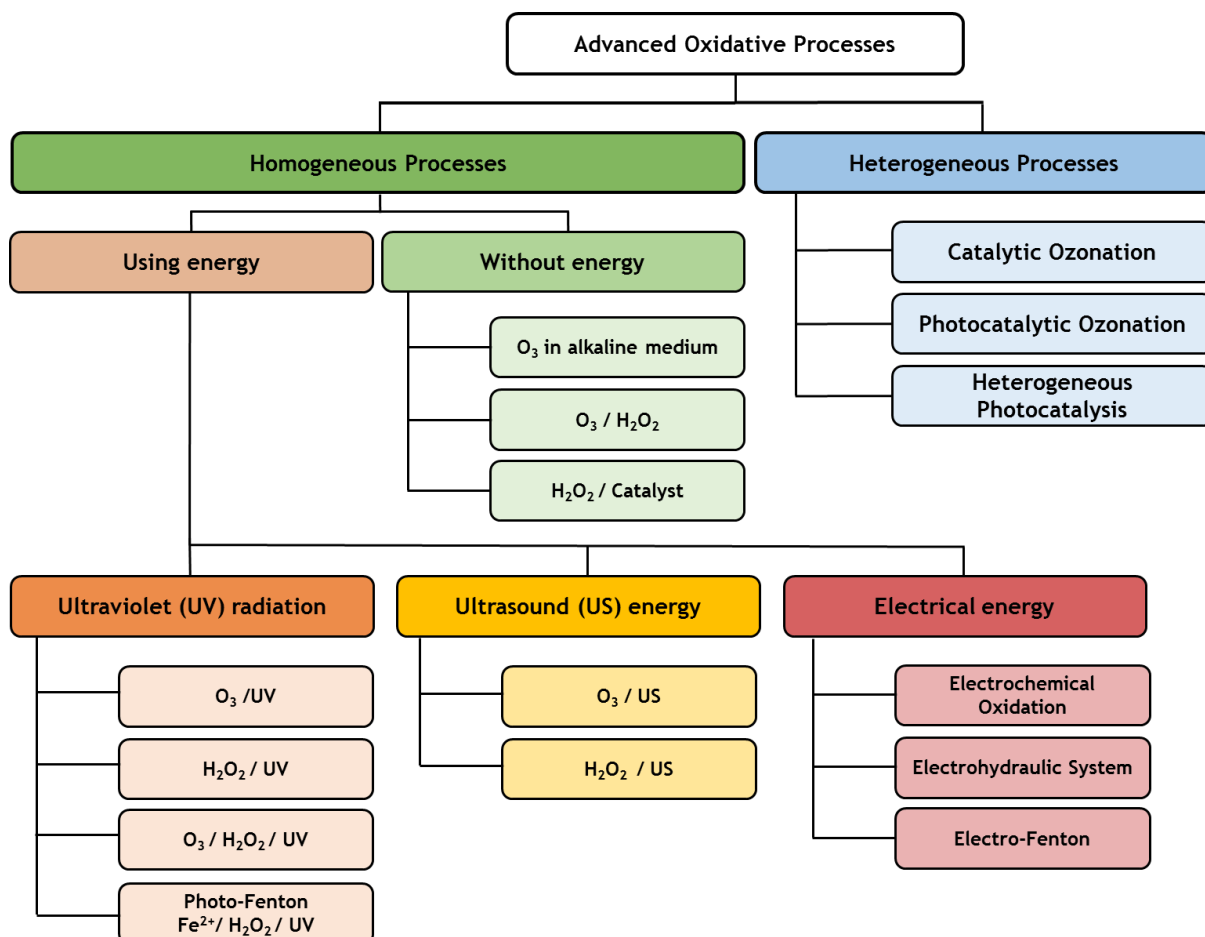


Figure 1.1: Classification scheme of different Advance Oxidation Processes (AOP) based on wastewater treatment technologies.^[47]

1.5.1 Photocatalytic materials

Many semiconductor materials exhibit photocatalytic properties; the illumination from visible or UV light causes the generation of a pair of oppositely charged particle, an electron (e^-) and a hole (h^+). The process is due to the promotion of the electron from the highest occupied electronic levels, the valence band (VB) to the lowest unoccupied ones, referred as to conduction band (CB). The promotion of the electron leaves a positive vacancy in the valence band, described in solid-state physics as a self-standing particle, a hole. The electronic transition and the consequent generation of the hole occur if the material receives an amount of energy equal or higher than the energy gap between the valence and conduction bands; a "region" also called the band gap in which the presence of electronic states is forbidden. Materials are classified as insulators, semiconductors and conductors on the basis of the magnitude of this energy gap. The band gap energy of most of semiconductors is in the range 1 - 5 eV, corresponding to visible and UV light wavelengths. Semiconductors differ from

conductive materials (metals), where the band gap is of the same order of magnitude of the electrons thermal energy or more often where the valence band is partly filled and hence the band gap does not need to be crossed. Also, semiconductors differ from insulators, for which the energy gap is not bridgeable by the energy of near-visible electromagnetic radiation. The presence of a bridgeable band gap is a necessary but not sufficient condition for the photocatalytic process to occur. The photo-generated charges should be able to migrate to the surface of the material and interact with the surrounding molecules, usually through reduction-oxidation reactions. Recombination and trapping of the charges have to be considered in order to increase the efficiency of the overall photocatalytic process.

Semiconducting oxides and chalcogenides generally present the best photocatalytic properties. Some examples are shown in Figure 1.2, with their band energies compared with the potential necessary for water splitting. Without doubt, the most commercially-employed photocatalytic material is titanium dioxide (TiO_2), which will be further described in the next sections. Apart from TiO_2 , numerous binary, ternary and quaternary compounds have been reported as effective for the photocatalytic degradation of different pollutants, even though performance is still generally inferior to TiO_2 .^[48] A review from 2010 listed almost 200 materials as having showed photocatalytic responses for water splitting,^[49] whereas several others have been classified useful for photocatalytic environmental remediation.^[48] The development of new synthesis methods, the discovery of new photoactive phases and the progressive research in band gap tailoring increase the potential for semiconductor photocatalytic materials to address the challenges in energy supply and environmental pollution, with applications in water splitting, degradation of organic pollutants, reduction of heavy-metal and several other AOPs.

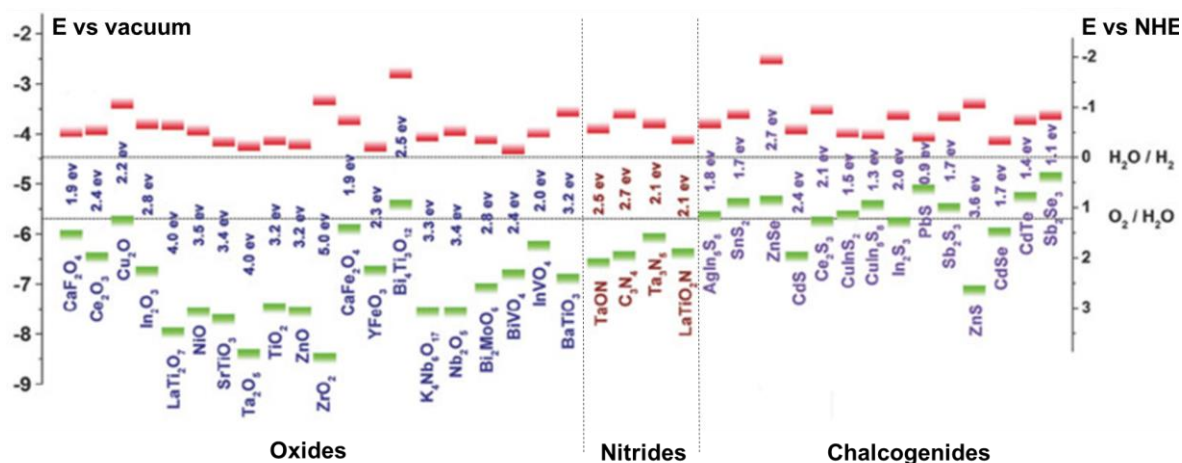


Figure 1.2: Band gap values and band-edge positions with respect to the vacuum level and NHE for selected semiconductors. Red bars represent the conduction-band edges, the green ones indicate the valence-band edges. The band energies are compared to the water redox reaction potentials.^[50]

1.6 Nanoparticles for environmental applications

Nanoparticles or nanostructured materials have always been object of research due to their interesting properties. Compared to bulk materials, the reduction to nanometric size gives access to a series of new mechanical, chemical, electrical, optical and magnetic properties. The radical change in material properties is due to the larger presence of superficial atoms, quantified by the high surface area to volume ratio.^[51] The high adsorption capacity of nanoparticles has proven to be particularly useful in environmental technologies, with applications in pollution monitoring and remediation of groundwater and soils, providing a cost-effective solution for major clean-up problems such as water decontamination from a wide range of pollutants, like chlorinated organic solvents, pesticides and toxic metal and metalloids.^[52]

High specific surface area and nano-size related properties are almost essential for the use of nanoparticles as water disinfection agents. The use of antimicrobial inorganic particles showed relatively limited toxicity and reduced risk of bacterial resistance development, compared with organic compounds generally used for disinfection.^[53] Nanoparticle toxicity depends on several factors, such as composition, surface modification and microorganism species. The general toxicity mechanism involves the attack and the structural destabilisation of the cell membrane of the microorganism by electrostatic interactions, reported for example in the case of nanoparticles of Al₂O₃ or ZnO.^[54]

Silver nanoparticles (Ag NPs) are probably the most famous and effective antimicrobial agent. Silver metal is renowned from ancient times for its purification properties, due to the release of Ag^+ ions, which establish a very strong interaction with the thiol groups of bacterial vital enzymes, inactivating their normal function, such as loss of DNA replication ability.^[55] Silver nanoparticles are less reactive than Ag^+ , allowing their use in clinical and therapeutic applications.^[56] The killing mechanism of Ag NPs involves the attack of the bacterial cell membrane with consequent destabilization of the plasma-membrane potential and release of intracellular adenosine triphosphate (ATP), depleting the energetic resources of the cell and leading to its death.^[57] Ag NPs are widely employed in several consumer products, such as antiseptic bandages, clothing materials, deodorants, cleaning agents and sprays.^[56] Ag-NPs have proved to be very effective in controlling the growth and activity of various microorganisms and inactivating microorganisms in aqueous suspensions, demonstrating their efficient application as a retarding agents for biofilm formation. However, silver nanoparticles are not effective for eradicating existing or mature biofilms or for use as a disinfectant. ^[58, 59, 60]

Metallic and ionic forms of copper produce hydroxyl radicals that damage essential proteins and DNA. Copper shows stronger toxicity than Ag-NPs towards eukaryotes, the family including fungi and other dangerous pathogenic agents. A solution with copper ions, complex copper species and Cu-doped particles have proved to be effective against fungi proliferation in aqueous environments. ^[61] Among non-oxide materials, MgF_2 has shown remarkable antimicrobial properties and inhibits biofilm growth from common pathogens. The nanoparticles are able to penetrate the cells and acidify their internal environment, causing potential membrane disruption and enhancing lipid peroxidation. The application of nano- MgF_2 to surfaces has been reported to enhance the resistance to bacterial colonisation for up to several days.^[62]

1.7 Titanium dioxide (TiO₂)

Titanium dioxide (TiO₂, also referred as to titania) is a remarkable material in terms of properties, technological applications, availability and cost-effectiveness. Thermal and chemical stability, relatively low toxicity and high biocompatibility make this material essential for everyday applications, mainly as a pigment for paints, food colouring (under the label E171) and sunscreen.^[63, 64, 65] In nature, TiO₂ occurs as three different polymorphic forms. The most abundant and thermodynamically stable is rutile,^[66] mostly used as a pigment. Two other metastable phases exist, anatase and brookite. The three polymorphs are all composed of TiO₆ octahedral units, organised in different spatial arrangements. Anatase and rutile both possess the tetragonal unit cell symmetry, with the octahedral units connected through the edges along the three spatial direction in zigzag arrangement in anatase, whereas in linear arrays for rutile. Because of the resulting symmetry, anatase has a body-centred cell (space group I4₁/amd) and rutile unit cell is primitive (P4₂/mnm). Brookite is the least common polymorph and is orthorhombic in symmetry (Pbca) due to the sharing of three edges between the TiO₆ units. The structures and the octahedral arrangement for the three polymorphs can be visualised in Figure 1.3.

Anatase is not particularly suitable as a pigment (it tends to chalk in painting), but it is the preferred crystalline phase for optimal photocatalytic performance under UV irradiation. This enhanced photoactivity has boosted interest in anatase with respect to multiple technological applications from basic heterogeneous photocatalysis to deodorant, water and air purification technologies and self-cleaning surfaces.^[67] The wide range of applications of TiO₂ has driven research interest towards the synthesis of nano-sized or nanostructured materials in an attempt to enhance properties through increased specific surface area, a higher number of high-energy or active sites and hierarchical porosity. Several nanostructures have been reported in the last decades, from nanoparticles, through nanotubes and wires to mesoporous structures.

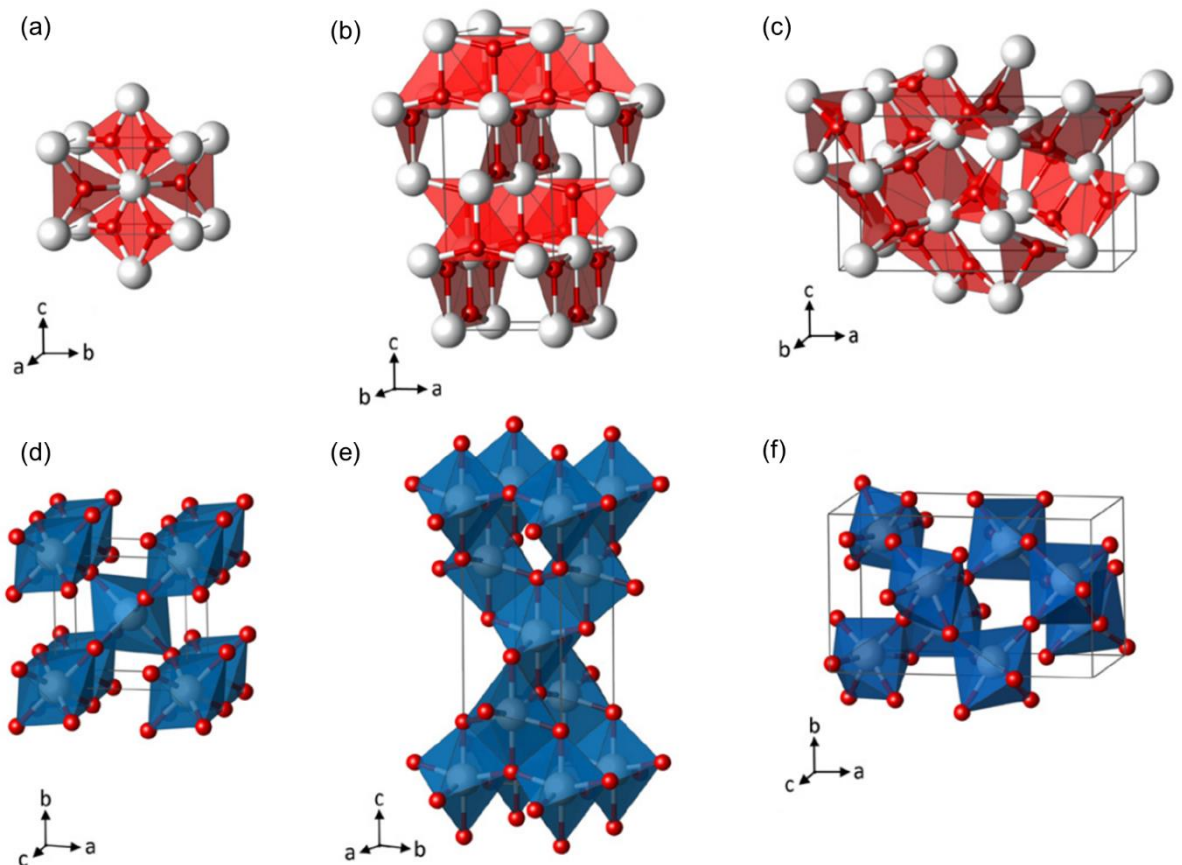


Figure 1.3: Structural representation using planar Ti_3O building-block model (upper images) and TiO_6 polyhedrals (lower images) for the three main TiO_2 polymorphic phases: (a, d) rutile, (b, e) anatase, (c, f) and brookite. Ti atoms are represented by white spheres, O with red ones. The axis orientation was arbitrary chosen to facilitate the representation of the structures.^[68]

1.7.1 Photocatalytic activity

The photocatalytic properties of TiO_2 were assessed for the first time in 1972, when Fujishima and Honda realised the possibility as performing water splitting using a Pt electrode coated with titania, providing the first experimental evidence of the photocatalytic activity of TiO_2 .^[69] The second seminal moment in the technological history of TiO_2 as a photoactive material is represented by the design of the first dye-sensitised solar cell (DSSC) in 1991 by Graetzel and O'Regan, in which a TiO_2 nanoparticle sol-gel thin film anode improved the efficiency of the cell while providing a low-cost solution for this kind of device.^[70]

Compared with other semiconductive oxides, TiO_2 has a relatively wide band gap, 3.25 eV for anatase and 3.03 eV for rutile,^[71] limiting the useful irradiation for photocatalytic activity to the UV region. The photocatalytic process is similar to the one reported in the previous section, with the reduction of Ti(IV) to Ti(III) by the photogenerated electrons, followed by reaction with the O_2 adsorbed on the

surface to create superoxide radical anions ($O^{\bullet 2-}$). A schematic representation of the process in water is given in Figure 1.4. In general, anatase shows superior properties compared to the other polymorphs, despite the wider band gap.^[72] The higher performance of anatase was initially attributed to the band edge positions, with the conduction band more positive in rutile compared to anatase. Anatase can generally exist with a higher specific surface area and smaller grain size, due to its higher thermodynamic stability at the nanometric scale; the opposite of the case for the bulk material. From the point of view of the electronic properties, unlike rutile and brookite, anatase has an indirect band gap and a smaller effective mass of charge carriers compared with rutile. Electrons and holes can therefore easily migrate towards the material surface.^[73] These properties lead to the higher surface adsorption capacity of anatase towards hydroxyl groups,^[74] the lower charge carrier recombination rate^[75] and the larger lifetime of the photo-generated holes and electrons.^[76]

Beside the different polymorphic structures, the photocatalytic activity of TiO_2 is strongly dependent upon the morphology, crystallite size, specific surface area and pore structure.^[77] Synthetic conditions hence dictate the performance of a photocatalytic material. The surface area plays a key role in the photocatalytic processes because of the increased number of active sites and the higher possibility to adsorb organic molecules and pollutants, facilitating the oxidation reactions. For this reason, nano-sized TiO_2 outperforms its bulk counterpart, presenting a high density of active surface sites due to the extremely high surface-to-volume ratio.^[78] On the other hand, a high degree of crystallinity is another important requirement for a good photocatalyst, since in this way the path of the charge carriers is not hindered by grain boundaries or other lattice defects, which could induce recombination. Unfortunately, those two conditions are often mutually exclusive. High crystallinity is achievable with high temperature treatments such as calcination, which irremediably reduces the surface area because of the growth of crystalline grains or collapse of delicate porous structures. Most of the research on TiO_2 photocatalysts aims for the optimal compromise between surface area and crystallinity.

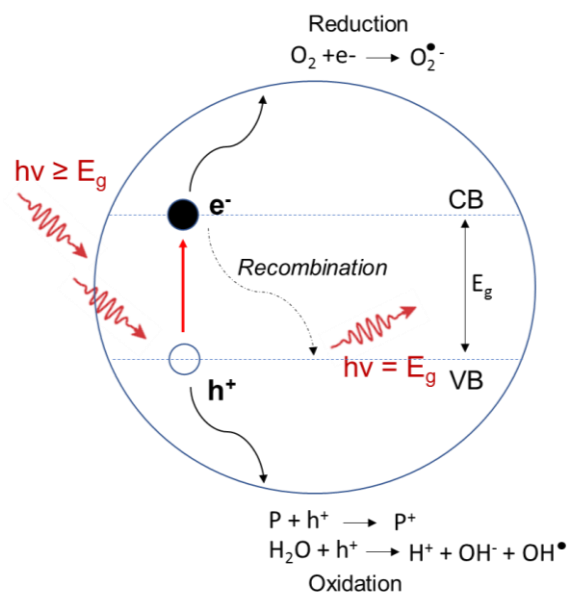


Figure 1.4: Mechanism of electron– hole pair formation in TiO₂ particle irradiated by photons with energy comparable with the material band gap. Example of reactions in the presence of pollutants (indicated with P) in water. (Adapted from Chong *et al.* [79])

1.7.2 Photo-induced hydrophilicity

Another remarkable characteristic of TiO₂ is its reversible amphiphilic surface. The TiO₂ surface, usually slightly hydrophobic, can be turned to a superhydrophilic one when exposed to UV-light. This interesting property was firstly reported in 1990, again by the group of Fujishima.^[80] A superhydrophilic surface presents a high affinity for water and polar liquids in general, allowing these liquids to spread uniformly, creating a thin liquid layer on the surface.

The superhydrophilicity mechanism has been explained by the rearrangement of polar groups on the TiO₂ surface due to reactions of the photo-generated holes with lattice atoms in their surroundings.^[81,82] Most of the photo-generated holes participate in the formation of OH• radicals when in contact with adsorbed water molecules or other adsorbed compounds. On the other hand, a limited amount of holes is trapped in lattice oxygen sites. The reaction of the holes with the TiO₂ weakens the bonds between the lattice Ti⁴⁺ and O²⁻. The weakened bonds are broken by water molecules, generating singly coordinated hydroxyl groups on the TiO₂ surface. The presence of those groups is thermodynamically unstable, increasing the surface energy and conferring superhydrophilic properties to the UV-irradiated surface (the mechanism is shown in Figure 1.5).^[83]

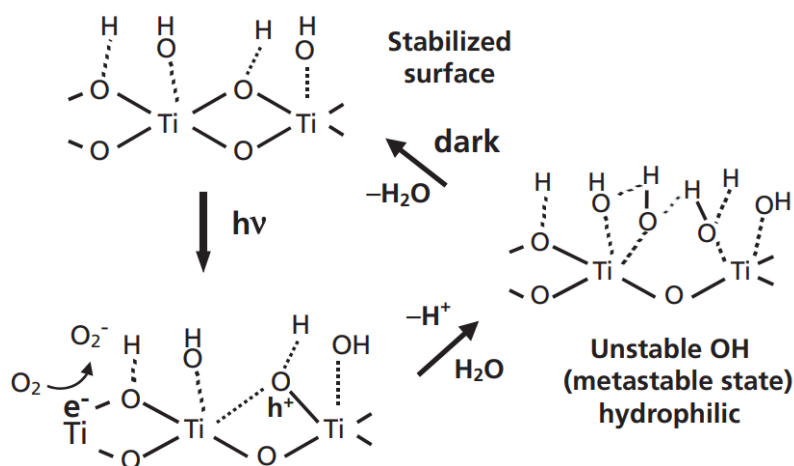


Figure 1.5: Schematic representation of the mechanism of reversible wettability of TiO₂ surface exposed to UV light irradiation and under dark. ^[84]

The newly discovered property of TiO₂ made the development of self-cleaning and anti-fogging surfaces possible. In the former application the thin layer of water produced on the surface is able to wash away the dirt. Dirt is indeed generally composed of hydrophobic matter and it is not able to form a stable attachment to the hydrophilic surface.^[85] As for anti-fogging applications, the functionalised surface prevents the condensation of water droplets, with the uniform thin film unable to scatter the light. This brings the advantage of not hindering sight through the transparent surface.

1.7.3 Visible light active TiO₂

The relatively wide band gap of TiO₂ is a physical limitation for the application of its photocatalytic properties in the visible light range. The band gap of anatase corresponds to a wavelength ($\lambda = 387$ nm) which limits the possible sunlight photo-activation to only 5% of the total solar spectrum.^[86] To extend the range of activation of TiO₂, modification of the band gap and edge positions is necessary. Visible-light active TiO₂ photocatalysts are often referred to as the second generation of photocatalytic material. ^[87]

A common research aim is to prevent major modification of the crystal structure of the photocatalyst, acting only on its electronic structure. ^[88] The principal methods can be roughly classified as doping and coupling techniques. Doping acts directly on the lattice structure, with insertion of non-metal anions or transition

metal cations. Coupling involves the intimate contact of TiO_2 with another material which could be an organic dye, a noble metal or another semiconductor. Doping acts directly on the electronic structure, by adding intermediate levels in the forbidden energy region. Depending on the proximity to the valence or the conduction bands, the intermediate levels are responsible for the trapping of photo-generated holes or electrons, respectively. Despite the efficient reduction of the band gap and the improvement of light-induced photoactivity, the insertion of transition metals leads to crystalline lattice instability, due to the different size or charge of the cations and additional charge carrier recombination centres.^[89] From this point of view, non-metal doping is more efficient and was initially attributed to the overlapping of the 2p bands of oxygen atoms with the equivalent states of the non-metal elements such as N,C,S and F. The band gap can narrow due to the production of isolated states in the forbidden region.^[90] More complex strategies have been developed exploiting the synergic action of the presence of two or more different anions or cations or metal/non-metal co-doping.^[91, 92]

Coupling is relatively less “invasive”; the energy levels of TiO_2 are paired with those of the coupled material, which is usually able to adsorb visible light efficiently and inject electrons into the conduction band of TiO_2 . This is the case for dye sensitisation. Alternatively, charges can be trapped by interfacial charge transfer mechanisms, avoiding fast recombination. Dye-sensitisation is widely used in photovoltaic systems (e.g. Dye-Sensitised Solar Cell, DSSC), but can also be applied in water splitting or pollutant degradation. The efficiency of the process is due to the rapidness of the process of electron injection, 2 to 3 orders of magnitude faster compared with the electron-hole recombination process. In addition to their electron trapping function, all noble metals such as Ag, Au and Pt have been also reported to promote electron injection through localised surface plasmon resonance (LSPR). The plasmon is responsible for the harvesting of a visible light photon and transferring electrons to TiO_2 either by direct injection or by a mediated electromagnetic field.^[93] Coupling with other semiconductors produces a heterogeneous junction which is efficient if the conduction band of one of the materials is more negative compared to the coupled material with a narrow band gap. The photogenerated electrons pass from a conduction band to a more positive one, with a mechanism similar to the electron injection in dye sensitisation. A common example of this strategy is represented by the junction

TiO₂-CdS, but Cu₂O, Fe₂O₃, Bi₂WO₆ and WO₃ also yield better performance under visible light compared to pristine TiO₂.^[94]

A very recent development towards simple activation of visible-light driven processes involves non-stoichiometric or defective structures, that are sometimes defined as “self-doping”. The presence of oxygen vacancies or the existence of partially occupied Ti³⁺ states generates impurity levels in the band gap, enhancing visible-light absorption.^[95] These stoichiometric defects are generally attributed to anionic doping or thermal treatment under an oxygen-deficient atmosphere. Very recently the possibility of reducing the band gap through oxygen excess defects has been demonstrated, due to the shift of the valence band and the reduction of the lattice parameters due to the bonding between interstitial and lattice oxygen atoms. The drawback of this defect approach is the reduction of the quantum efficiency due to the higher rate of electron-hole recombination.^[96]

1.7.4 Toxicity and antibacterial properties of TiO₂

TiO₂ is generally reported as a biocompatible and relatively non-toxic material. Even in the form of nanoparticles, TiO₂ shows negligible antimicrobial activity under dark conditions.^[97] Because of its high stability and biological inertness, TiO₂ materials with a particle size larger than 100 nm find application in food colorants, sunscreen and cosmetic creams, with low concern about potential toxicity. Several cytotoxic studies of nano-sized TiO₂ particles showed low or negligible toxicity compared with other nanoparticles, confirming the environmental and health safety of the material, except for the observation of pro-inflammatory effects in human endothelial cells.^[98]

On the other hand, exposure to UVA radiation activates the photocatalytic processes in the bulk and nanoscaled material. The photo-induced production of radicals, in particular superoxides, is the main cause of the complete decomposition of all sort of organic matter, from toxic organic molecules to microorganisms, making TiO₂ a benchmark material for AOPs in disinfection and purification treatments. The ROS generated during the photocatalytic process react violently with organic matter and microorganisms, leading to complete mineralisation to CO₂ and efficient removal of AOCs.^[99] The killing action of TiO₂ under suitable light irradiation has been described by two different mechanisms. Initially, the TiO₂ particles are in contact with the microorganism, allowing short-

lived ROS species to attack the cell wall without compromising the viability of the overall organism.^[100] The oxidative attack proceeds towards the cytoplasmic membrane, composed of polyunsaturated phospholipids.^[101] The lipid peroxidation progressively increases the cell permeability, causing leakage of intracellular components, such as potassium ions, RNA and proteins.^[102] The disruption of the internal equilibrium drives the cell to death. Nanoparticles can also enter the damaged cell, directly attacking the intracellular components and accelerating the cell destruction. This last mechanism was initially considered as the principal killing mode, due to the oxidative attack on coenzyme A, essential for the cell respiration.^[103] More specific mechanisms have been studied, associating for example the effect of photo-generated H₂O₂ in damaging specific parts of the organism's DNA^[104], similar to the killing mechanism of peroxygen disinfectants.^[105]

1.7.5 TiO₂ in water treatment and membranes

The application of the photocatalytic properties of TiO₂ to water treatment for pollutant removal and purification represents a cost-effective and environmentally-friendly alternative to conventional purification such as the use of chlorine. Photocatalytic processes in the presence of TiO₂ include the reduction of nitrates,^[106] CO₂ and heavy metal ions such as Cr(VI).^[107] TiO₂ nanoparticles have also been successfully employed as nanosorbents for heavy metals in water.^{[108][109]} The use of TiO₂-based catalyst in environmental applications is considered safer compared to other catalytic semiconductors, such as CdS or ZnO, due to the potential dissolution of the latter and subsequent production of harmful by-products.

The first TiO₂-based purification systems were based on the simple concept of TiO₂ particles dispersed in an aqueous suspension in the reactor. The simplicity of the idea (still widely reported) is counterbalanced by the difficulties in recovery and regeneration of the nanoparticles after the purification treatment. This has practical and economic disadvantages,^[110] with additional removal treatment such as coagulation or membrane separation required.^[111] Moreover, the relatively low toxicity and biocompatibility of the TiO₂ NPs is not enough to ease concerns over the unknown long-term effect on the environment due to unwanted release of nanoparticles and the generation of reactive radicals when the material is exposed

to sunlight. Furthermore, the agglomeration of the particles in water causes loss of surface area and active adsorption sites. Together with the reduction of the light penetration depth due to the strong adsorption by the nanoparticles, these factors limit the overall catalytic efficacy of the treatment.

For all these reasons, supported catalysts or nanocomposite materials, with nanoparticles bound or integrated onto the surface, constitute a more efficient and clean solution for environmental applications. The immobilization of TiO₂ on filtration membranes has proved particularly effective in the degradation of organic foulants. Moreover, the presence of TiO₂ in the membrane structure improves separation via the hydrophilic behaviour of the nanoparticles.^[112] Removal of pollutants, increasing permeability and establishment of a surface that is relatively difficult to attach to by microorganisms all make TiO₂ integration suitable in preventing membrane fouling.^[113]

Polymer and ceramic membranes have been extensively used as supports for nanosized TiO₂ in photocatalytic devices. The nanoparticles are integrated into the membrane by surface deposition via immersion or impregnation or alternatively by dispersing TiO₂ in the polymer solution, with modification of the membrane matrix after the casting process.^[111] Blended polymer membranes showed appreciable antibacterial performance and good immobilisation of the nanoparticles. However, this method has been reported to affect the phase separation process, generating uncontrollable anomalies in the membrane structure (in particular the internal porous structure).^[114] Moreover, agglomeration of the nanoparticles and poor compatibility with the surrounding polymer matrix are detrimental for membrane performance, with some cases reported of permeability decline caused by the blockage of the pores.^[115] The entrapment of the particle in the inner layer of the membrane drastically reduces the photo-sensitisation of the nanoparticles, with the polymer shielding penetration of activating light, reducing overall efficiency of the photocatalytic process. The blending process has also been reported to either only slightly modify or not significantly improve the hydrophilicity of the membrane.^[116,117]

Modification of the membrane surface by coating is considered a more efficient alternative. The surface of the membrane can be decorated with nanoparticles; TiO₂ can easily bind the functional groups frequently found in polymeric membranes. For instance, this could occur by binding two oxygen atoms of a carboxylate group or by forming hydrogen bonds between a carbonyl and/or

hydroxyl groups on the particle surface.^[118] The first membranes decorated with TiO₂ nanoparticles were prepared via immersion in colloidal suspension or impregnation in a pressurised vessel.^[119] Despite the lower pure water flux compared with unmodified membranes - due to pore blockage and the load of the particles on the surface - the presence of the TiO₂ nanoparticle coating proved to be an effective solution for antifouling. Higher stability and values of permeate flux in the presence of foulants or microorganisms could be obtained compared to the neat membranes.^[120]

Functionalization of the membrane surface via grafting or plasmochemical modification has been proposed to enhance particle adhesion. However, the few long-term studies on these membranes have showed poor stability of the coating due to the weak nature of the chemical bonds under the filtration conditions, causing shear stress on the surface and particle detachment.^[121] A stronger interfacial binding between the membrane surface and the nanoparticles is hence required to ensure long-term stability of surface-modified photocatalytic membranes.

1.8 Microwave-assisted hydrothermal synthesis

1.8.1 Hydrothermal/solvothermal methods

Among the several methods used for the controlled synthesis of highly ordered nanostructures, solution-based approaches are usually preferred due to the excellent control over morphology and size, flexibility and versatility of the method and relatively low energy consumption. Hydrothermal synthesis can be considered as a simple and effective strategy for this purpose.^[122] Hydrothermal synthesis has been historically conceived to describe the formation of rocks and minerals in the Earth's crust due to the presence of water at high temperature and pressure conditions.^[123] The simulation of this natural phenomenon led to the development of a synthesis technique for the production of crystalline nanoparticles or nanostructured materials. Remarkable results have been obtained in terms of the high purity of the products and precise control of size and composition.^[124] Unlike sol-gel or co-precipitation methods, hydrothermal synthesis gives highly crystalline products, which often do not require post-synthetic treatment such as calcination or annealing.

Hydrothermal (or solvothermal, when solvents other than water are used) reactions are based on the controlled dissolution of inorganic or organic precursors inside a pressurised vessel. The reaction is performed at a temperature higher than the boiling point of the solvent at a pressure far above the ambient value. The closed system allows the progressive increase of pressure, which has to be estimated prior to the reaction for safety reasons. Reaction conditions are often not supercritical, with most of the hydrothermal and solvothermal synthesis performed below the critical temperature of the solvent.^[125] Despite the relatively low reaction temperature compared to solid state reactions (373 - 513 K are the typical values for industrial or laboratory operations),^[126] the autogenous pressure reaches particularly high values, up to 10 MPa. Under these conditions many types of reaction are possible such as phase transformation reactions, crystallisation and precipitation.^[127]

To sustain these high values of pressure, hydrothermal/solvothermal reactors are PTFE-lined stainless steel autoclaves, sealed using bolts or screw cup systems. PTFE is employed for its remarkable chemical and thermal resistance. Overall, the autoclave is a closed and “blind” system. The control of the reaction is possible through indirect parameters, which can be classified as “internal” when related to the reaction system (concentration, pH value, time, pressure, organic additives or templates) or “external”, such as the modes of input energy or heating transfer. Zhang *et al.* classified two main hydrothermal routes: a first based on the initial precursor, grouped as recrystallisation of metastable precursors (RMP) such as amorphous colloids or small-size nanocrystals, reshaping bulk materials (RBM), indirect-supply reaction source (ISRS) and decomposition of single-source precursor (DSSP); A second classification involves the control of the internal conditions, distinguishing the reactions on the basis of the use of organic additive, template or substrate.^[128]

1.8.2 Microwave chemistry

Microwaves (MW) are defined as the portion of the electromagnetic spectrum ranging from 0.3 - 300 GHz in frequency, between the infrared and radio wave regions. All microwave instruments must work at a fixed frequency of 2.45 GHz ($\lambda=12.24$ cm) unless specifically authorized.^[129] The application of microwave heating to synthesis reactions has been defined as a breakthrough technology for

chemistry, due to its rapidity and reduction in energy consumption. The heating provided by microwave irradiation is uniform, volumetric and faster compared to conventional methods (conductive or convective heat transfer). Even in comparison with other radiative processes, the high heat rates of microwaves are due to the dielectric conversion of the electromagnetic radiation into heat. MW dielectric heating is based on two different mechanisms, dipolar polarisation and ionic conduction.^[130] Dipolar polarisation occurs when polar molecules (such as water) orientate following application of an alternating electric field (MW radiation). The electromagnetic field oscillations are relatively rapid, generating a difference in phase which ultimately results in rotation, frictions and collisions between the molecules with release of thermal energy.^[131] In the case of conduction, the alternate oscillation of charge carriers in solution following the microwave field generates an electrical or ion current. The collisions between the charged species with the surrounding molecules cause dissipation of the current and consequently dispersion of heat in the material by Ohm's law.^[132] In the absence of a conduction contribution, dielectric heating is the principal heating mechanism and the capacity of a molecule to be heated by MW irradiation can be estimated by considering its dielectric constant (ϵ'), which describes the ability of dipolar species to be polarised in an electric field and then store electromagnetic energy, and the dielectric loss factor (ϵ''), indicating the conversion efficiency from electromagnetic to thermal energy. The ratio of these two opposite terms, referred as to tangential loss (eq. 1.1), provides a quantification of the efficacy of microwave heating for a specific material or solvent at a given frequency and temperature, to which the tangential loss ($\tan\delta$) is strictly related:

$$\tan\delta = \frac{\epsilon''}{\epsilon'} \quad (\text{eq. 1.1})$$

Temperature and frequency also affect the MW penetration depth, which is defined as the point where 37% of the initially irradiated microwave power is still present.^[133] The penetration depth is inversely proportional to the tangential loss and it is the limiting parameter for the potential scale-up of microwave reactors. At room temperature, microwaves can penetrate water and most other organic solvents at a depth of only a few centimetres.

Unlike other heating processes, microwave irradiation is not able to induce chemical reactions by direct radiation absorption because of the low energy of the MW photons (10^{-5} eV at 2.45 GHz), even lower than Brownian motion and affecting only rotational movement of molecules in solution.^[134] The selection of the solvent plays a crucial role in microwave-assisted chemistry. Each solvent has a different behaviour under MW irradiation, defined by its own value of tangential loss. Indicatively, the polarity of the solvent is directly proportional to the absorption of microwave energy, with rapid increases of the temperature and the reaction rate as a consequence.

Microwave heating started with pioneering work in the late 80's, often using simple domestic microwave ovens (DMO) and modifying them to be more resistant to the laboratory conditions.^[135,136] The rapid development of the technique led to more refined instruments, such as microwave furnaces for heat treatments. Due to the dispersion of the different propagation modes over the entire cavity, the power density of the electromagnetic field is low compared with the cavity volume. The latest development is the selection of a single-mode, using self-tuning devices such as a circular waveguide, which allows the concentration of the power density in a smaller volume increasing the process efficiency.

1.8.3 MW-assisted hydrothermal/solvothermal synthesis

The application of microwaves to solvothermal and hydrothermal processes leads to incredible advantages compared to conventional heating, such as reduced processing time, with time scales reduced to minutes from the several hours or days of the conventional processes. In general, the resulting products present decreased particle size or narrower particle size distribution. When microwave dielectric heating is applied to a closed reaction system under pressurised conditions, the rate of chemical reaction is enhanced due to the increase of the system temperature. The solvents reach temperatures higher than the conventional boiling point, with a related effect on the autogenous pressure. The system is rapidly heated to a temperature that is in turn governed by the pressure.^[137]

MW-assisted hydrothermal synthesis requires a closed vessel made of a high-strength and thermal resistant polymeric material transparent to microwaves, such as polyetherimide, with a design similar to that of stainless steel autoclaves

used for conventional hydrothermal chemistry. These autoclaves were initially employed for microwave digestion processes, used for the dissolution of heavy metals in acidic media prior to further elemental analysis. In most modern microwave synthesis reactors, time and temperature are programmable. This last parameter is controlled by modulation of the microwave power and the experimental conditions can be perfectly optimized. However, the short penetration depth of MWs is a limiting parameter for reactor design, reducing also the product yield. Considering the high cost of dedicated MW reactors, MW-assisted techniques are still difficult to scale-up. Despite the development of more sophisticated microwave systems, the acid digestion reactor remains useful given high yields and the relative economic affordability. The use of such an “autoclave” has the same restrictions as conventional stainless steel autoclaves, with the internal conditions of the reaction impenetrable for observation. Moreover, microwave synthesis presents several challenges, for example direct control of essential parameter such as temperature and pressure is difficult (at least with less-sophisticated reactor designs), the decrease of the selectivity and reproducibility due to the increase reaction rate, and ultimately the concrete risk of explosion, due to the lower thermal and mechanical resistance of the polymeric enclosure. Non-modulated microwave heating results in an exponential heating rate, with total loss of control on pressure and temperature. Mismanagement in the reaction conditions and the prolonged exposure to microwave irradiation can seriously undermine the structural integrity of the autoclave. The challenge of the control of this synthesis approach is a relevant part of this thesis project.

1.9 Polyelectrolyte multilayers (PEMs)

“Because polymers are typically flexible molecules, the resulting superlattice architectures are somewhat fuzzy structures”

Prof. G. Decher

Polyelectrolyte Multilayers (PEMs or rarely PEMU) are macromolecular self-assembled structures composed of different polymeric species bound together mainly by electrostatic interaction. The simple assembly procedure and the large variety of polymers available make PEMs a versatile method for the production of multifunctional coatings, with precise control of thickness, chemical, structural and morphological properties at the nanometric scale.

Multilayer assembly is based on the alternate adsorption of polyelectrolyte species on a surface, where the only requirement is the presence of electrical or electrostatic charges. The principal interaction between polyelectrolytes is of an electrostatic nature. Polyelectrolytes possess naturally occurring electrical charges along their polymer backbone, due to the presence of charged or polarisable functional groups. The mutual interactions between different polyelectrolytes have been extensively studied in the past for the formation of polymer complexes in aqueous solution, more from a rheological and hydrodynamic point of view rather than for practical application purposes. However, Decher, Lvov and Moewald became aware of the possibility to harness the electrostatic interactions of oppositely charged polyelectrolytes to build ordinate self-assembled multilayers and create a stable coating.^[138] From that moment, the study on polyelectrolytes focused on the development of new potential applications exploiting all the possible combinations of and properties of this class of polymers.

The alternate deposition of oppositely charged or, generally speaking, interacting polyelectrolytes is defined as the Layer-by-Layer (LbL) technique, also termed Electrostatic Self-Assembly (ESA) or fabrication of an Ionic Self-Assembled Monolayer (ISAM)^[139] in early reports. LbL coating operations are based on the alternate contact of the substrate with different species. This deposition procedure could be described as self-assembly based on adsorption equilibria of interacting species. The principal (and the strongest) driving force for this

assembly is electrostatic. Oppositely charged polyelectrolyte species interact with the surface and between each other. The step-by-step deposition has also been found effective for other kinds of interaction, such as hydrogen or covalent bonding between macromolecules. For example, when substrate and polyelectrolyte possess the same sign of charge, eventual adhesion occurs by means of non-ionic bonding, such as hydrophobic interactions.^[140]

The original and most common technique for the application of the multilayer to a surface is dip coating, achieved by the alternate immersion of the substrate in different polyelectrolyte solutions, as shown in the schematic in Figure 1.6. Rinsing steps are aimed to remove the weakly bounded molecules, providing a stable layer for further deposition steps and hence reinforcing the structure of the whole multilayer. Other conventional deposition techniques, such as spray^[141] and spin coating^[142,143,144] have been successfully applied to PEM deposition processes.

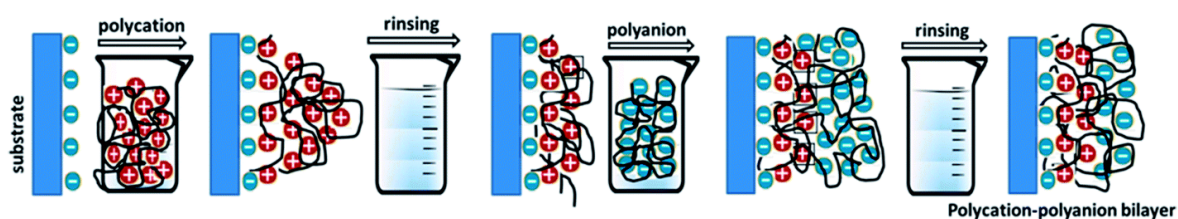


Figure 1.6: Scheme of a typical Layer-by-Layer (LbL) dip coating with immersion in oppositely charged polyelectrolyte solution.^[145]

The simple production of a PEM coating by LBL made this technique particularly versatile and useful in multiple technological applications. The control of the surface design features allows the use of PEM in optoelectronics,^[146,147] tissue engineering,^[148] electrocatalysis,^[149] nanofluidics,^[150, 151] drug delivery^[152,153] and chemical and biochemical sensing.^[154, 155]

1.9.1 Polyelectrolytes

Polyelectrolytes (PEs) are macromolecule with ionic or charged carrier groups along their backbone. Because of their unique structure, PE are the only class of polymers which can be easily solubilised in water. Polyelectrolytes are generally classified into three main categories. A first basic classification is between natural and synthetic PEs. The other categories generally involve the behaviour of the charged moieties of the polymer. Polyelectrolytes are divided in positive (or

cationic) and negative (or anionic), depending on the nature of the charge. Positive and negative PEs are generally referred as polycation and polyanion, respectively.

Finally, polyelectrolytes can be "weak" or "strong" depending on the behaviour of the charge as a function of the pH of the surrounding environment. This is probably the most important classification from an applied perspective. The charges on a weak polyelectrolyte are affected by pH, since the charged functional groups can be deprotonated or reduced, causing partial dissociation or ionisation of the charged group of the polyelectrolyte in water. The distribution of the charges on a weak polyelectrolyte is subjected to continuous fluctuation in time and space, making only an average distribution, possible from thermodynamic parameters.^[156]

Conversely, the charged functional groups carried on a strong polyelectrolyte are not affected by a change in pH. Strong polyelectrolytes are also classified as "quenched", since their charge is impossible to move along the backbone chain by altering the pH of the solution in which the polymer is dissolved. For the opposite reason, weak polyelectrolytes have been also defined "annealed".^[156]

1.9.2 Parameters influencing PEM structures

The secret of the versatility of the assembled multilayers resides in the diverse properties accessible through the principal assembly conditions such as pH, ionic strength or the selected combination of polyelectrolytes. The assembly conditions are fundamental for surface properties such as chemical functionality and the mechanical compliance of the coating. All the parameters responsible for the interactions between the polyelectrolyte influence the stability of the multilayer structure both during the self-assembly process and after, affecting the long-term stability. Mechanical, chemical, electrical or thermal external stimuli can alter the structure of the multilayer during or after the deposition process. This property is particularly useful for sensor or microfluidic applications, in which the external stimuli provide a switchable and reversible response. ^[157] Another example is the controlled destabilisation of part or of all the multilayer structure, sought in some particular application such as chemical gating, drug delivery ^[158, 159] and selective removal of the PEM coating when damaged or after the complete release of molecules or particles carried in its structure.

The chemistry of the multilayer defines its properties, in particular by the functional groups along the backbone chain. The nature and the behaviour in solution of the pendant groups define the classification of the polyelectrolytes in the categories of weak/strong and cationic/anionic and determine the interactions between the polymer chains in the multilayer structure. The properties of the coating can be tuned using different combinations of polyelectrolytes. The chemistry and the mutual interactions between different species affect the final properties.^[160] The selection of polyelectrolytes also affects the adsorption and growth kinetic of the multilayer. The layer self-assembly can follow linear or exponential growth kinetics. The linear growth is typical of polyelectrolytes characterised by strong interactions regardless of the number of layers,^[161] producing a stratified structure with no diffusion or interpenetration between chains of different layers.^[162] On the other hand, the layer thickness for exponentially growing multilayers can reach several microns after deposition of 10-15 bi-layers.^[163] with weaker interactions between the different polyelectrolytes and more hydrated and soft structures compared to linearly grown films.^[161, 164] This exponential growth behaviour is characteristic of naturally-derived polyelectrolytes, such as the hyaluronic acid/poly(L-lysine) system.^[165] According to Salomaki *et al.*, linear growth could be considered as an exponential build-up in which the diffusion rate is not sufficient to transport the polymer throughout the entire thickness of the layer.^[166]

Controlling the pH of the polyelectrolyte solution during assembly is a simple method to modify the conformational structure of a multilayer composed of weak polyelectrolytes. The presence of easily dissociable acid and alkaline functional groups on the chains is the cause of the pH-sensitive charge density or degree of protonation, with direct consequence on the intermolecular interactions in the self-assembly. The pKa of the dissociable groups is hence a key parameter for properties of the resulting multilayer. Ionic strength is another powerful parameter, influencing both the assembly process and the stability of the multilayer structure after its formation. Since polyelectrolytes in aqueous solution are always associated with counterions,^[167] these affect the charge compensation equilibrium. At low ionic strength the charge compensation depends uniquely on the oppositely charged couple of polyelectrolyte, defined as intrinsic compensation. The increase of the ionic strength leads to a shift towards extrinsic compensation, dependant on the presence of the counterions.^[168] For these

reasons, type, charge and concentration of counterions all affect important properties of the multilayer, such as thickness, stiffness and swelling behaviour.^[169, 170]

To exploit the modification induced by the ionic strength, electrolyte salts are added directly to the polyelectrolyte solution or as an alternative to the rinsing bath step or even at the end of the deposition process, exposing the multilayer to the concentrated salt solution as a post-assembly treatment. Ionic strength is generally modified using NaCl, with increase of the multilayer thickness directly related to the concentration used.^[171, 172, 173] The effect of the counterions is reversible, which is particularly useful for the production of stimuli-responsive PEM in biomedical applications.^[174]

Other minor parameters, such as the concentration of the polyelectrolyte, the temperature and the time of exposure to the polyelectrolyte solution during the LbL deposition influencing the self-assembly process and the multilayer structure. Concentration is generally directly proportional to the amount of deposited material and consequently to the resulting layer thickness. Experimental evidence showed the presence of a minimum value for stable layer adsorption^[175] as well as a saturation value, above which the increase of the polyelectrolyte concentration is not directly proportional to the thickness since different adsorption kinetics occur.^[175] The molecular weight of the polyelectrolyte chains as well as the degree of structural branching, does not significantly affect the multilayer assembly unless below a certain mass. In such a case, the polyelectrolyte is not able to participate in the cooperative interactions within the structure and is stripped off the multilayer if exposed to an oppositely charged polyelectrolyte with higher molecular weight, forming a free-complex in solution.^[176] Temperature is not particularly exploited as an assembly parameter. The increase of temperature during the assembly process alters the deposition kinetics, turning linear growth into exponential, depending on the pair of polyelectrolytes chosen.

1.9.3 PEM on filtration membranes

As a versatile and simple method to functionalise surfaces, PEMs found application in water treatment facilities and other filtration environments. They function as active and multifunctional coatings to improve specific properties, such as selective rejection and permeability, and to impart novel properties to surfaces, for example anti-adhesive or anti-bacterial functionalities. The water-based deposition technique and the high level of control and reproducibility on the coating parameters such as thickness make LbL deposition of PEM particularly appealing for modification of active surfaces. Depending on the final application, the multilayer coating could be highly permeable (for example in sensing applications or in filtration devices) or dense and impermeable, for instance in anticorrosion protection. Modifying membrane surfaces using polyelectrolytes is a simple process, with the layer-by-layer deposition facilitated by the natural charges occurring on polymer and ceramic membrane surfaces and the high compatibility between a polymeric surface and the polyelectrolyte layers. Thickness, density and porosity of the multilayer could be controlled at the nanometric scale, tailoring the composition and the properties of the active skin layer of the membranes. ^[177]

The potential applications of PEM-composite membrane are enormous,^[178] with several examples reported in reverse osmosis for water desalination, forward osmosis, low-pressure filtration processes, stimuli-responsive membranes, pervaporation dehydration ^[179] and even self-standing polyelectrolyte-based porous membrane. Fabrication of NF membrane for selective ion removal is to date the most reported application,^[180,181,182] with significant development in production of solvent resistant NF membranes (SRNF)^[183] and ion-exchange membranes (IEM).^[184]

One of the only weak points for the applicability of the PEMs in filtration is the unavoidable reduction of the pure water permeability due to the deposition of additional matter on the porous surface of the membrane. Depending on the final application, the permeability could be sacrificed for other properties (low-fouling) or increase of the selectivity, for example producing a NF membrane using a MF or UF membrane as support.^[183] When the increase of permeability is the main purpose of the modification, open or porous layer structures are preferred. Another concern about the long-term application of PEM-modified membranes is

their stability under filtration conditions, with the membrane exposed to changes in pH and ionic strength, or the presence of fouling agents with the subsequent need of cleaning processes. Similarly to other coatings, PEMs have been found to be very useful for the prevention of microorganism adhesion or even their eradication. The issue of bacterial contamination has dramatic consequences not only in filtration operations (establishment of biofouling) but also in a large amount of applications of biomaterials, such as biomedical devices (e.g. body tissue replacements such as catheters, vascular implants and heart valves).

1.9.4 PEM in antifouling and antimicrobial strategies

The action of different antifouling materials could be also combined in synergy, integrating nanoparticles, molecules and other polymers into the PEM structure. The most reported antifouling strategy with PEMs consists in the deposition of highly hydrated and "soft" molecules, principally polyethylene glycol (PEG).^[185] This strategy also proved to be effective when a strong polyanion is applied as a top layer (such as PSS or PAA).^[186]

Three main strategies are implemented in using PEM for the production of antibacterial coatings:^[187]

- realisation of an adhesive resistant surface to prevent the first step of bacterial interaction with the surface;
- a contact-killing approach, in which the functionalised surface has a physical bactericidal action;
- a release-killing approach, in which the multilayer coating gradually releases antimicrobial agents.

Contact-killing strategy mainly develops the interaction between polycation and the negatively charged outer membrane of most bacterial cells which are composed of acidic polysaccharides. The electrostatic interactions disrupt the integrity of the cell membranes, leading to leakage of intracellular components and the microorganism death. For instance, a detailed mechanism for the alteration of the outer membrane integrity in Gram-negative species involves the polycationic chains displacing Ca^{2+} , which is responsible for the stable contact between the outer membrane and the cell wall. The decrease in Ca^{2+} concentration causes the loss of integrity of the negatively charged outer

protective layer, also allowing the PE chains to penetrate the inner layer of the cell, with further deprivation of vital cytoplasmic components.^[188]

The release-killing approach is based on the release of agents in the surrounding environment. The release could occur by diffusion of the agents from the multilayer structure or due to the coating degradation. The most notorious approach for release-killing is the integration of Ag nanoparticles in a multilayer, in metallic (Ag^0) or ionic (Ag^+) form.^[189]

The production of a surface resistant to bacterial adhesion is generally based on two common properties of cytophobic surfaces: surface hydrophilicity and stiffness. Following this path, natural hydrophilic polyelectrolytes such as chitosan, heparin and hyaluronic acid or the integration by adsorption on the coating or functionalisation by grafting of highly hydrating molecules, such as PEG^[190] or polyzwitterionic molecules (poly(sulfobetaine methacrylate)^[191] to the polyelectrolytes have been reported to prevent bacterial adhesion.^{[192],[193]}

Stiffness, which is directly related to the multilayer structure, seems to affect the bacterial adhesion mechanism. The elastic modulus of the surface can be modulated by changing the architecture of the PEM without significantly changing the chemical properties of the film. More rigid and compact layers have been reported to increase the anti-adhesive power towards some bacteria.^[194] However, the exact correlation between elastic modulus of the surface and bacteria adhesion is still under debate.^{[195],[196]}

1.10 Nanocomposite coating by LbL technique

LbL technique is not limited to the self-assembly of charged polymers. The same approach can be adopted for the fabrication of organic/inorganic nanocomposite thin films, functionalising potentially any kind or shape of surface. The simple and inexpensive technique has been reported useful in the deposition or integration of several nanoparticles and other nanostructures, such as nanotubes and nanowires, different molecules and also biological polysaccharides, polypeptides, nucleic acids and different proteins have been successfully integrated in composite multilayers.^[197] This method has been widely applied to integrate binary inorganic colloids (e.g., sulfides, selenides, tellurides, and oxides of Cd, Pb, Ti, Fe, Mn, and Zn) in the multilayer structure, producing coatings with superhydrophobic, antireflective, antibacterial or catalytic properties.^[198]

The general assembly procedure requires the deposition of a first monolayer of polyelectrolyte, followed by exposition to a colloidal dispersion of particles with opposite charges on their surface. The strong adsorption of the nanoparticles onto the first polyelectrolyte multilayer is ensured by the combination of both electrostatic and hydrophobic interactions.^[199] Furthermore, the high surface charge density of the polyelectrolyte layer prevents the formation of a thick and rough coating of particles. The stability of the bonding between nanostructures and polyelectrolyte can be enhanced by functionalising the inorganic surface or by grafting suitable functional groups onto the polyelectrolytes.^[200] Thermal or chemical post-treatment can further enhance the mechanical stability and the immobilisation of the nanoparticles by cross-linking processes.

Several strategies have been proposed to improve the adhesion. *In situ* formation of nanoparticles within the multilayer structure is a common strategy for chemical reactive nanoparticles, such as Au, Ag, Pt or Cu. The multilayer can be exposed to a solution of metallic ions or the nanoparticle precursor can be mixed in solution with one of the constituent polyelectrolytes.^[201] The process is followed by exposition of the multilayer to a reducing agent, with the particles directly integrated in the macromolecular structure. The use of strong adhesive polyelectrolyte such as PEI has also proved efficient,^[189] with the formation of polycationic metal complexes due to the bonding between transition metal cations and the primary, secondary and tertiary amine groups of the polyelectrolyte.^[202] Apart from the formation of multilayers, due to their nature polyelectrolytes can be used to provide steric and electrostatic stabilisation for the production of colloidal suspensions. In the past, studies on the stabilisation of anionic precursor complexes of Au, Pd and Ag using polycations with quaternary ammonium functionalities (e.g. PDDA) have been reported.^[203]

1.11 Aim of the project

The design of nanostructured inorganic photoactive materials for water treatment applications is the main goal of this project. TiO_2 was chosen as target material because of its low cost, high abundance and relatively low toxicity compared to other photocatalysts.

The application of the microwave heating is aimed to fulfil the requirement of energy saving procedure, providing an extremely rapid synthetic technique which would benefit from the kinetics related to the fast heating process. Synthesis of colloidal objects with larger size than nanoparticles is sought in order to avoid the environmental and health concern related to the use of nanoparticles in water treatments, such as recovery difficulties, bioaccumulation and long-term effects, which fully comprehension has not yet been assessed.

The second goal of this project is the development of TiO_2 particles able to efficiently absorb solar light and convert it into electron-hole pairs for the activation of photocatalytic processes. This would overcome the intrinsic physical limit of TiO_2 , active only under UV light, reason why only 5% of the solar spectrum radiation can be efficiently exploited. Simple and cost-effective methods with relatively low impact on the environment, such as annealing under low content or oxygen-free atmospheres, have been privileged in the selection.

The last aim is the integration of TiO_2 for the development of a multifunctional coating for application in water and wastewater treatment processes, with specific focus on low-pressure filtration membrane. The inorganic particles will be anchored to the active layer of ultrafiltration membrane by means of simple electrostatic interactions. Other type of surfaces (Mylar, glass) will be used to better understand the adhesion mechanism, to characterise the coatings and to study their final properties and the influence of different substrates.

1.12 References

- ¹ World Health Organisation, UN-water global analysis and assessment of sanitation and drinking water (GLAAS) 2014 report: investing in water and sanitation: increasing access, reducing inequalities. Switzerland, 2014.
- ² M.T.M. Pendergast, E.M.V. Hoek, A review of water treatment membrane nanotechnologies, *Energy Environ. Sci.*, 2011, **4**, 1946–1971.
- ³ J. Zhu, Y. Su, X. Zhao, Y. Li, R. Zhang, X. Fan, Y. Ma, Y. Liu, Z. Jiang, Constructing zwitterionic ultrafiltration membrane surface via multisite anchorage for superior long-term antifouling properties. *RSC Adv.*, 2015, **5**, 40126–40134.
- ⁴ S.S. Sablani, M.F.A. Goosen, R. Al-Belushi, M. Wilf, Concentration polarization in ultrafiltration and reverse osmosis: a critical review, *Desalination*, 2001, **141**, 269-289.
- ⁵ Z.F. Cui, Y. Jiang, R.W. Field: Fundamentals of Pressure-Driven Membrane Separation Processes, in Z.F. Cui, H. S. Muralidhara, Membrane Technology, Elsevier, 2010.
- ⁶ R. Baker, *Membrane Technology and Applications*, Wiley (pp. 303-324)
- ⁷ R. Rosberg, Ultrafiltration (new technology), a viable cost-saving pretreatment for reverse osmosis and nanofiltration - A new approach to reduce costs, *Desalination*, 1997, **110**, 107-114.
- ⁸ M. Jahanshahi, A. Rahimpour, Developing thin film composite poly(piperazine-amide) and poly(vinyl-alcohol) nanofiltration membranes, *Desalination*, 2010, **257**, 129–136.
- ⁹ H. Karkhanechi, F. Razi, Improvement of antibiofouling performance of a reverse osmosis membrane through biocide release and adhesion resistance, *Separ. Purif. Technol.*, 2013, **105**, 106–113.
- ¹⁰ S.S. Kulkarni, E.W. Funk, N. Li, *Ultrafiltration*. In: Ho WSW, Sirkar KK (eds) Membrane Handbook, Van Nostrand, 1992.
- ¹¹ R. Baker, *Membrane Technology and Application* (2nd ed.), Wiley, 2004.
- ¹² B.A. Pulidoa, C. Waldrona, M.G. Zolotukhinb, S.P. Nunes, Porous polymeric membranes with thermal and solvent resistance, *J. Membr. Sci.*, 2017, **539**, 187-196.
- ¹³ S. Luque, D. Gómez, J.R. Álvarez, Industrial applications of porous ceramic membranes (pressure-driven processes), in: R. Mallada, M. Menendez (Eds.), Membrane Science and Technology, 13 Elsevier, 2008, pp. 177–216.
- ¹⁴ K.C. Khulbe, C.Y. Feng, T. Matsuura, *Synthetic Polymeric Membranes, Characterization by Atomic Force Microscopy*, Springer-Verlag Berlin, 2008.
- ¹⁵ M. Mulder, *Basic Principle of Membrane Technology*, Kluwer Academic Publisher, 1996.
- ¹⁶ L. Wang, J. Chen, Membrane and Desalination Technology (Handbook of Env. Eng. Vol. 13), Humana Press, 2003.
- ¹⁷ B. McVerry, J. Temple, Fabrication of Low-Fouling Ultrafiltration Membranes Using a Hydrophilic, Self-Doping Polyaniline Additive, *Chem. Mater.* 2013, **25**, 3597–3602.
- ¹⁸ W.J. Koros, Y. H. Ma, T. Shimidzu, Terminology for membranes and membrane processes (IUPAC Recommendations 1996), *Pure App. Chem.*, 1996, **6**, 1479-1489.
- ¹⁹ M. Hadidi, A.L. Zydney, Fouling behavior of zwitterionic membranes: Impact of electrostatic and hydrophobic interactions. *J. Membr. Sci.*, 2014, **452**, 97–103.
- ²⁰ G. De Luca, F. Bisignano, F. Paone, S. Curcio, Multi-scale modeling of protein fouling in ultrafiltration process. *J. Membr. Sci.*, 2014, **452**, 400–414.
- ²¹ R. Komlenic, Rethinking the causes of membrane biofouling. *Filtr. Sep.*, 2010, **47**, 26–28.
- ²² G. Amy, Fundamental understanding of organic matter fouling of membranes. *Desalination*, 2008, **231**, 44–51
- ²³ Z. Lewandowski, L.V. Evans, *Structure and function of biofilms*, Biofilms: recent advances in their study and control, Harwood Academic Publishers, 2000.
- ²⁴ A. Conte, G.G. Buonocore, A. Bevilacqua, M. Sinigaglia, M.A. Del Nobile, Immobilization of Lysozyme on Polyvinylalcohol Films for Active Packaging Applications, *J. Food Prot.*, 2006, **69**, 866–870.

- ²⁵ E.R. Kenawy, S.D. Worley, R. Broughton, The Chemistry and Applications of Antimicrobial Polymers: A State-of-the-Art Review, *Biomacromolecules*, 2007, **8**, 1359–1384.
- ²⁶ J. Mueller, R. H. Davis, Protein fouling of surface-modified polymeric microfiltration membranes, *J. Membr. Sci.*, 1996, **116**, 47–60.
- ²⁷ C.-C. Ho, A. L. Zydney, Protein Fouling of Asymmetric and Composite Microfiltration Membranes, *Ind. Eng. Chem. Res.*, 2001, **40**, 1412–1421.
- ²⁸ B. Van der Bruggen, M. Mänttari, M. Nyström, M. Drawbacks of applying nanofiltration and how to avoid them: A review. *Sep. Purif. Technol.*, 2008, **63**, 251–263.
- ²⁹ T.F. Speth, R.S. Summers, A.M. Gusses, Nanofiltration foulants from a treated surface water. *Env. Sci. Technol.*, 1998, **32**, 3612–3617.
- ³⁰ T. Boudou, T. Crouzier, K. Ren, G. Blin, C. Picart, Multiple Functionalities of Polyelectrolyte Multilayer Films: New Biomedical Applications, *Adv. Mater.*, 2010, **22**, 441–467.
- ³¹ S. Mulyati, R. Takagi, A. Fujii, Y. Ohmukai, T. Maruyama, H. Matsuyama, Improvement of the antifouling potential of an anion exchange membrane by surface modification with a polyelectrolyte for an electro dialysis process, *J. Membr. Sci.*, 2012, **417-418**, 137-143.
- ³² S.K. Hong, M. Elimelech, Chemical and physical aspects of natural organic matter (NOM) fouling of nanofiltration membranes. *J. Membr. Sci.*, 1997, **132**, 159–181.
- ³³ C.Y. Tang, J.O. Leckie, Membrane independent limiting flux for RO and NF membranes fouled by humic acid. *Env. Sci. Technol.*, 2007, **41**, 4767–4773.
- ³⁴ A.D. White, A.K. Nowinski, W. Huang, A.J. Keefe, F. Suna, S. Jiang, Decoding nonspecific interactions from nature, *Chem. Sci.*, 2012, **3**, 12, 3488-3494.
- ³⁵ F. Gao, G. Zhang, Q. Zhang, X. Zhan, F. Chen, Improved antifouling properties of Poly(Ether sulfone) membrane by incorporating the amphiphilic comb copolymer with mixed Poly(Ethylene glycol) and Poly(Dimethylsiloxane) brushes. *Ind. Eng. Chem. Res.*, 2015, **54**, 8789.
- ³⁶ S. Zhenga, Q. Yangb, B. Mi, Novel antifouling surface with improved hemocompatibility by immobilization of polyzwitterions onto silicon via click chemistry, *Appl. Surf. Sci.*, 2016, **363**, 619–626.
- ³⁷ J. Chapman, F. Regan, Nanofunctionalized Superhydrophobic Antifouling Coatings for Environmental Sensor Applications - Advancing Deployment with Answers from Nature, *Adv. Eng. Mat.*, 2012, **14**, B175-B184.
- ³⁸ C.M. Kirschner, A.B. Brennan, Bio-inspired antifouling strategies. *Annu. Rev. Mater. Res.*, 2012, **42**, 211–229.
- ³⁹ S.-T. Kang, A. Subramani, E.M.V. Hoek, M.A. Deshusses, M.R. Matsumoto, Direct observation of biofouling in cross-flow microfiltration: mechanisms of deposition and release, *J. Membr. Sci.*, 2004, **244**, 151–165.
- ⁴⁰ H. Ridgway, K. Ishida, G. Rodriguez, J. Safarik, T. Knoell, R. Bold, Biofouling of membranes: membrane preparation, characterization, and analysis of bacterial adhesion, *Biofilms*, 1999, **310**, 463–494.
- ⁴¹ M.R. Nejadnik, H.C. van der Mei, W. Norde, H.J. Busscher, Bacterial adhesion and growth on a polymer brush-coating, *Biomaterials*, 2008, **29**, 4117–4121.
- ⁴² I. Banerjee, R.C. Pangule, R.S. Kane, Antifouling coatings: recent developments in the design of surfaces that prevent fouling by proteins, bacteria, and marine organisms, *Adv. Mater.*, 2011, **23**, 690–718.
- ⁴³ E. Kiss, E.T. Heine, K. Hill et al., Membrane Affinity and Antibacterial Properties of Cationic Polyelectrolytes With Different Hydrophobicity, *Macromol. Biosci.*, 2012, **12**, 1181-1189.
- ⁴⁴ S. Liu, M. Lim, R. Fabris, C. Chow, M. Drikas, R. Amal, TiO₂ photocatalysis of natural organic matter in surface water: impact on trihalomethane and haloacetic acid formation potential. *Env. Sci. Technol.*, 2008, **42**, 6218-6223.
- ⁴⁵ S.N. Frank, A.J. Bard, Heterogeneous photocatalytic oxidation of cyanide ion in aqueous solution at TiO₂ powder, *J. Am. Chem. Soc.*, 1977, **99**, 303-304.
- ⁴⁶ B. Srikanth, R. Goutham, R. Badri Narayan, A. Ramprasath, K.P. Gopinath, A.R. Sankaranarayanan, Recent advancements in supporting materials for immobilised photocatalytic applications in waste water treatment, *J. Env. Manag.*, 2017, **200**, 60-78.

- ⁴⁷ J.O. Tijani, O.O. Fatoba, G. Madzivire, L.F. Petrik, A Review of Combined Advanced Oxidation Technologies for the Removal of Organic Pollutants from Water, *Water Air Soil Pollut.*, 2014, **225**, 2102 (pp 1-30).
- ⁴⁸ A. Di Paola, E. García-López, G. Marci, L. Palmisano, A survey of photocatalytic materials for environmental remediation, *J. Hazard. Mater.*, 2012, **211–212**, 3–29.
- ⁴⁹ X. Chen, S. Shen, L. Guo, S.S. Mao, Semiconductor-based Photocatalytic Hydrogen Generation, *Chem. Rev.*, 2010, **110**, 6503–6570.
- ⁵⁰ Q. Lu, Y. Yu, Q. Ma, B. Chen, H. Zhang, 2D Transition-Metal-Dichalcogenide-Nanosheet-Based Composites for Photocatalytic and Electrocatalytic Hydrogen Evolution Reactions, *Adv. Mater.*, 2016, **28**, 1917–1933.
- ⁵¹ G.M. Whitesides, Nanoscience, Nanotechnology, and Chemistry. *Small*, 2005, **1**, 172–179.
- ⁵² M.R. Wiesner, J.-Y. Bottero, *Environmental Nanotechnology, Applications and Impacts of Nanomaterials*, McGraw-Hill, 2007.
- ⁵³ M.J. Hajipour, K.M. Fromm, A.A. Ashkarran, D. Jimenez de Aberasturi, I. Ruiz de Larramendi, T. Rojo, V. Serpooshan, W.J. Parak, Antibacterial properties of nanoparticles, *Trends in Biotechnology*, 2010, **30**, 499-511.
- ⁵⁴ A. Thill, O. Zeyons, O. Spalla, F. Chauvat, J. Rose, M. Auffan, A.M. Flankll, Cytotoxicity of CeO₂ nanoparticles for Escherichia coli. Physico-chemical insight of the cytotoxicity mechanism. *Environ. Sci. Technol.*, 2006, **40**, 6151–6156.
- ⁵⁵ J.R. Morones, J.L. Elechiguerra, A. Camacho, K. Holt, J.B. Kouri, J.T. Ramírez, M.J. Yacaman, The bactericidal effect of silver nanoparticles, *Nanotechnology*, 2005, **16**, 2346-2453.
- ⁵⁶ X. Chen, H.J. Schluesener, Nanosilver: a nanoparticle in medical application, *Toxicol. Lett.*, 2008, **176**, 1-12.
- ⁵⁷ C.N. Lok, C.M. Ho, R. Chen, Q.Y. He, W.Y. Yu, H.Z. Sun, P.K.H. Tam, J.F. Chiu, C.M. Che, Proteomic analysis of the mode of antibacterial action of silver nanoparticles. *J. Proteome Res.*, 2006, **5**, 916-924.
- ⁵⁸ T. Nguyen, F. Roddick, L. Fan, Biofouling of Water Treatment Membranes: A Review of the Underlying Causes, Monitoring Techniques and Control Measures, *Membranes*, 2012, **2**, 804-840.
- ⁵⁹ N. Silvestry-Rodriguez, K.R. Bright, D.C. Slack, D.R. Uhlmann, C.P. Gerba, Silver as a residual disinfectant to prevent biofilm formation in water distribution systems. *Appl. Env. Microbiol.*, 2008, **74**, 1639–1641.
- ⁶⁰ A. Dror-Ehre, A. Adin, G. Markovick, H. Mamane, Control biofilm formation in water using molecularly capped silver nanoparticles. *Water Res.*, 2010, **44**, 2601–2609.
- ⁶¹ N. Cioffi, L. Torsi, Antifungal activity of polymer-based copper nanocomposite coatings, *App. Phys. Lett.*, 2004, **85**, 2417-2149.
- ⁶² J. Lellouche, A. Friedman, R. Lahmi, A. Gedanken, E. Banin, Antibiofilm surface functionalization of catheters by magnesium fluoride nanoparticles, *Int. J. Nanomed.*, 2012, **7**, 1175–1188.
- ⁶³ J.H. Braun, A. Baidins, R.E. Marganski, TiO₂ pigment technology: a review, *Prog. Org. Coat.*, 1992, **20**, 105-138.
- ⁶⁴ T.G. Smijs S. Pavel, Titanium dioxide and zinc oxide nanoparticles in sunscreens: focus on their safety and effectiveness, *Nanotechnol. Sci. Appl.*, 2011, **4**, 95-113.
- ⁶⁵ M. Skocaj, M. Filipic, J. Petkovic, S. Novak, Titanium dioxide in our everyday life; is it safe?, *Radiol Oncol.*, 2011, **45**, 227–247.
- ⁶⁶ Y. Hu, H.-L. Tsai, C.-L. Huangk, Effect of brookite phase on the anatase–rutile transition in titania nanoparticles, *Eur. Ceram. Soc.*, 2003, **23**, 691-696.
- ⁶⁷ S. Bum Kim, H.T. Hwang, S. Chang Hong, Photocatalytic degradation of volatile organic compounds at the gas–solid interface of a TiO₂ photocatalyst, *Chemosphere*, 2002, **48**, 437-444.
- ⁶⁸ M. Landmann, E. Rauls, W.G. Schmidt, The electronic structure and optical response of rutile, anatase and brookite TiO₂, *J. Phys.: Condens. Matter*, 2012, **24**, 195503.
- ⁶⁹ A. Fujishima, K. Honda, Electrochemical photolysis of water at a semiconductor electrode, *Nature*, 1972, **238**, 37-38.

- ⁷⁰ B. O'Regan, M. Graetzel, A low-cost, high efficiency solar cell based on dye-sensitized colloidal TiO₂ film, *Nature*, 1991, **353**, 737-740.
- ⁷¹ A. Sclafani, J.M. Herrman, Comparison of the Photoelectronic and Photocatalytic Activities of Various Anatase and Rutile Forms of Titania in Pure Liquid Organic Phases and in Aqueous Solutions, *J. Phys. Chem.*, 1996, **100**, 13655-13661.
- ⁷² K. Yanagisawa, J. Ovenstone, Crystallization of Anatase from Amorphous Titania Using the Hydrothermal Technique: Effects of Starting Material and Temperature, *J. Phys. Chem. B*, 1999, **103**, 7781-7787.
- ⁷³ J. Zhang, P. Zhou, J. Liu, J. Yu, New understanding of the difference of photocatalytic activity among anatase, rutile and brookite TiO₂, *Phys. Chem. Chem. Phys.*, 2014, **16**, 20382-20386.
- ⁷⁴ D.A.H. Hanaor, C.C. Sorrell, Review of the anatase to rutile phase transformation, *J. Mater. Sci.*, 2011, **46**, 855-874.
- ⁷⁵ A. Sclafani, J. M. Herrmann, Comparison of the Photoelectronic and Photocatalytic Activities of Various Anatase and Rutile Forms of Titania in Pure Liquid Organic Phases and in Aqueous Solutions, *J. Phys. Chem.*, 1996, **100**, 13655-13661.
- ⁷⁶ M. Xu, Y. Gao, E.M. Moreno, M. Kunst, M. Muhler, Y. Wang, H. Idriss, C. Woll, Photocatalytic Activity of Bulk TiO₂ Anatase and Rutile Single Crystals Using Infrared Absorption Spectroscopy *Phys. Rev. Lett.*, 2011, **106**, 138302.
- ⁷⁷ J.G. Yu, J.C. Yu, M.K.P. Leung, X.J. Zhao, W.K. Ho, J.C. Zhao, Effects of acidic and basic hydrolysis catalysts on the photocatalytic activity and microstructures of bimodal mesoporous titania, *J. Catal.*, 2003, **214**, 69-78.
- ⁷⁸ A. Panniello, M.L. Curri, D. Diso, A. Licciulli, V. Locaputo, A. Agostiano, R. Comparelli, G. Mascolo, Nanocrystalline TiO₂ based films onto fibers for photocatalytic degradation of organic dye in aqueous solution. *Appl. Catal. B*, 2012, **121-122**, 190-197.
- ⁷⁹ M.N. Chong, B. Jin, C.W.K. Chow, C. Saint, Recent developments in photocatalytic water treatment technology: a review. *Water Resources*, 2010, **44**, 2997-3027.
- ⁸⁰ R. Wang, K. Hashimoto, A. Fujishima, M. Chikuni, E. Kojima, A. Kitamura, M. Shimohigoshi, T. Watanabe, Light-induced amphiphilic surfaces, *Nature*, 1997, **388**, 431-432.
- ⁸¹ A. Fujishima, T.N. Rao, D.A. Tryk, Titanium dioxide photocatalysis, *J. Photochem. Photobiol. C*, 2000, **1**, 1-21.
- ⁸² K. Ikeda, H. Sakai, R. Baba, K. Hashimoto, A. Fujishima, Photocatalytic reactions involving radical chain reactions using microelectrodes, *J. Phys. Chem. B*, 1997, **101**, 2617-2620.
- ⁸³ K. Nakata, A. Fujishima, TiO₂ photocatalyst: Design and applications, *J. Photochem Photobiol C: Photochem. Rev.*, 2012, **13**, 169-189.
- ⁸⁴ K. Hashimoto, H. Irie, A. Fujishima, TiO₂ Photocatalysis: A Historical Overview and Future Prospects, *Jap. J. App. Phys.*, 2005, **44**, 8269-8285.
- ⁸⁵ L. Zhang, N. Zhao, J. Xu, Fabrication and application of superhydrophilic surfaces: a review, *J. Adhesion Sci. and Technol.*, 2014, **28**, 769-790.
- ⁸⁶ N. Zhou, V. Lopez-Puente, Q. Wang, L. Polavarapu, I. Pastoriza-Santos, Q.-H. Xu, Plasmon-enhanced light harvesting: Applications in enhanced photocatalysis, photodynamic therapy and photovoltaics. *RSC Adv.*, 2015, **5**, 29076-29097.
- ⁸⁷ M. Anpo, S. Kishiguchi, Y. Ichihashi, M. Takeuchi, H. Yamashita, K. Ikeue, B. Morin, A. Davidson, The design and development of second-generation titanium oxide photocatalysts able to operate under visible light irradiation by applying a metal ion-implantation method, *Res. Chem. Intermed.*, 2001, **27** (4-5), 459-467.
- ⁸⁸ J. Rashid, M.A. Barakat, S.L. Pettit, J.N. Kuhn, InVO₄/TiO₂ composite for visible light photocatalytic degradation of 2-chlorophenol in wastewater, *Environ. Technol.*, 2014, **35**, 2153-2159.
- ⁸⁹ M. Pelaez, N.T. Nolan, S.C. Pillai, M.K. Seery, P. Falaras, A.G. Kontos, P.S. M. Dunlop, J.W.J. Hamilton, J.A. Byrne, K. O'Shea, M.H. Entezari, D.D. Dionysiou, A review on the visible light active titanium dioxide photocatalysts for environmental applications, *Review Appl. Catal. B Environ.*, 2012, **125**, 331-349.
- ⁹⁰ V. Etacheri, G. Michlits, M.K. Seery, S.J. Hinder, S.C. Pillai, A Highly Efficient TiO_{2-x}C_x Nano-heterojunction Photocatalyst for Visible Light Induced Antibacterial Applications, *ACS Appl. Mater. Interfaces*, 2013, **5**, 1663-1672.

- ⁹¹ Y.W. Yao, L.H. Cui, Y. Li, N.C. Yu, H.S. Dong, X. Chen, F. Wei, Electrocatalytic Degradation of Methyl Orange on PbO₂-TiO₂ Nanocomposite Electrodes, *Int. J. Environ. Res.*, 2015, **9**, 1357-1364.
- ⁹² R.H. Zhang, Q. Wang, Q. Li, J. Dai, D.H. Huang, First-principle calculations on optical properties of C–N-doped and C–N-codoped anatase TiO₂, *Physica B*, 2011, **406**, 3417–3422.
- ⁹³ H.A. Atwater, A. Polman, Plasmonics for improved photovoltaic devices, *Nat. Mater.*, 2010, **9**, 205-213.
- ⁹⁴ I. Tamiolakis, I.N. Lykakis, G.S. Armatas, Mesoporous CdS-sensitized TiO₂ nanoparticle assemblies with enhanced photocatalytic properties: Selective aerobic oxidation of benzyl alcohols, *Cat. Today*, 2015, **250**, 180–186.
- ⁹⁵ A.G. Thomas, W.R. Flavel, R. Stockbauer, S. Patel, M. Gratzel, R. Hengerer, Resonant photoemission of anatase TiO₂ (101) and (001) single crystals, *Phys. Rev. B*, 2003, **67**, 035110.
- ⁹⁶ V. Etacheri, M.K. Seery, S.J. Hinder, S.C. Pillai, Oxygen Rich Titania: A Dopant Free, High Temperature Stable, and Visible-Light Active Anatase Photocatalyst, *Adv. Funct. Mater.*, 2011, **21**, 3744-3752.
- ⁹⁷ P.C. Maness, S. Smolinski, D.M. Blake, Z. Huang, E.J. Wolfrum, W.A. Jacoby, Bactericidal activity of photocatalytic TiO₂ reaction: toward an understanding of its killing mechanism. *Appl. Environ. Microbiol.*, 1999, **65**, 4094–4098.
- ⁹⁸ K. Peters, R.E. Unger, C.J. Kirkpatrick, A.M. Gatti, E. Monari, Effects of nano-scaled particles on endothelial cell function in vitro: studies on viability, proliferation and inflammation, *J. Mater. Sci. Mater. Med.*, 2004, **15**, 321-325.
- ⁹⁹ W.A. Jacobi, Mineralisation of bacterial cell mass on a photocatalytic surface in air, *Environ. Sci. Technol.*, 1998, **32**, 2650-2653.
- ¹⁰⁰ Z. Huang, P.C. Maness, D.M. Blake, E.J. Wolfrum, S.L. Smolinski, W.A. Jacoby, Bactericidal mode of titanium dioxide photocatalyst, *J. Photochem. Photobiol. A: Chem.*, 2000, **130**, 163-170.
- ¹⁰¹ O. Legrini, Photochemical processes for water treatment, *Chem. Rev.*, 1993, **93**, 671-698.
- ¹⁰² T. Saito, T. Iwase, J. Horis, T. Morioka, Mode of photocatalytic bactericidal action of powdered semiconductor TiO₂ on mutants streptococci, *J. Photochem. Photobiol. B: Biol.*, 1992, **14**, 369-379.
- ¹⁰³ T. Matsunaga, R. Tomoda, T. Nakajima, H. Wake, Photoelectrochemical sterilization of microbial cells by semiconductor powders, *Microbiol. Lett.*, 1985, **29**, 211-214.
- ¹⁰⁴ K. Hirakawa, M. Mori, M. Yoshida, S. Oikawa, S. Kawanishi. Photo-irradiated titanium dioxide catalyzes site specific DNA damage via generation of hydrogen peroxide. *Free Radic. Res.*, 2004, **38**, 439-447.
- ¹⁰⁵ G. McDonnell, A.D. Russell. Antiseptics and disinfectants: activity, action, and resistance. *Clin. Microbiol. Rev.*, 1999, **12**, 147–179.
- ¹⁰⁶ H. O'Neal Tugaoen, S. Garcia-Segura, K. Hristovski, P. Westerhoff, Challenges in photocatalytic reduction of nitrate as water treatment technology, *Sci. Tot. Environ.*, 2017, **599-600**, 1524-1551.
- ¹⁰⁷ X. Zhang, L. Song, X. Zeng, M. Li, Effects of Electron Donors on the TiO₂ Photocatalytic Reduction of Heavy Metal Ions under Visible Light, *Ener. Proc.*, 2012, **17**, 422 – 428.
- ¹⁰⁸ Q.D. Qin, Q.Q. Wang, D.F. Fu, J. Ma, An efficient approach for Pb(II) and Cd(II) removal using manganese dioxide formed in situ, *Chem. Eng. J.*, 2011, **172**, 68–74.
- ¹⁰⁹ R. Molinari, M. Mungari, E. Drioli, A.D. Paola, V. Loddo, L. Palmisano, M. Schiavello, Study on a photocatalytic membrane reactor for waste purification, *Catal. Today*, 2000, **55**, 71–78.
- ¹¹⁰ M.A. Albrecht, C.W. Evans, C.L. Raston, Green chemistry and the health implications of nanoparticles, *Green Chem.*, 2006, **8**, 417–432.
- ¹¹¹ R. Molinari, L. Palmisano, E. Drioli, M. Schiavello, Studies on various reactor configurations for coupling photocatalysis and membrane processes in water purification, *J. Membr. Sci.*, 2002, **206**, 399-415.
- ¹¹² X. Cao, J. Ma, X. Shi, Z. Ren, Effect of TiO₂ nanoparticle size on the performance of PVDF membrane, *Appl. Surf. Sci.*, 2006, **253**, 2003-2010.
- ¹¹³ T.H. Bae, T.M. Tak, Effect of TiO₂ nanoparticles on fouling mitigation of ultrafiltration membranes for activated sludge filtration, *J. Membr. Sci.*, 2005, **249**, 1-8.

- ¹¹⁴ G. Zhang, S. Lu, L. Zhang, Q. Meng, C. Shen, J. Zhang, Novel polysulfone hybrid ultrafiltration membrane prepared with TiO₂-g-HEMA and its antifouling characteristics, *J. Membr. Sci.*, 2013, **436**, 163–173.
- ¹¹⁵ V. Vatanpour, S.S. Madaeni, A.R. Khataee, E. Salehi, S. Zinadini, H.A. Monfared, TiO₂ embedded mixed matrix PES nanocomposite membranes: influence of different sizes and types of nanoparticles on antifouling and performance, *Desalination*, 2012, **292**, 19–29.
- ¹¹⁶ O.T. Alaoui, Q.T. Nguyen, C. Mbareck, T. Rhlalou, Elaboration and study of poly (vinylidene fluoride)–anatase TiO₂ composite membranes in photocatalytic degradation of dyes, *Appl. Catal. A: Gen.*, 2009, **358**, 13–20.
- ¹¹⁷ R.A. Damodar, S.-J. You, H.-H. Chou, Study the self-cleaning, antibacterial and photocatalytic properties of TiO₂ entrapped PVDF membranes, *J. Hazard. Mater.*, 2009, **172**, 1321–1328.
- ¹¹⁸ S.H. Kim, S.-Y. Kwak, B.-H. Sohn, T.H. Park, Design of TiO₂ nanoparticle self- assembled aromatic polyamide thin-film-composite (TFC) membrane as an approach to solve biofouling problem, *J. Membr. Sci.*, 2003, **211**, 157–165.
- ¹¹⁹ T.-H. Bae, T.-M. Tak, Effect of TiO₂ nanoparticles on fouling mitigation of ultrafiltration membranes for activated sludge filtration, *J. Membr. Sci.*, 2005, **249**, 1-8.
- ¹²⁰ S. Leong, A. Razmjou, K. Wang, K. Hapgood, X. Zhang, H. Wang, TiO₂ based photocatalytic membranes: A review, *J. Membr. Sci.*, 2014, **472**, 167–184.
- ¹²¹ Y. Mansourpanah, S.S. Madaeni, A. Rahimpour, A. Farhadian, A.H. Taheri, Formation of appropriate sites on nanofiltration membrane surface for binding TiO₂ photo-catalyst: performance, characterization and fouling-resistant capability, *J. Membr. Sci.*, 2009, **330**, 297–306.
- ¹²² Q. Yang, Z. Lu, J. Liu, X. Lei, Z. Chang, L. Luo, X. Sun, Metal oxide and hydroxide nanoarrays: Hydrothermal synthesis and applications as supercapacitors and nanocatalysts, *Prog. Nat. Sci.: Mat. Int.*, 2013, **23**, 351-366.
- ¹²³ K. Byrappa, M. Yoshimura, *Handbook of Hydrothermal Technology* (2nd ed.), Elsevier, Oxford, 2003.
- ¹²⁴ J. Li, Q. Wu, J. Wu, *Synthesis of Nanoparticles via Solvothermal and Hydrothermal Methods* in M. Aliofkhaezrai (ed.), *Handbook of Nanoparticles*, Springer, 2016.
- ¹²⁵ M. Rajamathi, R. Seshadri, Oxide and chalcogenide nanoparticles from hydrothermal/solvothermal, *Curr. Opin. Sol. St. Mat. Sci.*, 2002, **6**, 337–345.
- ¹²⁶ S. Feng, L. Guanghai, Chapter 4 - *Hydrothermal and Solvothermal Syntheses*. In R. Xu, W. Pang, Q. Huo, (eds), *Modern Inorganic Synthetic Chemistry*, Elsevier, 2011, pp 63-95.
- ¹²⁷ J. Chen, S. Wang and M. S. Whittingham, Hydrothermal synthesis of cathode materials, *J. Power Sources*, 2007, **174**, 442-448.
- ¹²⁸ W. Shi, S. Songa, H. Zhang, Hydrothermal synthetic strategies of inorganic semiconducting nanostructures, *Chem. Soc. Rev.*, 2013, **42**, 5714-5743.
- ¹²⁹ Y.-J. Zhu, F. Chen, Microwave-Assisted Preparation of Inorganic Nanostructures in Liquid Phase, *Chem. Rev.* 2014, **114**, 6462–6555.
- ¹³⁰ D. Stuerger, Microwave-Material Interactions and Dielectric Properties, Key Ingredients for Mastery of Chemical Microwave Processes, In *Microwaves in Organic Synthesis*, Eds. A. Loupy, (2nd Edition), Wiley-VCH, 2006.
- ¹³¹ C. Gabriel, S. Gabriel, E. Grant, B. Halstead, D. Michael, P. Mingos, Dielectric parameters relevant to microwave dielectric heating, *Chem. Soc. Rev.*, 1998, **27**, 213-224.
- ¹³² A. Metaxas, *Foundations of Electroheat: A Unified Approach*, John Wiley and Sons, 1996.
- ¹³³ M. Nüchter, B. Ondruschka, W. Bonrath, A. Gum, Microwave assisted synthesis – a critical technology overview, *Green Chem.* 2004, **6**, 128-141.
- ¹³⁴ C.O. Kappe, Controlled Microwave Heating in Modern Organic Synthesis, *Angew. Chem.*, 2004, **43**, 6250-6284.
- ¹³⁵ D. Villemin, F. Thibault-Starzyk, Domestic microwave ovens in the laboratory, *J. Chem. Educ.*, 1991, **68**, 346-350.
- ¹³⁶ M. Ali, S.P. Bond, S.A. Mbogo, W.R. McWhinnie, P.M. Watts, Use of a domestic microwave oven in organometallic chemistry, *J. Organomet. Chem.*, 1989, **371**, 11-13.

- ¹³⁷ M. Rajamathi, R. Seshadri, Oxide and chalcogenide nanoparticles from hydrothermal/solvothermal reactions, *Curr. Opin. Sol. St. Mat. Sci.*, 2002, **6**, 337-345.
- ¹³⁸ T. Boudou, T. Crouzier, K. Ren, G. Blin, C. Picart, Multiple functionalities of polyelectrolyte multilayer films: new biomedical applications, *Adv Mater.*, 2010, **22**, 441-467.
- ¹³⁹ Y. Lvov, K. Ariga, I. Ichinose, T. Kunitake, Assembly of Multicomponent Protein Films by Means of Electrostatic Layer-by-Layer Adsorption, *J. Am. Chem. Soc.*, 1995, **117**, 6117-6123.
- ¹⁴⁰ P.T. Hammond, Recent explorations in electrostatic multilayer thin film assembly, *Curr. Opin. Coll. Interf. Sci.*, 1999, **4**, 430-442.
- ¹⁴¹ P. Schaaf, J.-C. Voegel, L. Jierry, F. Boulmedais, Spray-assisted polyelectrolyte multilayer buildup: From step-by-step to single-step polyelectrolyte film constructions, *Adv. Mater.*, 2012, **24**, 1001-1016.
- ¹⁴² J. Cho, K. Char, J.D. Hong, K.B. Lee, Fabrication of Highly Ordered Multilayer Films Using a Spin Self-Assembly Method, *Adv. Mater.*, 2001, **13**, 1076-1078.
- ¹⁴³ P.A. Chiarelli, M.S. Johal, J.L. Casson, J.B. Roberts, J.M. Robinson, H-L. Wang, Controlled Fabrication of Polyelectrolyte Multilayer Thin Films Using Spin-Assembly, *Adv. Mater.*, 2001, **13**, 1167-1171.
- ¹⁴⁴ F. Fadhillah, S. M. J. Zaidi, Z. Khan, M. Khaled, F. Rahman, P. Hammond, Development of multilayer polyelectrolyte thin-film membranes fabricated by spin assisted layer-by-layer assembly, *J. Appl. Polym. Sci.*, 2012, **126**, 1468-1474.
- ¹⁴⁵ N. Joseph, P. Ahmadiannamini, R. Hoogenboom, I.F.J. Vankelecom, Layer-by-layer preparation of polyelectrolyte multilayer membranes for separation, *Polym. Chem.*, 2014, **5**, 1817-1831.
- ¹⁴⁶ A. Wu, D. Yoo, J.K. Lee, M.F. Rubner, Solid-state light-emitting devices based on the tris-chelated ruthenium(II) complex: 3. High efficiency devices via a layer-by-layer molecular-level blending approach, *J. Am. Chem. Soc.*, 1999, **121**, 4883-4891.
- ¹⁴⁷ O. Onitsuka, C. Fou, M. Ferreira, B.R. Hsieh, M.F. Rubner, Enhancement of light emitting diodes based on self-assembled heterostructures of poly(p-phenylene vinylene), *J. Appl. Phys.*, 1996, **80**, 4067-4071.
- ¹⁴⁸ C. Holmes, J. Daoud, P.O. Bagnaninchi, M. Tabrizian, Polyelectrolyte multilayer coating of 3D scaffolds enhances tissue growth and gene delivery: non-invasive and label-free assessment, *Adv. Healthc. Mater.*, 2014, **3**, 572-580.
- ¹⁴⁹ R.R. Carballo, V. Campo dall'Orto, J.A. Hurst, A. Spiaggi, C. Bonazzola, I.N. Rezzano, Covalently attached metalloporphyrins in LBL self-assembled redox polyelectrolyte thin films, *Electrochim. Acta*, 2008, **53**, 5215.
- ¹⁵⁰ H. Makamba, J.H. Kim, K. Lim, N. Park, J.H. Hahn, Surface modification of poly(dimethylsiloxane) micro-channels, *Electrophoresis*, 2003, **24**, 3607-3619.
- ¹⁵¹ J.P. De Rocher, P. Mao, J.Y. Han, M.F. Rubner, R.E. Cohen, Layer-by-layer assembly of polyelectrolytes in nanofluidic devices. *Macromolecules*, 2010, **43**, 2430-2437.
- ¹⁵² M.C. Berg, L. Zhai, R.E. Cohen, M.F. Rubner, Controlled drug release from porous polyelectrolyte multilayers, *Biomacromolecules*, 2006, **7**, 357-364.
- ¹⁵³ K.C. Wood, J.Q. Boedicker, D.M. Lynn, P.T. Hammon, Tunable drug release from hydrolytically degradable layer-by-layer thin films. *Langmuir*, 2005, **21**, 1603-1609.
- ¹⁵⁴ G. Decher, B. Lehr, K. Lowack, Y. Lvov, J. Schmitt, New nanocomposite films for biosensors: layer-by-layer adsorbed films of polyelectrolytes proteins or DNA, *Biosens. Bioelect.*, 1994, **9**, 677-684.
- ¹⁵⁵ T. Hoshi, H. Saiki, J.-I. Anzai, Amperometric uric acid sensors based on polyelectrolyte multilayer films, *Talanta*, 2003, **61**, 363-368.
- ¹⁵⁶ H.K. Yang, Polyelectrolyte Complexes and Multilayers, PhD dissertation at University of Freiburg – IMTEK, 2008.
- ¹⁵⁷ K. Glinel, C. Dejumat, M. Prevot, B. Scholer, M. Schonhoff, R.V. Klitzing, Responsive polyelectrolyte multilayers, *Coll. Surf, A: Physicochem. Eng. Aspects*, 2007, **303**, 3-13.
- ¹⁵⁸ J. K. Sun, X.F. Wang, J. Ji, Layer-by-Layer Assembly: The New Approach for Advanced Drug Release System. *Prog. Chem.*, 2009, **21**, 2682-2688.

- 159 I. Drachuk, O. Shchepelina, M. Lisunova, S. Harbaugh, N. Kelley-Loughnane, M. Stone, V.V. Tsukruk, pH-Responsive Layer-by-Layer Nanoshells for Direct Regulation of Cell Activity. *ACS Nano* 2012, **6**, 4266–4278.
- 160 S.T. Dubas, J.B. Schlenoff, Swelling and Smoothing of Polyelectrolyte Multilayers by Salt, *Langmuir*, 2001, **17**, 7725–7727.
- 161 N. Laugel, C. Betscha, M. Winterhalter, J.C. Voegel, P. Schaaf, V. Ball, Relationship between the growth regime of polyelectrolyte multilayers and the polyanion/polycation complexation enthalpy. *J. Phys. Chem. B*, 2006, **110**, 19443–19449.
- 162 G. Decher, Fuzzy nanoassemblies: Toward layered polymeric multicomposites. *Science*, 1997, **277**, 1232–1237.
- 163 P. Lavalle, C. Gergely, F.J.G. Cuisinier, G. Decher, P. Schaaf, J.C. Voegel, C. Picart, Comparison of the structure of polyelectrolyte multilayer films exhibiting a linear and an exponential growth regime: An in situ atomic force microscopy study. *Macromolecules*, 2002, **35**, 4458–4465.
- 164 L. Richert, A.J. Engler, D.E. Discher, C. Picart, Elasticity of native and cross-linked polyelectrolyte multilayer films. *Biomacromolecules*, 2004, **5**, 1908–1916.
- 165 C. Picart, P. Lavalle, P. Hubert, F.J.G. Cuisinier, G. Decher, P. Schaaf, J.C. Voegel, Buildup Mechanism for Poly(L-lysine)/Hyaluronic Acid Films onto a Solid Surface, *Langmuir*, 2001, **17**, 7414–7424.
- 166 M. Salomaki, I.A. Vinokurov, J. Kankare, Effect of Temperature on the Buildup of Polyelectrolyte Multilayers, *Langmuir*, 2005, **21**, 11232–11240.
- 167 J. A. Jaber, J. B. Schlenoff, Counterions and Water in Polyelectrolyte Multilayers: A Tale of Two Polycations, *Langmuir*, 2007, **23**, 896–901.
- 168 J.B. Schlenoff, H. Ly, M. Li, Charge and Mass Balance in Polyelectrolyte Multilayers, *J. Am. Chem. Soc.*, 1998, **120**, 7626–7634.
- 169 J.B. Schlenoff, S.T. Dubas, Mechanism of polyelectrolyte multilayer growth: charge overcompensation and distribution, *Macromolecules*, 2001, **34**, 592–598.
- 170 J. Wei, D. A. Hoagland, G. Zhang, Z. Su, Effect of Divalent Counterions on Polyelectrolyte Multilayer Properties, *Macromolecules*, 2016, **49**, 1790–1797.
- 171 G. Liu, S. Zou, L. Fu, G. Zhang, Roles of Chain Conformation and Interpenetration in the Growth of a Polyelectrolyte Multilayer. *J. Phys. Chem. B*, 2008, **112**, 4167–4171.
- 172 S.T. Dubas, J.B. Schlenoff, Factors Controlling the Growth of Polyelectrolyte Multilayers. *Macromolecules* 1999, **32**, 8153–8160.
- 173 J.B. Schlenoff, Charge Balance and Transport in Ion-Paired Polyelectrolyte Multilayers. In *Multilayer Thin Films*, 2nd ed.; G. Decher, J.B. Schlenoff, Eds., Wiley-VCH, 2012; Vol. 1.
- 174 J. Irigoyen, L. Han, I. Llarena, Z. Mao, C. Gao, S.E. Moya, Responsive Polyelectrolyte Multilayers Assembled at High Ionic Strength with an Unusual Collapse at Low Ionic Strength, *Macromol. Rapid. Comm.*, 2012, **33**, 1964–1969.
- 175 O. Mermut, C.J. Barrett, Effects of Charge Density and Counterions on the Assembly of Polyelectrolyte Multilayers, *J. Phys. Chem. B*, 2003, **107**, 2525–2530.
- 176 Z. Sui, D. Salloum, J.B. Schlenoff, Effect of Molecular Weight on the Construction of Polyelectrolyte Multilayers: Stripping versus Sticking, *Langmuir*, 2003, **19**, 2491–2495.
- 177 B.Su, T. Wangb, Z. Wangb, X. Gaoa, C. Gao, Preparation and performance of dynamic layer-by-layer PDADMAC/PSS nanofiltration membrane, *J. Membr. Sci.*, 2012, **423–424**, 324–331.
- 178 N. Joseph, P. Ahmadiannamini, R. Hoogenboom, I.F.J. Vankelecom, Layer-by-layer preparation of polyelectrolyte multilayer membranes for separation, *Polym. Chem.*, 2014, **5**, 1817–1831.
- 179 N. Wanga, G. Zhanga, S. Ji, Z. Qina, Z. Liu, The salt-, pH- and oxidant-responsive pervaporation behaviors of weak polyelectrolyte multilayer membranes, *J. Membr. Sci.*, 2010, **354**, 14–22.
- 180 H.Y. Deng, Y.Y. Xu, B.K. Zhu, X.Z. Wei, F. Liu, Z.Y. Cui, Polyelectrolyte membranes prepared by dynamic self-assembly of poly(4-styrenesulfonic acid-co-maleic acid) sodium salt (PSSMA) for nanofiltration (I), *J. Membr. Sci.*, 2008, **323**, 125–133.
- 181 H. Deng, Y. Xu, Q. Chen, X. Wei, B. Zhu, High flux positively charged nanofiltration membranes prepared by UV-initiated graft polymerization of methacrylateethyl trimethyl ammonium chloride (DMC) onto polysulfone membranes, *J. Membr. Sci.*, 2011, **366**, 363–372.

- ¹⁸² S. Ilyas, S.M. Abtahi, N. Akkilic, H.D.W. Roesink, W.M. de Vosa, Weak polyelectrolyte multilayers as tunable separation layers for micropollutant removal by hollow fiber nanofiltration membranes, *J. Membr. Sci.*, 2017, **537**, 220-228.
- ¹⁸³ S. Ilyas, N. Joseph, A. Szymczyk, A. Volodin, K. Nijmeijer, Wiebe M. de Vos, I.F.J. Vankelecom, Weak polyelectrolyte multilayers as tunable membranes for solvent resistant nanofiltration, *J. Membr. Sci.*, 2016, **514**, 322-331.
- ¹⁸⁴ Y. Wang, S. Wang, M. Xiao, D. Han, M.A. Hicknerb, Y. Meng, Layer-by-layer self-assembly of PDDA/PSS-SPFEK composite membrane with low vanadium permeability for vanadium redox flow battery, *RSC Adv.*, 2013, **3**, 15467.
- ¹⁸⁵ C. Cortez, J.F. Quinn, X. Hao, C.S. Gudipati, M.H. Stenzel, T.P. Davis, F. Caruso, *Langmuir*, 2010, **26**, 9720–9727.
- ¹⁸⁶ S. Garg, K. Vermani, A. Garg, R. Anderson, W. Rencher, L. Zaneveld, Development and characterisation of bioadhesive vaginal films of sodium polystyrene sulfonate (PSS), a novel contraceptive antimicrobial agent, *Pharm. Res.*, 2005, **22**, 584-595.
- ¹⁸⁷ L. Seon, P. Lavalle, P. Schaaf, F. Boulmedais, Polyelectrolyte Multilayers: A Versatile Tool for Preparing Antimicrobial Coatings, *Langmuir*, 2015, **31**, 12856–12872.
- ¹⁸⁸ N. Hilal, V. Kochkodan et al., Surface modified polymeric membranes to reduce (bio)fouling: a microbiologica study using *E. Coli*, *Desalination*, 2004, **167**, 293-300.
- ¹⁸⁹ J. Dai, M.L. Bruening, Catalytic Nanoparticles Formed by Reduction of Metal Ions in Multilayered Polyelectrolyte Films, *Nano Lett.*, 2002, **2**, 497-501.
- ¹⁹⁰ K.D. Park, Y.S. Kim, D.K. Han, Y.H. Kim, E.H.B. Lee, H. Suh, K.S. Choi, Bacterial adhesion on peg modified polyurethane surfaces. *Biomaterials*, 1998, **19**, 851–859.
- ¹⁹¹ Q. Liu, A.A. Patel, L. Liu, Superhydrophilic and underwater superoleophobic poly(sulfobetaine methacrylate)-Grafted glass fiber filters for oil–water separation. *ACS Appl. Mater. Interfaces*, 2014, **6**, 8996–9003.
- ¹⁹² H. Schmolke, S. Demming, A. Edlich, V. Magdanz, S. Buttgenbach, E. Franco-Lara, R. Krull, C.P. Klages, Polyelectrolyte multilayer surface functionalization of poly(dimethylsiloxane) (pdms) for reduction of yeast cell adhesion in microfluidic devices. *Biomicrofluidics*, 2010, **4**, 044113.
- ¹⁹³ F. Boulmedais, B. Frisch, O. Etienne, P. Lavalle, C. Picart, J. Ogier, J.C. Voegel, P. Schaaf, C. Egles, Polyelectrolyte multilayer films with pegylated polypeptides as a new type of anti-microbial protection for biomaterials. *Biomaterials*, 2004, **25**, 2003–2011.
- ¹⁹⁴ L. Richert, P. Lavalle, E. Payan, X.Z. Shu, G.D. Prestwich, J.F. Stoltz, P. Schaaf, J.C. Voegel, C. Picart, Layer by layer buildup of polysaccharide films: Physical chemistry and cellular adhesion aspects. *Langmuir*, 2004, **20**, 448–458.
- ¹⁹⁵ J.A. Lichter, M.T. Thompson, M. Delgadillo, T. Nishikawa, M.F. Rubner, K.J. Van Vliet, Substrata mechanical stiffness can regulate adhesion of viable bacteria. *Biomacromolecules*, 2008, **9**, 1571-1578.
- ¹⁹⁶ N. Saha, C. Monge, V. Dulong, C. Picart, K. Glinel, Influence of polyelectrolyte film stiffness on bacterial growth. *Biomacromolecules*, 2013, **14**, 520–528.
- ¹⁹⁷ T. Kruka, K. Szczepanowicza, D. Kregielb, L. Szyk-Warszynskaa, P. Warszynskia, Nanostructured multilayer polyelectrolyte films with silver nanoparticles as antibacterial coatings, *Coll. Surf. B: Biointerfaces*, 2016, **137**, 158-166.
- ¹⁹⁸ X. Zhang, X. Zana, Z. Su, Polyelectrolyte multilayer supported Pt nanoparticles as catalysts for methanol oxidation, *J. Mater. Chem.*, 2011, **21**, 17783-17789.
- ¹⁹⁹ N.A. Kotov, Layer-by-Layer Self-Assembly: The Contribution of Hydrophobic Interactions, *Nanostruct. Mater.*, 1999, **12**, 789-796.
- ²⁰⁰ G. Yang, H. Ma, L. Yu, P. Zhang, Preparation and characterization of layer-by-layer self-assembled polyelectrolyte multilayer films doped with surface-capped SiO₂ nanoparticles, *J. Coll. Interf. Sci.*, 2009, **333**, 776–781.
- ²⁰¹ Y. Liu, Y. Wang, R.O. Claus, Layer-by-layer ionic self-assembly of Au colloids into multilayer thin-films with bulk metal conductivity, *Chem. Phys. Lett.*, 1998, **298**, 315-319.
- ²⁰² L.A. Belfiore, E.M. Indra, Transition metal compatibilization of poly(vinylamine) and poly(ethylene imine), *J. Polym. Sci. B*, 2000, **38**, 552-561.

²⁰³ B. Sadeghi, A. Pourahmad, Synthesis of silver/poly(diallyldimethylammonium chloride) hybride nanocomposite, *Adv. Powder Technol.*, 2011, **22**, 669-673.

List of Abbreviations used in Chapter 2

AFM: Atomic Force Microscopy
CA: Contact Angle
DLS: Dynamic Light Scattering
DMO: Domestic Microwave Oven
DTA: Differential Thermal Analysis
EDX: Energy Dispersive X-ray Spectroscopy
FMH: Flash Microwave-assisted Hydrothermal synthesis
FRO: Forward Reverse Osmosis
FRR: Flux Recovery Ratio
FT-IR: Fourier Transform Infrared Spectroscopy
IEM: Ion-Exchange Membrane
LbL: Layer-by-Layer
ly: layer
MF: Microfiltration
MS: Mass Spectrometry
MW: Microwaves
MWCO: Molecular Weight Cut-Off
NF: Nanofiltration
NHE: Normal Hydrogen Electrode
PAA: Poly(acrylic acid)
PAN: Polyacrylonitrile
PAH: Poly(allylamine hydrochloride)
PDDA: Poly(diallyldimethylammonium chloride)
PE: Polyelectrolyte
PEI: Polyethyleneimine
PEM: Polyelectrolyte Multilayer
PES: Poly(ethersulfone)
PSS: Poly(sodium 4-styrenesulfonate)
PTFE: Polytetrafluoroethylene
PV: Pervaporation
PXD: Powder X-ray Diffraction
RhB: Rhodamine B

RO: Reverse Osmosis
SEM: Scanning Electron Microscopy
SPR: Surface Plasmon Resonance
SRNF: Solvent Resistant Nanofiltration
STA: Simultaneous Thermal Analysis
TEM: Transmission Electron Microscopy
TGA: Thermogravimetric Analysis
TMP: Transmembrane Pressure
TTIB: Titanium butoxide
TTIP: Titanium isopropoxide
UF: Ultrafiltration
US: Ultrasound
UV: Ultraviolet (radiation)
WPPM: Whole Powder Pattern Modelling
XPS: X-ray photoelectron spectroscopy

Chapter 2

Materials, methods and models

2.1 Materials

2.1.1 TiO₂ particle synthesis and post-synthetic treatment

All chemical and solvent used for the preparation of reagents and solution were ACS reagent grade or analytical grade and were used without further purification. De-ionised water was of Milli-Q grade. TiO₂ particles were prepared using titanium(IV) tetraisopropoxide (TTIP, Sigma Aldrich, 97% purity) and titanium(IV) butoxide (TTIB, Sigma Aldrich, 97%) stored under nitrogen to prevent hydrolysis. Solutions were prepared using absolute ethanol (AnalaR Normapur, VWR). Acidification of the solution was performed using hydrochloric acid (HCl, 37% v/v, Fluka), nitric acid (HNO₃, 70% v/v), sulphuric acid (H₂SO₄, 98% v/v, VWR), glacial acetic acid (CH₃COOH, 100% Sigma).

For the comparison with commercial materials and photocatalyst, TiO₂ anatase (99.9%, Sigma Aldrich) and TiO₂ rutile (99.99%, Sigma Aldrich) were used. Aeroxide® P25 (Acros) and Kronos 7000 (KronosClean 7000, Kronos Titan GmbH, Germany, received free of charge) were used as reference catalyst, for the degradation test for photocatalytic assessment. Rhodamine B (Sigma Aldrich, >95%) was selected as model organic molecule for the photodegradation experiments.

2.1.2 PEM-modified membrane preparation and characterisation

The following polyelectrolytes were used for the preparation of the solution for the multilayer assembly: Poly(acrylic acid) (PAA, Aldrich, average Mw 1800); Poly(allylamine hydrochloride) (PAH, [CH₂CH(CH₂NH₂·HCl)]_n Alfa Aesar); Poly(sodium 4-styrenesulfonate) (PSS, Mw 70k, Aldrich); Poly(diallyldimethylammonium chloride); (20 wt% solution in H₂O, Mw 200k-350k, Aldrich); Polyethyleneimine (PEI, branched, Mw 25k by LS, Mn 10k by GPC, Aldrich). Fouling tests were performed using Sodium alginate sodium salt, sodium chloride (NaCl, VWR), calcium chloride (CaCl₂, Fisher).

2.2 TiO₂ particles synthesis

2.2.1 Flash Microwave-assisted synthesis

The TiO₂ precursors were stored under nitrogen atmosphere to protect them from uncontrolled hydrolysis. Small aliquots of precursor (in liquid form at room temperature) were withdrawn for each use. At first, the solvent (water or ethanol) was cooled in an ice bath for at least 30 minutes. Once the solution reached a stable temperature (*ca.* 278 K), the precursor was added dropwise using a disposable syringe. The addition of the precursor was performed under continuous stirring, to improve the dispersion in the solution.

After at least 1 hour of mixing, an aliquot of 5-15 mL of the prepared solution were poured into a Teflon-lined microwave digestion autoclave. Reactions were performed in a multimode cavity (MMC) MW reactor based on a modified domestic microwave oven (DMO). The autoclave was maintained in the same position in the reactor at the highest amplitude of the propagating modes in the cavity. This position was previously determined using a quartz tube filled with graphite powder; the intensity of the thermal irradiation of graphite under the microwave field is indicative of the concentration of resonating microwave modes. The analysis of the hot spots was purely qualitative, with no photometric measurement of the emitted intensity.

The reactor vessels used were PTFE-lined microwave digestion bomb (Parr Instrument Company, U.S. Patent No. 4882128, 23 mL or 45 mL volume, with maximum temperature and pressure ratings of 523 K and 8.27 MPa respectively. At the end of the process, the digestion reactor was left to cool to room temperature. The resulting colloidal solution is centrifuged and washed with deionised water and absolute ethanol to remove unreacted precursor and/or by-products.

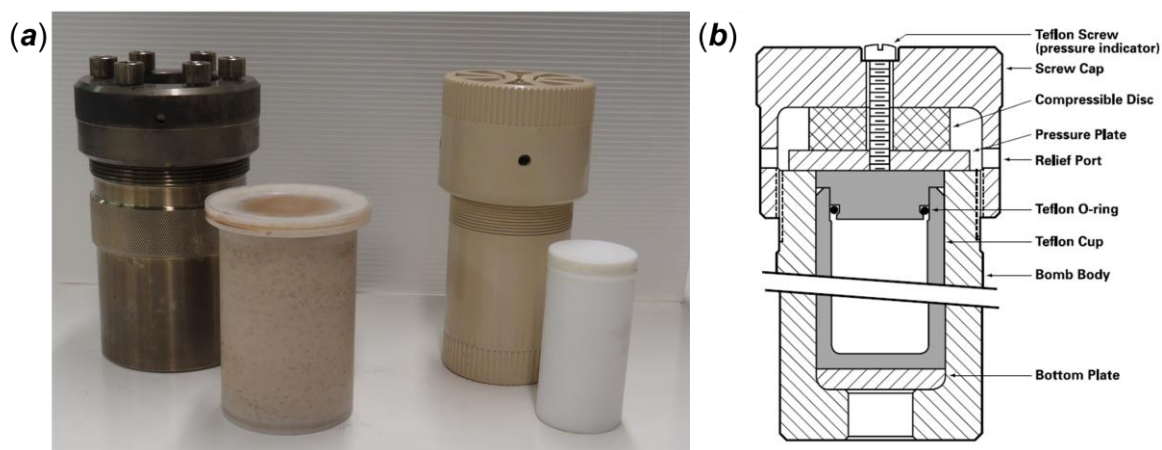


Figure 2.1: (a) Comparison between a conventional stainless steel autoclave for hydrothermal treatment and a MW-transparent autoclave; (b) schematic diagram of the structure of the MW-transparent autoclave.

2.2.2 Post-synthesis thermal treatments

2.2.2.1 Calcination and annealing

After preliminary structural and morphological analysis, all the samples produced by microwave-assisted hydrothermal synthesis were calcined in an electrical furnace at different temperatures (673, 773, 873 K) in order to remove the remains of the organic precursor and increase the degree of crystallinity. Calcination treatments were carried out in air for 3 h at a heating rate of 10 K/min in a box furnace. The powdered samples were placed in alumina crucibles or boats. At the end of the treatment, the samples were cooled to room temperature (no set ramp rate). Calcination under gaseous atmospheres was carried out in tube furnaces; samples in alumina or quartz boats were placed in the heating zone of the ceramic tube of the furnace, where the heating efficiency is maximised. The tube was closed at its ends with stainless steel flanges connected to the gas line. Several gases were used: Nitrogen (BOC, Oxygen free, 99.998%), Argon (BOC, Pureshield 99.998%), Ammonia (BOC, anhydrous, grade N3.8- 99.98%), 5% H₂ in Ar (BOC) and 5% H₂ in N₂ (BOC) mixture. The thermal treatment was performed at different temperatures (673, 773, 873 K) with a heating rate of 10 K/min. The reactive gases were fed into the tube furnace for approximately 30 min prior to heating to remove air (oxygen) from the system. The gas flow rate was kept constant during heating and cooling.

2.2.2.2 Vacuum post-synthesis treatments

Thermal treatment under vacuum was performed using two different configurations: static vacuum conditions using a quartz tube (10 mm inner diameter) or dynamic conditions directly connecting the quartz tube to the vacuum line for the entire duration of the thermal treatment. Tube sealing was performed using a glassblowing station equipped with a methane/oxygen flame. The vacuum is provided by a rotary pump (ensuring a pressure of 2-5 Pa) or a turbopump (providing a pressure of 10^{-4} to $5 \cdot 10^{-3}$ Pa). Dynamic vacuum reactions were performed in quartz tubes or in stainless steel flanged reactors. The thermal treatment was performed under constant vacuum using pot furnaces with a maximum operating temperature of 1673 K. Pressure was measured using a Pirani gauge.

2.2.2.3 Microwave solid state transformation and kinetic assessment

Solid state microwave reactions were performed using a CEM Discovery single-mode microwave reactor. The reactor, originally designed for liquid media, was modified for the reaction of solid material in the microwave cavity. The maximum incident MW power is 300 W, with stable operations at this temperature possible for a period of 10-15 minutes. The heating process can be enhanced using a microwave susceptor material, which generates heat when irradiated by microwaves. Materials such as carbon, SiC and CuO can provide heat to non-susceptible materials ^[1]. A different CEM single-mode reactor (not modified for solid state treatments) was used to replicate the synthesis conditions inside the digestion reactor in the MMC experiment (section 2.2.1), monitoring the temperature and pressure in situ allowing correlation with other experimental parameters such as the pH, type of acid and the degree of filling of the reactor.

2.3 PEM-modified surfaces

2.3.1 Coating technique

The principal deposition technique tested was dip coating of substrates directly into polyelectrolyte (PE) solutions. In general, polyelectrolyte solutions have a concentration of around 1-2 g/L. Other authors prefer to use the molecular weight

of the repeating unit of the polymer to give the concentration as a molarity; the concentration of the polyelectrolyte solution adopted is therefore ca. 10-20 mM.^[2] The solutions were adjusted to the target pH using a 1M solution of NaOH and HCl in MilliQ water (18 MΩ). Glass slides and Mylar foil were immersed exposing both sides to the polyelectrolyte solutions. For filtration membranes, surfaces were attached by their edges to a support, exposing only the active layer to the PE solution. Unfortunately, since the membrane was attached using insulating tape, the consecutive steps of deposition and rinsing weaken the adhesive strength, leading to partial permeation of the solution onto the support side of the membrane. Contamination due to dissolution of the glue on the tape when exposed to acidic or basic solutions was also a potential problem. Ultimately, this leads to reproducibility issues in measurements of the permeability and porosity analysis of the membrane. The best option for the adhesion of the polyelectrolyte multilayer (PEM) coating on the membrane was the use of a Mylar sheet, onto which the adhesive tape seemed to be more stable and easy to clean compared with other supports.

2.3.2 Surface preparation

Polymer membranes were removed from the original packaging and soaked in deionised water for at least 24 hours prior to use to remove excess of glycerol (the impregnated glycerol-ethanol solution acts as a plasticizer and humectant, preventing the active layer from drying completely). Brand new microscope glass slides (VWR BS 7011, low iron clear glass, 1.0 mm thickness) were used as received. A deeper surface cleaning can be obtained immersing the slides in a 1:1 mixture of NH₄OH solution (29% v/v) and H₂O₂ (30% v/v) for 90 min, with final rinse with de-ionised water.^[3] Immediately prior to PEM deposition, all surfaces were first cleaned by ultrasonication in a (1) 2:1 solution of IPA/water for 10 minutes and (2) for 5 minutes in a 2:3 solution of water and ethanol with 1 wt.% of KOH. This procedure ensures complete cleaning and the presence of negative charges on the substrate surface.^[4]

2.4 Powder X-ray Diffraction

2.4.1 Principles of the technique

Powder X-ray diffraction (pXRD or PXD) is a non-destructive qualitative and quantitative technique essential for the characterisation of solid crystalline materials. PXD allows identification of the crystalline phases in a sample, their relative quantitative abundance and ultimately determination and/or refinement of the structure.

The technique is based on diffraction phenomenon where the wavelength of an incident beam is comparable to objects in its path. A series of constructive and destructive interference phenomena result. The wavelength of X-rays is comparable to the interatomic distances (0.5 to 2 Å) in crystalline solid materials and so behave exactly like a grating illuminated by a light beam. Diffraction of X-rays is well described by Bragg's law.^[5]

$$n\lambda = 2d\sin\theta \quad (\text{eq 2.1})$$

where λ is the incident beam wavelength, d is the distance between lattice planes, θ is the angle of incidence, also known as Bragg's angle and n is an integer number which defines the order of diffraction ($n=1$ will identify first order, $n=2$ the second one and so on). The Bragg's law is based on a simple geometrical assumption: considering two monochromatic beams travelling in parallel direction, if the first beam is scattered elastically by an atom on the outer plane of the crystal, the second beam will be able to emerge from the crystal, always travelling parallel to the first scattered beam, only if scattered by an atom belonging to a plane parallel to the outer one. The second beam will travel for an additional distance in the crystal ($2d \cdot \sin(\theta)$, as shown in Figure 2.2), resulting in phase with the first beam and producing constructive interference. Depending on the orientation of the different crystal directions with respect to the incident beam, all the planes of the crystal will give a net signal at a certain angle.

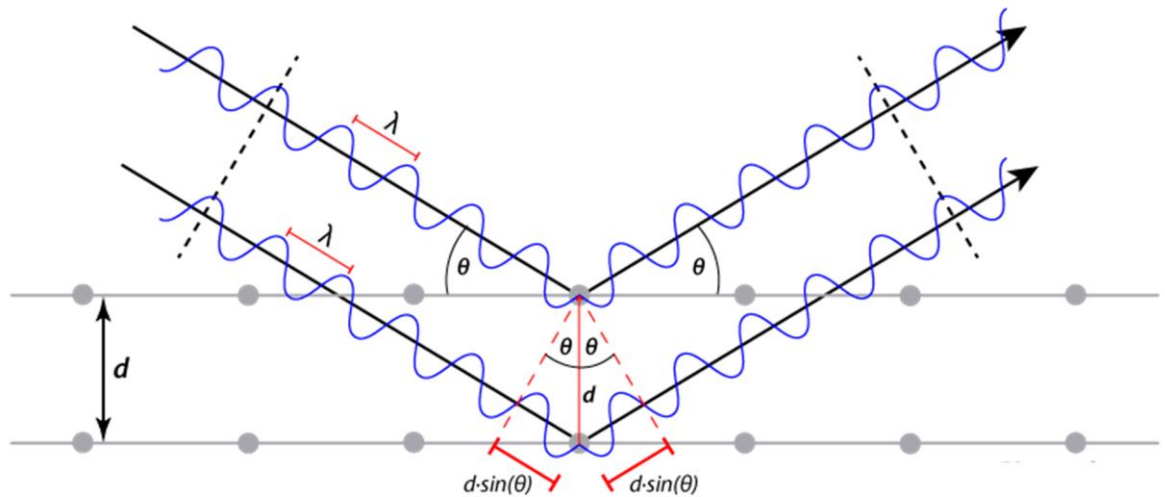


Figure 2.2: Schematic representation of the Bragg's law conditions for constructive interference of X-ray beams from atomic planes in a crystal. [6]

When the crystalline material is in powdered form, the single crystallites are ideally randomly oriented, with the different crystalline planes diffracting when the beam is incident at the appropriate angle. The irradiation of the powder over a wide angular range provides an accurate image of the crystalline structure. The series of verifying intensity peaks plotted as a function of the incident angle is called a diffraction pattern.

2.4.2 Data collection and analysis

Data collection was performed using a PANalytical X'Pert PRO MPD diffractometer equipped with an X'Celerator solid state detector and an X-ray monochromator. The X-ray generator operates at a voltage of 40 kV with a current of 40 A. The diffractometer has a Cu target and Cu K α 1 radiation ($\lambda=1.5406 \text{ \AA}$), is selected by the monochromator, removing the Cu α 2 and β emission and the problem of multiple peaks for the same (hkl) reflections.

The instrument is equipped with different sample stages, such as a simple indented glass holder or a spinning holder which enables rotation of the sample on an axis perpendicular to the beam during the measurement.

The X'Pert diffractometer was used in Bragg-Brentano reflection geometry. According to this configuration, a stationary source of X-rays irradiates a flat sample placed on a goniometer, which rotate exposing the sample surface at angle θ with respect to the incident beam, whereas the diffracted beam is collected at 2θ by a moving detector. The diffractometer could be used also for non-ambient

in situ measurements, with a furnace (HTK-1200N, Anton Parr), bringing the sample to the desired temperature under a constant flux (ca. 50 ml/min) of argon (for oxygen-free thermal decomposition) or compressed air.

Standard measurements were performed in the $15\text{-}85^\circ$ 2θ range, using a step size of 0.0167 or 0.0334° depending on the sought pattern resolution. A narrower step size provides more structural information when associated with a reasonably long time per step (at least 200 s/step). For instance, Rietveld refinement requires at least 3 h to obtain some data of suitable quality. A longer step size gives higher intensities, with even a short scan useful for phase identification. PXD samples were finely ground and placed inside the sample holder indent and levelled with a microscope glass slide to have a smooth, even and homogeneous surface. The slide should not be pressed in a particular direction to avoid superimposition of a certain orientation (when produces discrepancies in the relative intensities on the diffraction pattern; preferred orientation).

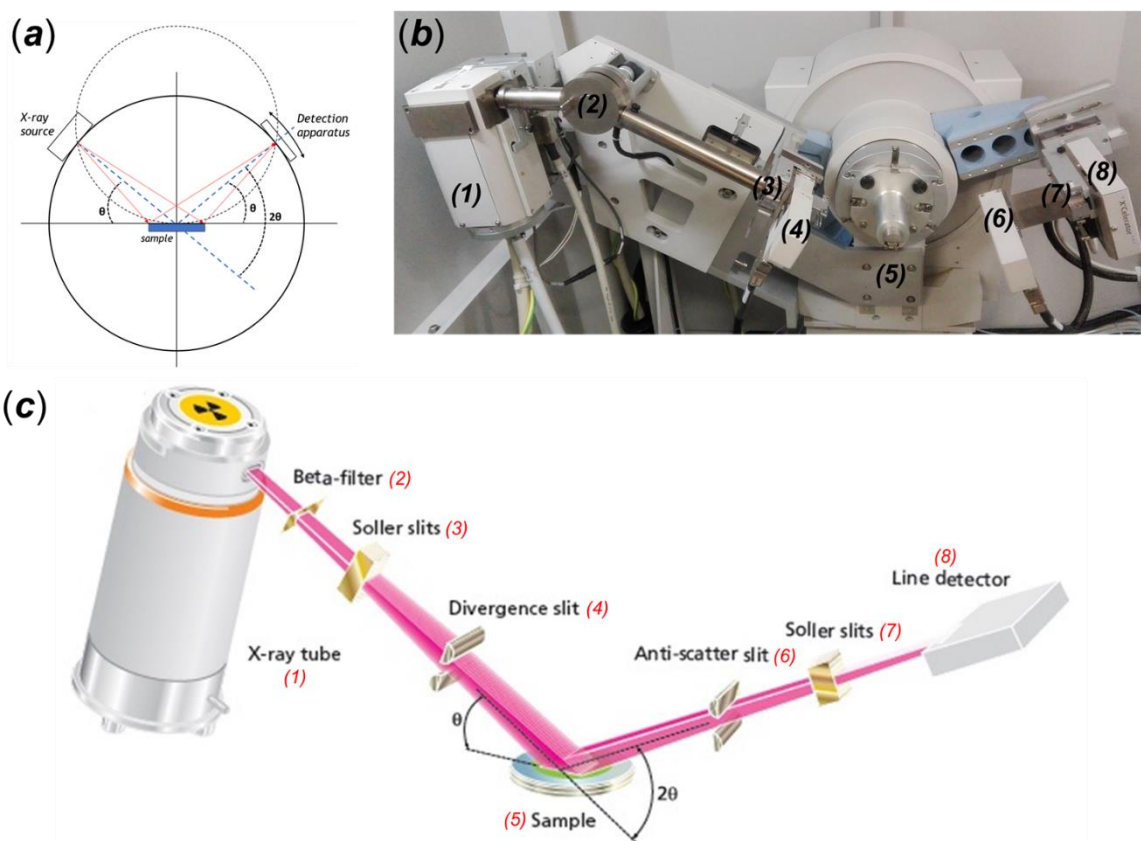


Figure 2.3: (a) schematic representation of the Bragg-Brentano geometry; (b) picture and (c) schematic diagram of the PANalytical X'Pert PRO MPD diffractometer, with numbers indicating the corresponding components. [7]

A pattern visualisation and analysis suite associated with the diffractometer (PANalytical HighScore Plus) allows the measurement of the peak position, intensity and full width at half maximum (FWHM) values and a direct comparison of a pattern with the ICDD (*International Center for Diffraction Data*) database.^[8] The PowderCell software was used for the comparison of the experimental data with the ICSD (*Inorganic Crystal Structure Database*) pattern library^[9] and for preliminary structure refinement to determine the approximate phase composition. The Winplotr package was used for the direct comparison of experimental patterns. More accurate analysis and interpretation of the diffraction data are reported in the sections below.

2.4.3 Rietveld refinement

Structure refinement enables a full comprehension of the crystalline structure of a material and the effect of modifications (change of symmetry, distortions due to interstitial or substitutional atoms, etc.) by comparison with a theoretical structure. Originally developed for constant wavelength neutron diffraction, has become the most used for the analysis of time-of-flight neutron and XRD data.^[10] The Rietveld refinement procedure involves the fitting of a structural model to one generated by the powder diffraction data. The main principle is the consideration of the whole set of individual reflections fitted using simple peak parameters, based on the assumption that the diffraction peak shape can be modelled by a linear combination of a Gaussian and a Lorentzian profile. The refinement is based on the non-linear least square best fit algorithm, in which the difference between the observed (y_i^{obs}) and the theoretical intensities (y_i^{calc}) is minimised through an iterative process:

$$f = \sum_i w_i (y_i^{obs} - y_i^{calc})^2 \quad (eq. 2.2)$$

where i represent the set of measurement steps and w_i is a weighting factor considering the uncertainty estimated for the observed (σ^2) intensities:

$$w_i = \frac{1}{\sigma^2 [y_i^{obs}]} \quad (eq. 2.3)$$

The method requires a good starting model, usually a similar or isotropic crystal structure. A series of structural (such as cell parameters, atom positions, thermal factors, site occupancy) and instrumental parameters (scale factor, relative position of the zero-point, background, shape parameters and asymmetry of the peaks, etc.) are iterated several times in order to reach convergence with a minimal difference between the pattern calculated from a theoretical model and the experimental data.

Rietveld refinement produces crystallographic data according to a model with an anticipated structure and yields the structural parameters for each crystalline phase identified and provides a quantitative determination of relative phase concentration. Several statistical factors are generated to evaluate the goodness of the fit to the model. These are defined as reliability (R) factors (Table 2.1).

Table 2.1: Statistical reliability factor for the structural refinement

<i>unweighted</i>		
	$R_p = \left[\frac{\sum_i y_i^{obs} - y_i^{calc} }{\sum_i y_i^{obs}} \right]$	(eq. 2.4)
<i>weighted</i>		
	$R_{wp} = 100 \left[\frac{\sum_i (y_i^{obs} - y_i^{calc})^2}{\sum_i w_i (y_i^{obs})^2} \right]^{1/2}$	(eq. 2.5)
	$R_{exp} = \left[\frac{(N - P + C)}{\sum_i w_i (y_i^{obs})^2} \right]^{1/2}$	(eq. 2.6)
	$\chi^2 = \left[\frac{R_{wp}}{R_{exp}} \right]^2$	(eq. 2.7)

The weighted profile factor (R_{wp}) is the most appropriate parameter for the determination of the quality of the refinement process. The best possible value for R_{wp} is given by the expected R (R_{exp}), which considers the number of observations (N), the number of parameters changed during the refinement (P) and the number of constraints (C). A convergence of R_{wp} towards R_{exp} is hence a good indication for the goodness of fit (χ^2): a χ^2 value close to 1 is considered as an acceptable indication of a meaningful fit.

2.4.4 Particle Size and Strain Analysis

X-ray diffraction patterns of nanostructured materials are characterised by a broadening of the intensity of the peaks caused by coherent scattering from nanocrystalline domains. Integral breadth (IB) methods are generally useful for the qualitative analysis of the peak broadening correlated to the average grain size and other structural causes of broadening such as the presence of lattice defects, micro-dislocation, etc.

Peak broadening is usually associated with the full width at half maximum (FWHM) intensity of the peak. The most popular integral breadth analysis which directly correlates the FWHM with the average grain size was formulated by Scherrer in 1918:^[11]

$$D = \frac{K\lambda}{\beta \cos\theta} \quad (\text{eq. 2.8})$$

In which β represents the FWHM in radians, λ is the wavelength of the X-rays, θ is the angle corresponding to the maximum intensity of the peak (always collected at 2θ in Bragg-Brentano geometry) and K is an empirical constant, reported by most authors to be ca. 0.9. The model proposed by Scherrer considers no causes of broadening other than size and assumes the crystallites all have the same size and shape.

A more accurate integral breadth analysis should include also the other contributions to the peak broadening, such as instrumental broadening (β_0) and other aberration causes, internal stress and micro-dislocation (quantified by the strain ε). The total broadening β could be approximately described as the quadratic sum of the three contributions:

$$\beta^2 = \left(\frac{K\lambda}{D \cos\theta} \right)^2 + (4\varepsilon \cdot \tan\theta)^2 + \beta_0^2 \quad (\text{eq. 2.9})$$

The Williamson-Hall method ^[12] simplifies this expression, considering the simple sum of the different contribution and extracting values of ε and D from the plot of the goniometric functions. Both the Scherrer and Williamson-Hall methods are purely empirical. Nonetheless, these approaches are useful for a semi-quantitative comparison of different products from the same synthesis for example.

2.4.5 Whole Powder Pattern Modelling (WPPM)

Whole Powder Pattern Modelling (WPPM) is a relatively novel approach for the microstructural investigation of nanocrystalline materials. In WPPM the calculated pattern, which is fitted to the experimental data, is generated from a physical model of the material microstructure. Unlike Rietveld refinement, WPPM does not use mathematical profile functions (Gaussian and Lorentzian profiles, fraction and breadth) to fit the pattern, but interprets the diffraction data in terms of physical parameters. ^[13] The method is based on the deconvolution of the Fourier Transform (FT) of the diffraction pattern peaks as sum of the FT components related with the causes of peak broadening. This approach has been shown to outperform the other models, providing results in agreement with size distribution derived from TEM imaging. ^[14] In this project, WPPM was used for the estimation of the grain size distribution of nanocrystalline materials. The calculation is based on the comparison of the pattern with a parametric model of the instrumental profile, obtained from the measurement of a standard sample (LaB₆, NIST SRM 660), and a broadening model considering the effect of the particle size. The diffraction domains are assumed to be spherical. Particle diameters follow a lognormal distribution, with its defining geometrical parameters (mean μ and standard deviation σ of the distribution) refined during the calculation process. ^[15]

WPPM analysis was performed using PM2K, a nonlinear least squares fitting software package. Prior to the analysis, the influence of the instrumentation on the diffraction pattern is evaluated. Instrumental broadening is calculated by employing the Caglioti expression for the FWHM ^[16] and a Lorentzian fraction parametrisation (η) to give the shape of the instrumental profile.

$$FWHM^2 = W + V \tan(\theta) + U \tan^2(\theta) \quad (\text{eq. 2.10})$$

$$\eta = a + b\theta + c\theta^2 \quad (\text{eq. 2.11})$$

where θ is the diffraction angle and all the other parameters are to be fitted for the profile of the standard. The apparent shift of the peak centroid caused by the divergence of the beam is calculated using a tangent polynomial series proposed by Wilson, ^[17] in which only the first five terms are generally considered:

$$\Delta(2\theta) = \sum_{i=0}^n a_i \tan^{i-1}(\theta) \quad (\text{eq. 2.12})$$

2.5 Spectroscopic technique for structural and physical characterisation

Spectroscopic analysis includes all techniques in which the signal produced by the interaction of electromagnetic radiation with matter is measured as a function of its wavelength, frequency or wavenumber. The interaction induces a transition in the energy levels of the molecule or compound, either rotational, vibrational or electronic depending on the intensity and frequency of the radiation. Since the energy levels are quantised, meaning that the possible levels are discrete, and the transition allowed according to particular selection rules, the resulting excitation to those levels gives indications about the structure of the sample.

2.5.1 FT-Infrared spectroscopy

Fourier transform infrared spectroscopy (FT-IR) is a qualitative and semi-quantitative technique based on the analysis of the vibration frequency of the atoms in molecules and compounds. The IR frequencies correspond to the vibrational level (4-60 kJ/mol) of a molecule or compound. The absorption of a certain frequency can be associated with the specific vibration of a chemical bond, functional group or an interaction with the surrounding atoms, providing a fingerprint of the material and important information about its structure. IR analysis can also define different vibration modes in a bond, such as stretching or twisting of the connected atoms. The intensity of the signal is depending on change in the dipole moment of the bond due to the absorption of energy and, secondarily, on the concentration of the specific compound in the sample (according to the Lambert-Beer law). The dipole moment depends directly on the charges and the relative position of the atoms involved in the bond. The vibration frequency (ν) can be calculated by the simplified representation of an oscillating spring connecting two masses, described by the Hooke's law:

$$\nu = \frac{1}{2\pi} \left(\frac{k}{\mu} \right)^{1/2} \quad (\text{eq. 2.13})$$

where k is the force constant of the bond and μ is the reduced mass, i.e. the sum of the reciprocal value of the masses of the atoms involved.

Commercial FT-IR spectrometers cover the range between 4000 and 400 cm^{-1} (2500 to 25000 nm). The analysis range is sometimes not particularly useful for the identification of the vibrational modes of bonding of metallic atoms in inorganic compounds, when resonate at frequencies corresponding to wavenumbers of ca. 600-400 cm^{-1} , where the resolution of the instrument is lowest.

FT-IR analysis was performed here with a Shimadzu IRAffinity-1S spectrometer, with measurements carried out with an accumulation of 50 runs and Happ-Genzel signal apodization. The instrument is equipped with an Attenuated Total Reflection (ATR) sample stage (Quest ATR diamond accessory, Specac). The IR generated by thermoelectric emission from a filament passes through a transparent crystal, a diamond in the case of the instrument used, with a range of transparency between 50 and 30000 cm^{-1}). The crystal is in contact with a highly reflective IR surface, generally a metal. If the sample is placed in contact with the surface, the reflected IR radiation will contain information about the sample. The depth of penetration of the IR in the sample depends on the refractive indices of the sample (n_2) and the crystal (n_1) and the incident/reflection angle (θ) and the wavelength (λ) of the IR radiation:

$$d_p = \frac{\lambda}{2\pi(n_1^2 \sin\theta - n_2^2)^{1/2}} \quad (\text{eq 2.14})$$

FT spectroscopy is based on non-dispersive light beam analysis, with an interferometer selecting or blocking periodically a series of wavelengths, generating constructive and destructive interferences. The absorption of the resulting beam is then processed by a terminal by using the Fourier transform, giving the typical spectrum in transmittance or absorbance (specular to each other).

2.5.2 Raman spectroscopy

Raman spectroscopy is another useful technique for the qualitative identification of compounds. The so-called Raman effect describes the inelastic scattering of a high intensity visible or near-visible light beam with a material. When a photon interacts with an atom it can be diffused or deflected (scattered). Looking deeper

at the interaction mechanism, the interaction excites the material at a molecular level. The energy of the radiation is not sufficient to promote the material to a higher electronic level, but powerful enough to access to a virtual state. The material decays from this state almost immediately. In the case of elastic scattering, the molecule returns to the same starting level (ground state) and for the principle of energy conservation, a photon with the same energy of the exciting one is re-emitted, producing what is called Rayleigh scattering. On the other hand, the molecule can fall to a higher or lower vibrational state, losing or gaining energy due to the interaction of the photon with a quantum of vibration (phonon). The interaction is then inelastic and the re-emitted photon will have a shifted frequency due to the difference between the initial and the final energetic state. When the frequency is lower compared to the original, the emission is called Stokes radiation; when it is higher, the emission is defined as Anti-Stokes radiation. The Raman shift is usually of the order of magnitude of a few nanometers (preferentially measured as wavenumber difference in cm^{-1}) and it is directly related to the vibrational state of the sample. A concise diagram of the Raman phenomena compared with the IR absorption and Rayleigh elastic scattering is shown in Figure 2.4.

Raman spectroscopy is complementary to IR analysis. Molecular vibration can be either active only in Raman spectroscopy, only in IR, active in both or in none of the spectroscopy. Raman modes correspond to a change in polarisation of the chemical bond, IR to a variation of the dipole momentum. Strongly polarised bonds such as C-O, N-O and O-H have weak or no Raman emission since the vibration does not affect the polarisation, causing on the other end a net charge movement and a dipolar change. C-C, C-H and C=C bonds are more affected by the polarisation change during the vibration, resulting in Raman active modes. In general, the activity of the different mode can be calculated analysing the molecular symmetry, applying the principles of the group theory. For some molecules, such as CO, the mutual exclusion principle applies, in which a molecular vibration cannot be active in both techniques at the same time.^[18]

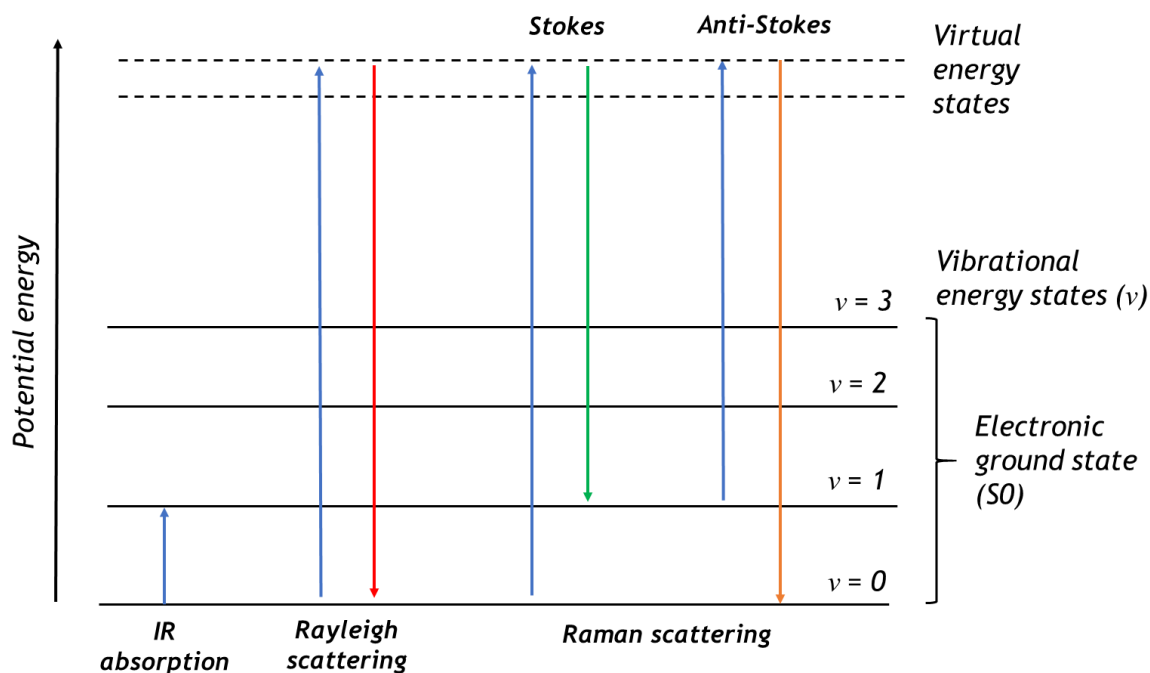


Figure 2.4: Schematic diagram of IR and Raman transition mechanisms, compared to Rayleigh (elastic) scattering and IR absorption.

Raman analysis was performed using a Horiba-Jobin Yvon LabRam HR confocal microscope. A Nd:YAG laser in the second harmonic (532 nm) and a He-Cd laser (325 nm) are the excitation sources of the apparatus for visible and UV light measurement respectively. The microscope is equipped with a 50x objective lens and a special 10x lens for UV radiation. A Synapse CCD detector collects the scattered radiation, with the spectra analysed with the software LabRam. The measurements were performed setting an acquisition time of 5 seconds, laser output variable between 10 and 25% depending on the crystallinity of the sample, and an accumulation of 20 measurements. The powdered samples were placed on a glass microscope slide and pressed creating a surface as even and as flat as possible to minimise signal noise.

2.5.3 UV-Vis spectroscopy

Unlike the previously described techniques, UV-Vis spectroscopy involves transition between electronic levels rather than the vibrational ones. The absorption of visible or near visible monochromatic light by a solid or liquid sample gives an indication as to the electronic structure of the material, in particular about the energy difference between occupied and unoccupied electronic levels. During the analysis, a wide spectrum of monochromatic wavelengths irradiates the sample. The amount of light absorbed (or transmitted) is compared to a reference (e.g. a measuring cell filled with pure solvent in the case of a liquid sample). In the basic instrumental configuration, two beams of monochromatic light travel in a parallel direction; one for the reference and the other for the sample. The instrument collects the two beams and calculates the difference in intensity between the light passing through the reference (I_0) and the sample (I). The intensity difference is plotted as an absorption spectrum. For a transmittance measurement, the total energy collected is normalised and the signal relative to the reference assigned the value of 100%. In most of the spectrometers, absorbance (A) and transmittance (T) are related by the formula:

$$A = 2 - \text{Log}(T) = 2 - \text{Log}\left(\frac{I}{I_0}\right) \quad (\text{eq. 2.15})$$

Because of its mathematical derivation, the values of absorbance are usually indicated in arbitrary unit (A.U.). The absorbance is also used to perform quantitative measurement, since its value is linearly dependent by the concentration of a material (generally a solute in solution) according to the Beer-Lambert equation:

$$A = \varepsilon Cl \quad (\text{eq. 2.16})$$

where C is the sample concentration, l is the optical path of the beam through the sample and ε is the extinction coefficient, inherently related to the material properties of the sample.

The resolution of the instrument depends on its components (detector, monochromator, optics). Usually absorption values fall from the Lambert-Beer linearity above 2 A.U., with a total saturation of the detectors at ca. 3-3.5 A.U. for the standard configuration of spectrometer. For instance, double monochromator UV-Vis can achieve 6 A.U. in absorbance (10^{-5} % of transmittance).

For all the measurements (absorbance, reflectance and transmittance on solution and solid state powder), a Shimadzu UV-Vis 2600 was used, provided with a 50 W halogen lamp and a D₂ lamp and equipped with a photomultiplier GaN detector.

2.5.4 Diffuse Reflectance UV-Vis (DR-UV-Vis) spectroscopy

Reflection describes the effect of light scattered back by a surface. Reflection is specular from an ideally planar surface without defects, at the light travelling back with an angle to the surface normal equivalent to the angle of incidence. Visible light specular reflection occurs from a mirror-like surface, whereas for all other surfaces the reflected light is scattered in all the possible directions, due to superficial roughness and imperfections. For opaque surfaces with negligible transmission, light can be absorbed or reflected. Measurement of diffuse reflection is hence useful for the determination of sample absorbance.

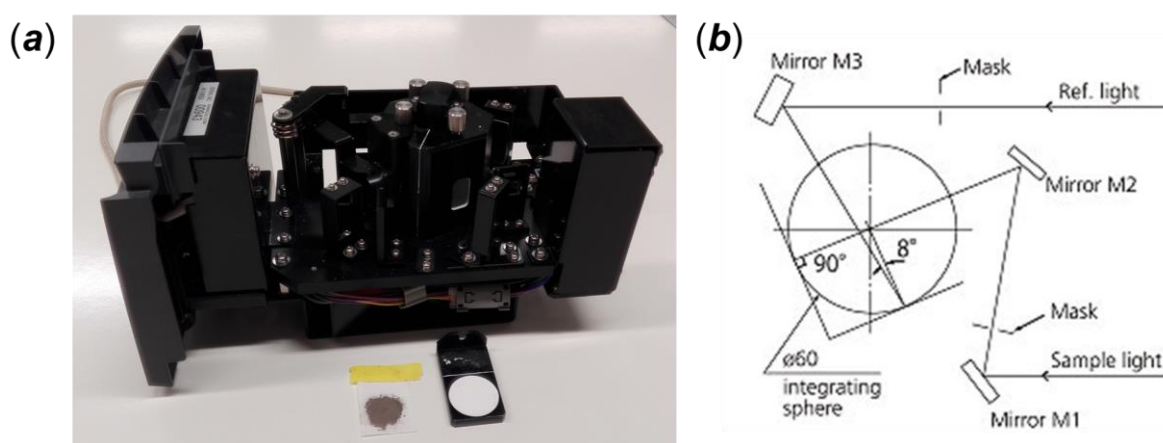


Figure 2.5: (a) Integrating sphere device, with BaSO₄ support and sample prepared for the measurement and (b) geometry of the integrating sphere (from Shimadzu).

Reflectance measurements require an integrating sphere attachment (ISR-2600 Plus) to the UV-Vis spectrometer. The reflectance or the absorbance are measured as a function of the wavelength of the incident radiation as in normal UV-Vis spectrometry. In the integrating sphere, the inclination of the sample and the reference with respect to the incoming beam allows the specular reflectance to exit undetected, with the diffuse reflectance is concentrated by the BaSO₄-coated inner walls of the sphere and collected by a photodiode. The beam is directed to the sample by a geometrical arrangement of parabolic mirrors. Barium sulphate is

also used for the baseline determination, since it reflects all radiation within the operative range of the spectrometer (190-1300 nm).

Band gap calculation

The optical band gap represents the energy required for a photon to be absorbed by a material. The absorption of the photon and associated energy is equivalent to the difference between the conduction and valence band. The optical band gap is not equivalent to the electronic band gap, defined as the energy necessary to produce a non-bound couple of a hole and an electron.

The determination of the optical band gap in semiconductors is easily extrapolated from its absorption spectrum according to the process originally proposed by Tauc, David and Mott.^[19, 20] The model, commonly known as Tauc's plot, proposes the proportionality between the band gap (E_g) and the absorption coefficient (α) of the material:

$$(h\nu\alpha)^{\frac{1}{n}} = A(h\nu - E_g) \quad (\text{eq. 2.17})$$

where h is the Planck constant, ν is the light frequency and A is a proportionality constant depending on the properties of the material. n is defined as power factor and its value depends on the nature of the optical transition probability.^[21] Briefly, a transition is direct when it does not involve a change in momentum and the sole interaction occurs only between the photon and the electron. A modification in momentum that defines an indirect transition involves an additional interaction with a phonon to promote the transition of the electron to the valence band. A transition can be classified as allowed or forbidden according to the momentum and energy conservation principle. The transition is generally allowed if the initial and final electronic states belong to two different bands; the intra-band transitions, in which the two states lay in the same band, are hence forbidden. The values of n (listed for each transition in Table 2.2) derive from the description of the electronic bands through their wavefunctions in function of the imaginary part of the dielectric constant of the material.^[19]

Table 2.2: Correlation exponential term for the Tauc expression

allowed	$n = 1/2$	$n = 2$
forbidden	$n = 3/2$	$n = 3$

A more refined model for the calculation of the band gap involves a description of optical properties considering the contribution of the scattering through the reflectance measurement. The Kubelka-Munk model is a two-flux model, with the light diffused by the sample travelling in the forward and reverse directions. [22] According to the Kubelka-Munk theory, [23, 24] the absorption coefficient (K) in the optical transition expression is weighted by the scattering coefficient (S). The ratio of the two coefficients is a function of the diffuse reflectance emerging from a theoretically infinite thick and opaque layer (R_∞): [25]

$$F(R_\infty) = \frac{K}{S} = \frac{(1 - R_\infty)^2}{2R_\infty} \quad (\text{eq. 2.18})$$

where $F(R_\infty)$ is the Kubelka-Munk function, which can be replaced in the Tauc's expression (eq. 2.17) giving:

$$(h\nu F(R))^{1/n} = A(h\nu - E_g) \quad (\text{eq. 2.19})$$

In both the Tauc and Kubelka-Munk model, the plot of $(h\nu F(R))^{1/n}$ as a function of the incident radiation energy generally gives generally a sigmoidal curve for a semiconductor. The characteristic slope is fitted as a linear interpolation. The intersection of the slope with the x-axis ($h\nu$) directly provides the value of the band gap. [26]

2.5.5 X-ray photoelectron spectroscopy (XPS)

XPS is one of the most powerful spectroscopic techniques for the quantitative elemental analysis, at the sample surface, in particular for light elements. The principle of XPS is conceptually similar to those of the other spectroscopic techniques already described. The excitation source in XPS is a focused beam of X-rays ($K\alpha$ from an aluminium target), with energy high enough to expel electrons from the inner core shells of atoms. The energy of the photo-emitted electrons is then analysed. The energy is characteristic of each type of atom in the sample and its electronic shell. The binding energy (E_B) of a particular electron in a specific element is given by:

$$E_B = E_p - (E_k + \phi) \quad (\text{eq. 2.20})$$

Where E_p is the energy of the exciting X-rays, E_k is the kinetic energy of the photo-emitted photon and ϕ is the work function, the minimum thermodynamic work to

extract an electron from a solid, bringing it to a point in the vacuum immediately outside the solid surface.

XPS analysis were performed by the Chemistry Research Laboratory in University of Oxford, using a VG-Escalab X-Ray Photoelectron Spectrometer VGX900 using Al $K\alpha$ radiation with an energy of 1486.6 eV at an operating pressure around 1×10^{-6} Pa. All spectra were fitted using XPS Casa program.

2.5.6 Electronic paramagnetic resonance (EPR)

Electron Paramagnetic Resonance (EPR) is a spectroscopic technique similar to NMR (Nuclear magnetic Resonance) and both analyses are performed by applying an external magnetic field. The magnetic momentum of an unpaired electron could align parallel or antiparallel to the applied field, splitting the electron state in two level distinct by their magnetic quantum number ($m_s = \pm 1/2$, +1/2 if parallel, -1/2 if antiparallel) and therefore with different energy. EPR spectroscopy is based on the application of a specific microwave frequency matching the difference between the two levels and promoting the transition from the parallel state (at lower energy and more occupied) to the antiparallel one. This resonance condition is achieved by sweeping the magnetic field strength, with the microwave frequency fixed. The energetic balance can be expressed by:

$$E = \pm \frac{1}{2} g \mu_B B_0 \quad (\text{eq 2.21})$$

$$\Delta E = \hbar \omega_0 = g \mu_B B_0 \quad (\text{eq 2.22})$$

where E and ΔE are the energy and energy difference of the split levels, B_0 is the intensity of the external magnetic field, μ_B is the Bohr magneton, g the Lande g -factor and ω_0 the resonant frequency.

The technique is particularly sensitive to the chemical environment of the unpaired electron. For example, the g is factor is affected by the spin-orbit coupling between the ground state of the atom and the excited state of the unpaired electron associated with the same atom. The coupling modifies the magnetic momentum, altering the calculated g -factor, which will be different from the value associated with a free electron (~ 2). The variation of the g -factor contains information on the electronic structure of the molecule and it is sensitive

to the size of the atom, since larger atoms exhibit a stronger spin-orbit coupling and resulting magnetic momentum. In the analysis of inorganic compounds, the technique is useful only in case of paramagnetic species. However, modification of the electronic structure of a diamagnetic material by doping or photoactivation could be responsible for the formation of an EPR active centre, as in case of Ti^{3+} reported in several cases after band gap modification of TiO_2 .^[27]

EPR measurements were performed on a Bruker EMX EPR spectrometer.

2.6 Elemental analysis (C, N, H)

The term elemental analysis usually refers to several different techniques (Atomic Absorption Spectroscopy, Titrations, Mass spectrometry, etc) aimed to quantify the exact concentration of a specific element in a sample. Combustion analysis is one of the simplest technique to determine the lighter elements of the periodic table, in particular hydrogen, nitrogen and carbon. ^[28] The sample is burnt at very high temperature (1173 K) in a pure oxygen atmosphere under static conditions. The combustion produces light gases such as H_2O (in the form of steam), CO_2 , N_2 and nitrogen oxides, carried by a helium flow. After catalytic reduction/oxidation and a series of traps, the residual gas is analysed by a series of high-precision thermal conductivity detectors, each containing a pair of thermal conductivity cells. The difference in thermal conductivity can be correlated with the quantity of the three elements.

The quantitative analysis of C, H and N in the sample was conducted using an Exeter Analytical CE-440 combustion analyser, which requires a very small amount of sample (*ca.* 5 mg), even though the accuracy of the result is dependent on the amount of sample. The measurements are performed in duplicate. The two different measurements should not differ to more than 0.3% in a homogeneous sample and the measurement is considered accurate if the experimental results are within an error of $\pm 0.3\%$ from the theoretical values.

2.7 Specific surface area determination

Specific surface area of the samples was measured by isothermal N₂ adsorption-desorption analysis. In the procedure, the sample is placed in a closed system, which is completely evacuated and progressively refilled with N₂, until the pressure reaches the atmospheric value. Subsequently, the sample is degassed again decreasing the pressure down to the value prior to the beginning of the measurement. All the operations are carried out at a constant temperature of 77 K, keeping the sample immersed in a liquid N₂ bath. The resulting absorption/desorption isotherms present a specific shape depending on the porosity of the sample. The presence of a hysteresis between the adsorption and desorption isotherms denotes a well-defined degree and distribution of porosity.^[29]

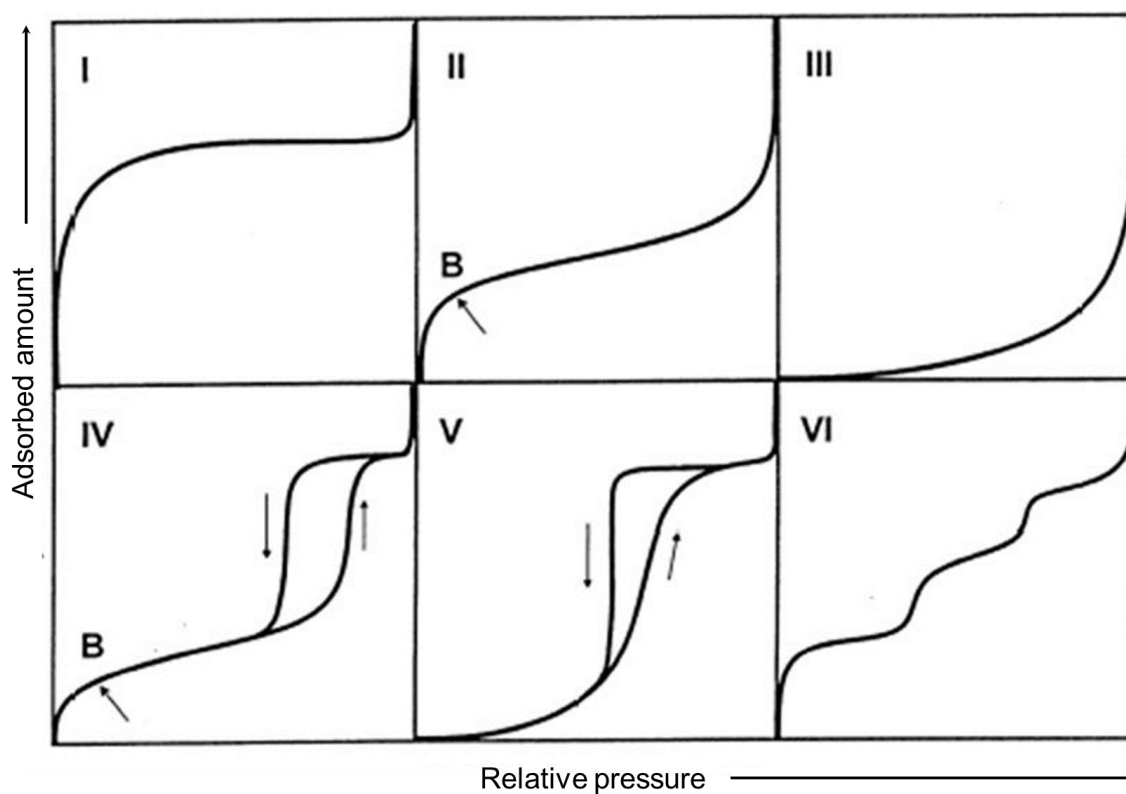


Figure 2.6: IUPAC classification of the adsorption/desorption isotherm for different materials: (I) microporous materials; (II) non-porous or macroporous materials; (III) materials in which lateral interactions between adsorbed molecules are strong with respect to the interactions between the adsorbent surface and adsorbate; (IV) mesoporous material with capillary condensation (hysteresis); (V) mesoporous materials presenting the same phenomena as the material of type III isotherm; (VI) stepwise multilayer adsorption on a uniform non-porous surface. The point B represents the achievement of adsorption of a complete N₂ monolayer on the analysed surface, with beginning of multilayer adsorption. ^[29]

Calculation of the surface area is mainly based on the Brunauer-Emmet-Teller (BET) theory, which calculate the surface area considering the physical adsorption of a monomolecular layer of gas molecule on the surface. [30] According to the BET theory, the adsorption isotherm can be described by the equation 2.23:

$$\frac{1}{v \left[\left(\frac{p_0}{p} \right) - 1 \right]} = \frac{C - 1}{C v_m} \left(\frac{p}{p_0} \right) + \frac{1}{C v_m} \quad (\text{eq 2.23})$$

where v is the volume of adsorbed gas, v_m is the volume of a single monolayer of gas adsorbed to the surface and p and p_0 are the equilibrium and the saturation pressure of N_2 respectively. The parameters of the equation can be calculated by plotting the first term of the equation as a function of the relative pressure. C is defined as the BET constant related to the enthalpy of adsorption of the adsorbate gas as a monolayer on the sample, providing an indication of the strength of the interaction between the gas molecule and the surface. The BET algorithm is usually applied to the initial part of the adsorption isotherm; as a rule of thumb, the values of p/p_0 between 0.05 and 0.3 are considered for the calculations.

N_2 adsorption/desorption measurements were performed using a Quantachrome EVO instrument, with the plot of the isotherm and the calculation of surface area and pore size distribution performed with the associated QuadraWin software.

2.7.1 Pore size distribution

The analysis of the N_2 isotherms is also a powerful instrument to determine the average pore size and pore distribution. Several algorithms are available for the calculation, each fitting a typical morphological situation (micropores, cylindrical slit-like pore shape, etc.). The most commonly used are the BJH algorithm or the Density Functional Theory (DFT) approach. BJH is a theory named after its original authors (Barrett, Joyner, Halenda) and extends the Kelvin equation for the determination of the pore size distribution in mesoporous solids.[31] The BJH approach considers the desorption process as the progressive reduction of the thickness of the adsorbed layers of gas molecules inside the pores.

Unlike the BJH model and other algorithm developed for the calculation of the pore size distribution, DFT is based on the simulation of the sorption and the phase behaviour of fluids in narrow pores on a molecular level instead of a macroscopic modelling of the gas adsorption/desorption, providing a more accurate and

realistic pore size analysis. Adopting this kind of approach, the experimental isotherm from a porous solid is described by the Generalized Adsorption Isotherm (GAI) equation:

$$N\left(\frac{p}{p_0}\right) = \int_{W_{min}}^{W_{max}} N\left(\frac{p}{p_0}, W\right) f(W) dW \quad (\text{eq 2.24})$$

in which the total adsorption isotherm $N(p/p_0)$ is given by the series of the individual isotherms of the single pores $N(p/p_0, W)$ weighted by a pore size distribution function ($f(W)$). The pore size distribution is calculated solving the GAI equation using a non-negative least square algorithm.

The models considering the thermodynamic equilibrium of nitrogen for materials presenting mixed pore shape matches with the desorption BJH, despite the overestimation of the pore size distribution. The most common model is the non-linear DFT (NLDFT), which is particularly effective for ordinate and definite pore structure, such as silica and zeolites. However, NLDFT models do not consider heterogeneous structures or more complex geometries besides slits, cylinders or spheres. The consequence of this simplification is that it induces a strong layering in the adsorbed phase, especially at low temperatures. Therefore, adsorption isotherms exhibit artificial steps in the region of multilayer adsorption

QSDFT model considers the solid as a distribution of solid atoms rather than as a source of the external potential field, as in the NLDFT analysis. DFT models consider the adsorption branch of the N_2 isotherm or the point in which the equilibrium of capillary condensation is achieved. [32]

2.8 Thermal analysis

2.8.1 Simultaneous thermogravimetric analysis (STA: TG-DTA)

Simultaneous thermogravimetric analysis (STA) is a combined technique giving access to important information such as thermal stability, identification of thermal events such as dehydration, decomposition, melting or phase transformations and calculation of parameter such as activation energy relative to an observed event. STA comprises thermal gravimetric analysis (TGA) and differential thermal analysis (DTA). TG analysis records the change of mass of the sample under a certain heating program; DTA is a comparative analysis of the sample with a reference, usually an empty alumina sample holder (the same used

for TG analysis. The difference in temperature between the sample and the reference is measured by using the same heating program. The thermal treatment was performed in this study under inert atmosphere, generally a flux of argon. Mass and sample temperature difference are recorded as a function of time and temperature. The simultaneous record of mass and temperature difference allows a precise classification of the thermal events, for instance structural or state changes not associated with loss of mass is decomposition or chemical reactions, where a mass change is appealed. The resulting DTA profile gives information about the thermodynamic nature of the event, specifically if an exothermic or endothermic process occurs.

The STA measurements were carried out using a Netzsch STA 409 PC instrument. The profiles are analysed using the Proteus Analysis Software associated with the instrument.

2.8.2 Mass spectrometry (MS)

Mass spectrometry is associated with the STA for the detection and quantification of the released gaseous compounds during thermal treatment. This spectrometry is based on the ionisation of the gaseous molecules by an electron source, with further application of an electric field (\vec{E}) and a magnetic field (\vec{B}) to select the ions on the basis of their mass-to-charge (m/z) ratio, according to Newton's second law of motion and Lorentz's law:

$$\left. \begin{array}{l} \vec{F} = m \cdot \vec{a} \\ \vec{F} = z(\vec{E} + \vec{v} \times \vec{B}) \end{array} \right\} \rightarrow \frac{m}{z} = \frac{(\vec{E} + \vec{v} \times \vec{B})}{\vec{a}} \quad (\text{eq 2.25})$$

where \vec{F} is the force resulting from the application of the fields, \vec{v} and \vec{a} are the velocity and the acceleration, respectively, of the ionised particles subjected to the fields.

MS analysis was performed with a Hiden Analytical HPR 20 spectrometer, equipped with a quadrupolar mass analyser designed for fast transient gas detection. The detector is composed of four rods to which are applied a radiofrequency (RF) and a direct current (DC) potential at the opposite pairs. The phase oscillation of the RF keeps the ionised molecules in the channel formed by the rods, while the application of a ramp of DC potential select the ions able to cross the channel

without colliding with the bars and reaching the collector at the end of the channel.

The gas detection was performed using the software MASsoft Pro associated with the instrument. Detection of argon as carrier gas was always monitored.

2.9 Colloidal dispersion stability

Small inorganic particles in aqueous suspension are characterised by the presence of a charged surface, resulting in interactions with the surrounding ions. Nonetheless, water molecules tend to adsorb to the surface of the particle, especially in the case of metal oxides. The ionic environment surrounding a particle in water is generally defined by a sphere of adsorbed molecules and ions, also known as the Stern layer, and a surrounding sphere in which loosely bound ions feel the influence of the attractive force of the particle, maintaining a certain freedom of movement but translating together with the particle. This sphere of influence is defined as a diffuse layer, limited by the slipping plane, which the ions inside the influence sphere cannot exit. The Stern and diffuse spheres define together the electrical double layer of a surface.

2.9.1 Dynamic Light Scattering (DLS)

Dynamic light scattering (DLS) is a powerful technique for the determination of the real size of particles and colloidal object in solutions. The principle of this technique is based on the interaction of laser light with particles dispersed in a liquid suspension. The particles are in Brownian motion, randomly colliding with molecules and particles in the surrounding media. The velocity and the size of the particles are related through the diffusion coefficient, according to the Stokes-Einstein equation (*equation 2.26*) the smaller the particles, the higher their diffusion coefficient (D) and hence their motion velocity.

$$r_H = \frac{kT}{6\pi\eta D} \quad (\text{eq. 2.26})$$

where r_H is defined as the hydrodynamic radius, k is the Boltzman constant, T is the absolute temperature and η is the liquid viscosity. When the size of a particle is relatively smaller compared with the wavelength (λ) of the incident radiation (approximately $<\lambda/20$), the radiation is scattered in different directions preserving

its energy, without any change in its wavelength. The illuminated particles in Brownian motion generate scattered radiation. If the scattering is observed in a certain direction, then the intensity of the scattered radiation fluctuates due to a series of constructive and destructive interference processes due to the random motion of the particles.

DLS considers a temporal correlation function of these intensity fluctuations, specifically the correlation with the intensity of the signal weakened over time. The autocorrelation function results in an exponential decay with time (*equation 2.27*). The decay rate depends on the size of the particles: for smaller and faster particles, the signal correlation will fade at a higher rate. [33]

$$G(t) = \langle I(t_0)I(t + t_0) \rangle = A + \left(\sum_i B_i e^{-\frac{t}{\tau_i}} \right)^2 \quad (\text{eq. 2.27})$$

The autocorrelation function can be considered as a combination of the decay rates related to each size class. The solution of the function gives a size distribution, quantified by the relative intensity of the scattered light. Using the Mye scattering theory, the intensity, of the light can be correlated to the volume or the number of particles per size class.

DLS (and zeta potential) were measured using two different Zetasizer Nano instrument (Malvern UK) in order to compare the results and estimate the error in size distribution.

2.9.2 Zeta-potential

The zeta potential is defined as the potential at the slipping plane of the electrical double layer. It provides a measurement of the effective charge density on a particle surface in solution and an indication of the stability of a colloidal suspension. The zeta potential is estimated through electrophoretic measurement. The velocity of the particle when a constant electrical field is applied to the colloidal surface, also known as electrophoretic mobility (u_E), is described by the Henry equation (*equation 2.28*):

$$u_E = \frac{2\varepsilon \zeta f(ka)}{3\eta} \quad (\text{eq. 2.28})$$

where the particle velocity is directly proportional to the dielectric constant of the surrounding media (ε) and inversely proportional to its viscosity (η). The

velocity of the particle is determined by the change in frequency of the light scattered from the laser. This technique is referred as Laser Doppler Electrophoresis (LDE). $f(ka)$ is defined as Henry's function. Its value is generally approximated to 1.5 for aqueous solution using the Smoluchowski approximation,^[34] which applies when the double layer is thin in comparison with the particle radius, indicating a moderate electrolyte concentration.^[35] In the case of non-aqueous measurement, a value of 1.0 is adopted for the Henry's function (Huckel approximation).^[36]

A general criterion for the definition of suspension stability is an absolute value of zeta potential above 30 mV. The zeta potential is highly dependent on the pH of the solution. The measurement of the zeta potential at different pH provides the identification of the isoelectric point (IEP) of the particles, which defines the situation in which there is no net charge on the particle surface. At the IEP, the colloidal system is in its least stable state.

The zeta potential was measured using the same instrument used for the DLS analysis. Zeta potential measurement were performed using a folded capillary cell with Cu contact (DTS 1070, Malvern Instrument UK). Suspensions for both DLS and zeta potential measurement are commonly prepared adding an electrolyte that does not interact with the compound in solution preventing a screening effect on other charged particles. The solutions most reported are 10^{-3} or 10^{-2} M KNO_3 .^[37]

2.10 Coating and thin film characterisation

2.10.1 Contact angle measurement

The surface wettability towards water or other liquids is evaluated with a very simple method, involving empirical observation of the behaviour of the test liquid on the surface. When a drop of liquid is on the surface, its shape is defined by the contact angle (CA); the angle between the surface and the drop shape profile at the interface between the two media and the surrounding atmosphere. The value of the contact angle is given at the equilibrium induced by the reciprocal interactions of the three media with each other.

The contact angle characterises the wettability of a surface. In the case of water, if the drop forms an angle with the surface below 90° , the surface is considered

hydrophilic, with strong affinity between the surface and water; on the other hand, if the contact angle is above 90°, the surface is classified as hydrophobic. The simplest method to measure the contact angle is the sessile drop method, in which a droplet of few µL of deionised water is deposited on the surface. The image of the drop is captured by a camera and the angle is estimated successively. The image capture should be taken almost immediately or at least a constant interval should be established between the deposition of the droplet and the angle measurement. For the wettability measurements, a Drop Shape Analyser (DSA25, KRÜSS GmbH, Germany) equipped with a Teli CCD Camera and automatic syringe was employed; DSA software was used to control the liquid drop on the surface. Contact angle values were estimated from a minimum number of 5 sampling points from 3 independent samples.

2.10.2 Atomic Force Microscopy (AFM)

Atomic Force Microscopy (AFM) is a very effective technique for the measurement of the sample morphology, surface topography and roughness. AFM provides a three-dimensional profile of the surface with nanometric resolution. The principle is based on the calculation of the force between a sharp nanometric probe (with a radius smaller than 10 nm) and the surface at a very short distance from the tip of the probe (same order of magnitude of the probe radius). A flexible cantilever holds the probe and deflects because of the interaction of the probe with the surface when they are very close or in contact. The measure of the deflection (x) gives the interaction force (K), according to the Hooke's law:

$$F = -kx \quad (\text{eq. 2.30})$$

where k is the elastic constant and depends on the cantilever material. The surface is scanned by the probe, with a topographic image extrapolated by the force value mapped during the scansion.

AFM measurements were performed using a Bruker Dimension Icon AFM with ScanAsyst®. The analysis of the surface images was performed using the Gwyddion software (version 2.49).^[38]

For the measurement of the surface roughness, average roughness (R_a) and Root-mean squared roughness (R_q). The former quantity is given by the formula:

$$R_a = \sum_{n=1}^N \frac{|Z_n - \bar{Z}|}{N} \quad (\text{eq. 2.31})$$

where Z_n is the height at the sample point n , \bar{Z} is the height of the centre plane and N is the total number of points in the sample area. R_q is given instead by the standard deviation of the Z values:^[39]

$$R_q = \sqrt{\sum_{n=1}^N \frac{(Z_n - \bar{Z})^2}{N}} \quad (\text{eq. 2.32})$$

2.10.3 Multi parametric Surface Plasmon Resonance (MP-SPR)

Surface Plasmon Resonance (SPR) spectroscopy is an optical technique particularly useful for the characterisation of the interaction of adhesive molecules (such as proteins) or the thickness of coatings. The SPR technique gives access to both *ex-situ* and *in-situ* analysis of the thickness, interaction energy and kinetics of the formation of the coating, with a relatively simple and economic setup.

SPR spectroscopy is based on plasmons, which could be basically described as the resonance of free electrons on a metal surface when excited by a powerful source, such as laser. The resonance produces an absorption maximum depending on the angle of the incident light beam. The angle at which the maximum occurs is referred as to resonance angle. In principle, since the plasmon resonance is strongly affected by the dielectric constant near the metal surface, any small variation of this parameter could influence the resonance angle. The resonance angle is sensitive to any change of the refractive index, generally shifting towards higher angles when new material is deposited.

In the multi-parametric SPR (MP-SPR) approach, the use of a second wavelength for the excitation provides more precise information about the thickness and the refractive index variation on the exposed surface. The laser excitation wavelengths usually employed are 670 and 785 nm. Typical measurements are performed in a range of incident angle between 37 and 78°. An SPR curve is generally produced measuring the reflection at a glass prism of a metal coated surface (generally gold) as a function of the incident angle. Apart from the resonance angle, identified in the spectrum as a parabolic minimum, the total internal reflection is another important feature of an SPR curve. The angle at

which the edge of total reflection occurs depends only on the difference of the dielectric constants of the glass prism and the medium in which the measurement is performed (air or water). This value is independent of the sample but it is highly influenced by the “buffer” used, that is any variation of dielectric constant of the supporting media (ionic strength, pH, type of solvent. The FWHM of the resonance peak could be defined as the “width of the plasmon” and it depends on the imaginary part of the dielectric constant of the metal. For example, a plasmon on a silver surface is much sharper than the one on gold. ^[40] At the SPR wavelength, organic molecules generally do not absorb light, resulting in $\epsilon'' = 0$. Any change of the broadening of the resonance peak is then caused by surface heterogeneities. Apart from the SPR curve itself, different parameters can be isolated and followed as a function of time using a sensogram. The measurement of the thickness and refractive index of a coating or a deposited layer could be performed using the double wavelength excitation or by measuring the plasmon resonance of the sample in two different media with a high difference in refractive index, such as water and air. It is preferable to use the double wavelength approach in the case of materials whose thickness could change by exposure to different media. This is the case of polymer and PEM coatings, which could easily swell in presence of water. Apart from the thickness and the optical properties of the adsorbed layers, SPR also provides information about the mass of the adsorbed matter, using the formula proposed by de Feijter:^[41]

$$m = t \frac{n_A - n_C}{\frac{dn}{dc}} \quad (\text{eq.2.33})$$

where t is the thickness of the adsorbed layer, n_A is the refractive index of the adsorbed layer, n_C is the refractive index of the cover medium and the differential dn/dc is the increment in the refractive index from molecule adsorption.

The sample used for SPR measurement is usually a chip made of glass and coated with a thin layer (50 nm) of gold. Between the glass and the gold, an ultrathin layer of chromium (2 nm) is deposited to provide stronger adhesion and stability to the gold layer. For *ex-situ* measurement, the sample is coated using different techniques (sol-gel, Langmuir Blodgett, CVD, ALD, LbL) and the SPR curve is compared with the bare chip as a reference. *In-situ* measurements are particularly useful for the analysis of the deposition of multiple layers on a surface, and provide the adsorption kinetics. A time-resolved kinetic SPR scan could identify

the deposition of each layer from its particular kinetic behaviour by following the resonance angle of the SPR curve.

The instrument used for the SPR measurement was a MP-SPR Navi™ 2000-150 instrument (BioNavis, Finland), with a maximum flow capacity of 300 $\mu\text{L}/\text{min}$.

2.11 Electron microscopy

2.11.1 Scanning Electron Microscopy (SEM)

Scanning Electron Microscopy (SEM) is a destructive imaging technique essential for the analysis of morphology at a micro- and nanoscale. The basic principle of electron microscopy is to overcome the diffraction limits of light limiting the magnification resolution in optical microscopy. A beam of accelerated electron is generated by the thermoionic effect from a LaB_6 filament and focused onto the sample using magnetic lenses. The instrument operates under high vacuum to preserve the filament from oxidation and to avoid interaction of the electron beam with atmospheric molecules.

Different signals are generated due to the collision of the electrons with the sample, providing different information about the sample topography and elemental composition.^[42] Elastic collisions produce reflected or back-scattered electrons (BSE), with energy higher than 50 eV, generally emerging from deep within the sample.^[43] Inelastic collisions are responsible for the emission of secondary electrons (SE), X-rays and Auger electrons. SE have 3-5 eV of energy generally produced a few nanometer from the surface of the sample, providing higher resolution for the reconstruction of the sample image compared with all the other signals.

SEM analysis was performed in the School of Chemistry using a Philips XL30 ESEM, operating with acceleration voltage of 20 V. The images were collected at a working distance of 5 mm and a maximum magnification of 10k x, above which it is impossible to distinguish any detail. This limited the size distribution analysis to particles with a diameter bigger than 200 nm. Most of the samples analysed required conductive coating, preventing the accumulation of electrical charges on the dielectric surface. The multiplication of signal from the surface and the reduction of secondary electrons is detrimental to the image quality and resolution. As an alternative to conductive coating, dielectric surfaces can be

observed by reducing the emission voltage or improving the quality of the vacuum. The samples were placed on an aluminium stub equipped with a conductive carbon adhesive tab. The as-prepared samples were sputter-coated with gold or palladium using a Polaron SC7640 plasma sputter coater. Due to the limited resolution of the instrument, high resolution SEM analysis was conducted with a Carl Zeiss Sigma variable pressure analytical SEM with Oxford microanalysis, belonging to the Imaging Spectroscopy and Analysis Centre (ISAAC), in the School of Geographical and Earth Sciences (GES). This microscope uses an operating voltage between 5 and 25 kV, with images collected at working distance of 5 mm. The instrument is equipped with Schottky thermal field emitter electron source and an In-lens secondary detector.

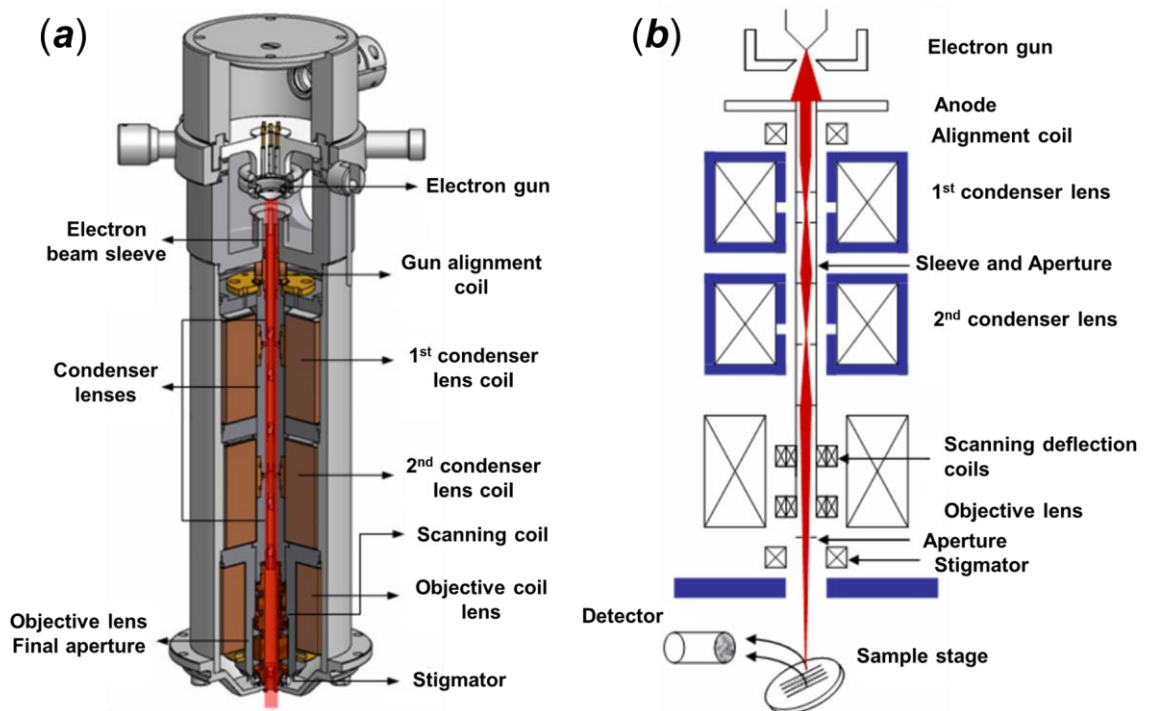


Figure 2.7: (a) Section view and (b) schematic diagram of the electron optical component of a scanning electron microscope (SEM).^[44]

2.11.2 Energy-dispersive X-Ray spectroscopy (EDX)

Energy-dispersive X-Ray spectroscopy (EDX or EDS) is a semi-quantitative analytical technique associated with SEM microscopy, useful for the determination of the elemental composition of a specimen. The same electron beam focused onto the sample for the SEM analysis promotes the excitation and expulsion of electrons from the inner shells of the atoms. The consequent formation of a vacant position causes the rearrangement in the atomic electronic structure, with the

decay of an electron from the outer shells and emission of radiation with an energy corresponding to the difference between the two transition levels, giving an emission of X-rays. The emission is strictly dependent on the atomic structure and correlates with the presence of a precise element and allows quantitative estimation. Due to the mechanism of generation of the detected X-rays, the technique is sensitive to elements with a K-shell. The analysis of light elements (conventionally below Beryllium, which was the standard material for detector windows until the 1980's) ^[45] is affected by low fluorescence yield (Auger emission is favoured), emission of low energy X-rays unable to leave the sample or even absorbed by the detector window and peak overlaps with L, M and N lines of heavier elements. ^[46]

2.11.3 Transmission Electron Microscopy (TEM)

Transmission Electron Microscopy (TEM) exploits the same basic principle as the SEM, where an image is generated by the interaction of a high-voltage accelerated electron beam with a specimen. The acceleration voltage of the electron beam is 100 keV, much higher compared with SEM, with an operating voltage of 120 kV against 20 kV of the latter instrument. Unlike the SEM, in which most of the collected signals emerge from the surface, in TEM the electron beam is transmitted through the sample, even if part of it is equally scattered. An obvious requirement for TEM analysis should be the transparency of the sample towards the electron and preparation of very thin samples with a thickness lower than 100 nm is essential.

The scattered electrons are also useful for crystal structure analysis. Considering the de Broglie equation, a moving electron can be equated to a wavelength, which in case of the scattered electrons is smaller than the atomic spacing, resulting in diffraction phenomena similar to those produced by X-rays. The exploitation of these signals is known as Selected Area Electron Diffraction (SAED or SAD). The collection of the scattered electrons produces a precise pattern reproducing the reciprocal lattice. The interaction of electrons from polycrystalline materials results in diffraction rings.

TEM analysis was performed using a FEI Tecnai TF20 microscope in the School of Physics and Astronomy at Glasgow University. For the image collection, a spherical aberration coefficient of 1.2 mm was used, resulting in 2.4 point resolution and

1.5 line resolution. The samples were prepared by dispersing the powder in acetone, placing some drops of the suspension on a copper grid.

2.12 Photocatalytic degradation

2.12.1 Organic dyes as pollutant model

The most common test used to evaluate the photocatalytic performances of a photocatalytic material is the controlled degradation of an organic dye. The experiment is carried out under illumination from different sources of light (depending on the band gap or on the specific application of the photocatalyst). From their molecular structures, organic dyes such as Rhodamine B, Methylene Blue or Methyl Orange II are good models for representative organic compounds, such as organic pollutants in wastewater. The molecules of commonly used dye are shown in Figure 2.8. The radicals produced by the photogenerated charge carriers attack the aromatic cycles of the organic dye. The aromatic groups absorb visible light, being the principle cause of this typical coloration.

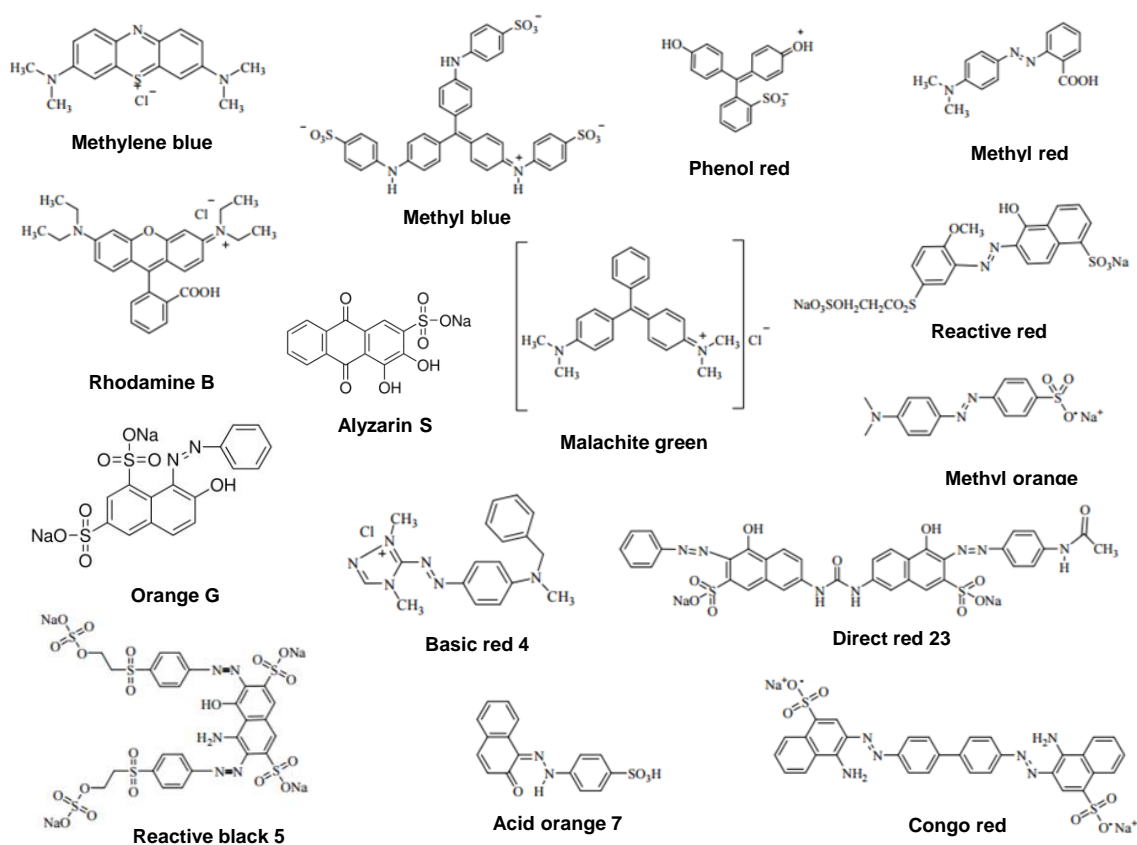


Figure 2.8: Examples of common organic dyes used in photodegradation evaluation tests. (adapted from [47]).

The degradation of those groups results in a progressive decolouration of the solution and consequently a drop in the absorption peak. Consequently, photocatalytic degradation of dyes can be followed by UV-Vis absorbance spectroscopy, measuring the change of the absorption intensity compared with the one of the initial non-irradiated solution. The dye concentration can be easily estimated using the expression:

$$C_{dye}(\%) = \frac{A_t}{A_0} \cdot 100 \quad (\text{eq. 2.34})$$

where A_0 and A_t are the initial absorbance and the absorbance after a certain exposure time (t) respectively. In wastewater treatment related analysis, the complete mineralisation of the degrading compound is also important. The degradation can thus also be followed by measuring the total organic carbon (TOC) or chemical oxygen demand (COD) in solution (equation 2.26):^{[3],[48]}

$$\% \text{ of mineralisation} = \left(1 - \frac{COD_t}{COD_0}\right) \cdot 100 \quad (\text{eq. 2.35})$$

The rate of the process of decolourisation of organic dyes is strictly dependent on the initial concentration of the dye. As this concentration increase, the colour removal efficiency decreases. Low concentration solutions have indeed led to reports of a faster degradation rate.^[3]

For a precise estimation of the degradation rate, the knowledge of the process kinetic is indispensable. In the case of unknown rate of degradation for the dyes, the experimental data could be fitted using an n-th order equation, following the Levenspiel model:^[49]

$$-r_{dye} = -\frac{dC_{dye}}{dt} = kC_{dye}^n \Rightarrow -\frac{dC_{dye}}{C_{dye}^n} = kdt \quad (\text{eq. 2.36 a})$$

$$-\int_{C_{dye,n}}^{C_{dye}} \frac{dC_{dye}}{C_{dye}^n} = k \int_0^t dt \Rightarrow C_{dye}^{(1-n)} - C_{dye,0}^{(1-n)} = (n-1)kt, n \neq 1 \quad (\text{eq. 2.36 b})$$

$$\frac{[C_{dye}^{(1-n)} - C_{dye,0}^{(1-n)}]}{(1-n)} = kt \quad (\text{eq. 2.36 c})$$

Using this equation, the degradation data can be plotted as a linear fit of the n-th order reaction.^[3] In most of the cases, photodegradation of organic dyes by semiconductors is a heterogeneous process, with the photocatalytic material dispersed in the dye solution. The degradation rate of photocatalytic oxidation

tested on various dyes in the presence of a TiO₂ catalyst satisfies the Langmuir-Hinshelwood (L-H) kinetics model:^[50]

$$r = -\left(\frac{dC}{dt}\right) = \frac{k_r KC}{1 + KC} \quad (\text{eq. 2.37})$$

where r is the rate of disappearance of the dye. K represents the equilibrium constant for the adsorption of the organic substrate onto the semiconductor particles, and k_r is the expression of the limiting rate of reaction at maximum coverage for the experimental conditions. When the concentration of the dye is very small (since the dyes are particularly colourful, the typical concentration values for photodegradation experiment are of the order of 10⁻⁵ mol/L or between 10 and 50 mg/L), the L-H kinetic expression can be simplified as:

$$\ln\left(\frac{C_t}{C_0}\right) = kt \quad (\text{eq. 2.38})$$

which is the most used expression to calculate the degradation rate for TiO₂-based catalysts. Both homogeneous and heterogeneous photodegradation of an organic dye in the presence of a TiO₂-based catalyst are reported to follow pseudo-first-order kinetics. The calculation of the apparent degradation rate constant is useful to standardise the outcomes of diverse degradation tests, often involving different operating conditions, setups, source of light, etc.

Rhodamine B (RhB) (Tetraethylrhodamine, also known as Basic Violet 10, Brilliant Pink B, Rhodamine O) is a xanthene class dye, highly soluble in water and in organic solvents. It is widely used as a colorant in textiles and the food industry, and is also a well-known water tracer fluorescent. When dissolved, RhB has a fluorescent bluish-red (or purple) colour. Rhodamine B represents a good general model of pollutants since it has been recently banned from use in foods and cosmetics because of its potential toxicity and carcinogenicity. For this reason, photodegradation of RhB is important with regard to the purification of dye effluents in wastewater treatments. ^[4, 51]

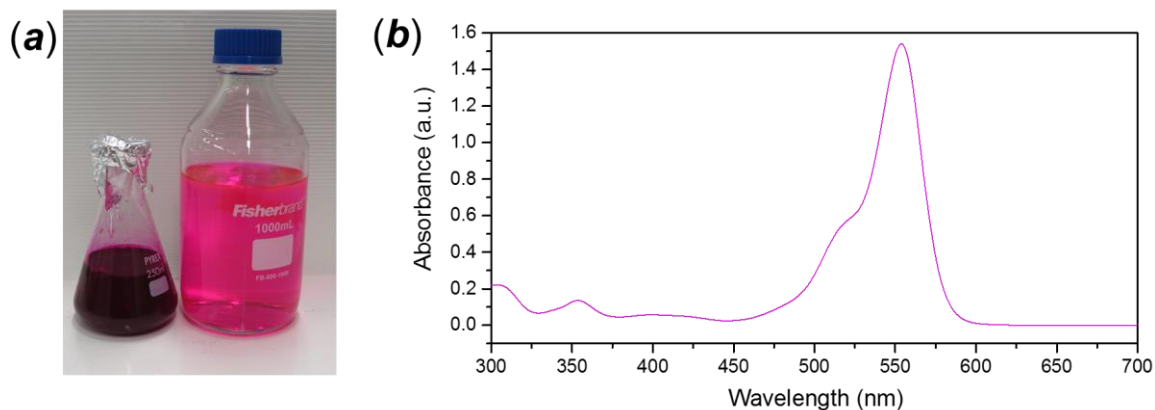


Figure 2.9: (a) picture of rhodamine solutions (10^{-3} M on the left and ca. $5 \cdot 10^{-5}$ M on the right) and (b) absorbance spectrum of rhodamine B in aqueous solution.

2.12.2 Degradation experiment

The dye solution had an approximate concentration of $1.5 \cdot 10^{-5}$ M, corresponding to ca. 1.6 A.U. (ca. 2.5% transmittance). A certain amount of photocatalyst was added to the solution, obtaining a final concentration of 1 or 0.5 g/L. The suspension was sonicated for 10 minutes to disperse the catalyst and stirred for at least 30 minutes, in order to establish equilibrium between adsorbed and desorbed dye molecules from the catalyst surface. 50 mL of suspension was poured into a beaker (250 mL or 100 mL) and exposed to the source of light under stirring. Tubular lamps were used for the illumination. A conventional fluorescent tube (Wotan L20W/23, power 20W, $T=3500$ K) was employed for the visible light radiation, whereas black light phosphorescent lamp (Norman Lamps, F20T8 BLB, 20W, $\lambda_{\max} = 365$ nm) and a low-pressure Hg vapour germicide lamp (LightTech G20T10, 20 W, $\lambda_{\max} = 256$ nm) were used for the UVA and UVC radiation experiment respectively. 2 mL of suspension was withdrawn from the beaker at regular interval. The sample was centrifuged for 20 minutes at 4000 rpm, extracting the supernatant for the UV-Vis measurement. A full spectrum of Rhodamine from 350-750 nm was recorded, minimizing peak intensity errors due to residual particles in suspension generating a non-zero background.

For the photocatalytic efficiency of the functionalised membranes, a batch experiment was performed. ^[52] The membrane was immersed in 12 mL of RhB solution, keeping the membrane soaked in darkness for 1 hour. The solution was then irradiated without stirring or gas bubbling. 2 mL aliquots of solution were measured at regular interval with the UV-Vis spectrometer and returned to the batch solution to monitor the same of volume throughout the entire experiment.

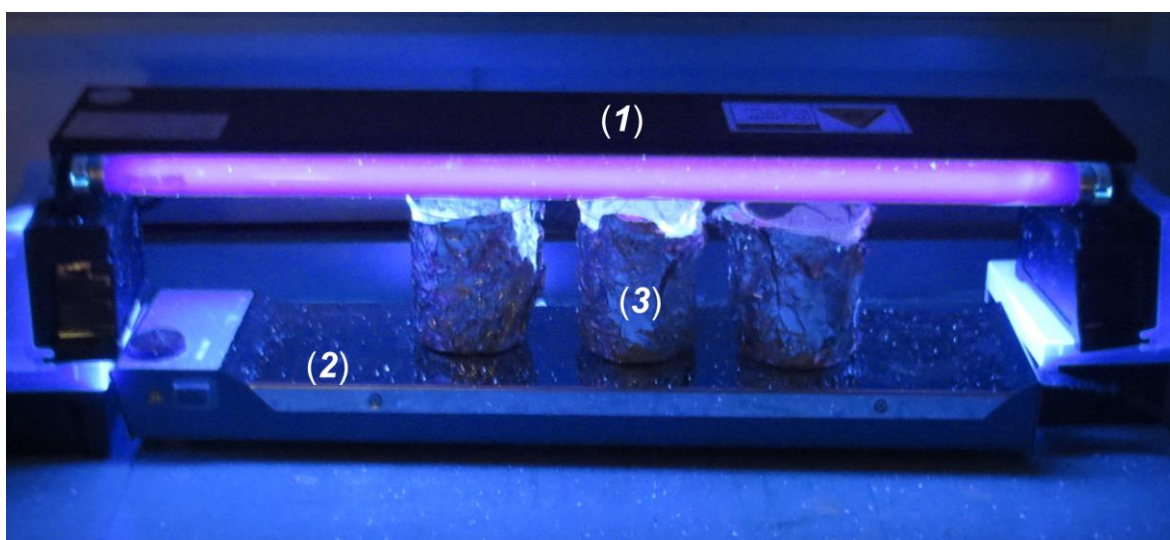


Figure 2.10: Picture of the degradation setup during operations using UVA light. The numbered items are (1) lamp for tube light bulbs, (2) multistirrer plate, (3) 250 mL borosilicate glass beakers wrapped in aluminium foil to maximise the light irradiation and avoid exposure to external luminous sources.

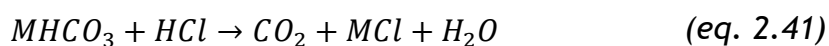
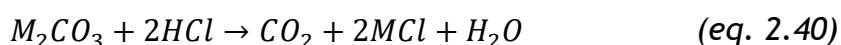
2.13 Total Organic Carbon (TOC) determination

The carbon species present in aqueous solution could be classified as organic or inorganic, depending on whether the carbon atoms belong to organic molecules or to gaseous carbonates, dissolved CO₂ or carbonate ions. The total amount of organic carbon present in a liquid sample is defined as Total Organic Carbon (TOC). A TOC analytical instrument is usually capable of detecting the total amount of carbon (including both organic and inorganic species, a sum referred to as Total Carbon - TC) and the amount of inorganic carbon (TIC or IC). The TOC value is given by the difference of these two quantities:

$$TOC = TC - IC \quad (\text{eq. 2.39})$$

The TC analysis is performed by combustion at 953 K in the presence of an oxidation catalyst. All the carbon species are converted to CO₂ and carried to an electronic dehumidifier by a constant flow of nitrogen (150 mL/min). The CO₂ is cooled and the water removed before it is flowed through a halogen scrubber for the final removal of chlorine and other halogens. The CO₂ is finally carried to a non-dispersive infrared (NDIR) gas analyser, which gives an analogue output signal (usually few mV). The integrated area of the signal peak is directly proportional to the concentration of CO₂, which is calculated through a set of calibration

curves. The amount of inorganic carbon (IC) is measured by acidification of the sample with HCl. When the pH goes below 3, all carbonate species are converted into CO₂



The produced CO₂ is then removed by sparging carrier gas through the sample and is detected by the NDIR detector.

TOC analysis was performed using a Shimadzu TOC-L Analyser, equipped with ASI auto sampler with 100 sampling positions available. The sample were collected in 9 mL vials. The TC and IC measurement was repeated three times for each sample. TOC can be used for the determination of the Molecular Weight Cut-Off (MWCO), an essential parameter for low-pressure filtration processes, indicating the range of molecular weights that could be rejected by the membrane. The observed or nominal MWCO is generally defined as the relative molecular weight of a compound with 90% of rejection. The MWCO is calculated by direct observation of the rejection of molecules with well-defined molecular mass, called solutes or tracers, for example proteins or small polymers, such as polyethylene glycol (PEG)^[53] and Dextrans.^[54] Solute should have very low or no interaction with the membrane surface.^[55] MWCO is generally calculated performing solute filtration and measuring their relative concentration of the solutes is usually performed by high performance size exclusion chromatography (HPSEC) or high-performance liquid chromatography (HPLC) with a refractive index (RI) detector,^[56] which allow a single filtration of multiple solutes at the same time. However, in the absence of these instruments, the filtration of separate solutes is a simpler (but more time consuming) method. The concentration of each fraction of solute was measured by TOC analysis.

2.14 Hydraulic characterisation of membranes

Filtration membrane performance is assessed prior to any modification or to their application in an operational process. The most important parameter is the initial permeate flux, which is measured by filtering pure de-ionised water through the membrane. The permeate flux (J) is defined as the ratio between the volume of

the permeate (V) and the time (t) in which that volume has been filtered, per the active filtration surface area (A):

$$J = \frac{V}{t \cdot A} \quad (\text{eq. 2.42})$$

The permeate flux is commonly reported in LMH (L/m²·h). Values in imperial units (GFD, gallons per feet per day) are frequently used in the case of US companies. The permeability of the membrane is calculated by normalising the permeate flux for the transmembrane pressure (TMP, Δp).

$$\text{Permeability} = \frac{J}{\Delta p} \quad (\text{eq. 2.43})$$

Transmembrane pressure is characteristic of the filtration process and represents the average applied pressure from the feed to the filtrate side, which is generally kept at ambient pressure:

$$\Delta p = \left(\frac{p_F - p_r}{2} \right) - p_f \quad (\text{eq. 2.44})$$

where p_F is the inlet or feed pressure, p_r is the outlet or retentate pressure and p_f is pressure on the permeate side. In general, once the membrane is placed in the filtration cell, the permeate flux is progressively decreases once the pressure or the flux applied, due to the compaction phenomenon. The value of the pure water permeability should be calculated after the end of the compaction phase, when the flux reaches a steady state. In the case of the addition of electrolytes (for example simulating wastewater filtration in a fouling experiment), the membrane has to be conditioned to the salt solution for a certain period of time. This process is called equilibration, and together with compaction is an important step to ensure good performance of a membrane and to avoid unexpected flux variation during the experiments.

When a membrane is put in operation, it is important to assess the filtration performance by measuring the retention or rejection. These indicate the concentration of the retained solute compared with the concentration of the feed solution:

$$R(\%) = \left(1 - \frac{C_p}{C_f}\right) \times 100 \quad (\text{eq. 2.45})$$

Where C_p indicates the concentration of the solute in the permeate and C_f is the original concentration in the feed solution.

2.14.1 Dead-end filtration

For a dead-end filtration cell, the apparatus is very similar to that used by Causserand *et al.* [57] and it is shown in Figure 2.11. The transmembrane pressure and consequently the feed flow rate is fixed using pressurised nitrogen, with a maximum operative pressure of 0.4 MPa. The filtrate side of the cell is at atmospheric pressure. The filtrate flux is measured by gravimetric method; collecting the filtrate using a balance with an accuracy of ± 0.01 g. The balance is connected to a terminal recording the weight at regular interval. A solvent-resistant stirred cell (Millipore, XFUF07601) designed for protein concentration and purification, with a maximum capacity of 0.3 L and total filtration area of $4 \cdot 10^{-3} \text{ m}^2$ was used all the operations in dead-end configuration. The maximum operative pressure of the cell is 0.6 MPa.[58] The pressure was controlled either using analogue pressure gauges (Wika) and digital pressure transmitters.

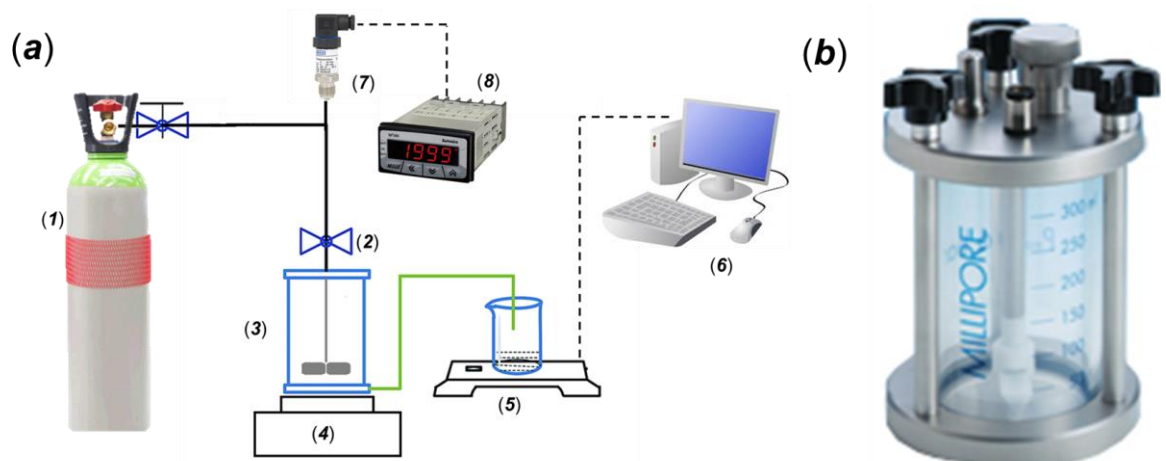


Figure 2.11: (a) schematic of the dead-end filtration system for membrane characterisation and fouling experiments. The numbered items correspond to (1) pressurised gas cylinder; (2) needle valve; (3) solvent-resistant stirring cell; (4) stirrer plate; (5) digital balance; (6) terminal for data collection; (7) pressure transducer; (8) digital panel meter for the pressure reading. (b) Image of the Millipore solvent-resistant stirred cell for volume concentration.

2.14.2 Fouling

The degree of fouling on a membrane surface is derived from the measurement of the permeate flux in presence of the foulant species. The permeability is different compared with operation performed in pure water. For the analysis of fouling, the resistance of the membrane is considered. This parameter is conceptually the opposite of the permeability and analogous to the concept of electrical resistance, in which the resistance of the membrane to the passage of the permeate is determined. The total resistance (R_t) of a membrane can be calculated adapting Darcy's law for water filtration:

$$J = \frac{\Delta p}{\eta R_t} \quad (\text{eq. 2.46})$$

where J is the permeation flux ($\text{m}^3\text{m}^{-2}\text{s}^{-1}$), ΔP is the transmembrane pressure (Pa) and η is the viscosity of the permeate (Pa s). Considering the analogy with an electric circuit, the membrane resistance can be modelled with a Voigt or in series approach,^[59] considering the sum of all the different contribution to R_t . Using a very simplified model, in addition to the intrinsic hydraulic resistance of the membrane (R_m), the other contributions could be clustered as reversible (R_r) and irreversible (R_{ir}) phenomena:

$$R_t = R_m + R_r + R_{ir} \quad (\text{eq. 2.47})$$

The different contributions to equation 2.38 can be experimentally determined by isolating the single causes of fouling;^[60] a general procedure consists of the measurement of the initial pure water permeability, followed by the determination of the permeation flux after the addition of different fouling agents to the system. Finally, the resistance of the membrane is evaluated after removal of the reversibly-attached foulants by cleaning (e.g. backflushing).^[61, 62] Regarding reversible fouling, the evaluation of the restoration of the membrane properties after cleaning is evaluated through the flux recovery ratio (FRR), given by the ratio of the permeate flux of the cleaned membrane to the original pure water flux.^[63]

The evaluation of fouling at laboratory scale considers a model of the foulant species, representing the principal causes of environmental fouling. An extensive study of organic fouling should consider three principal categories of species

detrimental for the membrane performances, polysaccharides, proteins and natural organic matter (NOM). This last category represents all the natural occurring effluent in fresh waters, including hydrophobic component such as carboxylic and phenolic functional groups, and hydrophilic species such as alkali (primary and secondary protein groups), acids (amino acids) and polysaccharides. Organic fouling can be evaluated using standardized NOM solution (the most famous is the one collected from the headwater of the Suwannee River ^[64]) or using model compounds such as bovine serum albumin (BSA); frequently used to study the attachment and the fouling of proteins ^[65].

For a very general evaluation of fouling effects, two other model compounds, humic acid (HA) and sodium alginate (SA), have been used extensively. The two simulate the humic hydrophobic substance and hydrophilic polysaccharide retrieved in NOM. Humic acid can be found in wastewater and is generally associated with the final products of biological and chemical degradation of dead organic matter such as plant and animal residues. Sodium alginate is a polysaccharide from brown algae and it is widely used because of its commercial availability and the formation of an extensive three-dimensional gel-like structure in the presence of Ca^{2+} .^[66] Divalent cations influence the interactions of the fouling agents in solution, usually causing agglomeration by complexing the organic molecules and enhancing the fouling on the filtration surface. In the case of humic acid, calcium forms complexes because of the high affinity for the carboxylic moieties of the molecule.^[67] The complexation neutralizes the charges of the molecule and depresses the mutual electrostatic repulsion, bridging the molecules and enhancing the surface fouling.^[68]

The selected fouling conditions were adapted from different studies of fouling on ultrafiltration membrane using alginate.^[69] The typical foulant concentration used ranged from 10-50 mg/L. The ionic strength of the solution was adjusted adding a concentration of 20 mM of NaCl. For the study of the effect of Ca^{2+} , CaCl_2 was added in concentrations of 0, 1 and 2 mM, ensuing that the ionic strength of the feed solution was kept constant. The influence of the pH was not considered, keeping the foulant solution neutral or buffered with NaHCO_3 . The permeability of the membrane was evaluated again after cleaning by rinsing the active side of the membrane with deionized water, re-measuring the permeate flux of the membrane.

2.15 References

- ¹ H.J. Kitchen, S.R. Vallance, J.L. Kennedy, N. Tapia-Ruiz, L. Carassiti, A. Harrison, A.G. Whittaker, T.D. Drysdale, S.W. Kingman, D.H. Gregory: Modern Microwave Methods in Solid-State Inorganic Materials Chemistry: From Fundamentals to Manufacturing, *Chem. Rev.*, 2014, **114**, 1170–1206.
- ² A. Garg, J.R. Heflin, H.W. Gibson, R.M. Davis: Study of Film Structure and Adsorption Kinetics of Polyelectrolyte Multilayer Films: Effect of pH and Polymer Concentration, *Langmuir*, 2008, **24**, 10887-10894.
- ³ B.P. Tripathi, N.C. Dubey, M. Stamm, Functional polyelectrolyte multilayer membranes for water purification applications, *J. Haz. Mat.*, 2013, **252–253**, 401-412.
- ⁴ J.-H. Kim, S. Shiratori, Characterisation of TiO₂/Polyelectrolyte Thin Film Fabricated by a Layer-by-Layer Self-Assembly Method, *Jap. J. App. Phys.*, 2005, **44**, 7588-7592.
- ⁵ W. H. Bragg, W. L. Bragg, The reflection of X-rays by crystals, *Proc R. Soc. Lond. A*, 1913, **88**, 428-438.
- ⁶ Bedingung für die konstruktive Interferenz von Wellen an einer Kristallschicht (*in German*) (<https://www.didaktik.physik.uni-muenchen.de>, *consulted on 25/11/2017*).
- ⁷ M. Ermrich, D. Opper, *XRD for analyst*, pp.28, PANalytical GmbH (2011).
- ⁸ International Center for Diffraction Data (ICDD) database (<http://www.icdd.com>, *consulted on January 2018*).
- ⁹ A. Belsky, M. Hellenbrandt, V.L. Karen, P. Luksch, New developments in the Inorganic Crystal Structure Database (ICSD): accessibility in support of materials research and design. *Acta Cryst. B*, 2002, **58**, 364-369.
- ¹⁰ H. M. Rietveld, The Rietveld method, *Phys. Scr.*, 2014, **89**, 9, 098002.
- ¹¹ P. Scherrer, Bestimmung der Grosse und der Inneren Struktur von Kolloidteilchen Mittels Rontgenstrahlen, *Göttinger Nachrichten Gesell.*, 1918, **2**, 98-100 (*in German*).
- ¹² G.K. Williamson, W.H. Hall, X-ray line broadening from filed Aluminium and Wolfram. *Acta Metall.*, 1953, **1**, 22–31.
- ¹³ P. Scardi, M. Ortolani, M. Leoni, WPPM: microstructural analysis beyond the Rietveld method, *Mat. Sci. Forum*, 2010, **651**, 155-171.
- ¹⁴ M. Leoni, T. Confente, P. Scardi, PM2K: a flexible program implementing Whole Powder Pattern Modelling, *Z. Kristallogr. Suppl.*, 2006, **23**, 249-254.
- ¹⁵ P. Scardi, M. Leoni, Advances in Line Profile Analysis for the Study of Nanocrystalline System, *ECS Trans.*, 2009, **3** (9), 125-131.
- ¹⁶ G. Caglioti, A. Paoletti, F.P. Ricci, Choice of collimators for a crystal spectrometer for neutron diffraction, *Nucl. Instr. Meth.*, 1958, **3**, 223-228.
- ¹⁷ A.J.C. Wilson, *Mathematical Theory of X-ray Powder Diffractometry*, Philips Technical Library Eindhoven, 1963.
- ¹⁸ J.R. Ferraro, K. Nakamoto, C.W. Brown, *Introductory Raman Spectroscopy* (2nd ed.), Academic Press, San Diego (US), 2003.
- ¹⁹ J. Tauc, R. Grigorovici, A. Vanacu, Optical Properties and Electronic Structure of Amorphous Germanium, *Phys. Status Solidi*, 1966, **15**, 627-637.
- ²⁰ E.A. Davis, N.F. Mott, Conduction in non-crystalline systems V. Conductivity, optical absorption and photoconductivity in amorphous semiconductors, *Philos. Mag.*, 1970, **22**, 903-922.
- ²¹ Y. Zhao, C. Li, X. Liu, F. Gu, H. Jiang, W. Shao, L. Zhang, Y. He, Synthesis and Optical Properties of TiO₂ Nanoparticles, *Mater. Lett.*, 2007, **61**, 79–83.
- ²² A.B. Murohy, Modified Kubelka–Munk model for calculation of the reflectance of coatings with optically-rough surfaces, *J. Phys. D: Appl. Phys.*, 2006, **39**, 3571–3581.
- ²³ P. Kubelka and F. Munk, Ein Beitrag Zur Optik Der Farbanstriche, *Z. Techn. Physik*, 1931, **12**, 593-601. (*in German*).
- ²⁴ P. Kubelka, New Contributions to the Optics of Intensely Light-Scattering Materials. Part I, *J. Opt. Soc. Am.*, 1948, **38**, 448-457.

- ²⁵ G. Kortüm, W. Braun, G. Herzog, Principles and Techniques of Diffuse-Reflectance Spectroscopy, *Angew.*, 1963, **2**, 333-341.
- ²⁶ M. Nowak, B. Kauch, P. Szperlich, Determination of energy band gap of nanocrystalline SbSI using diffuse reflectance spectroscopy, *Rev. Sci. Instr.*, 2009, **80**, 046107.
- ²⁷ B. Pattier, M. Henderson, A. Pöpl, A. Kassiba, A. Gibaud, Multi-approach Electron Paramagnetic Resonance Investigations of UV-Photoinduced Ti³⁺ in Titanium Oxide-Based Gels, *J. Phys. Chem. B*, 2010, **114**, 4424–4431.
- ²⁸ F. Pregl, *Quantitative Micro-Analysis of Organic Substances*, Springer, Berlin, 1917.
- ²⁹ K. S. W. Sing, D. H. Everett, R. A. W. Haul, L. Moscou, R. A. Pierotti, J. Roquerol, and T. Siemieniewska, Reporting Physisorption Data for Gas/Solid System with Special Reference to the Determination of Surface Area and Porosity, *Pure Appl. Chem.*, 1985, **57**, 603-619.
- ³⁰ S. Brunauer, P.H. Emmett, E. Teller, Adsorption of Gases in Multimolecular Layers, *J. Am. Chem. Soc.*, 1938, **60**, 309–319.
- ³¹ E. P. Barrett, L. G. Joyner, P. P. Halenda, The Determination of Pore Volume and Area Distributions in Porous Substances. I. Computations from Nitrogen Isotherms, *J. Am. Chem. Soc.*, 1951, **73**, 373-380.
- ³² P.I. Ravikovitch, G.L. Haller, A.V. Neimark, Density functional theory model for calculating pore size distributions: pore structure of nanoporous, *Adv. Coll. Interf. Sci.*, 1998, **76-77**, 203-226.
- ³³ J.B. Berne, R. Pecora, *Dynamic light scattering with applications to chemistry, biology, and physics*, Dover Publications (2nd ed.), New York, 2000.
- ³⁴ M. von Smoluchowski, in *Handbuch der Electricität und des Magnetismus*, ed. L. Grätz, Ambrosius Barth Verlag Leipzig, 1921, vol. II, p. 366.
- ³⁵ M. Kasuba, J. Corbett, F. McNeil Watson, High-concentration zeta potential measurements using light-scattering techniques, *Phil. Trans. R. Soc. A*, 2010, **368**, 4439–4451.
- ³⁶ A.S. Dukhin, P.J. Goetz, Characterization of Liquids, *Dispersions, Emulsions, and Porous Materials Using Ultrasound* (3rd ed.), Elsevier, 2017, p. 203.
- ³⁷ H. Strauss, H. Heegn, I. Strienitz, Effect of PAA adsorption on stability and rheology of TiO₂ dispersions, *Chemical Engineering Science*, 1993, **48**, 323-332.
- ³⁸ D. Necas *et al.*, Gwyddion 2.49, released on 15/08/2017.
- ³⁹ K. Bossu, B. Van der Bruggen, A. Volodin, J. Snauwaert, C. Van Haesendonck, C. Vandecasteele, Roughness and hydrophobicity studies of nanofiltration membranes using different modes of AFM, *J. Colloid. Interf. Sci.*, 2005, **286**, 632-638.
- ⁴⁰ K.-S. Lee, M.A. El-Sayed, Gold and Silver Nanoparticles in Sensing and Imaging: Sensitivity of Plasmon Response to Size, Shape, and Metal Composition, *J. Phys. Chem. B*, 2006, **110**, 19220-19225.
- ⁴¹ J.A. de Feijter, J. Benjamins, F. A. Veer., Ellipsometry as a tool to study the adsorption of synthetic and biopolymers at the air-water interface. *Biopolymers*, 1978, **17**, 1759–1772.
- ⁴² R. F. Egerton, *Physical Principles of Electron Microscopy*, Springer US, 2016.
- ⁴³ W. Zhou, Z.L. Wang, *Scanning Microscopy for Nanotechnology*. Springer-Verlag, New York, 2007.
- ⁴⁴ M.-J. Park, D.H. Kim, K. Park, D.Y. Jang, D.-C. Han, Design and fabrication of a scanning electron microscope using a finite element analysis for electron optical system, *J. Mech. Sci. Tech.*, 2008, **22**, 1734-1746.
- ⁴⁵ J. McCarthy, J. Friel, P. Camus, Impact of 40 Years of Technology Advances on EDS System Performance, *Microscopy and Microanalysis*, 2009, **15**, 484-490.
- ⁴⁶ J. Berlin, Analysis of Boron with Energy Dispersive X-ray Spectrometry, *Imaging and Microscopy*, 2011, **13**, 19-21.
- ⁴⁷ W.-K. Jo, R.J. Tayade, Recent developments in photocatalytic dye degradation upon irradiation with energy-efficient light emitting diodes, *Chin. J. Cat.*, 2014, **35**, 1781–1792.
- ⁴⁸ A. Aleboyeh, M.E. Olya, H. Aleboyeh, Electrical energy determination for an azo dye decolorization and mineralization by UV/H₂O₂ advanced oxidation process. *Chem. Eng. J.*, 2008, **137**, 518–524.
- ⁴⁹ O. Levenspiel, *Chemical Reaction Engineering* (3rd ed.). Wiley, Singapore, 1999.

- ⁵⁰ J. Cunningham, G. Al-Sayyed, S. Srijaranai, in: Aquatic and Surface Photochemistry, ed. G. Helz, R. Zepp, D. Crosby, Boca Raton: Lewis Publishers, CRC Press, 1994, p. 317 (Cp. 22).
- ⁵¹ N. Barka, S. Qourzal, A. Assabbane, A. Nounah, Y. Ait-Ichou, Factors influencing the photocatalytic degradation of Rhodamine B by TiO₂-coated non-woven paper, *J. Photochem. Photobiol., A*, 2008, **195**, 346-351.
- ⁵² R. Goei, Z. Dongc, T.-T. Lim, High-permeability pluronic-based TiO₂ hybrid photocatalytic membrane with hierarchical porosity: Fabrication, characterizations and performances, *Chem. Eng. J.*, 2013, **228**, 1030–1039.
- ⁵³ S. Platt, M. Mauramo, S. Butylina, M. Nyström, Retention of pegs in cross-flow ultrafiltration through membranes, *Desalination*, 2002, **149**, 417-422.
- ⁵⁴ K.J. Kim, A.G. Fane, R. Ben Aim, M.G. Liu, G. Jonsson, I.C. Tessaro, A.P Broek, D. Bargeman, A comparative study of techniques used for porous membrane characterization: pore characterization, *J. Memb. Sci.*, 1994, **87**, 35-46.
- ⁵⁵ C.M. Tam, A.Y. Tremblay, Membrane pore characterization-comparison between single and multicomponent solute probe techniques, *J. Memb. Sci.*, 1991, **57**, 271-287.
- ⁵⁶ S. Lee, G. Park, G. Amy, Determination of membrane pore size distribution using the fractional rejection of nonionic and charged macromolecules, *J. Membr. Sci.*, 2002, **201**, 191–201.
- ⁵⁷ C. Causserand, P. Aim, C. Vilani, T. Zambelli, Study of the effects of defects in ultrafiltration membranes on the water flux and the molecular weight cut-off, *Desalination*, 2002, **149**, 485-491.
- ⁵⁸ Solvent-resistant Stirred Cell XFUF07601, for 76 mm membranes (<https://www.merckmillipore.com>, consulted on 21/12/2017).
- ⁵⁹ M. Mulder, *Basic Principles of Membrane Technology*, Kluwer Academic Publishers, Dordrecht, 1996.
- ⁶⁰ T.-H. Bae, T.M. Tak, Preparation of TiO₂ self-assembled polymeric nanocomposite membranes and examination of their fouling mitigation effects in a membrane bioreactor system, *J. Membr. Sci.*, 2005, **266**, 1–5.
- ⁶¹ P. Rai, C. Rai, G.C. Majumdar, S.D. Gupta, S. De, Resistance in series model for ultrafiltration of mosambi (*Citrus sinensis* (L.) Osbeck) juice in a stirred continuous mode, *J. Membr. Sci.*, 2006, **283**, 116–122.
- ⁶² M. Cai, S. Zhao, H. Liang, Mechanisms for the enhancement of ultrafiltration and membrane cleaning by different ultrasonic frequencies, *Desalination*, 2010, **263**, 133-138.
- ⁶³ X. Li, X. Fang, R. Pang, J. Li, X. Sun, J. Shen, W. Han, L. Wang, Self-assembly of TiO₂ nanoparticles around the pores of PES ultrafiltration membrane for mitigating organic fouling, *J. Membr. Sci.*, 2014, **467**, 226–235.
- ⁶⁴ N.W. Green, D. McInnis, N. Hertkorn, P.A. Maurice, E.M. Perdue, Suwannee River natural organic matter: Isolation of the 2R101N reference sample by reverse osmosis, *Environ. Eng. Sci.*, 2015, **32**, 38–44.
- ⁶⁵ J. Liu, Z. Zhong, R. Ma, W. Zhang, J. Li, Development of High-Antifouling PPSU Ultrafiltration Membrane by Using Compound Additives: Preparation, Morphologies, and Filtration Resistant Properties, *Membranes*, 2016, **6**, 1-14.
- ⁶⁶ S. Lee, W.S. Ang, M. Elimelech, Fouling of reverse osmosis membranes by hydrophilic organic matter: implications of water reuse. *Desalination*, 2006, **187**, 313-321.
- ⁶⁷ S.K. Hong, M. Elimelech, Chemical and physical aspects of natural organic matter (NOM) fouling of nanofiltration membranes, *J. Membr. Sci.*, 1997, **132**, 159-181.
- ⁶⁸ C.L. Tiller, C.R. Omelia, Natural organic matter and colloidal stability. Models and measurements, *Colloids Surf. A*, 1993, **73**, 89-102.
- ⁶⁹ K. Katsoufidou, S.G. Yiantsios, A.J. Karabelas, Experimental study of ultrafiltration membrane fouling by sodium alginate and flux recovery by backwashing, *Jour. Memb. Sci.*, 2007, **300**, 137-146.

List of Abbreviations used in Chapter 3

- BET:** Brunauer-Emmett-Teller (*model for surface area measurement*)
- BJH:** Barrett-Joyner-Halenda (*model for pore volume and size distribution*)
- DMO:** Domestic Microwave Oven
- DR-UV-Vis:** Diffuse Reflectance-Ultraviolet-Visible light spectroscopy
- DSSC:** Dye-Sensitised Solar Cell
- DFT:** Density Functional Theory
- DTA:** Differential Thermal Analysis
- EDX:** Energy Dispersive X-ray Spectroscopy
- EPR:** Electron Paramagnetic Resonance
- FMH:** Flash Microwave-assisted Hydrothermal synthesis
- FT-IR:** Fourier Transform Infrared Spectroscopy
- FWHM:** Full Width at Half Maximum
- IMH:** Intermittent Microwave Heating
- MAWL:** Maximum Allowed Water Loading
- MS:** Mass Spectrometry
- MW:** Microwaves
- NLDFT:** Non-Local Density Functional Theory
- PTFE:** Polytetrafluoroethylene
- PXD:** Powder X-ray Diffraction
- QSDFT:** Quenched Solid Density Functional Theory
- SEM:** Scanning Electron Microscopy
- STA:** Simultaneous Thermal Analysis
- TEM:** Transmission Electron Microscopy
- TGA:** Thermogravimetric Analysis
- TTIB:** Titanium butoxide
- TTIP:** Titanium isopropoxide
- UV:** Ultraviolet (radiation)
- Vis:** Visible (radiation)
- WPPM:** Whole Powder Pattern Modelling
- XPS:** X-ray photoelectron spectroscopy

Sample labelling convention

CE: particles synthesised using HCl in ethanol

CW: particles synthesised using HCl in water

NE: particles synthesised using HNO₃ in ethanol

NW: particles synthesised using HNO₃ in water

Chapter 3

Flash microwave-assisted hydro/solvothermal synthesis of TiO₂ submicroparticles

3.1 Introduction

The successful application of TiO₂ materials in the development of different technologies led in recent years to the investigation of improved synthesis methods towards specific nanostructures. In environmental technologies, concerns over the dispersion and release of nanoparticles led to alternative approaches to reduce the long term environmental effects. One approach is to use nanostructured mesoporous particles, which possess some of the properties of nanoparticles, such as high surface area and catalytic activity, paving the way for potential application such as catalysis, energy storage and conversion.

A wide range of nanoparticles and nanostructures can be accessed through hydrothermal and solvothermal synthesis. High purity, crystalline products can be achieved through reaction at relatively low-temperatures in a closed-system. The application of microwave heating improves the efficiency of this strategy, reducing the time scale of the reactions and increasing the kinetics of crystallization from one to two orders of magnitude compared with conventional processes. The accelerated kinetics can give access to new crystalline phases and morphologies which are otherwise difficult to obtain. Microwave thermohydrolysis of transition metal salt solutions is a simple method adopted in the last two decades for the synthesis of uniform colloidal metal oxides.^[1] Microwave-assisted hydrothermal or solvothermal synthesis (MAHS or MASS) has been extensively used for the synthesis of several metal oxide nanostructures.^[2] This facile one-step synthesis has been firstly referred to as flash microwave synthesis in the works of Stuerger *et al.* ^[3,4] Similar to hydrothermal synthesis, the crystalline and morphological structure is tailored using alkaline or acid reagents, which facilitate the reactions and affect the crystal growth along preferential orientations. Other additives as surfactant or long chain molecules are often employed to form a template for the control of size and morphology.

The use of acid mediators is inspired by thermal dissolution of heavy metals for analytical analysis such as ICP or AAS.^[5] The first relevant work to report

“microwave digestion” of TiO₂ particles is from Komarneni *et al.* in 1999 using a pressure-controlled system.^[6] With the introduction in the market of new microwave devices, synthesis could become temperature-controlled. Pure digestion reactions were replaced by more controllable reactions in term of temperature and time. However, the production of nanostructures under high pressure and temperature conditions to force complex reactions such as crystallisation, the formation of ordinate agglomerate structures and phase transitions on a scale of seconds is still an exciting challenge. Detonation synthesis, for example, exploits the same principle and has been used to produce mixed-phase TiO₂ nanoparticles.^[7]

Self-assembly of nanoparticles in the production of hierarchical superstructures is a promising method for the synthesis of mesomaterials. The requirement of high purity, a defined crystalline structure and the preservation of high surface area drove the research work towards one-step and template-free synthesis, in order to avoid post-synthetic treatments. Unlike the conventional bottom-up approach, hydrothermal and solvothermal synthesis proved their capability of forming microspheres with hierarchical mesoporosity exploiting the simultaneous growth and aggregation of nanocrystals.^[8]

Fast kinetic reactions provided by microwave heating are a powerful tool for the production of stable agglomerated structures. Hydrothermal microwave heating maintains a constant temperature through modulation of the MW output power, shortening the reaction time compared with conventional hydrothermal synthesis. A different approach is to exponentially increase the temperature via the application of a constant incident power. Synthesis under these conditions is much faster but particularly difficult to control. The limiting threshold values of temperature and pressure are often achieved in a few minutes. Resuming the terminology adopted by Stuerger *et al.*,^[1] the synthesis will be referred as to **Flash Microwave-assisted Hydrothermal or Solvothermal** synthesis. For simplicity, in this thesis the synthesis will be denoted as **FMH** to indicate both hydrothermal and solvothermal approaches. The most recent work closely related to this project is that of Tian *et al.*, in which nearly spherical TiO₂ “aggregates” composed of nanocrystals are synthesised with a microwave-assisted technique using a single-mode reactor. The as-produced particles proved to have a better performance in dye-sensitised solar cells compared to commercial P25.^[9] The investigation of the

Flash Microwave approach to the synthesis of nanostructured TiO₂ involved the analysis and control of the principal synthesis parameters.

3.2 Aims

The development of a fast and simple technique for the synthesis of nanostructured TiO₂ microspheres is the ultimate research goal of the work described in this chapter. The application of microwave (MW) heating is used to accelerate the reaction rate and kinetics, reducing dramatically the time usually needed for hydrothermal reactions. The control of the final properties (morphological, structural, electronic) of the TiO₂ particles by means of the synthesis and experimental parameters is sought, without the help of surfactants or templating agents, developing a simple, cost-effective and extremely rapid synthetic procedure.

3.3 Synthesis of mesoporous TiO₂ sub-microparticles

3.3.1 Synthesis conditions

According to the classification by Zhang et al., the proposed synthesis is of the indirect-supply reaction source (ISRS) type. In this type of reaction, the precursor does not form a colloidal suspension when immediately in contact with the solution, with the precursor stable in solution for several days, as often witnessed by the solution transparency.^[10]

Four principal synthetic methods were studied for the optimisation of the production of the nanostructured TiO₂ spherical particles. Resuming a previous project in the same research laboratory,^[11] FMH synthesis in water mediated by HCl was originally performed. Titanium tetraisopropoxide (TTIP) was preferred as a starting material to TiCl₄, which has a strong exothermic reaction with water and is more difficult to handle in term of storage and preparation. TTIP was preferred also to ethoxide (very reactive) and butoxide, which was employed in a few reactions to compare the efficacy of the synthetic method. The original synthesis led to the immediate precipitation of non-crystalline products due to the fast hydrolysis reaction. Neither the reduction of the synthesis temperature using an ice bath nor the storage of the precursor under an inert atmosphere to prevent exposure to water and moisture had an effect on the precipitation

reaction. On the other hand, the use of ethanol as solvent prevented the rapid precipitation and the solution remained transparent. The four syntheses have been classified with a two-letter code (Table 3.1). The other synthesis conditions are indicated in brackets, especially precursor and acid concentration, which most affect the final characteristics of the sample. For example, particles synthesised via ethanolic routes in presence of HNO₃, using a 2 M acidic solution, 164 mM of precursor and 1 min of MW treatment were reported as **NE** (2 M, 164 mM, 1 min). For some specific characterisation, the parameters were explicitly mentioned. In some cases, volumetric ratio notation was used in alternative to the molarity for the precursor concentration, using for example 1:20 (1 part of precursor for 20 of solvent) instead of 164 mM.

Table 3.1: Summary of the synthesis parameters for the FMH-TiO₂ particles.

Sample label	Acid	Solvent	Other synthesis conditions
CE	HCl	Ethanol	Time:60-240 s, [HCl]:1,2M [TTIP]:328, 162 mM
CW	HCl	Water	Time:60-240 s, [HCl]:1,2M [TTIP]:328, 162 mM
NE	HNO ₃	Ethanol	Time:60-240 s, [HNO ₃]:0.5,1,2M [TTIP]:328, 162 mM
NW	HNO ₃	Water	Time:60-240 s, [HNO ₃]:0.5,1,2M [TTIP]:328, 162 mM

3.4 Characterisation of the as-synthesised sub-microparticles

3.4.1 Crystalline structure

The analysis of the powder XRD patterns revealed the presence of anatase for most syntheses. Unlike some hydrothermal methods, the patterns of the as-synthesised particles do not indicate a high degree of crystallinity, with generally only 6 or 7 of the characteristic peaks well-defined and low signal-to-noise ratio. Among the sets of synthesis conditions analysed, mildly acidic hydrothermal reactions led to more crystalline products. Solvothermal synthesis using ethanol and HNO₃ gave the lowest degree of crystallinity.

The PXD patterns of the four main synthesis types are compared in Figure 3.1. Synthesis using water as solvent led to higher crystallinity, probably due to the highest hydrolysis rate of the precursors. Addition of HCl ensures better crystallinity, with samples presenting very well-defined Bragg reflections. However, as will be shown in more details in the following sections, increasing acidity (especially concentration of HCl) can produce mixed phase samples, with progressive formation of rutile. For the least crystalline products (**NE** series, using ethanol and HNO₃), the clear presence of the most intense anatase peaks, despite their breadth and the low signal-to-noise ratio in the diffraction pattern, suggests a level of long range order and the presence of crystalline domains. According to the literature, a sample should contain at least 5% of crystalline domains for a crystalline phase to be discernible by XRD analysis.^[12] However, the estimation of the relative amounts of amorphous phase and crystalline phases is difficult to determine. As a comparison, Serpone *et al.* estimated 70-80% of amorphous phase in their 2-4 nm nanoparticles, with PXD patterns qualitatively very similar to the ones obtained for the **NE** particles.^[13] The reduced size of the crystallites can be nominated as the main cause of the peak broadening, together with the presence of amorphous domains or incompletely formed nanocrystallites. The formation of anatase is compatible with the presence of the nanocrystallites. As TiO₂ crystals reach the nanoscale, there is an energy crossover between the polymorphs, with anatase becoming the thermodynamically stable phase reversing the situation for the bulk material. Zhang and Banfield identified the threshold size above which rutile becomes more stable as *ca.* 14 nm.^[14]

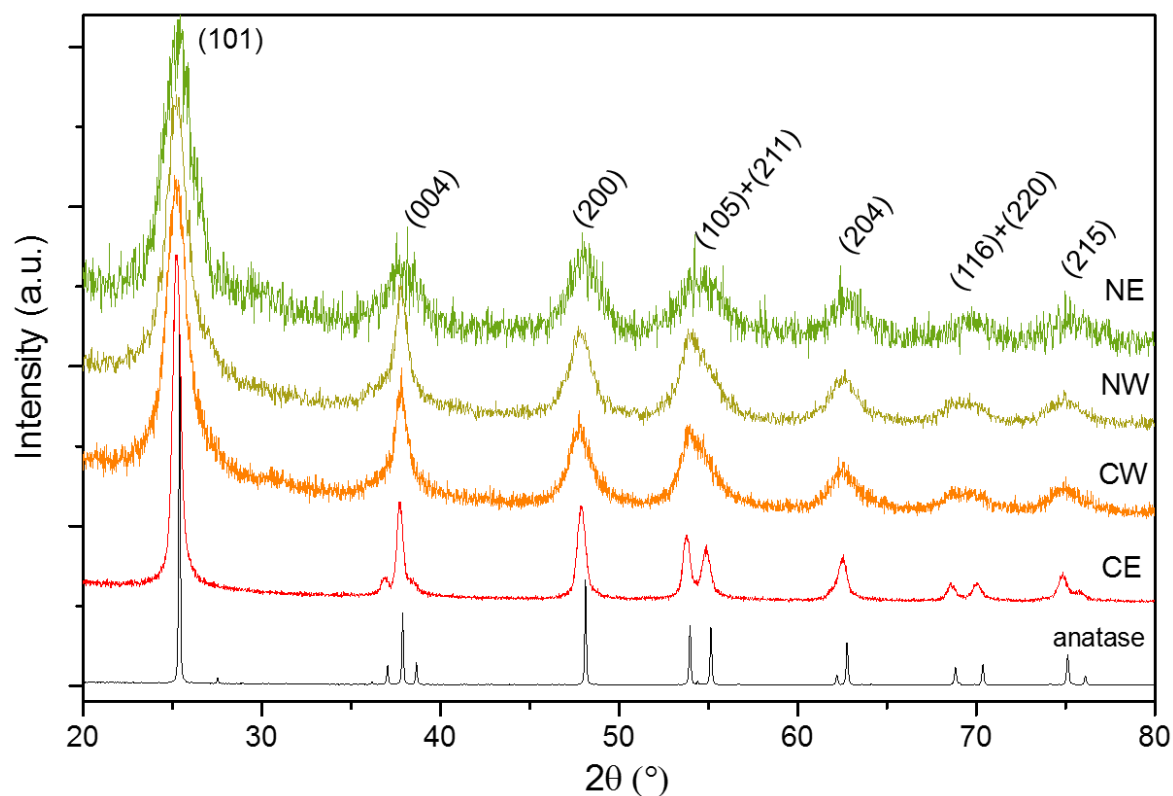


Figure 3.1: Representative PXD patterns for the principal synthesis series as compared with crystalline anatase. The pattern intensities have been normalised to simplify visualisation. The (hkl) values of the anatase peak were reported on the patterns.

Apart from qualitative phase identification, it was difficult to use PXD patterns for the investigation of the properties of the untreated particles, such as quantification of the crystalline grain size. The quality of the patterns is not sufficient for the effective implementation of algorithms such as Le Bail decomposition or Rietveld refinement for the calculation of cell parameters or distance and angles between atoms. In this case, the Scherrer equation can be used as an approximate means of comparison between the different synthesis conditions, giving at least a semi-empirical estimation of the average size of the primary crystallites. The application of the Scherrer equation (*equation 2.8*) was performed by fitting the (101) peak of anatase (or the (110) reflection of rutile) using a pseudo-Voigt profile line. The application of the equation to Aeroxide P25 gave a diameter of 23.4 nm without further correction for instrumental broadening. The calculated value is very close to the value reported in literature for this material. ^[15, 16] The average grain size for the untreated particles is in the range 3-20 nm, depending on the synthesis conditions. However, the reliability of results obtained below 6 nm is not high, due to the low quality of the patterns and

the weaknesses of Scherrer's method when applied to the majority of real particles (see section 2.4.4).

A recently adopted approach for the estimation of the grain size is given by the Whole Powder Pattern Modelling (WPPM), which considers the whole pattern profile and compares the peak widths to those of a standard (LaB₆) measured using the same instrumental conditions. The refinement results are shown in Figure 3.2 Figure 3.3 and Table 3.2. The grain size calculated using this method is lower than that approximated by Scherrer. Despite the unremarkable quality of the refinement, the crystallite size calculated using this approach appears more realistic and closer to the direct measurements from TEM, reported in the following sections.

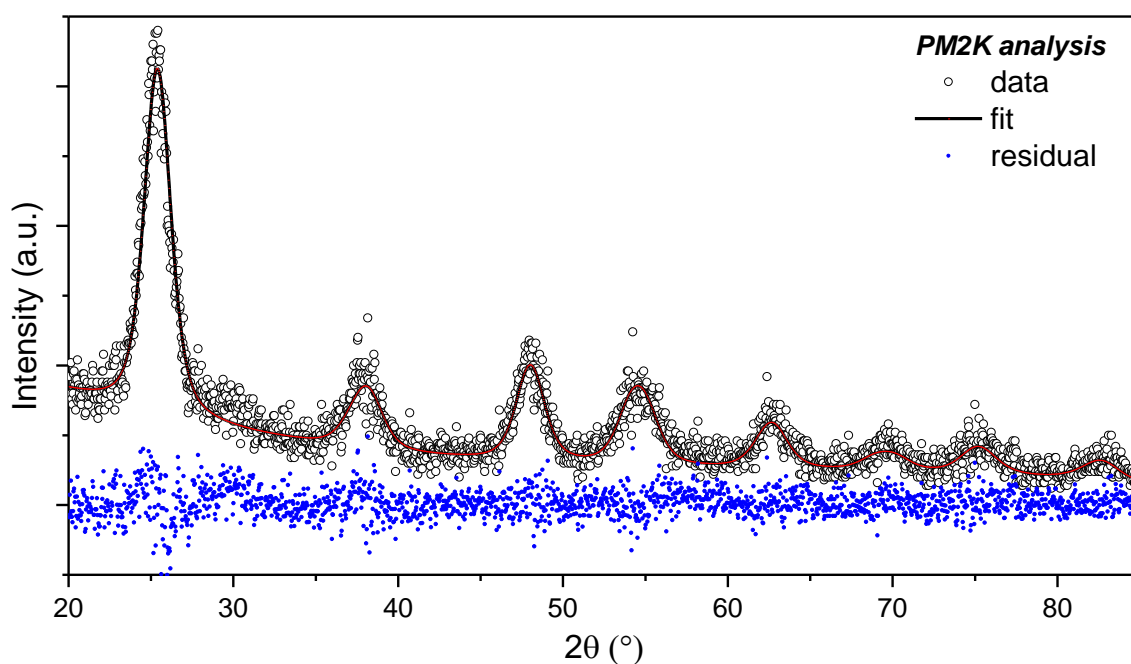


Figure 3.2: Profile fitting of a sample from the *NE* series of FMH-TiO₂ particles using the PM2K software

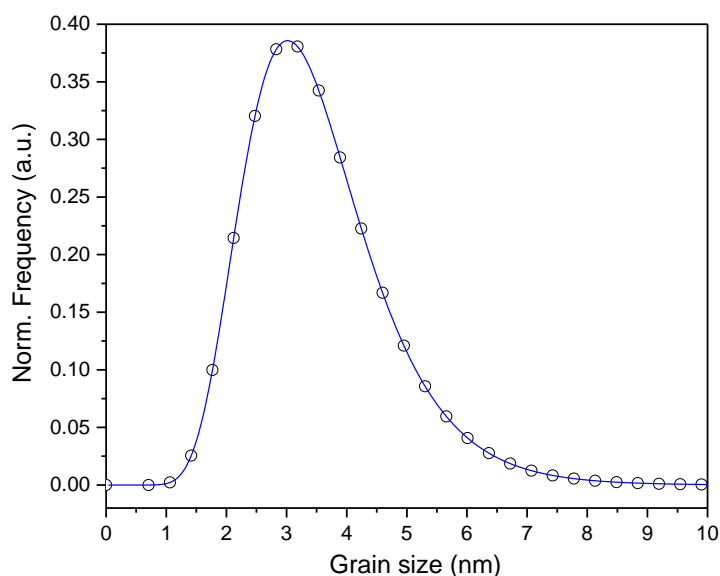


Figure 3.3: Example of log-normal distribution of the grain size diameter estimated using the WPPM method for FMH-TiO₂, NE sample (2 M HNO₃, 162 mM precursor concentration, 1 min MW treatment).

Table 3.2: Results of the WPPM refinement and size analysis compared with the Scherrer calculation.

FMH-TiO₂, NE series (2 M HNO₃, 162 mM TTIP, 1 min MW treatment)	
2θ (101) (°)	25.292 ± 0.017
FWHM (°)	1.876 ± 0.017
Scherrer's average grain size (nm)	4.34
WPPM calculation	
WPPM distribution peak (nm)	3.35 (3)
WPPM distribution width (nm)	0.33 (4)
Lattice parameters	
a (Å)	3.7974(1)
c (Å)	9.4935(94)
Fitting parameters	
μ	1.21(8)
σ	0.32(4)
No. of variables	46
No. of observation	1969
R _{wp} (%)	16.7
R _p (%)	18.6
χ ²	0.81
GOF	0.905

3.4.1.1 Effect of the acid type on the crystal structure

During the preliminary analysis for the individuation of the optimal condition for the development of the TiO₂ microsphere, four of the most common acids employed as mineralisers in conventional sol-gel or hydrothermal synthesis were considered, studying their influence on the morphology and crystalline structure of the products resulting from FMH in ethanol. In Figure 3.4 the crystal structures obtained using these various acids is reported. The four samples were produced using the same experimental conditions and the same nominal acid concentration (1 M). As already observed in the previous section, HCl-mediated synthesis gave the more crystalline products, followed by HNO₃. Acetic and sulphuric acid gave totally amorphous products.

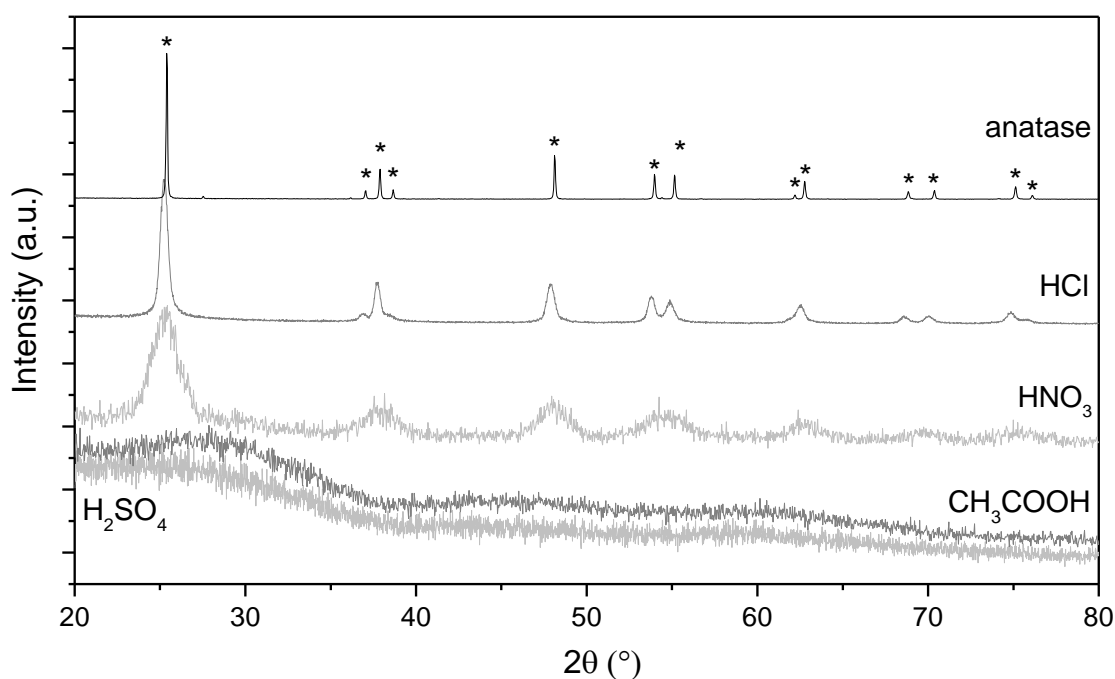


Figure 3.4: PXD patterns of TiO₂ samples synthesised using different acids of the same concentration (nominally 1 M) in ethanol. Crystalline anatase is also shown as a reference.

The effect of the concentration of the acid in solution was also studied. Only the samples of the *CE* series were selected, since the quality of the XRD patterns for NE samples was not good enough to compare the different synthesis conditions. The increase of acid concentration led to an initial increase of the crystallite size, at least up to 1 M HCl solution. However, further increase of the concentration led to broadening of the anatase peaks. Rutile peaks are also observable (Figure 3.5).

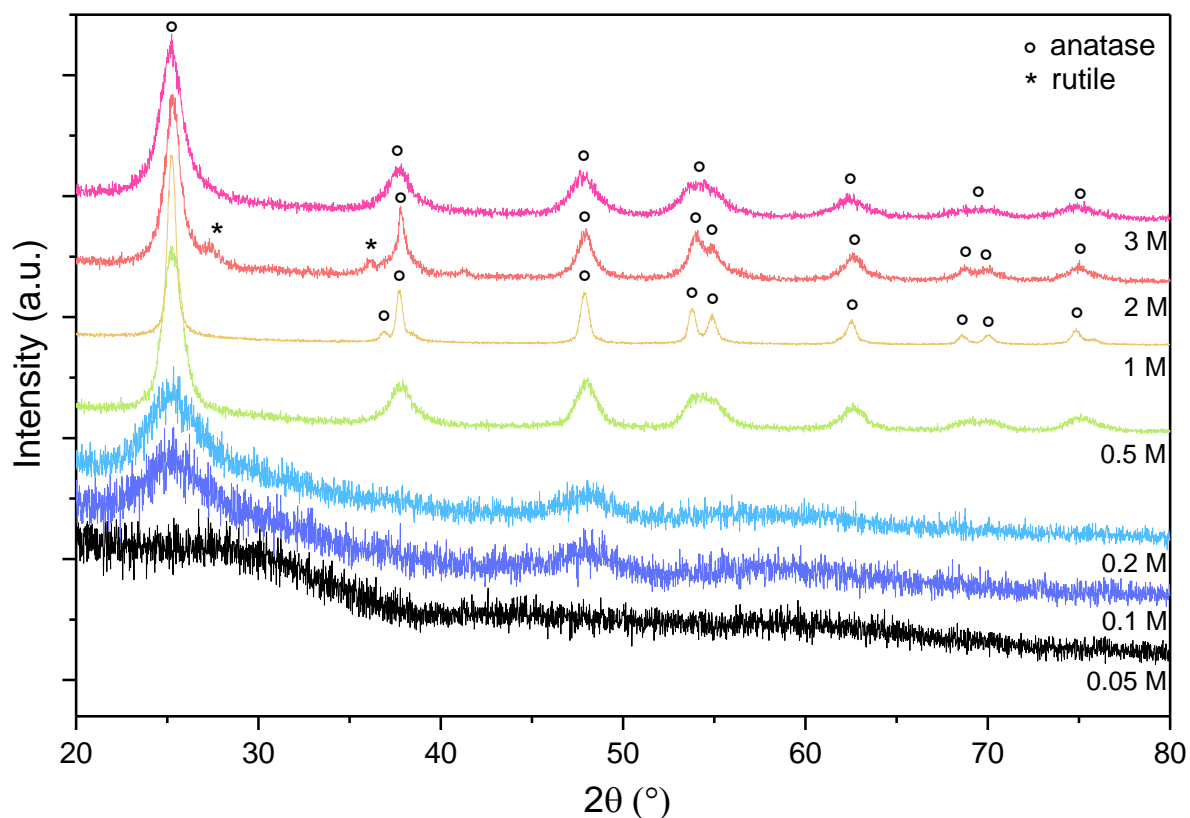


Figure 3.5: PXD patterns as a function of the acid concentration (HCl) in CE series samples (164 mM precursor concentration; treatment time 1 min at 750W MW power).

This phenomenon was observed for both the synthesis in ethanol (*CE*) and in water (*CW*). However, a series of attempts to replicate the precise relative concentration of the two polymorphs using 2 M HCl solution in ethanol was not successful, giving different amount of anatase and rutile in the different samples. It was not possible to identify a clear correlation between synthesis conditions and relative amounts of polymorphs, as shown in Figure 3.6. On the other hand, a further increase of the HCl concentration (3 M) led to formation of less crystalline anatase, in some cases almost amorphous products.

The unpredictability and difficult reproducibility of the results is likely due to the rapid kinetics involved by using MW heating, with the fast reactions favouring the random formation of a partially crystalline products or mixture of the two TiO₂ polymorphs.

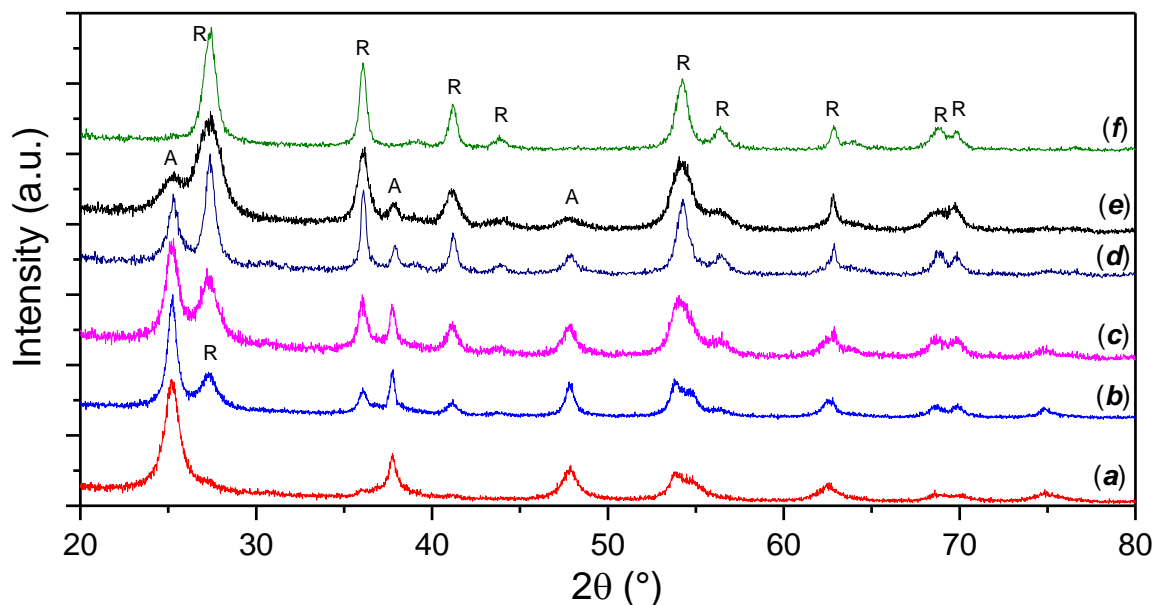


Figure 3.6: PXD patterns of samples prepared using 2 M HCl solution (if not otherwise indicated) as a function of different synthesis conditions: (a) 1.5 M acid concentration, 164 mM TTIP, 90 s MW synthesis; (b) 60 s MW synthesis, 164 mM TTIP; (c) 30 s MW synthesis, 164 mM TTIP; (d) 60 s synthesis in H₂O, 82 mM TTIP; (e) 90 s synthesis, 164 mM TTIP; (f) 60 s synthesis, 82 mM TTIP.

3.4.2 Morphology

Depending on the synthesis conditions, the particle size ranges from nanometric grains to sphere of up to a few microns in diameter. The particles can be described as sub-micrometric spheres, given an average diameter usually just below 1 μm . However, despite a certain control of the particle diameter and the distribution, the very fast kinetics of the process makes it difficult to achieve a narrow size distribution. The particles cannot be described as monodisperse, which is one of the main drawbacks of very fast synthesis, where the kinetics of nucleation and growth can be difficult to control. Despite the production of polydisperse particles, the particle distribution is still less broad than other syntheses reported in literature, with the further advantage of the incredibly rapid reaction time. SEM images of particles for some representative synthesis conditions are shown in Figure 3.7.

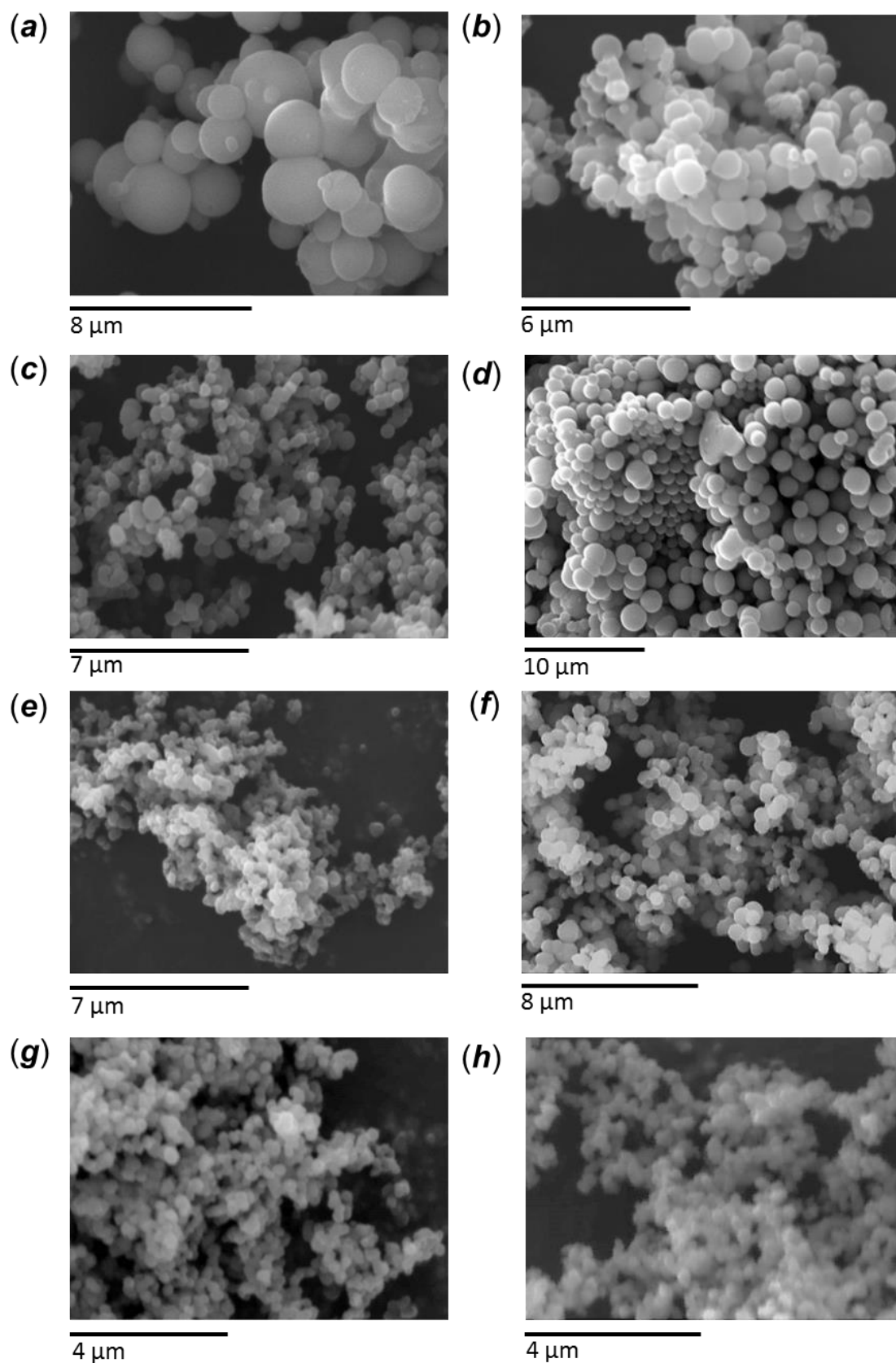


Figure 3.7: SEM images of selected FMH-TiO₂ samples (NE series) produced using different precursor and acidity concentrations. (a) 1M acid, 648 mM precursor; (b) 2 M acid, 648 mM precursor; (c) 2 M acid, 324 mM prec.; (d) 0.5 M acid, 324 mM prec.; (e) 2 M acid, 80 mM prec.; (f) 1 M acid, 80 mM prec.; (g) 1M acid, 40 mM prec; (h) 1 M acid, 20 mM prec.

In case of relatively broad size distribution the deviations from the average value is very high, with relative standard deviation (RSD) values ranging from 15% to 40%. In these latter cases the size distribution is multimodal, and so the average size is not representative of the true sample dimensions. The size distribution of the particles is also strongly influenced by the synthesis conditions. An example of the dependence on acid and precursor concentration is apparent for particles formed from ethanol in the presence of HCl (*CE* series), which size distributions are shown in Figure 3.8. The precise effect and influence of the synthesis conditions will be detailed in further sections.

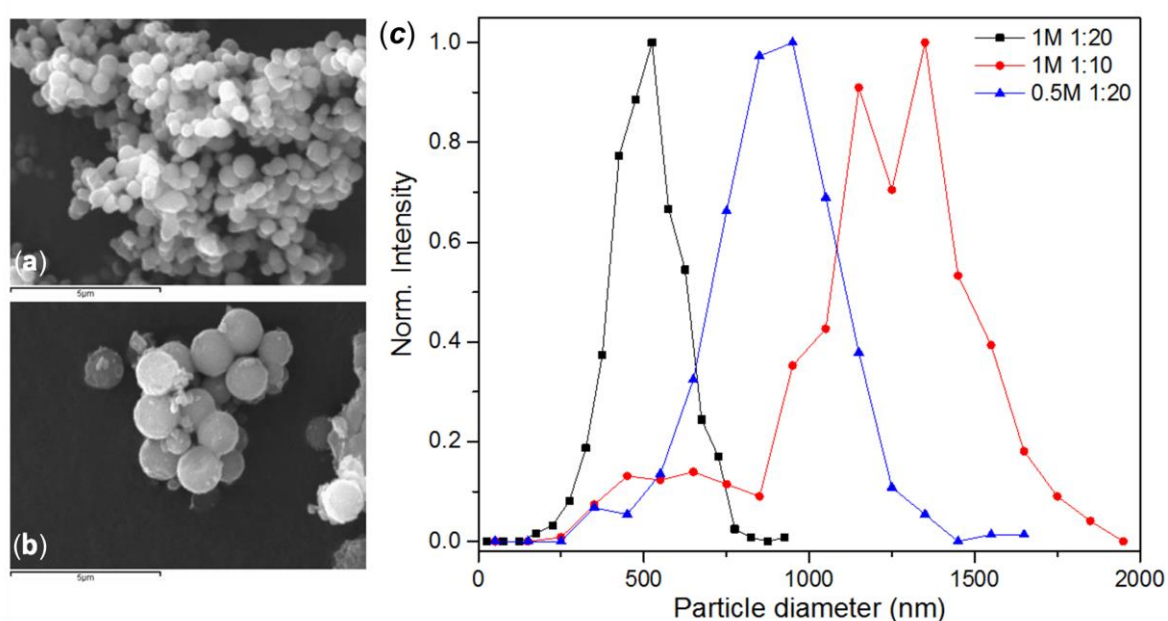


Figure 3.8: (a),(b) SEM images and (c) particle size distribution of FMH TiO₂ particles from the *CE* sample series (HCl as an acid mediator in ethanol solution). Each of the samples was produced using the same MW treatment time (1 min) at full power (700 W). Acid concentration and precursor concentration in volume are indicated in the graph respectively.

The size distribution of the particles has been estimated with the help of the software ImageJ[®], calculating the area of the ellipsoids encircling the particles and hence calculating the radius assuming the particles to be approximately spherical. In alternative, the Feret diameter (also referred to as the caliper diameter) can be used. The Feret diameter is defined as the normal distance between two parallel tangent planes or lines touching the particle surface, representing a measurement of tridimensional objects on a bidimensional plane; this method has been very popular in early particle characterisation, when only microscopic methods were available. [17] The comparison of the fitted ellipsoid

model with the Feret diameter led to a good agreement between the two methods, with a slight overestimation of the size of *ca.* 5% (Figure A.2 in the Appendix). The main limitations of this method, apart from the statistical inferences due to the limited amount of SEM image frames analysed, is related to the resolution of the instrument at the maximum magnification, rendering a precise evaluation of particles below *ca.* 200 nm impossible. The distribution calculated for some of the tested synthesis conditions are reported in Figure 3.9 and Figure 3.10. The size distributions were fitted using Gaussian curves, indicated with dotted lines in the graphs. For some of the samples, especially the ones synthesised with relatively large amount of precursor, multiple distributions were observed, indicated with dotted lines of different colours.

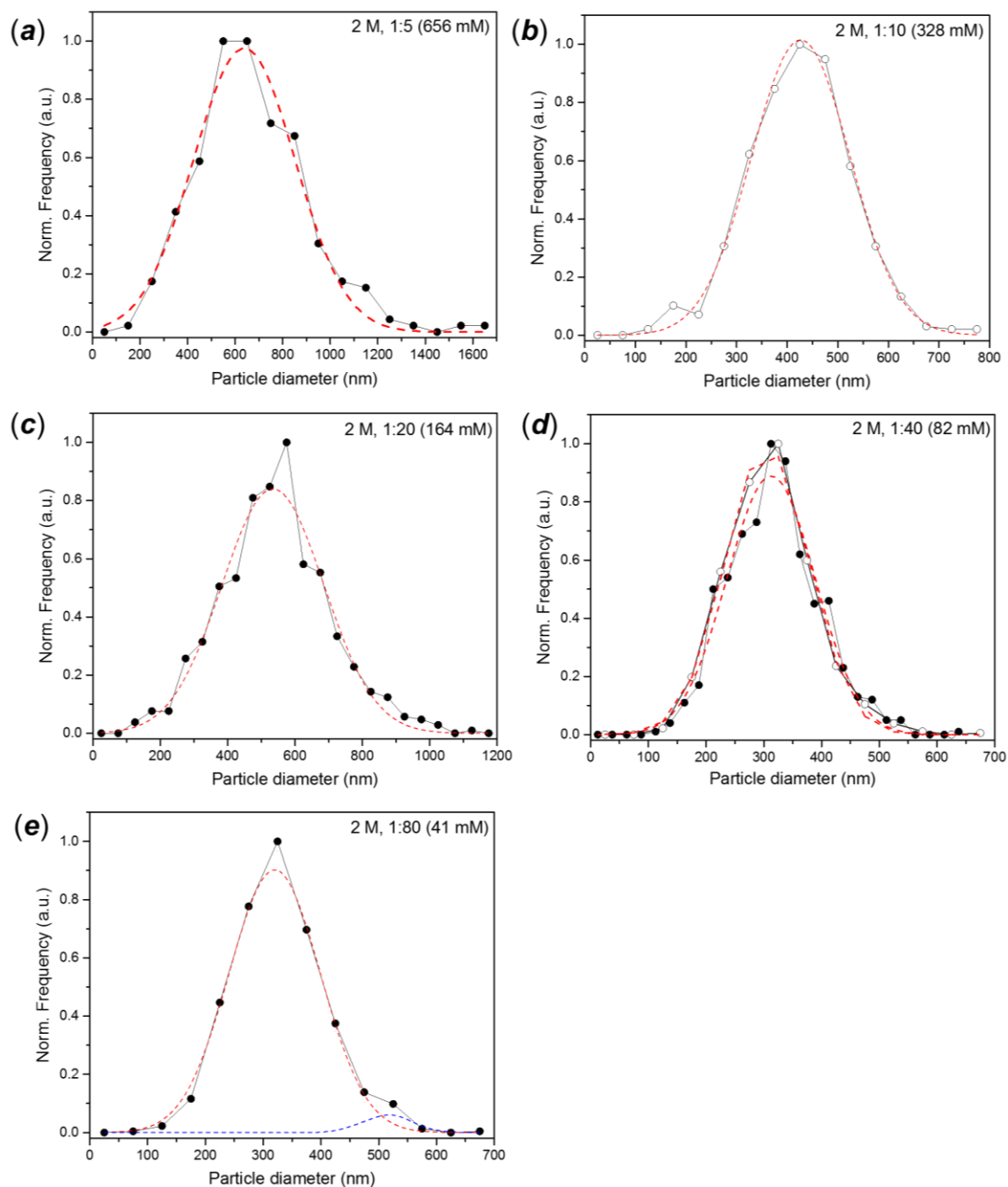


Figure 3.9: Particle size distribution of FMH-TiO₂ particles, NE series produced using 2 M HNO₃ solution and a precursor concentration of (a) 656 mM, (b) 328 mM, (c) 164 mM, (d) 82 mM, (e) 40 mM. The dots indicate the centre of the frequency bin, connected by continuous lines. The dotted lines indicate the Gaussian distribution calculated using the Fityk software. Different colours were used in case of multiple size distributions.

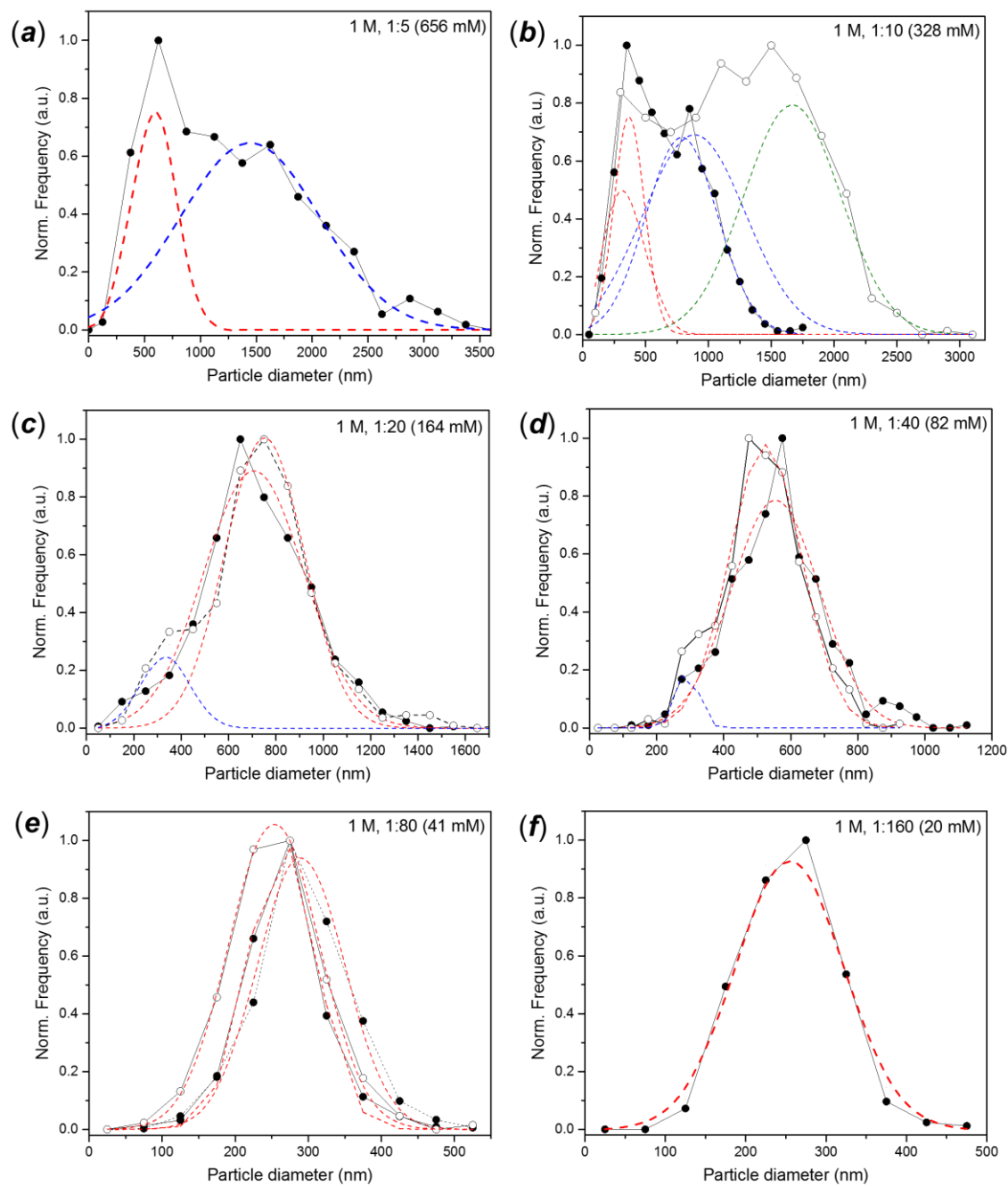


Figure 3.10: SEM size distribution of FMH-TiO₂ particles, NE series produced using 1 M HNO₃ solution and a precursor concentration of (a) 656 mM, (b) 328 mM, (c) 164 mM, (d) 82 mM, (e) 40 mM and (f) 20 mM. The dots indicate the centre of the frequency bin, connected by continuous lines. The dotted lines indicate the Gaussian distribution calculated using the Fityk software. Different colours were used in case of multiple size distributions.

The comparative analysis of different synthesis parameters by SEM imaging showed how the shape of the particles tends to be more smooth and spherical with an increase in the size, while smaller particles are more coarse and irregular. The eventual roughness observed on the particle surface using the high-resolution microscope (such as in Figure 3.11) is mainly due to the gold or platinum sputtered on the surface, required to avoid charging phenomena during SEM analysis.

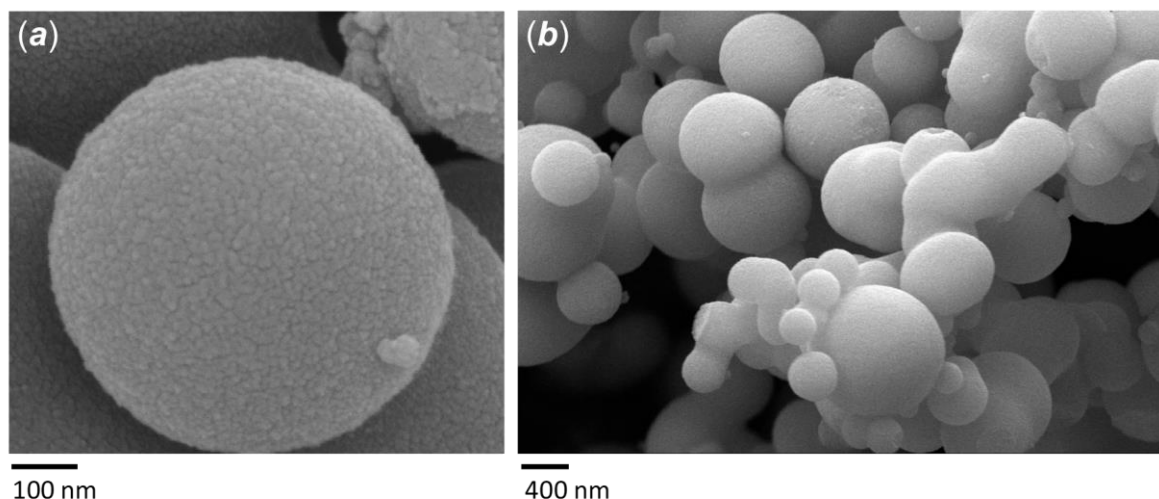


Figure 3.11: SEM images of the FMH-TiO₂ particles at high magnification. (a) The roughness of the particle surface is due to the gold sputtered for during the specimen preparation for the SEM analysis. (b) Polydisperse sample with coalescence phenomena between sub-micron particles.

Due to the very fast agglomeration kinetics, it is not unusual to observe morphological defects in the SEM images. Frequent phenomena of particle condensation occur when nuclei growing competitively are in close proximity (Figure 3.11 *b*), usually corresponding to an increase of treatment time. Cracks on the surface of the spheres become more prevalent as occurs the concentration of acid mediator is increased (examples in Figure 3.12). In this case, the structure of the particles is not sufficiently stable with tendency to break apart once the synthesis is finished or due to the drying process. Indeed, cracks are frequent in the larger particles, which suggest that there is an upper threshold in diameter for the formation of stable spheres.

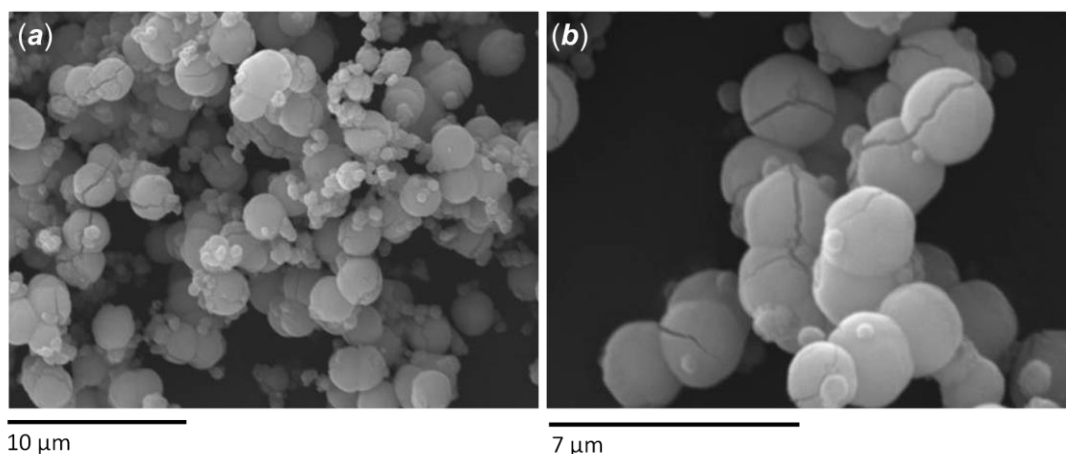


Figure 3.12: Examples of (a) the multimodal size distribution and (b) cracks present in the sub-micron spheres.

3.4.2.1 TEM and SAED analysis

TEM analysis clarified the structure of the microspheres produced by solvothermal synthesis with ethanol in the presence of either HCl (*CE* series) or HNO₃ (*NE* series) as mediator. The particles revealed a hierarchical structure with nanometric ultrafine primary nanocrystallites forming larger dense and compact secondary spherical particles. These secondary structures are difficult to penetrate with the electron beam during analysis, reducing the resolution of the images. The nano-sized crystallites are visible at the edges of the particles or in isolated clusters for which secondary aggregation did not occur. The crystallites are randomly oriented, as deduced by taking dark field images while applying a conical rotation of the sample. The different orientation of the sample with respect to the beam resulted in different “illuminated” crystallites. The particles produced using HCl presented a higher degree of crystallinity, with nanocrystals and diffraction fringes evident (Figure 3.13).

The analysis of the fringes revealed the orientation of the crystallites to be random. The normal direction to the parallel planes changes from one crystallite to its neighbours, producing micro-strain and other defects at their boundaries. The spacing between the diffraction fringes is ca. 3.9 Å, close to the larger interplanar distance in the anatase structure (3.52 Å for the (101) planes).^[18]

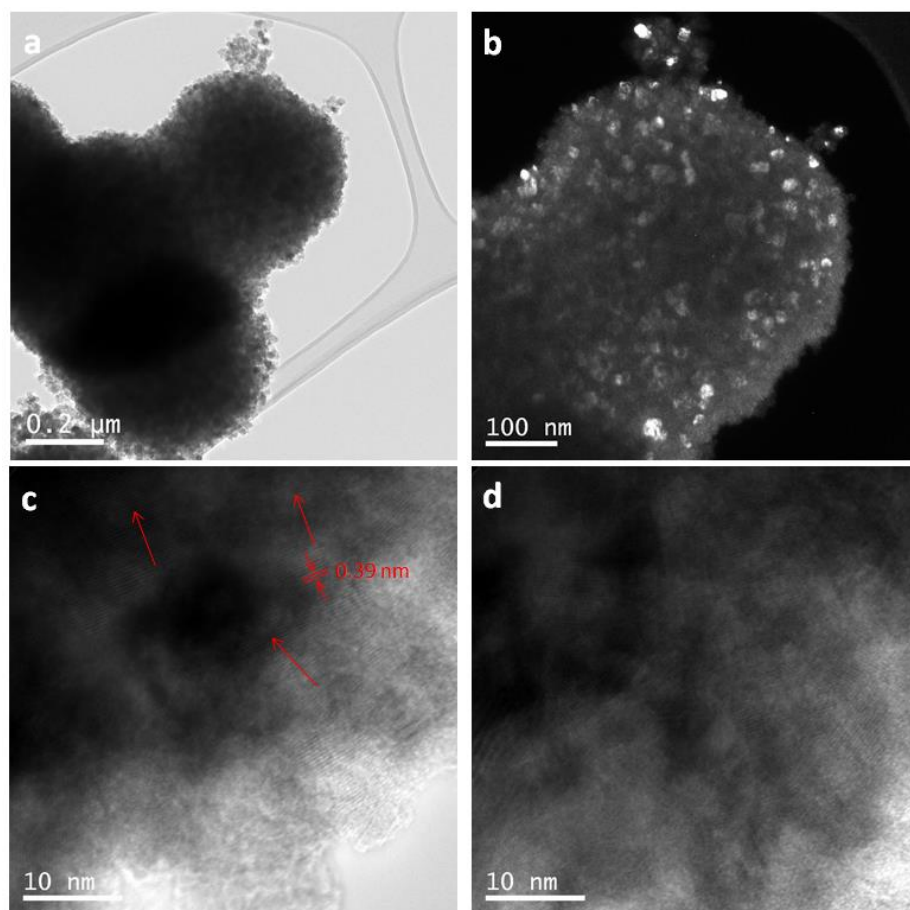


Figure 3.13: TEM analysis of TiO₂ microspheres, CE sample series (synthesised using a solution of 1M HCl in absolute ethanol, 1 min MW treatment at full power-700W). (a) bright field and (b) dark field image of a cluster of particles, (c) magnified details of the crystalline grains that comprise the particle.

Unlike the HCl-synthesised particles, the particles synthesised with HNO₃ present a lower degree of crystallinity. In this case it was impossible to observe any diffraction fringes or distinct crystallites. Discernible grains are visible only after calcination treatment (Figure 3.14 d). Despite this, the observation under conical rotation of dark field images reveals diffraction of many nanocrystallites uniformly distributed across the particles (Figure 3.14 b and Figure 3.15 a and b). Regardless of the lower crystallinity, the *NE* particles series have a narrow size distribution and generally passes a lower average particle size.

Very similar morphologies have been reported in the past in literature for the fabrication of microspheres for photoanodes in DSSC. Wang *et al.* reported a template-free synthesis in which the simple hydrolysis of titanium butoxide in an acetone solution giving a similar hierarchical structure, with broad size dispersion of the secondary particles. ^[19] Li *et al.* performed *solvothermal* synthesis with TTIP in anhydrous acetone and, despite obtaining a very broad size distribution,

the microsphere presented densely interconnected nanocrystallites and mesopores.^[20]

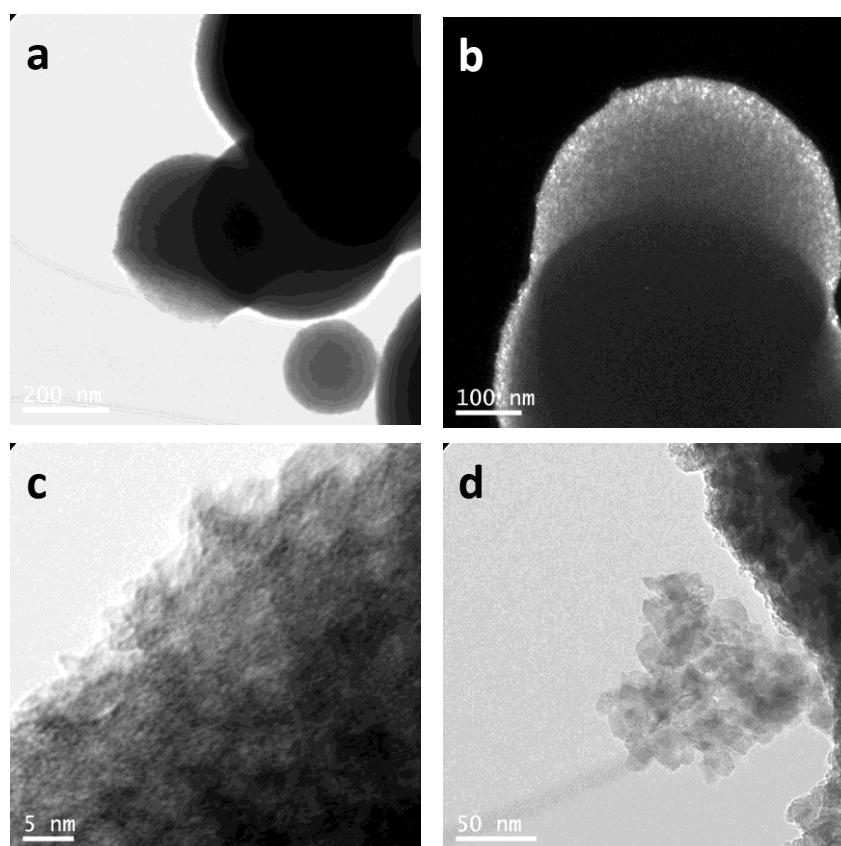


Figure 3.14: TEM analysis of TiO₂ microspheres from the NE series (synthesised using a solution of 2 M HNO₃ in absolute ethanol, 1 min MW treatment at full power-700W). (a) bright field and (b) dark field images; (c) high magnification of the detail of a particle edge and (d) a cluster of primary nanoparticles dissociated from the microsphere after calcination treatment (773 K, 3 h in air).

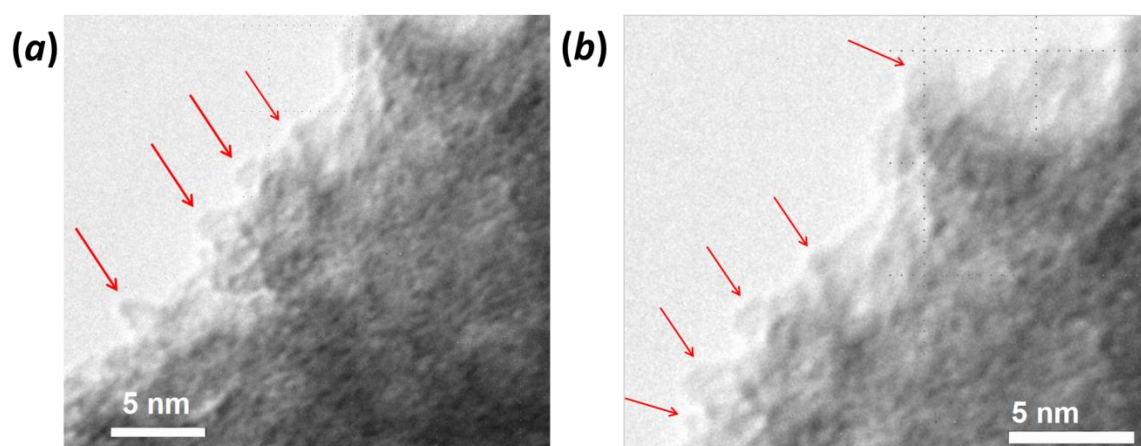


Figure 3.15: (a and b) Higher magnification (300k X) of the representative sample from the NE series (synthesised using a solution of 2 M HNO₃ in absolute ethanol, 1 min MW treatment at full power-700W), with primary crystallites observable at the edges marked with red arrows.

Under very specific conditions, rutile is formed in preference to anatase. Rutile is less interesting from a point of view of catalytic performance (the photocatalytic activity is lower compared to anatase), but various other applications are well known. [21,22] The rutile particles are composed of poorly crystalline acicular structures which probably form as intermediates between the primary growth of the crystallites and the formation of the microspheres. The rutile crystallites assembly in a radial direction, similarly to phalanxes in fingers (Figure 3.16 *d*). These structures have been observed only in the HCl-mediated ethanolic synthesis at high acid concentration (2 M); they were also previously reported for MW-assisted hydrothermal synthesis using HCl and TiCl_4 [11] and from conventional hydrothermal reactions of TiCl_3 with HCl in 2007. [23]

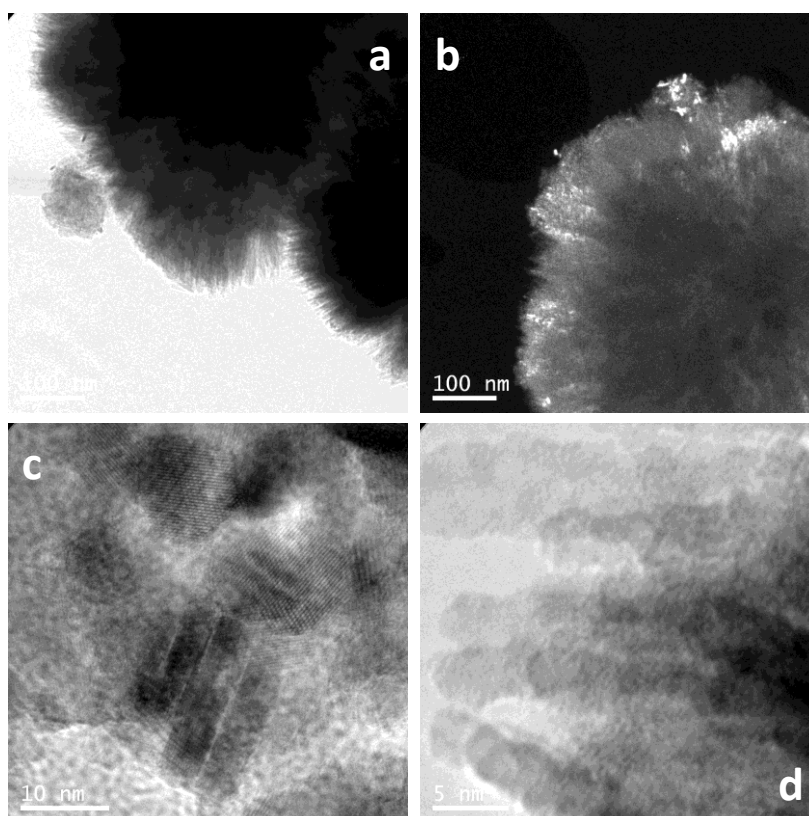


Figure 3.16: TEM analysis of particles synthesised using a solution of HCl 37% v/v in absolute ethanol (2 M HCl, 1 min MW treatment at full power). (a) Bright field and (b) dark field images of a cluster of particles; (c) magnified details of the primary nano-crystals that constitute the secondary particles and (d) detail of the nano-sized acicular structures.

However, it was difficult to replicate the same results using TTIP as precursor in a hydrothermal synthesis (i.e. using water as solvent) and high-resolution SEM images showed the presence of very small irregular nanoparticles, with sizes below 100 nm that coalesce to form larger irregular particles, as shown in Figure A.4 in the Appendix.

Further evidence of the presence of nanocrystals is provided by SAED analysis (Figure 3.17). In general, the observations from TEM and SAED were in agreement with the PXD analysis, with small crystallites or grains and little evidence of diffraction fringes confirming the poor crystallinity of the particles. The most intense powder rings can be indexed to the same reflections to the peaks observed in the PXD patterns for this series of samples. The diffraction of a perfect crystalline material would result in a series of spots representing the family of planes in the reciprocal lattice. The reduction of the crystallite size causes the degeneration of the spots into rings. A finer crystallite size produces a more continuous ring pattern, with rings of broader width. The thickness of the ring can be used as an inverse measure of the grain size. When the material is totally amorphous, all the discrete rings associated with a family of planes degenerate into a circular halo.^[24] In Figure 3.17, the difference in crystallite size between samples synthesised with HNO₃ and HCl is evident.

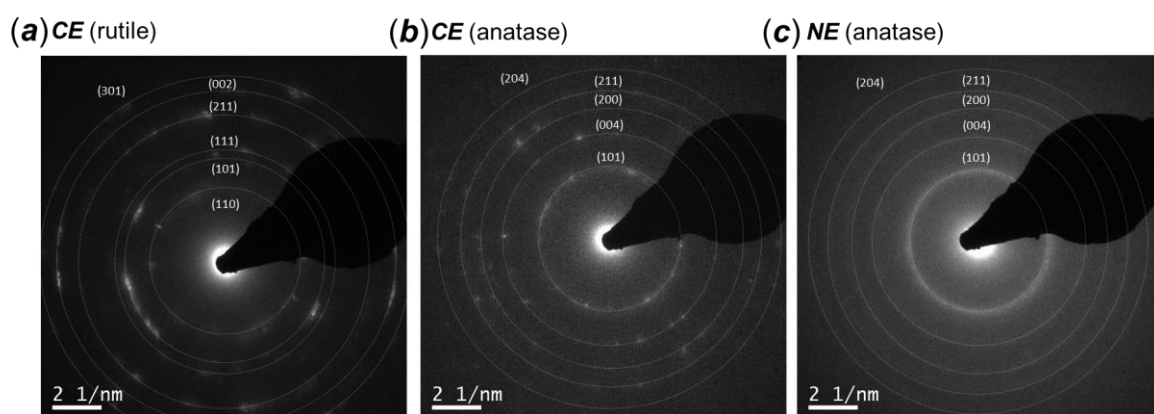


Figure 3.17: SAED analysis of the TiO₂ particles synthesised using ethanol as solvent. (a) CE series (2 M HCl in ethanol); (b) CE series (1 M HCl in ethanol); (c) NE series (2 M HNO₃ in ethanol). The rings are indexed and the crystalline phase is reported next to the sample label.

3.4.2.2 Effect of the acid type and concentration

Among the synthesis parameters influencing the formation and the final morphology of the secondary microspheres, acid type and concentration is the most relevant. Figure 3.18 summarise the average particle size and width of size distribution for the NE series (for which more data are available compared with the other synthesis), chosen because of the higher reproducibility and shape regularity compared to the other sample series. Generally, a larger concentration of acid led to smaller particle diameter and narrower distribution. However, it is

not recommended to increase the acid concentration, especially in the case of HNO_3 , which could release nitrous oxide contributing to by-products, impurities and ultimately an uncontrolled increase of the pressure. In Figure 3.18, some approximated trend for the most complete data sets are shown. The reduction of average size and size distribution is thus directly proportional to the concentration of the acid.

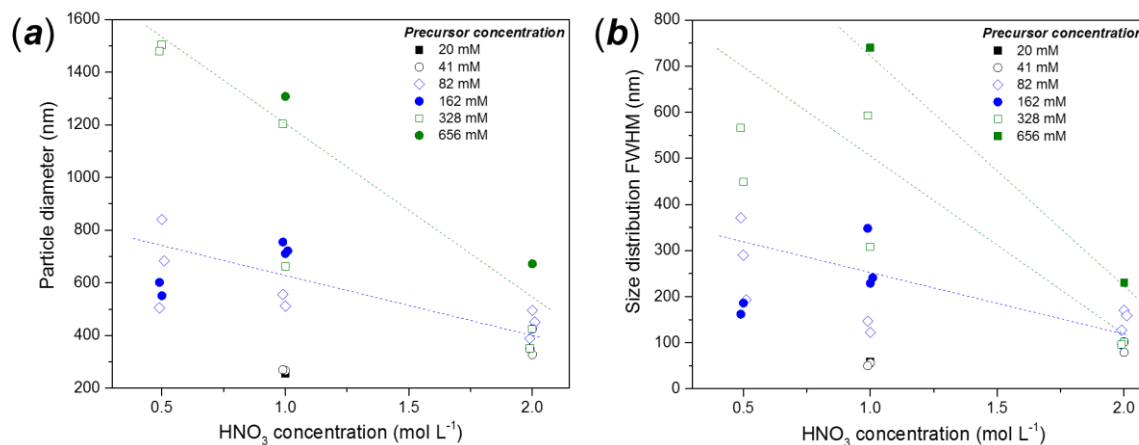


Figure 3.18: Size distribution analysis for the spherical microspheres of the *NE* series as a function of acid concentration, with (a) average particle diameter and (b) width of the size distribution calculated from the SEM images.

3.4.2.3 Effect of the precursor concentration

Precursor concentration and acidity of the precursor solution are the parameters that most affects the final morphology of the secondary particles. The increase precursor concentration was observed to increase the diameter of the spherical particles, together with broadening of the size distribution. In Figure 3.19 the example of particles belonging to the *NE* series obtained with 1 M HNO_3 is reported. Sphere size increases with higher precursor concentration. Lower precursor concentration of precursor usually led a narrower size distribution, with an average diameter of ca. 200-300 nm. As already mentioned, when the size of the particles is ≤ 200 nm, the SEM resolution limited the precision of the size distribution calculation.

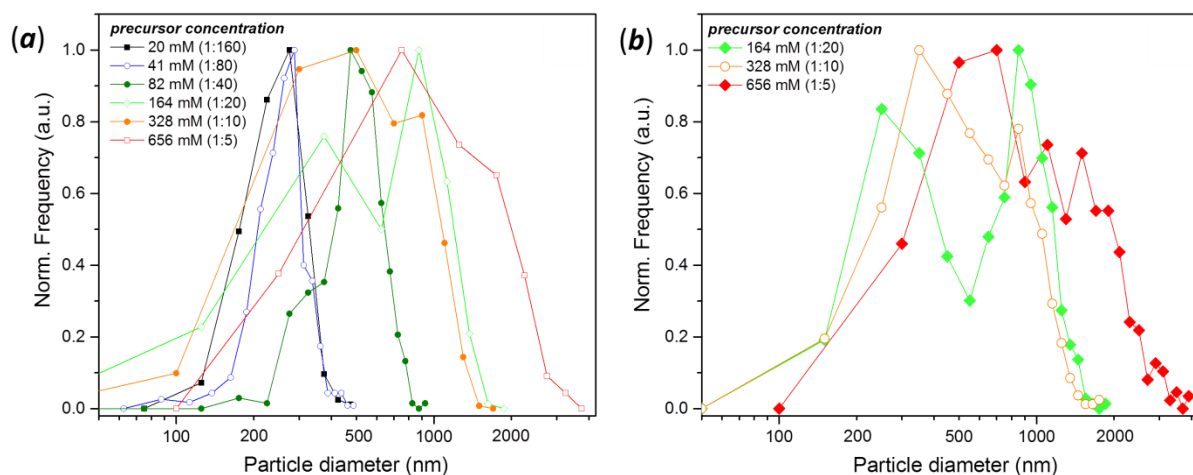


Figure 3.19: Particle size distribution, calculated by SEM image analysis, of NE series particles (1 M HNO₃, 1 min MW treatment at full power) as a function of the precursor concentration.

The reduction of particle size with precursor concentration is a well-known effect for the synthesis of spherical TiO₂ particles.^[25] In Figure 3.20, the average diameter of the spherical particles (a) and the width of the size distribution (b), calculated from the standard deviation of the measurement of the particle diameters) follows a precise trend, confirming that a similar formation mechanism to classic sol-gel and hydrothermal syntheses prevails. The phenomenon is particularly clear for the particles synthesised using 1 M HNO₃ (one of the most complete data set available), with the trend highlighted with a red line (Figure 3.20). Low acid concentration is not strong enough to ensure formation of spherical particles (e.g. a multimodal distribution observed at 0.5 M) while much higher concentration reduces the influence of the precursor on size (e.g. 2 M HNO₃).

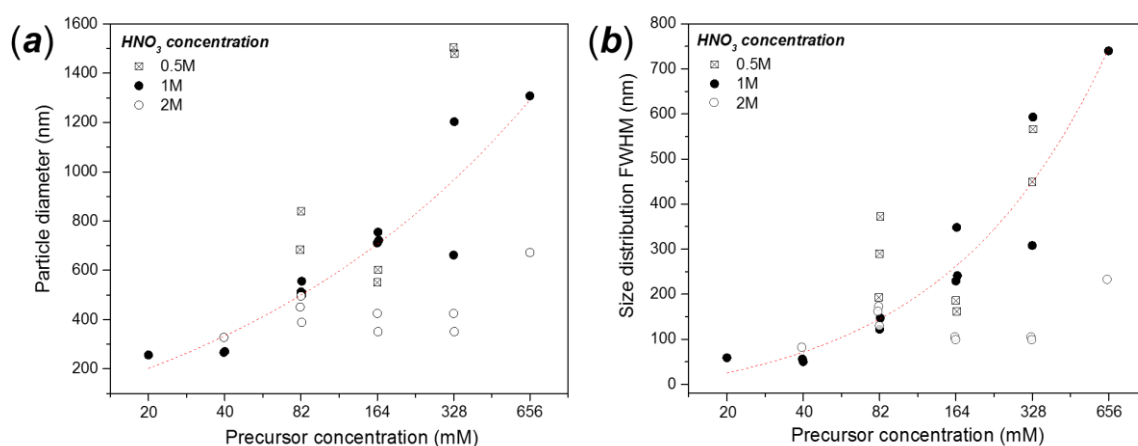


Figure 3.20: (a) Average particle size and (b) size distribution FWHM for particles in the NE series as a function of the precursor concentration, when varying the acid concentration.

3.4.3 Surface area and pore size

Surface area and pore size of the FMH-TiO₂ particles were measured through the analysis of nitrogen adsorption/desorption isotherms. As already mentioned in the introducing section, the shape of the isotherms reveals the porosity of the material, according to the IUPAC classification of the characteristic isotherm curves.^[26] Most of the isotherms can be classified as type II, typical of non-porous or microporous materials (Figure 3.21). However, the presence of a small hysteresis might indicate the presence of mesoporosity. Hysteresis is typical in type IV isotherms and is caused by the different rate between adsorption and desorption processes due to the condensation of the nitrogen inside the pores; on desorption the condensed nitrogen evacuates the pores at a different relative pressure compared to that required to fill the pores with gas originally.

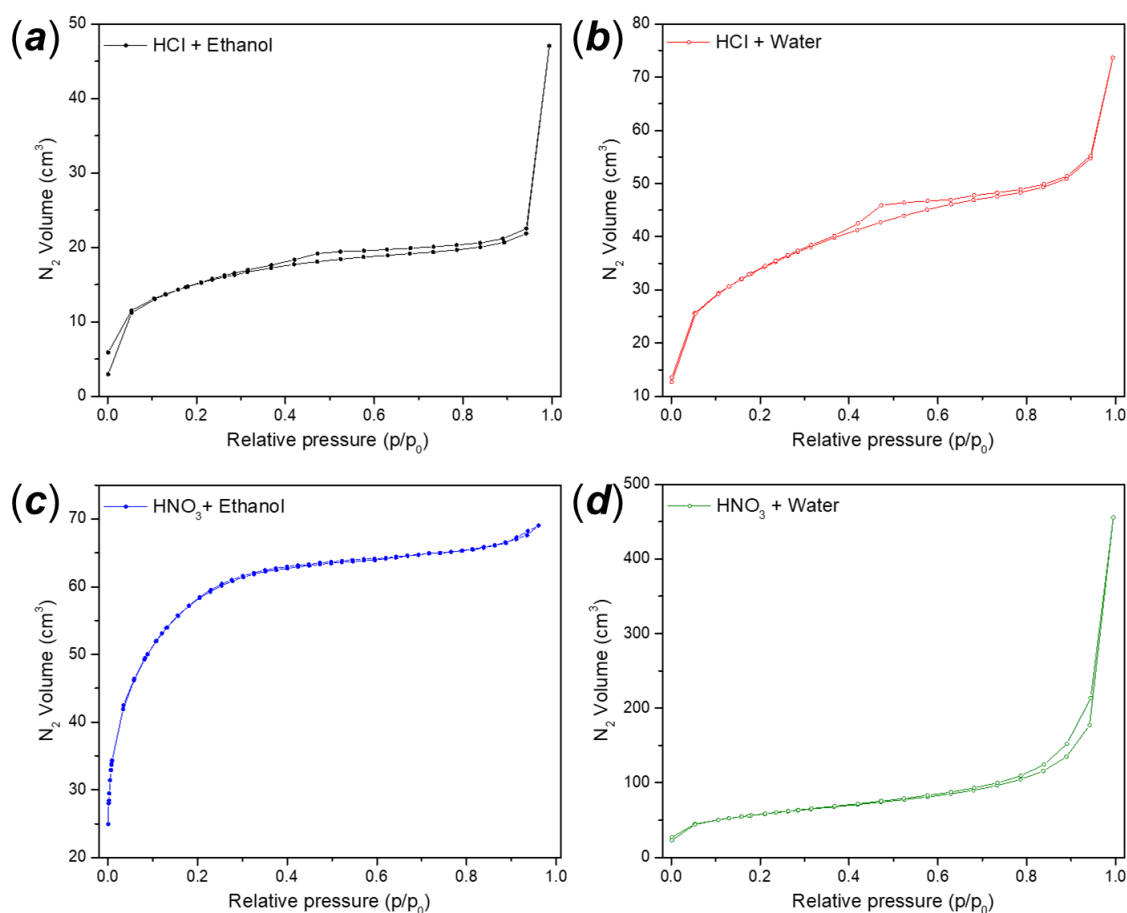


Figure 3.21: Nitrogen adsorption/desorption isotherms for as-synthesised materials. Following acids and solvents were used: (a) HCl (2 M) in ethanol (CE series); (b) HCl (2 M) in water (CW); (c) HNO₃ in ethanol (NE); (d) HNO₃ in water (NW)

The hysteresis phenomenon is mainly due to the capillary effect related to the size and shape of the pores. The shape of the hysteresis loop correlates with the material microstructure as determined by pore size distribution, pore geometry and the connectivity between the pores.^[27] From the isotherms in Figure 3.21 c, samples from the **NE** series appear to be the only ones to exhibit microporosity (IUPAC type I). The surface areas of these **NE** samples are the highest among the material prepared. A more detailed analysis of the **NE** samples revealed a progressive evolution of the pore size distribution and shape on varying the synthesis parameters; the acid and precursor concentration were the most important variables in this respect. Increased acidity led to a general increase in porosity, with an evolution from type I isotherms (typical of micropores) to type IV isotherms (characteristic of mesopores), as shown in Figure 3.22 and Figure 3.23.

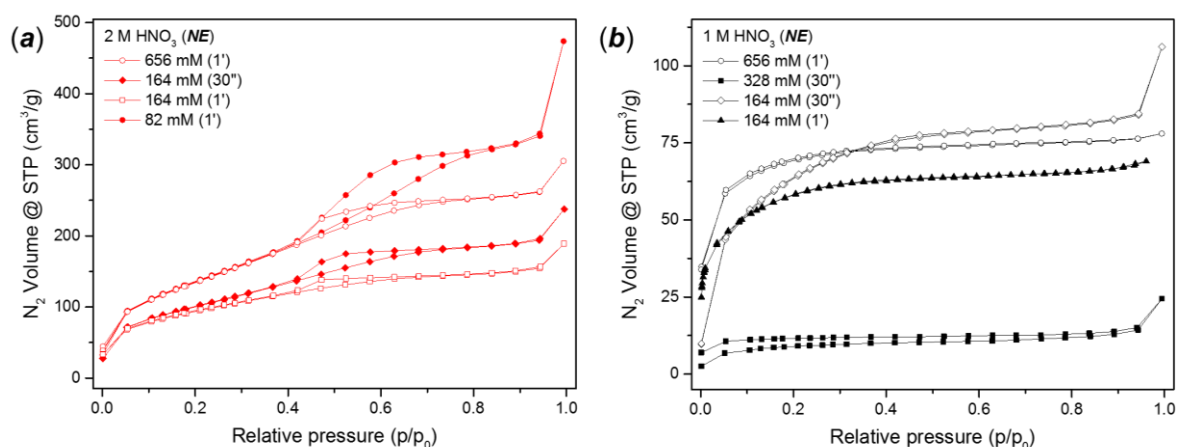


Figure 3.22: N₂ adsorption/desorption isotherms for some selected FMH-TiO₂ sample synthesised using (a) 2 M and (b) 1 M HNO₃ solution respectively

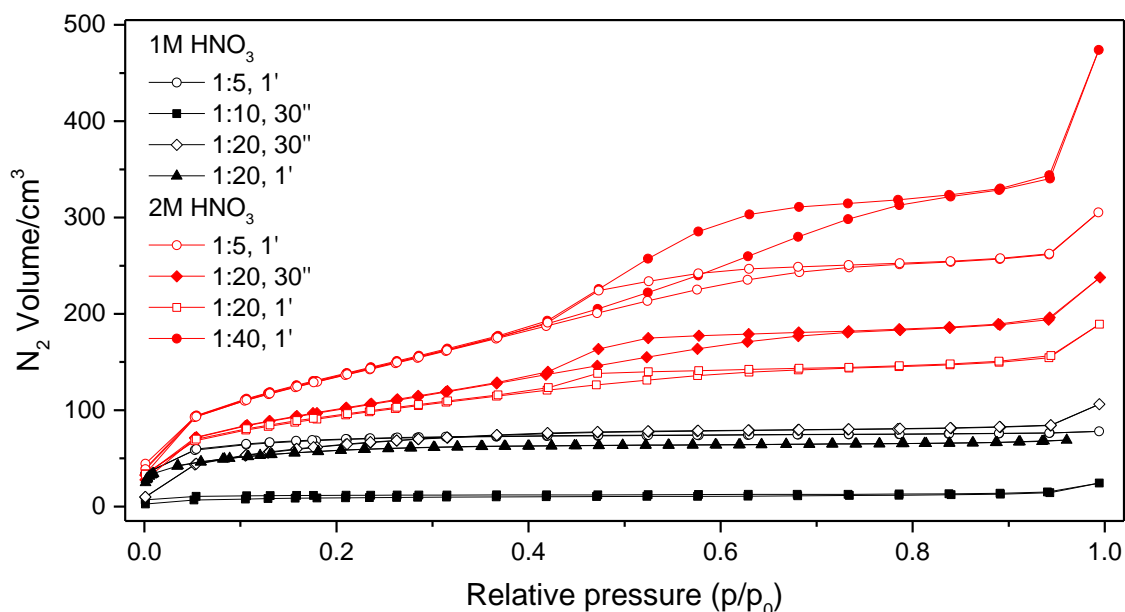


Figure 3.23: N_2 adsorption/desorption isotherms for the *NE* series, at different HNO_3 concentration.

The hysteresis loops observed for the mesoporous microspheres can be classified as “type A” according to the original De Boer system, suggesting the presence of an open mesoporosity with pore size invariant along the length of the pore.^[28, 29] This type of hysteresis can also be attributed to the H2 type under the IUPAC classification, which is associated with an ill-defined distribution of pore size and shape. Alternatively, the hysteresis shape might be considered as a degenerate H1 type, which suggests the presence of cylindrical pores.

3.4.3.1 Pore size distribution

The estimation of the pore size for mesoporous material was performed using the Barrett-Joyner-Halenda (BJH) equation and the Density Functional Theory (DFT) analysis. DFT models allow a better estimation of the pore distribution than thermodynamic methods, which underestimate the pore size for pore diameter below 10 nm. DFT calculations were performed with the help of the Quadrawin software (Quantachrome instruments), which has a library of DFT models for different adsorbate molecules (N_2 , Ar) and adsorbent material such as amorphous carbon, silica and zeolite. All the pre-set available DFT models were compared with the BJH results for the N_2 isotherms of a reference material (Aerioxide P25, with the results showed in Figure A.7 and Table A.2 in the Appendix). Four of these models were selected considering the presence mixed shape pores

(specifically cylindrical, slit and spherical), the adsorbent material and the calculation approach. Amorphous carbon was selected for three of the methods, considering the nanocrystalline/partly amorphous nature of the FMH-TiO₂ microspheres. However, one of the models considers silica, chosen to simulate an inorganic crystalline structure similar to TiO₂. Both non-local DFT (NLDF) and quenched solid (QSDFT) calculations were considered (a brief explanation of the different models is given in section 2.7.1)

Figure 3.24 shows the comparison of the different calculations of pore size distribution. Calculations based on the adsorption isotherm (Figure 3.24 a) revealed a broader pore distribution, with the DFT approaches providing a higher mean pore value compared to the classic BJH method. The method based on the desorption isotherms or on the equilibrium. The BJH pore distribution derived from the adsorption isotherm matches with the quenched solid state DFT (QSDFT) treatment for mixed pores types (cylindrical, slit and spherical) in carbon materials and with the non-local DFT implemented for mixed pores in silica-based materials.

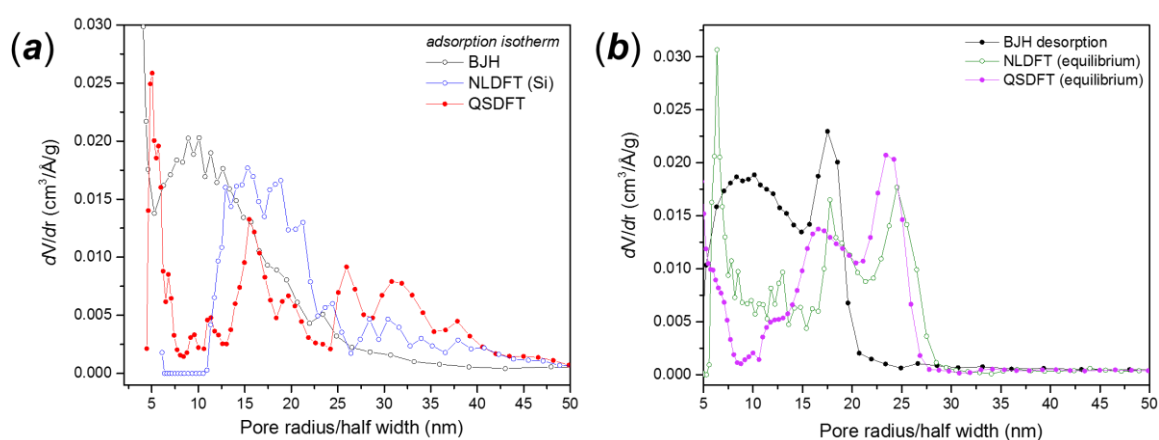


Figure 3.24: Pore size distribution of a representative sample of the NE series (2 M HNO₃, 162 mM, 1 min MW treatment) calculated by using (a) the adsorption isotherm and (b) the desorption or both isotherms, via BJH equation or DFT calculation.

Table 3.3: Surface area values for representative samples of the NE series (prepared using 2 M and 1 M HNO₃) using different calculation methods (calculation based on 3 measurement performed on 3 different samples from the same batch).

Precursor concentration	Surface area (m ² /g)		
	650 mM	162 mM	80 mM
BET	507.4 ± 17.9	369.4 ± 24.4	214.2 ± 15.2
BJH adsorption*	202.0 ± 13.8	148.0 ± 36.3	7.75 ± 3.8
BJH desorption*	246.6 ± 8.1	161.2 ± 28.1	7.93 ± 4.5
BJH adsorption	896.1 ± 14.1	739.9 ± 19.9	445.8 ± 14.3
BJH desorption	989.9 ± 15.5	563.1 ± 24.8	186.7 ± 17.0
NLDFT (C), adsorption	398.7 ± 6.3	307.0 ± 5.2	174.7 ± 5.2
QSDFT (C), adsorption	391.2 ± 6.2	289.8 ± 5.8	162.1 ± 5.6
QSDFT (C), equilibrium	387.7 ± 6.0	280.2 ± 5.4	162.5 ± 3.8
NLDFT (Si), equilibrium	385.2 ± 11.5	303.5 ± 8.9	207.8 ± 9.2

* considering $p/p_0 > 0.3$

The surface area has been calculated by applying the BET equation to the adsorption isotherm at low relative pressure values. The high values of surface area calculated for the samples support observation that the microspheres are comprised of nano-sized particles. Crude estimation can be made using an empirical formula for the deduction of particle diameter from the specific surface area (S), considering the simple ratio between mass and volume: ^[30]

$$d = \frac{6000}{\rho \cdot S} \quad (\text{eq. 3.1})$$

where d is the particle diameter and ρ is the skeletal density of the material, which considers the volume without including the porosity. The formula is based on the assumption of a uniform distribution of spherical particles, which is a reasonable approximation in our case. According to equation 3.10, if the spheres were dense agglomerates of diameter *ca.* 200 nm-1 μ m, then the surface area would be much smaller. The values of surface area correspond better to diameters of particles as estimated via WPPM and Scherrer's formula. A graphical representation of *equation 3.1* is shown for rutile and anatase in Figure 3.25, the estimated size of the particles and the BET surface area are superimposed on the plot for comparison.

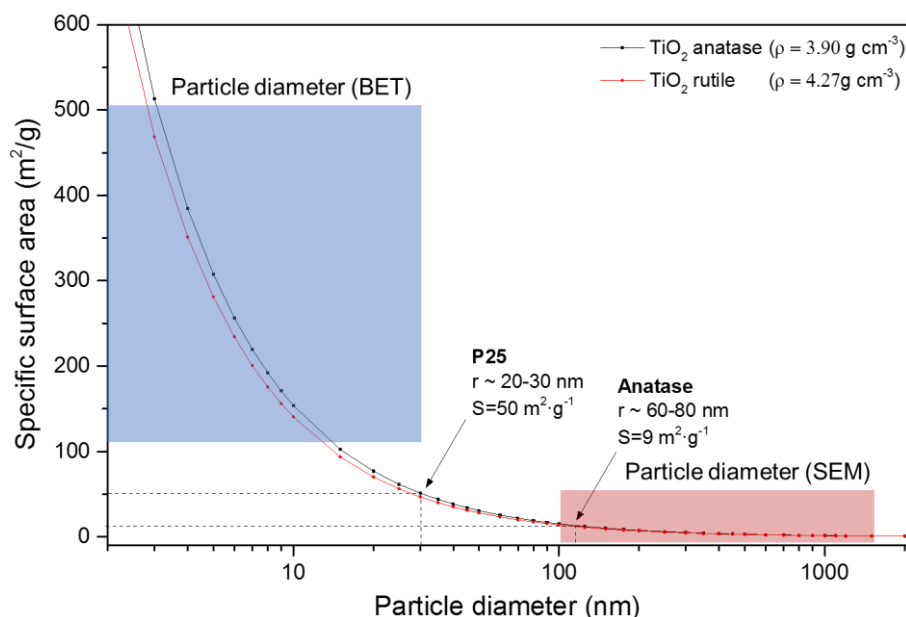


Figure 3.25: Plot of surface area against particle diameter for rutile and anatase according to *equation 3.10*. The range of experimentally determined BET surface areas and sphere diameters (from SEM) are shown for comparison. Typical surface areas for anatase and Aeroxide P25 particles are indicated for reference.

The values of surface area are also consistent with thermodynamic considerations. According to Ranade *et al.*, the surface enthalpy of anatase is lower than those of the other two titania polymorphs when the surface area of the particles is above c.ca 40 m²/g (~3500 m²/mol).^[31]

The parameter affecting the most the surface area is the acid concentration. As shown in Figure 3.26, the adsorption/desorption isotherms (for the *NE* series) can be divided in two distinct groups; particles synthesised with 1 M HNO₃ having a BET surface area in a range 100-200 m²/g, and particles with surface area from 250-450 m²/g, made using 2 M HNO₃. Such high values of specific surface area can be achieved via the mesoporosity of hierarchical structures, with wormhole-like pore structures.^[32]

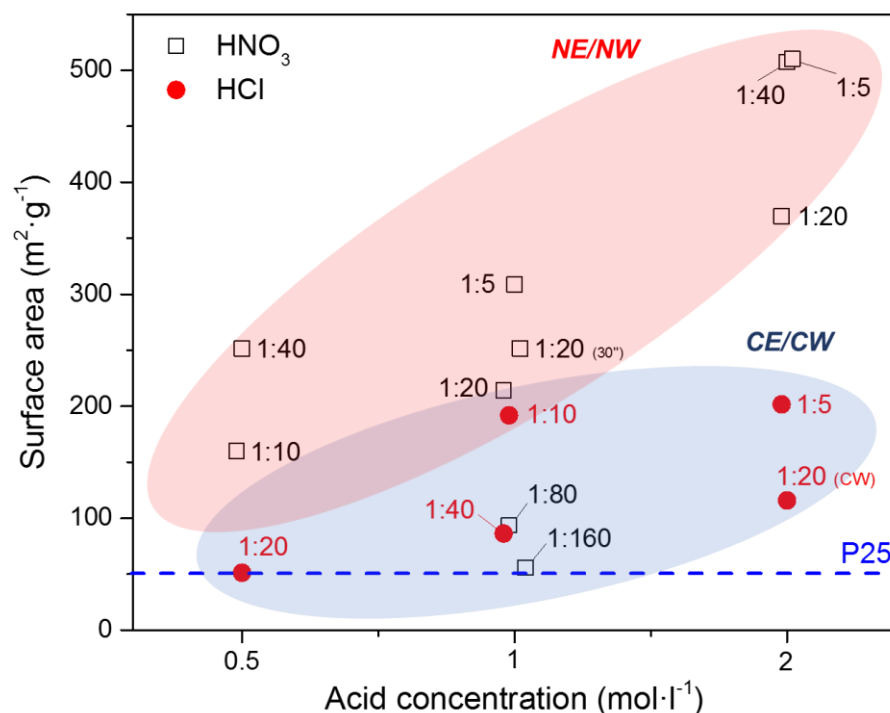


Figure 3.26: Distribution of surface area values as a function of acid and precursor concentration (indicated in volume proportion). The red ellipse regroups the sample synthesised using HNO_3 as acid mediator (except the samples produced with low precursor concentration, < 1:40 v/v) whereas the blue ellipse regroups the measurements performed on samples synthesised using HCl as acid mediator.

Finally, in Table 3.4 the values of surface area and pore size for different FMH- TiO_2 particles are compared with the average crystallite size (calculated by Scherrer method) and the particle diameter distribution, estimated via SEM images. The crystallite size is compared with the diameter calculated using *equation 3.1*. For the synthesis performed with HNO_3 as acid mediator (NE and NW series), the two values are relatively close. On the other hand, for the synthesis involving HCl the diameter estimated by BET is generally higher, due to the formation of bigger secondary particles, the enhancement of the agglomeration phenomena and subsequently the reduction of surface area. Furthermore, it was not possible to correlate the surface area to specific synthesis conditions and to other characteristics such as the estimated size of the primary crystallites and the final diameter of the microparticles. Formation of primary particles, agglomeration of secondary particles and internal structure of the microparticles appears to be independent from each other, with the three processes described by different mechanisms.

Sample	Isotherm type	BET surface (m ² /g)	BJH pore radius (Å)	BJH pore volume (cm ³ /g)	Crystalline size (nm)	BET diameter (nm)	SEM diameter ± distribution (nm)
NE							
0.5 M, 80 mM	I	251.5 ± 20.6	14.9 ± 3.7	0.022 ± 0.007	3.50	6.1	1165 ± 379 *
0.5 M, 328 mM	I	159.7 ± 15.4	17.5 ± 2.4	0.060 ± 0.011	2.67	9.6	1492 ± 566 *
1 M, 20 mM	II	55.7 ± 6.2	14.8 ± 3.9	0.014 ± 0.006	4.58	27.6	265 ± 59
1 M, 40 mM	II	106.2 ± 12.1	14.9 ± 3.9	0.049 ± 0.009	3.82	16.4	264 ± 57
1 M, 164 mM	I	214.2 ± 13.6	16.6 ± 2.5	0.014 ± 0.005	5.63	7.2	730 ± 273
1 M, 648 mM	I	251.5 ± 15.0	15.9 ± 1.9	0.011 ± 0.002	3.01	6.1	1308 ± 740
2 M, 80 mM	IV	510.1 ± 31.5	17.9 ± 3.5	0.642 ± 0.045	4.67	3.0	294 ± 93
2 M, 164 mM	IV	369.4 ± 17.4	17.5 ± 3.1	0.154 ± 0.011	3.84	4.2	496 ± 170
2 M, 648 mM	IV	507.4 ± 28.4	17.9 ± 2.7	0.316 ± 0.028	3.70	3.0	672 ± 230
NW							
2 M, 164 mM	II	202.9 ± 7.4	17.9 ± 4.0	0.647 ± 0.032	5.63	7.6	-
CE							
0.5 M, 164 mM	II	53.3 ± 5.3	15.9 ± 1.8	0.050 ± 0.008	6.72	28.9	-
1 M, 80 mM	IV	88.9 ± 6.1	17.5 ± 3.2	0.036 ± 0.007	8.32	17.3	-
1 M, 328 mM	IV	194.7 ± 12.0	17.5 ± 2.7	0.055 ± 0.014	8.07	7.9	-
2 M, 80 mM	IV	49.1 ± 2.6	18.5 ± 2.0	0.057 ± 0.002	9.56 (R)	31.3	-
CW							
1 M, 164 mM	IV	119.6 ± 9.1	17.9 ± 2.5	0.065 ± 0.012	11.52	12.9	-
2 M, 164 mM	IV	202.9 ± 14.5	17.9 ± 3.2	0.647 ± 0.055	8.59	7.6	-

Table 3.4: Surface area and pore size distribution data for some selected FMH-TiO₂ samples, compared with the crystalline size (calculated by Scherrer equation) and the secondary particle distribution (* used in case of multiple size distribution) (BET-BJH calculations based on 3 measurement performed on 3 different samples from the same batch, crystallite size estimated by Scherrer equation on single measurements using the same diffractometer conditions).

3.5 Spectroscopic characterisation

3.5.1 Raman spectroscopy

Raman analysis can be a powerful tool in the study of nanoparticles. Beyond being an easy way to identify characteristic vibration modes, it provides useful information about the long-range order and the size of crystallites.

According to the factor group analysis for the two main polymorphs of TiO_2 , the space group of anatase is associated with 15 optical modes, 10 if we consider their irreducible representation. Only six of these modes are Raman active ($A_{1g} + 2B_{1g} + 3E_g$), three are IR active ($A_{2u} + 2E_u$) and the mode B_{2u} is invisible by both spectroscopies. [33] In comparison, rutile has only 4 Raman active modes. [34] The Raman modes of anatase and rutile are described in the schematic in Figure 3.27. Anatase is characterised by a very intense $E_{g,I}$ mode (143 cm^{-1}) followed by another weaker E_g band ($E_{g,II}$, 197 cm^{-1}) and three medium intensity bands (B_{1g} , 399 cm^{-1} , A_{1g} 513 cm^{-1} , the second B_{1g} at 519 cm^{-1} overlapped to A_{1g} , $E_{g,III}$ 639 cm^{-1}). The strongest modes in rutile are the E_g (447 cm^{-1}) and A_{1g} (612 cm^{-1}), with a B_{1g} band in a very similar position to the anatase $E_{g,I}$ vibration.

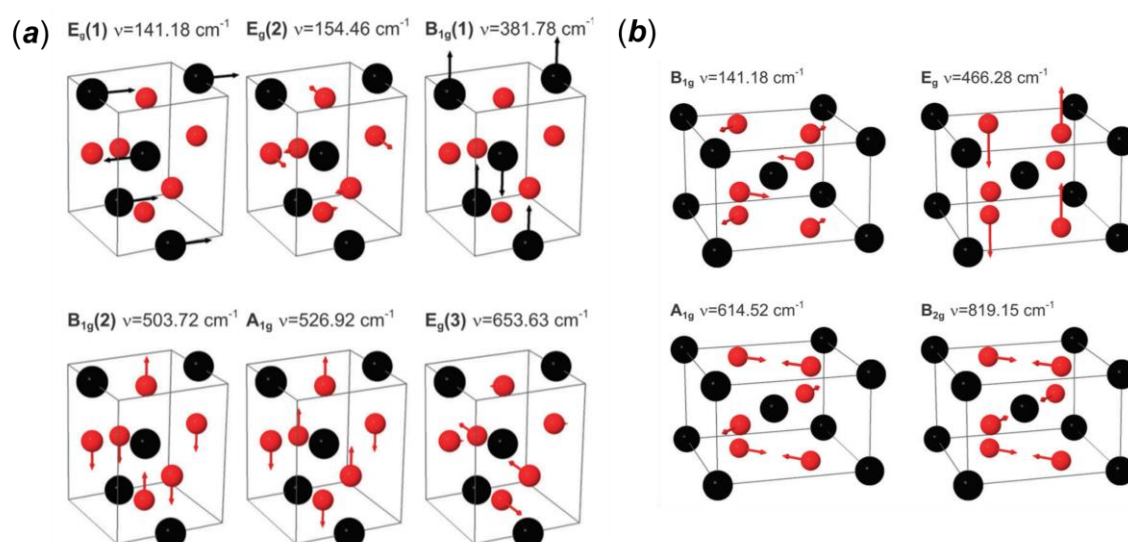


Figure 3.27: Schematic showing the active vibrational modes in (a) the anatase and (b) rutile lattice. [35]

For the analysis performed in this thesis, different conditions have been tested to improve the reproducibility and the accuracy of the results. The best results were obtained using an automatic baseline subtraction based on an 8-degree polynomial

algorithm. An example of the baseline subtraction is offered in Figure A.5 in the Appendix. After baseline subtraction, the peaks were fitted by means of a split Pseudo-Voigt function. By using this function, the combination of the Lorentzian and Gaussian contribute is weighed for the instrumental asymmetry of the signal. In Figure 3.28, the comparison between interpolations of the $E_{g,l}$ peak (belonging to a sample from the *NE* series) after baseline subtraction is reported. The split Pseudo-Voigt functions presents the best fit of the experimental data. Calculation of peak position and FWHM were determined using the Fytik software, implementing the Levenberg-Marquardt algorithm.

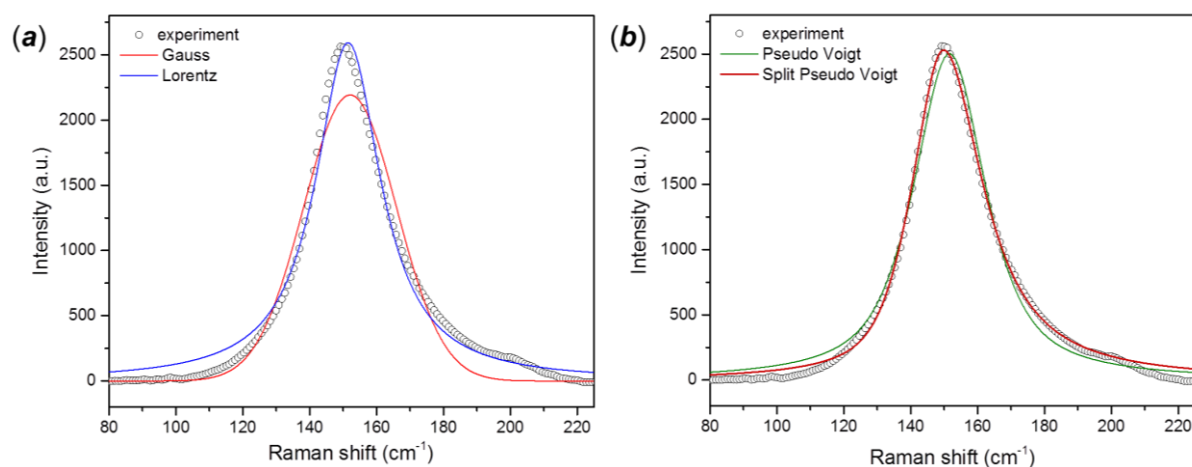


Figure 3.28: (a) Curve fitting of $E_{g,l}$ mode of a selected FMH-TiO₂ sample (*NE* series, 1 M HNO₃, 162 mM precursor, 1 min MW treatment) using Gaussian and Lorentzian curves; (b) fitting of the same data using Pseudo-Voigt and split Pseudo-Voigt curves.

Ultimately, the spectra were normalised considering the maximum intensity of the $E_{g,l}$ mode, which is normally the most intense for TiO₂ anatase.^[33]

The normalisation procedure does not affect the comparison of spectra provided that the same output power is used. Likewise, different time exposure or optical aperture, which are used to modulate the signal intensity, does not affect the comparative analysis after normalisation of the spectra, as shown in Figure A.6 in the Appendix.

In Figure 3.29, the corresponding Raman spectra of anatase, rutile and Aeroxide P25 (a combination between the two) are shown. Typical of the spectrum of rutile is also the presence of a second order band at 240 cm⁻¹, due to multiple-phonon scattering processes. The small band observed in Figure 3.29 and marked with (c) is likely due to anatase impurities in the rutile sample.

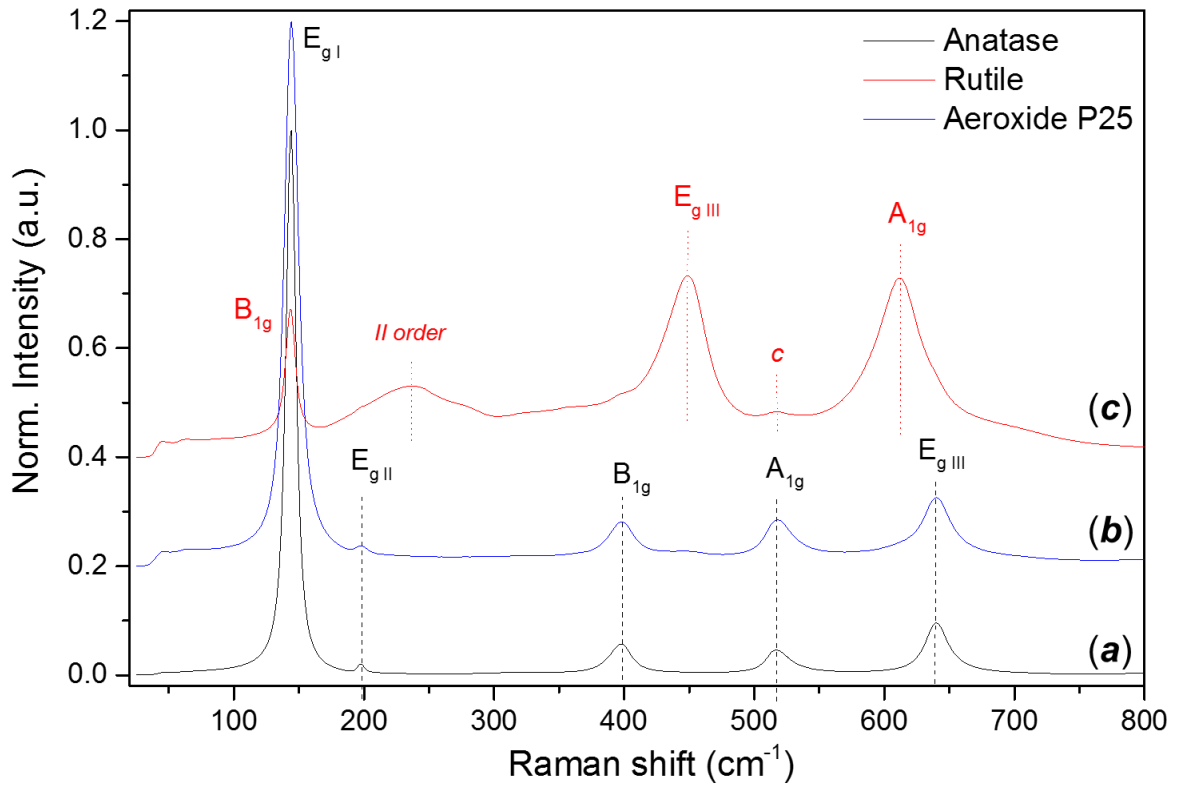


Figure 3.29: Raman spectra of (a) anatase, (b) Aeroxide P25 and (c) rutile (The spectra were collected, normalised and corrected with an appropriate scale factor).

The absolute intensity of the Raman bands is a good indicator of the degree of crystallinity and the long-range order of the material. A very good example is given by the differences in the Raman spectra of pure anatase and P25, which is a combination of the rutile and anatase. Pure crystalline anatase presents very intense peaks, with the $E_{g,I}$ mode entirely visible only for low laser power output (1%). On the other hand, P25 has much lower intensity despite the high crystallinity. The absolute intensity of the bands of P25 appeared 20 times weaker than those of anatase, despite the relatively high crystallinity of the material. Comparing the spectra, other discrepancies are evident, as shown in the analysis of the peak positions E_g and relative intensities in Table 3.5. The comparison between these materials is indicative of the effect of size and structural disorder. Despite its crystallinity, P25 has been reported as being ca. 10% amorphous. The comparison of the relative intensity of the most intense peaks has been previously reported as an indicator of the degree of crystallinity for nanomaterials. This analysis requires extreme care with regards to the instrumental parameters, which influence the absolute intensity and sometimes causes peak shift unrelated to the material itself.

Table 3.5: Band positions and relative intensity for the Raman spectra of commercial anatase (Sigma, 99.9%) and Aeroxide® P25 (results obtained from 3 measurement from samples from the same batch).

	Peak position		Relative intensity	
	<i>Anatase</i>	<i>P25</i>	<i>Anatase</i>	<i>P25</i>
$E_{g,I}$	143.92 ± 0.18	144.14 ± 0.15	$E_{g,I}$	100
$E_{g,II}$	197.53 ± 0.15	197.57 ± 0.21	$E_{g,II}$	2.05 ± 0.51
B_{1g}	397.65 ± 0.21	398.16 ± 0.35	B_{1g}	5.74 ± 0.32
A_{1g}	517.24 ± 0.16	518.05 ± 0.28	A_{1g}	4.64 ± 0.41
$E_{g,III}$	640.04 ± 0.10	640.00 ± 0.15	$E_{g,III}$	9.63 ± 0.36

The Raman analysis of the FMH-TiO₂ particles confirmed the phase identification provided by PXD analysis, with anatase as the main crystalline phase. Some common features are characteristic of the Raman spectra of the as-synthesised particles, such as a blueshift of the low frequency mode ($E_{g,I}$), a generalised peak broadening compared with the crystalline reference material and the enhancement of the initial low frequency shoulder. Peak broadening and shifting compared to anatase are evident in Figure 3.30, where the results of a multipoint analysis of NE series particles can be observed.

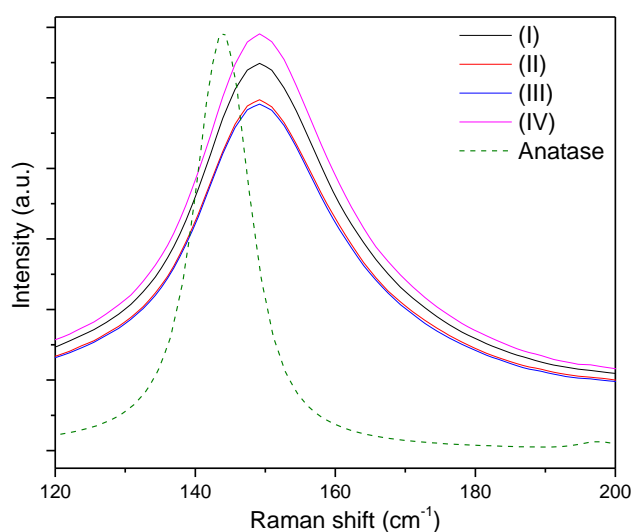


Figure 3.30: Detail of the $E_{g,I}$ mode in the Raman spectra of NE particles (2 M HNO₃, 162 mM TTIP concentration, 1 min MW synthesis) compared to anatase. The Roman numerals indicate the order of sampling points on the specimen.

The precursor concentration (which effect on the secondary particles has been already described in section 3.5.2.3) affects the size of the primary crystallites. The Raman spectra of the NE sample series are shown in Figure 3.31. The $E_{g,l}$ band broadens progressively and overall there is a decrease of absolute intensity and an increase in the background as the precursor concentration is reduced.

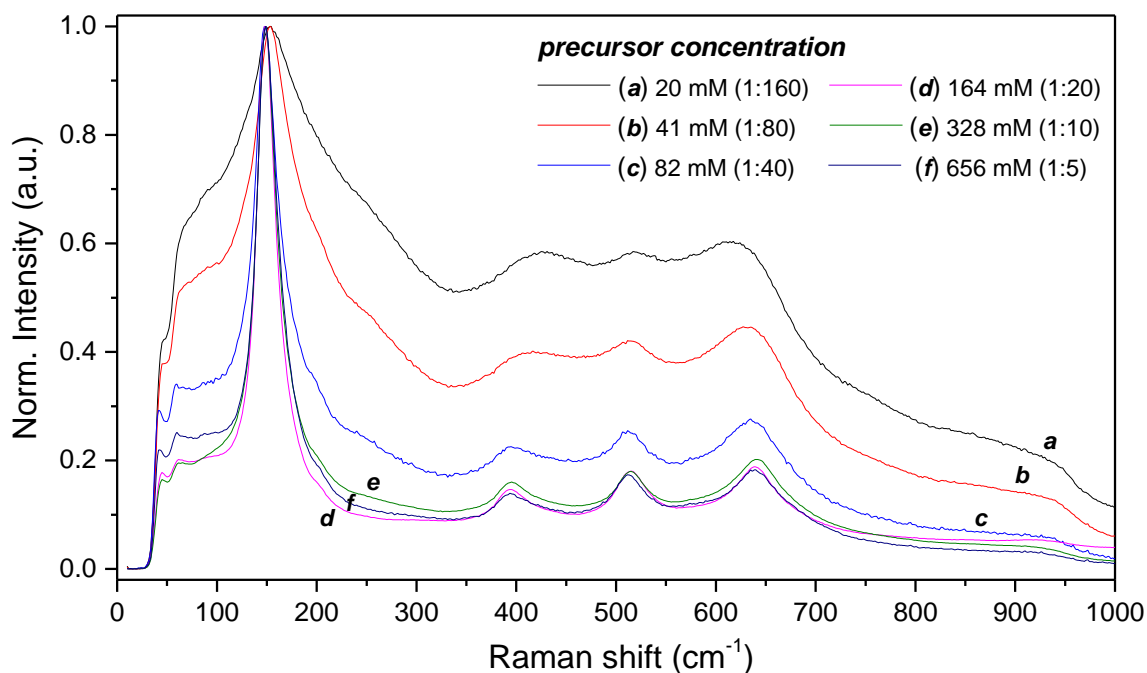


Figure 3.31: Raman spectra of the FMH-TiO₂ particles, NE series, as a function of the precursor concentration. The spectra were normalised using the $E_{g,l}$ mode peak intensity as the maximum value.

3.5.2 Optical properties

3.5.2.1 Optical properties of commercial references

Figure 3.32 shows the absorbance and reflectance spectra characteristic of commercial samples of rutile and anatase. As witnessed by the white colour of both samples, the reflectance is almost absolute in the entire range of visible light. The absorption edge, indicating the threshold energy for allowed electronic transition, is at *ca.* 416 nm for rutile and 382 nm for anatase. The Kubelka-Munk functions can be calculated from the reflectance spectra obtained via DR-UV-Vis spectroscopy. Figure 3.33 shows the functions for direct and indirect band gap calculation, with the result of the function interpolation listed in Table 3.6. The comparison of the values herein obtained is consistent with the literature, [36] apart from a discrepancy in the value of rutile.

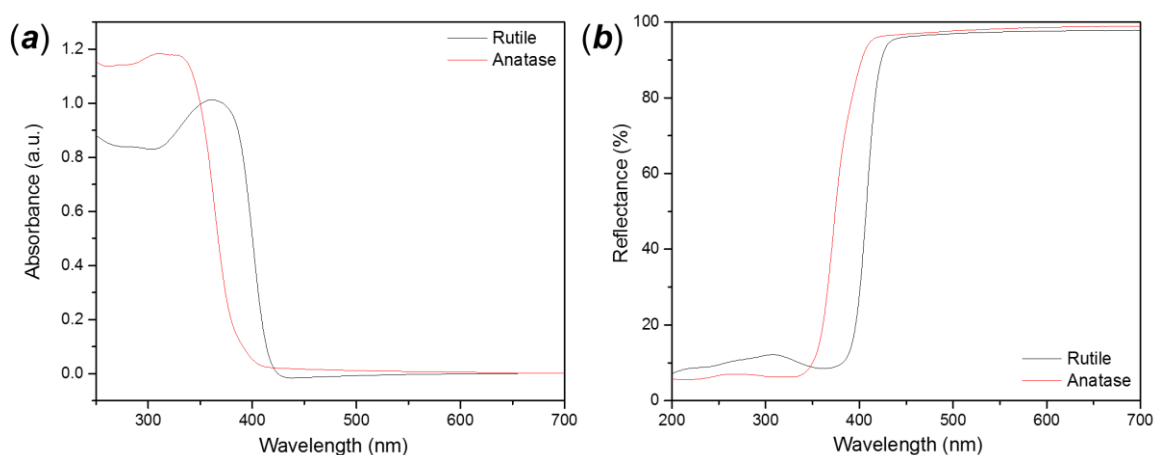


Figure 3.32: (a) Absorbance and (b) reflectance spectra for TiO_2 rutile and anatase.

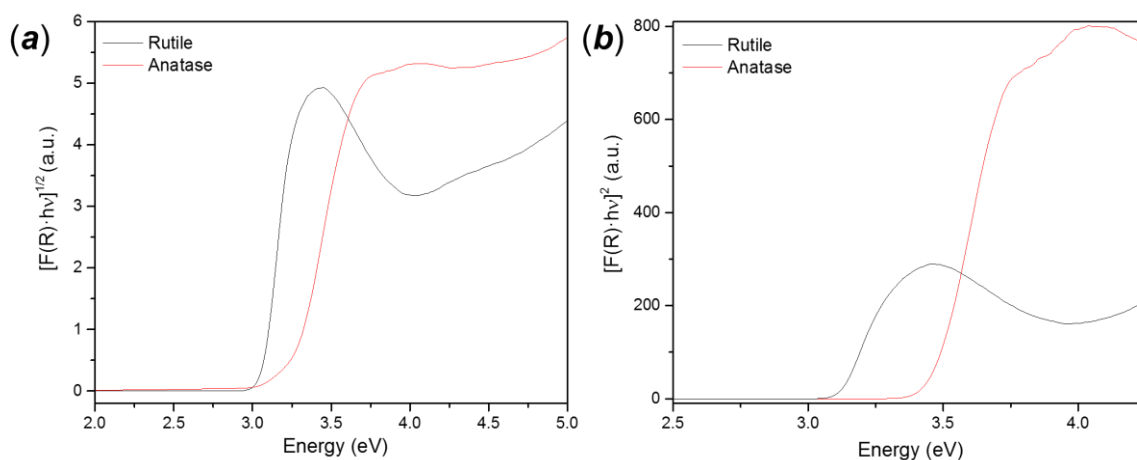


Figure 3.33: Band gap calculation for TiO_2 polymorphs; calculation of the Kubelka-Munk functions for (a) indirect and (b) direct band gap.

Table 3.6: Results of the band gap calculation for TiO₂ commercial anatase and rutile (the analysis of the errors is reported in Table A.1 in the Appendix)

Absorption edge (eV)	3.23	2.99
<hr/>		
Band gap		
direct (eV)	3.47	3.12
indirect (eV)	3.23	3.07

However, optical spectroscopies are generally unable to provide an accurate value for the band gap, often indicating only a single significant digit. Dedicated studies reported how the determination of the band gap is generally affected by theoretical and systematic errors, such as wrong fitting calculation or misinterpretation of the theory.^[37]

In this work, the linear fitting of the slope of the Kubelka-Munk function was performed considering a constant number of points around the respective points of inflection (e.g. 20 points in case of a 0.2 nm scan step) to improve the accuracy of the analysis. However, it was not possible to reduce the uncertainty in the band gap below ± 0.002 eV for crystalline materials and ± 0.005 eV for the FMH-TiO₂ samples, probably due to the lower uniformity of the material properties. Error calculations are reported in Table A.1 in the Appendix. The errors are almost certainly mainly due to the poor reproducibility of the synthesis technique rather than to inconsistency in the preparation of the DR-UV-Vis samples.

3.5.2.2 Optical properties of FMH-TiO₂

The band gaps of nanostructured materials can often be different from their bulk counterparts, when the particle size reaches quantum confinement limits. The measurement of the optical band gap for TiO₂ gives a good indication of the nature of the material, the degree of crystallinity, the polymorphic composition and the size of the primary particles. In this section, the different synthesis parameters have been correlated with the resulting optical properties. Diffuse reflectance UV-Vis spectroscopy (DR-UV-Vis) allows a precise measurement of the optical band gap in solid materials.

Figure 3.34 shows the reflectance spectra of four selected FMH-TiO₂ samples from the different synthesis categories, compared with commercial anatase. Despite the similar shape, the curves present several dissimilarities, including the spectral edge, which thus indicates optical band gaps different from that of anatase.

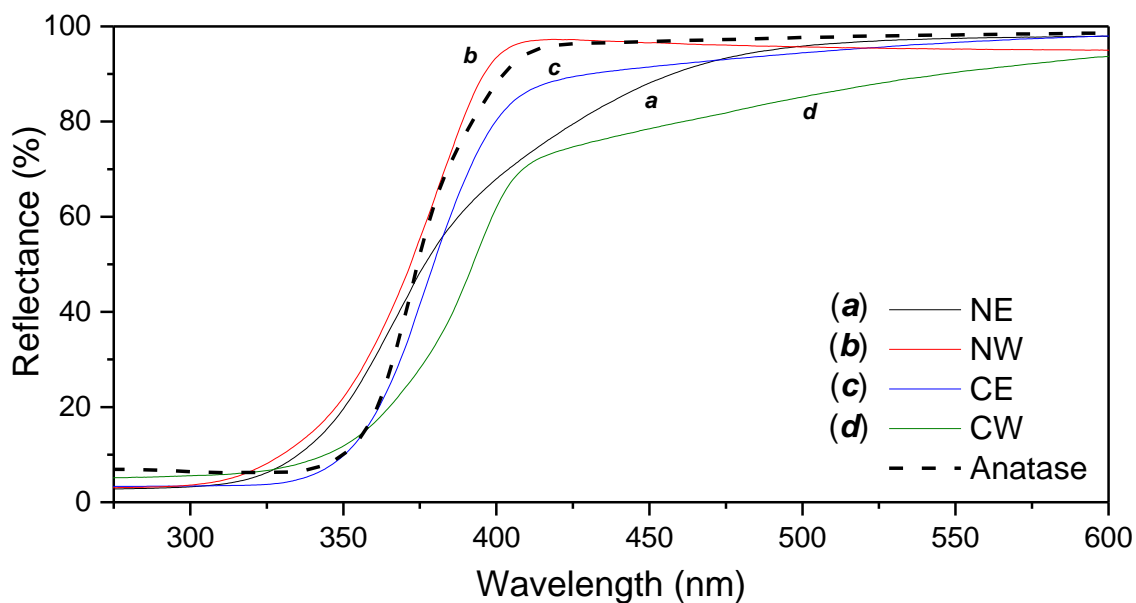


Figure 3.34: Reflectance spectra (obtained by DR-UV-Vis spectroscopy) of different FMH-TiO₂ samples compared with reflectance of commercial anatase (dashed line). All samples were synthesised using 2 M of acid (HNO₃ for NE, NW and HCl for CE, CW) and 162 mM of TTIP precursor.

The determination of the indirect and direct band gap for the FMH-TiO₂ samples is displayed in Figure 3.35. Apart from the sample belonging to the CW series, which has both values very close to those of anatase, all the other samples have indirect band gaps around 3.3-3.4 eV and direct of ca. 3.6-3.8 eV. A

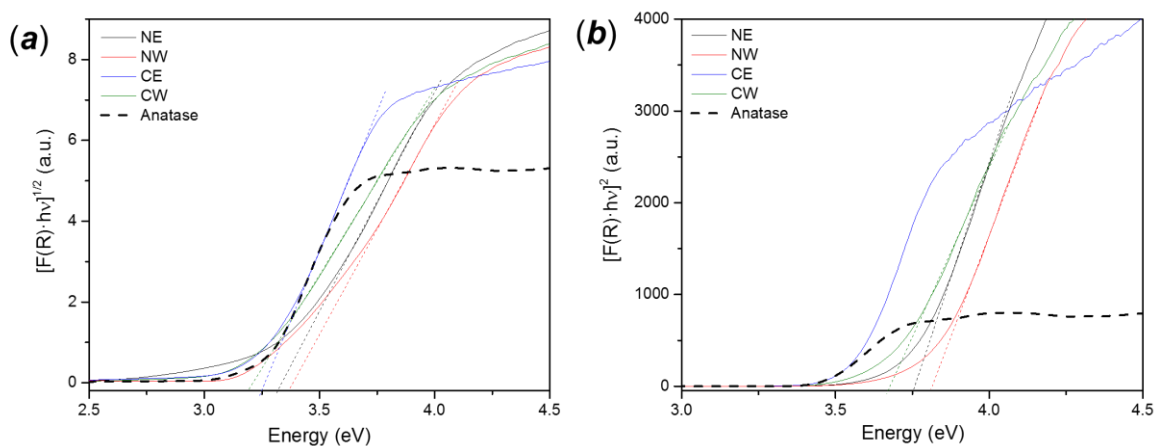


Figure 3.35: (a) Indirect and (b) direct band gap calculation of the selected FMH-TiO₂ samples using the Kubelka-Munk functions. The functions for anatase are represented with dashed lines.

Table 3.7: Optical band gap (indirect and direct) and Urbach energy (minimum and maximum values estimated from other synthesis conditions, e.g. treatment time) for FMH-TiO₂ particles, classified according to the synthesis conditions (type of acid and solvent), acid and precursor concentration.

Series	Acid conc. (M)	Precursor conc. (mM)	Indirect band gap (eV)	Direct band gap (eV)	Urbach energy (meV)	
NE	0.5	82	3.33-3.36	3.65-3.68	98-124	
		164	3.29-3.31	3.68-3.70	89-113	
		328	3.24-3.27	3.62-3.68	80-92	
	1	40	3.45	3.76-3.80	127-150	
		82	3.37-3.40	3.72-3.74	104-110	
		164	3.27-3.35	3.67-3.73	105-134	
	2	40	3.41-3.42	3.75-3.76	116-124	
		82	3.41	3.77	111-130	
		164	3.35-3.41	3.72-3.75	100-160	
		328	3.33-3.36	3.66-3.70	95-120	
		656	3.33	3.67	100-115	
CW	2	164	3.10-3.12	3.63	78-112	
		486	3.19-3.21	3.62-3.68	65-120	
CE	0.5	164	3.23-3.25	3.49-3.53	78-79	
		1	164	3.25-3.27	3.56-3.58	83-85
			328	3.22-3.23	3.60-3.62	83-85

3.5.2.3 Band gap and crystalline properties

Treatment time and MW power are among the synthesis parameters not significantly affecting the band gap. Crystallites obtained from the lowest precursor concentrations are most likely composed of an amorphous matrix with very small crystallites with it. The formation of very small crystallites is also implied from the optical properties, with an enhancement of the quantum size effect and a blue-shift in the band gap blue-shift of ca. 0.25-0.30 eV compared with crystalline anatase. The reduction of the precursor concentration leads to a progressive increase of the band gap, with a shift from 3.16 eV for a TTIP concentration of 650 mM towards 3.47-3.48 eV for a concentration of 20 mM.

From the calculation of the band gap for the different synthesis conditions, similar trends were observed for the samples of the *NE* series prepared with other HNO_3 concentration, with the results listed in Table 3.7. Figure 3.36 shows the correlation between the average values of indirect band gap and the precursor concentration. The indirect band gap increases with the decrease of the precursor concentration. The direct band gap follows the same trend.

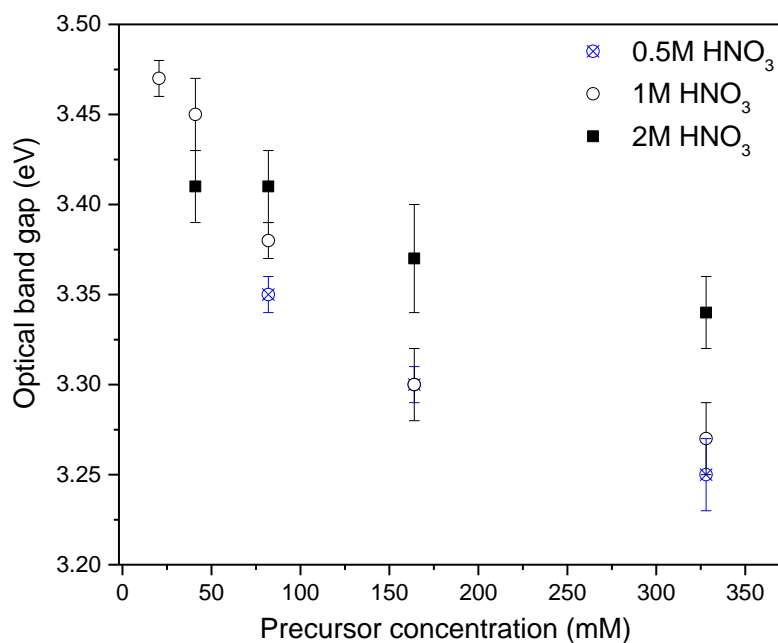


Figure 3.36: Effect of the precursor concentration on the indirect optical band gap of the TiO_2 particles in the *NE* series with varying acid concentration.

The correlation between indirect band gap and synthesis parameters (acid and precursor concentration) is displayed in the plot in Figure 3.37, in which all the values of indirect band gap have been reported. Despite the discrepancies from the average values (due to the influence of other parameter difficult to control, such as treatment time in the DMO), the correlation between the three parameters is evident, at least for the most investigated conditions.

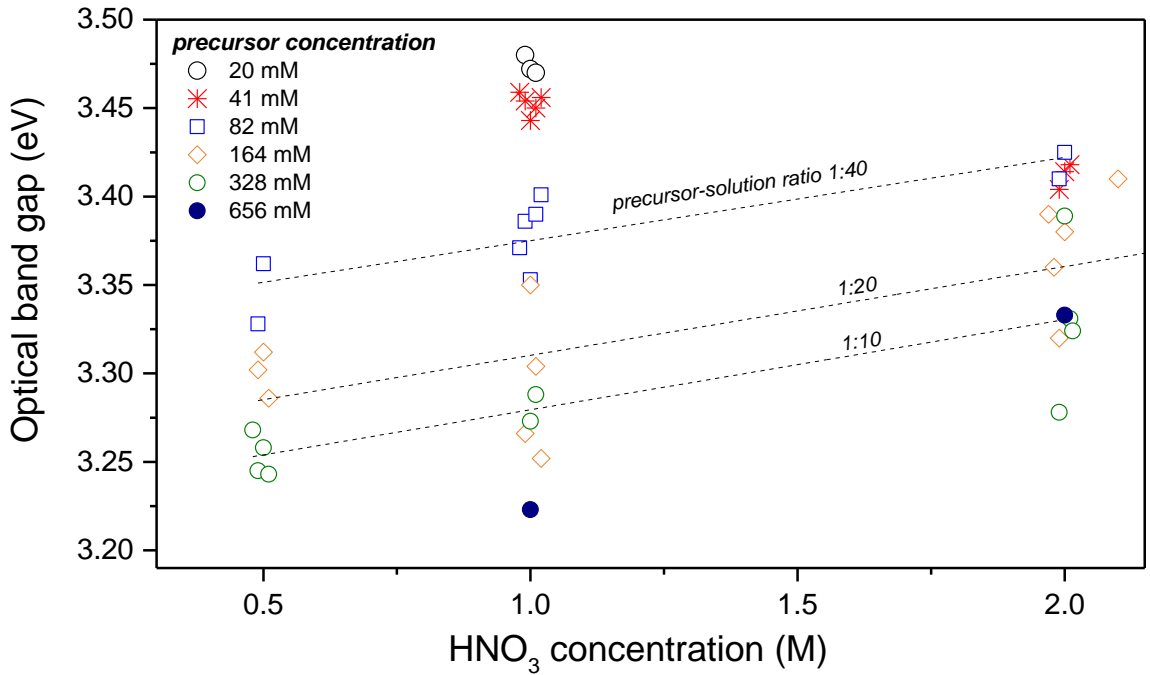


Figure 3.37: Effect of the acid concentration on the optical band gap for the *NE* series. The dotted lines indicate the precursor concentration in volume (1:10, 1:20 and 1:40 indicate 328 mM, 164 mM and 82 mM respectively)

3.5.2.4 Urbach energy

The reflectance spectra of the FMH-TiO₂ samples observed in Figure 3.34 differ from that of commercial anatase for a slightly different shape and the position of the edges. Unlike anatase, the slopes of the spectra for the FMH-TiO₂ are not constant, originating a non-zero absorbance region at energies below the estimated band gap. These spectral features are referred to as Urbach or band tails. The presence of the tails is typical of non-crystalline or partially amorphous semiconductor materials, in which the lack of long-range order modifies the valence and conduction bands, presenting a tail of localised states.^[38] Urbach tails are typical indicator of structural disorder and, for this reason, they are investigated for the characterisation of semiconductor thin films.^[39, 40]

The relationship between the absorption coefficient α and the energy ($h\nu$) is given by the empirical rule defined by Urbach:^[41]

$$\alpha = \alpha_0 \cdot \exp\left(\frac{h\nu}{E_U}\right) \quad (\text{eq. 3.2})$$

Where α_0 is a constant and E_U is the energy of the localised states or Urbach energy. Equation 3.2 can be transformed as follow

$$\ln(\alpha) = \ln(\alpha_0) + \left(\frac{hv}{E_U}\right) \quad (\text{eq. 3.3})$$

Structural disorder and defects are responsible for the formation of localised states at or near the conduction band level. The band tail is directly proportional to the density of localised state. [42]

In the band gap calculations, the Kubelka-Munk function is considered proportional to the absorption coefficient, which allows the substitution of the latter quantity in the Tauc's expression. In the same way, the Kubelka-Munk function could be replaced in *equation 3.3*, giving an estimation of the Urbach energy of the material. [43] The approximation is valid as soon as the scattering factor (S) is equal to the unity or constant. These conditions are generally valid in case of very small particles or sample thickness larger than the other dimensions. [44]

In Figure 3.38, the calculation of the Urbach energy for some representative sample chosen among the four types of FMH-TiO₂ synthesis performed in this thesis. The slope considered for the calculation is indicated in Figure 3.38 by a dashed line. Comparing the values reported in Table 3.7, the sample belonging to the NE series presents higher values (100-140 meV) of Urbach energies, which is expected due to the poor crystallinity of these samples.

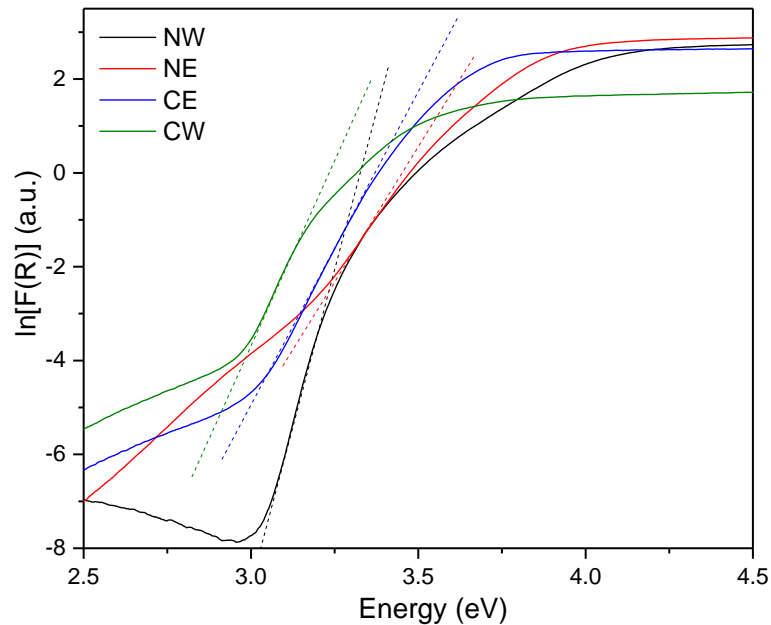


Figure 3.38: (a) Urbach energy calculation for representative FMH-TiO₂ samples for each type of synthesis.

3.5.3 Size determination by optical spectroscopy

3.5.3.1 Raman spectroscopy

The shift of Raman modes towards higher frequency, the asymmetric broadening and the appearance of a high-frequency shoulder are characteristic of the nanoscale reduction of the crystallite size of the material.^[45] This Raman band modification has been associated to different physical effects, such as phonon confinement^[46,47] or the presence of structural defects such as stoichiometric deficiencies.^[48] In the presence of phonon confinement, the selection rule for the Raman active modes (phonon momentum vector equal to 0) is broken, allowing all the phonons present in the Brillouin zone to contribute to the Raman scattering. This phenomenon is referred to as phonon dispersion and could be modelled using a Gaussian confinement function applied to the Raman intensity, described as a superimposition of a weighted Lorentzian function over the entire Brillouin zone (equation 3.4):

$$I(\omega) = \sum_{i=1}^2 \int_{BZ} \frac{\exp\left(-\frac{q^2 L^2}{2\alpha}\right)}{[\omega - \omega_i(q)]^2 + \left(\frac{\Gamma_0}{2}\right)^2} d^3 q \quad (\text{eq. 3.4})$$

where q is the phonon momentum, Γ_0 is the width of the profile line for the bulk material, L is the grain diameter assuming the crystallites to be spherical, ω is the mode frequency and α is the empirical coefficient related to the gaussian confinement function.^[49] From this expression it is possible to evaluate the frequency shift ($\Delta\omega$) and line width (Γ) of the $E_{g,l}$ mode:^[50,51]

$$\Delta\omega(L) = A \left[\frac{a}{L}\right]^\gamma \quad (\text{eq. 3.5})$$

$$\Gamma(L) = \Gamma_0 + B \left[\frac{a}{L}\right]^{\gamma'} \quad (\text{eq. 3.6})$$

where a is the parameter related to the network structure, L is the grain diameter, and all the other parameters relate to the phonon confinement. The origin of these latter parameters is often empirical. The model is not valid for crystallite smaller than 3-4 nm, considered as the critical size for this description of phonon dispersion and shape of the Brillouin zone.^[49] In our calculations, the empirical model proposed by Zhu *et al.* and Xue *et al.* were adopted,^[52, 53] in an

attempt to estimate the particle size from the characteristic of the $E_{g,l}$ mode, as shown in Figure 3.39.

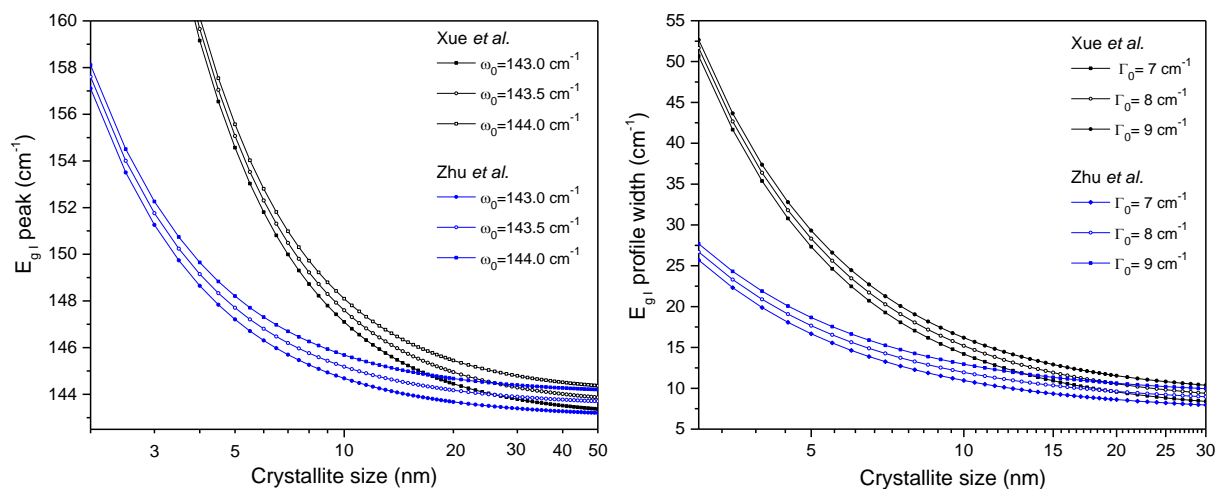


Figure 3.39: Blue-shift and broadening of the $E_{g,l}$ peak in nanocrystalline TiO_2 anatase, calculated according to the model proposed by Xue *et al.* and Zhu *et al.*, modifying the calculation using a different initial peak position (ω_0) and profile line (Γ_0), according to the variation of these values reported in literature. [45, 53]

Despite the discrepancies between the different models, measuring the modification of the $E_{g,l}$ mode profile as an indicator of the particle size was found to be more accurate than the Scherrer equation, based in case of the FMH TiO_2 particles (especially the *NE* series). The measurement of reference materials occasionally gave discrepancies of 1-2 cm^{-1} in comparison with the values reported in literature, in some cases even with the instrument perfectly calibrated. The parameters used in the comparative analysis of samples prepared under different synthesis conditions included the maximum intensity, peak wavenumber and FWHM of the $E_{g,l}$ mode and the relative intensity between the most intense mode and the others. Raman spectra of multiple sampling points (3 or 4) were necessary for the assessment of the inhomogeneity within a given sample. All the spectra were collected considering frequencies close to the Rayleigh scattering, quantifying the physical zero of the spectra to improve the accuracy of the normalisation. Raman spectra are generally collected from ca. 50-100 cm^{-1} and above to avoid the excitation wavelength, corresponding to the very intense Rayleigh scattering peak (a detailed explanation of the phenomenon is given in section 2.5.2). Immediately beyond the Rayleigh scattering, the Raman intensity for TiO_2 anatase is zero: this could be assumed as the real zero of the spectra. A shoulder appears at ca. 30-60 cm^{-1} . The shoulder defines the beginning of the background signal of the Raman spectrum. The low-frequency shoulder is present

also in samples with a high degree of crystallinity, even though its contribution is almost negligible compared to the intensity of the Raman bands. The relative intensity of this shoulder could be used as an important indicator for the determination of the structural disorder and degree of crystallinity. In previous studies, the strong background in Raman spectra of TiO₂ nanoparticles below 2.5 nm has been attributed to the presence of brookite (usually reported in the earliest stages of crystalline grain formation) or amorphous TiO₂.^[54]

3.5.3.2 Band gap

The association of electrons and holes in semiconductors, bound by Coulomb interactions into pair states, is represented as a quasi-particle defined as an exciton.^[55] When the size of the crystalline grains is comparable with the size of the exciton, the exciton undergoes quantum confinement, increasing its absorption energy and hence the band gap. The correlation between the crystallite size and the increase of the band gap has been estimated by Brus using the effective mass model (EMM):^[56]

$$\Delta E_g = \frac{\pi^2 h^2}{2R^2 \mu} - \frac{1.8e^2}{\epsilon R} \quad (\text{eq. 3.7})$$

where ΔE_g is the shift in band gap, R is the radius of nanoparticle, μ is the reduced mass of the exciton and ϵ the dielectric constant of the material. The exciton is represented by the couple of the photogenerated electron and hole, in the conduction and valence band respectively. The reciprocal of the reduced mass is calculated as the reciprocal of the effective mass of the charge carriers. An electron has a very different mass when in a material rather than as a free electron (m_e), due to the atomic interactions in the structure lattice. The same applies to holes.

The calculation of the band gap for the microparticles generally led to higher values compared to crystalline anatase. A blue-shift could confirm the presence of nanocrystalline structure according to the Brus theory. Significant differences in the band gap have been observed with changes in the synthesis parameters related to solution preparation, such as precursor concentration and acid concentration. From our observations, the precursor concentration strongly

affects both the optical properties and crystallite size. The quantum size effect is particularly evident at lower concentration (below 100 mM of alkoxide precursor). In Figure 3.40, the calculation of the effect of the quantum size on the optical band gap according to the Brus equation (equation 3.7) according to different model is reported. The discrepancies between the methods are mainly due to the consideration of the reduced masses of the charge carriers. In most of the cases the exciton radius is calculated only as a function of the effective mass of the electrons, such as in the Grätzel model, where the effect of the valence band is considered negligible.^[61] Another fault in the different models is the estimation of the dielectric constant for anatase, ranging from 31 to 184.^[61] The value has been reported to vary depending on the synthesis method and other factors such as the crystalline anisotropy.^[57] In this thesis, models considering a reduced effective mass of ca. 1-2 times the value of m_e , such as in case of Hoffman, Kasinski and Enright,^[58,61,62] were considered the most accurate. Satoh *et al.* confirmed these findings by applying the Brus equation to a semiempirical model based on TEM, AFM and band gap measurements of TiO₂ nanoparticles.^[59]

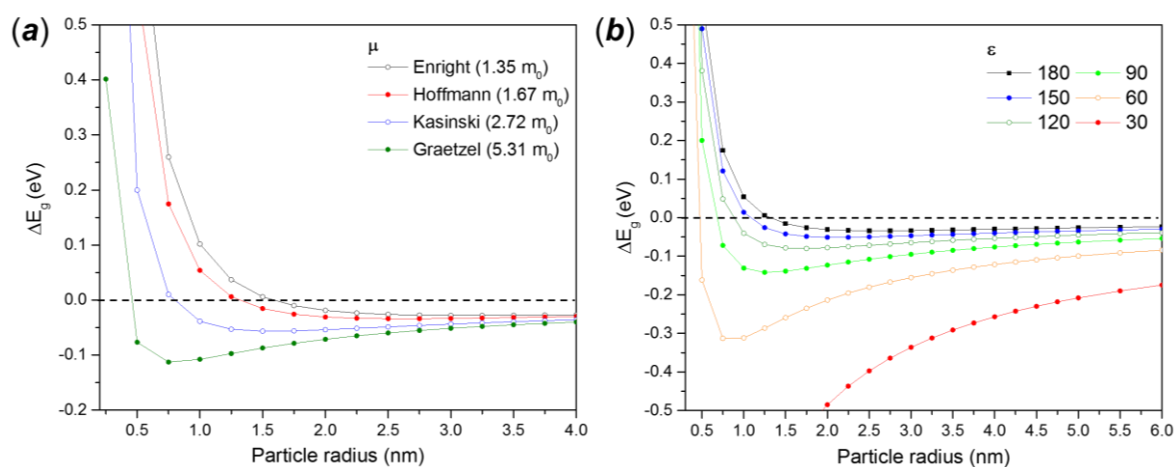


Figure 3.40: Comparison of the different model for the evaluation of the quantum-size effect developing the Brus equation in function of (a) the reduced mass μ and (b) the dielectric constant of the material. ^[60, 61, 62, 63, 69]

Serponi *et al.* concluded by reviewing all the proposed models (some of which are included in Figure 3.40), that the diameter threshold for the quantum-size effect could be narrowed to the range 1-4 nm. For all the blue-shift phenomena seen to occur with larger grain size, they proposed an alternative explanation by attributing the phenomena to the presence of Franck-Condon direct transitions in the indirect band gap semiconductor.^[13] Another cause of band gap blue-shift other than the quantum size effect is the Burstein-Moss effect, due to the

accumulation of localised states in the conduction band which increases the Fermi level and gives the electrons the possibility higher energy transitions. However, this phenomenon has been reported for degenerate semiconductors (such as InSb), in which an excess of doping levels creates a new series of energy states, even though the effect was observed also in ZnO thin films.^[64, 65]

3.5.3.3 Quantum-size effect in nanostructured TiO₂ microparticles

Due to the very broad peaks in the XRD pattern (low crystallite size), it was difficult to deduce the average particle size using the Scherrer equation or to estimate particle size by Raman analysis. For the *NE* series, it is possible to observe how the increase of the acid concentration led to a general blueshift of the band gap (Figure 3.37). According to the Brus equation, the increase of the optical band gap of anatase corresponds to a reduction of the crystallite size below the threshold at which quantum size effect occurs (< 10 nm). These findings are contradicting the trend reported for acid-mediated hydrothermal synthesis, in which the presence of the acid accelerates the crystal growth, with a larger grain size observed for stronger acidic solutions.^[66] An increase in band gap has been reported also by Calleja *et al.* in sol-gel syntheses with hydrolysis ratios below 50. The amorphous microporous samples in this previous study gave a band gap from 3.42-3.48 eV, when was not explained by the authors but which might be attributed to the quantum size effect in the nanoparticles.^[67]

Despite the different approaches reported in literature based on the calculation of the reduced mass or the consideration of the effective Rydberg energy,^[68] the quantum size effect of the band gap has been generally observed below a particle radius of 4 nm. Thapa *et al.* claimed a blue-shift of 0.54 eV for a primary particle radius of 6 nm,^[69] with Satoh *et al.* reporting the same shift for anatase particles with a radius of 1.3 nm.^[114] Due to the difficulties involved in the calculation of the reduced effective mass for the charge carriers, the knowledge of the quantisation threshold is still uncertain.

3.6 Examples of comparative analysis

3.6.1 Effect of treatment time

The effect of the treatment time on the particle characteristics was studied for the *CW* series, using 2 M HCl and a 164 mM precursor concentration. PXD, Raman and optical characterisation data were compared in an attempt to find a correlation between the duration of the MW treatment and the particle properties. Qualitative analysis of the peak broadening in the PXD patterns (Figure A.9 in the Appendix) indicated an increase in particle size. More information on the size of the crystallites was obtained by using the Scherrer expression (*equation 2.8*) and from the blueshift of the $E_{g,l}$ band in the Raman spectra (Figure 3.41).

The data are reported in Table 3.8. According to the calculation from the PXD, the crystallite size is not apparently affected by the treatment time until the first minute of reaction. However, reactions become less controllable if performed for a longer period, variable according to the synthesis conditions. In some cases, reactions have to be terminated because of an increase in autogenous pressure beyond the operational limits of the autoclave. The quality of the final products is affected, by-products are formed and longer cooling times are required.

The crystallite grains calculated by Scherrer increase starting from 90 s. The crystallite growth is also displayed by the position and the width of the $E_{g,l}$ band in the Raman spectra. For the set of experiments reported in Table 3.8, the presence of rutile can be observed after 150 s, identified in both PXD and Raman analysis. This is likely related to the stability inversion between anatase and rutile over certain particle sizes, which fit with the correlation between treatment time and particle growth. For treatments ≤ 90 s, experimental evidence of an effect of irradiation time on particle size is weaker. The Scherrer particle size and information from Raman spectra are probably affected by experimental errors (and perhaps theoretical limitations) due to the very small grain size.

The effect of the progressive increase in crystallite size with irradiation time is also evidenced by the optical band gap (Figure A.10 in the Appendix), progressively shifting from about 3.3 eV towards the values reported for bulk anatase and then after the transition, for rutile.

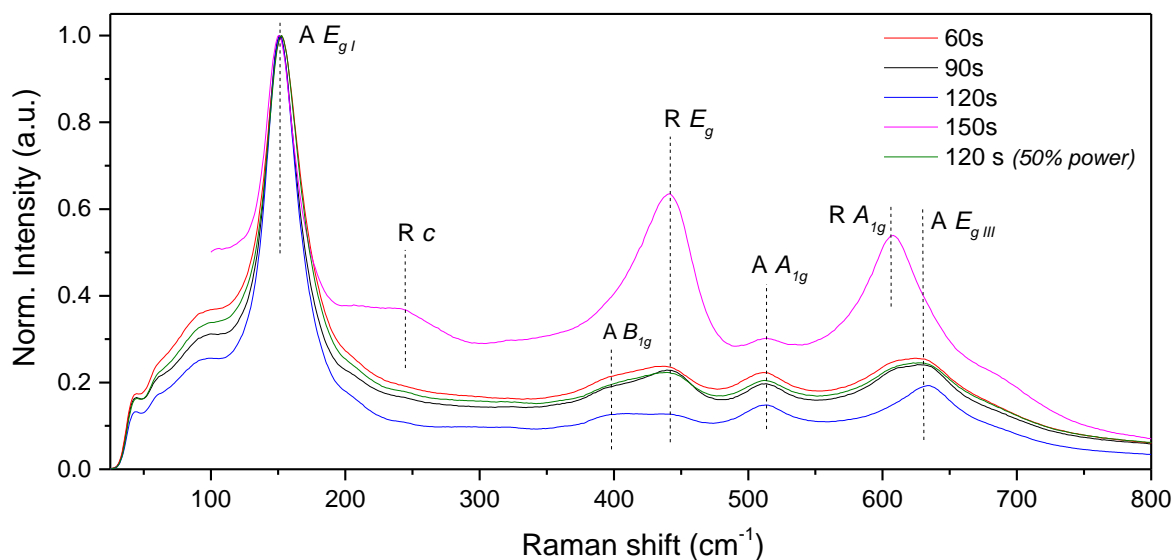


Figure 3.41: Raman spectra for the CW series of FMH-TiO₂ particles (TTIP conc. 164 mM, HCl 2 M solution) as a function of the MW treatment time.

Table 3.8: Effect of the treatment time on selected characteristics of the FMH-TiO₂ particles, CW series (TTIP conc. 164 mM, HCl 2 M solution). (Raman and band gap results obtained from 3 measurement from samples from the same batch; crystallite size estimated by Scherrer equation on single measurements using the same diffractometer conditions; band gap error ≤ 0.01 if not indicated).

Treatment time (s)	Crystallite size (nm)	Band gap (eV)		Raman (cm ⁻¹)	
		<i>ind</i>	<i>dir</i>	<i>E_{g,I} peak</i>	<i>E_{g,I} FWHM</i>
30	6.5	3.29	3.75	153.74 ± 0.27	30.30 ± 0.23
60	6.7	3.22	3.69	151.88 ± 0.17	27.48 ± 0.34
90	6.8	3.19	3.52	149.13 ± 0.37	24.14 ± 0.21
120	9.3	3.09	3.44	146.59 ± 0.13	21.23 ± 0.19
150	13.7	3.08	3.51	144.33 ± 0.16	17.52 ± 0.20

3.6.2 MW pulsed regime

One way to counter the rapid increase of autogenous pressure under constant microwave irradiation is to employ a pulsed regime of microwave irradiation. The autoclave is heated for a set time, cooled and re-heated for the same reaction time interval. The method, also defined as *intermittent microwave heating (IMH)* has been used in solid state synthesis to achieve better control of reaction temperature by tuning the heating and relaxation time.^[70]

The MW pulsed treatment was used to reproduce the same synthesis conditions of the sample NE (2 M acid concentration, 164 mM precursor concentration), applying different number of 1 minute cycles. The autoclave was left to cool down for at least 1 hour between two successive cycles. Three samples were produced applying 1, 2 and 5 cycles. The results of the characterisation analysis of these sample is reported in Table 3.9. Increasing the treatment time by the number of pulse cycles led to an increase of the crystallite size, as evidenced from values calculated by the Scherrer analysis. The intensity and the definition of the peaks in Raman spectra increase as well with the number of cycles, indicating an increase of the crystallinity of the sample. (Figure 3.42 *a*). The structural change is also evidenced by the band gap, with the quantum size related blue-shift progressively reduced, with the band gap moving towards the values reported for crystalline anatase. (Figure 3.42 *c*) Conversely, the number of heating cycles does not affect the size distribution of the secondary particles, as shown in Figure 3.42 *b*.

Table 3.9: Selected characteristics of particles prepared by MW-pulsed treatment (1 min reaction per cycle); Results obtained from 3 measurement from samples from the same batch; band gap error ≤ 0.01 if not indicated.

	1 st cycle	2 nd cycle	5 th cycle
Average particle size ^(a) (nm)	253 \pm 76	229 \pm 57	252 \pm 58
Average crystallite size ^(b) (nm)	4.46	4.57	4.98
Raman E _{g,I} shift (cm ⁻¹)	148.65 \pm 0.06	148.47 \pm 0.21	147.57 \pm 0.20
Raman E _{g,I} FWHM (cm ⁻¹)	24.53 \pm 0.11	23.69 \pm 0.42	23.13 \pm 0.11
BET surface area (m ² /g)	490.0 \pm 24.3	364.2 \pm 33.9	283.3 \pm 34.3
Average pore size ^(c) (Å)	18.52 \pm 1.97	22.01 \pm 1.81	18.50 \pm 3.48
Average pore volume ^(c) (cm ³ /g)	0.44 \pm 0.03	0.51 \pm 0.02	0.23 \pm 0.04
Optical band gap (ind, eV)	3.44	3.26	3.20
Optical band gap (dir, eV)	3.79	3.68	3.58
Urbach energy (meV)	125 \pm 4	105 \pm 5	106 \pm 12

^(a) calculated from SEM images

^(b) calculated by Scherrer equation (XRD data), single measurement using same diffractometer conditions

^(c) calculated using the BJH method on desorption isotherms

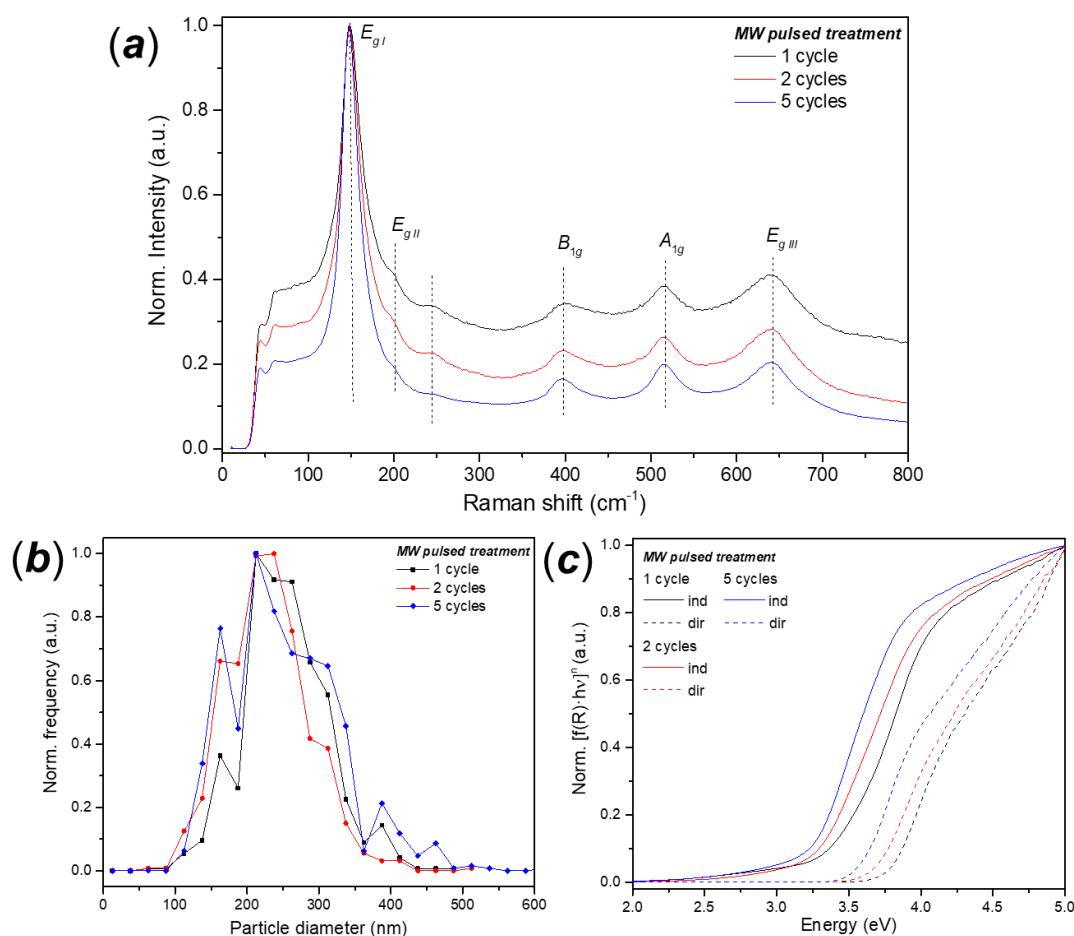


Figure 3.42: (a) Raman spectra, (b) SEM particle size distribution and (c) band gap analysis of samples prepared by pulsed MW synthesis using 1 min cycle (1, 2 and 5 cycles are shown respectively).

As the crystallinity of the sample increase, the number of cycles affect also the surface area, which is reduced by *ca.* 40% from the 1st to the 5th cycle. However, the pore size distribution and the pore volume are almost unchanged. A possible mechanism of pore structural reorganisation might involve a progressive reduction of the intergranular porosity, with the pore preserving their volume since the densification process does not involve the entire volume of the particles, but it is progressively extending to the rest of the particle cycle after cycle.

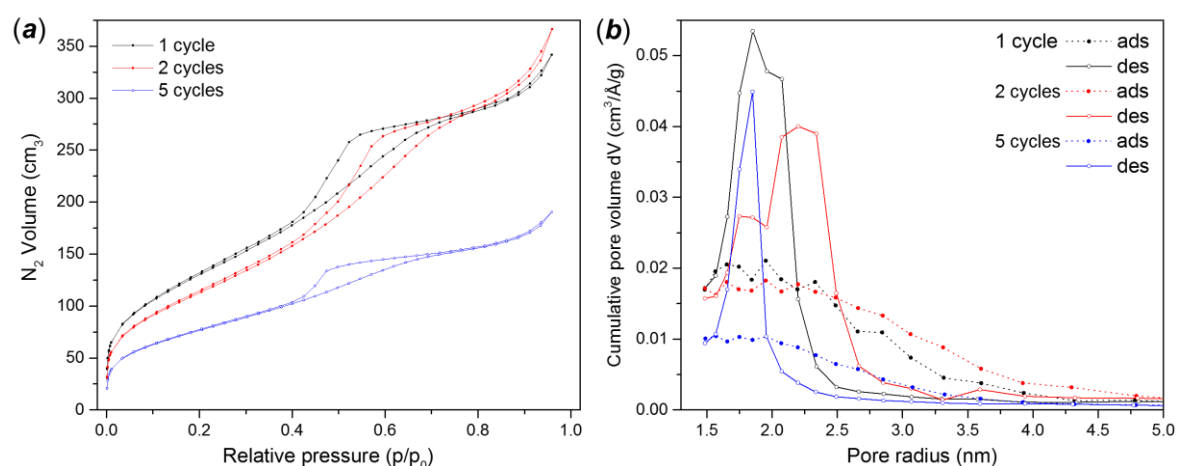


Figure 3.43: (a) N₂ adsorption/desorption isotherms for the MW-pulsed FMH-TiO₂ samples and (b) pore size distribution using BJH calculation for the adsorption and desorption branches of the isotherms.

Pulsed MW treatment is a way to increase the duration of the MW treatment without exceeding the pressure of the autoclave. Hanlon *et al.* adopted this procedure for the synthesis of Mg(OH)₂ nanoplates using 1 min intervals up to a total time of 6 min.^[71] Etacheri *et al.* adopted the same method to create C-doped nanoparticles with mixed crystalline phases composed of anatase and brookite from TTIP in water in an open system under MW irradiation for 10 min intervals. The fraction of brookite was enhanced with the number of intervals, with the particles showing remarkable photocatalytic and antibacterial properties without the necessity of post-synthesis treatments.^[72]

3.6.3 Influence of the solvent

The formation of microparticles was observed only using ethanol as a solvent. Hydrothermal synthesis led to the formation of irregular micrometric fragments with irregular surface. The presence of partially formed spherical particles incorporated into the fragments is frequently observable (Figure 3.44 *a* and *b*), such as synthesising the particles by using an HCl solution in water (*CW* series), with secondary aggregation phenomena occurring and formation of bulky fragments rather than particles with a defined morphology and/or shape. On the other hand, hydrothermal synthesis mediated by HNO₃ (*NW* series) led to the formation of very small granules, agglomerating to form larger irregular but distinct particles (Figure 3.44 *c* and *d*). HR-SEM showed the size of the single granules to vary between 50-80 nm.

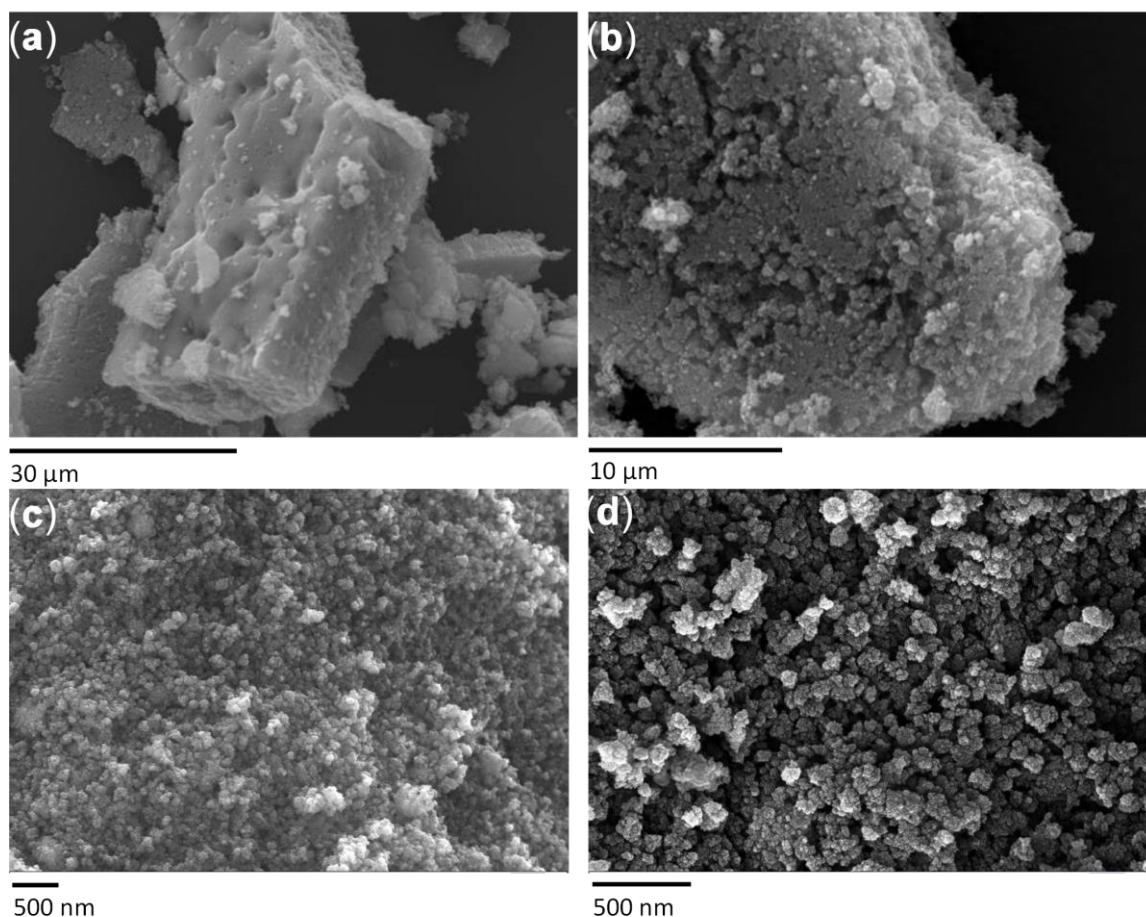


Figure 3.44: Examples of particles and agglomerates from (*a*, *b*) the *CW* series (2 M HCl, 162 mM precursor, 90 s MW treatment) and (*c*, *d*) the *NW* series (1 M HNO₃, 162 mM precursor, 90 s MW treatment).

Different hydrolysis ratios (water:ethanol) were also investigated. The sample analysed and the relative data are reported in Table 3.10. The secondary spherical particles became progressively smaller as the hydrolysis ratio increases. In term of crystalline structure, the presence of water enhances the crystallinity, with more defined and less broaden peak observed in the PXD patterns (Figure 3.45). Further investigation aimed to understand the role of the water content in the final morphology of the microparticles. The general effect observed analysing different relative amount of water evidenced a reduction of the secondary particle diameter until complete disappearance of a definite shape. Despite the larger crystallite size, the primary particles aggregate irregularly, forming bulky fragments when the relative concentration of water is over 60% (Figure 3.46). The increase in water content increases the crystallinity and hence reduces the surface area, with the particles progressively losing their typical mesoporosity. The N_2 adsorption/desorption isotherms showed in Figure 3.47 indicates a transition from a type IV to a type I, with the mesopores progressively reduced to micropores (Figure 3.47 b).

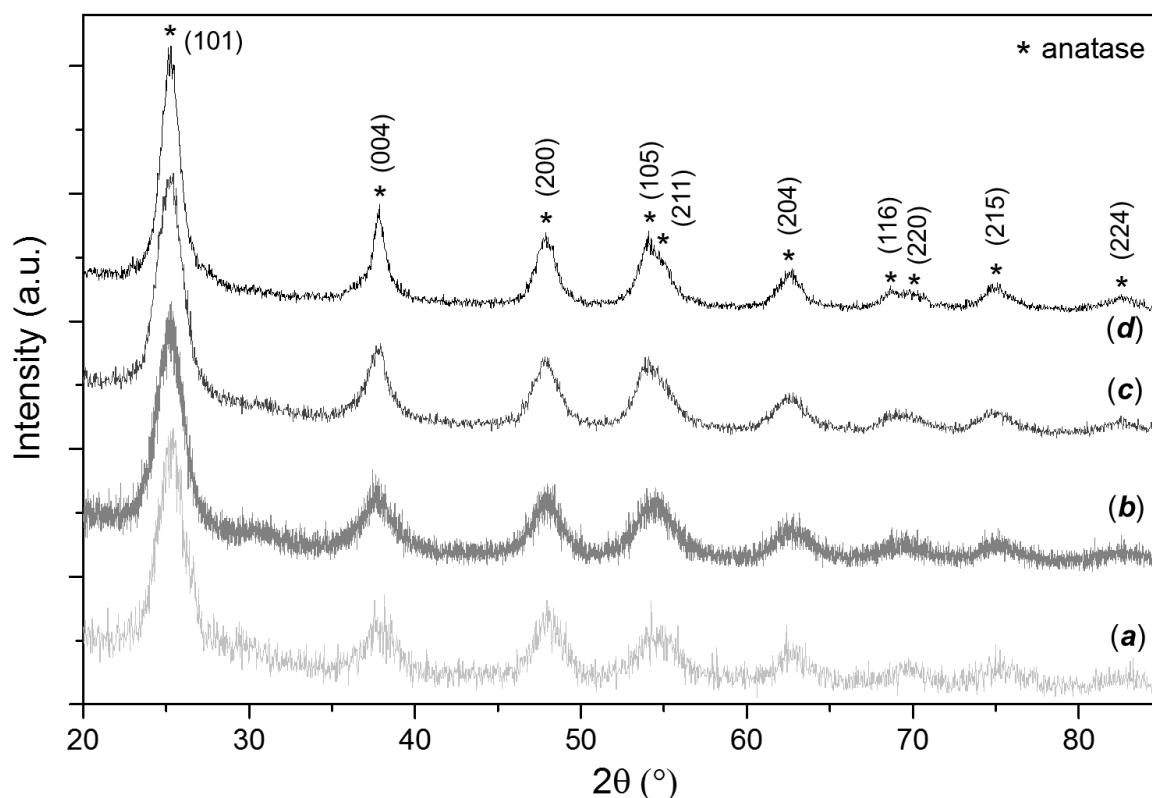


Figure 3.45: PXD patterns for samples produced with pure ethanol (*NE* series), pure water (*NW* series) and at various water:ethanol ratios: (a) pure ethanol; (b) 1:3; (c) 1:1; (d) pure water.

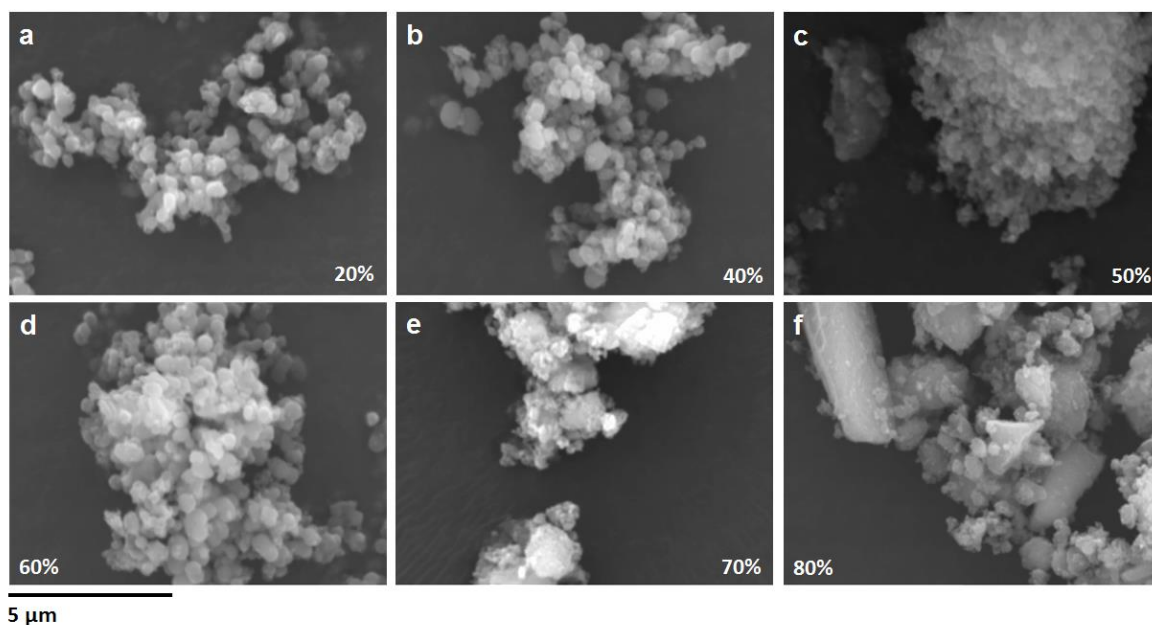


Figure 3.46: SEM images of TiO₂ particles synthesised using different hydrolysis ratios (the relative concentration of water in ethanol is indicated in the images: (a) 20%; (b) 40%; (c) 50%; (d) 60%; (e) 70%; (f) 80%.

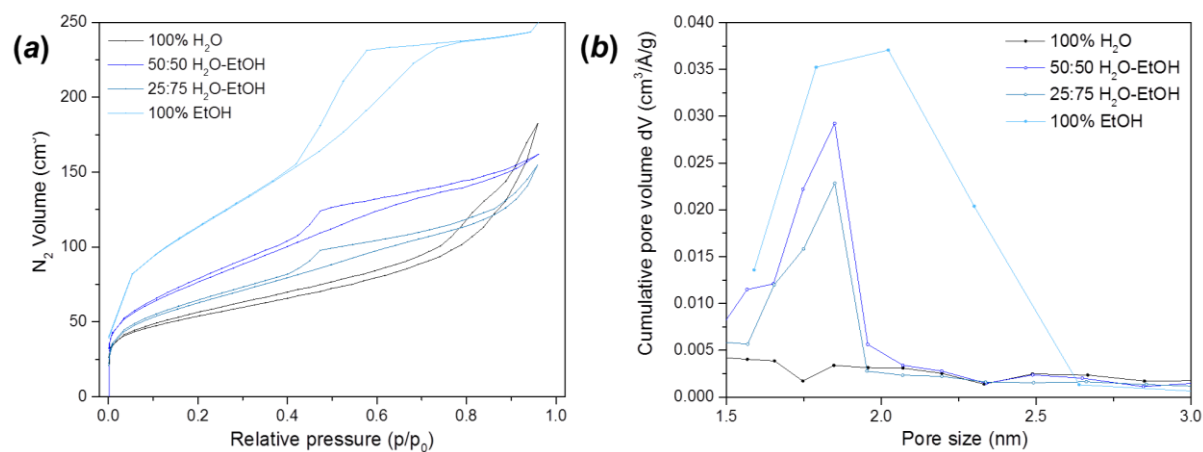


Figure 3.47: (a) N₂ adsorption-desorption isotherms and (b) BJH pore size distribution analysis for different samples of ethanol-water ratios in the HNO₃-mediated synthesis

Table 3.10: Selected characteristics for particles produced using different ratios of ethanol and water (HNO₃-mediated synthesis); results obtained from 3 measurement from samples from the same batch; band gap error ≤ 0.01 if not indicated.

Water:Ethanol	Water	1:1	1:3	Ethanol
Hydrolysis ratio	318	165	73	18
Average particle size (nm) ^(a)	6.0	4.5	4.3	3.6
Raman E _{g,l} shift (cm ⁻¹)	150.16 ± 0.13	152.25 ± 0.10	151.20 ± 0.34	149.25 ± 1.00
Raman E _{g,l} FWHM (cm ⁻¹)	26.74 ± 0.32	28.79 ± 0.15	26.40 ± 0.06	24.56 ± 0.26
BET surface area (m ² /g)	196.8 ± 5.8	279.9 ± 18.7	221.3 ± 4.8	414.3 ± 16.5
Avg. pore volume (cm ³ /g)	0.60 ± 0.07	0.16 ± 0.04	0.17 ± 0.08	0.31 ± 0.07
Avg. pore size (Å)	14.86 ± 1.54	18.50 ± 2.01	18.50 ± 3.19	20.23 ± 2.84
Indirect Optical band gap (eV)	3.27	3.29 (± 0.11)	3.26 (± 0.08)	3.39
Direct Optical band gap (eV)	3.50	3.69 (± 0.13)	3.72 (± 0.06)	3.75
Urbach energy (meV)	64 ± 17	83 ± 8	101 ± 12	120 ± 10

^(a) calculated by Scherrer equation (XRD data), single measurement using same diffractometer conditions

3.7 Surface analysis, composition and impurities

3.7.1 XPS analysis

XPS analysis was performed with the *NE* series clarifying the nature of any impurities. For Ti the classic 2p_{1/2} (458 eV) and 2p_{3/2} (465 eV) peaks characteristics of Ti⁴⁺ species such as Ti-O and Ti-O-Ti are present (Figure 3.48). Another small peak at lower binding energy (around 456.2 eV) can also be observed, which can be attributed to non-stoichiometric defects such as the formation of Ti³⁺, generally reported at lower binding energy compared to Ti⁴⁺ (typically 457.7 eV).^[73] A very broad signal at 529.5 eV is compatible with the O 1s binding energy for O²⁻ in TiO₂ (528.5-529.7 eV).^[74] The broadening was attributed to the convolution of two secondary peaks at 527.5 and 532 eV. The O 1s peak located at ca. 533 eV is assigned to the binding energy of absorbed oxygen (hydroxyl) on the TiO₂ surface (530.54-533.77 eV).^[75] The results of the peak intensity integration and the calculation of the composition of the analysed sample are reported in Table 3.11.

Table 3.11: XPS integrated signal for the selected *NE* series sample using Casa® software.

	Position	FWMH	Area	At %
Ti 2p _{3/2}	460.45	2.834	16688.12	15.15
O 1s	531.45	3.490	19708.16	47.70
C 1s	286.45	3.291	5239.50	37.15

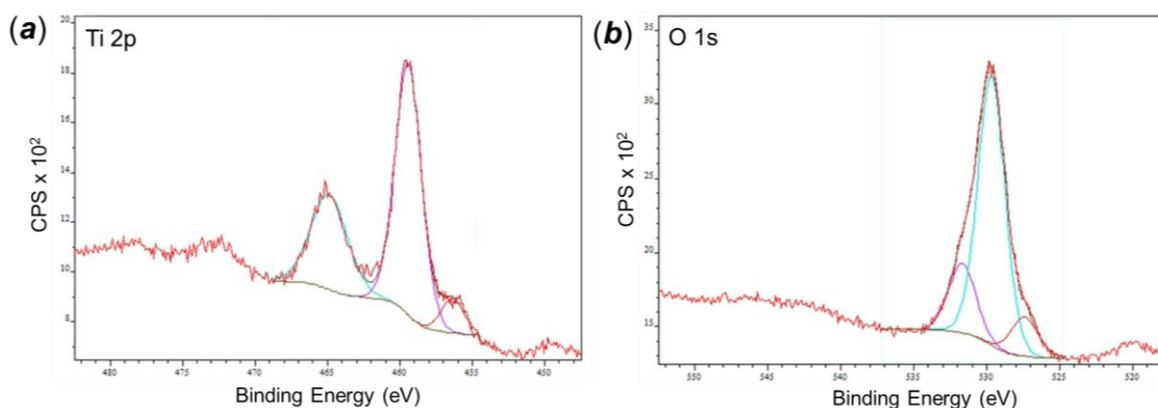


Figure 3.48: XPS of the selected *NE* series sample (2 M HNO₃, 162 mM TTIP, 1 min MW treatment), showing the peak fitting for (a) the Ti_{2p} and (b) O_{1s} signals.

Unfortunately, the sample was prepared in a way similar to the SEM analysis, dispersing the fine powder on a carbon sticker, which contributes to the C 1s signal. In order to exclude the signal from the carbon tape, the C 1s peak was compared with the same obtained for P25 treated with ammonolysis (see section 4.5), which in principle should not contain any relevant amount of carbon. The “carbon-free” sample presents a central peak at 284.8 eV, with the possible contribution of weaker signal at around 286.3 eV, contributing to broaden asymmetrically the main peak. The untreated TiO₂ particles present the main peak in the same position of the N-doped P25, with two smaller distinct peaks at the sides, located at 288.5 and 281.8 eV.

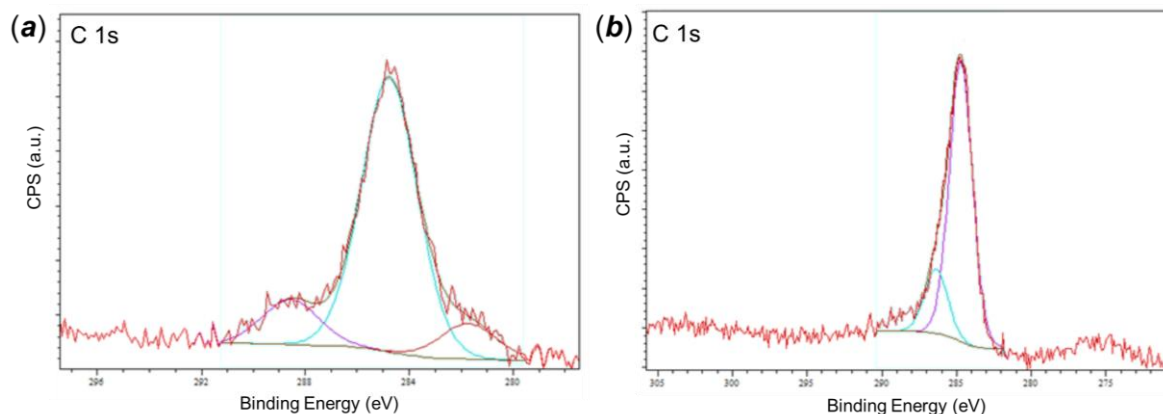


Figure 3.49: XPS peak fitting for the C 1s signals of (a) NE series FMH-TiO₂ submicroparticles and (b) Aeroxide P25.

The peak at *ca.* 285 eV can be attributed to graphitic-like C-C, C=C and C-H bonds and can be generally attributed to adventitious carbon, in this case the presence of the carbon tab, common to the two samples.^[72] The peak at 288.5 might be attributed to oxidised carbon (e.g. C=O bonds, typically at 289 eV) or to C-O (appearing at lower energies, at *ca.* 287.5 eV). The formation of surface carbonate species, reported at 286.1 and 288.4 eV in sucrose-modified TiO₂ material cannot be ruled out.^[76]

The signal at 281.7 eV compares well with the C 1s peak for a Ti-C bond.^{[77],[78]} This suggests the possible substitution of oxygen by carbon in the TiO₂ lattice. However, the signal is not compatible with the peaks reported for Ti 2p. The binding energy for a Ti-C bond is reported to be 454.7 eV,^[77, 79] whereas Ti-N gives a signal at 456.3 eV,^[80] (more compatible with our findings). Despite these results, the analysis of nitrogen (N 1s, expected at 397 eV) did not produce any relevant signals. However, the XPS spectra of N-doped samples (extensively described in chapter 4) did not show either of these peaks in the N 1s region.

3.7.2 Thermal analysis

Thermogravimetric analysis (TG) revealed typical mass losses of *ca.* 10-17% for the TiO₂ materials (Figure 3.50). Around 70% of this lost mass is released within the first 200 K of the heating program (generally 5 K/min, maximum temperature between 973-1473 K, analysis under constant argon flow). The amount of mass loss was not specifically attributed to the synthesis conditions of the sample. The investigation about the nature of the released material proceeded with combustion microanalysis of selected FMH-TiO₂ microparticle samples. Results of

selected set of experiments are reported in Table 3.12. Combustion microanalysis revealed the presence of consistent concentrations of C and H, with negligible traces of N. Except for one isolated sample, the concentration of nitrogen traces is relatively high (more than 1%) for the particles produced in presence of very acid solutions (2 M) of HNO₃. The FMH-TiO₂ samples produced using HCl showed less organic impurities and negligible presence of nitrogen compared to those synthesised in presence of HNO₃.

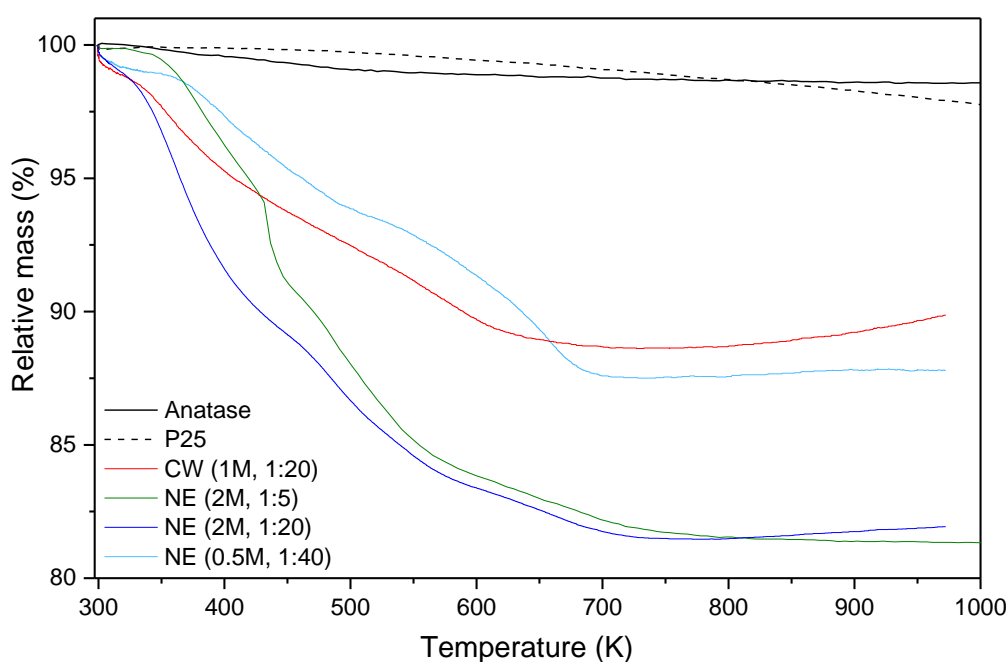


Figure 3.50: Thermogravimetric(TG) analysis of selected TiO₂ samples produced under different synthetic conditions.

Table 3.12: CHN combustion microanalysis results for some representative FMH-TiO₂ samples (results obtained from double measurement on the same batch)

Elements (wt%)	C	H	N
Samples			
NE (2 M, 648 mM)	2.32 ± 0.09	0.96 ± 0.04	1.32 ± 0.12
NE (2 M, 162 mM)	3.09 ± 0.14	1.20 ± 0.05	0.78 ± 0.06
NE (1 M, 80 mM)	2.11 ± 0.00	1.43 ± 0.07	0.17 ± 0.00
NE (0.5 M, 80 mM)	3.37 ± 0.06	2.28 ± 0.15	1.07 ± 0.07
NE (1 M, 40 mM)	1.94 ± 0.07	2.09 ± 0.07	0.17 ± 0.00
NW (2 M, 162 mM)	1.25 ± 0.08	1.05 ± 0.11	0.84 ± 0.03
NW (2 M, 80 mM)	2.32 ± 0.11	1.47 ± 0.00	0.13 ± 0.00
CE (1 M, 324 mM)	0.33 ± 0.00	1.43 ± 0.06	0.02 ± 0.00
CW (2 M, 162 mM)	0.43 ± 0.04	1.68 ± 0.12	0.03 ± 0.00

Differential Thermal analysis (DTA) showed one clear thermal event for all samples (Figure 3.51); an endothermic peak occurring between 325-340 K, depending on the sample, which can be associated with the desorption of water molecules adsorbed on the surface. This feature was previously reported in sol-gel synthesised TiO₂ within the same temperature range, followed by an exothermic peak corresponding to the release and decomposition of organic species within the range 473-623 K.^[81] In some of the samples this peak is evident, whereas in other is not detected (more details are provided in Figure A.12 and A.13 in the Appendix).

Finally, further information regarding the precise nature of sample impurities are provided by the evolved gas analysis (mass spectrometry), performed simultaneously with the TG-DTA and reported in Figure 3.52; according to the previous results, all the possible low molecular weight molecules containing N, C, H and O were analysed. Due to the limited selection of low molecular weight compounds, the weights of the molecular fragments analysed overlap (Table A.4 in the Appendix). Despite the broad peak observed in the IR analysis, the precise amount of water was not detectable through mass spectrometry. The water signal in the mass spectrum is probably masked by the higher signal from the carrier gas (argon, 10⁻⁶ Pa), especially if compared with the other impurities (Figure A.11 in the Appendix), which are two or three orders of magnitude less intense.

As shown in Figure 3.52, some of the samples synthesised using HNO₃ gave clear evidence of the release of compounds which MS signals are compatible with the release of nitrous oxide (N₂O, MW ~44 g/mol) and nitric oxide (NO, MW ~30 g/mol), whereas analysis excluded the presence of nitrogen dioxide (MW ~30 g/mol), since its complementary mass signal at 46 g/mol was absent. On the other hand, it is difficult to discriminate between carbon dioxide (MW ~44 g/mol) and nitrous oxide because these molecules present collateral fragments having the same molecular weight.

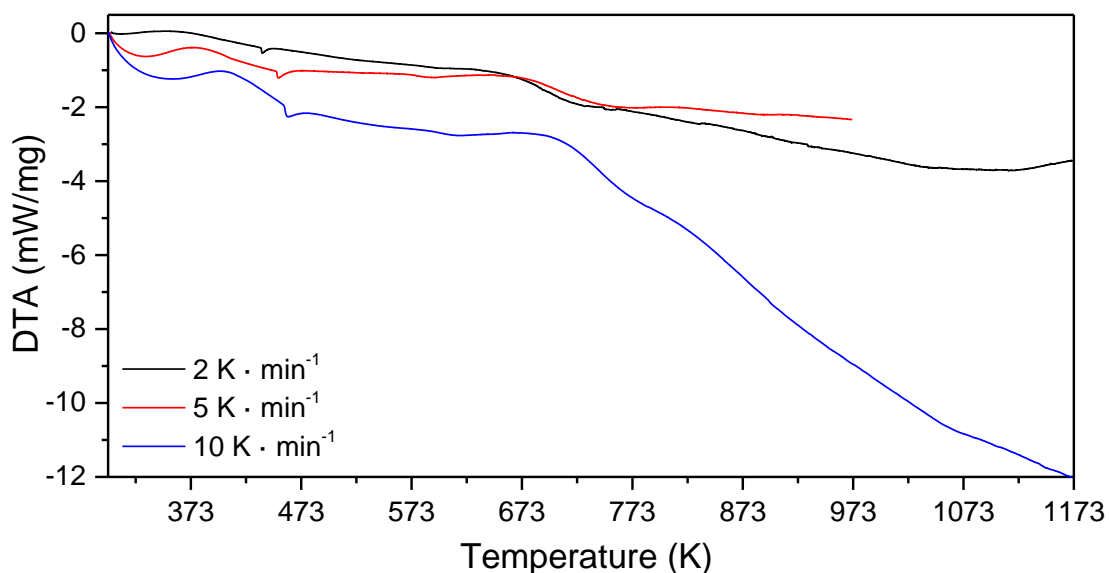


Figure 3.51: Differential thermal analysis (DTA) of a representative FMH-TiO₂ sample (NE series, 2 M, 324 mM) using different heating ramps.

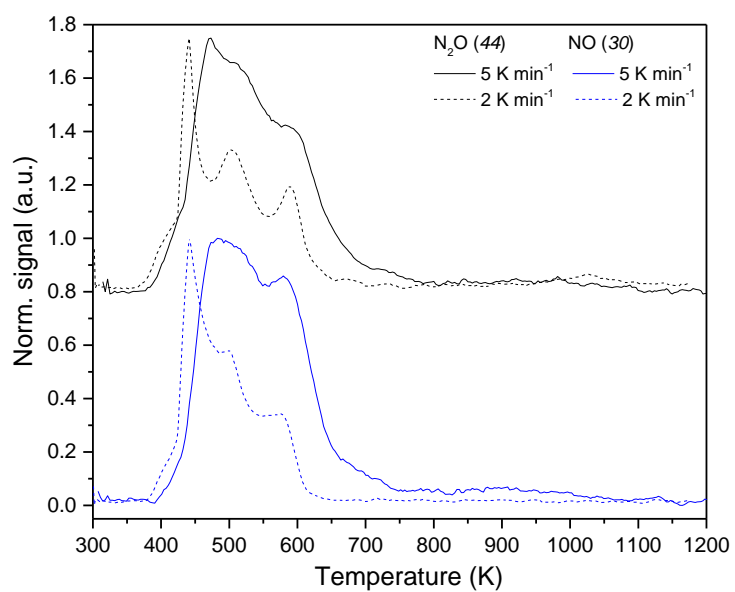


Figure 3.52: Evolved gas MS analysis of the signal presumably associated to N₂O (MW: 44) and NO (MW: 30) for the FMH-TiO₂ sample (NE series, 2 M, 324 mM)

3.7.3 FT-IR and Raman analysis of the impurities

The IR analysis of the particle surface revealed *in primis* the presence of hydroxylated surfaces in all the syntheses; hydroxyl groups are likely due to the presence of adsorbate water or exposed hydroxylated moieties from the Ti-O network. The broad signal between 3600-3200 cm^{-1} and the peak at 1640-1623 cm^{-1} (Figure 3.53) are indicative of O-H stretching and bending of water, respectively.^[82, 83]

The Ti-OH bending mode for bulk anatase has been also reported at 1605 cm^{-1} .^[84] An increase in dimers can further shift the signal, implying a large amount of water molecules adsorbed on the surface. Bezrodna *et al.* also reported the presence of $\delta(\text{Ti-OH})$ at 1222, 1137 and 1048 cm^{-1} , with the latter two bands representing strong H-bonding with water molecules.^[85] These two bands are perhaps observable for the FMH-TiO₂ particles (Figure 3.53), even though the attribution of the vibration band in this spectral region is made difficult by the presence of multiple signal not associated to TiO₂.

Regardless of the solvent used, the influence of the type of acid is evident (Figure 3.53). Syntheses mediated by HCl result in a sample “free” from impurities compared with those produced using HNO₃. However, in the HCl samples, the $\nu(\text{O-H})$ band is slightly shifted, lying at higher frequency (*ca.* 3100 cm^{-1}), with no shift in the $\delta(\text{O-H})$ band. A broad -OH stretching is usually associated with hydroxyl groups in carboxylic acid, with a strong signal in the range 3400-2500 cm^{-1} .

Conversely, the -OH stretching shift for the particles synthesised in the presence of HNO₃ is not as strong as in the sample of **CE/CW** series, but the group of signals between 1600-1000 cm^{-1} is a clear sign of the presence of impurities. The amount and type of impurities changes from sample to sample depending on the synthesis conditions.

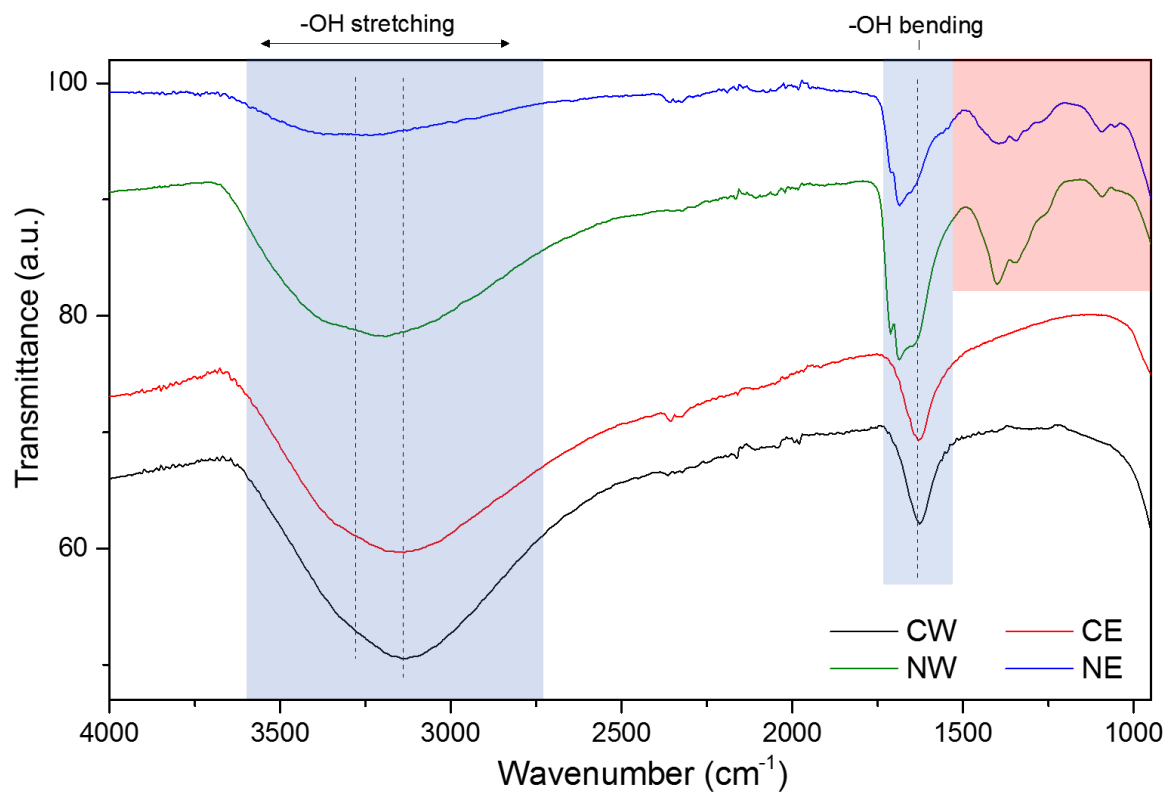


Figure 3.53: IR spectra of typical samples from each series. The spectra are displaced on the intensity scale for better visualisation. The IR vibrations typical of the hydroxyl groups are marked in blue, the spectral region in which the signals not related to TiO_2 occur are marked in red.

3.7.3.1 Identification of the impurities

In the samples in this work, thermal treatments progressively reduced both organic moieties and hydroxyl groups present on the surface of TiO₂ particles. Traces of functional groups are still present after a thermal treatment of 3 h at 573 K, almost completely absent at 773 K and not visible at 873 K (Figure 3.54).

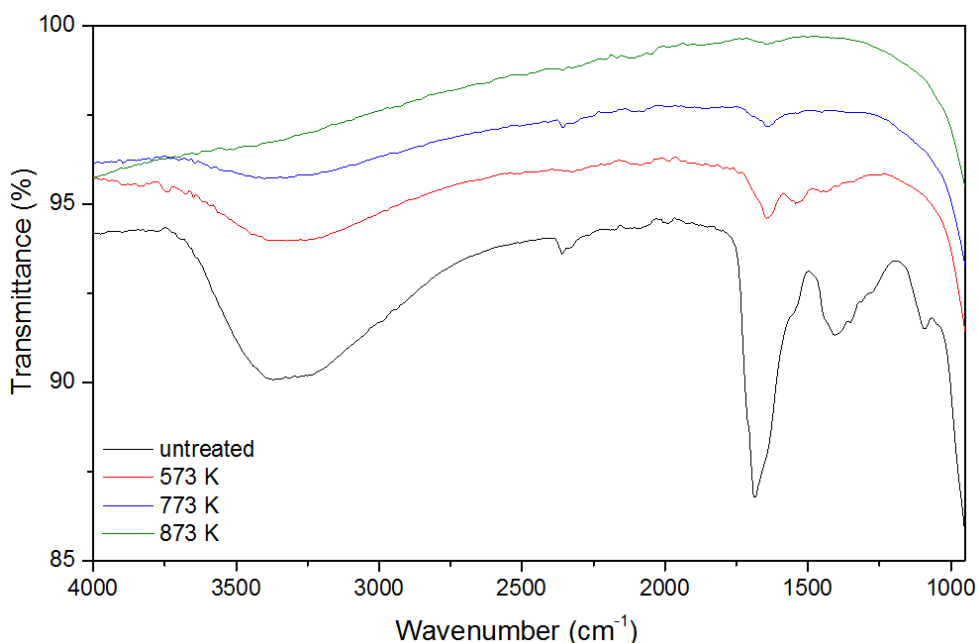


Figure 3.54: IR spectra of MW-synthesised particles (1:20 TTIP, HNO₃ 2 M, 1min) before and after thermal treatment under oxidizing atmosphere at different temperatures.

Considering Figure 3.55, the bands in the fingerprint region are difficult to identify because of the weak signal intensity. In order to investigate the possible origin of these signal, the IR spectra were compared with similar acid-mediated hydrothermal synthesis from the literature. One of the possible source of impurities could be the precursor. However, signals related with the precursor molecule were not observed, since none of the signals reported in literature (stretching, scissoring and bending modes of C-H observed at 2920, 1463 and 1005 cm⁻¹, respectively) [86] apart from the Ti-O bonds at 630 cm⁻¹, are present. Presence of residual acid molecules might be the origin of the bands in the region 1600-1700 cm⁻¹. Gaseous HNO₃ has been reported to have strong IR absorption at 1711 cm⁻¹, however the band shifts to 1677 cm⁻¹ when adsorbed to a surface, [87] which could be compatible with the IR band (b), which is very strong when it occurs. Moreover, absorption bands at 3400 and 1420 cm⁻¹ can be associated with stretching and bending of the N-H bond. This could explain the shift in the O-H

stretching region and the nature of the peak (**d**), more evident in the samples produced with higher concentration of HNO₃. Bands occurring at ca. 1440-1450 cm⁻¹ can be attributed to the presence of nitrates and ammonium groups. [88] By-products and impurities related to HNO₃ can also be observed, such as non-coordinated NO₂⁻ (reported at 1260 cm⁻¹), and NO₃⁻ (1350 cm⁻¹), which can be associated with the bands (**g**) and (**f**), respectively. [89]

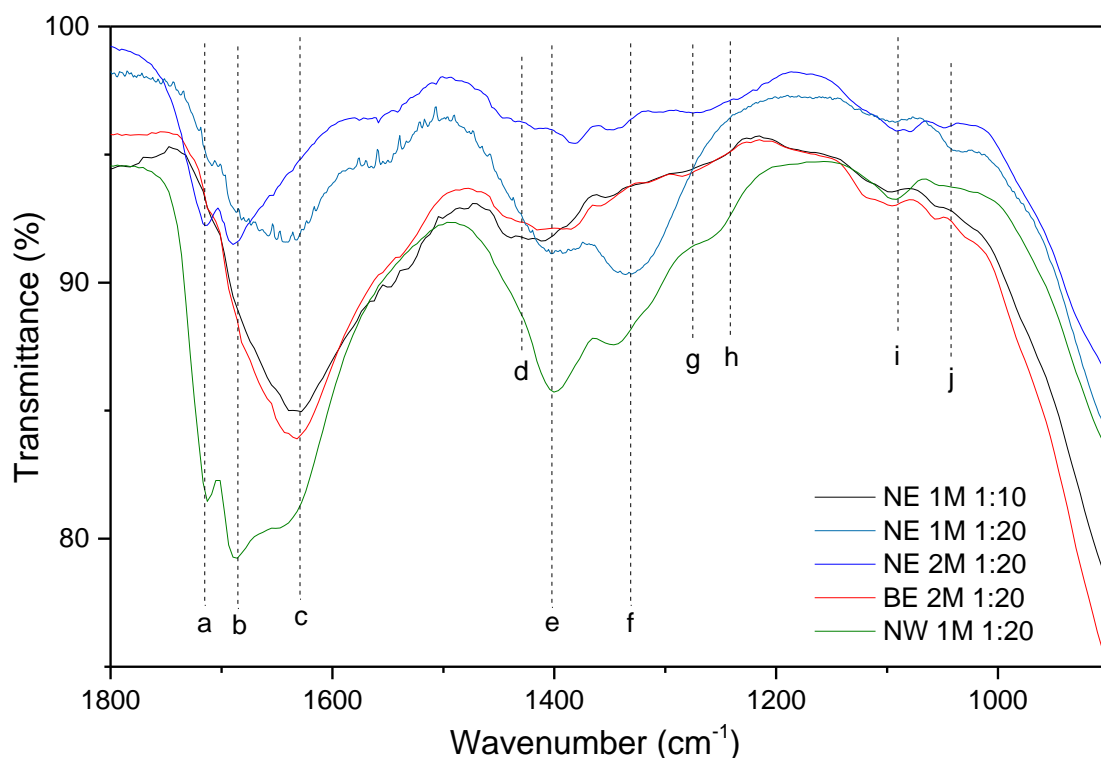


Figure 3.55: IR spectra of different FMH-TiO₂ particles belonging to the NE, NW and BE series, (where BE uses titanium tetrabutoxide instead of TTIP), in the spectral region 1800-900 cm⁻¹. The most relevant IR modes are marked with dashed lines and labelled.

The band at 1715 cm⁻¹ (**a**) is characteristic for the stretching of C=O in a free carboxylic acid group as observed by Urlaub *et al.* in a TiO₂ sol-gel coating using a complexed form of Ti isopropoxide as precursor. [90] Vasconcelos *et al.* attributed the bands at 1638 cm⁻¹ and 1445 cm⁻¹ ((**c**) and (**d**) respectively) to the asymmetric and symmetric stretching vibrations of the COO group, forming a bidentate bridging coordination complex with Ti atoms, [91] although the same combination of COO vibrations is reported occurring at 1536 and 1435 cm⁻¹. They attributed the band at 1080 cm⁻¹ (corresponding to our band (**i**)) to the bridging vibrations of Ti-O-C, which were reported as isopropoxy groups by Urlaub *et al.* Strong bands between 1680-1780 cm⁻¹ are usually associated with the stretching of carbonyl

groups (C=O).^[92] The band at 1047 cm⁻¹ has been reported for the C-N stretching vibrations of aliphatic amines, which could be associated to the weak band (j).^[93]

Table 3.13: List of the IR bands observed for the FMH-TiO₂ particles, with their assignment (signal wavenumbers in cm⁻¹ indicated in brackets).

Band	Wavenumber (cm ⁻¹)	Ti, O related bands	C-impurities	N-impurities
(a)	1715		C=O stretching ^[90] COO monodentate stretching (1720)	
(b)	1685		COO asymmetric stretching (1685)	HNO ₃ (1690) ^[87]
(c)	1632	-OH bending ^[90]		
(d)	1435			Nitrites, NH ₄ ⁺ ^[88]
(e)	1405		CH ₂ bending (1400)/ CO vibration (COH, 1414) ^[90]	
(f)	1345-1335		CH ₃ , δ(CH ₂ CH ₃) ^[89]	NO ₃ ⁻
(g)	1275		COO symmetric stretching (1276), δ (CO)	NO ₂ ⁻ ^[89]
(h)	1242		CO from alcohol or carbonile (1246)	
(i)	1090		Ti-O-C bending ^[90] (1080)	
(j)	1040	Ti-OH (1048)	C-N aliphatic amines (1047) ^[85]	

The presence of impurities in the *NE* series samples was noted also by Raman analysis of the low frequency peaks, especially in the region between 1000-1500 cm⁻¹ (Figure 3.56). Carbonate ions bands at 1064 and 1415 cm⁻¹ have been reported in the case of carbon-doped TiO₂ heterojunctions.^[94]

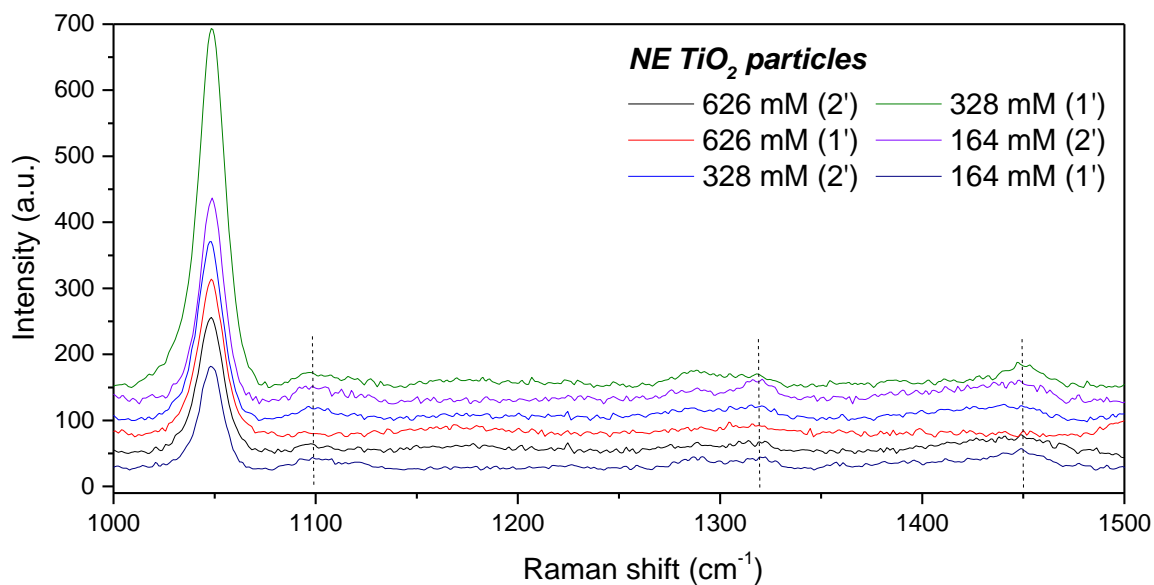


Figure 3.56: Raman spectra of some samples from the NE series in the lower frequency region in which N and C-based impurities generally occur.

3.8 Discussion

3.8.1 Hydrothermal conditions under microwave heating

The main drawback of the flash MW-assisted synthesis is the lack of available information concerning the actual conditions inside the autoclave during the reactions. The issue is mainly due to practical and technological limitations, partially overcome for conventional hydrothermal synthesis by using autoclaves provided with pressure gauges and thermocouples. For MW-assisted reactions, the most recent generation of MW reactor employs glass vessels, with temperature reading performed by an IR sensor and pressure measurement carried out with piezoelectric devices on elastic and deformable lids. One of these new classes of reactor, an integrated single-mode MW-cavity (CEM Discovery®), was used to analyse the internal condition of the MW-transparent digestion bomb used for the TiO₂ particle synthesis. The MW-cavity was used to simulate similar synthesis conditions performed in the multimode DMO, despite the evident difference between the two reactors and the lower pressure limit achievable by the single-mode cavity (around 17 bars versus the maximum 80 bars of the digestion bomb).

3.8.2 Theoretical calculations

Reactions in a sealed vessel are known for the generation of autogenous pressure. The temperature increase from a constant heating process generates a corresponding increase in pressure. The volume of heated water increases establishing a continuous equilibrium between the vapour and the liquid phase. At the same time the increase of pressure increases the boiling point of the liquid phase, allowing higher temperature to be used in the liquid phase compared to non-pressurised reactions in open systems. This situation exists below the critical temperature, above which water exists under supercritical conditions.

Analysis of the conditions inside a sealed vessel has been performed in terms of the change of pressure and volume as a function of temperature. The first rigorous experimental analysis describing the relationship between these three parameters in hydrothermal conditions was performed by Kennedy in 1950. [95] The pressure-temperature diagram for pure water, later elaborated by Rabenau and reported in Figure 3.57 *a*, describes the effect of the volume of liquid filling the autoclave. When the autoclave is filled below 32% of its volume, water will vaporise before reaching supercritical conditions, with temperature and pressure following the vapour-liquid equilibrium curve up to the critical temperature (647 K); if the autoclave is filled above 32%, the meniscus formed between the fluid and the vapour is curved upwards, with the liquid filling the entire autoclave below the critical temperature. [96] After the critical temperature the liquid totally transforms into a dense gas or supercritical fluid. [97] The phenomenon never occurs under normal operation in a Teflon-lined autoclave, unless the filling ratio is above 80%, mostly because of the limited continuous service temperature of Teflon (523 K).

For low temperature reactions, an estimation of the autogenous pressure in a closed system can be obtained using a cubic equation of state (EOS). [98] A practical example for hydrothermal reactions was reported by Rajamathi and Seshadri, who used the Peng-Robertson equation to estimate the change in molar volume during the reaction: [99]

$$p = \left[\frac{RT}{V_m - b} \right] - \left[\frac{a}{V_m^2 + 2bV_m - b^2} \right] \quad (\text{eq. 3.8})$$

$$\text{where:} \quad a = 0.45724 \frac{RT_c}{p_c} \left[1 + f_\omega (1 - T_r^{1/2}) \right]^2 \quad (\text{eq. 3.9})$$

$$b = 0.07780 \frac{RT_c}{p_c} \quad (\text{eq. 3.10})$$

$$\text{and } f_\omega = 0.37464 + 1.54226\omega - 0.26992\omega^2 \quad (\text{eq. 3.11})$$

where V_m is the molar volume, T_c and p_c the critical temperature and pressure respectively, T_r the ratio between the temperature T and the critical temperature, R is the gas constant and ω is the Pitzer acentric factor (equation 3.12), which could be considered as a correction factor to the ideal model in which the molecule is assumed to be spherical. The values of the critical parameters are reported in the Appendix.

$$\omega = -\log\left(\frac{p}{p_c}\right)_{\frac{T}{T_c}=0.7} - 1 \quad (\text{eq. 3.12})$$

The authors developed the equation extrapolating the molar volume as the first of the real solutions of the cubic equation, to obtain a series of isobaric curves, as showed in Figure 3.57 *b* for toluene. The molar volume was corrected for the filling factor dividing the former over the latter parameter.

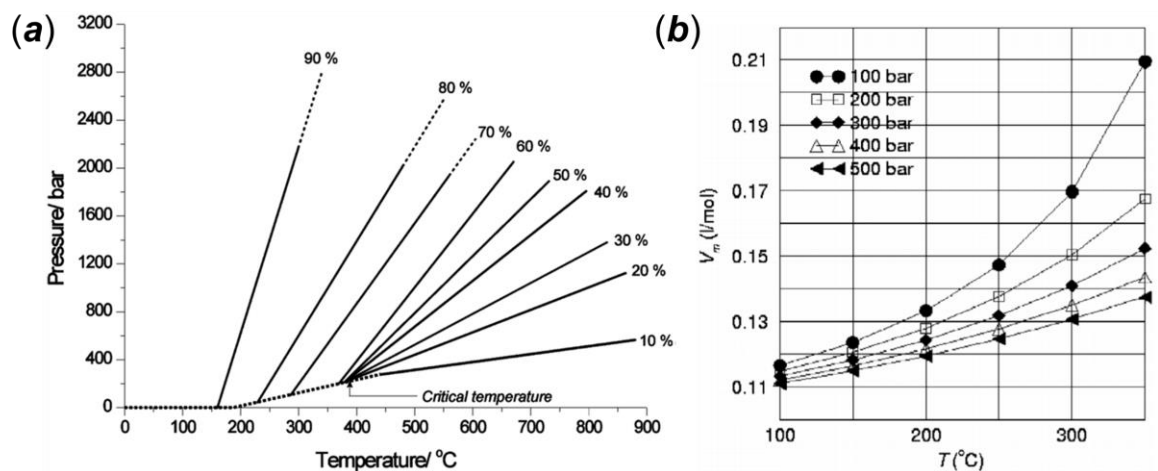


Figure 3.57: (a) Kennedy-Rabenau pressure-temperature diagram for hydrothermal conditions ^[96] and (b) Rajamathi-Seshadri application of the Peng-Robertson equation for the estimation of the molar volume of toluene inside a pressurised vessel. ^[99]

The values of the molar volume for water and ethanol were recalculated using the same method. The disadvantage of this method is the difficult determination of the effect of the pressure when this parameter is below a certain value (10 MPa for water and 2.5 MPa for ethanol, as shown in Figure 3.58 *a* and *b*, respectively), for which the pressure change has no effect on the curves.

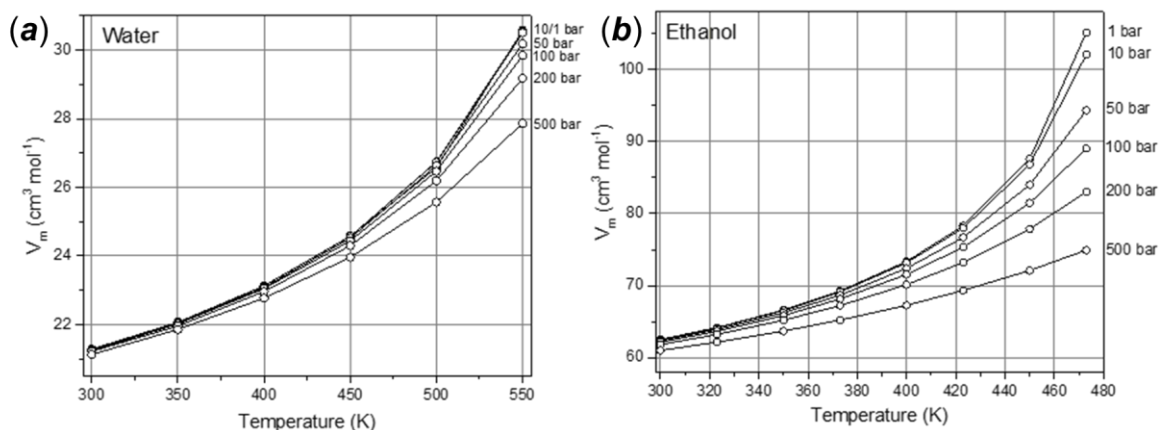


Figure 3.58: Calculation of the molar volume for (a) water and (b) ethanol using the Peng-Robertson equation to give isobaric curves as a function of temperature.

The Peng-Robertson equation is also useful for the calculation of the pressure and temperature conditions at which the equilibrium between the liquid and the vapour phase is established. From the solution of the cubic EOS is it possible to calculate the fugacity of the two phases, which are in equilibrium when they have the same fugacity value.^[100] The equilibrium conditions are reported in the graph in Figure 3.59 *a* for water, ethanol and ethylene glycol, this last very common in MW hydrothermal synthesis due to its high loss tangent value.^[2] The values of molar volume can be also useful to determine the Maximum Allowable Water Loading (MAWL), given by the ratio between the vessel volume and a volume multiplier, in turn given by the ratio of the specific volume at STP and at the treatment temperature. The factor is corrected for 0.9, giving a further 10% of safety margin.^[101] The volume multiplier represents an estimation of the volume expansion inside the autoclave. The calculations of the estimated volume expansion for water, ethanol and ethylene glycol are reported in the graph in Figure 3.59 *b*.

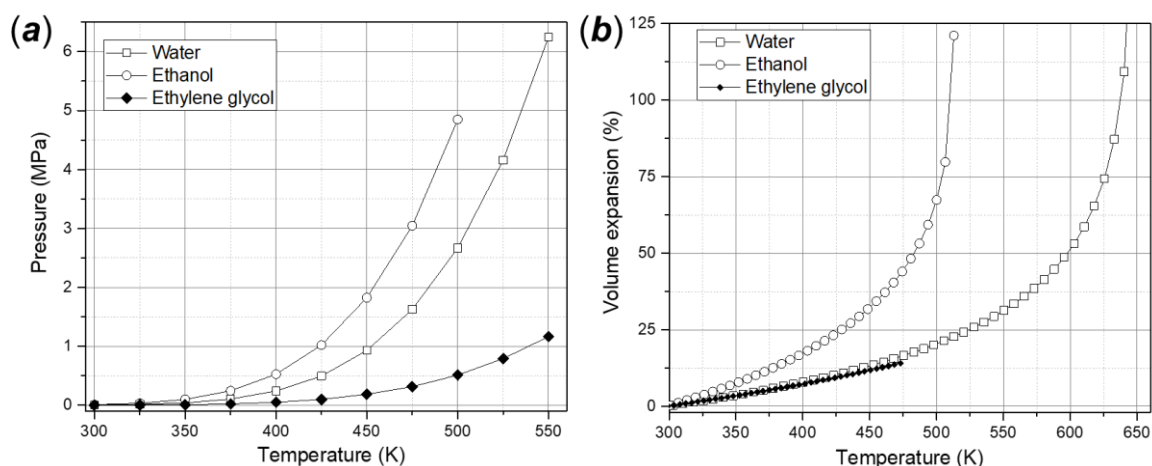


Figure 3.59: (a) Pressure-temperature diagram at equilibrium conditions and (b) estimated volume expansion in a sealed vessel for different solvents.

3.8.3 *In-situ* measurement

Modern microwave heating devices allow a good control of temperature and pressure. In an attempt to compare the pressure and temperature conditions inside the digestion bomb in the MW hydrothermal experiments, alternative experiments using a single-mode microwave cavity (CEM Discovery®) were performed. The in-situ conditions of the microwave autoclave in the former reactions were “simulated” in the latter experiments by varying different parameters affecting the synthesis conditions, such as solvent, type and concentration of acid, filling factor and MW power. The method has several limitations, mainly due to the different maximum pressure limit (nominally 80 bars for the digestion bomb and 20 bars for the single-mode cavity), the different vessel materials (MW transparent polymer and PTFE for the bomb, quartz for the single-mode cavity) and the relatively low accuracy of the temperature and pressure sensors in the single-mode experiments.

For safety reasons, the reactions were eventually stopped just before the safety pressure limit (250 psi = ca. 17.2 bars) to avoid damage to the instrument. The pressure sensor of the instrument is not precise enough to build a pressure-temperature curve. Despite three repeats for each given set of experimental conditions, the precision of the measurements by using the pressure sensor was low. The precision of the instrument is especially low below 0.15-0.2 MPa (examples are shown in Figure 3.62 and A.18 in the Appendix).

The temperature profiles for the MW heating of de-ionised water as a function of applied power are shown in Figure 3.60. All the curves show a steep temperature increase followed by a long plateau. The reactions were performed for at least 10 min without any sign of instability in the temperature profile. These kinds of heating curves have been reported previously for the MW heating of organic solvents.^[102] The steady-state conditions were attributed to the balance between heat flowing out of the system and the heat produced by the system.^[102] The behaviour shown in Figure 3.60 perfectly represents what is described by Rajamathi and Seshadri as a process of heating to a temperature that is in turn governed by pressure.^[99] At low MW power, the heating rate is slow enough to allow a gradual increase of the pressure, with the temperature stabilizing at a steady value. An increase in power causes a rapid increase of the temperature with an exponential increase of pressure, with the pressure rising faster than the temperature.

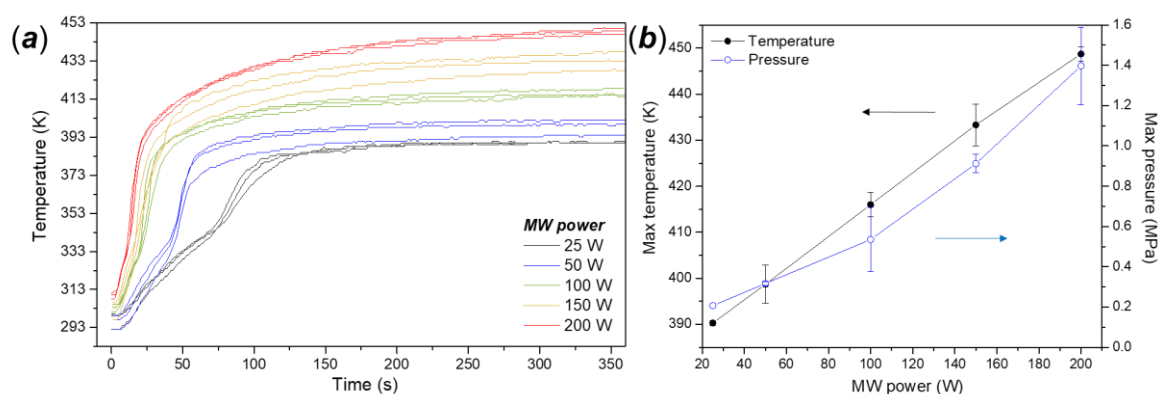


Figure 3.60: (a) Temperature profiles and (b) maximum values for temperature and pressure as a function of MW power for deionised water (filling factor 30%) using the single-mode reactor.

Also notable from Figure 3.60 is how the shape and gradient of the heating curves change with the MW power. The transition time from the initial heating rate to the second decreases with increasing MW power. These heating profiles demonstrate how it would be possible to perform reactions at a constant temperature by applying a fixed MW incident power. To the first approximation, maximum values of temperature and pressure can be fit linearly as a function of the MW power. (Figure 3.60 b). A more detailed analysis can also give important information about the heating power, as performed by Dudley *et al.* calculating the heating rate for some MW-absorbing molecules from the initial linear increase of temperature, obtaining the heating power using mass and heat capacity of the

molecules.^[102] However, a multistage profile was observed for low power irradiation, with a change of slope that apparently does not correlate with an increase of pressure (Figure A.18 in the Appendix). This initial temperature variance could signify the presence of two distinct heating mechanisms. The deviation in temperature rate is progressively reduced with an increase of incident power or on changing the MW adsorbing capacity of the solvent, determined by its dielectric loss (section 1.8.2). It is for example totally absent in the heating profile for absolute ethanol (Figure 3.61), which has higher dielectric loss compared with water. The missing temperature profiles were fitted using different sigmoidal functions, among which the Gompertz function showed the best fit for the temperature profile, assuming a similar trend for higher MW power. The missing data are due to the overcome of the pressure limit at the imposed conditions (over 50 W of MW power). As shown in Figure 3.62, the pressure rate increases rapidly towards the safety operating limit of the instrument, not allowing the supposed achievement of the temperature plateau.

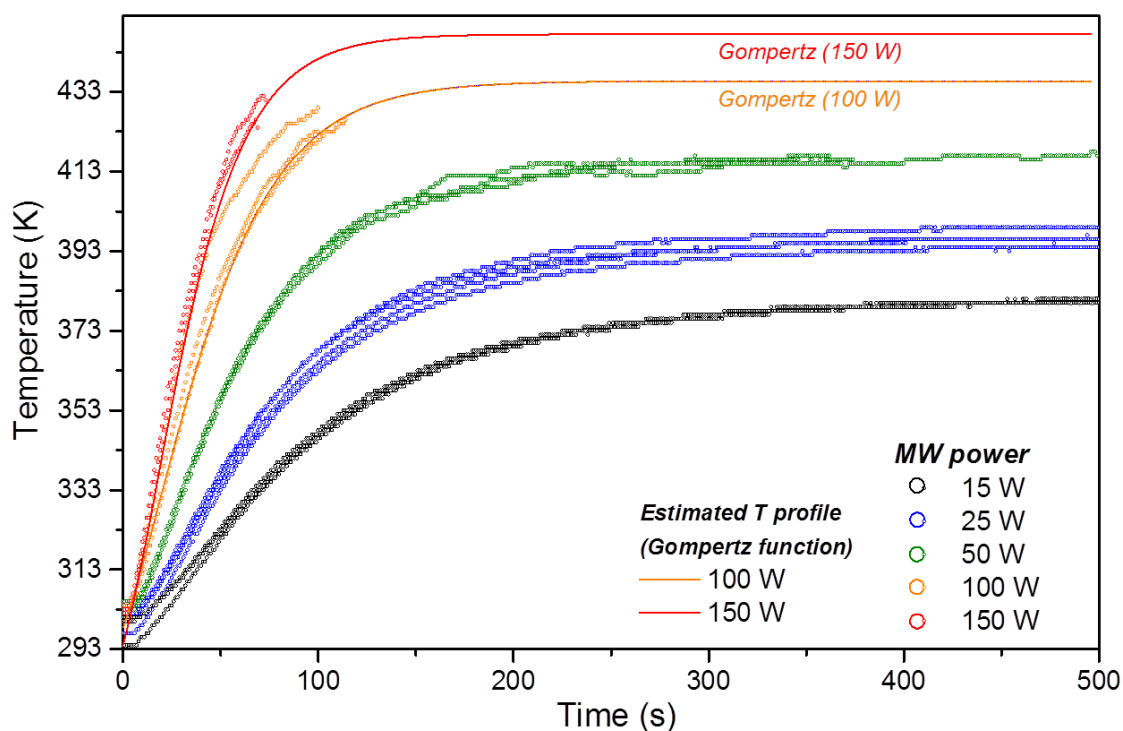


Figure 3.61: Temperature profiles for MW heating of absolute ethanol (3 mL) at different applied MW power. Incomplete temperature profiles have been fit and extrapolated by using Gompertz sigmoidal functions.

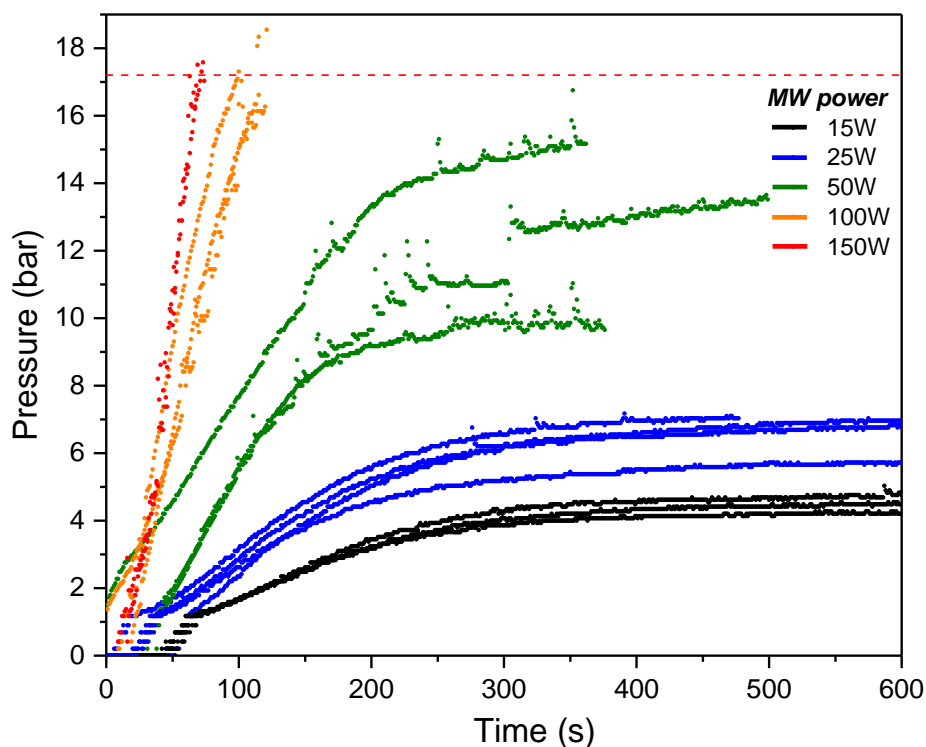


Figure 3.62: Pressure profiles for MW heating of absolute ethanol (3 mL) at different applied MW power.

The main drawback of the FMH synthesis is the relative lack of control over the synthesis parameters and the inherent difficulties in following the synthesis conditions *in situ* inside the reactor. Apart from a comparison with the theoretical model and the *in-situ* observation of the effect of MW heating on operational parameters such as pressure and temperature the only possible methods of investigation involves *ex situ* observation of the effect of the controllable parameters (such as precursor concentration, acidity of the precursor solution, treatment time, etc.) on the final products. In addition to the major variables above, the effect of stirring,^[103] the position of the autoclave in the MM-MW reactor, the conditions of the liner, the presence of impurities, the time of ageing of the solution before the treatment and the drying process were investigated briefly in order to achieve optimal conditions. Their treatment will not be discussed at length in this work.

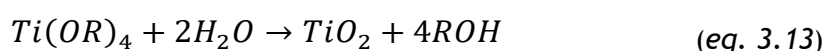
The main advantage of the FMH synthesis is the template-free and surfactant-free synthesis of nanostructured spherical particles. The rapid growth kinetics provided by microwave heating in association with hydrothermal/solvothermal conditions, facilitates the formation of the spherical hierarchical structures. The average size

distribution of the particles is strongly affected by the synthesis parameters, allowing some control over morphology. The possibility of a template-free synthesis of particles with a precise shape is an attractive prospect. The proposed synthesis is mediated only by an inorganic acid rather than by a surfactant, carboxylic acid or other kind of templating molecule as would commonly be used in shape-selective methods. The formation of irregular microspheres by flash-MW synthesis was firstly reported by Komarneni *et al.* from the hydrolysis of $TiCl_4$ in presence of high concentration (3 M) of HCl.^[6]

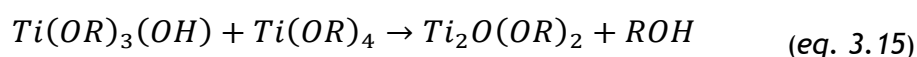
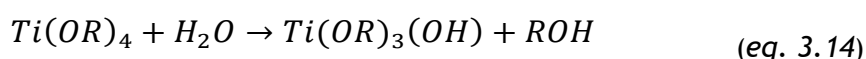
3.8.4 Principles of the reaction

Spherical nanostructured TiO_2 submicroparticles were prepared according to the synthetic method described in section 2.2. The mediation of an inorganic acid for phase-selective TiO_2 synthesis has often been reported for sol-gel and hydrothermal methods. Preparation of oxide nanoparticles by acid- or base-catalysed hydrolytic methods such as polycondensation of alkoxy compounds is particularly popular for the synthesis of dioxide, such as these of Si, Ti and Zr.^[104] Synthesis of TiO_2 via a hydrolytic route is made difficult by the high reactivity of the precursors (e.g. $TiCl_4$, tetraalkoxides) towards water, with uncontrolled condensation of products differing in size and structure, ultimately leading to the formation of amorphous TiO_2 .^[105]

The aqueous route for the synthesis of TiO_2 from an alkoxide precursor is generally described as a hydrolysis reaction:

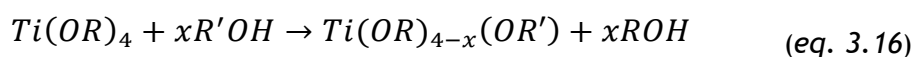


In this conventional route, the alkoxide is firstly hydrolysed, with the formation of TiOH units, which condense to produce Ti-O-Ti bridges, the backbone of the future crystalline particles. The two different mechanisms can be described using the following reactions: ^[106]



The control of the kinetics of hydrolysis and condensation leads to the formation of products differing in final properties, such as porosity, size distribution and

crystalline structure. For this reason, the relative hydrolysis and condensation rates are important parameters in sol-gel or hydrothermal synthesis. The kinetics of the reactions depends principally on the type of alkoxide group and the solvent. For example, titanium tetraisopropoxide is more reactive with water compared to other primary alkoxides (butoxide, ethoxide); the steric hindrance of the isopropoxyl groups in the former prevents the oligomerisation of the molecule.^[107] The hydrolytic polycondensation of alkoxides generally leads to uncontrolled self-condensation and consequent precipitation of particulate material. The control of molecular interactions during the hydrolysis is essential to regulate the final properties of TiO₂.^[108] Hydrolysis-condensation mechanisms can be controlled by adjusting the amount of water, using a different solvent or by the presence of a critical amount of acid. When solvents such as alcohols are used instead of water, the reaction with metal alkoxide described in *equation 3.13* becomes:



The interchange between alcohol and alkoxide is facilitated in the case of low steric hindrance. The exchange reaction could be considered as a nucleophilic substitution at the metal centre. According to Schubert, the metal centre of the alkoxide could be considered as a Lewis acid; depending on the nature of the alkoxo group, the lighter alkoxides are not present in the form of monomers because of the formation of alkoxo-bridges between two or three Ti atoms. In alcoholic solution, the formation of the alkoxo-bridges competes with interactions between the acid centre and the Lewis basic solvent; the aggregation between alkoxide molecules is prevented by the formation of a stable alcohol adduct.^[109] The effect of changing the solvent is evident in the reaction of TiCl₄ with ethanol, which is very slow at room temperature and requires heat to promote the formation of crystalline aggregates.^[9] A very common synthesis procedure is the pre-mixing of the alkoxide with a long chain alcohol (such as isopropanol) in order to protect the precursor from uncontrolled hydrolysis. This reaction is often performed in an alkaline or acidic environment, with the acid or the base functioning catalytically. The presence of the acid is important for several reasons. Firstly, acid promotes hydrolysis at the expense of condensation. In sol-gel synthesis, the effect is visible with the production of a turbid gel rather than a precipitate.^[110] During hydrolysis, the Ti ions in the alkoxide increase their

coordination from 4 to 6 by using their vacant d-orbitals to accept oxygen electron pairs from nucleophilic ligands, such as hydroxyl groups, leading to the formation of octahedral structures. The presence of the acid reduces the coordinating groups to -OH and -OH₂ and simplifies the structure.^[111, 112] The acidic environment favours the formation of Ti(OH)₂⁺ species, which combine with the acid anions in the octahedral configuration. Depending on the coordination position and the affinity of the acid anion with the Ti centre, the subsequent condensation of the octahedral unit via olation or oxolation can lead to the different TiO₂ polymorphs, with the mechanism shown in Figure 3.63.^[113]

The proper choice of solvent and acid anions is also useful in controlling the crystalline phase in the final product. The crystalline habit is strongly influenced by the polymerisation mechanism of the TiO₆ octahedral units. Selective adsorption on reaction sites inhibits the growth along certain directions or facets, promoting or preventing the formation of a specific polymorph. The arrangement of the TiO₆ units determines the final crystal structure, with the crystal growth proceeding using cis-coordination sites (corresponding to the octahedra's edges) for the zig-zag packing typical of anatase. Conversely, the linear arrangement occurring in rutile is due to the bridging of different TiO₆ units through trans-coordination sites (the corners of the octahedra).^[114] Face sharing does not occur in TiO₆ octahedra because of the high repulsive energy between the tetravalent metal centres.^[112]

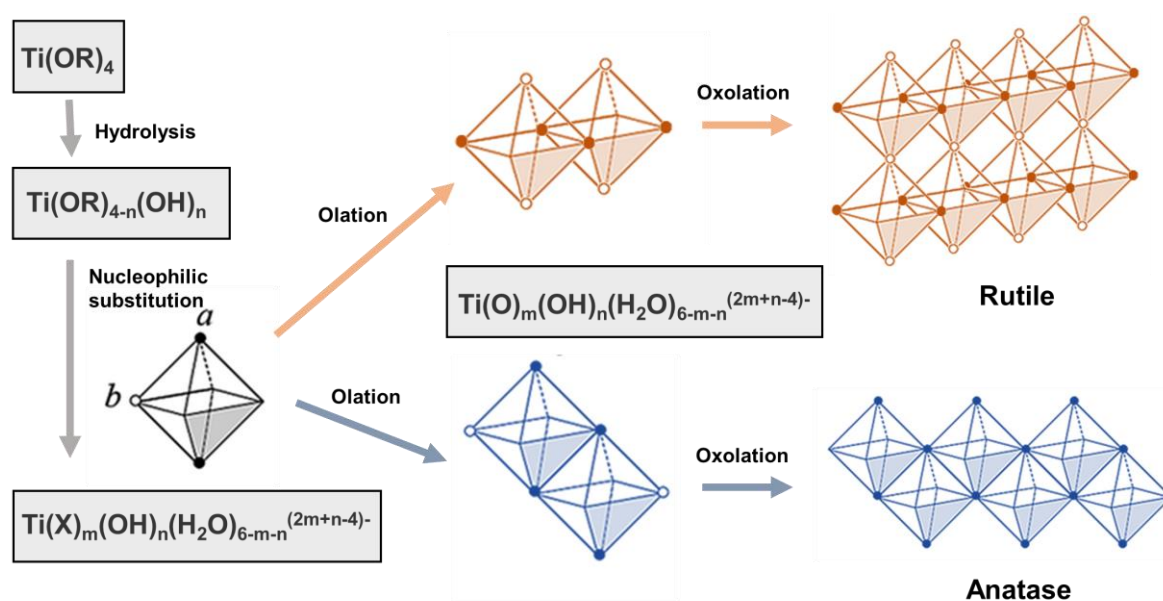


Figure 3.63: Schematic mechanism of acid-mediated synthesis of anatase or rutile in sol-gel and hydrothermal processes. Adapted from Li *et al.* ^[113]

Ultimately, the reduced pH prevents agglomeration of the TiO₂ nanoparticles forming during the reactions, since the isoelectric point of the oxides is between pH 5 and 7. A more acid (or basic) pH would charge the particles, leading to electrostatic repulsion. This colloidal stabilisation will be discussed in the following chapters. The presence of chlorides and nitrates has been shown to affect the peptization process in sol-gel synthesis, breaking the initial large aggregates due to fast hydrolysis into aggregates smaller than 20 nm and primary particles, producing a stable TiO₂ nanoparticle colloidal suspension.^[115]

The fast heating rate provided by microwave irradiation enables solvolysis and the rapid condensation of small crystalline grains in spherical aggregates. The heating rate acts on the nucleation-growth mechanism at the onset, preventing the growth of bigger crystals. From this point of view, the combination of ethanol and microwave heating removes the need for protective agent. The kinetic rate can also influence the resulting crystalline phase. Gopal *et al.* proposed a phase-selective TiO₆ condensation mechanism based on the orientation of three octahedral units, in which the linear combination which gives rutile is thermodynamically favourable because it maximises the distance between metal centres. However, it is also statistically unfavoured compared with other arrangements in which the chain is skewed to produce anatase. Despite a higher activation energy, crystallisation of anatase is preferred kinetically and consequently at higher temperatures.^[112]

3.8.5 Kinetic mechanism of microsphere formation

The formation mechanism of TiO₂ microspheres with hierarchical porosity has been investigated by several authors. One of the most complete study is the one of Cadman *et al.*, which identified three different levels of product from the acid-catalysed partial hydrolysis of Ti alkoxides in alcohol (benzyl alcohol). The primary particles originate from the hydroxylation of the alkoxide precursor, with subsequent condensation of the hydroxylated unit to form nuclei. The secondary particles are generated by agglomeration of the primary particles, driven by thermal energy and catalysed by the presence of the acid. The successive agglomeration of the secondary particles eventually leads to tertiary structures with final characteristics depending on the surface properties of the secondary unit and the synthesis conditions (e.g. hydrolysis ratio).^[116]

The size distribution of the FMH-TiO₂ sub-microspheres obtained in the work described herein is not optimal but can be considered relatively acceptable compared with other syntheses. Good control of the secondary structure has been reported using conventional methods, for example SiO₂ or polymeric colloidal spheres produced by the Stöber method as a template for TiO₂ sol-gel synthesis, followed by a calcination or etching step to remove the template and obtain hollow microspheres.^[117] Eiden-Assman *et al.* reported the production of monodisperse amorphous TiO₂ micro and submicrospheres, with a deviation of $\pm 5\%$ in mean diameter, synthesised by the simple hydrolysis of titanium ethoxide in alcoholic solution in the presence of NaCl or KCl, with size controlled by the concentration of the electrolytes.^[118] The width of the size distribution in our case is due to the accelerated reaction rate given by the MW heating. A rapid formation of highly crystalline particle aggregates with a very wide particle size distribution using microwave-assisted methods was reported by Wang and Cao simply using ethanol and TiCl₄.^[119] The authors described the formation of the particles using a kinetic model of burst nucleation developed by LaMer.^[120, 121] The particles are produced by a homogeneous nucleation mechanism in which the metal ions are reduced forming a critical composition of atomic species in solution forming seeds or nuclei. The nuclei are generated simultaneously as soon as supersaturation is achieved. Subsequent growth occurs immediately without additional nucleation because the burst nucleation dramatically reduces the precursor concentration, restoring the sub-saturation conditions.

According to the LaMer model, the colloidal particles are formed by the aggregation of the primary particles, smaller units generally with a size within the range of 5-20 nm, as observed in our case. The absolute size of the final particles strongly depends on the size and aggregation behaviour of these primary units.^[122] The nuclei aggregate in spherical secondary agglomerates driven by minimization of surface energies according to the Gibbs-Thomson law. Gibbs-Thomson model considers the energy balance in the nucleating system, defining a minimum or critical size above which the formed nuclei are stable; otherwise their energy is too high, leading to redissolution.^[123] The polydisperse distribution is likely to occur when the condensation reaction rate is slow, such as in alcoholysis reactions. Zhang *et al.* improved the size distribution of particles by controlling the condensation reaction with urea, with the alkaline conditions accelerating the condensation rate and providing uniform nuclei.^[124] On the other hand, the

presence of acid leads to the rapid dissolution of nuclei with a size smaller than the critical dimension, defined by the Gibbs model. Only larger, more stable nanoparticles remain undissolved. The critical size also correlates with the hydrothermal temperature, with the formation of larger particles observed at higher temperatures.^[125]

Since nucleation and growth process are influenced by the heating rate, the exploitation of fast reaction kinetics to control the nucleation process selectively in order to narrow the particle size distribution particles has been widely applied. The most effective commercial TiO₂ photocatalyst, Aeroxide P25, is produced by flame pyrolysis, in which the precursor solution is nebulised through a high temperature flame.^[126] Another example is detonation synthesis, in which high temperature and pressure conditions are rapidly generated by a controlled explosion;^[127] this method has been reported for the synthesis of mixed-phase TiO₂ nanoparticles.^[128] In MW heating, the rapid achievement of the reaction temperature (see section 3.8.3) enables the formation of a large amount of crystal nuclei. The nucleation process is immediately followed by the rapid growth of nuclei. A higher population of nuclei with smaller sizes can be achieved by MW heating as compared to conventional heating. Moreover, increasing MW power leads higher heat rates, enhancing the homogeneous nucleation process, producing smaller particles with a narrower size distribution.

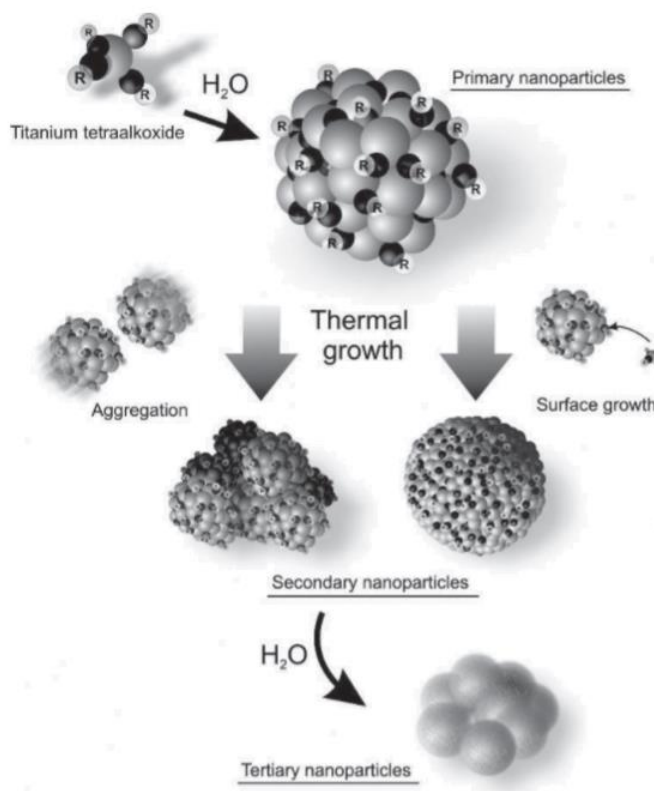


Figure 3.64: Mechanism of formation of primary, secondary and tertiary particles in alcohol-mediated synthesis of TiO₂ nanoparticles (from Cadman *et al.* ^[116]).

3.8.6 Precursor concentration

The reduction of the concentration of precursor in acid-mediated FMH synthesis leads to the reduction of both the crystallite size and the secondary particle diameter. The results of the influence of the precursor are not in agreement with the findings of Chae *et al.*, which correlated the increase of the precursor concentration with the reduction of the nanoparticles size. The higher the quantity of precursor molecules, the higher the number of nuclei, with the growing phase hindered by mutual competition amongst the numerous crystallites formed. However, the effect of the mutual competition is suppressed above a certain concentration, when the small sized TiO₂ nanograins tend to agglomerate to minimise the energy of the system.^[129]

3.8.7 Treatment time and MW power

The treatment time is, together with the MW power, the parameter most directly connected to the reaction temperature and consequently to the pressure inside the autoclave.

Increasing treatment time in general leads to an increase of crystallite size and the degree of crystallinity, as is also observed in conventional hydrothermal synthesis. The longer the irradiation time, the higher the quantity of heat transferred to the solution. The effect was studied for the *CW* series, using 2 M HCl and a 164 mM precursor concentration. For this series of samples, it is impossible to test the impact of the treatment time on the morphology, because under these synthesis conditions there is no formation of particles with defined shape. The treatment time is the most critical parameter, since the wrong estimation of the reaction time could lead to an overheating of the reactor or even to an explosion due to an uncontrolled increase of pressure. Considering the kinetics of these MW-assisted syntheses, the existence of a minimum time for the stable nucleation of the particles was assessed. In both syntheses with the MW-transparent digestion bomb and in trials with the single-mode reactor, a threshold time for the stability of the particles was observed. Below 15 seconds of irradiation, despite the initial formation of a colloidal suspension witnessed by a change in turbidity, the particles were easily dissolved in water during the washing steps. This phenomenon is perfectly described by the non-achievement of the nucleation peak in the LaMer model and re-dissolution of the precursor in monomeric units.

Despite, in some cases, an increase in secondary particle size with longer irradiation times, the size distributions from SEM revealed no clear trend. This suggests that once the particles are formed according to the LaMer mechanism, there is no further agglomeration of crystallites to induce secondary particle growth. Extending the treatment time further led to agglomeration of the secondary particles to form larger porous structures of no specific morphology.

The most obvious direct effect of the applied MW power is its enhancement of the degree of crystallinity, manifested as a narrowing of the PXD peak width and an increase of the Raman peak intensity.

3.8.8 Acid mediator

The type of acid is known to have a strong effect on the crystalline phase. Considering the affinity of the acid anions for the Ti^{4+} centre, a stronger bonding with the titanium atom should inhibit the structural rearrangement, increasing this way the activation energy for the crystallisation of rutile and hence promoting the formation of pure anatase. According to this principle, weaker bonded anions such as NO_3^- and Cl^- anions should promote the formation of rutile, unlike strong bonded ions such as sulphate, fluoride and acetate anions.^[130]

According to Guo *et al.* however the size of the anion principally determines the TiO_2 phase rather than coordination strength, with smaller anions resisting elimination longer than the aquo-ligands during the olation (condensation of TiO_6 units due to the progressive removal of at the expenses of bound water molecules). Always according to their theory, the acid anions tends to occupy a specific position in the octahedral coordination, affecting the progressive removal of equatorial or apical ligands and hence leading to the formation of the different TiO_2 polymorphs (Figure 3.63). In particular, condensation through the equatorial edges gives linear chains leading to rutile, whereas initial removal of bigger anions leads to the formation of skewed structures which condense to produce anatase.^[131] From all the experimental evidence, a series of anions was established, as shown in

Figure 3.65, which loosely resembles the Hoffmeister series.^[132]

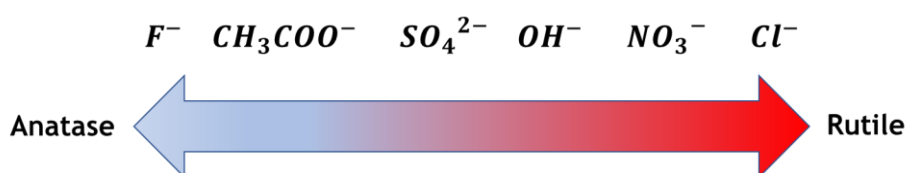


Figure 3.65: Pseudo-Hoffmeister series for the tendency of acid anions to form anatase or rutile in acid-mediated sol-gel or hydrothermal syntheses.

The rule seems to apply for Cl^- under almost all conditions, for example, with the formation of rutile nanoparticle even below the thermodynamic stability threshold (~14 nm).^[133] However, variable results have been observed using HNO_3 , which was often reported to produce pure anatase via sol-gel and hydrothermal synthesis.^[139]

Gopal *et al.* identified two distinct formation regions for anatase and rutile in the precipitation of crystalline TiO_2 in sol-gel syntheses mediated by HNO_3 (Figure

3.66).^[134] Formation of anatase was observed at relatively high temperature at the very early steps of the reaction. Hydrothermal reactions occur at higher temperature than sol-gel reactions and, following LaMer kinetics, the burst nucleation occurs even faster under MW heating. The accelerated kinetic would also explain our finding of anatase crystals also in presence of chlorine.

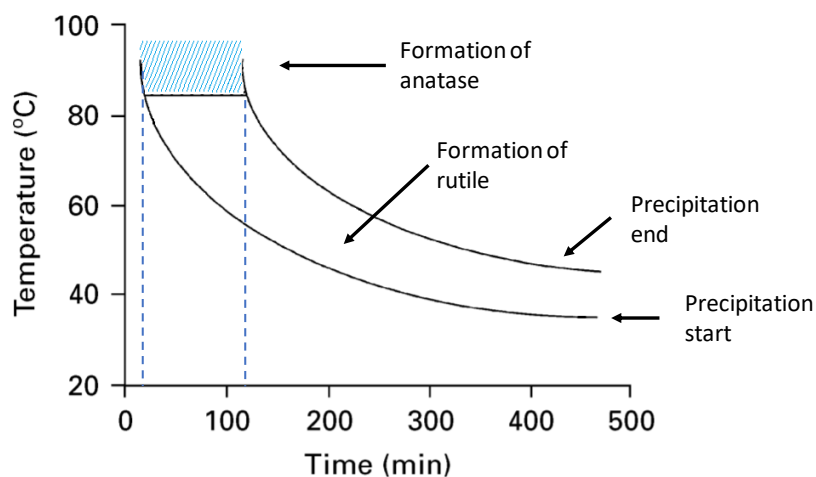


Figure 3.66: Time-temperature-precipitation diagram for acid-mediated sol-gel synthesis of crystalline TiO_2 in the presence of HNO_3 (adapted from ref. [134]).

For H_2SO_4 and CH_3COOH , the kinetics are probably too fast to allow the formation of ordered nanocrystals, with the precipitated TiO_2 in amorphous form. Moreover, from the point of view of the morphological control, these acids promoted the formation of unshaped agglomerates with no interest from the point of view of the morphology.

Another potential cause for the poor yield in terms of quality using these acids is the water amount present in commercial grade acid, a parameter which should be considered in acid-mediated synthesis in organic solvents. As reported in the following section, the amount of water is an essential parameter for production of TiO_2 particles. The amount of water present in some of the most common grades of acid is reported in Table A.7 in the Appendix. The hydrolysis ratio is more than doubled using the same concentration of HCl rather than HNO_3 . The low quantity of water can slow excessively the condensation reactions, since the precursors are not fully hydrolysed. As soon as the nuclei form, they aggregate irregularly to minimise the surface energy. Synthesis with H_2SO_4 and CH_3COOH were not investigated further in this study. The same phenomenon was not observed for HNO_3 , following the behaviour proposed according to the pseudo-Hoffmeister

series, as observed by Izumi *et al.* using stronger acids.^[130] The other properties (conductivity, pH) of the acidic solution used are reported in Table A.8, A.9 and A.10 in the Appendix. The unequivocal formation of anatase in conditions which would favour rutile can be explained by using the theory of phase selection according to Bekkerman *et al.*, with the transition to rutile promoted by a higher concentration of acid. Since H⁺ species adsorb to the TiO₆ units during particle growth, the repulsion due to their increase in solution (i.e. higher concentration) would tend to force the octahedra into a linear arrangement, breaking the statistical rules of the three adjacent units.^[135]

Besides phase selection and degree of crystallinity, the nature and the concentration of the acid influence also the final morphology of the particles in the FMH synthesis. A threshold acid concentration below which the distinct particles are not produced has been observed by carrying out reactions with very low acid concentration. For HCl, isolated particles were not observed at 0.2 M or lower, with formation of unshaped agglomerated structures. An increase of the acid concentration is usually associated with larger surface area and increased porosity (section 3.5.3). The N₂ adsorption/desorption isotherms showed an increased mesoporosity moving towards higher acid concentration, as observed for both solvents (ethanol and water) and both acids (HNO₃ as reported in Figure 3.23, HCl shown in Figure 3.67). This result is not in agreement with the analysis of Hu *et al.*, in which a decrease of surface area is reported when the pH is low, despite a corresponding reduction in primary particle size. ^[136]

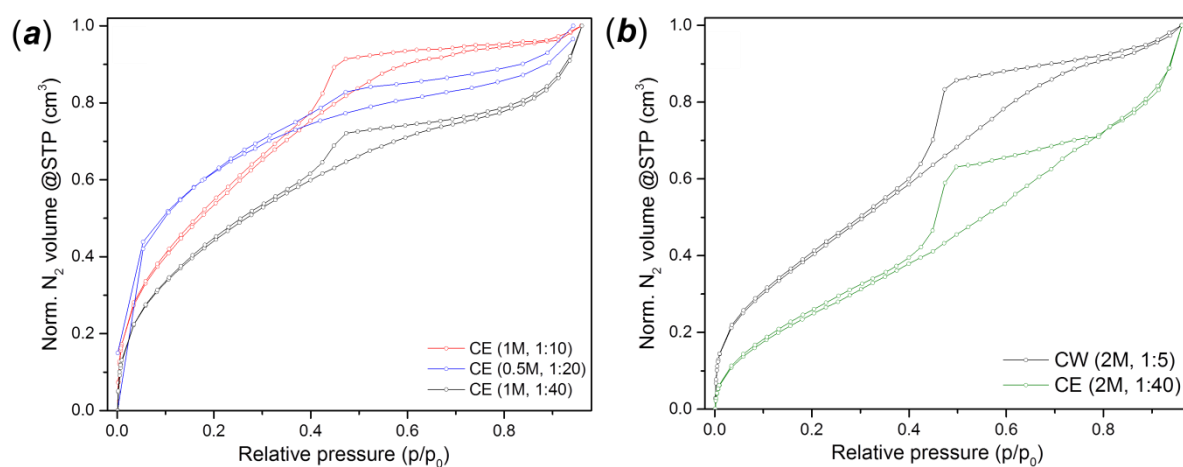


Figure 3.67: N₂ adsorption/desorption isotherms for the CE/CW series, with different concentrations of HCl.

The analysis of the morphology and the surface area of the microspheres led to the conclusion that higher acid concentration reduces the particle size. The rate of agglomeration is supposed to accelerate in the presence of acid, with crystallites creating voids as they combine, leading to mesoporosity and larger values of specific surface area.

3.8.9 Effect of the solvent

The selection of the solvent affects the equilibrium and the relative kinetics of the hydrolysis and condensation reactions of the Ti precursors. The conditions can dictate the final characteristics of the resulting products, especially the final morphology and particle size. The molar ratio between water and titanium is defined as the hydrolysis ratio (r) and is considered to be one of the fundamental parameter for the control of the two reactions involved in the particle formation (precursor hydrolysis and condensation of monomeric unit by dehydration or dealcoholation).^[137] Two precise regimes can be defined depending on the value of r . If $r < 10$, the reaction of an alkoxide will result in monodisperse spherical aggregates of nanoparticles of 0.5-1 nm. Conversely, an increase in water content causes acceleration of the nucleation and growth of the particles to second time scales.^[115] As discussed in section 3.3.1, the use of water as a solvent leads to the rapid hydrolysis of the precursor, generating nuclei of $\text{Ti}(\text{OH})_4$ within seconds. The solution turns cloudy because of the colloidal dispersion of the nuclei. Without the presence of a surfactant and/or template, a hydrothermal approach will not produce spherical particles. The presence of a less polar solvent hence appears to be fundamental for the formation of spherical secondary particles.

Chae *et al.* analysed the effect of the hydrolysis ratio on the particle size in acid-mediated HT synthesis in the water-ethanol system. The authors claimed that ethanol-rich conditions led to particle size reduction, with the lowest value obtained using a volumetric ratio of 8:1.^[129] Lower hydrolysis ratios were found to lead to poor crystallisation due to insufficient hydrolysis. These observations are in agreement with the ethanolic syntheses conducted in this project.

Differences in the type of adsorption isotherm and hence porosity can be also attributed to the different hydrolysis ratio. Calleja *et al.* correlated the surface area and pore size distribution with the hydrolysis ratio, finding that an increase in water content leads to a reduction of the surface area. They also observed a

progressive change from type I to type IV isotherms and then to type II with increasing hydrolysis ratio in sol-gel synthesis using TTIP. They observed a progressive transformation from a totally amorphous microporous material to those with increased mesoporosity and finally microporous material with a well-defined crystalline structure.^[67]

3.8.10 Impurities

One of the characteristics of the as-prepared TiO₂ particles is the yellowish coloration of the powder, even after washing the original colloidal suspension with de-ionised water and ethanol. The yellow coloration was particularly prevalent for samples synthesised with ethanol-HNO₃ (**NE** series). TiO₂ colours other than white are often associated with residues from the synthesis, external element and even doping substitution. The observed irregular mesoporosity could be due to the presence of amorphous domains of TiO₂ or the presence of carbonaceous impurities. The as-synthesised particles are not only composed of amorphous or crystalline TiO₂ but also some other residues probably originated from some unexpelled precursor fragments or reaction by-products, as shown by the thermal and surface characterisation analysis.

The presence of carbonaceous impurities in the particles can be assessed using surface and elemental analysis. Unfortunately, EDX spectroscopy could not provide useful qualitative or quantitative information, because of the strong background from the carbon tabs used for the preparation of the SEM samples and the lower sensitivity of the technique towards lighter atoms such as carbon and nitrogen. XPS revealed the possible presence of Ti-C bonds, whereas weak IR band around 1080 cm⁻¹ can be attributed to the vibration of Ti-O-C.

Thermal analysis confirmed a consistent loss of mass, up to 10% of the original weight of the sample, between the temperature of release of the adsorbed water and the crystallisation/phase transition of TiO₂. Apart from the hypothesis of release of structural water, the mass loss is sometimes accompanied by an exothermic thermal event. Similar results were obtained by Sibū *et al.*, which observed exothermic decomposition of nitrates at around 600-700 K and the removal of structural hydroxyls between 660-680 K, this latter process involved a mass loss but not distinct DTA peak.^[138]

Mass spectrometry of the evolved gas did not clarify the nature of the impurities released during heating. The release of by-products of HNO₃ (such as NO) are not unusual in synthesis mediated by this acid. The eventual release of CO₂ cannot be excluded, since the signal originated by its mass fragments are overlapping with those of N₂O. The simultaneous presence of both carbonaceous and nitrite/nitrate impurities can be still considered as a valid option. Gombac *et al.* noted evolution of NO at 493 K and progressive release of CO and CO₂ from 473 and 873 K in particles produced by sol-gel synthesis in ethanol using Ti-butoxide as a precursor.^[139]

3.9 Conclusion

In this chapter, synthesis of TiO₂ nanostructured particles by Flash-MW hydrothermal synthesis was extensively analysed, deeply investigating the particle formation mechanisms, the control of the synthesis parameters and their effect on the final products. The main findings of this study can be summarised as follows:

- Constant power MW heating associated to solvothermal method provides a very rapid (minute scale) method for the synthesis of TiO₂ particles;
- Nanostructured TiO₂ mesoporous spherical sub-microparticles with very high surface area (200-500 m²/g) were obtained by means of this technique
- Almost perfect spherical shape was obtained without use of surfactant or templating agents;
- Synthesis conditions such as acid mediator and precursor concentration are essential for the control of the synthesis in terms of size distribution, porosity, etc.;

The FMH method constitutes a very fast synthetic method compared to conventional and MW-assisted hydrothermal reaction, adopting the method for the synthesis of nanostructured spherical particles as never reported before. The reaction time was reduced from the several hours necessary for hydrothermal using conventional heating to a minute scale process, outclassing also other MW-assisted process, based on power modulation to control temperature and pressure of the reaction system. Furthermore, *in situ* analysis of the heating conditions demonstrated the achievement of a thermal equilibrium applying constant MW power to a closed reactor, with constant temperature and pressure controllable by means of the applied MW power.

The described methodology offers control over the final characteristics of the particles, such as morphological and structural properties. Selection of the acid and precursor type and their concentration, together with the selection of the solvent, are all factors letting to supersede the limited control over the internal parameters (pressure, temperature) intrinsic of the digestion bomb/multimode reactor system.

The internal structure of the TiO₂ particles is interesting from the point of view of nanostructuration. The particles are composed of nanometric grains, which size is as small as 2-3 nm, as confirmed by direct observation by TEM, with the presence of a dense agglomeration of nanometric primary particles composing the spherical secondary units. The properties of the nano-grains are transferred to the secondary structure as confirmed by different experimental evidences. Quantum confinement effect typical of nanosized particles were observed in optical band gap measurement, with a blue-shift to 3.4-3.5 eV (depending on the synthesis conditions) compared to the 3.2 of bulk crystalline anatase. Raman modes were also affected by the nanostructuration, with the E_{g,1} mode peak located around 149-152 cm⁻¹ and its FMWH above 20 cm⁻¹, as reported in literature for TiO₂ nanoparticles below 5 nm. A further proof of the presence of very small nanocrystals is the difficult application to the models used to predict the particle size from the effect of the quantum confinement, models failing in presence of particles smaller than 3-4 nm.

The synthetic procedure involves incorporation of organic impurities, representing 10-20 wt% of the final mass of the as-synthesised particles. These impurities, identified in residual chain from the incomplete reaction of the precursor and evolution of NO-N₂O (notably in case of synthesis with HNO₃ in ethanol), might have a role in the production of the mesoporosity. Moreover, the presence of impurities contributes to the structural disorder of the particles, with presence of electronic localised states marked with higher Urbach energies (*ca.* 100 meV) compared to bulk anatase or other TiO₂ nanoparticles (e.g. P25).

Finally, the high specific surface area, with values ranging between 200 and 500 m²/g, proved the presence of a porosity network formed by the intergranular voids between primary crystallites. Particles produced in more acidic environment presents enhanced porosity, with higher value of surface area and hierarchical distribution of pores, with the existence of small micropores together with open mesoporosity (5-20 nm of pore diameter) with irregular distribution and shape. This last property is peculiar for the application of the FMH-TiO₂ particles in purification processes, potentially enhancing the adsorption capacity of the system and offering a higher number of active sites in photocatalytic reactions, improving the overall efficiency of these last.

3.10 References

- ¹ P. Rigneau, K. Bellon, I. Zahreddine, D. Stuerger, Microwave flash-synthesis of iron oxides nanoparticles, *Eur. Phys. J. AP*, 1999, **7**, 41-43.
- ² Y. Zhu, F. Chen, Microwave-Assisted Preparation of Inorganic Nanostructures in Liquid Phase, *Chem. Rev.*, 2014, **114**, 6462–6555.
- ³ C. Bosquet-Berthelin, D. Chaumont, D. Stuerger, Flash microwave synthesis of trevorite nanoparticles, *J. Sol. St. Chem.*, 2008, **181**, 616-622.
- ⁴ E. Gressel-Michael, D. Chaumont, D. Stuerger, From a microwave flash-synthesized TiO₂ colloidal suspension to TiO₂ thin films, *J. Colloid. Int. Sci.*, 2005, **285**, 674-679.
- ⁵ R.E. Burau, *Lead*, in C.A. Black (eds), *Methods of Soil Analysis, Part 2, Chemical and Microbiological Properties*, American Society of Agronomy, Soil Science Society of America, Madison (WI, U.S.A.), 2nd ed., 1982, vol. 9.2, pp. 347–366.
- ⁶ S. Komarneni, R. K. Rajhaa, H. Katsuki, Microwave-hydrothermal processing of titanium dioxide, *Mat. Chem. Phys.*, 1999, **61**, 50-54.
- ⁷ Y. Qu, C. Sun, G. Sun, X. Kong, W. Zhang, Preparation, characterization, and kinetic and thermodynamic studies of mixed-phase TiO₂ nanoparticles prepared by detonation method, *Res. Phys.*, 2016, **6**, 100-106.
- ⁸ H. Wang, J. Chen, S. Hy, High-surface-area mesoporous TiO₂ microspheres via one-step nanoparticle self-assembly for enhanced lithium-ion storage, *Nanoscale*, 2014, **6**, 14926.
- ⁹ X. Wang, J. Tian, C. Fei, L. Lv, Y. Wang, G. Cao, Rapid construction of TiO₂ aggregates using microwave assisted synthesis and its application for dye-sensitized solar cells, *RSC Adv.*, 2015, **5**, 8622- 8629.
- ¹⁰ W. Shi, S. Song, H. Zhang, Hydrothermal synthetic strategies of inorganic semiconducting nanostructures, *Chem. Soc. Rev.*, 2013, **42**, 5714-5743.
- ¹¹ J.B. Gallagher, Synthesis of nanostructured materials with potential renewable energy generation applications. PhD thesis (2015), University of Glasgow.
- ¹² W.T. Sproull, *X-Rays in Practice*; McGraw-Hill, New York, 1946, p 430.
- ¹³ N. Serpone, D. Lawless, R. Khairutdinov, Size Effects on the Photophysical Properties of Colloidal Anatase TiO₂ Particles: Size Quantization or Direct Transitions in This Indirect Semiconductor?, *J. Phys. Chem.*, 1995, **99**, 16646-16654.
- ¹⁴ H. Zhang, J.F. Banfield, Thermodynamic analysis of phase stability of nanocrystalline titania, *J. Mater. Chem.*, 1998, **8**, 2073-2076.
- ¹⁵ T. Ohno, K. Saruwaka, K. Tokieda, K. Matsumura, Morphology of a TiO₂ Photocatalyst (Degussa, P-25) Consisting of Anatase and Rutile Crystalline Phases, *J. Catal.*, 2001, **203**, 82-86.
- ¹⁶ G. Colon, M.C. Hidalgo, J.A. Navio, Photocatalytic deactivation of commercial TiO₂ samples during simultaneous photoreduction of Cr(VI) and photooxidation of salicylic acid, *J. Photochem Photobiol. A*, 2001, **138**, 79-85.
- ¹⁷ H.G. Merkus, *Particle Size Measurements: Fundamentals, Practice, Quality*, Springer, 2009, pp. 15-16.
- ¹⁸ M. Horn, C.F. Schwerdtfeger, E.P. Meagher, Refinement of the structure of anatase at several temperatures, *Zeitschrift fur Kristallographie, Kristallgeometrie, Kristallphysik, Kristallchemie*, 1972, **136**, 273-281.
- ¹⁹ J. Wang, Y. Zhou, Y. Hu, R. O'Hayre, Z. Shao, Facile Synthesis of Nanocrystalline TiO₂ Mesoporous Microspheres for Lithium-Ion Batteries, *J. Phys. Chem. C*, 2011, **115**, 2529–2536.
- ²⁰ Z. Li, Y. Que, L. Mo, W. Chen, Y. Ding, Y. Ma, L. Jiang, L. Hu, S. Da, One-Pot Synthesis of Mesoporous TiO₂ Microspheres and Its Application for High-Efficiency Dye-Sensitized Solar Cells, *ACS Appl. Mater. Int.*, 2015, **7**, 10928–10934.
- ²¹ K. Mohd, M. Hasmaliza, Effect of Rutile on Modulus of Rupture in Ceramic Glaze, *Proc. Chem.*, 2016, **19**, 10-14.

- 22 Y. Man, L. Mu, Y. Wang, S. Lin, G.L. Rempel, Q. Pan, Synthesis and Characterization of Rutile Titanium Dioxide/Polyacrylate Nanocomposites for Applications in Ultraviolet Light-Shielding Materials, *Pol. Compos.*, 2014, **36**, 8-16.
- 23 Y.B. Zhang, X.J. Feng L. Jiang, Synthesize TiO₂ microspheres self-assembled from nanorods via hydrothermal treatment, *Sci. Chin. Ser. B: Chem.*, 2007, **50**, 175-178.
- 24 D.B. Williams, C.B. Carter, *Transmission Electron Microscopy*, Springer, 2009.
- 25 X. Jang, T. Herricks, Y. Xia, Monodispersed Spherical Colloids of Titania: Synthesis, Characterisation and Crystallization, *Adv. Mater.*, 2003, **15**, 1205-1209.
- 26 K.S.W. Sing, D.H. Everett, R.A.W. Haul, L. Moscou, R.A. Pierotti, J. Rouquerol, T. Siemieniewska, Reporting physisorption data for gas/solid systems with special reference to the determination of surface area and porosity. *Pure Appl. Chem.*, 1985, **57**, 603-619.
- 27 A. Zeid, A. Othman, A Review: Fundamental Aspects of Silicate Mesoporous Materials, *Materials* 2012, **5**, 2874-2902.
- 28 J. H. De Boer, *The structure and properties of porous materials*. Butterworths, London, 1985, 389, 68-94.
- 29 S. Patra, C. Davoisne, H. Bouyanfif, D. Foix, F. Sauvage, Phase stability frustration on ultra-nanosized anatase TiO₂, *Scientific Reports*, 2015, **5**, 10928.
- 30 F. Rouquerol, J. Rouquerol, K. Sing, *Adsorption by Powders & Porous Solids*, Academic Press, London, 1999.
- 31 M. R. Ranade, A. Navrotsky, H. Z. Zhang, J. F. Banfield, S. H. Elder, A. Zaban, P. H. Borse, S. K. Kulkarni, G. S. Doran and H. J. Whitfield, Energetics of Nanocrystalline TiO₂, *Proc. Natl. Acad. Sci.*, 2002, **99**, 6476-6481.
- 32 D.S. Kim, S. Kwak, The hydrothermal synthesis of mesoporous TiO₂ with high crystallinity, thermal stability, large surface area, and enhanced photocatalytic activity, *App. Cat. A: Gen.*, 2007, **323**, 110-118.
- 33 T. Ohsaka, F. Izhumi, Y. Fujiki, Raman Spectrum of Anatase, TiO₂, *J. Raman Spectr.*, 1978, **7** (6), 321-324.
- 34 S.P.S. Porto, P.A. Fleury, T.C. Damen, Raman Spectra of TiO₂, MgF₂, ZnF₂, FeF₂, and MnF₂, *Phys. Rev.*, 1967, **154**, 522-526.
- 35 O. Frank, M. Zukalova, B. Laskova, J. Kürti, J. Koltaib, L. Kavan, Raman spectra of titanium dioxide (anatase, rutile) with identified oxygen isotopes (16, 17, 18), *Phys. Chem. Chem. Phys.*, 2012, **14**, 14567-14572.
- 36 K.M. Reddy, S.V. Manorama, A.R. Reddy, Bandgap studies on anatase titanium dioxide nanoparticles, *Mat. Chem. Phys.*, 2003, **78**, 239-245.
- 37 B.D. Vriezicke, S. Patel, B.E. Davis, D.P. Birnie, Evaluation of the Tauc method for optical absorption edge determination: ZnO thin films as a model system, *Phys. Stat. Solid. B*, 2015, **252**, 1700-1710.
- 38 S.J. Ikhmayies, R.N. Ahmad-Bitarb, A study of the optical bandgap energy and Urbach tail of spray-deposited CdS:In thin films, *J. Mater. Res. Tech.*, 2013, **2**, 221-227.
- 39 F. Leblanc, Y. Maeda, M. Ando, M. Wakagi, T. Minemura, Accurate Determination of the Urbach Energy of aSi:H Thin Films by Correction for the Interference Effect, *Jpn. J. Appl. Phys.*, 1994, **33**, L1755-1758.
- 40 J.C. Hebig, I. Kühn, J. Flohre, T. Kirchartz, Optoelectronic Properties of (CH₃NH₃)₃Sb₂I₉ Thin Films for Photovoltaic Applications, *ACS Energy Lett.*, 2016, **1**, 309-314.
- 41 F. Urbach, The Long-Wavelength Edge of Photographic Sensitivity and of the Electronic Absorption of Solids, *Phys. Rev.*, 1953, **92**, 1324.
- 42 A.S. Hassanien, A.A. Akl, Influence of composition on optical and dispersion parameters of thermally evaporated non-crystalline Cd₅₀S_{50-x}Se_x thin films, *J. Alloy Comp.*, 2015, **648**, 280-290.
- 43 B. Choudhury, M. Dey and A. Choudhury, Defect generation, d-d transition, and band gap reduction in Cu-doped TiO₂ nanoparticles, *Int. Nano Lett.*, 2013, **3**, 25.
- 44 M. Nowak, B. Kauch, P. Szperlich, Determination of energy band gap of nanocrystalline SbSi using diffuse reflectance spectroscopy, *Rev. Sci. Instr.*, 2009, **81**, 046107.

- ⁴⁵ K. Zhu, M. Zhang, Q. Chen, Z. Yin, Size and phonon-confinement effects on low-frequency Raman mode of anatase TiO₂ nanocrystal, *Phys. Lett. A*, 2005, **340**, 220-227.
- ⁴⁶ W.F. Zhang, Y.L. He, M.S. Zhang, Z. Yin, Q. Chen, Raman scattering study on anatase TiO₂ nanocrystals, *J. Phys. D*, 2000, **33**, 912-916.
- ⁴⁷ Y. Iida, M. Furukawa, T. Aoki, T. Sakai, Raman Spectrum of Ultrafine Anatase Powders Derived from Hydrolysis of Alkoxide, *Appl. Spectrosc.*, 1998, **52**, 673-678.
- ⁴⁸ J.C. Parker, R.W. Siegel, Calibration of the Raman spectrum to the oxygen stoichiometry of nanophase TiO₂, *Appl. Phys. Lett.*, 1990, **57**, 943-945.
- ⁴⁹ D. Bersani, P.P. Lottici, X.-Z. Ding, Phonon confinement effects in the Raman scattering by nanocrystals, *Appl. Phys. Lett.*, 1998, **72**, 73-75.
- ⁵⁰ C.J. Doss, R. Zallen, Raman studies of sol-gel alumina: Finite-size effects in nanocrystalline AlO(OH), *Phys. Rev. B*, 1993, **48**, 15626.
- ⁵¹ V. Swami, A. Kuznetov, L. Dubrovinsky, R.A. Caruso, D.G. Shchulkin, B.C. Muddle, Finite-size and pressure effects on the Raman spectrum of nanocrystalline anatase TiO₂, *Phys. Rev. B*, 2005, **71**, 184302.
- ⁵² K. Zhu, M. Zhang, Q. Chen, Z. Yin, Size and phonon-confinement effects on low-frequency Raman mode of anatase TiO₂ nanocrystal, *Phys. Lett. A*, 2005, **340**, 220-227.
- ⁵³ X. Xue, W. Ji, Z. Mao, H. Mao, Y. Wang, X. Wang, W. Ruan, B. Zhao, J.R. Lombardi, Raman Investigation of Nanosized TiO₂: Effect of Crystallite Size and Quantum Confinement, *J. Phys. Chem. C*, 2012, **116**, 8792-8797.
- ⁵⁴ H. Chang, P.J. Huang, Thermo-Raman Studies on Anatase and Rutile, *J. Raman Spectr.*, 1998, **29**, 97-102.
- ⁵⁵ S.W. Koch, M. Kira, G. Khitrova, H. M. Gibbs, Semiconductor excitons in new light, *Nature Mat.*, 2006, **5**, 523-531.
- ⁵⁶ L.E. Brus, Electronic wave functions in semiconductor clusters: experiment and theory, *J. Phys. Chem.*, 1986, **90**, 2555-2560.
- ⁵⁷ T. Soga, *Nanostructured Materials for Solar Energy Conversion*, Elsevier, 2006, pp. 230-231.
- ⁵⁸ B. Enright, D. Fitzmaurice, Spectroscopic Determination of Electron and Hole Effective Masses in a Nanocrystalline Semiconductor Film, *J. Phys. Chem.* 1996, **100**, 1027-1035.
- ⁵⁹ N. Satoh, T. Nakashima, K. Yamamoto, Metastability of anatase: size dependent and irreversible anatase-rutile phase transition in atomic-level precise titania, *Nature Scientific Reports*, 2013, **3**, 1959.
- ⁶⁰ J. Zhang, P. Zhou, J. Liub, J. Yu, New understanding of the difference of photocatalytic activity among anatase, rutile and brookite TiO₂, *Phys. Chem. Chem. Phys.*, 2014, **16**, 20382-20386.
- ⁶¹ C. Kormann, D.W. Bahemann, M.R. Hoffmann, Preparation and characterization of quantum-size titanium dioxide, *J. Phys. Chem.*, 1988, **92**, 5196-5201.
- ⁶² J.J. Kasinski, L.A. Gomez-Jahn, K.J. Faran, S. M. Gracewski, R.J. Dwayne Miller, Picosecond dynamics of surface electron transfer processes: Surface restricted transient grating studies of the n-TiO₂/H₂O interface, *J. Chem. Phys.*, 1989, **90**, 1253-1269.
- ⁶³ M. Grätzel, *Heterogeneous photochemical electron transfer*, CRC press Boca Raton, 1989.
- ⁶⁴ E. Burstein, Anomalous optical absorption limit in InSb. *Phys. Rev.*, 1954, **93**, 632-633.
- ⁶⁵ K. G. Saw, N. M. Aznan, F. K. Yam, S. S. Ng, S. Y. Pung, New Insights on the Burstein-Moss Shift and Band Gap Narrowing in Indium-Doped Zinc Oxide Thin Films, *PLoS One*, 2015, **10**, e0141180.
- ⁶⁶ M. Wu, G. Lin, D. Chen, G. Wang, D. He, S. Feng, R. Xu, Sol-Hydrothermal Synthesis and Hydrothermally Structural Evolution of Nanocrystal Titanium Dioxide, *Chem. Mater.*, 2002, **14**, 1974-1980.
- ⁶⁷ G. Calleja, D.P. Serrano, R. Sanz, P. Pizarro, A. Garcia, Study on the Synthesis of High-Surface-Area Mesoporous TiO₂ in the Presence of Nonionic Surfactants, *Ind. Eng. Chem. Res.*, 2004, **43**, 2485-2492.
- ⁶⁸ Y. Kayanuma, Quantum-size effects of interacting electrons and holes in semiconductor microcrystals with spherical shape, *Phys. Rev. B*, 1988, **38**, 9797-9805.

- ⁶⁹ R. Thapa, S. Maiti, T.H. Rana, U.N. Maiti, K.K. Chattopadhyay, Anatase TiO₂ nanoparticles synthesis via simple hydrothermal route: Degradation of Orange II, Methyl Orange and Rhodamine B, *J. Mol. Cat. A: Chem.*, 2012, **363-364**, 223-229.
- ⁷⁰ P.K. Shen, S. Yin, Z. Li, C. Chen, Preparation and performance of nanosized tungsten carbides for electrocatalysis, *Electr. Acta*, 2010, **55**, 7969–7974.
- ⁷¹ J.M. Hanlon, L.B. Diaz, G. Balducci, B.A. Stobbs, M. Bielewski, P. Chung, I. MacLaren, D.H. Gregory, Rapid surfactant-free synthesis of Mg(OH)₂ nanoplates and pseudomorphic dehydration to MgO, *Cryst. Eng. Comm.*, 2015, **17**, 5672-5679.
- ⁷² V. Etacheri, G. Michlits, M. K. Seery, S.J. Hinder, S. C. Pillai, A Highly Efficient TiO_{2-x}C_x Nano-heterojunction Photocatalyst for Visible Light Induced Antibacterial Applications, *ACS Appl. Mater. Interf.*, 2013, **5**, 1663–1672.
- ⁷³ L.B. Xiong, J.-L. Li, B. Yang, Y. Yu, Ti³⁺ in the Surface of Titanium Dioxide: Generation, Properties and Photocatalytic Application, *J. Nanomat.* 2012, 831524.
- ⁷⁴ Y.G. Zhang, L.L. Ma, J.L. Li, Y. Yu, In Situ Fenton Reagent Generated from TiO₂/Cu₂O Composite Film: a New Way to Utilize TiO₂ under Visible Light Irradiation, *Environ. Sci. Tech.*, 2007, **41**, 6264-6269.
- ⁷⁵ J. Li, L. Liu, Y. Yu, Y. Tang, H. Li, F. Du, Preparation of highly photocatalytic active nano-size TiO₂-Cu₂O particle composites with a novel electrochemical method, *Electrochem. Comm.*, 2004, **6**, 940-943.
- ⁷⁶ S. Koliyat Parayil, H.S. Kibombo, C. Wu, R. Peng, J. Baltrusaitis, R.T. Koodali, Enhanced photocatalytic water splitting activity of carbon-modified TiO₂ composite materials synthesized by a green synthetic approach, *Int. J. Hydr. En.*, 2012, **37**, 8257-8267.
- ⁷⁷ J. Park, T. Back, W.C. Mitchel, S.S. Kim, S. Elhamri, J. Boeckl, S. B. Fairchild, R. Naik, A.A. Voevodin, Approach to multifunctional device platform with epitaxial graphene on transition metal oxide, *Scientific Reports*, 2015, **5**, 14374.
- ⁷⁸ J.E. Krzanowski, R.E. Leuchtner, Chemical, Mechanical, and Tribological Properties of Pulsed-Laser-Deposited Titanium Carbide and Vanadium Carbide, *J. Am. Ceram. Soc.*, 1997, **80**, 1277-1280.
- ⁷⁹ E. Enko, T.L. Barr, S. Hardcastle, E. Hoppe, A. Bernasik, J. Morgiel, XPS study of the cBN-TiC system, *Cer. Int.*, 2001, **27**, 637-643.
- ⁸⁰ I. Strydom, S. Hofmann, The contribution of characteristic energy losses in the core-level X-ray photoelectron spectroscopy peaks of TiN and (Ti,Al)N studied by electron energy loss spectroscopy and X-ray photoelectron spectroscopy, *J. Electron Spectr. Related Phenom.*, 1991, **56**, 85-103.
- ⁸¹ L. You-ji, C. Weia, Photocatalytic degradation of Rhodamine B using nanocrystalline TiO₂-zeolite surface composite catalysts: effects of photocatalytic condition on degradation efficiency, *Catal. Sci. Technol.*, 2011, **1**, 802-809.
- ⁸² X. Jiang, T. Herricks, Y. Xia, Monodisperse Spherical Colloids of Titania: Synthesis, Characterization, and Crystallization, *Adv. Mater.*, 2003, **15**, 1205-1208.
- ⁸³ V. Etacheri, M. Seery, S. Hinder, S. Pillai, Nanostructured Ti_{1-x}S_xO_{2-y}N_y Heterojunctions for Efficient Visible-Light-Induced Photocatalysis, *Inorg. Chem.*, 2012, **51**, 7164-7173.
- ⁸⁴ D.J.C. Yates, Infrared Studies of the Surface Hydroxyl Groups on Titanium Dioxide, and of the Chemisorption of Carbon Monoxide and Carbon Dioxide, *J. Phys. Chem.*, 1961, **65**, 746-753.
- ⁸⁵ T. Bezrodna, G. Puchkovska, V. Shymanovska, J. Baran, H. Ratajczak, IR-analysis of H-bonded H₂O on the pure TiO₂ surface, *J. Mol. Struc.*, 2004, **700**, 175–181.
- ⁸⁶ J.V. Bell, J. Heisler, H. Tannenbaum, J. Goldenson, Infrared Spectra of Metal Isopropoxides, *Anal. Chem.*, 1953, **25**, 1720-1724.
- ⁸⁷ M. Mochida, B.J. Finlayson-Pitts, FTIR Studies of the Reaction of Gaseous NO with HNO₃ on Porous Glass: Implications for Conversion of HNO₃ to Photochemically Active NO_x in the Atmosphere, *J. Phys. Chem. A*, 2000, **104**, 9705-9711.
- ⁸⁸ D. Dolat, N. Quici, E. Kusiak-Nejmana, A.W. Morawski, G. Li Puma, One-step, hydrothermal synthesis of nitrogen, carbon co-doped titanium dioxide (N,C TiO₂) photocatalysts. Effect of alcohol degree and chain length as carbon dopant precursors on photocatalytic activity and catalyst deactivation, *App Cat B: Env*, 2012, **115-116**, 81–89.

- ⁸⁹ J. A. Navio, C. Cerrillos, C. Real, Photo-induced Transformation, upon UV Illumination in Air, of Hyponitrite Species $N_2O_2^{2-}$ Preadsorbed on TiO_2 Surface, *Surf. Interface Anal.*, 1996, **24**, 355–359.
- ⁹⁰ R. Urlaub, U. Posset and R. Thull, FT-IR Spectroscopic Investigations on Sol-Gel-Derived Coatings from Acid-Modified Titanium Alkoxides, *J. Non-Cryst. Solids*, 2000, **265**, 276-284.
- ⁹¹ S. Doeuff, M. Henry, C. Sanchez, J. Livage, Hydrolysis of Titanium Alkoxides: Modification of the Molecular Precursor by Acetic Acid, *J. Non-Crystalline Solids*, 1987, **89**, 206-216.
- ⁹² <https://webspectra.chem.ucla.edu/irtable.html> (accessed December 2017).
- ⁹³ N. A. Órdenes-Aenishanslins, L. A. Saona, V.M. Durán-Toro, J. P. Monrás, D. Margarita Bravo, J. M. Pérez-Donoso, Use of titanium dioxide nanoparticles biosynthesized by *Bacillus mycoides* in quantum dot sensitized solar cells, *Microbial Cell Factor.*, 2014, **13**, 90.
- ⁹⁴ E.B. Scheetz, B. White, Vibrational spectra of the alkaline earth double carbonates, *Am. Mineral.*, 1977, **62**, 36-50.
- ⁹⁵ G.C. Kennedy, Pressure-Volume-Temperature relations in water at elevated temperatures and pressures, *Am. J. Sci.*, 1950, **248**, 540-564.
- ⁹⁶ A. Rabenau, The Role of Hydrothermal Synthesis in Preparative Chemistry, *Angew. Chem. Int. Ed. Engl.*, 1985, **24**, 1026-1040.
- ⁹⁷ J.W. Nielsen, R.R. Monchamp, *The Use of Phase Diagrams in Crystal Growth*, in *Phase Diagrams, Materials Science and Technology*, Elsevier, 1970, Vol. 3, pp. 36-37.
- ⁹⁸ J.M. Smith, H.C. van Ness, M.M. Abbott, *Introduction to Chemical Engineering Thermodynamics*, McGraw-Hill, 6th edn. Singapore, 2001.
- ⁹⁹ M. Rajamathi, R. Seshadri, Oxide and chalcogenide nanoparticles from hydrothermal/solvothermal reactions, *Curr. Op. Sol. St. Mat. Sci.*, 2002, **6**, 337-345.
- ¹⁰⁰ J.R. Elliott, C.T. Lira, *An Introduction to Applied Thermodynamics* (2nd. ed.).
- ¹⁰¹ Parr Instrument Company, *Safety in the Operation of Laboratory Reactors and Pressure Vessels*, 2005.
- ¹⁰² G. B. Dudley, R. Richertb, A. E. Stiegman, On the existence of and mechanism for microwave specific reaction rate enhancement, *Chem. Sci.*, 2015, **6**, 2144-2152.
- ¹⁰³ S. Komarneni, M. Katsuki, Microwave-hydrothermal synthesis of barium titanate under stirring condition, *Ceram. Int.*, 2010, **36**, 1165-1169.
- ¹⁰⁴ M. Niederberger, Nonaqueous Sol-Gel Routes to Metal Oxide Nanoparticles, *Acc. Chem. Res.*, 2007, **40**, 793–800.
- ¹⁰⁵ A. Chemseddine, T. Moritz, Nanostructuring titania: Control over nanocrystal structure, size, shape, and organization. *Eur. J. Inorg. Chem.*, 1999, **235**, 45.
- ¹⁰⁶ C. Sanchez, J. Livage, M. Henry, F. Babonneau, Chemical Modification of alkoxide precursors, *J. Non-Cryst. Sol.*, 1988, **100**, 65-76.
- ¹⁰⁷ M.N. Cullinane, S.J. Chard, G.F. Price, B.B. Millward, G. Langois, Organic derivatives of titanium II, Preparation and properties of some ortho-esters, *J. Appl. Chem.*, 1951, **1**, 400-406.
- ¹⁰⁸ B. Yoldas, Hydrolysis of titanium alkoxide and effects of hydrolytic polycondensation parameters, *J. Mat. Sci.*, 1986, **21**, 1087-1092.
- ¹⁰⁹ U. Schubert, Chemical modification of titanium alkoxide for sol-gel processing, *J.Mater.Chem.*, 2015, **15**, 3701-3715.
- ¹¹⁰ C. Wang, J.Y. Ying, Sol-Gel Synthesis and Hydrothermal Processing of Anatase and Rutile Titania Nanocrystals, *Chem. Mater.*, 1999, **11**, 3113-3120.
- ¹¹¹ J. Livage, M. Henry, C. Sanchez, Sol-gel chemistry of transition metal oxides, *Prog. Solid St. Chem.*, 1988, **18**, 259-341.
- ¹¹² M. Gopal, W.J. Moberly, Y Chan, L.C. De Jonghe, Room temperature synthesis of crystalline metal oxides, *J. Mat. Sci.*, 1997, **32**, 6001- 6008.
- ¹¹³ Y. Li, Y. Yang, M. Guo, M. Zhang, Influence of acid type and concentration on the synthesis of nanostructured titanium dioxide photocatalysts from titanium-bearing electric arc furnace molten slag, *RSC Adv.*, 2015, **5**, 13478-13487.

- ¹¹⁴ N. Satoh, T. Nakashima, K. Yamamoto, Metastability of anatase: size dependent and irreversible anatase-rutile phase transition in atomic-level precise titania, *Nature Scientific Reports*, 2013, **3**, 1959.
- ¹¹⁵ G. Oskam, A. Nellore, R. Lee Penn, P.C. Searson, The Growth Kinetics of TiO₂ Nanoparticles from Titanium(IV) Alkoxide at High Water/Titanium Ratio, *J. Phys. Chem. B*, 2003, **107**, 1734-1738.
- ¹¹⁶ C.J. Cadman, A. Pucci, F. Cellesi, N. Tirelli, Water-Dispersible, Ligand-Free, and Extra-Small (<10 nm) Titania Nanoparticles: Control Over Primary, Secondary, and Tertiary Agglomeration Through a Modified “Non- Aqueous” Route, *Adv. Funct. Mater.*, 2014, **24**, 993–1003.
- ¹¹⁷ C. Wang, F. Wang, Y. Zhao, Y. Li, Q. Yue, Y. Liu, Y. Liu, A.A. Elzatahry, A. Al-Enizi, Y. Wu, Y. Deng, D. Zha, Hollow TiO_{2-x} porous microspheres composed of well crystalline nanocrystals for high-performance lithiumion batteries, *Nano Res.*, 2016, **9**, 165–173.
- ¹¹⁸ S. Eiden-Assmann, J. Widoniak, G. Maret, Synthesis and Characterization of Porous and Nonporous Monodisperse Colloidal TiO₂ Particles, *Chem. Mater.*, 2004, **16**, 6-11.
- ¹¹⁹ X. Wang, J. Tian, C. Fei, L. Lv, Y. Wang, G. Cao, Rapid construction of TiO₂ aggregates using microwave assisted synthesis and its application for dye-sensitized solar cells, *RSC Adv.*, 2015, **5**, 8622-8629.
- ¹²⁰ V. K. La Mer, R. H. Dinegar, Theory, Production and Mechanism of Formation of Monodispersed Hydrosols, *J. Am. Chem. Soc.*, 1950, **72**, 4847-4854.
- ¹²¹ V. K. LaMer, Nucleation in Phase Transitions, *Ind. Eng. Chem.*, 1952, **44**, 1270-1277.
- ¹²² G. H. Bogush, C.F. Zukoski, Studies of the Kinetics of the Precipitation of Uniform Silica Particles through the Hydrolysis and Condensation of Silicon Alkoxides, *J. Colloid Int. Sci.*, 1991, **142**, 1-18.
- ¹²³ G. Kaptay, The Gibbs Equation versus the Kelvin and the Gibbs-Thomson Equations to Describe Nucleation and Equilibrium of Nano-Materials, *J. Nanosci. Nanotechnol.*, 2011, **12**, 1-9.
- ¹²⁴ Y. Zhang, S. Zhang, K. Wang, F. Ding, J. Wu, Surfactant-Free Solvothermal Method for Synthesis of Mesoporous Nanocrystalline TiO₂ Microspheres with Tailored Pore Size, *J. Nanomat.*, 2013, 294020.
- ¹²⁵ Q. Zhang, L. Gao, Preparation of Oxide Nanocrystals with Tunable Morphologies by the Moderate Hydrothermal Method: Insights from Rutile TiO₂, *Langmuir*, 2003, **19**, 967-971.
- ¹²⁶ B. Ohtani, O.O. Prieto-Mahaney, D. Li, R. Abe, What is Degussa (Evonik) P25? Crystalline composition analysis, reconstruction from isolated pure particles and photocatalytic activity test, *J. Photochem. Photobiol. A: Chem.*, 2010, **216**, 179-182.
- ¹²⁷ X. Li, Y. Qu, X. Xie, Z. Wang, R. Li, Preparation of SrAl₂O₄: Eu²⁺, Dy³⁺ nanometer phosphors by detonation method, *Mat. Lett.*, 2006, **60**, 3673–3677.
- ¹²⁸ Y. Qu, C. Sun, G. Sun, X. Kong, W. Zhang, Preparation, characterization, and kinetic and thermodynamic studies of mixed-phase TiO₂ nanoparticles prepared by detonation method, *Res. Phys.*, 2016, **6**, 100–106.
- ¹²⁹ S.Y. Chae, M.K. Park, S.K. Lee, T.Y. Kim, S.K. Kim, W.I. Lee, Preparation of Size-Controlled TiO₂ Nanoparticles and Derivation of Optically Transparent Photocatalytic Films, *Chem. Mater.*, 2003, **15**, 3326-3331.
- ¹³⁰ F. Izumi, The Polymorphic Crystallisation of Titanium(IV) Oxide under Hydrothermal Conditions. II) The Roles of Inorganic Anions in the Nucleation of Rutile and Anatase from Acid Solutions, *Bullet. Chem. Soc. Jap.*, 1978, **51**, 1771-1776.
- ¹³¹ Y. Li, Y. Yang, M. Guo, M. Zhang, Influence of acid type and concentration on the synthesis of nanostructured titanium dioxide photocatalysts from titanium-bearing electric arc furnace molten slag, *RSC Adv.*, 2015, **5**, 13478- 13487.
- ¹³² Y. Zhang, P.S. Cremer, Interactions between macromolecules and ions: the Hofmeister series, *Curr. Opin. Chem. Bio.*, 2006, **10**, 658-663.
- ¹³³ L. Li, J. Yan, T. Wang, Z.-J. Zhao, J. Zhang, J. Gong, N. Guan, Sub-10 nm rutile titanium dioxide nanoparticles for efficient visible-light-driven photocatalytic hydrogen production, *Nature Comm.*, 2015, **6**, 5881.
- ¹³⁴ M. Gopal, W.J. Moberly Chan, L.C. De Jonghe, Room temperature synthesis of crystalline metal oxides, *J. Mat. Sci.*, 1997, **32**, 6001- 6008.

- ¹³⁵ L.I. Bekkerman, I.P. Dobrovolskii, A.A. Ivakin, Effect of composition of titanium(IV) solutions and precipitation conditions on solid-phase structure, *Russ. J. Inorg. Chem.*, 1976, **21**, 233.
- ¹³⁶ Y. Hu, H.-L. Tsai, C.L. Huang, Phase transformation of precipitated TiO₂ nanoparticles, *Mat. Sci. Eng.*, 2003, **A344**, 209-214.
- ¹³⁷ Q. Zhang, L. Gao, J. Guo, Effects of Calcination on the Photocatalytic Properties of Nanosized TiO₂ Powders Prepared by TiCl₄ Hydrolysis, *App. Cat. B: Environ.*, 2000, **26**, 207-215.
- ¹³⁸ C.P. Siby, S. Rajesh Kumar, P. Mukundan, K.G.K. Warriar, Structural Modifications and Associated Properties of Lanthanum Oxide Doped Sol–Gel Nanosized Titanium Oxide, *Chem. Mater.*, 2002, **14**, 2876–2881.
- ¹³⁹ V. Gombac, L. De Rogatis, A. Gasparotto, G. Vicario, T. Montini, D. Barreca, G. Balducci, P. Fornasiero, E. Tondello, M. Graziani, TiO₂ nanopowders doped with boron and nitrogen for photocatalytic applications, *Chem. Phys.*, 2007, **339**, 111–123.

List of Abbreviation used in Chapter 4

- BET:** Brunauer-Emmett-Teller (*model for surface area measurement*)
BJH: Barrett-Joyner-Halenda (*model for pore volume and size distribution*)
DFT: Density Functional Theory
DR-UV-Vis: Diffuse Reflectance-Ultraviolet-Visible light spectroscopy
DSSC: Dye-Sensitised Solar Cell
DTA: Differential Thermal Analysis
EDX: Energy Dispersive X-ray Spectroscopy
EPR: Electron Paramagnetic Resonance
FMH: Flash Microwave-assisted Hydrothermal synthesis
FT-IR: Fourier Transform Infrared Spectroscopy
HPLC: High-Performance Liquid Chromatography
MS: Mass Spectrometry
MW: Microwave (radiation)
NHE: Normal Hydrogen Electrode
PTFE: Polytetrafluoroethylene
PXD: Powder X-ray Diffraction
RhB: Rhodamine B
SEM: Scanning Electron Microscopy
STA: Simultaneous Thermal Analysis
TEM: Transmission Electron Microscopy
TGA: Thermogravimetric Analysis
TOC: Total Organic Carbon
TTIB: Titanium butoxide
TTIP: Titanium isopropoxide
UV: Ultraviolet (*radiation*)
Vis: Visible light (*radiation*)
XPS: X-ray photoelectron spectroscopy

Sample labelling

- NE:** particles synthesised using HNO₃ in ethanol
SV: Static Vacuum
DV: Dynamic Vacuum

Chapter 4

Towards active visible-light photocatalysis: reducing treatment and vacuum activation

4.1 Introduction

The highest performance of TiO₂ is observed when it is irradiated by ultraviolet light, at wavelengths corresponding to the band gap (*ca.* 3.25 eV, 387 nm). For higher wavelength, the efficiency of titania is much lower. Inevitably this limits TiO₂ as a photoactive material, preventing its exploitation under sunlight or other visible light sources. Only 5% of the solar spectrum at the Earth's surface is in the UV region. However, TiO₂ is to date unchallenged by other materials given the cost-benefit balance for technological applications. The extension of TiO₂ photoactivity towards longer wavelengths has been a focal point of research for decades, allowing the access to the so-called "second generation" of photocatalysts.^[1,2] All visible-light activation or sensitisation methods modify the electronic levels of the material in order to reduce the band gap, creating intermediate levels or junctions to promote the electronic transitions. The principal methods to achieve this were introduced in chapter 1 (section 1.7.3). The most successful doping methods often involve the use of relatively expensive materials, such as lanthanides, or expensive techniques such as ion implantation, all factors which discourage scaling-up visible-light active catalyst production.^[3] To date, commercial materials are limited to a handful of products. In other cases, despite the use of less expensive materials (e.g. transition metals, carbon-containing compounds), the doping process introduces further impurities in the original structure, causing thermal or structural instability and most of all increasing the density of recombination centres. Despite the potential ability of the impurity levels to trap the charge carriers, these delays fast recombination and allowing the migration of the carriers to the particle surface, the presence of recombination centres could be detrimental because of the progressive quenching of the trapped charges.^[4] Although some photocatalysts have proved to be promising under visible light, they are ineffective in specific applications due to their electronic structure (e.g. not a negative enough flat band potential for H₂ reduction in water splitting)^[5] or due to their instability in water (e.g. CdS).^[6]

For all these reasons, combining a simple synthesis procedure for nano-sized TiO₂ with a similarly simple and efficient doping technique could pave the way for the realisation of an affordable commercial product. The use of non-oxidizing atmospheres in the post-synthesis treatment can improve the quality of the final product.

4.1.2 Aims

The final purpose of the experimental investigation of this chapter is production of visible-light active photocatalyst. In particular, calcination, reducing treatments and vacuum activation were selected as simple methods to improve the photocatalytic activity of the mesoporous TiO₂ sub-microparticles prepared by Flash Microwave-assisted hydrothermal synthesis (FMH), which synthesis was previously described (chapter 3). The samples treated with the different procedures have to show improvement of the photodegradation properties towards a model organic molecule, rhodamine B, used as representative of a general pollutant. The ultimate goal is to outperform the photodegradation of rhodamine by commercial TiO₂ reference materials, such as Aeroxide® P25, which represents the benchmark for TiO₂ catalysts.

The selected methods represent relatively-environmentally friendly and cost-effective procedure compared to more complex doping techniques. Calcination aims to “imitate” the properties of P25 tuning the composition of anatase and rutile. On the other hand, reducing treatment and vacuum activation are designed to induce stoichiometric defects in the TiO₂ structure, such as Ti³⁺, or interstitial/substitutional defects of atoms not originally present, nitrogen for instance. Furthermore, other methods, such as hydrogenation direct MW irradiation of powdered samples, were also chosen with the purpose of introduce useful modification for the improvement of the photocatalytic properties.

4.2 Synthesis and treatments

4.2.1 Calcination

FMH-TiO₂ particles were calcined at different temperature and times in box muffle furnaces. The calcination treatments were performed in at constant heating rate (10 K/min). All samples were collected after cooling to room temperature.

Reference samples (anatase) and commercial catalyst (P25, Kronos) underwent a similar treatment to allow comparison.

4.2.2 Post-synthesis thermal treatment under specific atmosphere

4.2.2.1 Inert gases

Calcination under inert gas was performed under a constant gas flow in a tube furnace. The samples were placed in alumina boats and put in the heating zone of the furnace. The furnace was sealed with flanges directly connected to the gas line. The tube was purged with pure nitrogen or argon for at least 30 min prior to heating. The samples were calcined at different temperature, ranging from 573-973 K.

4.2.2.2 Reactive atmosphere

Using the same setup described in the previous section, ammonia and hydrogen were used as reactive gases for the particle post-treatments. In particular, NH₃ was used for thermal ammonolysis, based on the thermal dissociation of ammonia into N₂ and H₂:



This reaction occurs in a single step and is exothermic, with $\Delta H_{298K}^0 = -54.6$ kJ/mol and thermodynamically favoured at a temperature higher than 454 K (181 °C). However, the complete conversion of ammonia into the two gases occurs at higher temperature, depending on the heating rate. For instance, the NH₃ dissociation onset was reported at 843 K using a temperature program of around 3 K/min. [7] As an alternative to ammonia, hydrogen was used in 5% by volume mixtures with inert gases (argon or nitrogen) in order to verify the possibility of directly reducing the treated material.

4.2.2.3 Post-synthesis vacuum activation

Vacuum annealing was performed using two different configurations, in a flanged stainless steel vessel (under continuous pumping, in dynamic conditions) and in a sealed quartz tube (under static conditions). The quartz tubes were sealed under “low” (2 to 5 Pa) and “medium” (10⁻⁴ to 5·10⁻³ Pa) vacuum using a methane-oxygen

flame. The flanged reactor vessel was evacuated at the same pressures and placed in an apposite furnace. The sealed tubes were heated in a box furnace in conditions analogous to the calcination under air.

4.2.2.4 Microwave activation under vacuum

Attempt were also made to study the effect of direct MW irradiation on TiO₂ samples under vacuum. The samples were sealed under vacuum in glass tubes and irradiated without the use of MW susceptor (a substance which can efficiently absorb MW radiation and convert to heat, such as SiC and graphite). In some cases, a rotary pump was connected directly to open tubes to perform reactions under dynamic conditions. The MW treatment was performed in a single-mode (SM) MW cavity (CEM Discovery), modified to perform solid state reactions.

4.3 Overview of commercial photocatalysts

4.3.1 Aeroxide[®] P25

P25 is considered the benchmark for TiO₂-based photocatalysis, presenting the best performance in processes such as pollutant degradation or water splitting.^[8,9] P25 is produced in a process similar to flame spray pyrolysis (Aerosil[®] process, designed for the production of fumed silica). TiCl₄ is vaporized, mixed with air and hydrogen and passed through a burner at temperatures between 1273 - 2673 K.^[10] The process leads to a distinctive structure for the photocatalyst, with very small crystalline grains (around 20 nm) and the simultaneous presence of both anatase and rutile, with the former the predominant phase (*ca.* 80 wt%). Apart from the beneficial effects of the nanometric size, the secret of the good performance of this catalyst is ascribed to the polymorphic homojunction. Among the different theories proposed to explain the superior photocatalytic efficiency compared to single polymorphs, the close contact between the two crystalline phases would efficiently separate the photo-induced charge carriers, with the electrons migrating to anatase and the holes remaining in the rutile phase.^[11] The suppression of the recombination processes enhances the promotion of photocatalytic reactions, since the charge carriers are free to move towards the material surface. The exact relative concentration of the two polymorphs is still under debate, with the concentration of anatase reported in the range 70-85%.

The Rietveld refinement performed on the PXD pattern of P25 gave around 85% of anatase, and 18% rutile (Figure 4.1 and Table 4.1). Recently, the presence of an additional amorphous component in the structure of P25 has been demonstrated through comparison of different mixtures of anatase and rutile and by the addition of a standard such as corundum or CaF_2 . The amount of amorphous phase had been estimated in the range between 8 -13%. [12] Besides experimental and systematic errors, the discrepancies reported for the characteristics of P25 (see for example the surface area and pore characteristic values in section 3.5.3) are allegedly due to some modification of the production protocols by the supplier company. Newer formulations contain more and smaller grains of anatase, increasing the surface area to $61 \text{ m}^2/\text{g}$ from the previously reported $50 \pm 15 \text{ m}^2/\text{g}$. [13]

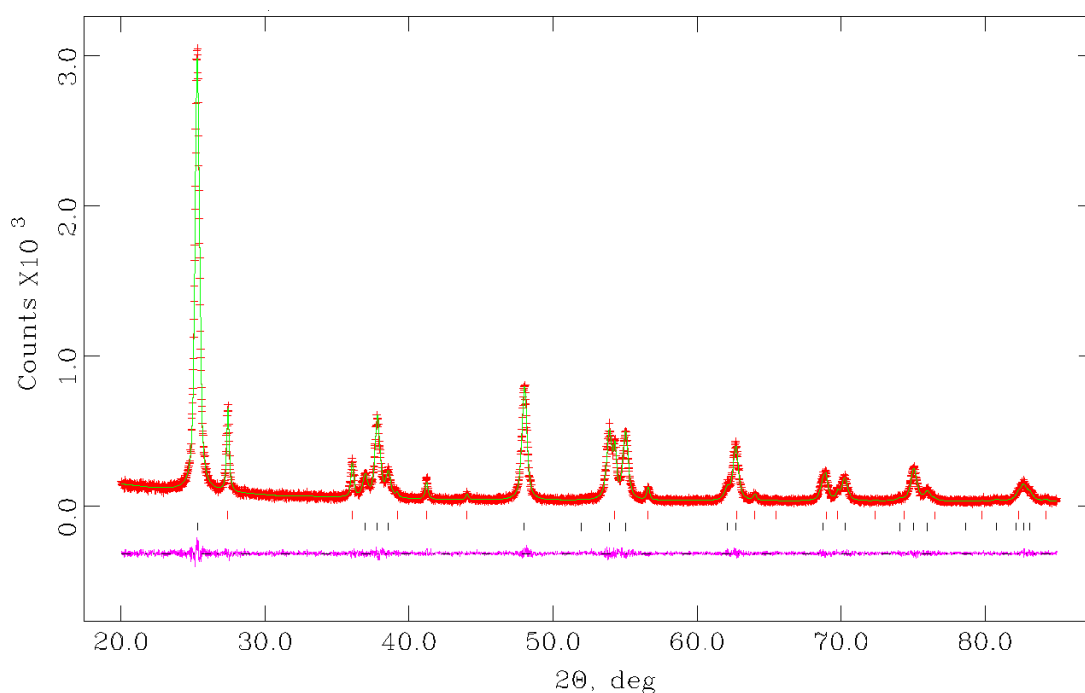


Figure 4.1: Rietveld refinement against PXD data for Aerioxide P25: experimental pattern (red), calculated pattern (green) difference profile (purple) and tick marks for anatase (blue) and rutile (red) phases.

Table 4.1 Result of the Rietveld refinement for Aeroxide P25, with the estimated relative concentration of the two polymorphs.

	Anatase	Rutile
Lattice parameters		
a(Å)	3.786(1)	2.960(2)
c(Å)	9.507(4)	4.595(2)
V(Å ³)	136.287(1)	62.480(8)
Molecular weight (g/mol)	296.28	144.847
Density (g/cm ³)	3.617	3.850
Phase Fraction (wt%)	0.853	0.147
<hr/>		
No. of variables	33	
No. of observations	4187	
R _{wp} %	6.85	
R _p %	5.53	
χ ²	1.124	

4.3.2 Kronos7000

Kronos VLP 7000 was one of the first commercial TiO₂-based visible-light active photocatalyst. It appears as a light beige powder. According to the information provided by the supplier, this photocatalyst could be used for a wide range of indoor and outdoor photodegradation processes. The activation under visible light irradiation should be provided by carbon doping.^[14] The structural characteristics and physical properties of this material are very similar to the FMH-TiO₂ microspheres described in the previous section. As observed in Figure A.19 in the Appendix, the PXD peaks can be associated unequivocally to anatase. The crystalline structure of Kronos is typical of nanocrystalline material, with occurrence of quantum size broadening which causes peak overlapping and loss of signal definition, since not more than eight peaks are distinguishable. The Scherrer calculation provided a crystallite size of ca. 10 nm, comparable with previously reported results.^[14,15,16] However, Tobaldi *et al.* reported a bimodal distribution of grains, centred at 3 and 10 nm.^[16] As for P25, the presence of amorphous phase is still under debate, with the reported content of the anatase phase between 87.5 - 95% and no indication about the nature of the remaining percentage.^[17, 18] Apart from a similar microstructure to the FMH-TiO₂ microspheres, Kronos also has a high surface area, reported to be ca. 250 m²/g for the commercial catalyst.

In Figure 4.2, the comparison between the optical behaviour of the commercial photocatalysts and the single TiO₂ polymorphs clearly evidence how the structural differences have an effect on the electronic structure of the materials. Comparing the absorption edges (Figure 4.2 **a**), the rutile edge is at lower frequency, corresponding to a direct band gap of ca. 3.02 eV. In P25 and Kronos, the shapes of the Kubelka-Munk function (Figure 4.2 **b**) is characteristic of the polymorph structures. P25 exhibits a convolution of the anatase and rutile (coexisting phases in the material) contributions.

Kronos displays an indirect band gap of 3.30 eV, comparable with the value of 3.28 eV reported by Tobaldi *et al.* [16] The value is higher compared with the one reported for pure anatase, presumably due to the quantum-size blueshift already observed in the FMH-TiO₂ nanostructured particles described in the previous chapter. Another important feature for Kronos is the tail at the base of the sigmoidal slope in the absorption spectra. The presence of this non-zero absorption tail, defined as an Urbach tail, reveals the presence of localised states in the band gap.^[19] For this material, the localised states are attributed to C-doping, which reduces the energy required for an optical transition and shifts the photon absorption towards visible-light wavelengths.^[20] The comparison between pure anatase, Aeroxide P25 and Kronos structural and corresponding optical properties is summarised in Table 4.2.

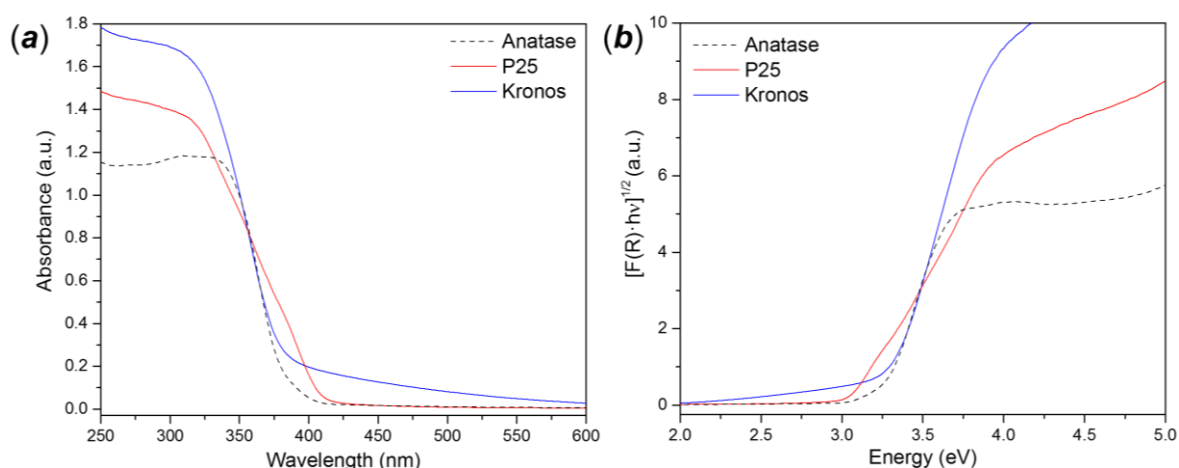


Figure 4.2: (a) Absorbance spectra and (b) Kubelka-Munk function transformation for the optical indirect band gap for pure anatase, rutile, Aeroxide® P25 and Kronos7000.

Table 4.2: Principal characteristics and properties of pure anatase, Aeroxide P25 and Kronos7000 (Raman and band gap results obtained from 3 measurement from samples from the same batch; grain size estimated by Scherrer equation on single measurements using the same diffractometer conditions; band gap error ≤ 0.01 if not indicated).

	Anatase	Aeroxide P25	Kronos7000
Average grain size (nm)	85.1	23.5	9.8
Phase composition (% Anatase)	100	85	100
Optical band gap (indirect) (eV)	3.23	3.09	3.30
Optical band gap (direct) (eV)	3.47	3.63	3.63
Urbach energy (meV)	64 ± 2	40 ± 2	93 ± 4
BET surface area (m ² /g)	9 ± 2	50 ± 4	250 ± 12

4.4 Effect of the oxidative calcination of FMH-TiO₂

Calcination is a standard post-synthetic step for sol-gel and hydrothermal processes. The as-synthesised products usually contain impurities due to organic precursors or other molecules involved in the synthesis (surfactant or templating molecules). The calcination process guarantees a higher degree of purity and crystallinity, expelling organic moieties and impurities.^[21] On the other hand, the high temperature treatment could lead to loss of initial morphology, loss of internal porosity due to the collapse of the mesoporous structure and consequent reduction of the surface area, one of the most important parameters for the photocatalytic performance of the material.^[22] The optimal balance between degree of crystallinity and surface area is probably the best recipe for the production of an undoped catalyst with performance comparable to the commercial products. In this section the principal post-synthetic treatment for the microparticles previously prepared (chapter 3) is described in detail and compared with the application of the same procedure to the single polymorphs and the commercial photocatalysts.

4.4.1 Crystallite growth and phase transition

In Figure 4.3, the *ex-situ* study of the thermal evolution of the FMH-TiO₂ particles is reported. The crystallinity of the sample is improved with an increase of the temperature (all treatments were performed for 3 hours, with a heating rate of 10 K/min) with the phase transition starting at 773 K and rapidly evolving, as witnessed by the appearance of the rutile peaks in the pattern at 873 K.

A very simple method to determine the relative percentage of anatase and rutile is given by the correlation between the integrated intensity of the most intense peak for both phases; (101) for anatase ($2\theta = 25.30^\circ$) and (110) for rutile ($2\theta = 27.44^\circ$), based on an empirical correlation firstly proposed by Spurr and Myers:^[23]

$$\chi_R = \frac{1}{1 + 0.884 \left(\frac{I_{A(101)}}{I_{R(110)}} \right)} \quad (\text{eq. 4.2})$$

where χ_r is the relative concentration of rutile and I_A and I_R are the intensities of the two peaks. The analysis is relatively simple since the two peaks lie very close to each other. The original formula has since been modified to consider the

presence of brookite or to fit the experimental data more accurately using a quadratic expression.^[24] For example, the conversion rate for the particles in Figure 4.5 is around 50% of rutile, all evolved in 100 K of temperature.

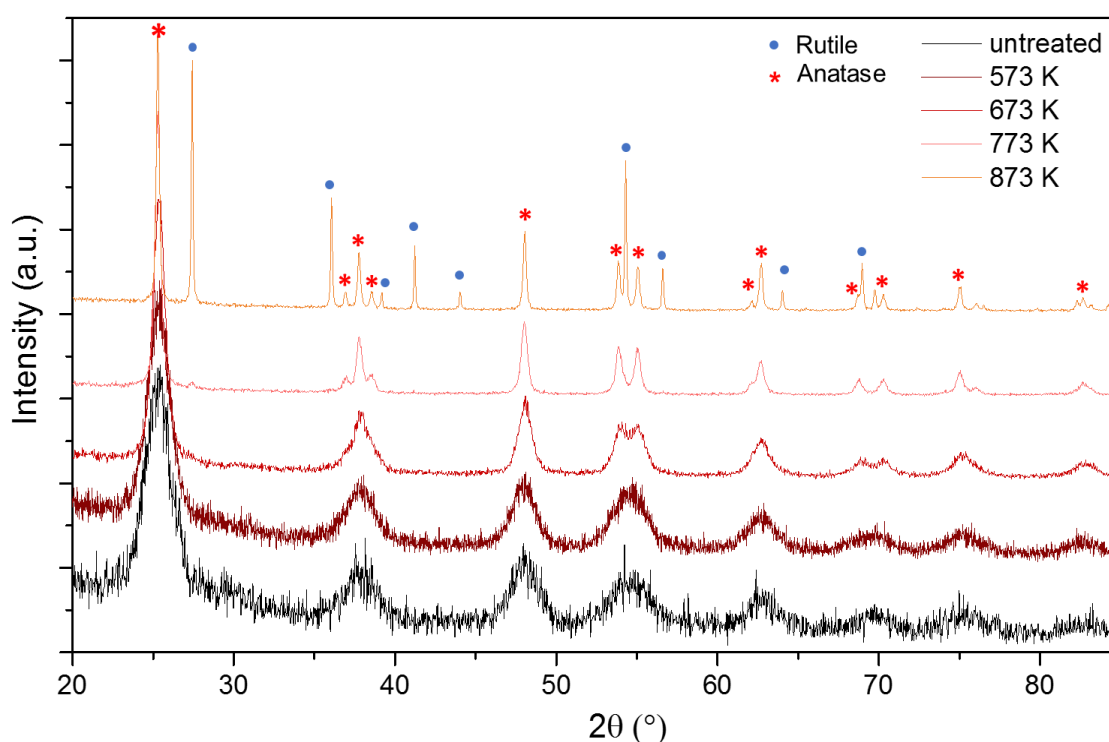


Figure 4.3: Thermal evolution of the crystalline structure of the as-synthesised FMH-TiO₂ particles (series *NE*, 2 M HNO₃ concentration, 162 mM (1:20 in volume) precursor concentration, 1 min treatment at full MW power) under an oxidative atmosphere. The intensity values of the PXD patterns were all normalised to simplify the visual comparison.

Other *ex situ* analyses were performed on different FMH-TiO₂ samples Figure 4.4 *a* shows the grain size of some of the samples calcined in air at different temperatures (773 K, 823 K and 873 K) around that of the observed anatase-to-rutile transition. Different synthesis conditions lead to different structural properties, thus also the thermal evolution will change accordingly, as observed from the data. Particles synthesised using water behaves differently compared to the other produced by ethanol, despite only one sample was tested. Unlike the particles described in Figure 4.3, none of the samples analysed showed phase transition up to 873 K.

Further investigation considered a broader selection of samples. Crystal growth evolution and phase transition were investigated performing *in situ* variable temperature PXD measurements under flowing inert gas (argon) to purge the reaction chamber from released impurities. Figure 4.4 *b* plots the particle size (by Scherrer's formula) against temperature for some selected FMH-TiO₂ samples. The

complete transformation from anatase to rutile was not observed for the analysed samples.

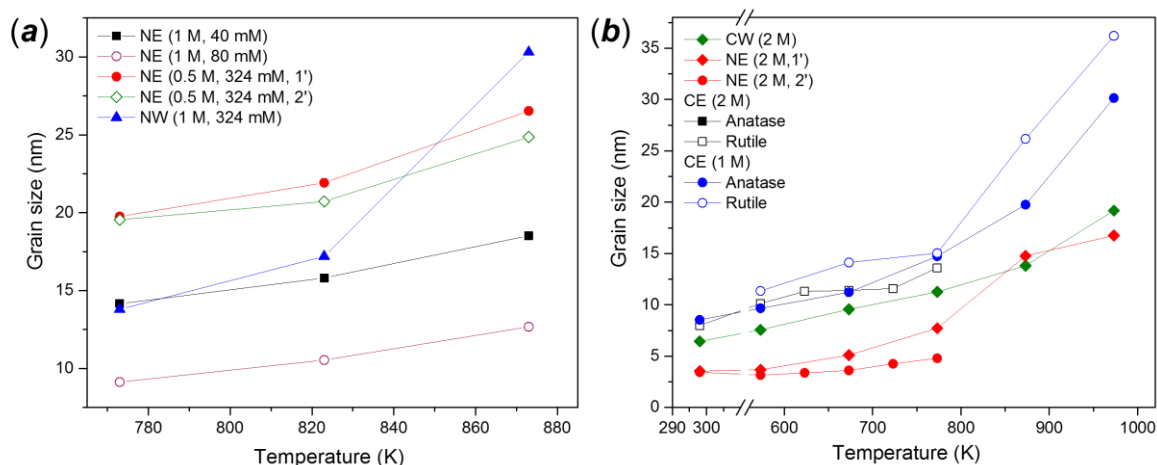


Figure 4.4: Calculation of the average grain size of (a) representative FMH-TiO₂ samples calcined at different temperatures (773, 823 and 873 K) and (b) calcined under constant flow of argon during *in situ* variable temperature measurement (heating ramp 5 K/min).

A more detailed study of the transformation process was performed using two of the samples used for the *in-situ* analysis, one chosen because of the presence of rutile as the most abundant phase (*CE* series, 2 M HCl, 162 mM TTIP) and the other containing rutile phase after calcination (*CE* series, 1 M HCl, 162 mM TTIP). The *in situ* variable temperature PXD of these two samples are shown in and respectively. As shown in Figure 4.5, the relative fractions of anatase and rutile is constant with temperature, whereas the grain size increases (at the expenses of smaller grains).

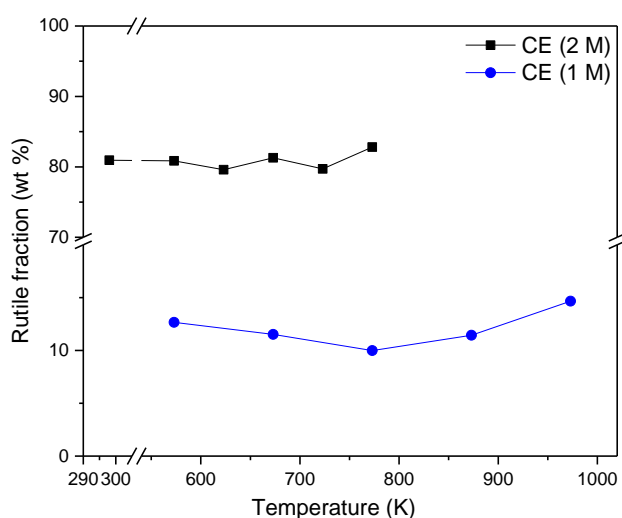


Figure 4.5: Calculation of phase fraction of rutile calculated by integrated intensity from the *in-situ* temperature PXD measurement of different samples. The *in-situ* measurements were performed under a constant argon flow with a heating ramp of 5 K/min.

The precise anatase-to-rutile transition temperature changes with the characteristic of the sample. Among in situ variable temperature measurements, STA analysis represents a very accurate method for the individuation of the precise thermal event. Generally, the anatase-rutile transition is a discrete exothermic event in the differential thermal analysis (DTA) profile.^[25] Figure 4.6 shows the DTA analysis for commercial anatase, Aeroxide P25 and two FMH-TiO₂ samples of the *NE* series, included the one previously described in Figure 4.3. For P25 and anatase, the exothermic transition was observed as a broad exothermic peak occurring with approximately the same amount of energy released (4.39 and 4.46 mW/mg respectively) but at very different temperatures (1023 K for P25, 1446 K for anatase). The transformation of anatase to rutile in P25 has been reported at ca. 1000 K previously.^[26] For the FMH-TiO₂ samples the same event can be observed, but the energy involved is much lower compared to the other two more crystalline materials. For the sample *NE* (2 M acid conc., 162 mM precursor conc.), the temperature of the peak corresponds to the expected transition temperature, as observed from the *ex situ* analysis. On the other hand, the other sample presents a transition temperature higher than P25, which confirms the findings of the *in-situ* temperature variable analysis, in which all samples did not achieve the complete phase transition up to 1000 K.

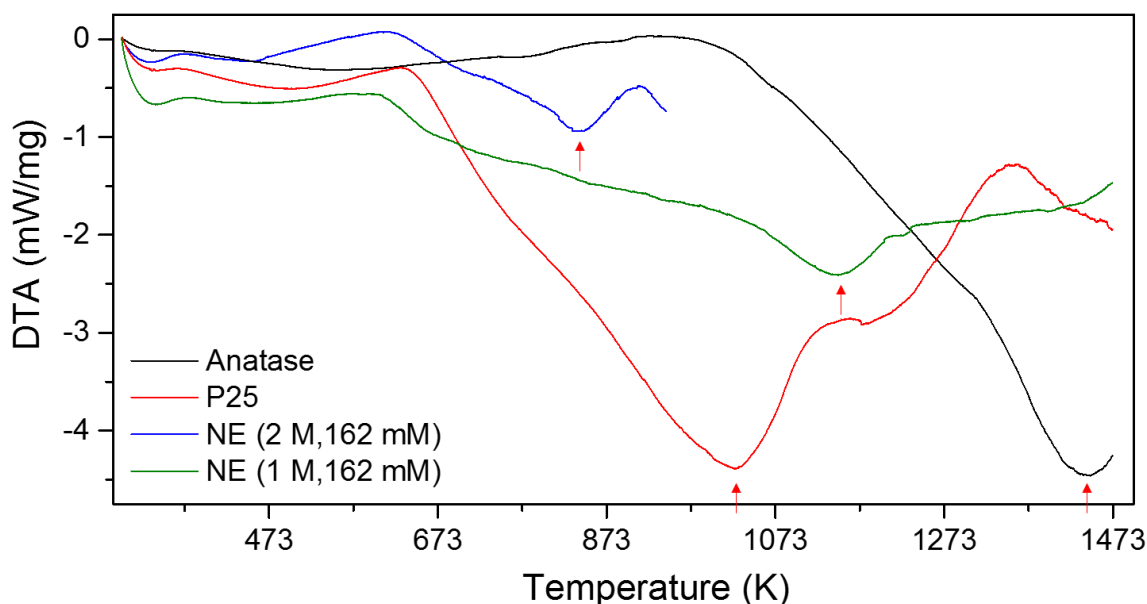


Figure 4.6: Differential thermal analysis (DTA) of commercial anatase, Aeroxide P25 and two representative FMH-TiO₂ samples (*NE* series, 1 M and 2 M acid concentration, both synthesised using 162 mM of precursor concentration).

4.4.2 Optical properties

Regarding the optical properties of the FMH-TiO₂ particles, calcination has the effect of decreasing the band gap values (both direct and indirect), closer to those reported for bulk anatase (Figure 4.7) as would be expected following the growth of the crystallites. The presence of rutile in the crystalline structure of the sample calcined at the highest temperature examined (973 K) has no effect on the optical properties, in contrast to P25 with its mixed phase composition (Figure 4.2). This shed light on the microstructural nature of this catalyst, which are still under debate.^[13] In the calcined particles, the band gap is progressively and uniformly shifted towards the values of rutile. Similar behaviour has been observed by Satoh *et al.* with an almost neat transition of the band gap values in quantum-size TiO₂ by means of optical wave guide (OWG) spectroscopy, corresponding to the irreversible transition to rutile.^[65]

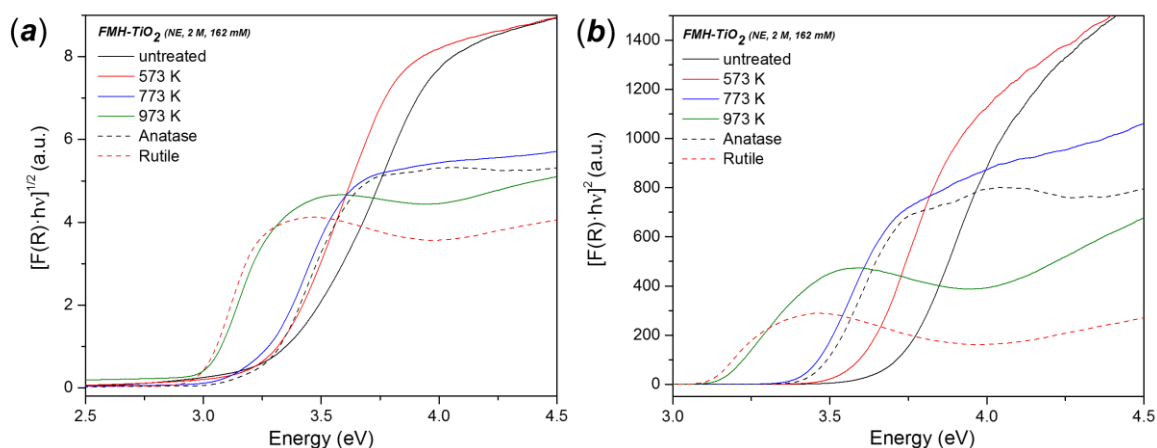


Figure 4.7: Kubelka-Munk functions for (a) direct and (b) indirect band gap calculations of the sample reported in Figure 4.3 as a function of the calcination temperature.

Table 4.3: Band gap and Urbach energy calculations for some representative FMH-TiO₂ samples (acid and precursor concentrations indicated respectively) calcined at different temperature. (calculations based on 3 measurements on the same sample, standard deviation for band gap measurement ≤ 0.01 if not indicated).

Sample	Temperature (K)	Indirect band gap (eV)	Direct band gap (eV)	Urbach energy (meV)
NE (2 M, 162 mM)	<i>untreated</i>	3.38	3.73	110 \pm 13
	573 K	3.30	3.60	84 \pm 5
	773 K	3.22	3.43	73 \pm 3
	973 K	3.01	3.16	48 \pm 5
NE (1 M, 162 mM)	<i>untreated</i>	3.34	3.63	102 \pm 8
	773 K	3.20	3.38	70 \pm 3
	823 K	3.19	3.37	73 \pm 1
	873 K	3.19	3.38	73 \pm 2
NE (1 M, 648 mM)	<i>untreated</i>	3.20	3.38	65 \pm 2
	573 K	3.17	3.35	62 \pm 3
	673 K	3.14	3.32	58 \pm 2
	773 K	3.14	3.32	63 \pm 2

4.4.3 Surface area and pore size

Figure 4.8 *a* shows the N₂ adsorption-desorption isotherms of the products of calcination of the selected **NE** series samples (2 M acid, 162 mM precursor) at different temperature. Calcination reduced the total volume uptake of nitrogen, (hence specific surface area), but increased the level of hysteresis in the isotherms at $T \leq 673$ K, before reduction of hysteresis at $T = 773$ K, as shown in. The results of the calcination on surface area and porosity are shown in Table 4.4. Similarly, the BJH analysis showed an initial increase of pore volume and average pore size up to 673 K, with subsequent reductions at 773 K. The experimental data seem to identify an optimum temperature at which the porosity is enhanced, with clear presence of mesopores (3.5-4 nm of average radius from BJH calculation, shown in Figure 4.8 *b*).

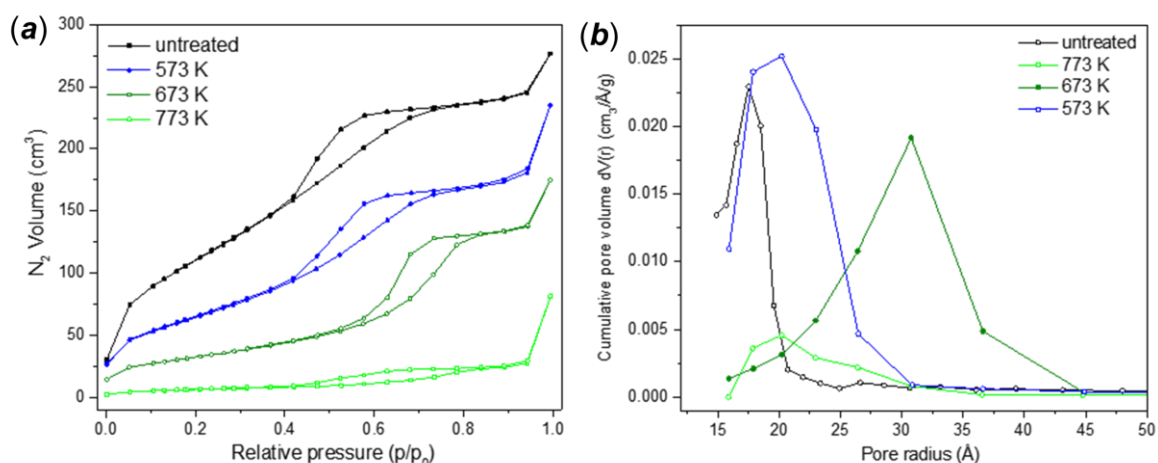


Figure 4.8: (a) Nitrogen adsorption/desorption isotherms and (b) BJH pore size distribution (calculated from the desorption isotherms) for a representative sample belonging to the *NE* series (2 M HNO₃ in ethanol, 162 mM precursor concentration, 1 min MW treatment) before and after calcination (573 – 773 K).

Table 4.4: BET and BJH calculations for the nitrogen adsorption/desorption isotherms of the representative sample belonging to the *NE* series (2 M HNO₃ in ethanol, 162 mM precursor concentration, 1 min MW treatment) before and after calcination (573 – 773 K), which isotherms and BJH porosity are shown in Figure 4.8. (calculations based on 3 repeats on the same sample).

Sample	BET surface area (m ² /g)	BJH pore volume (cm ³ /Å/g)		BJH pore radius (Å)	
		<i>Des</i>	<i>Ads</i>	<i>Des</i>	<i>Ads</i>
Untreated	429.1 ± 9.2	0.37 ± 0.03	0.34 ± 0.03	17.52 ± 0.40	14.86 ± 1.13
573 K	245.8 ± 23.2	0.34 ± 0.03	0.32 ± 0.03	20.21 ± 1.63	22.93 ± 1.97
673 K	112.1 ± 4.8	0.28 ± 0.03	0.27 ± 0.02	30.78 ± 0.62	36.46 ± 9.54
773 K	26.8 ± 3.2	0.14 ± 0.05	0.14 ± 0.01	20.22 ± 0.01	30.87 ± 9.87

4.4.4 Effects of the treatment time

A first estimation of the calcination time on the phase composition and grain size of FMH-TiO₂ microparticles was performed calcining some representative samples belonging to the *NE* series (2 M HNO₃, 162 mM TTIP), for 1, 2 and 3 hours at the temperature chosen for the previous calcination (773 K) and successively performing PXD analysis on these samples. From the PXD patterns showed in Figure 4.9, the crystalline size measured observing from the PXD peak broadening and estimated by the Scherrer's equation (listed in Table 4.5) showed a progressive increase, even though the main crystal growth occurred within the first hour of treatment, with a growth of the crystallite of roughly 400%.

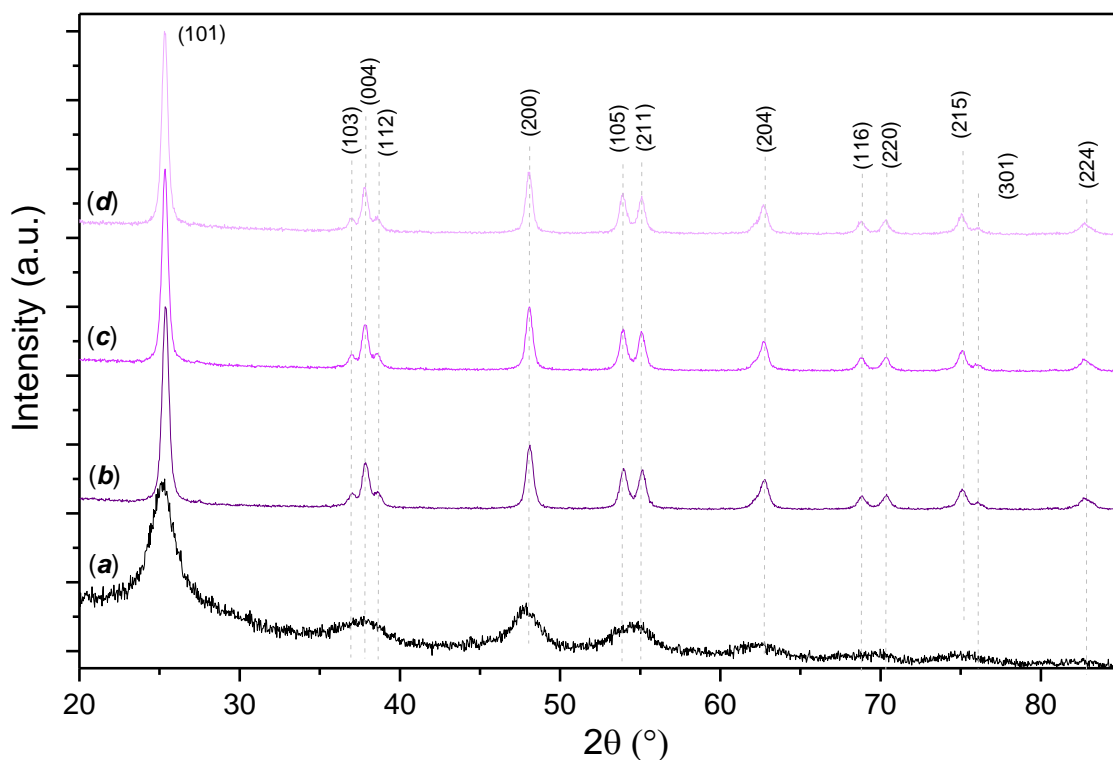


Figure 4.9: PXD patterns for the study of the duration of the calcination for a representative sample of FMH-TiO₂ microparticles. (a) untreated sample and calcined at 773 K for (b) 1h, (c) 2h and (d) 3h.

The effect of the treatment duration on the crystal structure and particle size was also assessed by *in situ* PXD in the angular range $23^\circ < 2\theta / ^\circ < 30^\circ$, which include the most intense peaks of anatase and rutile, (101) and (110) respectively. The heating time was extended up to 8 hours. The data reported in Figure 4.10 show that extended calcining has a limited effect on the crystal growth, with the principal modification occurring within the first 1-2 hours of treatment. Prolonged heating can lead to the progressive transformation of anatase components to rutile above a certain temperature. As shown in Figure 4.10 *b*, the phase transformation appears to be temperature dependent, regardless the initial composition of the sample. P25, which already contains around 20% of rutile, maintains a constant concentration of anatase throughout the full treatment at 773 K. At 973 K, the energy of the thermal treatment is high enough to promote the phase transition, even though the crystalline size growth up to a certain level, after which the grains are directly converted to rutile.

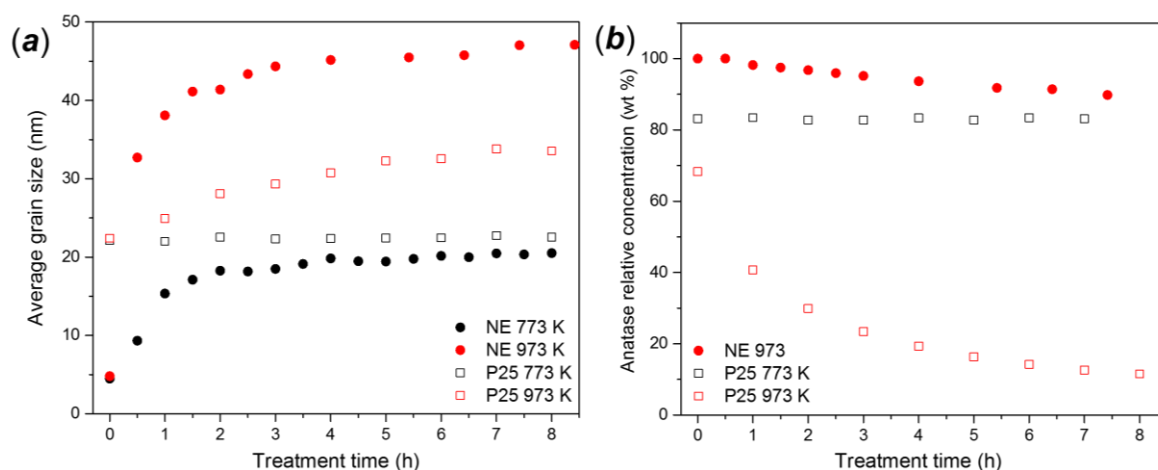


Figure 4.10: (a) Average crystallite size of the particles and (b) relative content of anatase as a function of the treatment time for Aeroxide P25 and FMH-TiO₂ samples.

N₂ sorption isotherms and pore estimation by BJH and DFT methods for the FMH-TiO₂ samples after different calcination times are shown in Figure 4.11. As reported in the previous section, the pore shape fit geometrical models for pores rather than showing irregularity, with cylindrical shape evidenced by typical hysteresis (resembling the H1 IUPAC classification) and accordingly to the DFT model applied to the sorption isotherms, fitting with cylindrical pores observed in carbonaceous material from equilibrium isotherms (Figure 4.11). The duration of the treatment progressively reduces the pore radius, the pore volume and the surface area. The increase of the crystallite size is also witnessed by the reduction of the optical band gap with values closer to that of crystalline anatase. As shown in Figure 4.12, the Kubelka-Munk functions for both indirect and direct band gap changed their shapes, with disappearance of the Urbach tail at lower energies. The band gap values are then slowly changing towards that of bulk anatase, consistently with the increase of the crystallite size, as listed in Table 4.5.

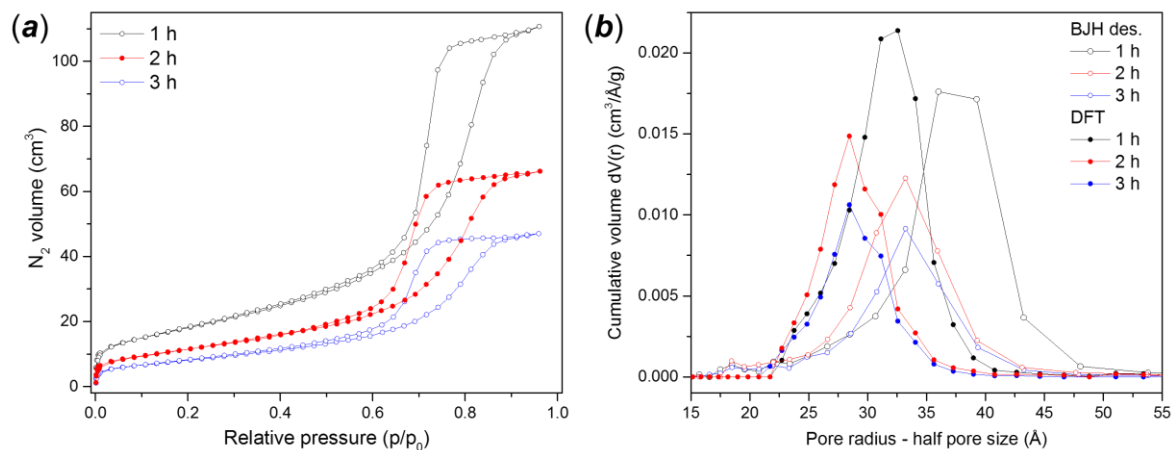


Figure 4.11: (a) N_2 adsorption/desorption isotherms and (b) pore size distribution of FMH-TiO₂ (3 M HNO₃, 162 mM TTIP, 1 min MW treatment) calcined at 773 K for 1, 2 and 3 hours respectively.

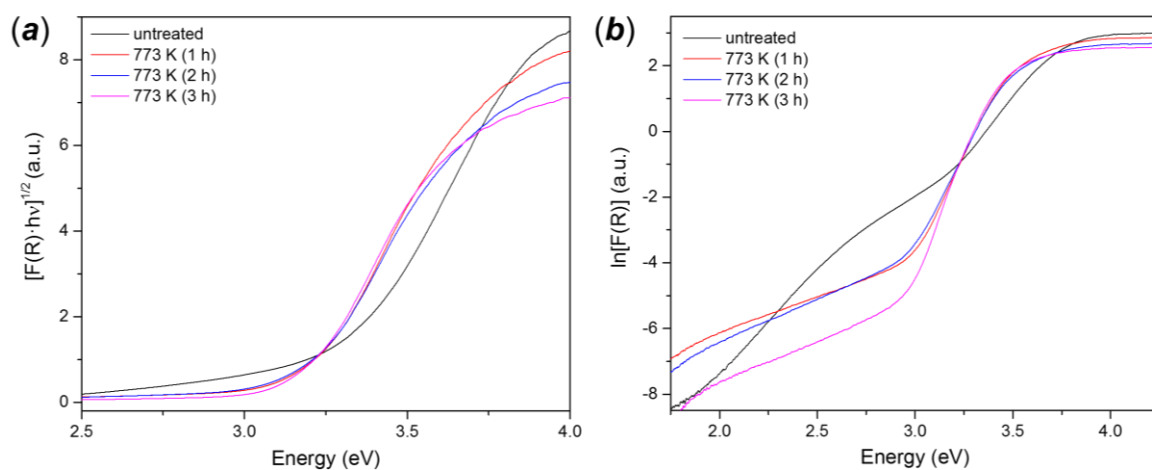


Figure 4.12: Kubelka-Munk functions for the determination of (a) the direct optical band gap and (b) Urbach localised states for the samples calcined in air at constant temperature for different time.

Table 4.5: Influence of the heating time on the microstructural parameters of particles calcined at 773 K (calculations based on 3 measurement on the same sample, standard deviation for band gap measurement ≤ 0.01 if not indicated).

	untreated	1h	2h	3h
Avg. grain size (nm) ^(a)	4.4	16.5	17.3	17.9
BET surface (m ² /g)	-	67.8 \pm 7.2	43.2 \pm 3.7	30.7 \pm 5.3
BJH(d) pore volume (cm ³ /g)	-	0.184 \pm 0.031	0.113 \pm 0.026	0.079 \pm 0.035
BJH(d) avg. pore radius (Å)	-	36.02 \pm 6.34	33.21 \pm 6.53	33.20 \pm 5.31
Band gap, ind.(eV)	3.29	3.20	3.19	3.18
Band gap, dir. (eV)	3.63	3.50	3.47	3.42
Urbach energy (meV)	134 \pm 7	85 \pm 2	80 \pm 2	63 \pm 4

^(a) calculated by Scherrer equation (XRD data), single measurement using same diffractometer conditions

The elemental microanalysis of H, C and N revealed the presence of only traces of these elements (Table A.11 in the Appendix). This suggests all impurities are removed at 773 K. The decrease of carbon and hydrogen suggests that carbonaceous impurities are due to unreacted or trapped precursor molecules, as previously described in section 3.8. Nitrogen impurities are present in small traces. Assuming these latter impurities to originate from the presence of HNO₃ in the synthesis procedure (e.g. giving nitrous oxide), the STA analysis reported in the previous chapter confirmed the release of the impurities below the standard calcination temperature, resulting in minimal residual presence for the samples described in this section. The reduction of the impurities after calcination is also represented by the progressive reduction of the Urbach energy for the localised states, probably caused by the impurities rather than by the presence of nano-sized crystallites.

4.4.5 Inert gas calcination of FMH-TiO₂ materials

The effect of calcination under atmospheres other than air at different temperature for FMH-TiO₂ particles is shown in Figure 4.13. The analysis of the structural properties from the PXD patterns of the calcined particles revealed a lower degree of crystallisation under inert atmosphere compared to the same treatment under air. The effect was observed for both N₂ and Ar atmospheres, but also for thermal annealing under constant NH₃ (ammonolysis reaction) or under

vacuum, which will be further described in detail. The lack of oxygen seemingly slows the crystal growth process.

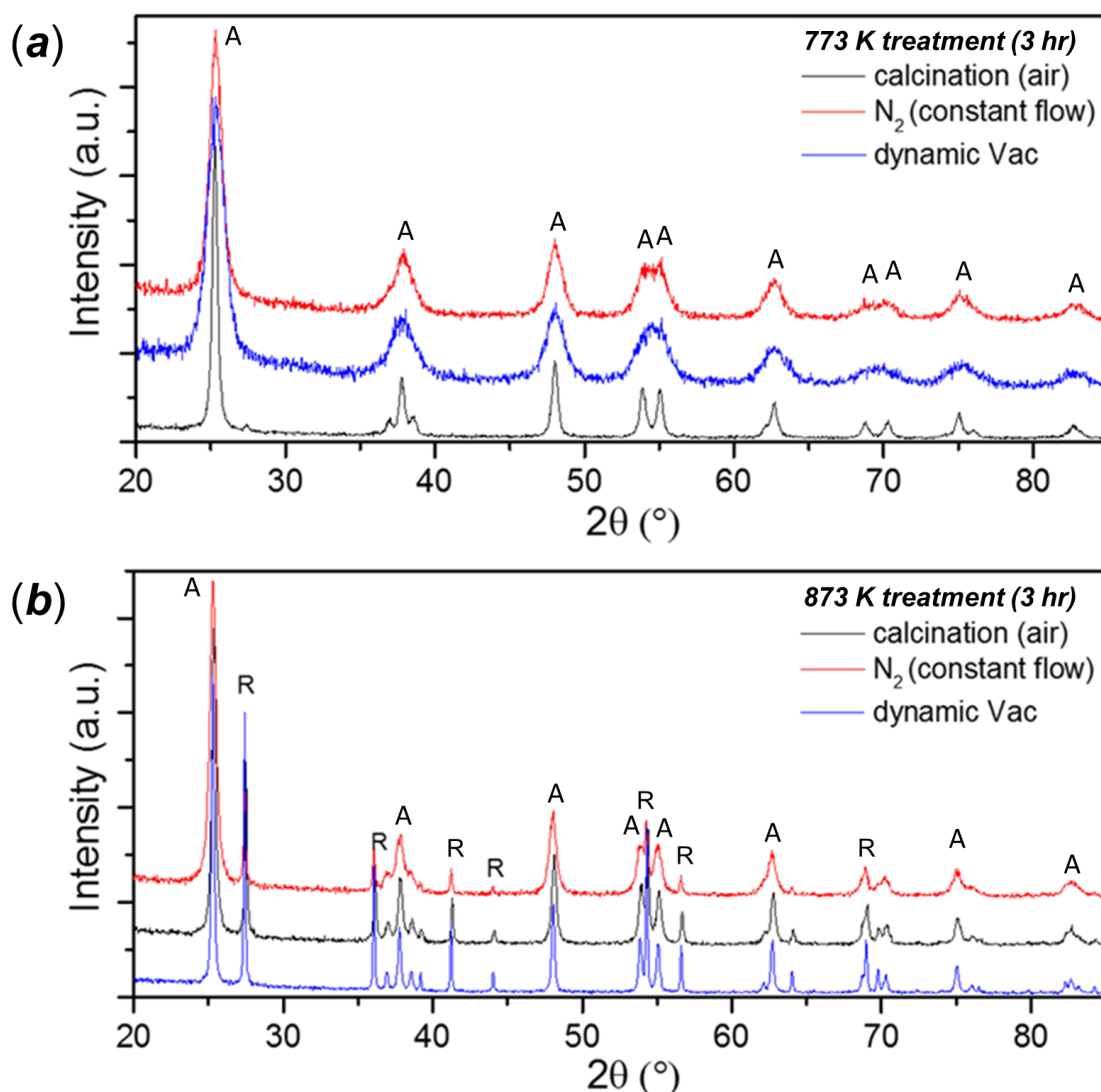


Figure 4.13: Comparison of PXD patterns of representative samples of FMH-TiO₂ particles (2M HNO₃, 162 Mm TTIP, 1 min MW treatment, the same described in the previous section) calcined under different conditions (air, N₂ or dynamic vacuum) at (a) 773 K and (b) 873 K.

A similar effect was observed measuring the surface area of the samples compared with the standard calcination treatment, with slower reorganisation of the pores and reduction of the mesoporosity due to the oxygen-poor atmosphere. This effect is a direct consequence of the slower kinetic of crystallisation of the nanograins composing the spherical particles. These findings agree with other results previously reported in the literature. [27]

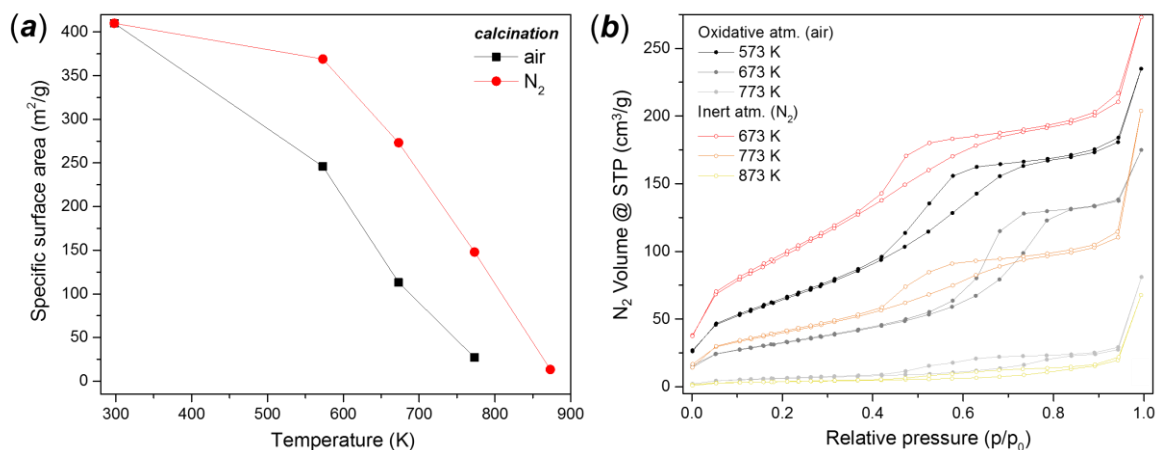


Figure 4.14: Surface area values (a) and N₂ adsorption-desorption isotherms (b) of the FMH-TiO₂ particles in function of the temperature and the atmosphere of the annealing treatment

Figure 4.15 shows the optical properties of the FMH-TiO₂ samples. The FMH-TiO₂ particles turned brown or grey depending on both the initial TiO₂ synthesis conditions and the subsequent calcining conditions. The modification looks similar to the one observed for the vacuum-activated samples (extensively described in the following sections), allowing to suppose that a similar process could be involved. The complete results of the analysis of the optical properties, surface area and pore size analysis are listed in Table A.12 in the Appendix.

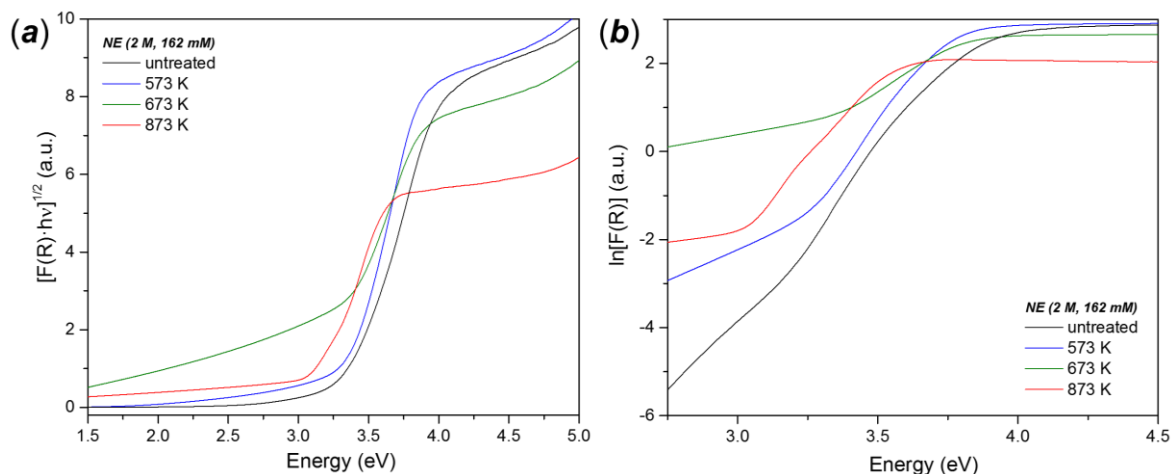


Figure 4.15: Effect of sintering under N₂ on the optical properties of the FMH-TiO₂ particles, through the observation of the Kubelka-Munk functions for (a) indirect band gap and (b) Urbach localised states.

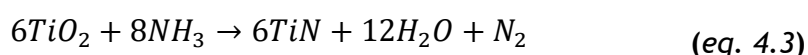
4.5 Nitrogen doping by ammonolysis treatment

The demonstration through first-principle calculations and experiment of successful visible light activation or sensitisation of TiO₂ through nitrogen doping by Asahi in 2001 marked the beginning of the development of the second generation of photocatalytic materials. [4] To date, substitution of lattice oxygen atoms with non-metal elements is considered an efficient method for the modification of the TiO₂ band gap. Compared with doping with transition metal cations, non-metal substitution generally leads to higher thermal stability and a lower density of recombination centres because of the insertion of smaller atoms, more compatible with the lattice size, and the least invasivity of the process. Nitrogen doping is one of the simplest methods to achieve band gap modification without adversely affecting the other properties of the material.

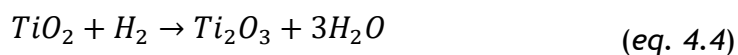
4.5.1 Ammonolysis

Ammonolysis is historically the simplest method to obtain a visible light-active TiO₂-based photocatalyst. The thermal dissociation of NH₃ causes the adsorption of nitrogen atoms inside the TiO₂ lattice, together with the reducing atmosphere due to the presence of hydrogen causing the production of Ti³⁺ defects. As a result, the overlapping of the 2p orbitals of N with those of the oxygen and the appearance of Ti³⁺ intermediate states located just below the conduction band cause the overall reduction of the band gap.

A complete ammonolysis of TiO₂ leads to production of pure nitride, in which the valence of Ti is reduced from +4 to +3. Starting from pure anatase, the reaction proceeds with the transformation of anatase into rutile and the subsequent formation of rock-salt structure TiN, according to the reaction:



The reaction can be described in three stages, considering the thermal dissociation of NH₃ (*equation 4.1*), an intermediate reduction of TiO₂ in Ti₂O₃ due to the presence of hydrogen released by ammonia decomposition and the ultimate reduction of TiO₂.^[28] The second intermediate stage can be described as in *equation 4.4*:



If the temperature is not high enough to complete this last reaction, oxygen is progressively replaced by nitrogen atoms, instead producing non-stoichiometric intermediate structures (TiO_{2-x}). Mild ammonolysis conditions leads to interstitial insertion of nitrogen atoms, in the TiO_2 lattice forming Ti-O and Ti-N bonds. Interstitial doping is also responsible for the production of oxygen vacancies. A higher temperature of ammonolysis can promote substitutional doping, with progressive direct replacement of oxygen with nitrogen. Substitutional doping also creates oxygen vacancies, to maintain charge balance. Apart from the oxygen vacancies and the presence of nitrogen atoms, the reducing atmosphere should favour the formation of Ti^{3+} centres, which could also be responsible for the increase of the photoactive response under visible light. [3]

In this work, the ammonolysis temperature was chosen within the range 573-973 K and mostly targeting 773 K. Treatment at 773 K has been reported previously for TiO_2 nanoparticles, to give modified optical properties with retention of crystal structure. [29] Ammonolysis was first replicated on pure crystalline anatase and the other commercial standards (P25, Kronos) to verify the reported procedure. Ultimately, the same process was applied to the FMH- TiO_2 particles, in order to improve their catalytic response under visible light.

4.5.2 Structural analysis

PXD revealed the structural changes due to the ammonolysis treatment (Figure 4.16). The structure of pure anatase is not affected by the treatment even at very high temperature (a maximum of 973 K was tested). At 973 K, the reactions led to the presence of a small peak at ca. $2\theta = 43^\circ$, signifying of the beginning of the transformation into TiN, (the most intense peak, (200), is at this angle). Analysis of the patterns reveals a typical shift of peaks towards higher values of 2θ , indicating a contraction of the cell volume. On the other hand, the peak broadening increases up to a certain temperature and then decreases. In P25, the effect of the ammonolysis on the structure is more evident, with an onset of nitridation at 823 K and a full transition to TiN observed at 973 K (Figure 4.16 *b*). For the FMH-TiO₂ particles, the behaviour depends on the properties of the sample. PXD pattern at 973 K of the NE series sample produced with a precursor concentration of 648 mM shows the presence of a broad TiN (200) peak together with the signals associated to nanocrystalline anatase (Figure 4.16 *c*). On the other hand, the sample produced with 162 mM of precursor (Figure 4.16 *d*) resulted in a transition resembling that of P25 at the same temperature. In this case, nanocrystalline anatase is totally converted in TiN, with the presence of additional secondary crystalline phases which attribution is difficult, with some peaks associated to non-stoichiometric TiO₂ structures, which will be partially investigated in the following sections. The nanocrystallinity lowers the transition temperature compared to more crystalline materials (such as commercial anatase).

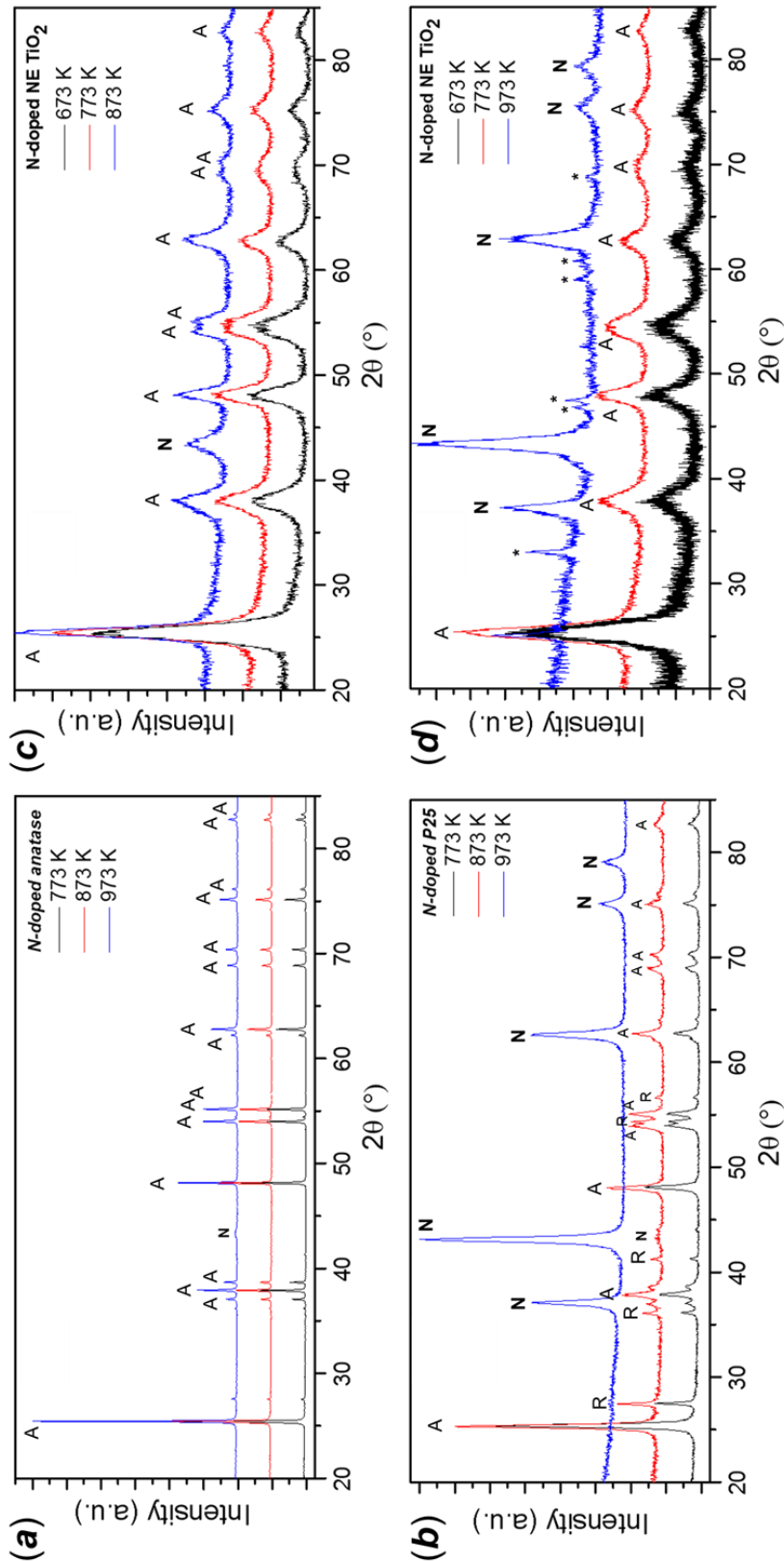


Figure 4.16: PXD patterns of (a) commercial anatase, (b) Aeroxide P25, FMH-TiO₂ particles (NE series, 2 M HNO₃, with (c) 648 mM and (d) 162 mM precursor (TTIP) concentration after ammonolysis (constant flow NH₃, 3 hrs, heating rate 10 K/min) at different temperature. (A indicates anatase, R rutile, N (bold) TiN and (*) the unidentified peaks).

4.5.3 Optical properties

Ammonolysis led to a characteristic change of colour of the samples, with an initial yellow colour turning to green and intensifying with the increase of temperature. Samples became almost black at the highest temperature tested (923 K).

The absorbance spectra of ammonolysed anatase are shown in Figure 4.17. The absorbance is not negligible in the visible and near-IR light regions, with an effect enhanced by the ammonolysis temperature.

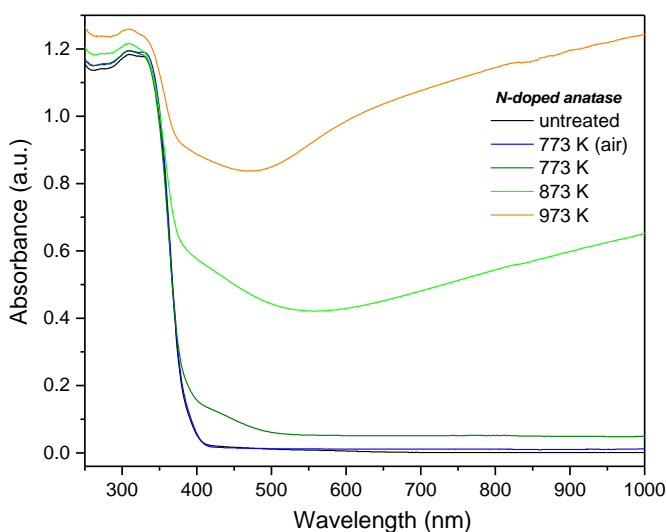


Figure 4.17: Absorbance spectra of ammonolysed anatase at different temperatures.

Figure 4.18 shows the indirect band gap analysis for anatase, P25 and the two representative FMH-TiO₂ samples which crystalline structure has already been described in Figure 4.16. Ammonolysis shifts the band gap towards lower energies (visible light) with a progressively appearance more pronounced absorption tail which begins to resemble a “secondary band gap”. However, a significant change in band gap occurs only at very high temperatures. Using the normal criteria established for the determination of the band gap, the materials modified at the highest temperature should absorb light in the IR region (0.36 eV corresponding to 3400 nm!), beyond the range of the measurement. For these samples, an alternative estimation of the band gap was performed considering the Kubelka-Munk functions at lower energies as a baseline, as shown in Figure A.23 in the Appendix.

The optical functions progressively lose their characteristic sigmoidal shape, with the appearance of multiple changes in slope. At this level of investigation, it is difficult to define a situation of multiple band gap values, which would correspond

to a partial modification of the original structure without altering the initial properties, for example considering anatase ammonolysed at 873 K, which crystalline structure is totally anatase (Figure 4.16 a). Analysis of the optical functions appeared to show more of an enhancement of the Urbach tail rather than a consistent shift of the absorption edge.

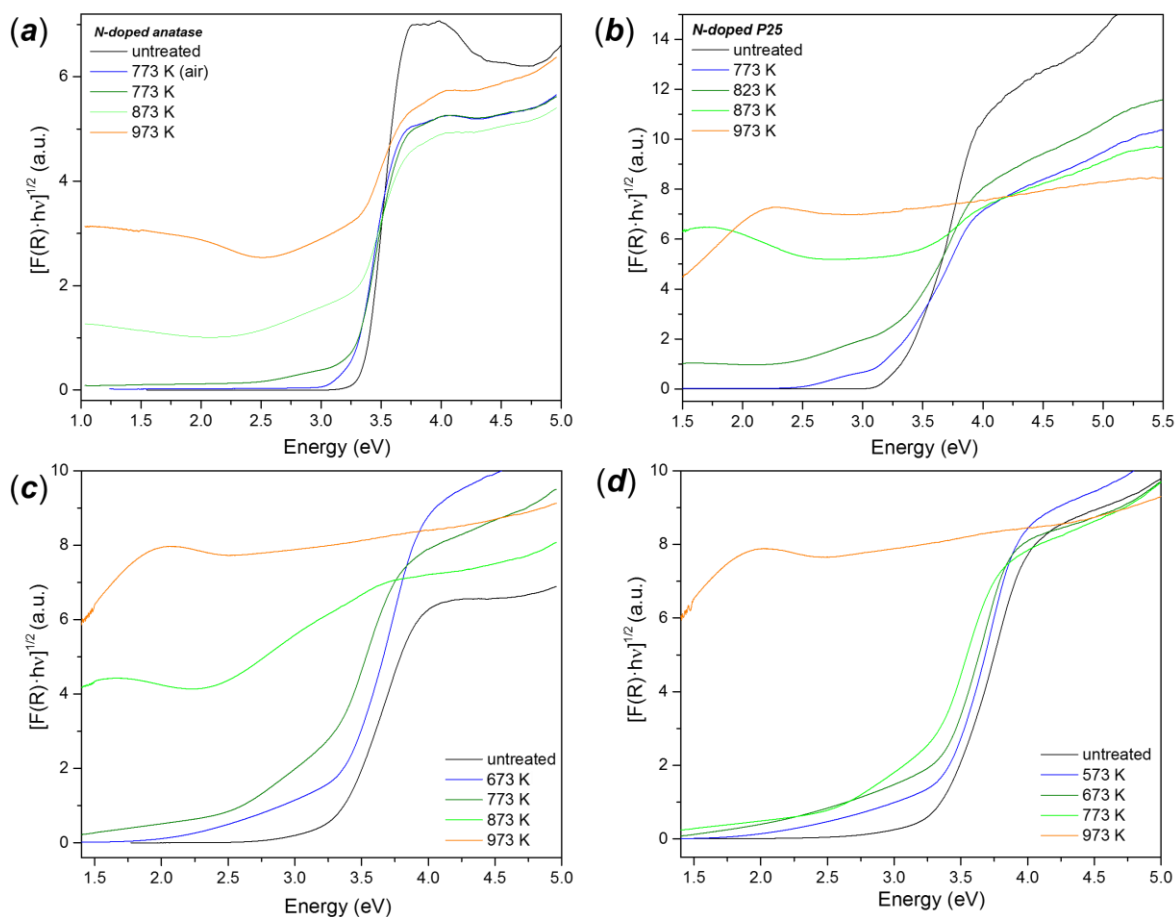


Figure 4.18: Kubelka-Munk function transformations for the indirect band gap of (a) commercial anatase, (b) P25, NE series, 2 M HNO₃, with (c) 648 mM and (d) 162 mM precursor (TTIP) concentration, after ammonolysis at different temperatures.

The results of the band gap analysis for anatase, P25 and FMH-TiO₂ particles after ammonolysis are listed in Table 4.6 and Table 4.7 respectively.

Table 4.6: Summary of the optical band gap and Urbach energy values of P25 and anatase after ammonolysis treatment at different temperatures (calculations based on 3 measurements on the same sample, standard deviation for band gap measurement ≤ 0.01 if not indicated).

	T(K)	Band gap (ind) (eV)	Band gap (dir) (eV)	Urbach energy (meV)
Anatase	<i>untreated</i>	3.23	3.47	64 \pm 2
	773	3.24, 2.20	3.47	76 \pm 5
	873	3.09, 1.25	3.44	221 \pm 21
	973	2.79	3.36	380 \pm 18
	P25	<i>untreated</i>	3.09	3.63
	773	3.16, 2.49	3.62	192 \pm 11
	823 (2h)	3.07, 1.79	3.63	289 \pm 8
	823	2.98, 2.47*	3.60	440 \pm 12
	873	2.22, 0.45	3.42 (3.56*)	1023 \pm 25
	973	0.56	1.55	934 \pm 37

Table 4.7: Summary of the optical band gap and Urbach energy values of FMH-TiO₂ (NE series, 2 M HNO₃) after ammonolysis treatment at different temperatures (calculations based on 3 measurements on the same sample, standard deviation for band gap measurement ≤ 0.01 if not indicated).

Precursor conc.	T(K)	Band gap (ind) (eV)	Band gap (dir) (eV)	Urbach energy (meV)
162 mM	<i>untreated</i>	3.36	3.72	110 \pm 13
	573	3.34	3.68	155 \pm 5
	673	3.26	3.62	186 \pm 9
	773	3.12, 2.56	3.49	213 \pm 6
	973	2.44	2.48	(1800 \pm 194)
648 mM	<i>untreated</i>	3.42	3.66	104 \pm 12
	673	3.07	3.52	172 \pm 7
	773	2.53, 2.26	3.26	410 \pm 6
	873	2.37	2.26	(1331 \pm 239)
	973	2.47	2.49	*

Despite the same crystalline structure, the nitridation of P25 over a certain temperature (973 K from PXD in Figure 4.16 b) has optical functions similar to pure TiN but with different values of band gap. TiN has been reported to have a direct band gap (3.4 eV in thin films).^[30] Here, TiN exhibits a direct band gap of 2.43 eV and an indirect band gap of 1.81 eV (Table 4.6). The value of the direct band gap is very close to the one observed for the loss of reflectivity at 2.5 eV in TiN films associated with an intraband electronic transition.^[31] A more detailed comparison between the nitridating and the reverse transformation from TiN to TiO₂ will be provided in section 4.7.3.

4.5.4 Efficacy of doping

Elemental analysis techniques were used in an attempt to determine the amount of nitrogen in the samples described in the previous section (Table 4.7). The results relative to doping of anatase and P25 are shown in Table 4.8.

EDX was not able to quantify nitrogen in the structure. Analysis of samples of anatase and P25 ammonolysed between 773 - 973 K detected presence of non-negligible nitrogen only in one of the sample (the one treated at the lowest temperature). EDX does indicate, however, that the oxygen content in the samples appears to decrease with increasing ammonolysis temperature, with the biggest reduction in oxygen between 873 - 973 K.

Nitrogen content was also analysed by CHN microanalysis. The combustion analysis detected nitrogen trace at 773 K (less than 0.5%wt) and consistently higher amounts at 973 K. The increase of nitrogen could be compatible with the decrease of oxygen in the structure, since one of the mechanisms proposed for the doping is the progressive substitution of oxygen with nitrogen atoms and formation of vacancies, as shown in *equation 4.5*:

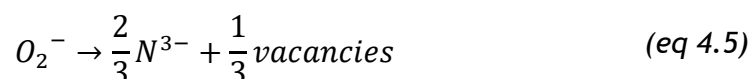


Table 4.8: Elemental analysis results on anatase and P25 under thermal ammonolysis treatment at different temperature.

	T(K)	Ti (%at)	O (%at)	Ti/O ratio	N (*) (%wt)
Anatase	773	28.00 ± 0.97	72.00 ± 0.98	0.39	n.d.
	873	30.02 ± 9.66	69.98 ± 10.61	0.43	0.42 ± 0.01
	973	36.97 ± 12.30	63.03 ± 15.80	0.59	1.84 ± 0.06
P25	773	27.15 ± 2.45	72.85 ± 2.65	0.37	0.23 ± 0.01
	823	26.34 ± 2.07	73.66 ± 2.25	0.36	2.00 ± 0.01
	873	27.68 ± 1.86	68.04 ± 2.06	0.41	5.63 ± 0.13(**)
	973	29.91 ± 4.84	34.13 ± 1.93	0.88	n.d. (**)

*CHN microanalysis results, wt %

**4.46 ± 0.94 and 35.67 ± 5.27 by EDX, not detected for all the other measurements#

4.5.5 Thermal analysis

STA analysis was performed on both P25 and FMH-TiO₂ samples after ammonolysis. Thermogravimetric analysis (Figure A.24 in the Appendix) of N-doped P25 (873 K, 3 hours) and N-doped NE particles (773 K, 3 hours) revealed a negligible loss of mass for the former and a loss of around 3% for the latter, probably due to the release of impurities (carbonaceous residual or nitrous oxide deriving from the synthesis process) surviving the ammonolysis treatment. PXD patterns of the two samples were collected after the STA analysis. The original anatase structure of the N-doped FMH-TiO₂ particles was almost totally converted to rutile (Figure A.25 in the Appendix), with only 2% of anatase content measured by comparison of the integrated intensities by the Spurr-Meyer equation (equation 4.2). On the other hand, the relative content of anatase to rutile in the N-doped P25 was 54:46 compared to the initial of 84:16. The PXD pattern of the sample P25 treated under NH₃ at 873 K before and after the STA is shown in Figure 4.19. The pattern for P25 exhibits broad peaks not belonging to either anatase or rutile. The analysis of the region around the most intense peak of rutile (110) and the portion of the pattern between 41 - 46° 2θ suggests the formation of TiN and the possible presence of reduced titanium oxides, including Ti₄O₅, Ti₃O₅.^[32,33] The characteristics of these crystalline structure are reported in Table A.13 in the Appendix.

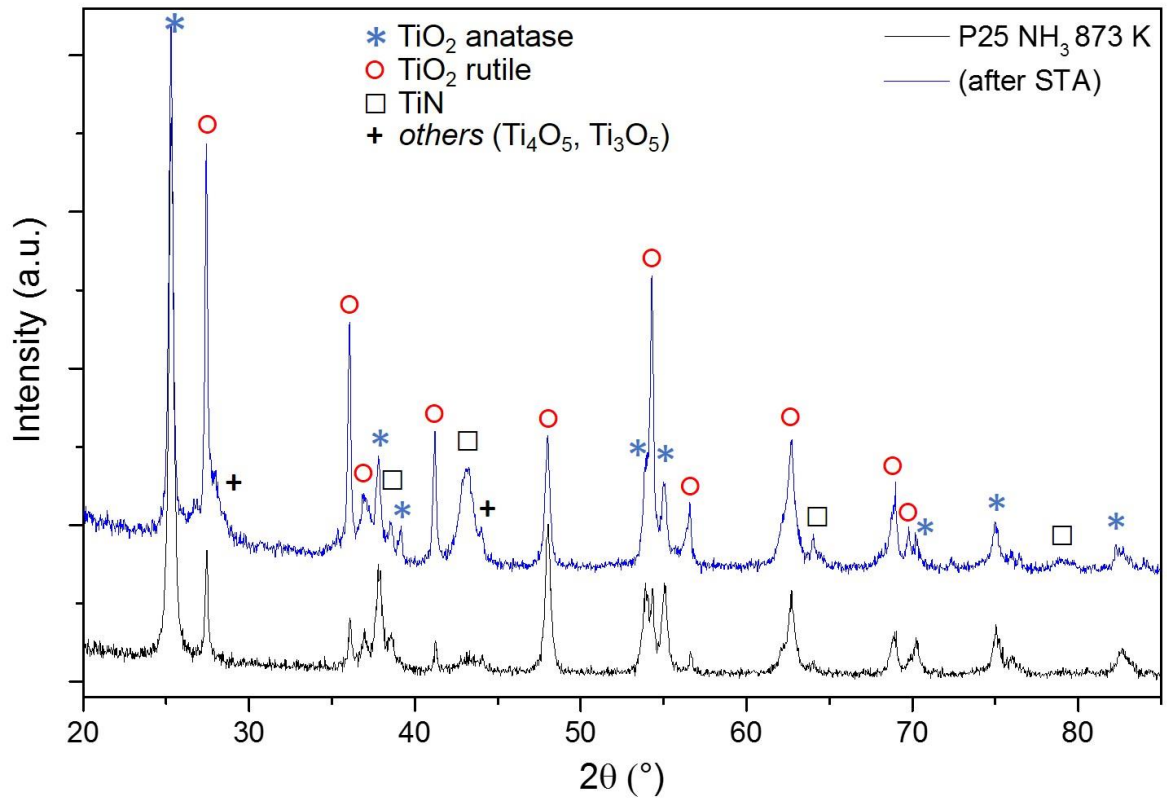


Figure 4.19: PXD patterns of the P25 treated under ammonolysis at 873 K before and after the TG-DTA analysis (heating program: 1173 K under Ar, heating ramp 5 K/min)

DTA profiles of the two samples did not show a clear peak corresponding to the phase transition as observed in Figure 4.6. The thermal profile of the FMH-TiO₂ particles, for which the transition to rutile was almost complete, shows what can be considered as a very broad peak at the end of the descending slope. The slope can thus indicate the beginning of the phase transition, with length and inclination of the profile slope depending on the initial composition of the sample and the eventual coexistence of rutile grains, as in case of ammonolysed P25 (Figure 4.20).

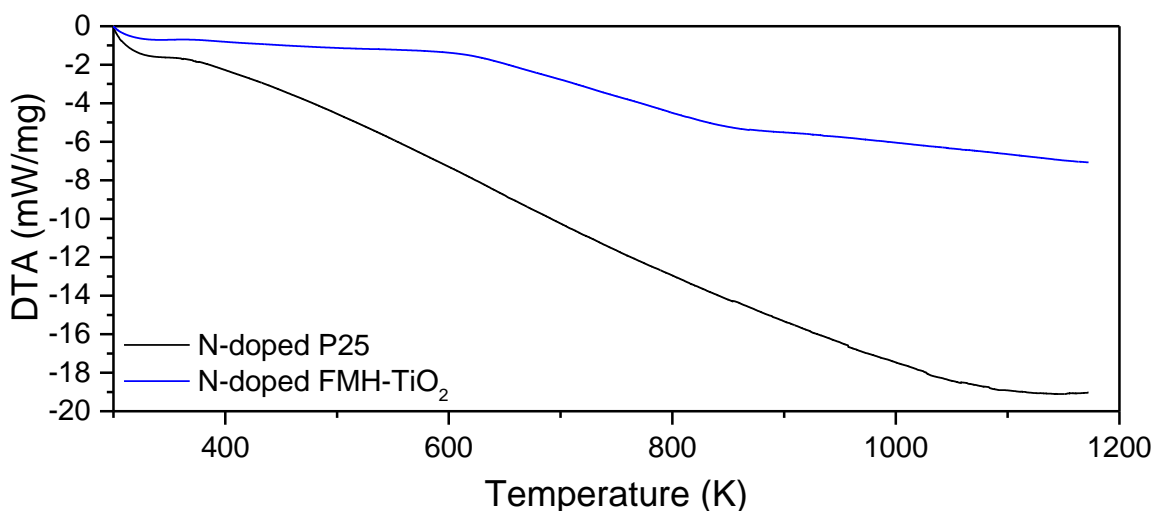


Figure 4.20: DTA profiles of ammonolysed P25 and FMH-TiO₂ particles (NE series, 2 M, 648 mM, ammonolysed at 773 K for 3 hrs). the thermal program consisted of a 5 K/min heating ramp up to 1173 K under constant argon flow.

Evolved gas MS analysis revealed progressive release of molecular nitrogen principally at 500 and 900 K (Figure 4.21 *a*). N₂O is also detected but at much lower levels (Figure 4.21 *b*). The N₂O release occurs in the same temperature range as samples prior to ammoniation (section 3.8.2). This further suggests incomplete release of gaseous impurities during ammonolysis.

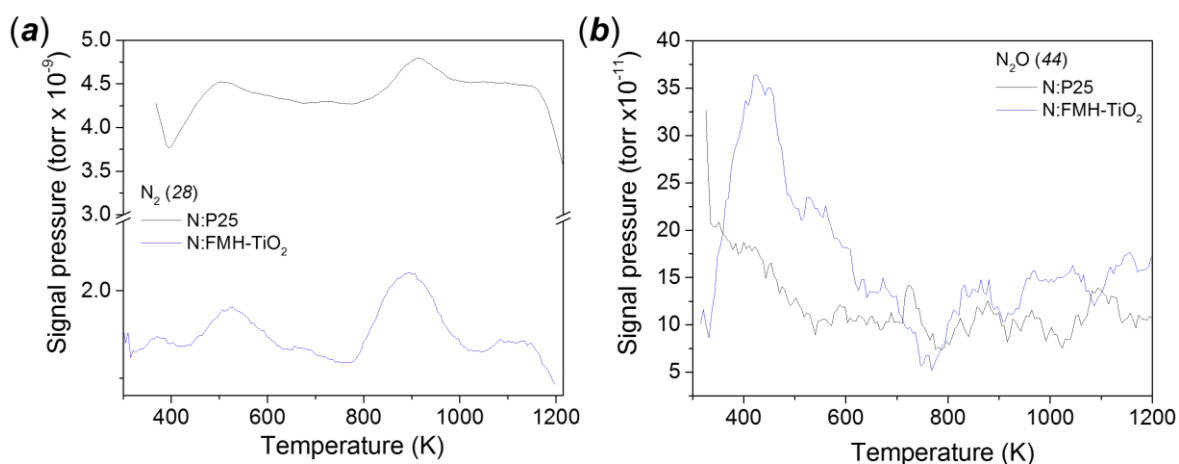


Figure 4.21: MS evolved gas analysis of the nitrogen doped samples (P25 treated under NH₃ constant flux, 873 K for 3 hours and NE – 1M HNO₃, 648 mM TTIP ammonolysed at 773 K for 3 hours). (*a*) analysis of released N₂ (MW:28) and (*b*) N₂O (MW:44).

The change in optical properties due to the STA (heating ramp under inert gas constant flow) were investigated in Figure 4.22. The optical properties of the selected FMH-TiO₂ samples after STA are similar to rutile (Table 4.9), as PXD analysis would also suggest. Conversely ammoniated P25 showed an increase in absorption at lower wavelengths (at which usually TiO₂ is totally transparent). The results might indicate the evolution of the change of the electronic structure, such as previously observed for the localised states of the ammoniated samples, associated with the growth of secondary phases.

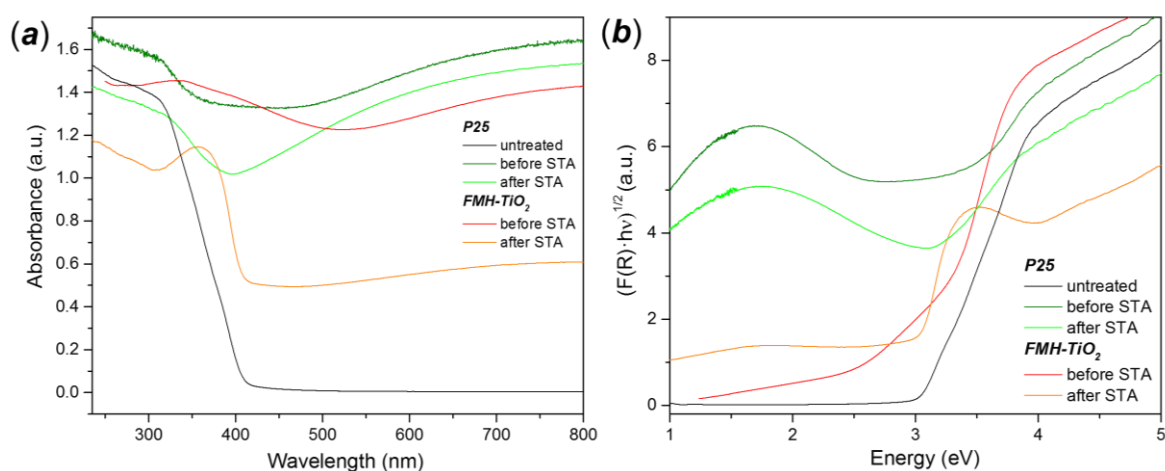


Figure 4.22: (a) Absorbance spectra and (b) Kubelka-Munk functions for the calculation of the indirect band gap of ammoniolysed samples before and after STA.

Table 4.9: Optical properties of the selected ammoniolysed FMH-TiO₂ samples, before and after STA analysis, compared to P25 underwent the same treatment. (optical measurement results obtained from 3 measurements from samples from the same batch; band gap error ≤ 0.01 if not indicated).

		Band gap (ind) (eV)	Band gap (dir) (eV)	Urbach energy (meV)
NE (1 M, 648 mM)	<i>untreated</i>	3.42	3.66	104 \pm 12
	NH ₃ (873 K)	2.37	2.26	(1331 \pm 239)
	STA	2.93	3.13	114 \pm 11
P25	<i>untreated</i>	3.09	3.63	40 \pm 2
	NH ₃ (873 K)	2.22, 0.45	3.42 (3.56)	1023 \pm 25
	STA	3.01 (2.28)	3.30	932 \pm 49

4.6 Vacuum activation

As reported in the previous section, NH_3 has a dramatic effect on the structural and physical properties of the treated materials. A milder alternative to obtain comparable effects could be to anneal under vacuum. This TiO_2 “self-doping” has been hence considered as an alternative solution to ammonolysis via a simple one-step reaction. Self-doping is defined as the modification of the original structure by insertion of structural defects, such as vacancies and/or ions of reduced valence. In case of TiO_2 , self-doping involves reduction of Ti^{4+} to Ti^{3+} generally caused by the presence of oxygen vacancies. Oxygen vacancies are the most common defects in metal oxides, with important consequences for heterogeneous catalysis. The vacancies constitutes important active sites for adsorption and subsequent reaction, increasing the overall efficiency of the catalyst.^[34, 35] Oxygen vacancies are reported to introduce a localised donor level at 0.75 to 1.18 eV below the bottom of the conduction band,^[36,37] allowing absorption at lower frequency compared to the band gap itself.^[38] The formation of Ti^{3+} defects is improved by the increase of the annealing treatment time and temperature and reduction of pressure.^[39] One of the first example of improved visible-light photocatalysis through inducing vacancies in nanostructured TiO_2 is attributed to Chen *et al.*, who first described the properties of black hydrogenated nano-anatase. The material was hydrogenated with 2 MPa H_2 at 473 K, for 5 days maintaining the original crystal structure and particle size but with colour determined by changes in electronic structure.^[40] Another way to introduce structural defects in TiO_2 is to perform hydrothermal synthesis using a strong reducing agent, such as NaBH_4 . Such reactions are reported to affect the sample morphology and colour but not the crystal structure, with an improvement to photocatalytic activity under visible light associated to a modified electronic structure.^[41] A simpler visible-light activation can be performed by heating under vacuum, leading to non-stoichiometric TiO_{2-x} phases,^[42] for example reduction of polycrystalline anatase under vacuum under high vacuum ($\sim 10^{-3}$ Pa) for several hours led to the formation of Ti^{3+} species, detected by EPR spectroscopy.^[43]

4.6.1 Structural and physical modifications

Some selected sample batches among the FMH-TiO₂ particles were annealed under vacuum, both in quartz tubes sealed under vacuum (static regime) and in stainless steel reactor connected to a vacuum apparatus (dynamic regime) during the entire reaction time. The average pressure was ca. 1 Pa for the dynamic vacuum treatment and 200 kPa for the sealed tubes, with heating rate of 10 K/min for both regimes. Reactions performed under static vacuum generally led to a lighter coloration of the products compared to what was observed for dynamic vacuum samples. An intense odour was detected when the sealed samples were opened, which could be associated with nitric oxide release (as described in section 3.8.2). All the samples treated under static vacuum were brown/grey. Dynamic vacuum treatment resulted in darker coloured samples under otherwise the same conditions. The colour change is enhanced by the level of vacuum and the temperature of the treatment. An example of the progressive darkening of the samples with the temperature and the duration of the treatment is given in Figure 4.23. The colour modification is similar to that reported by Ren *et al.*;^[41] the effect of the vacuum treatment may differ depending on the initial structure morphology and composition of the samples. In case of P25 and commercial anatase, the original clear white colour appeared dull, with no other evident changes.

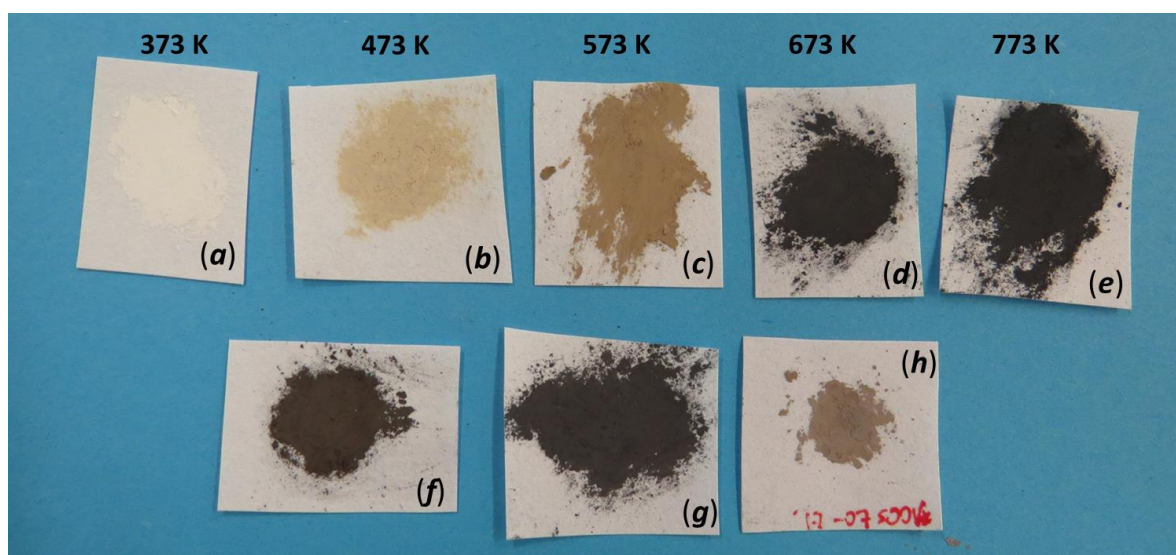


Figure 4.23: Examples of specimens of vacuum-activated FMH-TiO₂ (series NE; 2 M HNO₃, 162 mM precursor concentration) after heating for 3 h under dynamic vacuum at (a) 373K, (b) 473 K, (c) 573 K, (d) 673 K and (e) 773 K or at 773 K for (f) 30 min and (g) 1 hr; (h) was produced under static vacuum conditions (static pressure around 2 kPa, 3hr thermal treatment at 773 K)

The XRD analysis of the powdered samples revealed that the crystal structures were seemingly unchanged after vacuum heating (Figure 4.24). Unlike the ammonolysis treatment, the vacuum annealing conditions were not sufficient to alter the crystal structure of the sample, with the transition to rutile occurring at almost the same temperature as in air.

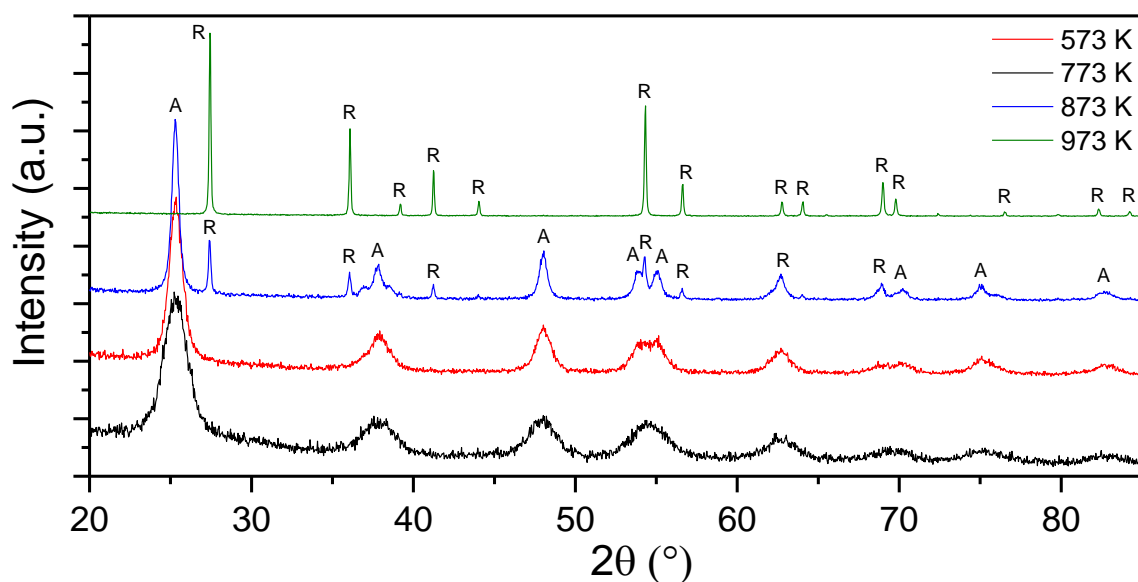


Figure 4.24: PXD patterns of FMH-TiO₂ particles (series NE, 2 M HNO₃, 162 mM precursor concentration) annealed under dynamic vacuum at different temperatures (R and A signifying rutile and anatase peaks respectively).

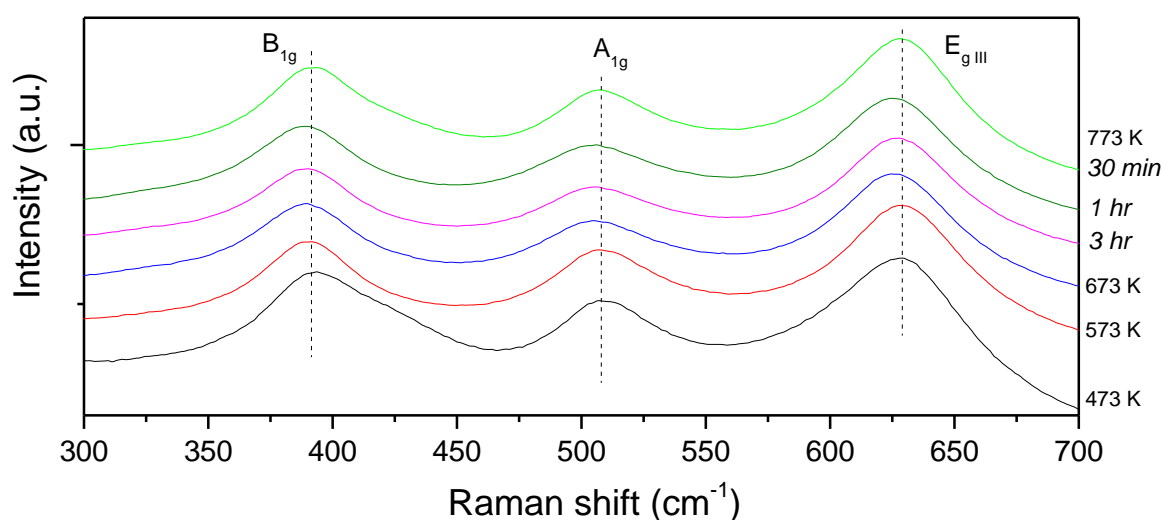


Figure 4.25: Raman bands of the FMH-TiO₂ particles annealed under dynamic vacuum at different temperature and treatment duration. The individuation of the principal modes (relative to TiO₂ anatase) are indicated.

In Table 4.10, key features of the Raman spectra are correlated with crystallographic data. The redshift of the bands would not be expected from an increase of grain size after heating. The reduction of the consequences of the quantum size effect (as samples are heated) is compensated by the structural disorder associated with the oxygen vacancies and the formation of Ti^{3+} . Indeed, peak broadening and redshift are more consistent in the sample with higher structural disorder, as confirmed by the analysis of the Urbach localised states in the following section (the optical properties of the same series of samples are reported in Table 4.13).^[44]

Table 4.10: Collection of selected structural data and Raman spectral features for FMH-TiO₂ samples annealed under dynamic vacuum at different temperature and duration. (Raman calculation based on 3 measurements from samples from the same batch).

<i>Temperature</i>	473 K	573 K	673 K	773 K	773 K	773 K
<i>Duration</i>	3h	3h	3h	30 min	1h	3h
Average crystalline size (nm) ^(a)	3.8	4.1	8.7	6.1	7.4	11.1
$E_{g,I}$ (cm ⁻¹)	148.84 ± 0.11	148.70 ± 0.21	149.78 ± 0.23	148.59 ± 0.22	149.66 ± 0.08	149.53 ± 0.71
$E_{g,I}$ FWHM (cm ⁻¹)	25.37 ± 0.30	24.08 ± 0.08	24.56 ± 0.06	22.94 ± 0.08	24.63 ± 0.09	23.89 ± 0.12
B_{1g} (cm ⁻¹)	392.55 ± 1.38	390.98 ± 0.34	389.21 ± 0.58	391.54 ± 0.77	388.95 ± 1.29	389.36 ± 1.44
A_{1g} (cm ⁻¹)	509.26 ± 0.24	508.67 ± 0.76	505.02 ± 0.43	507.64 ± 0.21	504.46 ± 0.81	506.00 ± 1.89
$E_{g,III}$ (cm ⁻¹)	630.13 ± 0.80	629.40 ± 0.49	625.48 ± 0.44	629.12 ± 0.45	625.53 ± 0.72	627.32 ± 1.50

^(a) calculated by Scherrer equation (XRD data), single measurement using same diffractometer conditions

As in the case of the samples calcined in air, the IR spectra of the vacuum heated samples revealed the progressive disappearance of the IR bands related to the impurities of the FMH-TiO₂ samples. (Figure 4.26). Microanalysis of some selected samples confirmed the presence of C (*ca.* 1%) with the dynamic vacuum heated sample presenting also traces of H, which are compatible with organic fragments. Nitrogen was instead absent in all the samples analysed. The results of the analysis are reported in Table 4.11.

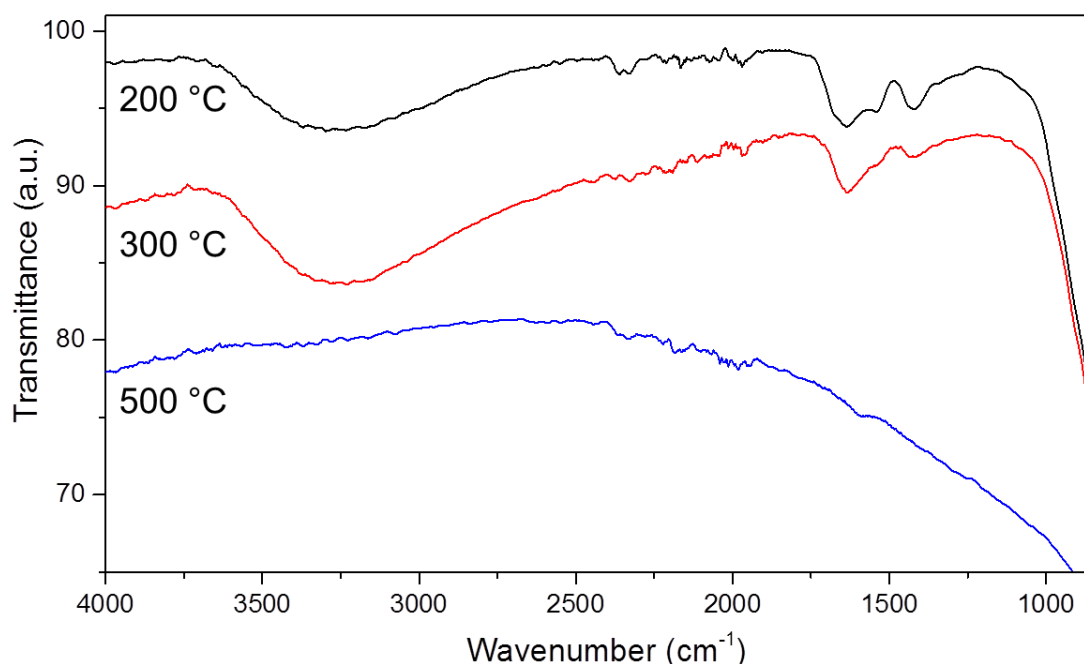


Figure 4.26: IR spectra of NE (2 M, 162 mM) FMH-TiO₂ particles calcined under dynamic vacuum at different temperatures.

Table 4.11: Combustion CHN microanalysis for some representative vacuum heated FMH-TiO₂ samples (SV indicates “static vacuum”, DV indicates “dynamic vacuum” conditions); results obtained from double measurement on the same batch.

Sample	Treatment	C (wt%)	H (wt%)	N (wt%)
NE (2 M, 164 mM)	SV, 473 K	0.95 ± 0.08	0.31 ± 0.02	0.01 ± 0.00
NE (2 M, 164 mM)	SV, 573 K	0.61 ± 0.03	0.07 ± 0.01	0.02 ± 0.01
NE (2 M, 648 mM)	DV, 773 K	1.43 ± 0.04	0.95 ± 0.07	0.05 ± 0.00

4.6.2 Optical properties

4.6.2.1 Static vacuum conditions

As suggested by the changes in colour, the band gap decreases with increasing annealing temperature (Figure 4.27). The vacuum treated samples lose reflectance in the spectral region in which usually TiO₂ has high reflectivity. The vacuum treated samples are hence absorbing light at wavelength lower than those corresponding to the band gap. At high temperature the samples also reflect before the absorption edge. The Kubelka-Munk functions show that vacuum heating above 773 K increases both the direct and indirect band gap.

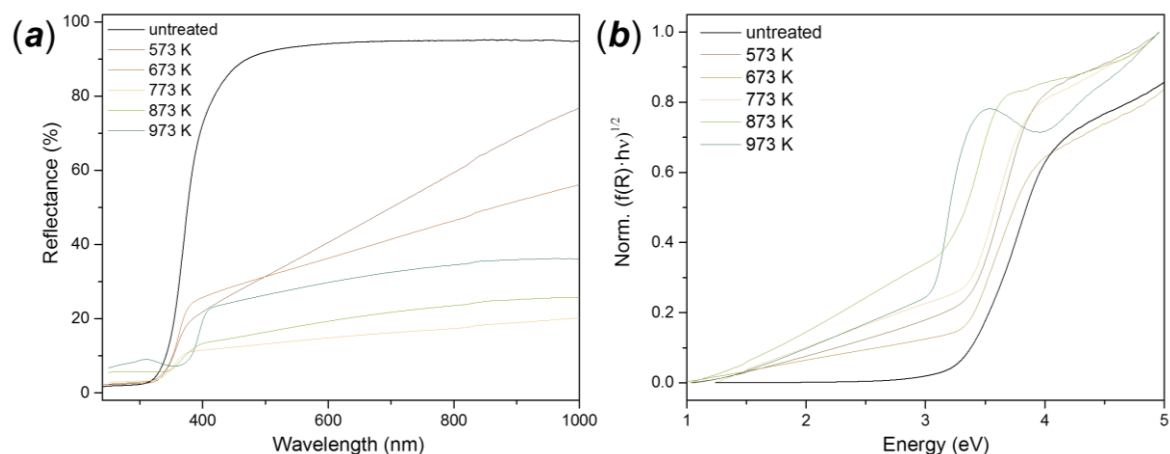


Figure 4.27: (a) Diffuse reflectance spectra and (b) Kubelka-Munk plots for to the indirect band gap for the NE series (2 M HNO₃, 162 mM (1:20 volume) prec. conc.) after heating under static vacuum (The Kubelka-Munk function plots were normalised to facilitate the comparison; calculations were performed on the non-normalised functions).

Table 4.12: Results from DR-UV-Vis analysis for the NE samples heated under static vacuum. (calculations based on 3 measurements on the same sample, standard deviation for band gap measurement ≤ 0.01 if not indicated).

	T(K)	Ind. Band gap (eV)	Dir. Band gap (eV)	Urbach energy (meV)
NE (2M, 162 mM)	<i>untreated</i>	3.38	3.73	110 \pm 13
	573	3.23	3.62	209 \pm 13
	673	3.18	3.61	189 \pm 23
	773	3.01	3.52	315 \pm 19
	873	2.81	3.31	340 \pm 23
	973	2.89	3.13	164 \pm 14

Another peculiarity of the optical behaviour of the static vacuum samples is the significant absorption tail, which slopes seem to increase progressively. The Urbach energy values initially decrease after annealing and subsequently increase. The presence of the Urbach tail is evidence of structural disorder. The ultimate increase of the indirect band gap and the abruptly change of the direct band gap to value close to that of bulk rutile over a certain temperature, together with the decrease of the Urbach energy, are probably correlated to the transition to rutile.

4.6.2.2 Dynamic vacuum conditions

The optical behaviour of the samples heated under dynamic vacuum were modified significantly, as reported in Table 4.12 for static vacuum and in Table 4.13 for dynamic vacuum. Figure 4.28, shows the loss of the characteristic sigmoidal shape in the DR-UV-Vis spectrum (similar to the nitrated samples

described in section 4.5.3). The vacuum heating caused progressive generation of mid-gap localised states, as witnessed by the increase of the Urbach contribution for darker materials. In Figure 4.28 *b* it is possible to observe the width of the linear slope in the Kubelka-Munk functions progressively narrowing with the increase of the temperature, corresponding in the absorbance spectra to a decrease of the absorption edge, together with its shift towards visible light wavelengths.

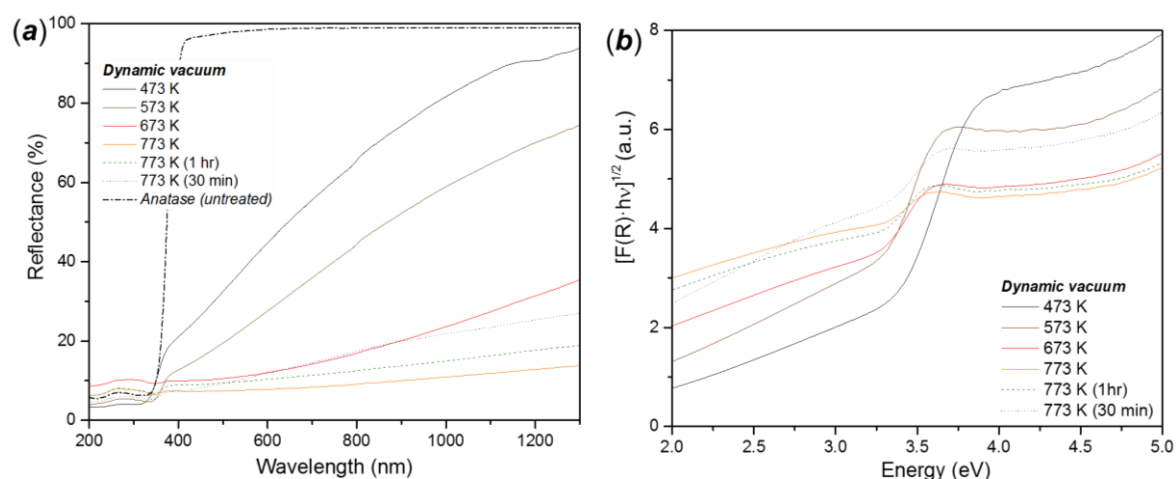


Figure 4.28: (a) DR-UV-Vis spectra and (b) Kubelka-Munk function for the indirect band gap for dynamic vacuum annealed FMH-TiO₂ samples at different annealing temperatures and times (3 hrs when not indicated).

Table 4.13: Results of the optical analysis for the samples produced under dynamic vacuum conditions (calculations based on 3 measurements on the same sample, standard deviation for band gap measurement ≤ 0.01 if not indicated).

	T (K)	Ind. Band gap (eV)	Dir. Band gap (eV)	Urbach energy (meV)
NE (1:20, 2 M)	<i>untreated</i>	3.38	3.73	110 \pm 13
	473	3.17	3.57	229 \pm 9
	573	3.09	3.37	269 \pm 11
	673	1.95	3.07	958 \pm 64
	773	2.66	3.25	455 \pm 13
	773 (30 min)	2.29	3.16	779 \pm 23
	773 (1 hr)	2.42	3.17	659 \pm 29

4.6.3 Thermal stability

TG-DT Analysis of vacuum annealed samples revealed no loss of mass. One of the samples produced under static vacuum conditions (773 K, 3 hrs) was considered for analysis as a representative of the vacuum heated materials. The mass of the sample was essentially constant throughout the entire temperature program (5

K/min up to 1173 K), apart from a slight increase due to systematic errors in the measurement (e.g. buoyancy effect of the weighing system at high temperatures) of the instrument. The DTA scan revealed a weak and very broad endothermic peak centred at ca. 540 K. The sample retained its original colour and phase composition post TG-DTA suggests almost negligible reoxidation of Ti^{4+} , as could be expected under inert conditions. By contrast, the *in situ* oxidation (in air) during variable temperature PXD resulted in white samples, with the anatase structure even at 973 K, the temperature at which the rutile phase starts to appear.

In Figure 4.29 shows the optical properties of another FMH- TiO_2 sample (NE series, 2 M HNO_3 , 648 mM precursor concentration) annealed under static vacuum conditions for different duration time. Similarly to what observed for the calcination in air, prolonging the vacuum treatment had no effect neither on the degree of crystallinity (by PXD analysis, shown in Figure A.27 in the Appendix) nor on the density of structural defects, as shown by the constant shape of the optical characteristics (reflectance, Kubelka-Munk functions), at least up to the 5th hour of treatment. Re-oxidation was tested on the sample treated for longer time (7 hrs) simply by calcining it under air at 673 K for 3 hrs. The effect of the re-oxidation is witnessed by the colour change and hence of the electronic structure of the sample, DR-UV-Vis shows that re-oxidation leads to spectra and Kubelka-Munk transformations more similar to those of the untreated samples as might be expected as oxygen vacancies are filled.

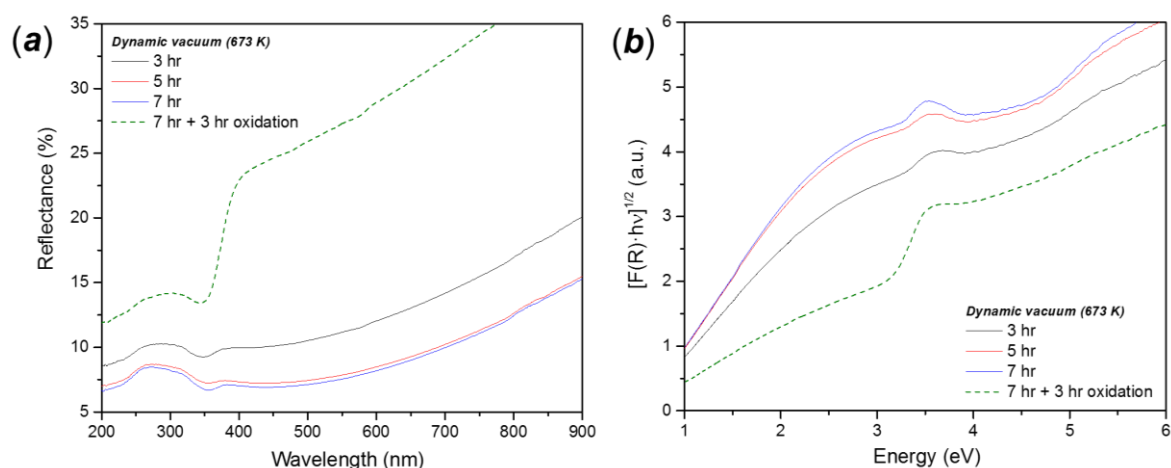


Figure 4.29: (a) Reflectance spectra and (b) Kubelka-Munk transformations for indirect band gap for NE series (2M HNO_3 , 1:5 precursor concentration) samples previously heated at 673 K under dynamic vacuum.

Table 4.14: Results of the optical analysis for selected samples produced under dynamic vacuum conditions at constant temperature (673 K) for different times. The results include also the re-oxidation experiment performed on the sample heated under dynamic vacuum for 7 hours and then calcined in air at the same temperature for 3 hours. (3 measurements on the same sample, standard deviation for band gap measurement ≤ 0.01 if not indicated).

	Ind. Band gap (eV)	Dir. Band gap (eV)	Urbach energy (meV)
3h	0.55 (3.29)	2.68 (3.30)	479 \pm 25
5h	0.65 (3.27)	2.31, 1.64	377 \pm 35
7h	0.44 (3.26)	2.62, 1.64	359 \pm 29
7h + 3h (reox.)	2.60 (3.18)	3.19	412 \pm 17

4.7 Efficacy of the reducing treatment

4.7.1 XPS analysis

Four representative samples were analysed, focusing on the observation of the Ti 2p and O 1s signal and the detection of nitrogen and carbon. The samples and the XPS data are listed in Table 4.15 (the full data for the ammonolysed samples are shown in Table A.14 in the Appendix).

Table 4.15: List of samples analysed by XPS, with the peak position and the atomic concentration, calculated from the integrated intensity of the signal, for Ti, O and C (no N was detected). NE (2 M HNO₃, 162 mM prec. Concentration, 1 min MW treatment) was selected as representative sample for the different thermal treatments.

	XPS signal position (eV)			Atomic concentration (%)		
	Ti 2p _{3/2}	O 1s	C 1s	Ti	O	C
P25 (NH ₃ , 773 K)	458.77	530.77	284.77	16.11	50.22	33.67
NE (NH ₃ , 773 K)	459.25	530.25	284.25	19.24	50.41	30.35
NE (Ar, 673 K)	458.03	530.03	248.03	17.05	47.01	35.94
NE (St.Vac., 773 K)	460.13	531.03	286.13	13.38	40.93	45.69

High resolution XPS spectra in the Ti 2p and O 1s regions for P25 and a sample of FMH-TiO₂ from the NE series are reported in Figure 4.30. In both cases, the Ti 2p_{3/2} signal is slightly shifted compared to the value reported in literature for stoichiometric TiO₂, (458.6 eV, and to a lower energy than the peak in the ammonolysed P25).^[45] The presence of a double O 1s signal is generally ascribed to both oxygen in the crystal lattice and that adsorbed on the surface (528.5-529.7 eV and 530.54-533.57 eV, respectively).^[81] Conflicting with the other

experimental evidences, XPS showed no presence of nitrogen for any of the ammoniated samples.

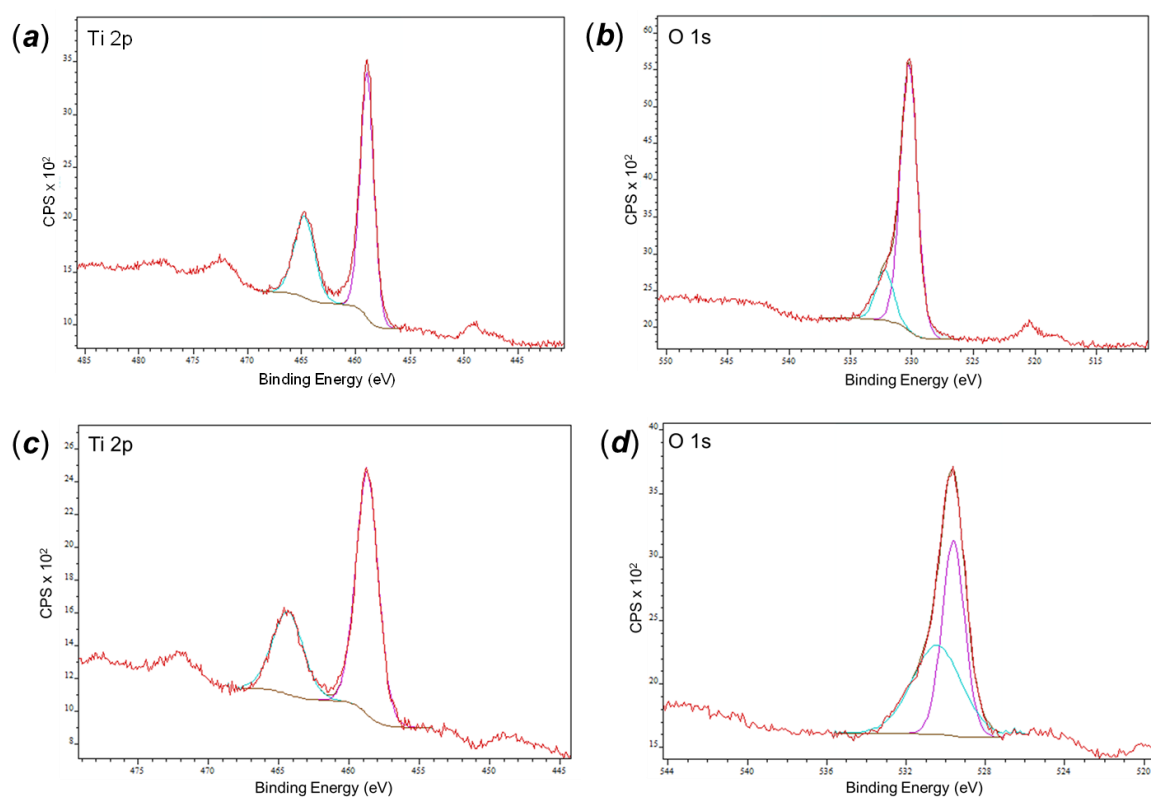


Figure 4.30: XPS spectra in the Ti 2p and O 1s regions respectively for (a,b) N-doped Aeroxide P25 (commercial TiO₂ photocatalyst) and (c,d) the N-doped FMH-TiO₂ particles (NE series, 2 M HNO₃, 162 mM precursor concentration, 1 min MW treatment).

The vacuum annealed sample analysed by XPS showed a shift in the Ti 2p_{3/2} signal consistent with the presence of Ti³⁺, as shown in Figure 4.31 a, with the peak at 460.13 eV. On the other hand, the Ti 2p_{1/2} signal correspond to the same binding energy of the other sample analysed (ca. 465 eV). The O 1s signal (Figure 4.31 b) consists of the peak at ca. 530 eV, broaden by a secondary contribute centred at ca. 532 eV. The characteristics of this signal are identical compared to the O 1s observed in ammonolysed P25 (Figure 4.30 b).

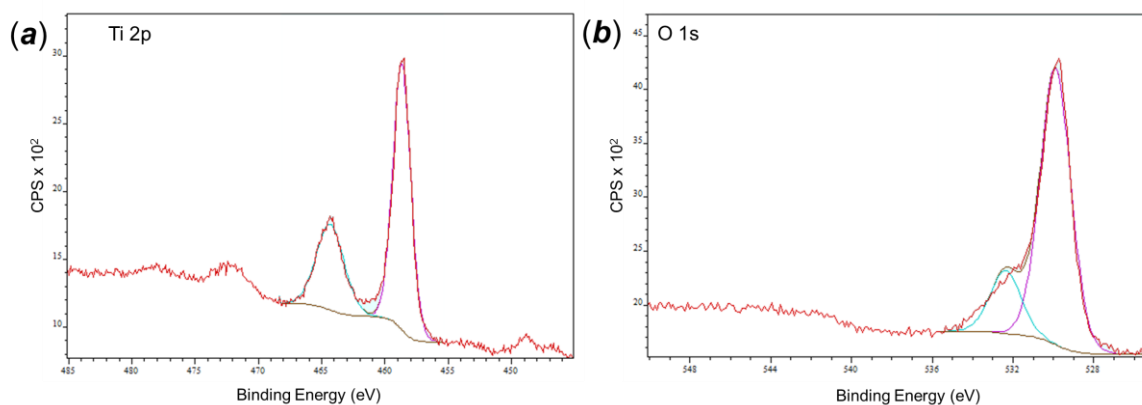


Figure 4.31: XPS analysis of the Ti 2p and O 1s signals for vacuum annealed FMH-TiO₂ (series NE, 2 M, 1:20 v/v precursor concentration, vacuum treatment 773 K, static conditions, 3 hrs).

Figure 4.32 shows the Ti 2p and O 1s signals of the FMH-TiO₂ sample annealed under constant flow of Ar. This sample presents the lowest binding energies for both 2p_{3/2} (458.03 eV) and O 1s (530.03) among all the other samples considered.

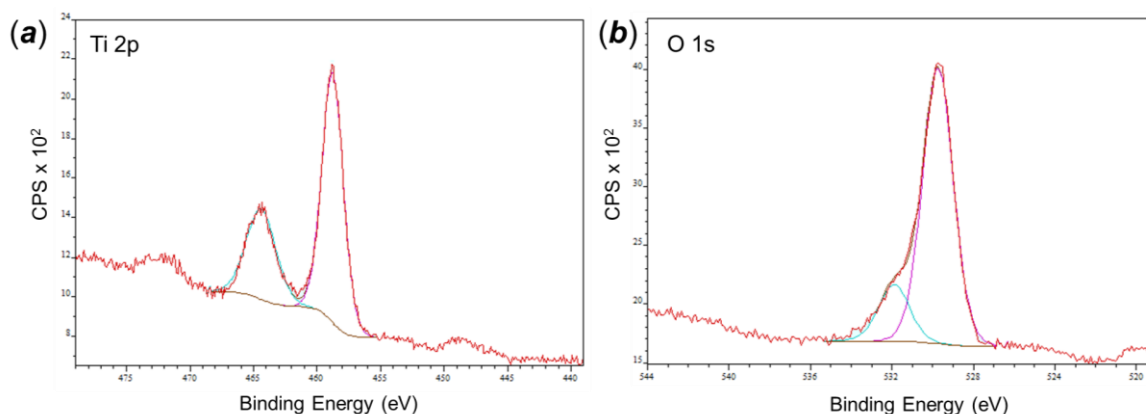


Figure 4.32: XPS analysis of the Ti 2p and O 1s signals for FMH-TiO₂ (series NE, 2 M, 1:20 v/v precursor concentration) annealed under Ar atmosphere (673 K, 3 hrs).

Also in the FMH-TiO₂ sample calcined under static vacuum, nitrogen was not detected. This result is totally expected, since the residual nitrogen from the synthesis procedure is released during the thermal treatment, as observed from the STA analysis on the as-synthesised particles (section 3.8.2) and the absence of relevant signal from the MS evolved gas analysis previously reported in this chapter.

4.7.2 EPR analysis

EPR was chosen to detect the presence of Ti^{3+} or other paramagnetic species induced by the reducing treatments. Some representative samples described in the previous sections were selected, including ammonolysed P25 and FMH- TiO_2 particles annealed under NH_3 , static and dynamic vacuum. The description of the samples and the corresponding EPR signals are listed in Table 4.16.

Nitrogen-doped P25 gave a very low intensity signal, partially masked by the signal produced by copper atoms with unpaired electrons from the instrument resonator (the strong peak at ca. 3300 Gauss observed in Figure 4.33).^[46] It was possible to detect a clear signal only for the sample treated at higher temperature (873 K), with a g value of 1.998, which could be associated with superficial Ti^{3+} defects.

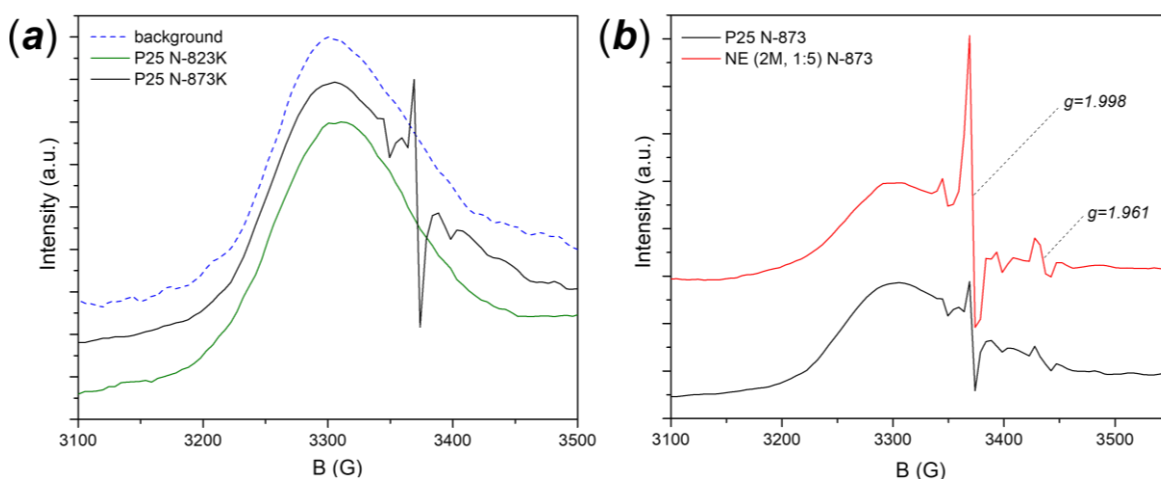


Figure 4.33: EPR spectra of (a) ammoniated P25 and (b) of ammoniated FMH- TiO_2 compared to ammoniated P25.

In the FMH- TiO_2 particles after ammonolysis, the same signal appeared stronger with a further resonance at $g = 1.961$, compatible with the formation of bulk Ti^{3+} defects. In both samples, the intensities of the signals suggest that ammonolysis has generated a low concentration of structural defects. Since bulk Ti^{3+} is more stable than superficial Ti^{3+} , the presence of the former species would extend the lifetime and the operational capacity of the photocatalyst. Despite the weakness of the signal, the presence of bulk Ti^{3+} indicates that FMH- TiO_2 can be more easily modified than the more crystalline material (P25).

Unlike the ammoniated samples, the particles heated under vacuum or under inert gas (argon) displayed a sharp and strong EPR signal with $g = 2.001$ - 2.004 , associated with superficial Ti^{3+} (Figure 4.34). Figure 4.34 b shows the EPR signal of the vacuum heated sample collected at different temperature. The signal shifts

towards higher g values (lower B) at 125 K. Moreover, two almost symmetric signals appeared around the main signal, with g values 2.040 and 1.969.

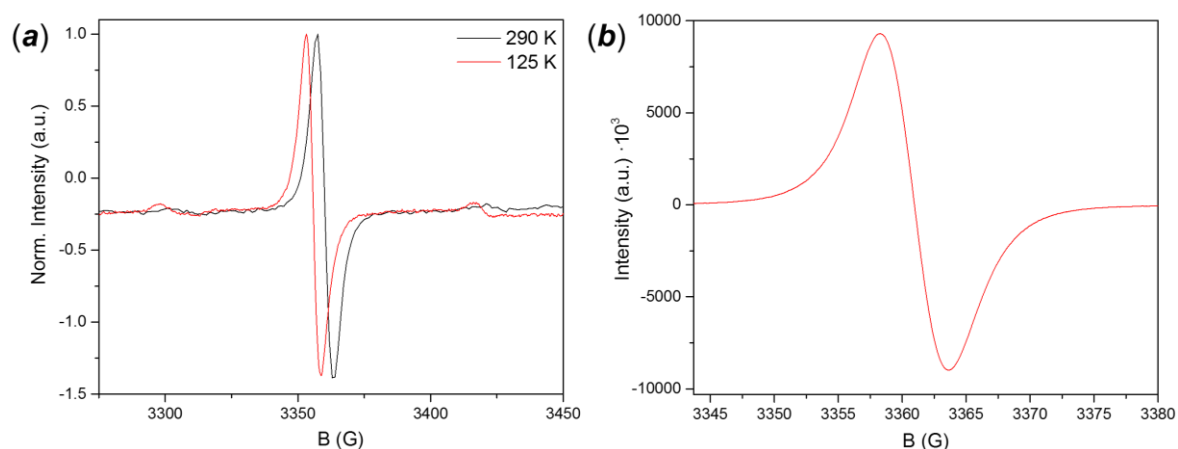


Figure 4.34: EPR spectra of FMH-TiO₂ particles calcined (a) under static vacuum and (b) under dynamic vacuum conditions. The EPR of (a) was collected at different temperatures indicated in the graph.

Table 4.16: List of the sample selected for the EPR analysis with their corresponding g values.

Sample	Post-synthesis treatment	T (K)	B (Gauss)	g
P25	NH ₃ , 873 K	290	3371.27	1.998
		290	3435.70	1.961
		140	3371.21	1.998
NE (2 M, 648 mM)	NH ₃ , 873 K	290	3371.84	1.998
		290	3435.19	1.961
NE (2 M, 648 mM)	Ar, 773 K	290	3359.53	2.005
NE (1 M, 648 mM)	Dyn. Vac., 673 K	290	3361.40	2.004
NE (2 M, 162 mM)	St. Vac., 773 K	290	3358.97	2.005
NE (1 M, 162 mM)	Dyn. Vac., 773 K	290	3360.23	2.005
		125	3355.80	2.007
		<i>peak (a)</i>	125	3302.26
	<i>peak (b)</i>	125	3419.82	1.969

4.7.3 Comparison with reverse oxidation reaction

Ultimately, the reduction of TiO_2 (commercial catalyst, FMH particles or other materials) proposed in this thesis would result in complete nitridation (TiN) or to reduced oxides (Ti_2O_3 or TiO). The analysis of the opposite reactions was performed in an attempt to find evidence of similarities and hence shed light on the transformation of TiO_2 after ammonolysis and vacuum annealing. Commercial TiN (Aldrich, 99%) and Ti_2O_3 (Johnson-Matthey) were oxidised under air at different temperature using constant treatment duration and heating rate. The temperature range was chosen between 573 - 973 K, where the physical modifications of the samples were more evident. All samples were thus analysed via PXD for phase characterisation and DR-UV-Vis for determination of the electronic structure.

Titanium nitride is a ceramic material which appears matt brown when it is pure, it becomes grey at 773 K turning progressively to white through different shades of yellow as it is heated in air. The transition to TiO_2 occurs between 723 - 773 K, with the formation of both rutile and anatase, with rutile dominating as the temperature is increased.

Ti_2O_3 oxidises in air to rutile TiO_2 between 723 - 773 K (similar to TiN), consistent with the findings of Morikawa and Asahi.^[47] Ti_2O_3 changes colour from the original dark purple progressively to green to yellow, to pale yellow and finally almost white at 973 K (Figure 4.35). This colour scale was observed for the TiO_2 nitridation, which would also imply Ti^{3+} due to the reducing atmosphere caused by the NH_3 thermal dissociation.

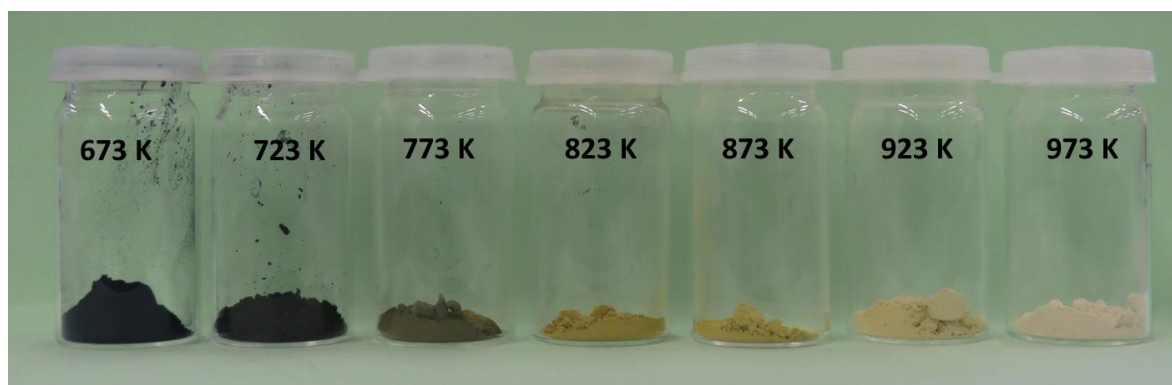


Figure 4.35: Colour of samples as commercial Ti_2O_3 (Johnson-Matthey) is oxidised at different temperatures (3 hours thermal treatment, heating rate 10 K/min)

The analysis of the DR-UV-Vis spectra revealed a clear transition from the Ti_2O_3 structure (more metallic) to the classic sigmoidal shape observed in semiconductor materials such as TiO_2 (Figure 4.37). The material treated at 773 K, when the predominant crystalline structure is composed of Ti^{4+} atoms. At this temperature, both direct and indirect band gap indicates the presence of two distinct values.

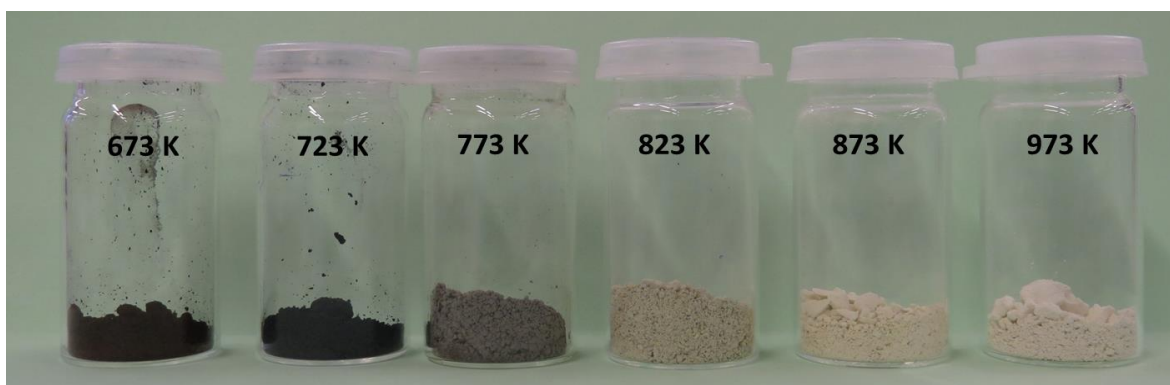


Figure 4.36: Colours of the samples of commercial TiN (Aldrich, 99%) after heating in air at different temperatures (3 hours thermal treatment, heating rate 10 K/min).

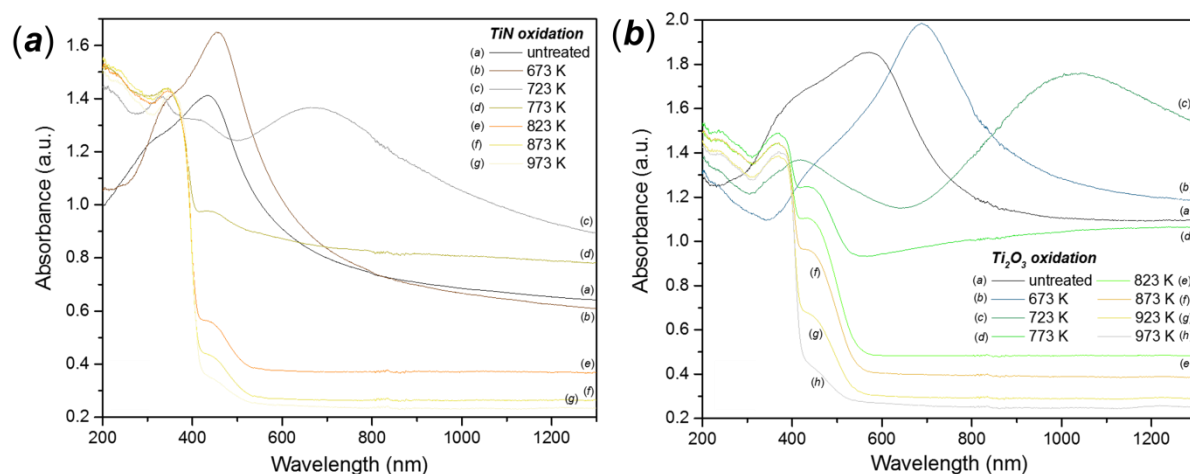


Figure 4.37: Absorbance spectra of (a) TiN and (b) Ti_2O_3 after progressive oxidation at different temperature.

4.8 Other reductive thermal treatments

4.8.1 Hydrogen atmosphere

Recently, hydrogenation has been shown to increase lattice disorder with the production of mid-gap states, responsible for visible light absorption. The macroscopic effect of hydrogenation is a drastic change in colour of TiO₂, which usually becomes black. Similarly to ammonolysis, the interaction of H₂ with TiO₂ has been described as a three-stage process, strongly depending on the temperature of the treatment. H₂ interacts with the oxygen atoms in the lattice above 573 K transferring electrons and abstracting oxygen. Above 723 K electron transfer occurs at the Ti⁴⁺ centres, which are reduced to Ti³⁺. Electron transfer from the oxygen vacancies to Ti⁴⁺ then occurs at 833 K, generating further Ti³⁺ defects.^[93] Unlike the generation of structural defects under vacuum, hydrogenation provides stable superficial and bulk functionalisation, potentially enhancing the lifetime and efficiency of the photocatalyst.^[48]

Conventional hydrogenation is usually performed at relatively low temperature (473 K) and high pressure (2 MPa), which requires special equipment. Lu *et al.* recently reported hydrogenation of P25 at room temperature, under an atmosphere of 3.5 MPa of H₂ for three weeks.^[49]

Here, milder hydrogenation conditions were used. 5% H₂ in nitrogen (forming gas) or argon, used at the same temperatures as the ammonolysis reactions previously described, was not able to modify commercial anatase or P25. This thermal treatment was almost identical to a conventional calcination in air. However, reduction by forming gas of TiO₂ has been reported to generate a reduced TiO_{2-x} (x ~ 0.01), at 1373 K.^[50] Also, equivalent heating of the FMH-TiO₂ particles only led to further crystal growth as identified by PXD patterns with narrower peaks. However, the treatment led to a complete transformation of the sample colour, from white to brown/black, similar to the vacuum heated samples. Figure 4.38 shows the optical functions for a representative FMH-TiO₂ sample (2 M HNO₃, 162 mM precursor concentration, 1 min MW treatment) before and after the hydrogenation under forming gas atmosphere. The band gap is narrowed as width of the linear slope, with the presence of a non-zero tail after the absorption edge.

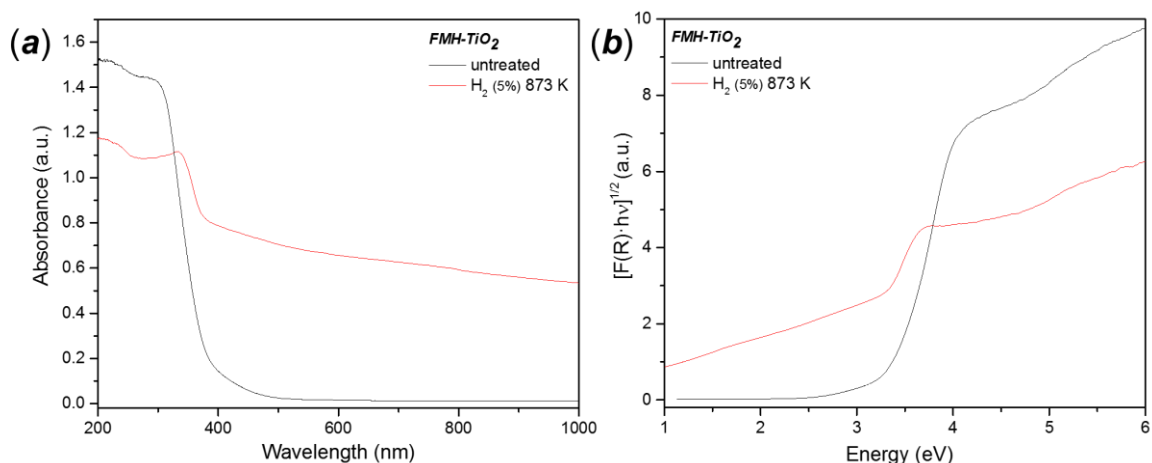


Figure 4.38: (a) Absorbance spectra and (b) Kubelka-Munk transformation for the indirect band gap for the hydrogenated FMH-TiO₂ particles

The effects of the mild hydrogenation treatment are similar with those from annealing under inert or oxygen-poor atmosphere, with notable defects forming only from TiO₂ samples of low crystallinity.

4.8.2 Microwave heating

In addition of being a useful tool to improve heating in inorganic and organic synthesis reactions, MW heating is also useful in solid state reaction. Attempts to calcine both crystalline materials and as-synthesised particles were made using a single-mode MW reactor. The reactions were performed under vacuum (in sealed quartz tubes), under a protected atmosphere (flowing inert gases such as N₂ and Ar), under flowing ammonia or under a dynamic vacuum.

A number of transition metal binary oxides has been reported to exhibit strong interaction with microwave radiation.^[51] The capacity to generate heat when irradiated makes dielectric oxides useful as MW susceptors, facilitating high temperature synthesis of oxides or inducing sintering.^[52] Vaidhyanathan *et al.* reported that TiO₂ could be heated to 873 K (average temperature of the polymorphic transformation) in only 15 min of irradiation at 2.45 GHz within a multimode cavity with a maximum output power of 1 kW.^[53]

Figure 4.39 *a* shows the polymorphic transformation of commercial anatase by MW heating under static vacuum after between 30 seconds and 4 minutes of treatment. The samples were coloured between grey and blue. A blue coloration is indicative of Ti³⁺ in both anatase and rutile TiO₂.^[54] The analysis of the electronic spectra of the modified materials (Figure 4.39 *b*) confirms the modification of the

band gap, with the evident presence of a double slope, due to the coexistence of the two polymorphs.

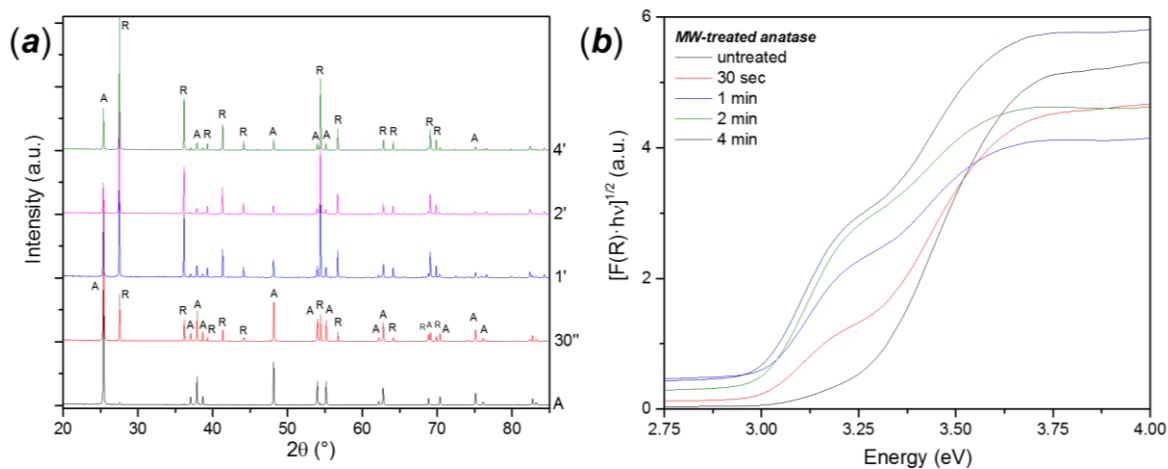


Figure 4.39: (a) PXD patterns and (b) Kubelka-Munk function for indirect band gap of commercial anatase heated in a MW cavity for 0.5 – 4 min. “A” denotes anatase peaks, “R” denotes rutile peaks.

Table 4.17: Phase composition and optical properties of commercial anatase MW-heated under vacuum as a function of the treatment time. (3 measurements on the same sample, standard deviation for band gap measurement ≤ 0.01 if not indicated).

MW treatment (s)	Anatase (wt %) ^(a)	Indirect band gap (eV)	Direct band gap (eV)	Urbach energy (meV)
30	72.9	3.19, 2.98	3.42	47 ± 1, 127 ± 9
60	29.1	2.95, 2.96	3.32, 3.11	69 ± 2, 263 ± 11
120	17.2	2.82, 2.98	3.32, 3.11	58 ± 1, 241 ± 22
240	20.7	2.96, 3.00	3.35, 3.10	53 ± 1, 339 ± 12

^(a) calculated by Spurr-Myers formula, single measurement using same diffractometer conditions

4.9 Photocatalytic properties

The photocatalytic properties of the samples were assessed by controlled degradation of an organic dye (rhodamine B) in aqueous solution. The degradation experimental setup is described in chapter 2. The results of photocatalytic tests depend on many experimental factors, including the instrumental apparatus (light source and power intensity, geometry of the photoreactor, etc.), the type of dye and its concentration, the concentration of the catalyst and other variables (solution pH, temperature).^[55] For this reason, the most efficient way to assess the performance of a material synthesised in house is by comparison with a reference material under the same conditions. Tests with anatase or commercial TiO₂ photocatalyst (Aeroxide[®] P25, Kronos 7000) were compared to analogous work in the literature citing the same dye (rhodamine B) and an unequivocal reference material (one of the previously mentioned commercial catalysts). These tests were also useful to validate the reproducibility of the measurement performed using degradation apparatus and protocol here adopted.

As shown in Table 4.18, the degradation rates do not correlate linearly with the catalyst concentration, as reported by several authors.^[55] Despite the supposed good photocatalytic properties described for the Kronos catalyst, the degradation performance using rhodamine B was much lower than expected, both under UV and visible light irradiation. A graphical representation of the degradation data for the commercial reference material is given in Figure 4.40.

Table 4.18: Results of degradation test for the reference materials, using different concentration of photocatalyst in Rhodamine aqueous solution (calculations based on 3 repeats of the degradation experiment with the same material).

	Degradation constant (UV) (10^{-3} min^{-1})	Deg. Rate at 20 min (%)	Deg. Rate at 60 min (%)	Degradation constant (VIS) (10^{-3} min^{-1})	Deg. Rate at 20 min (%)	Deg. Rate at 60 min (%)
P25						
250 mg/L	64.6 ± 8.4	72.0 ± 1.6	99.5 ± 0.6	3.9 ± 1.6	3.3 ± 1.8	14.8 ± 3.8
500 mg/L	97.3 ± 8.8	82.7 ± 7.0	100	5.2 ± 1.2	5.7 ± 1.8	18.8 ± 3.8
1 g/L	103.7 ± 6.8	84.2 ± 1.9	100	6.4 ± 0.3	9.9 ± 0.8	31.7 ± 0.8
Anatase						
1 g/L	70.5 ± 4.4	74.3 ± 1.4	100	5.4 ± 0.7	10.3 ± 1.2	22.5 ± 2.5
Kronos						
500 mg/L	4.6 ± 0.4	7.4 ± 0.9	38.6 ± 6.3	0.8 ± 0.3	2.3 ± 0.5	4.8 ± 1.7
1 g/L	8.2 ± 1.9	21.5 ± 1.1	82.5 ± 2.4	4.2 ± 0.4	9.5 ± 1.6	30.4 ± 3.2

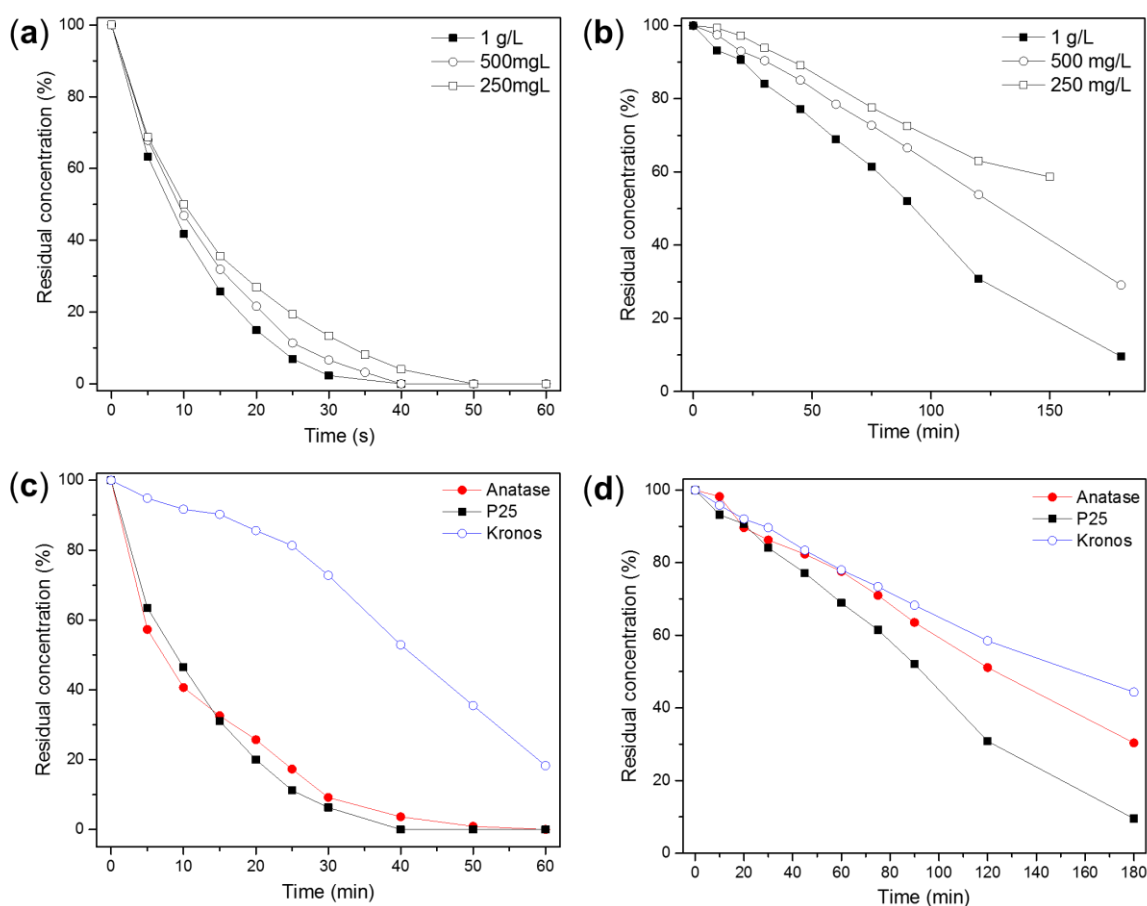


Figure 4.40: Results of the degradation experiment for different concentration of Aeroxide P25 (a) under UVA and (b) under visible light irradiation; comparison between degradation experiment of the reference materials (commercial anatase, P25 and Kronos7000, 1 g/L in Rhodamine solution) performed (c) under UVA and (d) under visible light irradiation.

4.9.1 Untreated particles

Degradation tests on untreated FMH-TiO₂ samples were not initially considered. Few preliminary tests gave negligible photoactivity under both UV and visible light. However, more accurate tests were performed selecting samples representative of different synthesis conditions (acid and precursor concentration) reputed to affect the structure of the final product. The sample analysed are listed in Table 4.19. The powdered sample was mixed to rhodamine B solution ($1.5 \cdot 10^{-5}$ mol/L) preparing a suspension with concentration 500 mg/L. The suspensions were sonicated for 10 min to enhance the dispersion of the sample and then stirred under dark for at least 30 min. This would ensure the achievement of the adsorption-desorption equilibrium between particles and dye molecules in the suspension.

Table 4.19: List of the untreated FMH-TiO₂ sample, with degradation performance under UVA and visible light (calculations based on 2 repeats of the degradation experiment with the same material).

Sample	Degradation constant (UV) (10^{-3} min^{-1})	Deg. rate at 60 min (%)	Degradation constant (VIS) (10^{-3} min^{-1})	Deg. rate at 60 min (%)
P25	97.3 ± 8.8	100	5.2 ± 1.4	18.8 ± 3.8
NE (1 M, 40 mM)	2.6 ± 0.3	13.2 ± 1.1	8.3 ± 2.4	37.2 ± 1.3
NE (2 M, 324 mM)	1.3 ± 0.4	7.7 ± 1.0	4.8 ± 1.3	24.2 ± 2.1
CE (2 M, 162 mM)	7.8 ± 1.6	37.4 ± 2.1	7.7 ± 2.6	36.3 ± 3.8
CW (2 M, 162 mM)	6.4 ± 1.8	28.3 ± 2.5	2.1 ± 0.4	10.7 ± 1.1
<i>(only visible light test)</i>				
NE (1 M, 80 mM)	-	-	7.2 ± 0.6	40.4 ± 4.2
NE (1 M, 80 mM , 15 s)	-	-	10.8 ± 2.7	44.0 ± 3.7
NE (0.5 M, 80 mM)	-	-	5.2 ± 2.3	39.0 ± 3.0
NE (0.5 M, 162 mM)	-	-	11.2 ± 1.8	41.9 ± 2.8

The degradation tests performed on FMH-TiO₂ particles resulted in not relevant photocatalytic activity under UV light illumination. However, irradiation with visible light progressively reduced the rhodamine concentration. The estimated degradation rates are in some cases comparable with the same concentration of P25 under the same conditions.

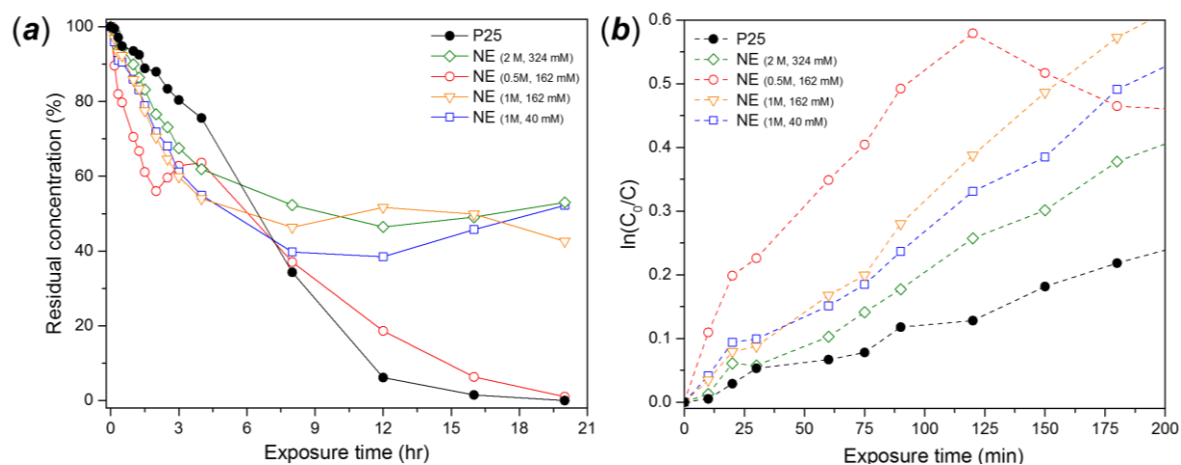


Figure 4.41: (a) degradation curve and (b) apparent degradation rate for selected FMH-TiO₂ particles under visible light (P25 is included as a comparison)

Figure 4.42 shows the evolution of the UV-Vis spectra of the rhodamine B solution during degradation. For P25 (Figure 4.42 a), absorption shifts towards shorter wavelengths during degradation. By the time that the compound is almost totally degraded by the photocatalytic reaction, the band shift is significant. This band shift is considerable for the FMH-TiO₂ sample (Figure 4.42 b). The absorption peak is finally centred at 498 nm. The observed shift in the rhodamine peak arises from the progressive degradation of the original molecule into smaller fragments. The degradation path proceeds with the progressive de-ethylation of the four N-ethyl groups bound to the xanthene structure. The original molecule has an absorption peak at 553 nm. A single de-ethylation step causes a peak shift to 539 nm, then progressively as remaining ethyl groups are detected, 522 nm, 510 nm and finally with the removal of all the ethyl groups brings the peak shifts to 498 nm.^[56] At this point, the rhodamine solution appears yellow, as shown from the picture in Figure 4.43.

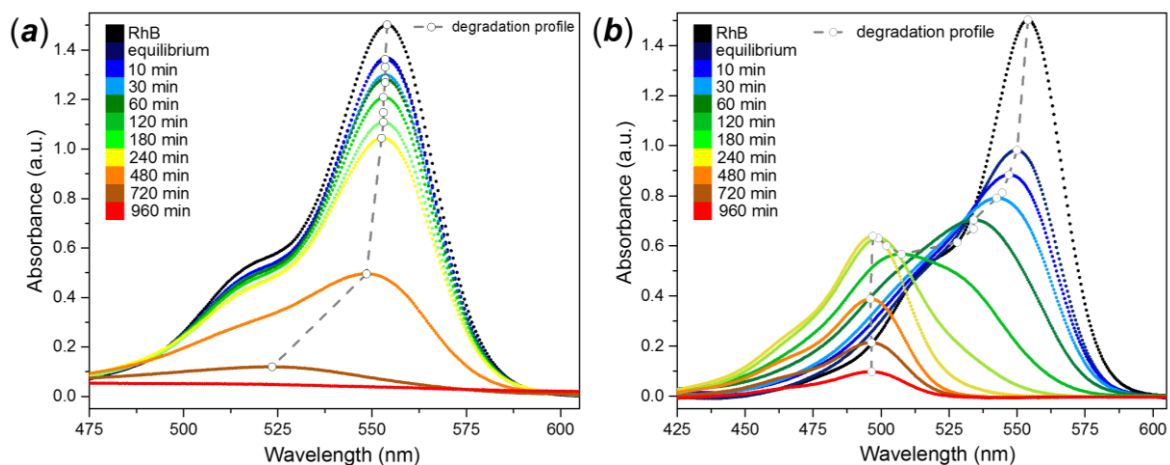


Figure 4.42: Rhodamine UV-Vis spectra using (a) P25 and (b) FMH-TiO₂ as a catalyst for its degradation under visible light. The dashed trend line indicates the maximum value for each spectrum.



Figure 4.43: Image of the rhodamine solution collected after degradation under visible light in the presence of FMH-TiO₂ particles ((a) NE, 0.5 M, 162 mM and (b) NE, 1 M, 40 mM)

After ethyl group removal, the dye is in a form similar to rhodamine 110 (3,6-diamino-9-(2-carboxyphenyl) chloride, absorbing at the same frequency) and the degradation proceeds further with the cleavage of the chromophore group, into smaller fragments until complete mineralisation. Once the chromophore group is destroyed, it is impossible to follow the degradation using UV-Vis, requiring other techniques such as TOC, HPLC or mass spectrometry. In the case of FMH-TiO₂, the degradation proceeded after de-ethylation with the cleavage of the fluorescent group of Rh110 towards complete mineralisation, causing reduction of the absorbance peak without a further shift from 498 nm. At the end of the

degradation test, the FMH sample was light purple indicating residual adsorption of rhodamine at the surface.

Some further understanding of the degradation mechanism can be obtained by following the absorption wavelength of the single de-ethylation products. The degradation curves for each part of the molecule as successive ethyl groups are removed are shown in Figure 4.44. For P25 (Figure 4.44 *a*), the concentration of each molecular part decreases uniformly. Conversely, the degradation process using FMH-TiO₂ proceeds by progressive accumulation of the de-ethylation products, slowing consistently once the concentration of the lowest de-ethylated compound is at its maximum (Figure 4.44 *b*).

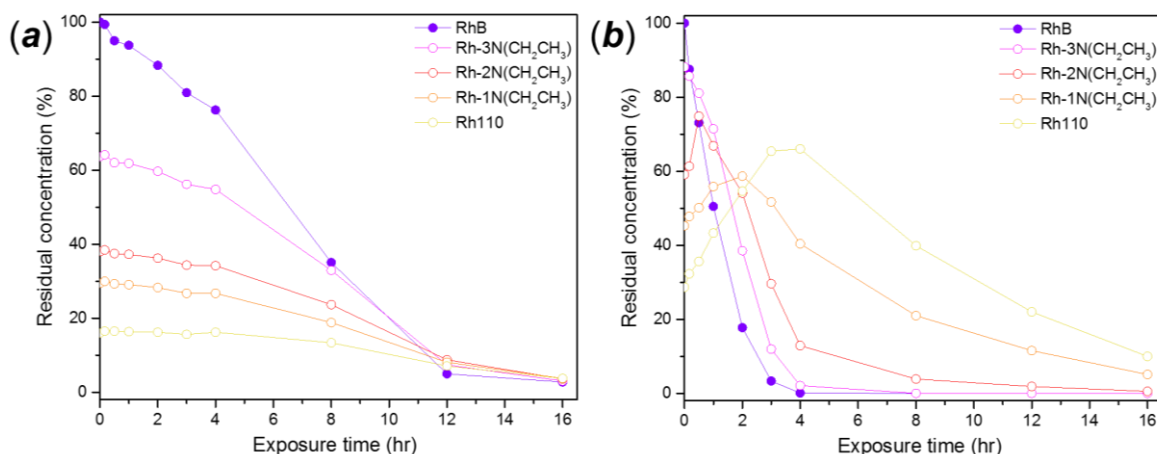


Figure 4.44: Degradation curves for the 5 degrees of N-ethylation of the Rhodamine molecule (RhB contains 4, Rh110 none) for (a) P25 and (b) FMH-TiO₂ particles (b) under visible light irradiation

This mechanism of degradation is not reported elsewhere in literature. Furthermore, according to the analysis of the optical properties of these samples, the band gap is widened by the nanocrystallinity, preventing the efficient absorption of photons with energy corresponding to the band gaps of anatase of P25. The high value of surface area of these particles might contribute towards the mechanism since the best performance was obtained with particles which synthesis conditions (such as NE particles produced using 0.5 M HNO₃) led to lower surface areas compared to the other sample tested. A common point in all the degradation experiments performed is the initial adsorption observed after the experiment preparation phase, in which the suspension of catalyst in rhodamine solution is sonicated to enhance the dispersion and then stirred to ensure the adsorption/desorption equilibrium of the organic dye. The importance and the

consequences of the dye adsorption on the particle surface will be detailed in the further section.

4.9.2 Effect of the thermal treatment

4.9.2.1 Calcination under air (oxidative treatment)

Degradation tests were also performed using FMH-TiO₂ particles calcined at different temperature. The synthesis conditions of the particles and the correspondent calcination treatment are reported in Table 4.20. Despite an improvement towards the degradation under UVA light compared to the as-synthesised particles, calcination in air was detrimental to the photocatalytic performance under visible light (Figure 4.45).

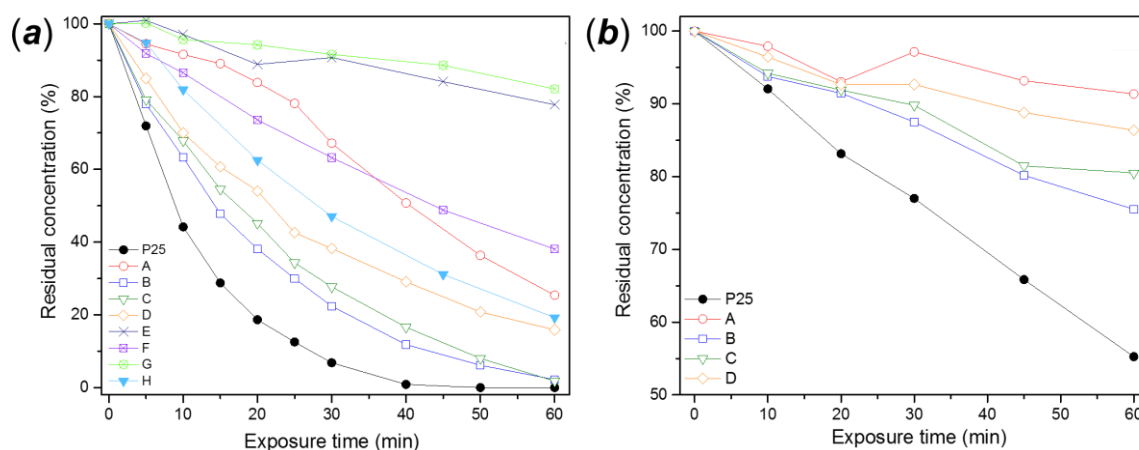


Figure 4.45: Degradation curves for selected FMH-TiO₂ samples calcined in air (synthesis conditions and calcination temperature are reported in Table 4.20, all samples treated for 3 hrs using a heating ramp of 10 K/min), under (a) UVA and (b) visible light (P25 is included as a comparison).

All the samples tested lost the photoactivity displayed by the untreated FMH-TiO₂ samples. This further confirms the link between the photocatalytic properties of the particles and their structure, in particular crystallite size and surface area. The loss of photocatalytic performance is probably influenced not only by crystallite size but also by the relative amount of rutile, since for some of the samples the calcination temperature triggered the polymorphic transition. The crystal growth has some conflicting consequences. On one side, the loss of the nano-size restores the band gap towards the values reported for the bulk crystalline material, allowing less energetic photons to generate electrons and holes. On the other hand, larger crystals imply longer path for the charge

diffusion, increasing the chance of recombination during the migration towards the surface.

Table 4.20: Structural characteristics and degradation performance of the samples tested (Figure 4.45); calculations based on 2 repeats of the degradation experiment with the same material.

Sample	Average size (<i>a</i>) (nm)	Relative amount of rutile(<i>b</i>) (%)	Degradation constant (UV) (10^{-3} min^{-1})	Deg. rate at 60 min (%)	Degradation constant (VIS) (10^{-3} min^{-1})	Deg. rate at 60 min (%)
P25	23.0	15.0	97.3 ± 8.8	100	5.2 ± 1.4	18.8 ± 3.8
<i>NE series</i>						
A (2M, 162 mM, 773 K)	22.3	0	32.5 ± 4.5	74.6 ± 2.5	1.3 ± 1.6	8.6 ± 4.5
B (2M, 162 mM, 873 K)	38.0	49.9	49.3 ± 5.9	97.8 ± 4.0	4.6 ± 0.6	24.5 ± 4.0
D (2M, 324 mM, 873 K)	39.5	30.1	31.2 ± 5.7	84.1 ± 4.1	2.3 ± 1.1	13.6 ± 3.5
<i>NW series</i>						
C (2M, 162 mM, 573 K)	10.3	0	42.3 ± 7.2	98.2 ± 3.7	3.7 ± 1.5	19.5 ± 5.4
<i>NE series (UV only)</i>						
E (1M, 324 mM, 873 K)	39.5	0	4.2 ± 0.9	22.2 ± 3.7	-	-
F (2M, 80 mM, 923 K)	35.7	67.0	16.1 ± 2.9	61.9 ± 4.9	-	-
G (2M, 162 mM, 973 K)	49.3	97.4	3.2 ± 1.6	17.9 ± 5.1	-	-
H (2M, 162 mM, 773 K)	15.3	0	27.9 ± 1.4	80.8 ± 4.5	-	-

(*a*) and (*b*) calculated by Scherrer and Spurr-Myers formula respectively (from XRD data), single measurement using same diffractometer conditions.

4.9.3 Effect of reductive treatments

4.9.3.1 Nitrogen-doped samples

A series of photocatalytic tests was performed on the ammonolysed samples, both commercial (P25, Kronos) and FMH-TiO₂. With the same protocol adopted in the previous tests, the catalyst was mixed with the rhodamine solution and exposed to UV and visible light (in separate experiments). The results of the degradation tests are reported in Table 4.21. The values for untreated P25 and Kronos are different compared with those previously reported in Table 4.18 because the degradation setup was slightly modified for this experiment, using 100 mL beakers instead of 250 mL ones. The former configuration implies lower net irradiance compared to the latter because of the less exposed surface.

Table 4.21: Degradation performance of commercial TiO₂ photocatalyst ammonolysed at different temperature (calculations based on 2 repeats of the degradation experiment with the same material).

	Degradation constant (UV) (10 ⁻³ min ⁻¹)	Deg. Rate at 60 min (%)	Degradation constant (VIS) (10 ⁻³ min ⁻¹)	Deg. Rate at 60 min (%)
P25				
untreated	59.5 ± 5.2	100	4.6 ± 1.6	19.8 ± 3.5
NH ₃ 773 K	6.1 ± 1.2	34.6 ± 3.5	1.7 ± 1.8	10.5 ± 3.7
NH ₃ 873 K	1.7 ± 0.3	9.2 ± 1.6	<i>n.d.</i>	0.8 ± 1.7
Kronos				
untreated	4.9 ± 1.4	30.0 ± 3.3	0.7 ± 0.9	4.9 ± 2.9
NH ₃ 773 K	1.6 ± 0.8	6.5 ± 3.8	0.6 ± 0.7	5.1 ± 3.0

Despite the modification of the optical properties and the preservation of the anatase structure, the ammonolysis treatment caused a dramatic reduction of the photocatalytic properties under both UV and visible light. The structural defects (vacancies, mid-gap states) introduced in the structures probably acts as recombination centres rather than trapping the charge carriers. Excessive nitrogen dopant sites have been reported to produce new electron-hole recombination sites.^[57] P25 treated under NH₃ at 773 K degrades *ca.* 30% of the initial concentration of rhodamine in the same period of time in which the unmodified material would have completely removed the dye (Figure 4.46). The photocatalytic performance is worse also for Kronos. Degradation tests performed using P25 ammoniated at higher temperature (likely containing larger amounts of nitrogen and defects), showed no degradation under visible light and barely degraded 10% rhodamine B with respect to the original concentration under UVA after 1 h.

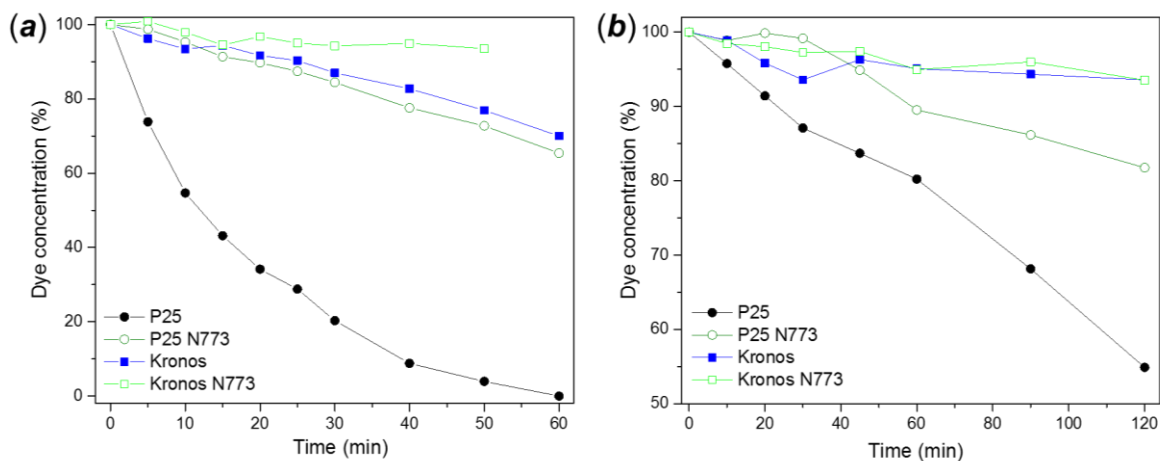


Figure 4.46: Degradation curves of P25 and Kronos ammonolysed at 773 K (N773), mixed in solution with RhB (dye concentration $1.5 \cdot 10^{-5}$ mol/L, catalyst concentration 500 mg/L) under (a) UVA and (b) visible light.

The results appear to be in total disagreement with the literature. Gao *et al.* successfully doped TiO₂ rutile nanorods with nitrogen using the same methodology adopted in the work herein; with a degradation activity towards methylene blue under UV light comparable to the untreated particles and which showed a strong improvement under visible light, with no activity showed by the equivalent untreated material. The optical characteristics of these particles are very similar to these reported herein, with the exception that of a stronger N 1s signal associated with the Ti-N bond was detected by XPS analysis.^[58] Silveyra *et al.* slightly modified the ammonolysis approach, nebulising a suspension of air, TiO₂ powder and ammonia solution through a tube furnace. The process shifted the band gap towards visible light absorption but improved the photocatalytic activity only for samples heated at 873 K. The treatment at higher temperature restored the photocatalytic activity to the level of the unmodified P25. The authors imputed it to the decrease of surface area.^[59]

4.9.3.2 Vacuum-heated samples

Unlike the case of ammonolysis samples, the formation of structural defects (Ti^{3+} /oxygen vacancies) led to an increase in photocatalytic activity for FMH- TiO_2 samples. Degradation of rhodamine B is comparable or better than P25 under UV irradiation, with outstanding results under visible light. The degradation curves reported in Figure 4.47 compares the performance of similar FMH- TiO_2 samples modified under either static or dynamic vacuum. Both samples performed better under visible light compared to P25.

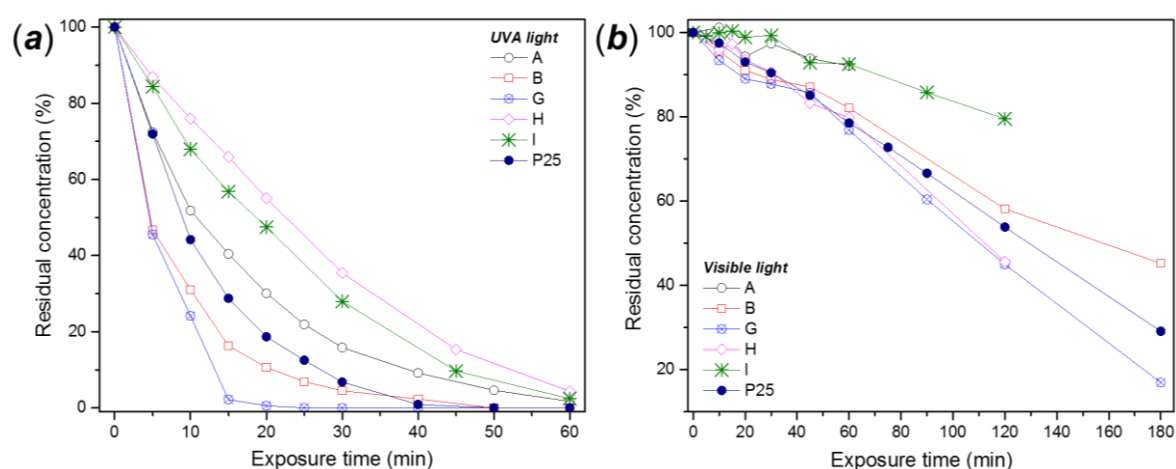


Figure 4.47: Comparison of degradation curves for rhodamine B using P25 and vacuum annealed FMH- TiO_2 samples under (a) UVA light and (b) visible light. (the description of the samples, together with the complete degradation data, is reported in Table 4.23).

The temperature of the vacuum treatment has been reported to influence the photocatalytic activity. Despite no changes in structure, samples treated at 673 K did not show the same activity as those treated at 773 K, (subsequently selected as the optimal temperature). Further increase of temperature is detrimental, similar to the consequences of higher temperature ammonolysis. Samples prepared at 873 K showed no degradation activity. Increased lattice disorder could lead to generation of recombination centres in this case, totally quenching the pairs of photogenerated carriers.

The structures, optical properties and photocatalytic performance of the samples are reported in Table 4.23, with the description of the sample synthesis reported in Table 4.22. As previously mentioned, a pivotal factor in these experiments is the adsorption-desorption equilibrium. The organic dye tends to be adsorbed and desorbed by the photocatalyst. After a certain period of time, an equilibrium between the two processes is established. As a result, the concentration of the

dye in solution becomes lower than the original value, with a constant number of molecules adsorbed on the catalyst surface. For example, in the experiment using 500 mg/L concentration of P25, the relative adsorption averaged 2.5-3%, with peaks of 8% in some isolated experiments. However, untreated FMH-TiO₂ samples showed a rapid increase in adsorption value, with the concentration at the beginning of the experiment lowered by 10-12% (Figure 4.50 a). In case of the vacuum activated particles, the values reported for the dye initial adsorption are even higher (Table 4.23, marked in blue), with degradation experiment starting using an initial dye concentration less than 50% than the original solution. In all the degradation profiles, the starting point was considered as the concentration of the dye just before the irradiation, after the full establishment of the adsorption-desorption equilibrium. Excluding this criterion, the absolute values of dye concentration after photodegradation in the presence of the vacuum-activated samples would be even lower than the values reported in Figure 4.47. Some examples are shown in Table 4.23.

Table 4.22: Description of the FMH-TiO₂ vacuum heated samples reported in Table 4.23 (SV indicates static vacuum, DV indicates dynamic vacuum); the asterisk (*) indicates 20% autoclave filling factor batches rather than 10% (conventionally adopted for the FMH-TiO₂ synthesis)

	Synthesis conditions	Vacuum heating		Synthesis conditions	Vacuum heating
A	NE (2 M, 648 mM)	SV, 673 K	F	BE (2 M, 162 mM)	SV, 773 K
B	NE (2 M, 648 mM)*	SV, 773 K	G	NE (2 M, 648 mM)	SV, 773 K
C	NE (2 M, 162 mM)	SV, 773 K	H	NW (2 M, 324 mM)	SV, 773 K
D	NE (2 M, 162 mM)*	SV, 773 K	I	NW (2 M, 324 mM)	DV, 773 K
E	NE (1M, 162 mM)*	SV, 773 K	L	NE (1 M, 162 mM)	SV, 773 K

	A	B	C	D	E	F	G	H	I	L	P25
Direct band gap (eV)	3.14	2.98	2.98	2.93	3.16	2.86	2.97	2.96	3.01	2.88	3.09
Indirect band gap (eV)	3.58	3.39	3.36	3.33	3.44	3.34	3.43	3.54	3.44	3.35	3.63
Urbach energy (meV)	190 ± 23	257 ± 19	244 ± 23	286 ± 31	150 ± 12	328 ± 37	280 ± 21	100 ± 8	221 ± 16	245 ± 13	40 ± 2
Degradation constant UV (10 ⁻³ min ⁻¹)	64.7 ± 3.5 ± 8.5	105.5 ± 18.5	135.6 ± 18.5	104.4 ± 11.7	54.1 ± 14.0	155.5 ± 15.4	267.3 ± 32.1	29.4 ± 7.2	37.7 ± 4.2	479.0*	97.3 ± 8.8
Degradation rate at 60 min - UV (%)	98.3 ± 2.3	100	100	100	100	100	100	95.6 ± 1.0	97.6 ± 2.3	100	100
Degradation constant VIS (10 ⁻³ min ⁻¹)	1.5 ± 0.3	4.7 ± 2.0	5.3 ± 1.6	2.8 ± 0.8	3.4 ± 2.5	6.5 ± 1.6	7.2 ± 2.8	4.0 ± 1.7	1.3 ± 0.5	16.1 ± 3.7	5.2 ± 1.4
Degradation rate at 60 min - VIS (%)	7.9 ± 2.4	18.0 ± 4.5	27.6 ± 2.9	17.2 ± 4.9	14.0 ± 2.5	50.4 ± 3.6	23.1 ± 17.3	20.2 ± 3.5	7.5 ± 2.3	59.7 ± 7.1	18.8 ± 3.8
Initial adsorption (%)	13.0 ± 0.2	44.0 ± 2.5	46.8 ± 2.9	47.1 ± 2.7	14.7 ± 4.6	55.6 ± 7.7	80.3 ± 5.9	29.5 ± 4.0	19.2 ± 3.5	65.0 ± 1.3	2.6 ± 1.5
Degradation rate at 60 min - VIS, considering initial adsorption (%)	21.6 ± 2.5	54.6 ± 1.7	63.7 ± 2.3	58.6 ± 2.4	26.6 ± 2.1	74.0 ± 1.9	91.2 ± 2.2	43.9 ± 2.3	25.2 ± 4.1	93.7 ± 2.8	26.58 ± 3.8

Table 4.23: Optical-electronic characteristics of the vacuum heated samples with the corresponding photocatalytic performance observed in the rhodamine degradation experiments. (calculations based on 2 repeats of the degradation experiment with the same material).

4.9.3.3 Other synthesis

Thermal treatment under inert gases (N₂, Ar) or under hydrogen atmosphere, despite the modification of the band gap of the FMH-TiO₂ samples, resulted in only a modest improvement of the photocatalytic activity. The formation of any localised states or structural defects does not produce effects similar to those observed for the vacuum activated samples.

Regarding in particular hydrogenation process, the inefficacy in producing relevant transformations in crystalline materials such as P25 is confirmed by the degradation results, which are not improved compared with the original material but even slightly reduced.

The MW-direct heating of anatase, despite the changes in structure and optical properties, did not improve the photocatalytic performance. Preliminary experiments (Figure A.31 in the Appendix) showed no improvement for modified anatase under visible light and a worse performance under UVA light. The deterioration of the photoactivity under UVA light can be attributed to the presence of rutile, but also to the further reduction of the surface area (already low for crystalline anatase). A better control of the MW irradiation in term of emitted power, cavity design and use of microwave susceptor.

4.10 Discussion

4.10.1 Calcination

In general, FMH-TiO₂ particles showed a transition temperature between 773 - 1073 K, depending on the original synthesis conditions. Compared with pure anatase, the TiO₂ submicroparticles showed a lower transition temperature. Hu *et al.* demonstrated how the pH of the precursor solution influences the transition temperature, with the onset of the phase transition as low as 723-773 K for particles synthesised with at lower pH.^[60] In our experiments, the onset of the transformation to rutile was observed at ca. 873 K. Since anatase is the most photoactive TiO₂ polymorph, the calcination conditions should not achieve the transition to rutile. For pure anatase, the transition is reported to occur between 673-1373 K, although it rapidly occurs above 923 K in air, with the efficacy of the conversion related to the duration of the thermal treatment.^[61] The transition is

strongly depending on the heating conditions,^[62] initial particle size and the presence of structural defects or external impurities.^[63,64] For this reason, the sample preparation and synthesis highly influences the transition temperature. The phase transition does not occur at a precise temperature because no phase equilibrium is involved, and the transformation is irreversible.

Since the ultimate goal of the post-synthesis treatment is the improvement of the degree of crystallinity without loss of the anatase structure, the optimal calcination temperature without protective atmosphere was estimated to be between 773-873 K, where the observed transformation to rutile was minimal for the majority of the samples tested. A preliminary study to correlate synthesis parameters, transition temperature and grain size did not provide more detailed information, mainly due to the uncertainty about the original grain size for the untreated particles and due to the systematic errors from the low precision of the furnaces employed for the thermal treatment, with temperature oscillation up to ± 25 K in some cases. Satoh *et al.* claim that the presence of unreacted precursor, residual particles below a critical size and the presence of amorphous material are all factors affecting the anatase-rutile transition temperature in sol-gel and similar TiO₂ synthesis.^[65] As similarly reported by Qu *et al.*, the anatase crystallites are free to grow and expand even in the presence of rutile below the phase transition temperature, with subsequent conversion of anatase to rutile above the transition.^[66] Patra *et al.* found the transition to rutile starts when the crystallite size of anatase grains achieves a value of *ca.* 32 nm. The transformation was complete when the grain sizes reach *ca.* 60 nm.

DTA analysis of particle calcination clarified that the different temperature for the anatase-to-rutile transition depends on the initial crystalline structure and crystallite size. The simultaneous presence of rutile domains in the structure of P25, mainly consisting of anatase, is the cause of its lower transition temperature compared to anatase^[67] and some of the FMH-TiO₂ particles, presenting nanocrystallinity. TiO₂ nanoparticles have been reported to undergoing densification or sintering at around 773 K, identified in DTA profile with an endothermic peak. However, the phase transformation occurred around 923-1073 K, masking the thermal event with a broad exothermic signal. The broadening of the exothermic transition peak (observed in other DTA profile in this thesis, such as in Figure 4.20) has been attributed to heterogeneity of the nanoparticle size.^[68]

The thermal event broadening can thus be used to compare the distribution and the homogeneity of the nanocrystallites composing the FMH-TiO₂ particles.

As for the surface area measurements, increased calcination temperature and duration have a detrimental effect on the surface area and pore volume of the particles; natural consequence of the growth of the primary and secondary particles in the FMH-TiO₂ samples. The size and shape of the pores drastically changes during the calcination process (Figure 4.8). The increase of pore volume observed at 673 K, just before the total loss of porosity, might be attributed to an internal reorganisation of the irregular pores of the untreated particles. The same thermal effect was described by Liu *et al.*, even though the authors interpreted the data as a monotonic increase of pore size due to the reconstruction of the pore structure during calcination. The discrepancy could be due to their calculation of the pore size using a single-point method rather than by more complex algorithms.^[69]

4.10.2 Reducing treatments

Calcination under non-oxidative atmosphere is reported to alter the thermal growth of the crystallites, generally slowing down the kinetics of the processes associated to the oxidative treatment. One example is the production of a non-radiative centre at high temperature (>1473 K), quenching the typical photoluminescence of a Ti⁴⁺ centre ($\lambda = 580$ nm).^[70] However, there are few studies in the literature about the direct consequences of annealing under inert atmospheres. Wu *et al.* increased H₂ production from a methanol/water solution by calcining a TiO₂ sol-gel at 673 K under Ar, outperforming P25.^[71]

The macroscopic effect of the thermal treatment under inert gases is a change of the samples' colour. The phenomena occurred only for the FMH-TiO₂ particles and not for all the commercial "reference" materials (pure crystalline anatase, P25 or Kronos). For these latter very crystalline materials, heating under a different atmosphere makes little difference compared to the equivalent treatment in air. For example, the temperature and the kinetics of the anatase-rutile phase transition has been reported to be the same both in air and under vacuum. ^[61] All treatments under oxygen-free or oxygen-poor atmospheres involve an easier modification of the band gap compared with more crystalline samples, such as the commercial reference materials, creating localised states, trapping centres in the

band gap or the possibility to extract oxygen atoms from the lattice and reduce the amount of impurities. Furthermore, calcination under inert atmosphere is potentially useful for the preservation of the initial high values of surface area or at least a limitation of the total disappearance of the mesoporous structure after the calcination process.

N-doping optimises the optical response of TiO_2 towards solar radiation. After ammonolysis, the initial white colour of the material is reported to turn yellow, green or light grey.^[72] Irie *et al.* observed a change in colour starting at 823 K, with the annealed powders turning from pale yellow to dark green in a temperature window of just 50 K.^[88]

Similar spectra and values of band gap to those observed in this thesis were reported for materials nitridated by other means, such as insertion of ammonium chloride during sol-gel synthesis.^[73, 74] Livraghi *et al.* observed a modification of the absorption edge only in the upper part of spectra (higher wavelengths), with the original band gap unchanged.^[74] This suggests an increase in the density of the localised states in the band gap as the principal effect of the ammonolysis treatment. This would also explain the change in colour and concur with observations previously that localised Ti^{3+} yield “green TiO_2 ” doped with nitrogen. The reduction of the metal centre is indeed reputed responsible of the change in band gap rather than the presence of N atom in the lattice.^[75]

Vacuum heating of anatase has been reported to produce a colour change from white to light grey above 873 K,^[61] whereas a blue coloration was observed as a consequence of annealing under high-vacuum (10^{-8} Pa), due to the production of reduced Ti^{3+} species.^[76] The result was not achieved with our setup probably because the pressure was too high to promote vacuum-activated reduction. However, Xing *et al.* managed to induce reduced states in P25 with a treatment at only 470 K in a vacuum furnace, supposedly with a minimum pressure of 1 Pa, well above the pressure used in our experiments. According to their findings, the efficacy of the reduction of the Ti^{4+} centres depends on the duration of the treatment. The reduced material showed an improved performance in dye degradation and hydrogen evolution experiments. ^[77] The darkening of the powders under vacuum has been observed also in other wide band-gap semiconductors, such as SnO_2 and ZrO_2 and can be attributed to oxygen deficiency. The hypothesis is supported by the reversibility of the colour change after calcination under oxidative conditions, as observed also in the re-oxidation

experiment reported in section 4.6.3.^[71] Initially the removal of oxygen ions and the creation of oxygen vacancies was believed to enhance the anatase-to-rutile transformation. However, treatment under vacuum would rather enable the formation of interstitial trivalent Ti centres, delaying the polymorphic transition due to the less coordination centres available for the lattice rearrangement of the O²⁻ anions.^[78]

Raman spectra of the vacuum-heated samples were almost identical to those for the untreated samples, (as observed by Ren *et al.*^[41]). Under heavy hydrogenation conditions, new bands not attributable to any of the three TiO₂ polymorphs were reported for “black TiO₂”.^[40] The new bands have been associated to the activation of zone-edge and Raman-forbidden modes, with the structural disorder breaking down the selection rule for Raman transition.^[79] Even the darkest vacuum-heated FMH-TiO₂ samples presented the Raman modes commonly observed for anatase, (Figure 4.25). A more detailed analysis of the peak positions and shape revealed a subtle redshift and broadening likely due to both the quantum size effect (typical of the nanocrystalline structure and described in section 3.9.7.1) and the presence of structural defects. As a comparison, Khan *et al.* reported a 10% increase of the E_g FWHM due to oxygen vacancies generated by high energy electron beam irradiation.^[80]

4.10.3 Efficacy of the reducing treatments

XPS can provide evidence of elements and their oxidation states at the surface of a material. Hence changes to the TiO₂ structure as a consequence of the heating treatments described previously can be probed effectively. For example, formation of Ti³⁺ and the presence of nitrogen should be detectable. The presence of reduced Ti states shifts the binding energy of the Ti 2p_{3/2} state in TiO₂ from the original 459.5 eV (Ti⁴⁺) by ca. 1.4 eV (to 457.7 eV) for Ti³⁺,^[81] whereas even greater shifts are associated with Ti²⁺ (3.1 eV) and Ti⁰ (4.1 eV) states.^[82] The XPS Ti 2p peak in TiO₂ is sharp, whereas the presence of Ti³⁺ can produce a broad convoluted signal that shifts towards lower binding energies.^[39, 83]

N-doped TiO₂ usually shows two characteristic N 1s signals, at 396 eV and 401 eV. The peak at 396 eV is generally expected in case of nitridic species^[84] or substitutional nitrogen,^[4] such as for the Ti-N bond.^[85] The signal at higher binding energy corresponds to molecularly chemisorbed nitrogen.^[86] The effect of a

specific nitridation method can be assessed by observing the intensity of these signals and their persistence after Ar sputtering. Nitriding of TiO₂ via ammonia should lead to the incorporation of N atoms from the outer surface of the particles, with the production of a core-shell structure in which the core could be relatively free from dopants (depending on temperature and treatment time). [87] The total absence of a clear signal attributable to the presence of nitrogen is not completely unexpected. Irie *et al.* reported a very low intensity N 1s peak for samples calcined under NH₃ (at 823, 858 and 873 K for 3h) giving dopant concentrations of 0.5, 1.1 and 1.9%, respectively (Figure 4.48). [88] Similarly, Yuan *et al.* observed only a weak signal at 396 eV, barely distinguishable from the background, despite using a high concentration of urea as a source of nitrogen and a relatively low calcination temperature (623 K). Despite this, their samples showed a red-shift in the band gap and acceptable photocatalytic activity to H₂ evolution, consistent with successful N-doping. [86]

As for the atomic concentration, the atomic ratio of the identified elements is similar to the results from EDX. Excluding the presence of carbon, the atomic percentage of titanium derived from the integration of the signal was estimated as 24.3% for the N-doped P25 and 27.7% for the N-doped FMH-TiO₂ particles.

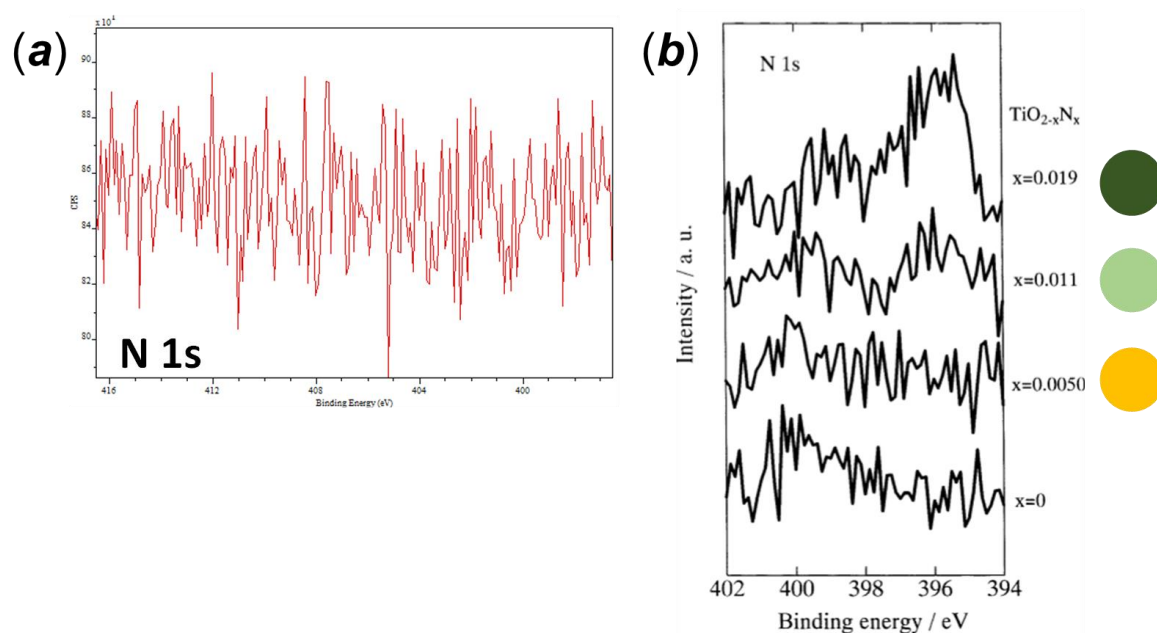


Figure 4.48: Comparison between the XPS analysis of the N 1s signal performed (a) on the N-doped P25 and (b) the data reported by Irie *et al.* (ref [88], coloured circles added according to the sample description reported by the authors).

4.10.3.1 EPR

Another method to identify reduced Ti species is EPR spectroscopy. The reduction of Ti^{4+} to Ti^{3+} in TiO_2 generates paramagnetic species, with one unpaired electron and hence EPR active. Stoichiometric diamagnetic TiO_2 , (included P25) is EPR silent. The EPR signal from Ti^{3+} is sensitive to its location on the surface or in the bulk of TiO_2 . The g-factor is significantly lower for surface Ti^{3+} compared to the bulk species; the former with $g = 1.998$ and the latter with $g = 1.961$. The two signals also differ in shape, with a sharper signal for bulk interstitial centres and a broader response for superficial ions. The g-values are also sensitive to unpaired electron density and symmetry of the local surroundings, (such as the presence of vacancies and impurities in the nearest coordination sphere or from surface modifications).^[89, 83] For example, a signal from superficial Ti^{3+} ions might from $g = 1.99$ - 1.94 depending on the surrounding environment.^[90]

Superficial Ti^{3+} is generally considered unstable under illumination in air or in the presence of electrolytes, undergoing oxidation by air or dissolved oxygen in water.^[91] The presence of this Ti^{3+} EPR signal can be explained by the reduction of the adsorbed atmospheric O_2 to O^{2-} by the surface Ti^{3+} and can be attributed to the presence of an unpaired electron trapped in an oxygen vacancy (giving a g-value of ca. 2.002).^[92, 93] The nature of this signal is still under debate, however. In some cases, the resonant signal at $g = 2.002$ has been associated with the presence of unpaired electrons in the structure.^[94] Some authors claimed that in some cases the two signals related to oxygen vacancies and superficial Ti^{3+} are both present and indistinguishable because the weak g tensor anisotropy would cause the overlapping between the two signals, convoluted in a single resonance around $g = 1.98$ - 2.00 .^[77] As a result, the EPR spectrum of Ti^{3+} can be considered as a superposition of two derivatives of Lorentzian lines with very similar g values.^[95]

4.10.4 Degradation performance

4.10.4.1 Crystalline structure and defects

The crystal structure and microstructure of the photocatalyst are essential for the efficient transport of photo-generated electrons and holes. Reduced crystal size increases the number of boundaries between crystalline domains, which would favour recombination and/or slow down the migration of the charges from the bulk to the surface. However, Anpo *et al.* reported enhanced photocatalytic activity of TiO₂ when the particle size is reduced to less than 10 nm, attributing the phenomenon to a quantum confined structure, inducing localised states, and the reduced size of the exciton formed by the photo-generated electron/hole pair. These effects compensate for the increased number of grain boundaries and other structural defects. Moreover, the nanometric size facilitates the diffusion of the charges towards the surface for photocatalysis.^[96]

In case of untreated FMH-TiO₂, the photocatalytic activity under visible light could be also attributed to impurities, generating localised states and lowering the frequency range of the absorption. In the previous chapter the two principal sources of impurities were suggested to be NO (in the case of HNO₃-mediated syntheses) and residual carbonaceous impurities from the precursor. NO has been reported not to alter the electronic structure of the material, segregating in pores, which would explain also the multistep release observed during the temperature program in the simultaneous thermal analysis. On the other hand, residual carbon could be considered as a dopant. Several synthesis methods have reported successful production of C-doped TiO₂ photocatalysts using the precursor itself as a source of carbon.^[97]

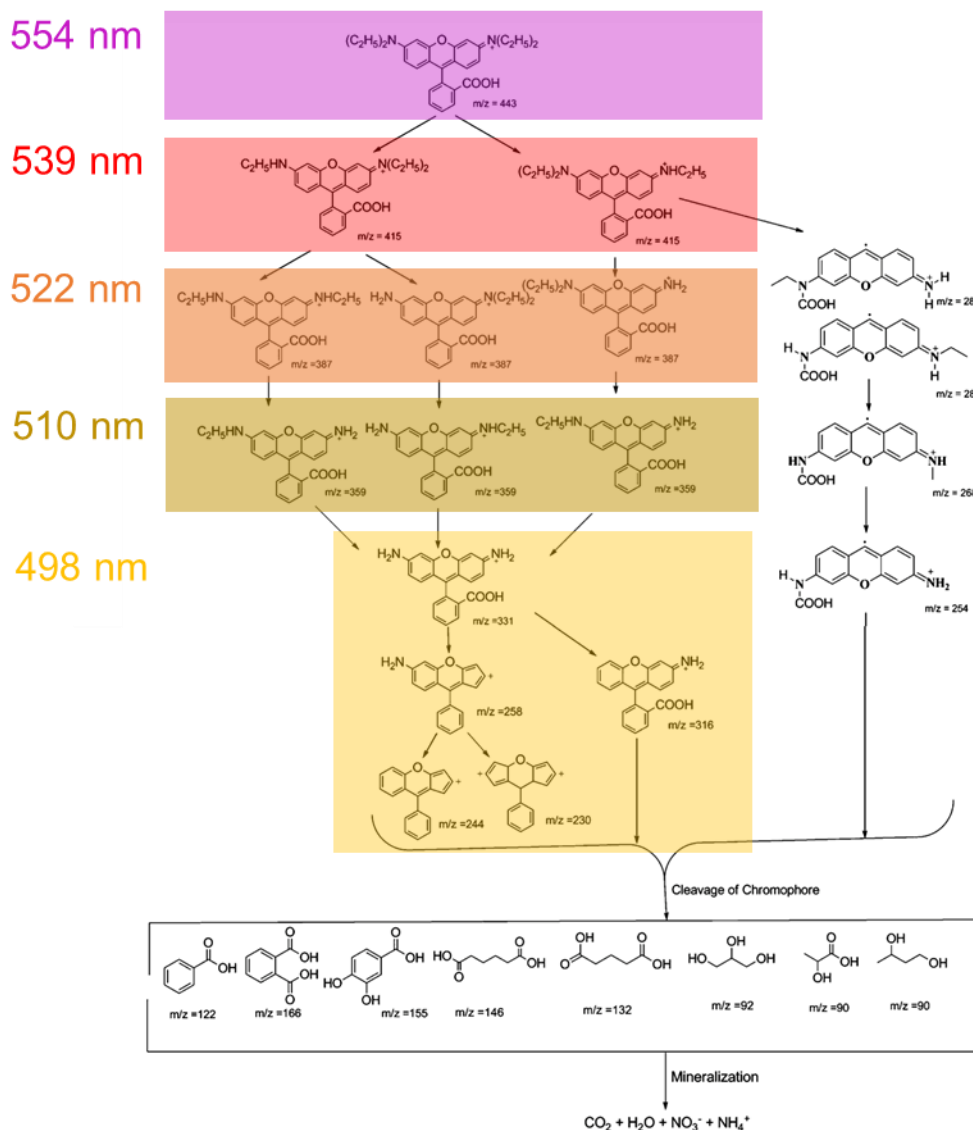


Figure 4.49: Proposed mechanism of degradation of rhodamine B (adapted from Jo *et al.* [98])

The effect of such impurities (N and C inserted during synthesis) is difficult to assess univocally. Xiao *et al.* observed a moderate increase of the photocatalytic activity under visible light compared to the undoped particles when using glucose as a carbon source in hydrothermal synthesis. In this case the optical properties (band gap, absorption edge) were unchanged apart from the appearance of Urbach tails in the absorption spectra.^[99] Parida and Naik reported an N-doped structure produced by co-precipitation with urea, producing a material showing higher photocatalytic activity under visible light compared to P25, but with lower performance under UV irradiation.^[100] This behaviour is similar to the untreated FMH-TiO₂ samples. The authors though neither explain the exact mechanism nor considered the absorption capacity, despite pronounced mesoporosity in their samples. One of the possible explanations for the different photocatalytic activity

under visible and UV light could originate from the lower mobility of the electrons in the localised states compared with those in the valence band. The carriers excited by visible-light are trapped in localised states without recombining, with subsequent migration towards the surface. Higher energy (UV light) promotes the transition to the conduction band, where the mobility is higher, leading to recombination. Another explanation can be found in the non-efficient absorption of the UV photons, with energy higher than the gap reduced by the localised states and the electrons promoted to these last, with the energy difference emitted as phonons (enhancing “non-vertical” transitions).

Calcination of samples in air has a sintering effect on the FMH-TiO₂ particles, increasing crystallinity and long-range order of the structure. The treatment also decreases porosity, reducing pore volume and, consequently, the surface area of the particles. Because of the improved crystallinity, degradation tests on annealed samples showed an improvement in photocatalytic activity under UVA light. Unfortunately, despite the improvement, the observed degradation rates are not comparable with commercial standards.

In this chapter, two contrasting phenomena regarding defects have been observed. Defects introduced by ammonolysis are detrimental towards photoactivity perhaps because of the high structural disorder generated. The insertion of nitrogen (probably in interstitial position due to the lack of evidence of the presence of Ti-N bonds) and the production of Ti³⁺ defect centres both in the bulk and on the surface increase the number of potential recombination centres. The reduction of surface area from heating under NH₃ is also detrimental. This is consistent with Hu *et al.* where the efficiency of N-doping was improved by the quantum-sized crystal, the presence of rutile as a secondary phase and the high surface area; after calcination the proposed material performed worse than the untreated samples.^[101] By contrast, the enhanced photoactivity of the vacuum activated samples can be explained by both nanocrystallinity and the presence of the structural defects such as Ti³⁺ and oxygen vacancies. A high concentration of these defects leads to the generation of a vacancy state just below the valence band, lowering the band gap and promoting photoactivity under visible light.^[102] As reported in section 4.7.2, the presence of only superficial Ti³⁺ and oxygen vacancies can be detrimental for the photocatalytic activity in the long term or with re-use, since the oxidative process can remove the surface defects restoring stoichiometric conditions (i.e. TiO₂). However, the presence of bulk defects, such

as Ti^{3+} observed in N-doped samples, could induce a stable source of recombination centres for the photoinduced charge carriers, quenching the photocatalytic activity of the material.^[103]

4.10.4.2 Catalyst sensitisation

As already mentioned, the initial concentration of the dye during the degradation experiment was measured after the assumed achievement of the adsorption-desorption equilibrium between the dye and the catalyst surface. Compared with the original concentration of the dye, which was assumed to be almost constant for all the different experiments, a dramatic reduction of was noted due to the adsorption equilibrium, especially in case of the vacuum activated samples. A higher capacity of dye adsorption was also observed for the untreated FMH-TiO₂ samples compared with the reference materials. The adsorption capacity is partially lost after most of the post-synthetic treatments (except the vacuum-activation), correlating the phenomenon to the higher surface area of the untreated particles. Figure 4.50 compares the initial adsorption of rhodamine to the catalyst and the degradation rate, calculated from the results of the photodegradation experiment on the untreated FMH-TiO₂ samples described in the previous section.

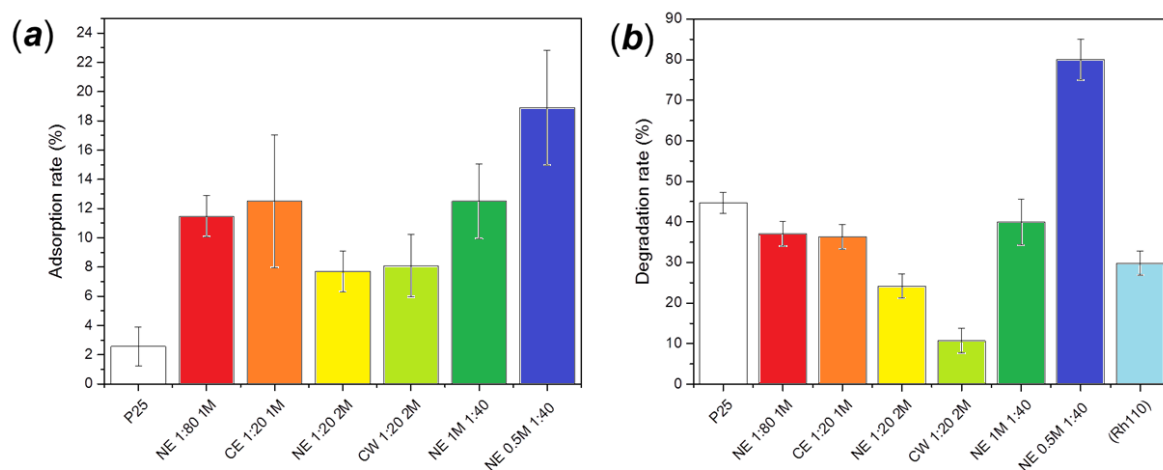


Figure 4.50: (a) Initial adsorption and (b) degradation rate under visible light after 1 hour for some of the untreated FMH-TiO₂ samples. In figure (b), the light blue bar indicates the degradation relative to the final Rh110 by-product (calculations and standard deviations estimated on double measurement using the same sample for the degradation experiment).

Even in samples showing moderate and low photoactivity, such as the FMH-TiO₂ samples annealed under air at 873 K, showed an initial reduction of the rhodamine

concentration of almost 9% immediately after sonication which remained constant after stirring in the dark.

The initial surface adsorption is strictly correlated with the increase of the degradation efficiency of the photocatalyst. This effect is sometimes referred to as "activity under dark", usually occurring in photocatalytic degradation performed using mesoporous or high surface area materials. Xu *et al.* reported a 50% of the degradation efficiency was only due to the absorption phenomena in nanostructures composed of a mixture of nanocrystals and mesoporous spheres, forming a bigger structure with the (001) facets exposed.^[104] It is well known that high surface area leads to higher photocatalytic activity.^[105] Untreated FMH-TiO₂ present particularly high surface areas (at least 150 m²/g for the particles belonging to the *NE* series), which could explain the relatively high adsorption values and the relatively high photocatalytic activity (at least under visible light). The adsorption abilities of the organic dyes onto the photocatalytic particle surface can be investigated through the calculation of absorption equilibrium constants. The absorption behaviour of organic molecules on TiO₂ powder can be described considering the absorption coefficient in the Langmuir-Hinshelwood equilibrium used to fit the degradation process associated with heterogeneous photocatalysis. The precise effect of the surface area in TiO₂ photocatalyst is still under investigation. When large surface arises through nanostructuring, the influence the quantum size effect is considered to be a predominant in determining photocatalytic activity.^[96] Slimen *et al.* investigated the dark adsorption on an activated carbon-TiO₂ catalyst, using the Lagergreen model for the adsorption-desorption equilibrium. In their findings, calcination under an inert atmosphere results in a higher adsorption capacity principally due to the higher surface area.^[27]

A higher adsorption capacity could also represent a drawback for photocatalytic activity. Reduction of photoactivity has been reported when the concentration of the organic dye was increased. A higher amount of adsorbed molecules prevents photons being absorbed by the catalyst, reducing the photogeneration of charge carriers and the production of radicals on the surface.^[106]

4.11 Conclusions

The results reported in this chapter can be highlighted in the following key points:

- FMH-TiO₂ particles shows higher degradation rate compared to P25 under visible light, following predominantly a mechanism of selective de-ethylation;
- Calcination and reducing ammonolysis were not able to improve notably the photocatalytic performance of the tested materials;
- Annealing under vacuum provided promising results, with higher degradation rate under both UV and visible light compared to commercial TiO₂ catalysts;
- Adsorption processes in solution are the key for the improvement of the photocatalytic performances;

Despite their structural characteristics (band gap of 3.2-3.5 eV), FMH-TiO₂ particles are not active under UVA light. However, degradation under visible light of rhodamine B is higher or comparable to that observed for P25 (apparent degradation rate constant of $5.2 \cdot 10^{-2} \text{ min}^{-1}$ and degradation rate after 1 hour of *ca.* 20% of the original dye concentration). A deeper analysis of the mechanism showed a very fast initial de-ethylation of rhodamine followed by a slower cleavage of the chromophore groups. The first de-ethylation step observed using selected FMH-TiO₂ is 3 times faster compared to P25. Notably, 10% of the original concentration of dye is adsorbed onto the particle surface, compared with the *ca.* 2.5% adsorbed on P25.

Calcination of the FMH-TiO₂ particles is potentially useful in control of the composition in anatase and rutile, which combination is supposed to be the reason behind the higher catalytic performances of Aeroxide P25. However, the initial high surface area is lost during the process, which should be considered in the experimental design. At intermediate temperature (573-673 K) before the polymorphic transition, the pore structure reorganised with formation of cylindrical pores, before to shrink and disappear at higher calcination temperatures. Due to this process, the FMH-TiO₂ particles lost both the adsorption capacity and photoactivity under visible light, being able to degrade rhodamine under UV but at lower rates (apparent constant of $2.5 \cdot 10^{-2} \text{ min}^{-1}$ under UVA,

$2.4 \cdot 10^{-3} \text{ min}^{-1}$ under visible light) compared with P25 (degradation constant of $9.7 \cdot 10^{-1} \text{ min}^{-1}$ under UVA light).

Ammonolysis process successfully modified the electronic properties of both commercial TiO_2 samples and FMH- TiO_2 particles. The absorption capacity of the samples was efficiently shifted towards visible light, with optical band gap reduced to *ca.* 2.5 eV at 773 K of treatment. Above this temperature, structural changes occurred, with activation of the transformation from anatase to rutile or the onset of secondary phases, such as TiN or non-stoichiometric titanium oxides. Ammonolysis is responsible for the formation of non-stoichiometric defects, in particular generation of Ti^{3+} centres both in the bulk and on the particle surface, as shown by EPR analysis. However, the photocatalytic performances of the particles are not improved compared with the sample calcined in air and with commercial materials, which optical properties were also successfully modified in terms of visible light absorption.

Vacuum annealing modified as well the optical properties and electronic structure of FMH- TiO_2 , with negligible effect on commercial samples. The net modification of the absorption capacity led to the reduction of the band gap in a range of values between 1.90 and 2.80 eV, depending on original synthesis conditions and annealing temperature. The onset of the polymorphic transformation was observed above 773 K, subsequently chosen as optimal treatment temperature. Vacuum treatment gave to the particles increased structural disorder, displayed by the higher Urbach energy values (above the *ca.* 200 meV observed for some ammonolysed sample in the range 673-773 K) and the shift of the Raman modes. Moreover, EPR analysis revealed the presence of O^{2-} vacancies ($g = 2.002\text{-}2.005$), excluding formation of deep defects (bulk Ti^{3+}). Vacuum heating, even under medium vacuum (10^{-3} - 10^{-4} bars), had no significant effect on commercial (and more crystalline) materials.

Vacuum heated FMH- TiO_2 particles showed remarkable results in photodegradation of rhodamine B both under visible and UVA light. The apparent degradation rate constant was generally higher or comparable with that of Aeroxide P25 for the UVA experiment, with a maximum of almost $2.7 \cdot 10^{-1} \text{ min}^{-1}$ compared with of P25. Under visible light, the rates appeared lower than P25, with apparent constant values between 1 and $7 \cdot 10^{-3} \text{ min}^{-1}$. However, considering the reduction of the dye concentration due to the adsorption processes, the degradation rates after 1 hour around 60-70%, compared with the *ca.* 25% of P25.

Highest degradation rates were observed in sample with higher rhodamine adsorption capacity (Table 4.23 and Figure 4.50).

Encouragingly, direct irradiation with MW of anatase powder led to partial conversion into rutile in just about 30 seconds, with blue coloration of the sample indicating possible formation of Ti^{3+} centres. Despite the presence of both rutile and anatase reminding the composition of P25, preliminary photocatalytic experiment showed reduction of the performance compared to the original material, probably due to the reduction of surface area or to the formation of rutile, exceeding the optimal proportion with anatase.

It can be concluded that the performance of both as-synthesised and vacuum heated are strongly dependant on their structure, with nanocrystals conferring high surface area, enhancing adsorption of the organic molecules and facilitating the photocatalytic reactions, occurring prevalently once the photogenerated carriers migrate to the particle surface.

4.12 References

- ¹ M. Anpo, S. Kishiguchi, Y. Ichihashi, M. Takeuchi, H. Yamashita, K. Ikeue, B. Morin, A. Davidson, The design and development of second-generation titanium oxide photocatalysts able to operate under visible light irradiation by applying a metal ion-implantation method, *Res. Chem. Intermed.*, 2001, **27**, 459-467.
- ² C.H. Langford, Photocatalysis - A Special Issue on a Unique Hybrid Area of Catalysis, *Catalysts*, 2012, **2**, 327-329.
- ³ F. Zuo, L. Wang, T. Wu, Z. Zhang, D. Borchardt, P. Feng, Self-Doped Ti³⁺ Enhanced Photocatalyst for Hydrogen Production under Visible Light, *J. Am. Chem. Soc.*, 2010, **132**, 11856-11857.
- ⁴ R. Asahi, T. Morikawa, T. Ohwaki, K. Aoki, Y. Taga, Visible-Light Photocatalysis in Nitrogen-Doped Titanium Oxides, *Science*, 2001, **293**, 269-271.
- ⁵ A. Kudo, K. Omori, H. Kato, A novel aqueous process for preparation of crystal form-controlled and highly crystalline BiVO₄ powder from layered vanadates at room temperature and its photocatalytic and photophysical properties, *J. Am. Chem. Soc.*, 1999, **121**, 11459-11461.
- ⁶ W. Shangguan, A. Yoshida, Photocatalytic hydrogen evolution from water on nanocomposite incorporating cadmium sulphide into the interlayer. *J. Phys. Chem. B*, 2002, **106**, 12227-12230.
- ⁷ C.H. Shin, G. Bugli, G. Djega-Mariadassou, Preparation and Characterization of Titanium Oxynitrides with High Specific Surface Areas, *J. Solid State Chem.*, 1991, **95**, 145-155.
- ⁸ B. Ohtani, O.O. Prieto-Mahaney, D. Li, R. Abe, What is Degussa (Evonik) P25? Crystalline composition analysis, reconstruction from isolated pure particles and photocatalytic activity test. *J. Photochem. Photobiol. A: Chem.*, 2010, **216**, 179-182.
- ⁹ A. Mills, S.-K. Lee, A web-based overview of semiconductor photochemistry-based current commercial applications, *J. Photochem. Photobiol. A: Chem*, 2002, **152**, 233-247.
- ¹⁰ Evonik Industries, AEROXIDE®, AERODISP® and AEROPERL® Titanium Dioxide as Photocatalyst, Technical Information 1243.
- ¹¹ D.C. Hurum, A.G. Agrios, K.A. Gray, T. Rajh, M.C. Thurnauer, Explaining the Enhanced Photocatalytic Activity of Degussa P25 Mixed-Phase TiO₂ Using EPR, *J. Phys. Chem. B*, 2003, **107**, 4545-4549.
- ¹² D.M. Tobaldi, R.C. Pullar, M.P. Seabra, J.A. Labrincha, Fully quantitative X-ray characterisation of Evonik TiO₂ P25®, *Mat. Lett.*, 2014, **122**, 345-347.
- ¹³ X. Jiang, M. Manawan, T. Feng, R. Qian, T. Zhao, G. Zhou, F. Kong, Q. Wange, S. Dai, J.H. Pan, Anatase and rutile in evonik aerioxide P25: Heterojunctioned or individual nanoparticles?, *Catalysis Today*, 2018, **300**, 12-17.
- ¹⁴ A. Manassero, M.L. Satuf, O.M. Alfano, Evaluation of UV and visible light activity of TiO₂ catalysts for water remediation, *Chem. Eng. J.*, 2013, **225**, 378-386.
- ¹⁵ M.J. Hernández Rodríguez, E. Pulido Meliána, O. González Díaz, J. Arana, M. Macías, A. González Orivec, J.M. Dona Rodríguez, Comparison of supported TiO₂ catalysts in the photocatalytic degradation of NO_x, *J. Molec. Cat. A: Chem.*, 2016, **413**, 56-66.
- ¹⁶ D. M. Tobaldi, M.P. Seabra, G. Otero-Irurueta, Y.R. de Miguel, R. J. Ball, M. K. Singh, R.C. Pullara, J. A. Labrincha, Quantitative XRD characterisation and gas-phase photocatalytic activity testing for visible-light (indoor applications) of KRONOClean 7000®, *RSC Adv.*, 2015, **5**, 102911.
- ¹⁷ R. Quesada-Cabrera, A. Mills, C. O'Rourke, Action spectra of P25 TiO₂ and a visible light absorbing, carbon-modified titania in the photocatalytic degradation of stearic acid, *Appl. Catal. B*, 2014, **150-151**, 338-344.
- ¹⁸ <http://kronostio2.com/en/component/jdownloads/finish/99/288>, (accessed January 2018).
- ¹⁹ A.S. Hassanien, A.A. Akl, Influence of composition on optical and dispersion parameters of thermally evaporated non-crystalline Cd₅₀S_{50-x}Se_x thin films; *J. Alloy Comp.*, 2015, **648**, 280-290.
- ²⁰ H. Irie, Y. Watanabe, K. Hashimoto, Carbon-doped Anatase TiO₂ Powders as a Visible-light Sensitive Photocatalyst, *Chem Lett.*, 2003, **32**, 772-773.
- ²¹ Y. Lin, S. Inoue, Y. Matsumura, J.C. Chen, Effect of preparation conditions in sol-gel method on yellow phosphor with wide spectrum, *AIP Advances*, 2017, **7**, 015208.

- 22 J.N. Kondo, T. Yamashita, K. Nakajima, D. Lu, M. Haraa, K. Domenb, Preparation and crystallization characteristics of mesoporous TiO₂ and mixed oxides, *J. Mater. Chem.*, 2005, **15**, 2035–2040.
- 23 R.A. Spurr, H. Myers, Quantitative Analysis of Anatase-Rutile Mixtures with an X-Ray Diffractometer, *Anal. Chem. Res.*, 1957, **29**, 760-762.
- 24 L. E. Depero, L. Sangaletti, B. Allieri, E. Bontempi, R. Salari, M. Zocchi, C. Casale, M. Notaro, Niobium-titanium oxide powders obtained by laser-induced synthesis: Microstructure and structure evolution from diffraction data, *J. Mater. Res.*, 1998, **13**, 1644 -1649.
- 25 L. You-ji, C. Weia, Photocatalytic degradation of Rhodamine B using nanocrystalline TiO₂–zeolite surface composite catalysts: effects of photocatalytic condition on degradation efficiency, *Catal. Sci. Technol.*, 2011, **1**, 802-809.
- 26 Y.-H. Tseng, H.Y. Lin, C-S. Kuo, Y.-Y. Li, C.-P. Huang, Thermostability of nano-TiO₂ and its photocatalytic activity, *React. Kinet. Catal. Lett.*, 2006, **89**, 63-69.
- 27 H. Slimen, H. Lachheb, S. Qourzal, A. Assabbane, A. Houasac, The effect of calcination atmosphere on the structure and photoactivity of TiO₂ synthesized through an unconventional doping using activated carbon, *J. Env. Chem. Eng.*, 2015, **3**, 922-929.
- 28 G. Tomandi, M. Mangler, J. Woltesdorf, Evidence of nanopores in sol–gel based TiO₂ and TiN ultrafiltration membranes, *Mat. Chem. Phys.*, 2000, **63**, 139-141.
- 29 S. Yang, L. Gao, Photocatalytic activity of nitrogen doped rutile TiO₂ nanoparticles under visible light irradiation, *Mat. Res. Bull.*, 2008, **43**, 1872–1876.
- 30 M. N. Solovan, V.V. Brus, E.V. Mastruk, P. D. Maryanchuk, Electrical and optical properties of TiN thin films, *Inorganic Materials*, 2014, **50**, 40-45.
- 31 P. Patsalas, N. Kalfagiannis, S. Kassavetis, Optical Properties and Plasmonic Performance of Titanium Nitride, *Materials*, 2015, **8**, 3128-3154.
- 32 M. Onoda, Phase Transitions of Ti₃O₅, *J. Solid State Chem.*, 1998, **136**, 67-73.
- 33 A.I. Gusev, A.A. Rempel, A.J. Magerl, Disorder and Order in Strongly Nonstoichiometric Compounds: Transition Metal Carbides, Nitrides and Oxides, Springer, 2013.
- 34 G. Pacchioni, Oxygen Vacancy: The Invisible Agent on Oxide Surfaces, *Chem. Phys. Chem.*, 2003, **4**, 1041-1047.
- 35 S. Polarz, J. Strunk, V. Ischenko, M.W.E. van den Berg, O. Hinrichsen, M. Muhler, M. Driess, On the Role of Oxygen Defects in the Catalytic Performance of Zinc Oxide, *Angew. Chem.*, 2006, **45**, 2965-2969.
- 36 M. K. Nowotny, L. R. Sheppard, T. Bak, J. Nowotny, Defect Chemistry and Electrical Properties of Titanium Dioxide. 1. Defect Diagrams, *J. Phys. Chem. C*, 2008, **112**, 590-601.
- 37 X. Pan, M.-Q. Yang, X. Fu, N. Zhang, Y.-J. Xu, Defective TiO₂ with oxygen vacancies: synthesis, properties and photocatalytic applications, *Nanoscale*, 2013, **5**, 3601-3614.
- 38 R. Sanjines, H. Tang, H. Berger, F. Gozzo, G. Margaritondo, F. Levi, Electronic structure of anatase TiO₂ oxide, *J. App. Phys.*, 1994, **75**, 2945-2951.
- 39 F. Guillemot, M.C. Porte, C. Labrugere, C. Baquey, Ti⁴⁺ to Ti³⁺ Conversion of TiO₂ Uppermost Layer by Low-Temperature Vacuum Annealing: Interest for Titanium Biomedical Applications, *J. Colloid. Int. Sci.*, 2002, **255**, 75-78.
- 40 X. Chen, L. Liu, P.Y. Yu, S.S. Mao, Increasing Solar Absorption for Photocatalysis with Black Hydrogenated Titanium Dioxide Nanocrystals, *Science*, 2011, **331**, 746-749.
- 41 R. Ren, Z. Wen, S. Cui, Y. Hou, X. Guo, J. Chen, Controllable Synthesis and Tunable Photocatalytic Properties of Ti³⁺-doped TiO₂, *Scientific Report*, 2014, **5**, 10714, 1-9.
- 42 W. Fang, Y. Zhou, C. Dong, M. Xing, J. Zhang, Enhanced photocatalytic activities of vacuum activated TiO₂ catalysts with Ti³⁺ and N co-doped, *Catalysis Today*, 2016, **266**, 188-196.
- 43 E. Serwicka, ESR Study on the interaction of water vapour with polycrystalline TiO₂ under illumination, *Colloids and Surfaces*, 1985, **13**, 287-293.
- 44 X. Xue, W. Ji, Z. Mao, H. Mao, Y. Wang, X. Wang, W. Ruan, B. Zhao, J.R. Lombardi, Raman Investigation of Nanosized TiO₂: Effect of Crystallite Size and Quantum Confinement, *J. Phys. Chem. C*, 2012, **116**, 8792-8797.

- 45 L.B. Xiong, J.-L. Li, B. Yang, Y. Yu, Ti³⁺ in the Surface of Titanium Dioxide: Generation, Properties and Photocatalytic Application, *J. Nanomat.* 2012, **2012**, 831524.
- 46 H. Rupp, Binuclear Copper Electron Paramagnetic Resonance Signals of a-Methemocyanin of Helix pomatia, *Z. Naturforsch.*, 1980, **35 c**, 188-192.
- 47 T. Morikawa, R. Asahi, T. Ohwaki, A. Aoki, Y. Taga, Band-Gap Narrowing of Titanium Dioxide by Nitrogen Doping, *Jpn. J. Appl. Phys.*, 2001, **40**, 561-563.
- 48 X. Chen, L. Liu, P.Y. Yu, S.S. Mao, Increasing solar absorption for photocatalysis with black hydrogenated titanium dioxide nanocrystals, *Science*, 2011, **331**, 746-750.
- 49 H. Lu, B. Zhao, R. Pan, J. Yao, J. Qiu, L. Luo, Y. Liu, Safe and facile hydrogenation of commercial Degussa P25 at room temperature with enhanced photocatalytic activity, *RSC Adv.*, 2014, **4**, 1128-1132.
- 50 B. Vaidhyanathan, D.K. Agrawal, R. Roy, Microwave-Assisted Synthesis and Sintering of NZP Compounds, *J. Am. Ceram. Soc.*, 2004, **87**, 834-842.
- 51 E. Reguera, C. Diaz-Aguila, H. Yee-Madeira, On the changes and reactions in metal oxides under microwave irradiation, *J. Mater. Sci.*, 2005, **40**, 5331-5334.
- 52 H.J. Kitchen, S.R. Vallance, J. L. Kennedy, N. Tapia-Ruiz, L. Carassiti, A. Harrison, A. G. Whittaker, T. D. Drysdale, S. W. Kingman, D.H. Gregory, Modern Microwave Methods in Solid-State Inorganic Materials Chemistry: From Fundamentals to Manufacturing, *Chem. Rev.*, 2014, **114**, 1170-1206.
- 53 B. Vaidhyanathan, A.P. Singh, D.K. Agrawal, T.R. Shrout, R. Roy, Microwave Effects in Lead Zirconium Titanate Synthesis: Enhanced Kinetics and Changed Mechanisms, *J. Am. Ceram. Soc.*, 2001, **84**, 1197-1202.
- 54 V. N. Kuznetsov, N. I. Glazkova, R.V. Mikhaylov, N. Serpone, *In situ* study of photo- and thermo-induced color centers in photochromic rutile TiO₂ in the temperature range 90–720 K, *Photochem. Photobiol. Sci.*, 2016, **15**, 1289-1298.
- 55 L. You-ji, C. Wei, Photocatalytic degradation of Rhodamine B using nanocrystalline TiO₂-zeolite surface composite catalysts: effects of photocatalytic condition on degradation efficiency, *Catal. Sci. Technol.*, 2011, **1**, 802-809.
- 56 J. Xie, X. Lu, J. Liu, H. Shu, Brookite titania photocatalytic nanomaterials: Synthesis, properties, and applications, *Pure Appl. Chem.*, 2009, **81**, 2407-2415.
- 57 H. Irie, Y. Watanabe, K. Hashimoto, Nitrogen-Concentration Dependence on Photocatalytic Activity of TiO_{2-x}N_x Powders, *J. Phys. Chem. B*, 2003, **107**, 5483-5486.
- 58 S. Yang, L. Gao, Photocatalytic activity of nitrogen doped rutile TiO₂ nanoparticles under visible light irradiation, *Mat. Res. Bull.*, 2008, **43**, 1872-1876.
- 59 R. Silveyra, L. De La Torre Saenz, W. Antunez Flores, V. Collins Martinez, A. Aguilar Elguezabal, Doping of TiO₂ with nitrogen to modify the interval of photocatalytic activation towards visible radiation, *Cat. Today*, 2005, **107-108**, 602-605.
- 60 Y. Hu, H.-L. Tsai, C.-L. Huang, Phase transformation of precipitated TiO₂ nanoparticles, *Mat. Sci. Eng.*, 2003, **A344**, 209-214.
- 61 A. W. Czanderna, C. N. Ramachandra Rao, J. M. Honig, The anatase-rutile transition part I- Kinetics of the transformation of pure anatase, *Trans. Faraday Soc.*, 1958, **54**, 1069-1073.
- 62 R.D. Shannon, Phase transformation studies in TiO₂ supporting different defects mechanism in vacuum-reduced and hydrogen reduced Rutile, *J. Appl. Phys.*, 1964, **35**, 3414-3416.
- 63 A.A. Gribb, J.F. Banfield, Particle size effects on transformation kinetics and phase stability in nanocrystalline TiO₂, *Am. Mineralog.*, 1997, **82**, 717-728.
- 64 S. Hishita, I. Mutoh, K. Koumoto, H. Yanagida, Inhibition mechanism of the anatase-rutile phase transformation by rare earth oxides, *Ceram. Int.*, 1983, **9**, 61-67.
- 65 N. Satoh, T. Nakashima, K. Yamamoto, Metastability of anatase: size dependent and irreversible anatase-rutile phase transition in atomic-level precise titania, *Nature Scientific Reports*, 2013, **3**, 1959.
- 66 Y. Qu, C. Sun, G. Sun, X. Kong, W. Zhang, Preparation, characterization, and kinetic and thermodynamic studies of mixed-phase TiO₂ nanoparticles prepared by detonation method, *Res. Phys.*, 2016, **6**, 100-106.

- ⁶⁷ W. Li, C. Ni, H. Lin, C.P. Huang, S. Ismat Shah, Size dependence of thermal stability of TiO₂ nanoparticles, *J. Appl. Phys.*, 2004, **96**, 6663–6668.
- ⁶⁸ W.F. Sullivan, S.S. Cole, Thermal chemistry of colloidal titanium dioxide, *J. Am. Ceram. Soc.*, 1959, **42**, 127–133.
- ⁶⁹ J. Liu, T. An, G. Li, N. Bao, G. Sheng, J. Fu, Preparation and characterization of highly active mesoporous TiO₂ photocatalysts by hydrothermal synthesis under weak acid conditions, *Microporous and Mesoporous Materials*, 2009, **124**, 197–203.
- ⁷⁰ R. Plugaru, A. Cremdes, J. Piqueras, The effect of annealing in different atmospheres on the luminescence of polycrystalline TiO₂, *J. Phys.: Condens. Matter*, 2004, **16**, S261-S268.
- ⁷¹ N. Wu, M. Lee, Z. Pon, J. Hsu, Effect of calcination atmosphere on TiO₂ photocatalysis in hydrogen production from methanol/water solution, *J. Photochem. Photobiol. A: Chem.*, 2004, **163**, 277-280.
- ⁷² X. Chen, S. S. Mao, Titanium Dioxide Nanomaterials: Synthesis, Properties, Modifications, and Applications, *Chem. Rev.*, 2007, **107**, 2891–2959.
- ⁷³ X. Cheng, X. Yu., Z. Xing, L. Yang, Synthesis and characterisation of N-doped TiO₂ and its enhanced visible-light photocatalytic activity, *Arab. J. Chem.*, 2016, **9**, S1706-S1711.
- ⁷⁴ S. Livraghi, M. Paganini, E. Giamello, A. Selloni, C. Di Valentin, G. Pacchioni, Origin of Photoactivity of Nitrogen-Doped Titanium Dioxide under Visible Light, *J. Am. Chem. Soc.*, 2006, **128**, 15666–15671.
- ⁷⁵ H. Noda, K. Oikawa, T. Ogata, K. Matsuki, H. Kamata, Preparation of Titanium(IV) Oxides and Its Characterization, *Chem. Soc. Jpn.*, 1986, **8**, 1084-1090.
- ⁷⁶ E. Asari, R. Souda, A study of reactivity of O₂-gas on the TiO₂ (1 1 0) surface: low and heavily reduced surfaces, *Vacuum*, 2002, **68**, 123-129.
- ⁷⁷ M. Xing, J. Zhang, F. Chen, B. Tian, An economic method to prepare vacuum activated photocatalysts with high photo-activities and photosensitivities, *Chem. Comm.*, 2011, **47**, 4947-4949.
- ⁷⁸ R.D. Shannon, J.A. Pask, Kinetics of the anatase–rutile transformation, *J. Am. Ceram. Soc.*, 1965, **48**, 391– 398.
- ⁷⁹ X. Chen, L. Liu, Peter Y. Yu, S.S. Mao, Increasing Solar Absorption for Photocatalysis with Black Hydrogenated Titanium Dioxide Nanocrystals, *Science*, 2011, **331**, 746-749.
- ⁸⁰ M.M. Khan, S.A. Ansari, D. Pradhan, M.O. Ansari, D.H. Han, J. Lee, M.H. Cho, Band gap engineered TiO₂ nanoparticles for visible light induced photoelectrochemical and photocatalytic studies, *J. Mater. Chem. A*, 2014, **2**, 637-644.
- ⁸¹ Y.G. Zhang, L.L. Ma, J.L. Li, Y. Yu, *In situ* Fenton reagent generated from TiO₂/Cu₂O composite film: a new way to utilize TiO₂ under visible light irradiation, *Environ. Sci. Technol.*, 2007, **41**, 6264–6269.
- ⁸² L.Q. Wang, D.R. Baer, M.H. Engelhard, Creation of variable concentrations of defects on TiO₂(110) using low-density electron beams, *Surf. Sci.*, 1994, **320**, 295-306.
- ⁸³ L.B. Xiong, J.-L. Li, B. Yang, Y. Yu, Ti³⁺ in the Surface of Titanium Dioxide: Generation, Properties and Photocatalytic Application, *J. Nanomat.*, 2012, **2012**, 831524.
- ⁸⁴ H. Kisch, S. Sakthivel, M. Janczarek, D.J. Mitoraj, A Low-Band Gap, Nitrogen-Modified Titania Visible-Light Photocatalyst, *J. Phys. Chem. C*, 2007, **111**, 11445-11449.
- ⁸⁵ N.C. Saha, H.G. Tompkins, Titanium Nitride Oxidation Chemistry: An X-ray Photoelectron Spectroscopy Study, *J. Appl. Phys.*, 1992, **72**, 3072-3079.
- ⁸⁶ J. Yuan, M. Chen, J. Shi, W. Shanggun, Preparations and photocatalytic hydrogen evolution of N-doped TiO₂ from urea and titanium tetrachloride, *Int. J. Hydr. En.*, 2006, **31**, 1326-1331.
- ⁸⁷ R. Asahi, T. Morikawa, H. Irie, T. Ohwaki, Nitrogen-Doped Titanium Dioxide as Visible-Light-Sensitive Photocatalyst: Designs, Developments, and Prospects, *Chem. Rev.*, 2014, **114**, 9824–9852.
- ⁸⁸ H. Irie, Y. Watanabe, K. Hashimoto, Nitrogen-Concentration Dependence on Photocatalytic Activity of TiO_{2-x}N_x Powders, *J. Phys. Chem. B*, 2003, **107**, 5483-5486.
- ⁸⁹ A. I. Kokorin, D.W. Bahnemann (eds), *Chemical Physics of Nanostructured Semiconductors*, VSP-Brill, Academic Publishers, 2003.

- ⁹⁰ J.C. Conesa, J. Soria, Reversible Ti³⁺ Formation by H₂ Adsorption on M/TiO₂ Catalysts, *J. Phys. Chem.*, 1982, **86**, 1392-1395.
- ⁹¹ M. Anpo, M. Che, B. Fubini, E. Garrone, Generation of superoxide ions at oxide surfaces, *Topics in Cat.*, 1999, **8**, 189-198.
- ⁹² R.F. Howe, M. Gratzel, Electron-paramagnetic-res observation of trapped electrons in colloidal TiO₂. *J. Phys. Chem.*, 1985, **89**, 4495-4499.
- ⁹³ H. Liu, H.T. Ma, X. Z. Li, W.Z. Li, M. Wu, X.H. Bao, The enhancement of TiO₂ photocatalytic activity by hydrogen thermal treatment, *Chemosphere*, 2003, **50**, 39-46.
- ⁹⁴ V.M. Khomenko, K. Langer, H. Rager, A. Fett, Electronic absorption by Ti³⁺ ions and electron delocalization in synthetic blue rutile, *Phys. Chem. Minerals*, 1998, **25**, 338-346.
- ⁹⁵ B. Pattier, M. Henderson, A. Pöpl, A. Kassiba, A. Gibaud, Multi-approach Electron Paramagnetic Resonance Investigations of UV-Photoinduced Ti³⁺ in Titanium Oxide-Based Gels, *J. Phys. Chem. B*, 2010, **114**, 4424-4431.
- ⁹⁶ M. Anpo, M. Takeuchi, The design and development of highly reactive titanium oxide photocatalyst operating under visible light irradiation, *J. Catal.*, 2003, **216**, 505-516.
- ⁹⁷ K. Palanivelu, J.S. Im, Y.-S. Lee, Carbon Doping of TiO₂ for Visible Light Photo Catalysis - A review, *Carb. Sci.*, 2007, **8**, 214-224.
- ⁹⁸ W.-K. Jo, R.J. Tayade, Recent developments in photocatalytic dye degradation upon irradiation with energy-efficient light emitting diodes, *Chin. J. Cat.*, 2014, **35**, 1781-1792.
- ⁹⁹ Q. Xiao, L. Gao, One-step hydrothermal synthesis of C,W-codoped mesoporous TiO₂ with enhanced visible light photocatalytic activity, *J. Alloys Comp.*, 2013, **551**, 286-292.
- ¹⁰⁰ K.M. Parida, B. Naik, Synthesis of mesoporous TiO_{2-x}N_x spheres by template free homogeneous co-precipitation method and their photo-catalytic activity under visible light illumination, *J. Coll. Interf. Sci.*, 2009, **333**, 269-276.
- ¹⁰¹ S. Hua, A. Wanga, X. Li, H. Lowe, Hydrothermal synthesis of well-dispersed ultrafine N-doped TiO₂ nanoparticles with enhanced photocatalytic activity under visible light, *J. Phys. Chem. Solids*, 2010, **71**, 156-162.
- ¹⁰² I. Justicia, P. Ordejon, G. Canto, J. L. Mozos, J. Fraxedas, G. A. Battiston, R. Gerbasi, A. Figueras, Designed Self-Doped Titanium Oxide Thin Films for Efficient Visible-Light Photocatalysis, *Adv. Mater.*, 2002, **14**, 1399-1402.
- ¹⁰³ F. Zuo, L. Wang, T. Wu, Z. Zhang, D. Borchardt, P. Feng, Self-Doped Ti³⁺ Enhanced Photocatalyst for Hydrogen Production under Visible Light, *J. Am. Chem. Soc.*, 2010, **132**, 11856-11857.
- ¹⁰⁴ W. Wang, C. Lu, Y. Ni, F. Peng, Z. Xu, Enhanced performance of {0 0 1} facets dominated mesoporous TiO₂ photocatalyst composed of high-reactive nanocrystals and mesoporous spheres, *Appl. Surf. Sci.*, 2013, **265**, 438-442.
- ¹⁰⁵ J. Liu, T. An, G. Li, N. Bao, G. Sheng, J. Fu, Preparation and characterization of highly active mesoporous TiO₂ photocatalysts by hydrothermal synthesis under weak acid conditions, *Microporous and Mesoporous Mat.*, 2009, **124**, 197-203.
- ¹⁰⁶ T.S. Natarajan, M. Thomas, K. Natarajan, H.C. Bajaj, R.J. Tayade, Study on UV-LED/TiO₂ process for degradation of Rhodamine B dye, *Chem. Eng. J.*, 2011, **169**, 126-134.

List of Abbreviations used in Chapter 5

- AFM:** Atomic Force Microscopy
- ANOVA:** Analysis Of Variance
- BET:** Brunauer-Emmett-Teller (*model for surface area measurement*)
- BJH:** Barrett-Joyner-Halenda (*model for pore volume and size distribution*)
- CA:** Contact Angle
- DLS:** Dynamic Light Scattering
- FT-IR:** Fourier Transform Infrared Spectroscopy
- HSD:** Honestly Significant Difference
- LbL:** Layer-by-Layer
- ly:** layer
- Is:** Ionic Strength
- MWCO:** Molecular Weight Cut-Off
- NF:** Nanofiltration
- PAA:** Poly(acrylic acid)
- PAN:** Polyacrylonitrile
- PAH:** Poly(allylamine hydrochloride)
- PDDA:** Poly(diallyldimethylammonium chloride)
- PE:** Polyelectrolyte
- PEI:** Polyethyleneimine
- PEM:** Polyelectrolyte Multilayer
- PES:** Poly(ethersulfone)
- PSS:** Poly(sodium 4-styrenesulfonate)
- PXD:** Powder X-ray Diffraction
- QCM-D:** Quartz Crystal Microbalance with Dissipation monitoring
- RO:** Reverse Osmosis
- SEM:** Scanning Electron Microscopy
- SPR:** Surface Plasmon Resonance
- TFC:** Thin-Film Composite (*membrane*)
- TMP:** Transmembrane Pressure
- TOC:** Total Organic Carbon
- UF:** Ultrafiltration
- UV:** Ultraviolet (*radiation*)
- WAXD:** Wide Angle X-ray Diffraction

Chapter 5

TiO₂-Polyelectrolyte Multilayers (PEMs) composites for membrane filtration

5.1 Introduction

Polyelectrolytes provide versatile means to functionalise surfaces, creating or enhancing innovative properties. In the introductory part, electrostatic assembly of polyelectrolytes in multilayered structures defined as polyelectrolyte multilayers (PEMs) were discussed extensively in the last decades.^[1] PEMs are of great importance in surface engineering since their discovery in the early 1990's, with applications in several technological fields, such as optical, biomedical and environmental. ^[2, 3, 4]

Because of their nature of charged and large molecules, polyelectrolytes can be also useful to enhance the dispersion of colloidal suspensions. As water soluble charged species, polyelectrolytes can functionalise colloidal particles, stabilising their suspension through both steric and electrostatic repulsion mechanisms.

Due to their versatility, PEMs have been previously reported to have an important role in the production of antifouling and antibacterial coating (section 1.9). Polyelectrolytes can adsorb onto any surface with a minimum charge density regardless of the geometry of the object, allowing the deposition of a uniform nanometric film. PEMs are built by applying a single layer of polyelectrolyte to the surface, followed by the deposition of a second polyelectrolyte with opposite charge. This process is called layer-by-layer (LbL) and involves the self-assembly of adsorbing molecules. The deposition process can be performed in water, simply by immersing the substrate in the polyelectrolyte solution (dip coating) or, in alternative, using other conventional liquid phase thin film deposition processes, such as spray or spin coating. ^[5, 6]

As versatile and multifunctional coatings, PEMs are suitable for application in polymer membranes.^[7] The membrane active layer can be functionalised, allowing modification of properties such as hydrophilicity or surface roughness. ^[8] These particular characteristics are potentially responsible for the reduction of the adhesive power of organic substances, responsible for membrane fouling in real life situations.

The integration of inorganic particles within the multilayer coating can potentially attribute novel properties to the surface. Self-cleaning is one of the most interesting applications.^[9] Specifically, semiconductor materials are useful for this purpose due to their capacity of increasing the surface energy inducing superhydrophilicity. Among oxide semiconductors, TiO₂ has shown remarkable properties for this application.^[10]

5.1.1 Aims

In this section of work, two main issues were addressed. Firstly, it was decided to investigate whether a potential protective coating for an ultrafiltration membrane (UF) could be fabricated with only a limited loss of hydraulic performances. The polymeric coating is basically a hindrance for the porous structure of the membrane active layer, reducing dramatically the permeability of the membrane. PEMs have been successfully applied to nanofiltration (NF) and reverse osmosis (RO) membrane, where higher pressure is involved, and the rejection capacity is relatively more important compared to the overall permeability. The simple method of the layer-by-layer (LbL) assembly can be transferred to any charged entities. The second aim was to demonstrate how polyelectrolytes (previously reported to form nanocomposite coatings with several nanoparticles)^[11, 12] might be efficiently employed in the stabilisation of TiO₂ nanoparticles as nanocomposite coating onto a filtration membrane. The characteristics of the new surface and the preliminary performance of the modified membrane were explored using the available characterisation techniques. This preliminary study involved deposition of polyelectrolyte multilayers (PEMs) on different surfaces in an attempt to study more in general the different properties of the coating, specifically wettability, on surface other than membranes.

5.2 Polyelectrolyte multilayers (PEMs) for environmental applications

One of the primary aims of the functionalisation of surfaces in environmental applications is to provide protection against microorganisms and to prevent or delay the adhesion of organic substances (the fouling effect). For this reason, anti-adhesive and intrinsic anti-bacterial properties are the optimal combination for the multilayer. The former can be achieved by modifying the wettability of the system. Organic matter, which is generally of a hydrophobic nature (humic fractions) do not generally adhere to hydrophilic or superhydrophilic surfaces. ^[13] Hydrophilic self-cleaning surfaces are based on this enhanced wettability, with water spreading uniformly across the surface forming a protective film against the adhesion of dirt. ^[14] As for the antibacterial properties, cationic polyelectrolytes are known for their cytotoxic properties, with the positively charged chain disrupting the negatively charged cell membrane of microorganisms, ultimately causing their elimination. ^[15,16]

5.2.1 Selection of polyelectrolytes and conditions

A brief description of the nature of the polyelectrolytes is provided in chapter 1. A large variety of charged molecules can be classified as polyelectrolytes, both synthetic and natural. The scope of this project is to investigate the polyelectrolyte as a relatively inexpensive surface functionalisation technique. For this reason, commonly used polyelectrolyte species, easy to retrieve in the market and relatively inexpensive, were considered. The selected species with their characteristics and colloidal properties are listed in Table 5.1. The conductivity of the polyelectrolyte in solution was measured by a conductivity meter. Despite the narrow selection of species, a wide number of combinations is available for the deposition conditions. The properties of the multilayer can be via several factors, principally pH, ionic strength and polymer concentration. In Table 5.2, the concentrations of the different polymers are compared. It is common procedure to use the repeating unit as reference for the concentration, regardless of the molecular weight distribution. The actual concentration of the polyelectrolyte solutions was calculated through measurement of the total organic carbon (TOC).

In order to confer potential antimicrobial activity to the membrane, polycations were often selected as the outermost layer of the membrane coating. Poly(diallyldimethylammonium chloride) (PDDA) possesses quaternary ammonium groups in cyclic units in its chemical structure, carrying a permanent positive charge along its chain. An uppermost layer of this polymer shows antimicrobial activity due to the killing action of the contact with the cationic groups.^[17,18] Despite its antibacterial properties, this polyelectrolyte is generally considered safe towards human health. PDDA is already widely employed in food processing, water treatments and several medical and biological applications.^[19, 20] Poly(allylamine hydrochloride) (PAH) has been also proposed as contact-killing polyelectrolyte. Due to the exposition of charge neutral system when combined with Poly(sodium 4-styrenesulfonate) (PSS) or Poly(acrylic acid) (PAA) in low pH solution, the uncharged amine groups of the PAH chains are protonated, causing cell membrane disruption.^[21]

Table 5.1: Characteristic of the polyelectrolyte species investigated in this project.

	Charge	Concentration (mM x repeat unit)	TOC Concentration (mg/L)	pH	Conductivity ($\mu\text{S cm}^{-1}$)
PAA	-	10	355	3.48	147
PAH	+	10	340	5.04	397
PDDA	+	10	895	5.10	597
PSS	-	10	393	6.90	682
PEI	+	(1 g/L)	490	10.3	338

Three specific systems of synthetic polyelectrolytes are efficiently combining antifouling and antibacterial properties: (PAA/PAH)_n assembled at low pH; (PDDA/PSS)_n and (PSS/PAH)_n, both in alkaline environment. Despite being one of the most investigated polyelectrolytes in association to PAA, PAH is relatively more expensive compared with the other in Table 5.1. The system composed of PSS and PDDA was preferred. The pH of the polyelectrolyte solutions has to be compatible with the tolerance of the membrane materials, which is between 2-3 and 10-11, variable depending on the type of polymer (Table 5.3).

In Table 5.2, the effect of the concentration on initial pH and conductivity is also reported. The variation of pH with the concentration is totally expected, as the increase of the concentration of polyanion tend to reduce the H⁺ in solution, and

vice versa for the polycation. The conductivity of the solution is proportional to the concentration of the polyelectrolyte, as expected increasing the amount of charged chains in solution.

Table 5.2: effect of the concentration of polyelectrolyte on the solution conductivity for strong polyelectrolytes.

	Concentration	pH	Conductivity ($\mu\text{S cm}^{-1}$)	TOC
PSS	<i>5 mM</i>	6.54	331	393
	<i>10 mM</i>	6.75	651	783
	<i>20mM</i>	6.90	1294	1555
PDDA	<i>5 mM</i>	5.36	301	341
	<i>10 mM</i>	4.95	571	855
	<i>20mM</i>	4.29	1104	1413

5.2.2 Adhesion mechanism and kinetics

The adsorption kinetic of the different polyelectrolytes was evaluated using *in-situ* Multiparameter Surface Plasmon Resonance (MP-SPR) spectroscopy. The polyelectrolyte solutions were flown onto a gold-coated glass chip, exposed to a double wavelength laser beam. The resulting plasmon resonance is directly correlated with the properties of the coating, such as thickness and refractive index. The SPR is a very sensitive technique, detecting thicknesses of few nanometers due to the variation of the refractive index on the surface. The main features of a typical SPR curve can be represented in form of a sensogram as a function of the time.

The variation in thickness is given by the minimum resonance angle in the SPR curve. Plotting the minimum as a function of the time gives an estimation of the variation of the thickness of the coating on the gold chip throughout the duration of the experiment.

Figure 5.1 shows a typical sensogram for the resonance angle measured during the deposition of a PDDA/PSS multilayer, with both polyelectrolyte solutions having 10 mM concentration (based on the polymer repeating unit) and adjusted to pH 10. In the graph, the response of the two exciting wavelengths on the same multilayer are shown. The optical properties (dielectric constant and refractive index) of a material are wavelength-dependent. Subsequently, the plasmonic resonance will be different for the same material using the two laser frequency available for the instrument used. The comparison between the different responses potentially allows a deeper analysis in terms of thickness estimation and multilayer structure.

The increase of the signal corresponds to the injection of the polyelectrolyte in the system and the subsequent decrease indicates the rinsing step with deionised water. The alternate injection-rinsing, as during the layer-by-layer deposition, generates a characteristic ladder plot, in which each step corresponds to the deposition of a single layer.

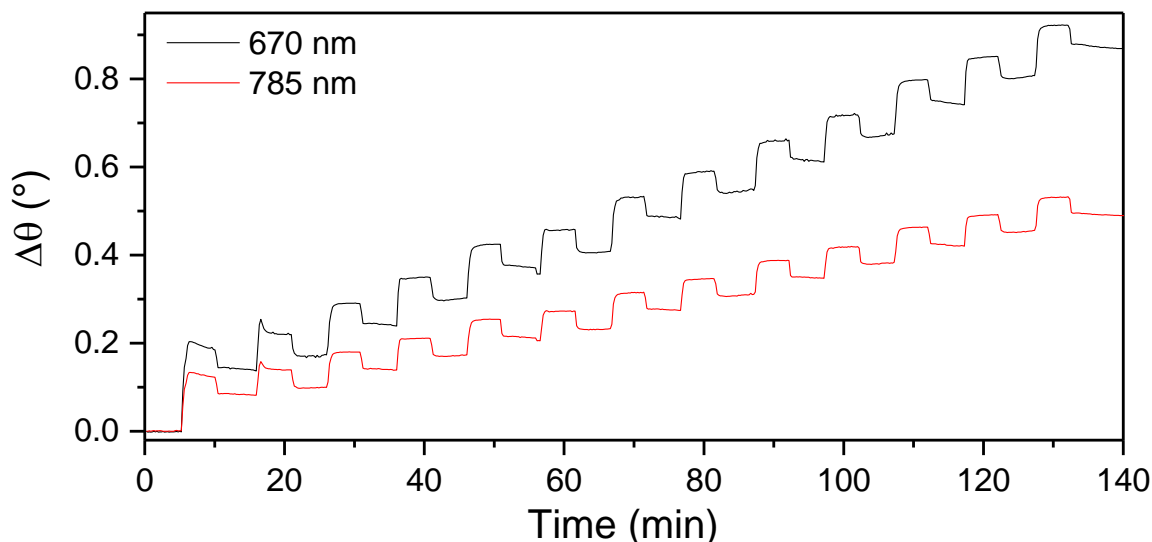


Figure 5.1: SPR sensogram for the minimum resonance angle of a (PDDA/PSS) multilayer, deposited on gold coated surface exposing it to the polyelectrolyte solutions (both 10 mM concentration and pH 10) for 5 min using a flow rate of 20 $\mu\text{L}/\text{min}$. Rinsing step ca. 5 min at 50 $\mu\text{L}/\text{min}$ flow rate.

The sensogram gives indication about the kinetics of the deposition process. The polyelectrolyte molecules adhere almost immediately to the surface, with the amount of polyelectrolytes remaining constant or slightly increasing during the injection phase. When the surface is rinsed, the loosely bonded polymer chains are released. However, the drop of thickness is due to the exposure of the layers to a different pH, since the rinsing water is neutral, with compression of the multilayer structure.

The comparison between the different adsorption profiles for each layer deposition of the (PDDA-PSS) multilayer is shown in Figure 5.2. The amount of material adsorbed and the thickness of the multilayer are directly proportional with the value of resonance angle. Figure 5.2 shows that shifting the different adsorption profile on the same scale results in almost no differences between the layers. The profiles describe the deposition mechanism, with rapid increase of the signal intensity (contact and adhesion of the polyelectrolyte with the surface), a stabilisation period (establishment of the adsorption equilibrium) and a rapid drop followed by a second stabilisation (rinsing step with removal of loosely bound polymer chains). The only exception is the very first layer deposited on the gold surface (PDDA1) for which both the adsorption curve and the compression/release of loosely bonded polyelectrolyte due to the rinsing step are different from the rest of the layers.

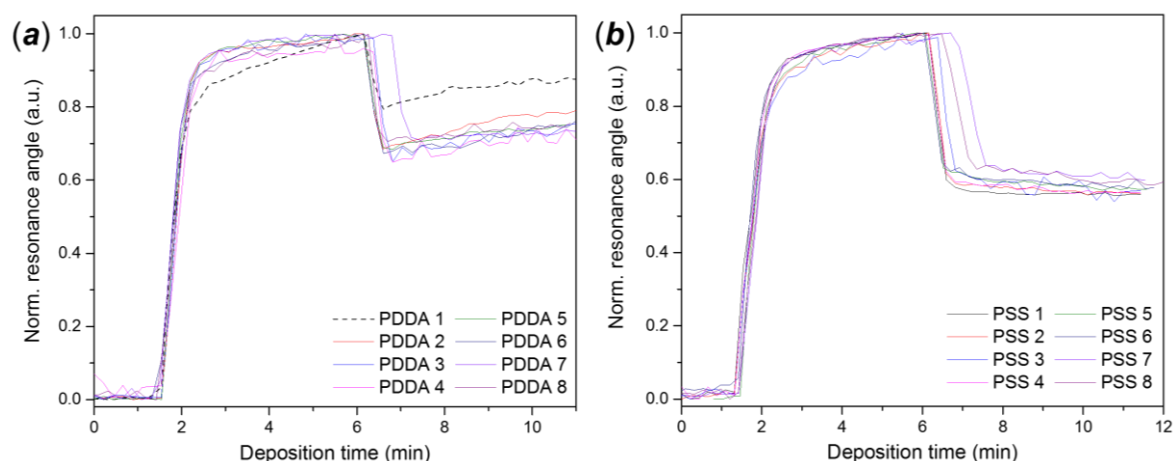


Figure 5.2: Adsorption profiles of the different layers of (a) PDDA and (b) PSS in the PDDA/PSS multilayer reported on the same scale.

5.2.2.1 Influence of the pH

The different deposition steps of a PAH/PAA multilayer are reported in Figure 5.3. Apart from the very first layer, the two polyelectrolytes present a very distinct adsorption profile, much steeper for PAH. According to the SPR curves, the maximum adsorption efficiency occurs within instants after the insertion of the polyelectrolyte solution. Depending on the type of polymer, the adsorbed molecule can slightly accumulate on the surface (such as in case of PAA) or slowly desorb (as for PAH), with the effect being more marked after the first couple of layers.

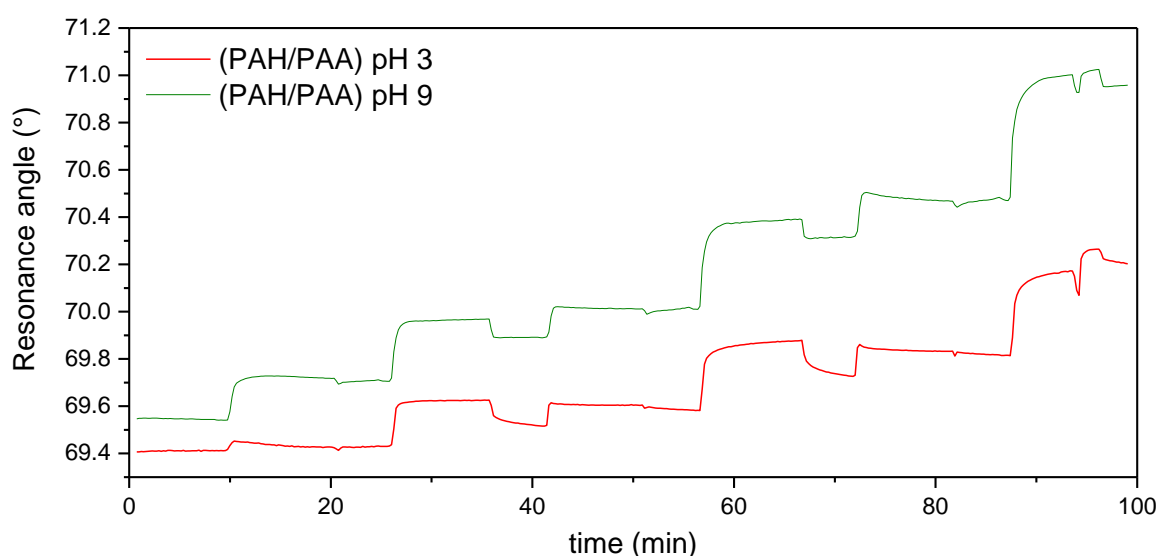


Figure 5.3: SPR Kinetic mode measurement of the *in-situ* deposition of PAH/PAA multilayer at pH 3 and PAH/PSS at pH 9 (excitation laser wavelength 670 nm, deposition time 10 minutes, flow rate 10 $\mu\text{L}/\text{min}$, rinsing time 5 minutes at 50 $\mu\text{L}/\text{min}$, deposition on Au coated chip)

PAH and PAA are both weak polyelectrolytes, implying that their charge density is strongly affected by the pH of the solution. The plasmonic resonance curve at basic pH occurs at higher angles compared with the same multilayer deposited under acidic conditions. Higher resonance angles indicate higher thickness of the coating on gold. This can be correlated with a higher amount of material deposited or a weaker charge density, with the polymeric structure of the multilayer more open and loosen, increasing the total volume of the structure.

5.2.2.2 Ionic strength

The influence of the ionic strength (Is) of the polyelectrolyte solutions is shown in Figure 5.4, in which the same multilayer structure (PDDA-PSS) is compared by SPR measurement using 0, 150 and 500 mM of NaCl respectively. As evident from the plot, the resonance angle (and hence the multilayer thickness) increases with the ionic strength. For the measurement at Is = 500 mM, the SPR curve at $\lambda = 670$ nm was out of the range of the measurement after the 4th bi-layer because of its thickness, making necessary the comparison with the curve at $\lambda = 785$ nm, which has a lower angular value and thus can appreciate thicker coatings (dashed green sensogram in Figure 5.4). For this last measurement, the sensogram shows instability of the multilayer structure with the increase of the number of layers (hence of the thickness). The deposition of a layer of polycation (PDDA), the subsequent rinsing step caused thickness decrease, which can be either attributed to removal of loosely attached chains or rapid compression of the multilayer structure due to the exposure to a solution with zero ionic strength such as deionised water.

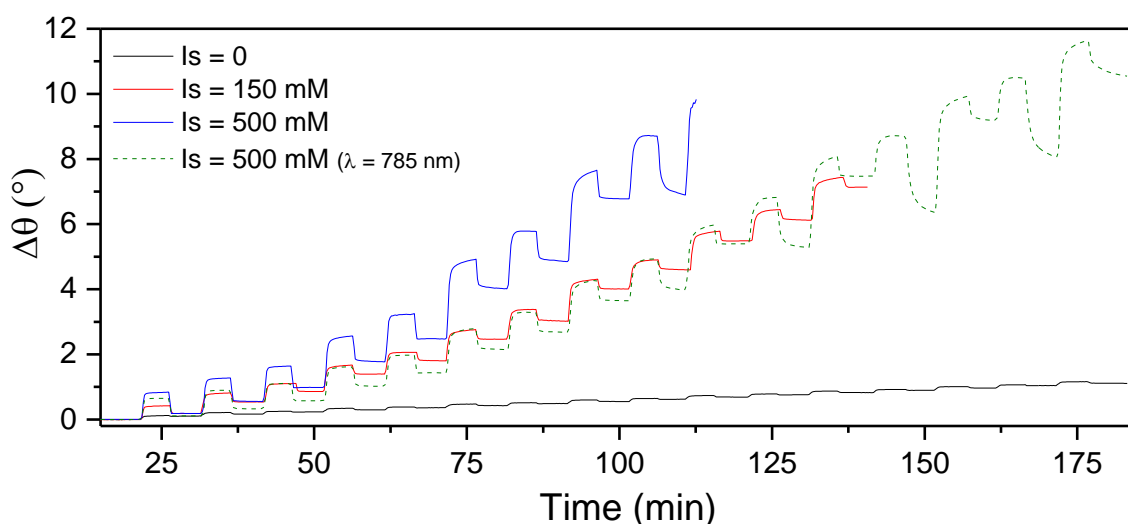


Figure 5.4: SPR curves (resonance angle) for deposition of PDDA-PSS multilayer (10 mM concentration, pH 10) at different ionic strength (adjusted with NaCl); flow rate 20 $\mu\text{L}/\text{min}$, rinsing time 5 minutes at 50 $\mu\text{L}/\text{min}$, deposition on Au coated chip.

Figure 5.5 shows the effect of the variation of the pH for the rinsing water. In the experiment, pH 10 deionised water was used as buffer for the deposition, rinsing the gold surface when the polyelectrolyte solutions were not injected. The decrease of thickness after the injection phase is limited by the exposure to the same pH used for the deposition process. In the specific case, the layers composed by PDDA appeared more sensitive to the change of pH, with the multilayer thickness growing both during the deposition and the rinsing step, while the thickness remains constant when the outermost layer consists of PSS.

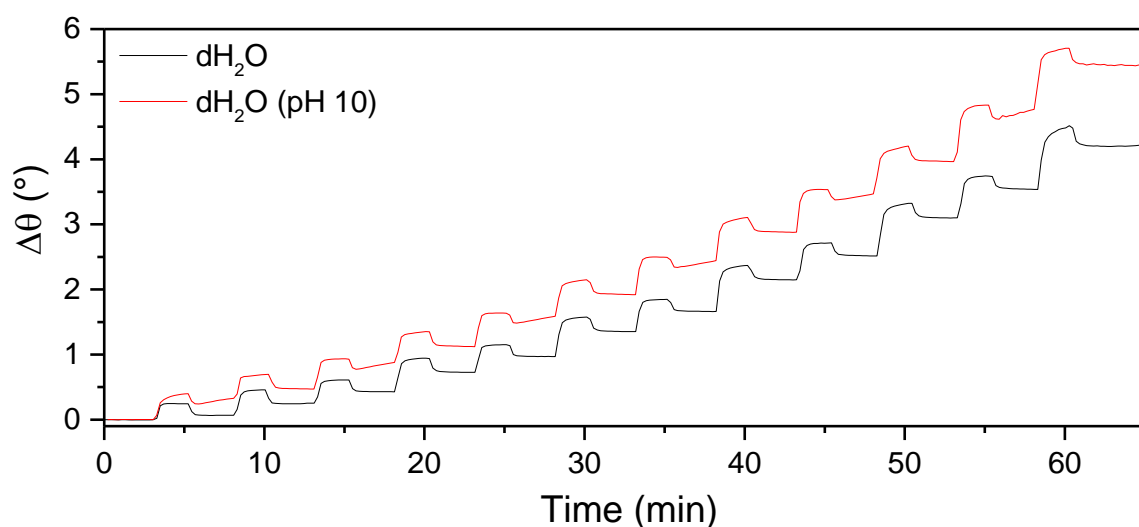


Figure 5.5: SPR curves (resonance angle) for deposition of PDDA-PSS multilayer (10 mM concentration, pH 10, $I_s = 100 \text{ mM NaCl}$) using deionised water at neutral pH and pH 10 (adjusted with 1 M NaOH solution). Flow rate 20 $\mu\text{L}/\text{min}$, rinsing time 5 minutes at 50 $\mu\text{L}/\text{min}$, deposition on Au coated chip).

5.2.2.3 Deposition time

In the previous section, the change in resonance angle due to the deposition of a single layer of polyelectrolyte was estimated in less than 1 minute. However, it is necessary to evaluate the exact effect of the deposition time on the stability of the layer and the structure of the additional layer built over it.

In Figure 5.6, the deposition of the same multilayer was performed using different injection time of the polyelectrolyte solutions. The sensogram corresponding to a 10 min deposition per layer shows the full establishment of the equilibrium between the surface and the polyelectrolyte solution, at least for the first layers. When the number of layers increases, the deposition time is not enough to establish the equilibrium, as shown by the incomplete sigmoidal curves for the outmost layers. When the deposition time is reduced to 5 min per layer, less time is available for reaching the equilibrium. Consequently, the subsequent layers appear to be thinner. This effect is more evident considering the 2 min deposition.

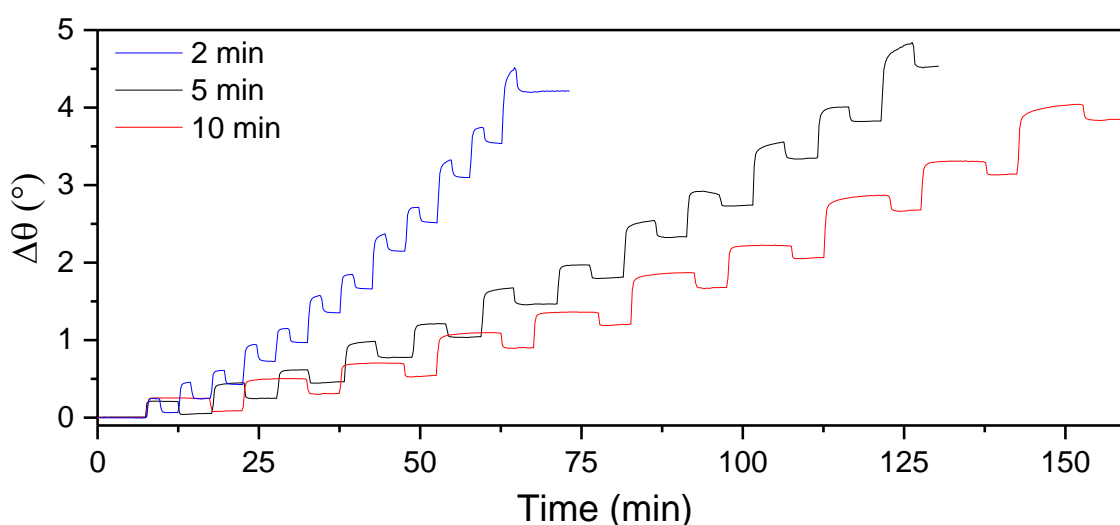


Figure 5.6: SPR curves (resonance angle) for the deposition of a PDDA/PSS multilayer (10 mM concentration, pH 10, Is 100 mM NaCl) using different injection times. Flow rate 20 $\mu\text{L}/\text{min}$, rinsing time 5 minutes at 50 $\mu\text{L}/\text{min}$, deposition on Au coated chip.

Due to the complexity of the multilayer structure and the limited availability of gold-coated chips, it was not possible to determine precisely the thickness of the multilayer. However, since the shift of the resonance angle can be assumed directly proportional to the increase of the multilayer thickness, it was possible at least to determine the growth trend of the multilayer under different conditions. As an example, the sensogram reported in Figure 5.6 can be converted in thickness growth curves, as reported in Figure 5.7. The graph was plotted considering both the maximum shift observed during the deposition step (Figure 5.7 *a*) and the shift value observed during the rinsing step approximately 1 min before the deposition of the following layer (Figure 5.7 *b*). In both cases, the increase of the deposition time led to increase of thickness of the multilayer. In case of short deposition time (e.g. 2 min), the multilayer grows faster but at the expenses of the thickness, probably due to the shorter stabilisation time of the new layer over the one previously applied.

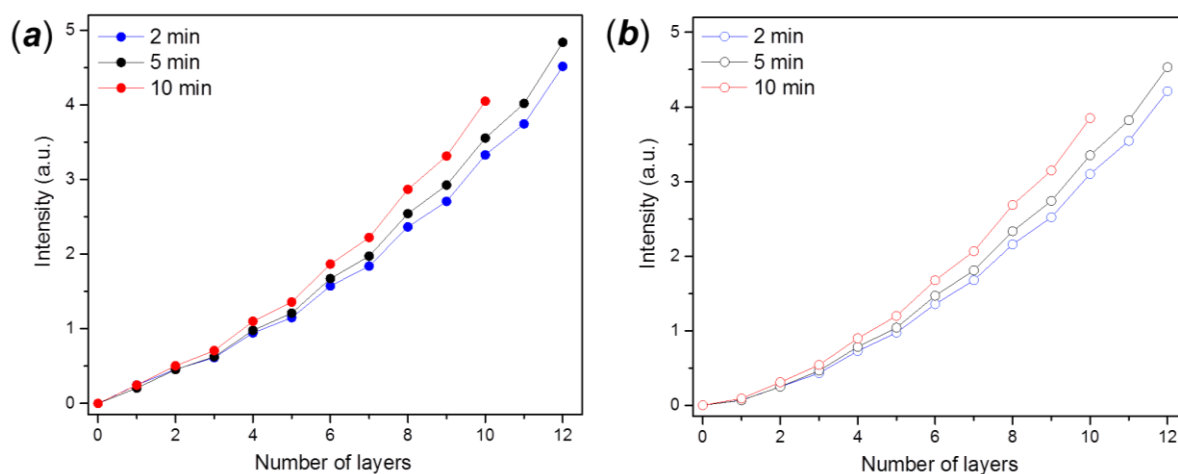


Figure 5.7: (a) maximum intensity during deposition step and (b) shift values observed during the rinsing step approximately 1 min before the deposition of the following layer as a function of the number of layers, calculated from the SPR curve in Figure 5.6.

5.2.3 Surface characterisation of PEM-modified surfaces

5.2.3.1 Optical characterisation

Different conventional spectroscopic techniques were implemented for the detection of the multilayers on different surfaces. Figure 5.8 provides some examples of transmittance measurement on glass slides (*a*) and FT-IR measurement on a plastic (polypropylene) sheet (*b*). The transmittance measurements were performed using the integrating sphere attachment associated with the UV-Vis spectrometer. A clean glass slide was used as reference, with the coated slide placed just before the integrating sphere along the optical path of the beam light.

The presence of the PEM on the slide determines a loss of transmittance, corresponding to the absorption by the polymeric coating. Absorption is generally occurring in the spectral region between 250 -350 nm, with the maximum absorbance at *ca.* 260 nm. The measurement range is limited between the low-absorbance of the coating in the visible light region and the range of absorbance of the glass slides, transparent to wavelength longer than 250 nm.

Due to the low intensity of the monochromatic light, the resolution of this technique is not particularly high, with limited information provided. The measurement is sensitive only towards the thickness of the multilayer, as displayed by the different transmission of PEM coating produced under different conditions (Figure 5.8 *b*). The presence of chitosan (a natural polycation) inserted into the (PAH-PAA) multilayer caused a dramatic change of the spectra. Further attempts to correlate the shape of the transmittance spectra with the nature of the polyelectrolyte used did not give successful results (Figure A.32 in the Appendix). FT-IR measurement was unable to detect any band related to the presence of the PEM coating. The deposition of multiple layer resulted in a decrease of the transmittance value, without masking the original bands of the substrate, as shown in Figure 5.8 *b*.

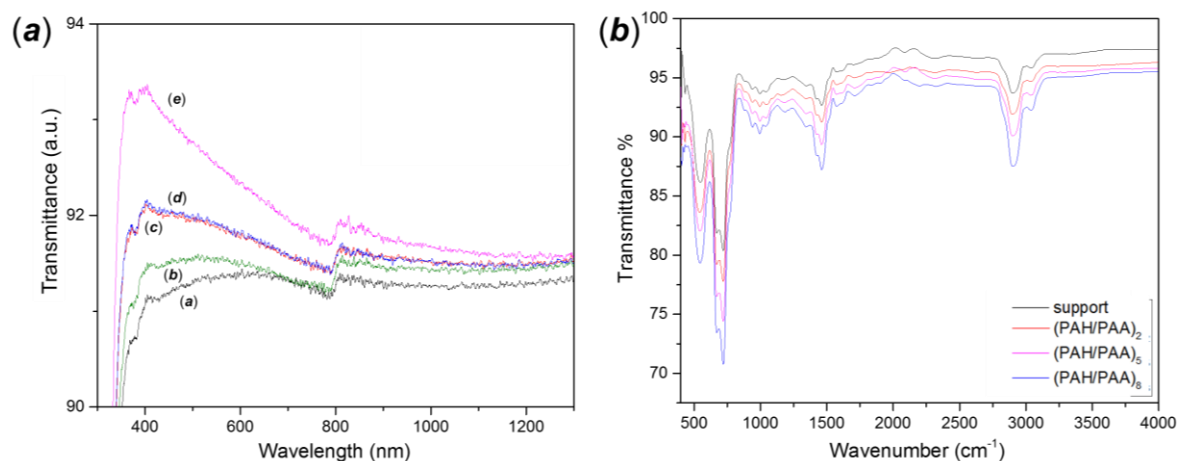


Figure 5.8: (a) UV-Vis transmittance measurements on PEM-coated microscope glass slides. Different PEMs were used: (a) uncoated slide; (b) (PAH-PAA)₅, 5 min/ly; (c) (PAH-PAA)₅, 10 min/ly; (d) (PAH-PAA)₅, 10 min/ly; (e) (PAH-PAA)(CHI-PAA)₃(PAH-PAA), 10 min/ly. (b) FT-IR of (PAH-PAA)_n multilayers coating on polypropylene support, all layers applied with 10 min/ly deposition.

5.2.3.2 Contact angle

The measurement of the contact angle allowed the indirect detection of the presence of the polyelectrolyte coating on the surface. Few nanometer of thickness can dramatically affect the wettability of the surface, turning it more hydrophilic or hydrophobic depending on the polyelectrolyte species and the deposition conditions. A concrete example of the effect of the different type of multilayer on the wettability of a glass slide measurement through contact angle observation is reported in Figure 5.9. The multilayer (PDDA-PSS) gave to the slide, generally very hydrophilic, values of contact angle around 35-40°. One-way ANOVA analysis and Tukey HSD *post-hoc* test were used to assess the statistical significance of the difference among measurements. [1] Despite the statistical analysis showed generally significance of the results, the comparison in pairs of the data demonstrated not significant differences between the samples, mostly limited to the type of multilayer rather than the other deposition conditions (e.g. immersion time). With similarities with what previously observed in the kinetic analysis, the structure of the multilayer built starting from the polyanion is slightly different. However, the increased hydrophobicity of (PSS-PDDA)₅ compared with (PDDA-PSS)_{5.5}, with the presence of PDDA is the outermost layer in both samples,

¹ One-way Analysis of Variance (ANOVA) and Tukey HSD (Honestly Significant Difference) were conducted assuming a confidence interval of 95% (significance level $\alpha = 0.05$) for all the contact angle and water uptake in this chapter. All calculations were performed using the software Minitab 17 and GraphPad Prism 7.4

appears to be not statistical significant. Different the case of a more compact layer such as (PAH-PAA), deposited under acidic conditions. The type of outermost layer affects the surface wettability only under prolonged immersion time, for which the exposure of PAA resulted in a more hydrophilic behaviour of the surface.

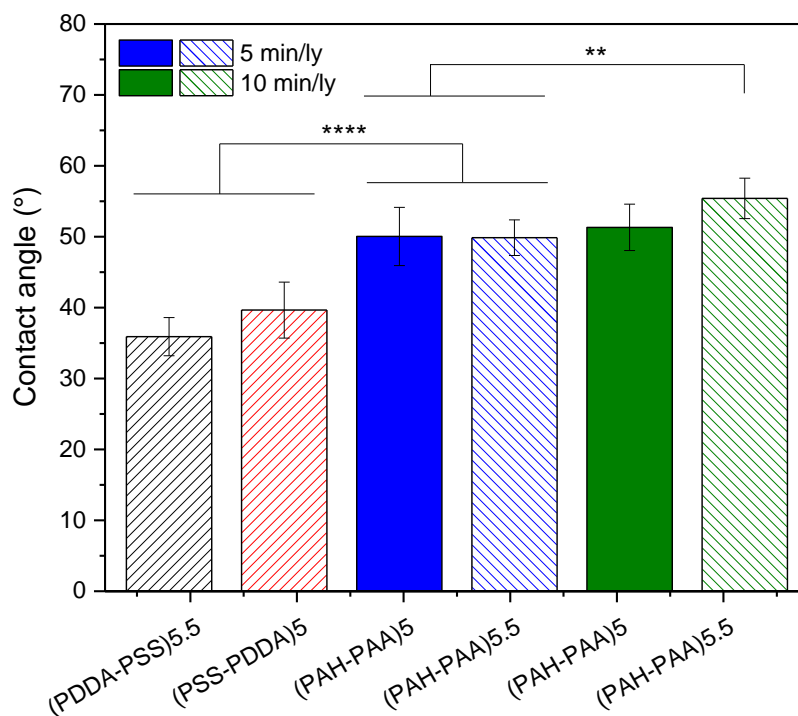


Figure 5.9: Contact angle measurement on microscope glass slide coated using different PEM under different deposition conditions (time of immersion, outermost layer). Statistical analysis is reported for significant results: * $P \leq 0.05$, ** $P \leq 0.01$, * $P \leq 0.001$, **** $P \leq 0.0001$. P values were calculated using one-way analysis of variance (ANOVA).**

5.3 Polyelectrolyte-TiO₂ composites

5.3.1 Dispersion of TiO₂ particles in aqueous solution

One of the main problems of the integration of nanoparticles in composite systems is their dispersibility and compatibility with the chemical environment, specifically the affinity with the solvent in which the system is dispersed. [22] The application of TiO₂ particles in aqueous systems is critical, because of the tendency to agglomerate. In most cases, this means reduction of the nano-size related properties such as photocatalytic degradation. [23, 24]

The stability of colloidal suspension of commercial TiO₂ particles used in this thesis was studied, analysing the zeta potential of the different suspension at different pH values (Figure 5.10). The pH of the suspensions (100 mg/L for all the samples) was adjusted using NaOH and HCl solutions. The pH in correspondence of the zeta potential zero is defined as the isoelectric point of the particles. At this condition, the particle surface carried no net electrical charge. [25] The isoelectric point reported for TiO₂ varies from 4.5 to 6.8 depending on the particle size, shape and crystalline structure. [26, 27] This explain the differences between the three suspension analysed, with the nanocrystalline samples presenting a higher isoelectric point compared with “bulky” anatase powder. The zeta potential defines also the stability of a colloidal suspension. From the data reported in Figure 5.10, it is reasonable to assume that colloidal suspensions of TiO₂ particles are stable at pH values well below or above the isoelectric point. Because of its relatively low isoelectric point, anatase suspension presents higher stability (more negative zeta potentials) at high pH values compared to Kronos and P25.

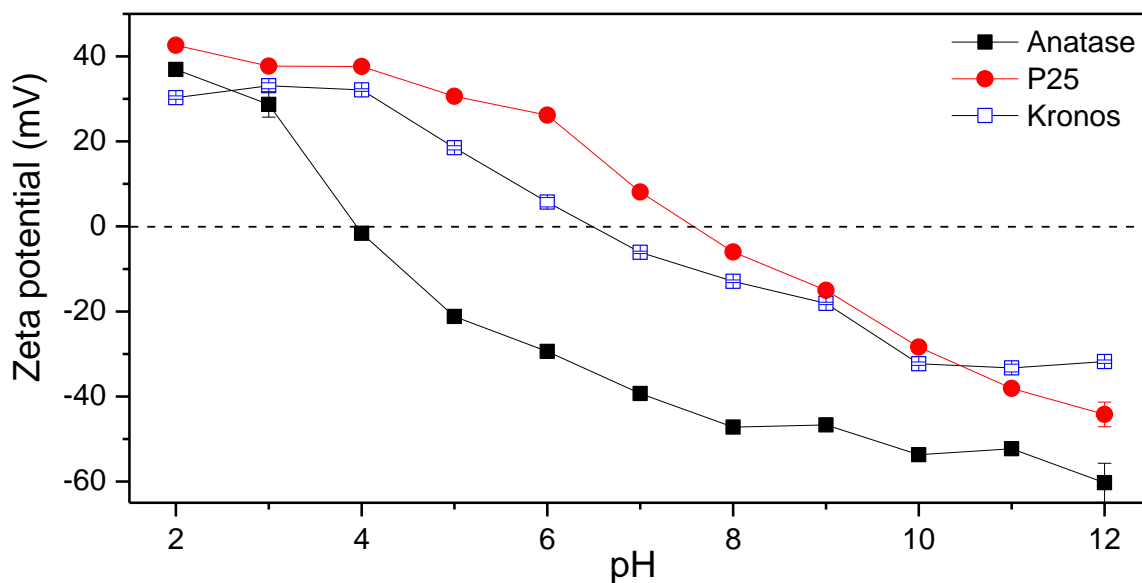


Figure 5.10: Zeta potential measurement for anatase, P25 and Kronos (100 mg/L suspension) at different pH values. For each pH value, the measurement was repeated 4 times. The complete results are reported in Table A.20 in the Appendix.

The Dynamic Light Scattering (DLS) analysis of the colloidal suspension of anatase, P25 and Kronos 7000 shows the increased stability of the solution at pH values far from the isoelectric points. The suspensions lose the electrical stability when the pH is close to the pH_{iso} , around which the particle size measured by DLS increases to micron size due to the agglomeration process. Apart from the pH, also the ionic strength of the solution has a strong influence on the stability of the colloidal suspension. The example of the zeta potential and DLS particle size of a 100 mg/L P25 suspension with the change of ionic strength is reported in Figure 5.11. The increase of the concentration of NaCl destabilise the particle suspension, with the zeta potential decreasing below the stability threshold (30 mV) [28] and the nanoparticle aggregation becoming critical, forming micron-sized clusters.

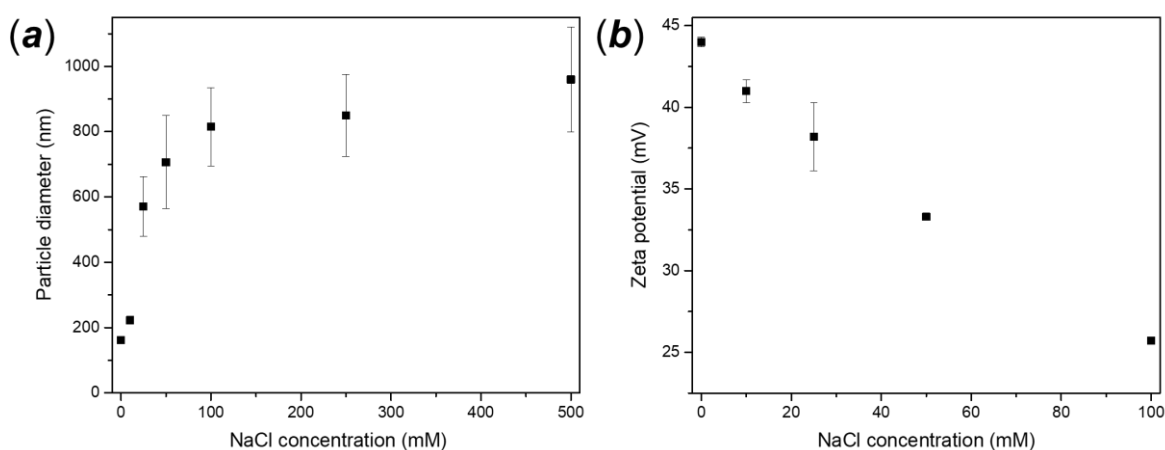


Figure 5.11: (a) DLS Z-average particle diameter and (b) zeta potential measurement of TiO₂ P25 nanoparticles suspension (100 mg/L) in the presence of different concentration of NaCl.

5.3.2 Integration of TiO₂ nanoparticles into PEMs

The integration of photoactive nanoparticles into the multilayer structure represents one of the final goals of this project. A successful integration requires the decoration of the membrane (or any other) surface with the nanoparticles, without loss of the nanoparticles properties (e.g. surface area, photocatalytic activity) and improving the properties of the surface modified with the nanoparticles (e.g. hydrophilic behaviour, antifouling properties).

The criterion for the selection of the integration methods was based on their simplicity, for example avoiding complex functionalisation of the particles with other molecules rather than the polyelectrolytes. The most popular technique consists of the integration of TiO₂ particles (nanostructures or micron-sized powder) in a composite multilayer using the polyelectrolytes as building units. The method exploits the presence of a surface charge distribution occurring on the oxide particles in water. The charges interact with those present on the polyelectrolyte chains, binding the particles in the structure through electrostatic interactions (Figure 5.12). Oxide particles in an aqueous suspension present a superficial charge due to the hydroxyl groups and superficial oxygen atoms. The defective nature of the surface leads to protonation or formation of hydrogen bonding, facilitated by the high superficial energy and the consequent thermodynamic rearrangements.

The charged particle interacts in the same way as polyelectrolyte, despite the lower charge density, binding with oppositely charged species. The resulting multilayer consists of alternate layers of charged particles and polyelectrolytes, with the particles anchored between two layers of oppositely charged polyelectrolytes, potentially preventing their unwanted release.

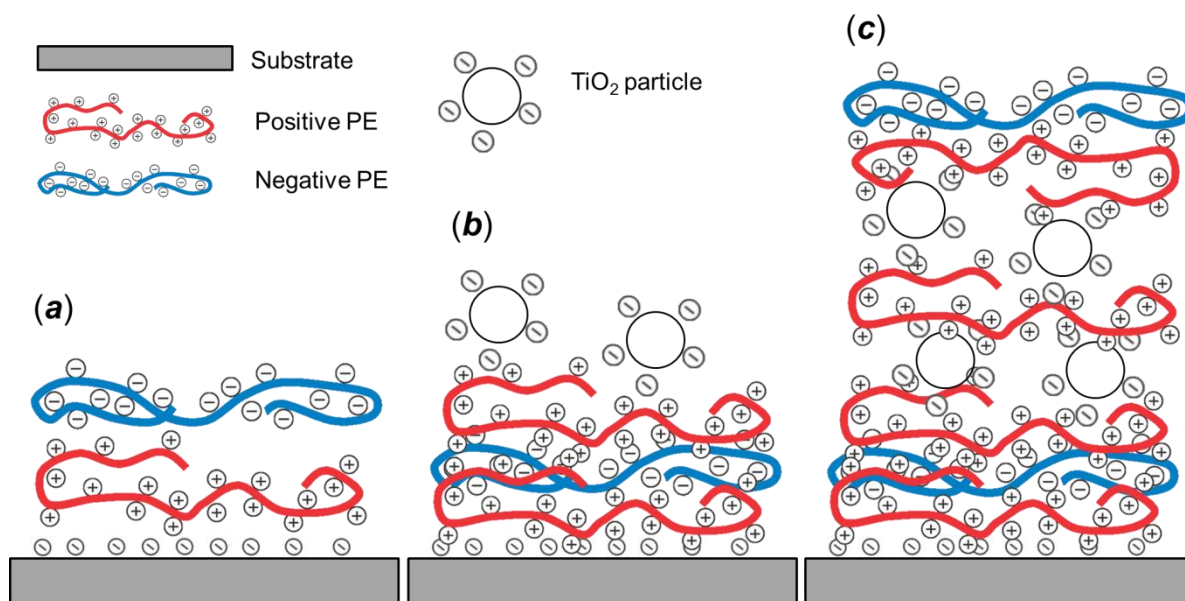


Figure 5.12: Schematic of the composite TiO₂-PEM multilayer assembly: (a) deposition of the polyelectrolytes on the substrate with priming function; (b) exposure of the substrate in a colloidal suspension of negatively charged TiO₂ particles; (c) exposure of the coated surface to other polyelectrolyte solution and TiO₂ particle suspension.

The pH of the suspension needs to be adjusted accordingly to the chosen polyelectrolyte combination. For example, the insertion of positively charged particles replacing a polycationic layer requires low pH values. If the polyelectrolyte solutions are deposited in basic conditions, the effect of the exposure of the acidic suspension on the multilayer structure has to be carefully considered, avoiding possible destabilisation or drastic changes of the structural properties. Comparing the zeta potential values of the particle suspensions (Figure 5.10), the pH tolerance of the membranes (Table 5.3) and the compatibility with the other deposition conditions, the combination of negatively charged particles at pH 9-10 with basic polyelectrolyte solutions such as (PDDA-PSS) and (PAH-PSS) has been preferred to the other options.

The surfaces were alternatively immersed in the oppositely charged polyelectrolyte solutions. For the integration of the inorganic particles, immersion in alkaline TiO₂ suspension replaced the polyanion for the intermediate layers in the coating. The first two bi-layer always consisted of only polyelectrolytes, in order to provide a priming layer for a stable adhesion of the particles to the multilayer and for stabilise the entire structure. The immersion time is indicated in minutes per layer (**min/ly**, used as a notation for the whole chapter).

In Figure 5.13 some example of TiO₂-composite multilayer deposited on Mylar foils are reported. The deposition of the particles on these surfaces did not appear

uniform. Further attempts to improve the deposition procedure (acceleration of drying phase, nitrogen flow drying after each deposition step, stirring of the rinsing solution) did not affected the quality of the coating.

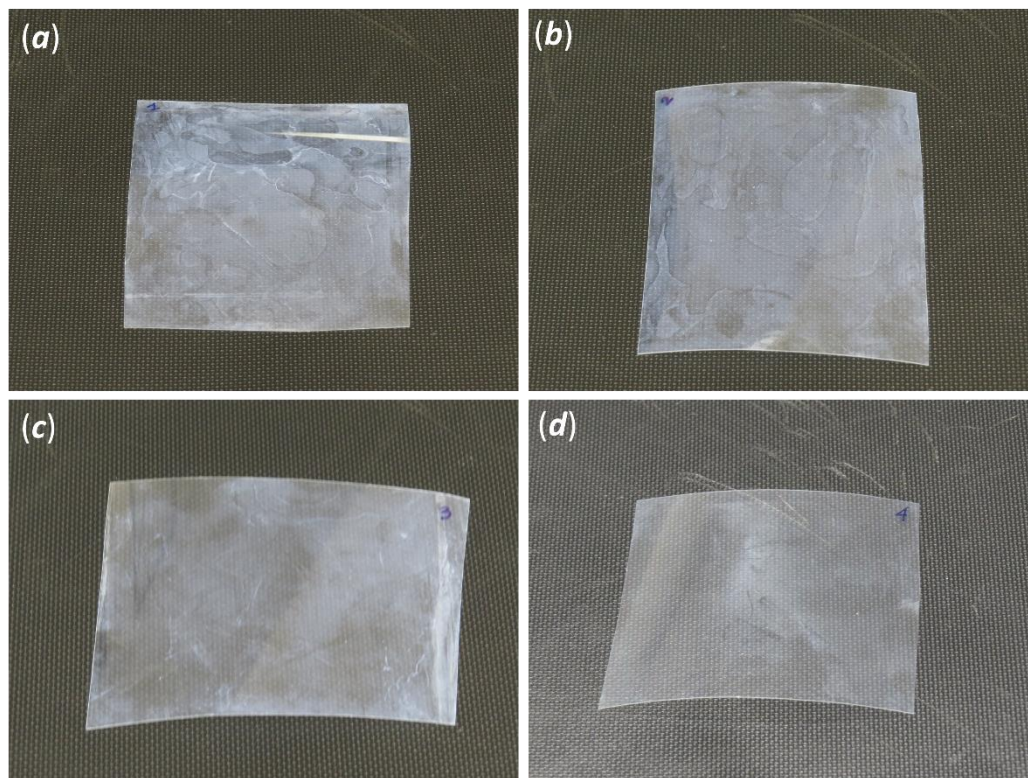


Figure 5.13: Deposition of TiO_2 -composite PEM on Mylar sheets; (a) $(\text{PDDA-PSS})_3(\text{PDDA-TiO}_2)_3$, with TiO_2 exposed, (b) $(\text{PDDA-PSS})_3(\text{PDDA-TiO}_2)_{3.5}$, with PDDA exposed, all layer deposited with an immersion time of 10 min. (c) $(\text{PDDA-PSS})_3(\text{PDDA-TiO}_2)_3$ and (d) $(\text{PDDA-PSS})_3(\text{PDDA-TiO}_2)_{3.5}$, with immersion time of 10 min for the polyelectrolytes and 20 min for TiO_2 .

5.3.2.1 Adsorption kinetic

The SPR curves in Figure 5.14 shows the effect of the insertion of TiO₂ using the layer-by-layer deposition. The pH of the suspension (*ca.* 10) confers negative charges to the oxide particle surface, promoting the interaction with a positive counterpart such as a polycationic layer. The adsorption kinetics of the TiO₂ particles is very different from that of the polyelectrolyte. The injection of the TiO₂ suspension in the system caused a progressive increase of the resonance angle for the entire deposition period. This behaviour differs from that of polyelectrolytes, which adsorption achieves equilibrium with the substrate in few tenth of seconds. Because of the lower conductivity of the suspension compared to the polyelectrolyte solutions (5 to 10 times more conductive), the charged site of the polyelectrolyte layer can establish electrostatic interactions with a higher number of particles. The thickness of the TiO₂ layer is proportional to its concentration and to the deposition time. Unlike polyelectrolyte layers, the thickness of TiO₂ layers is not affected by the rinsing step. This can be due to a good adhesion of the particles on the multilayer surface or to the different behaviour of the inorganic particles to the change of deposition conditions (e.g. pH of the rinsing water) which is likely to modify the polyelectrolyte configuration in the multilayer structure.

Figure 5.14 shows also the evolution of the TiO₂ composite multilayer. Due to the difference in conductivity and the smaller number of charged sites, the adhesion of the subsequent polyelectrolyte layer is limited. After the rinsing step, the resonance angle (and thus the thickness) is unchanged regardless of the concentration of TiO₂ used. Despite of this, the positive charge of the outermost part of the multilayer seems to be refreshed, with a new layer of TiO₂ ready to be deposited. However, each deposition cycle reduces the capacity of the multilayer to integrate new layers of TiO₂ particles.

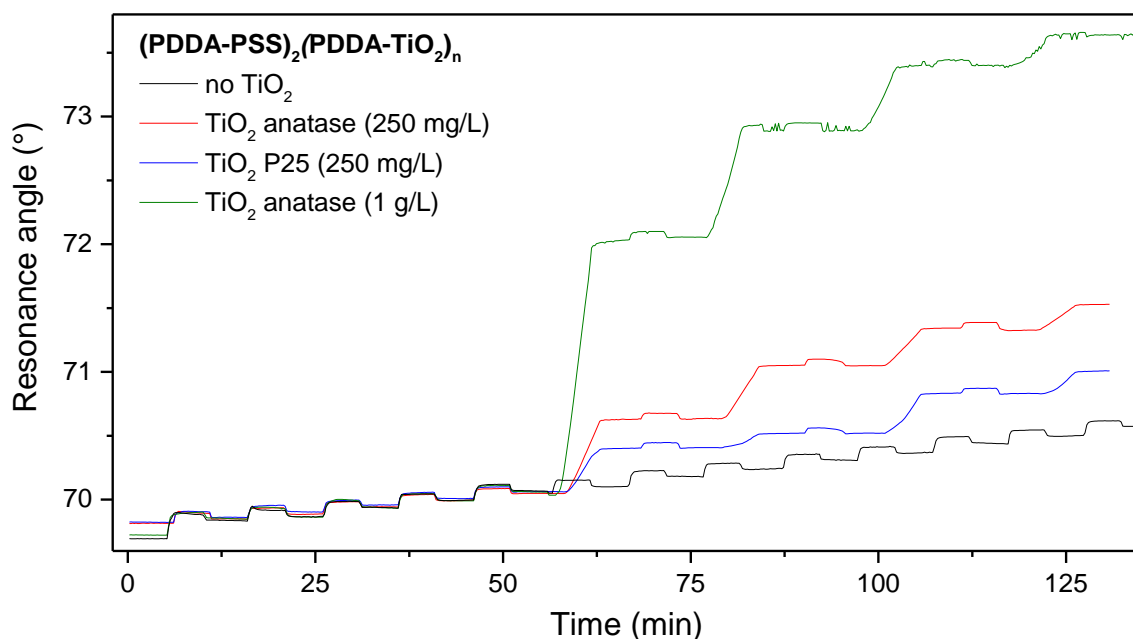


Figure 5.14: SPR resonance angle curves for (PDDA-PSS)₂(PDDA-TiO₂)_n multilayer integrated with TiO₂ suspensions at different concentration as anionic layer (ionic strength 0, pH 10.5)

Figure 5.15 shows the effect of an insufficient charge density for the multilayer build-up. A TiO₂-composite (PDDA-PSS) multilayer is compared to a standard one built with polyelectrolytes only. The suspension used had a concentration of 150 mg/L. The thickness of the first TiO₂ layer is already lower compared to that of the PSS layer deposited on the other system, unlike what was observed in the situation described in Figure 5.14. The subsequent deposition of layers of particles and positive polyelectrolyte cannot balance the charge density, not achieving the conditions to sustain a new layer. The multilayer stops growing because the surface reaches its electrical equilibrium, with the thickness remaining constant. After the 3rd alternate TiO₂-polycation layer, the particles are not able to adhere to the surface, as was occurring with the polycation in excess.

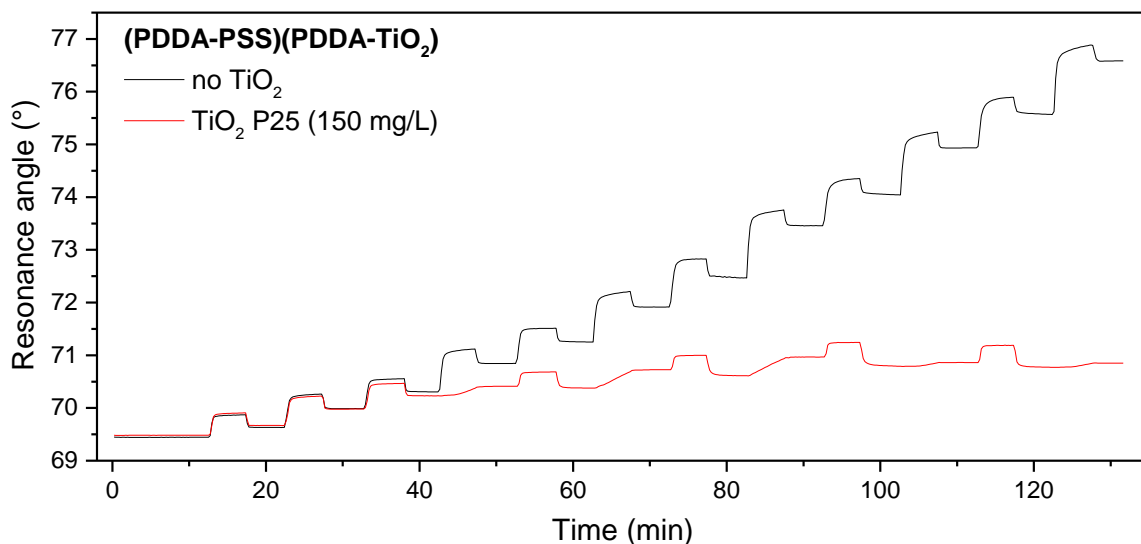


Figure 5.15: SPR resonance angle curves of a (PDDA-PSS) multilayer compared to the same structure integrated with TiO₂ particles (P25, 150 mg/L, pH 10.5).

5.3.2.2 Transmittance

Figure 5.16 shows the transmittance of a glass slide after deposition of a TiO₂ composite multilayer on microscope glass slides. The presence of the multilayer (in this case a (PAH-PAA)_n system deposited under acidic conditions) is detected by a small absorption peak at ca. 260 nm. The integration of the TiO₂ layer increases the peak intensity (or conversely the loss in transmittance, as shown in Figure 5.16). The absorbance is proportional to the amount of TiO₂ deposited. It is not surprising that the glass slide immersed 20 min in the TiO₂ suspension resulting in a lower absorbance than the one immersed for only 15 min. When the TiO₂ particles saturates the polyelectrolyte charges on the multilayer, the surface achieves the electrical equilibrium, as observed in the previous section, and cannot host additional particles even if other oppositely charged polyelectrolyte layers are added. The additional layer of (TiO₂-PAA) in the multilayer **B** increased its absorption peak compared to the multilayer **A**, which has only 2 TiO₂ composite bi-layers. Transmittance measurement can thus be useful to estimate the number of composite bi-layers or the amount of TiO₂ integrated into the multilayer. However, this analysis requires the preparation of precise standards to convert the spectroscopic signal into a quantitative data.

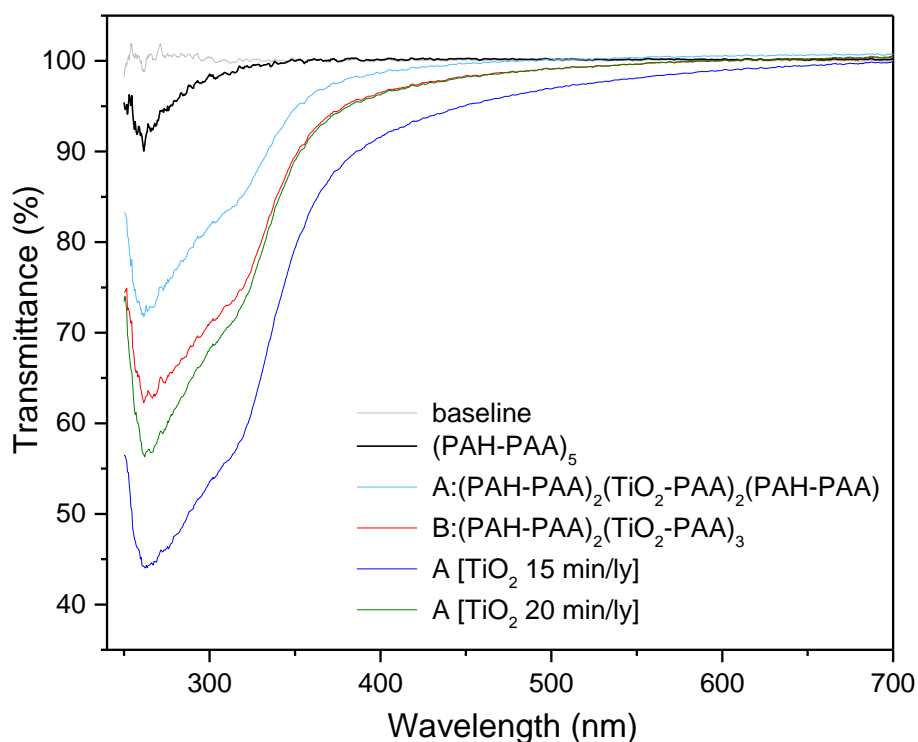


Figure 5.16: Transmittance spectra of glass slides coated with TiO₂ composite (PAH-PAA) multilayers, with different combination of TiO₂ and polyelectrolyte layers or different deposition time (10 min when not indicated).

5.3.2.3 Contact angle

In Figure 5.17, the effect of different multilayer structures containing TiO₂ nanoparticles on the measured values of contact angle was observed. The analysis provided important information about the efficacy of the integration process, such as the increase of the hydrophilicity of the multilayer directly related to the increase of TiO₂ concentration in suspension and to the number of TiO₂ layers. The direct exposure of TiO₂ as outmost layer resulted in a further increase of wettability. On the other hand, more complex combinations of multilayer, such as separating adjacent TiO₂ composite bi-layer with a polyelectrolyte bi-layer resulted in the elimination of the effect of the presence of the nanoparticles on the surface wettability (“purple” sample in Figure 5.17). The superficial properties of the coating, which are usually determined by the outermost layers, are thus also affected by the inner structure of the multilayer. Statistical analysis confirmed the significance of these results.

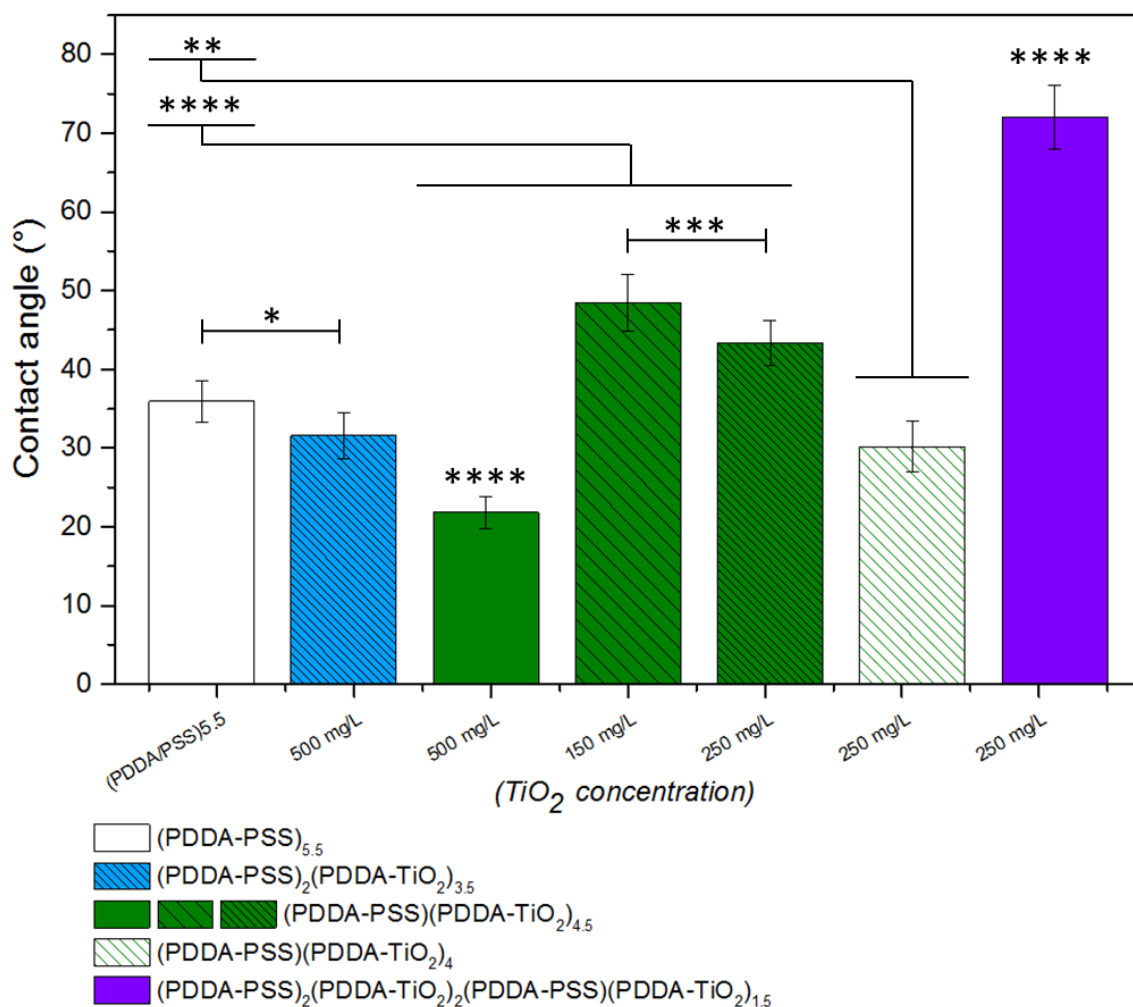


Figure 5.17: Contact angle measurement on glass slide coated with different configuration of TiO₂ integrated composite multilayer (PDDA-PSS). Statistical analysis is reported for significant results: * P ≤ 0.05, ** P ≤ 0.01, *** P ≤ 0.001, **** P ≤ 0.0001. P values were calculated using one-way analysis of variance (ANOVA).

Another reasonable observation is the increase of the hydrophilic behaviour of the surfaces with the concentration of TiO₂ in suspension, reported in different kind of multilayers ((PDDA-PSS) in Figure 5.17 and (PAH-PSS) in Figure 5.18 a. The effect of the lower concentration of TiO₂ did not lead to significant changes in contact angle, unlike the addition of higher concentration of TiO₂ (500 mg/L) to the multilayer.

Due to its very high adhesion capacity, PEI is often used as a priming agent for the surfaces to be functionalised using PEM coating. The initial pH of PEI in solution is relatively high compared to the other polyelectrolytes (around 10.3-10.5, depending on the polymer concentration) and for this reason adjustment of the pH at the level of the other solution using an acidic solution was necessary. The multilayers produced using PEI appeared more hydrophilic. Also, the difference

between the mixed multilayer PEI-PSS-PDDA and the multilayer produced with PEI only is statistical significant. These results confirm the enhanced hydrophilicity of PEI associated to TiO_2 , probably due to the higher adhesive interactions between the branched polymer and the inorganic particles.

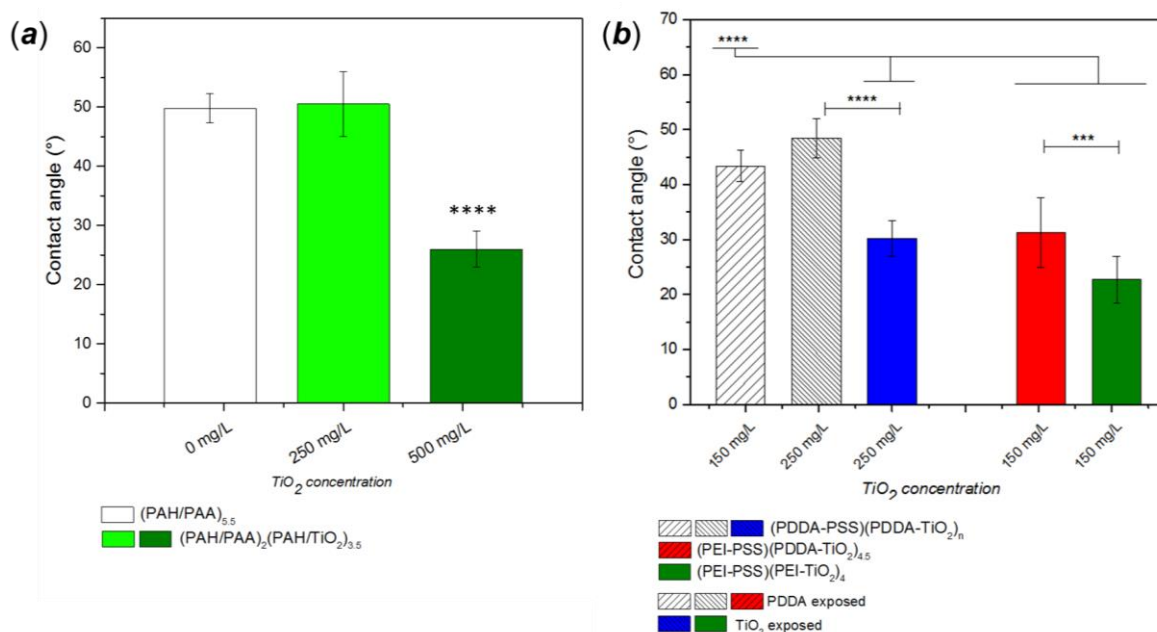


Figure 5.18: Contact angle of glass slides modified with (a) different concentration of TiO_2 nanoparticle suspension integrated in a $(\text{PAH/PAA})_n$ multilayer and (b) different combinations of PEI on a TiO_2 modified $(\text{PDDA-PSS})_n$ multilayer. Statistical analysis is reported for significant results: * $P \leq 0.05$, ** $P \leq 0.01$, * $P \leq 0.001$, **** $P \leq 0.0001$. P values were calculated using one-way analysis of variance (ANOVA).**

5.3.3 Stabilising effect of polyelectrolytes

Functionalisation with larger molecules is one of the possible strategies to improve the stability of colloidal suspension of nanoparticles. Conversely to the electrostatic repulsion effect obtained by altering the pH below or above the isoelectric point of the material in suspension, the attachment of long-chain molecules on the particle surface provides steric hindrance against the agglomeration process, with a stabilising effect on the colloidal suspension.^[29, 30] The use of polyelectrolytes as stabilisers has been already reported in case of both polycations (e.g. PAH)^[31] and polyanions (PAA).

In order to improve the dispersive performances of TiO_2 , the stabilisation by polyelectrolyte adhesion was tested on P25 suspension (100 mg/L). Two different methodologies were tested to prove the stabilising effect of the different

polyelectrolytes used for the preparation of protective coatings in both basic and acidic environments.

The suspension at a basic pH had TiO₂ particles negatively charged. The zeta potential value indicate that the suspension can be considered stable, as the value is below the accepted threshold of stability (over +30 mV or below -30 mV). The results of the stabilisation with polycation are shown in Figure 5.19 *a*. The insertion of PDDA appeared to revert the surface charge. However, the particles in the new suspension showed DLS diameter higher than that of the original suspension, with no significant improvement of the colloidal stability, as displayed by the relatively low value of zeta potential. Increasing the concentration of PDDA can be detrimental for the suspension, as shown for the DLS diameter and zeta potential value of the suspension prepared using 20 %_{wt} of polyelectrolyte. On the other hand, PAH led to a destabilisation of the suspension at low concentration, partially stabilising the solution using higher amount of polyelectrolyte, with the effect of reversing the charges.

The results of the stabilisation of positively charged particles (acidic pH) and polyanion are shown in Figure 5.19 *b*. PSS has a stronger stabilisation capacity than PAA, even at higher concentrations. The addition of PAA to the TiO₂ suspension led to destabilisation of the suspension. PAA is not able to revert the charge of the particles (the zeta potential values remained positive even at higher concentrations) unlike PSS, in which a net negative charge was observed at the lowest dispersant concentration (2.5 %). The higher dispersion capacity of the strong polyelectrolyte is also evidenced by the hydrodynamic diameter of the particles in suspension (Figure 5.20). The particles did not show aggregation when using PDDA. On the other hand, PAA has the worst performance, with progressively increase of the particle diameter, indicating destabilisation of the suspension.

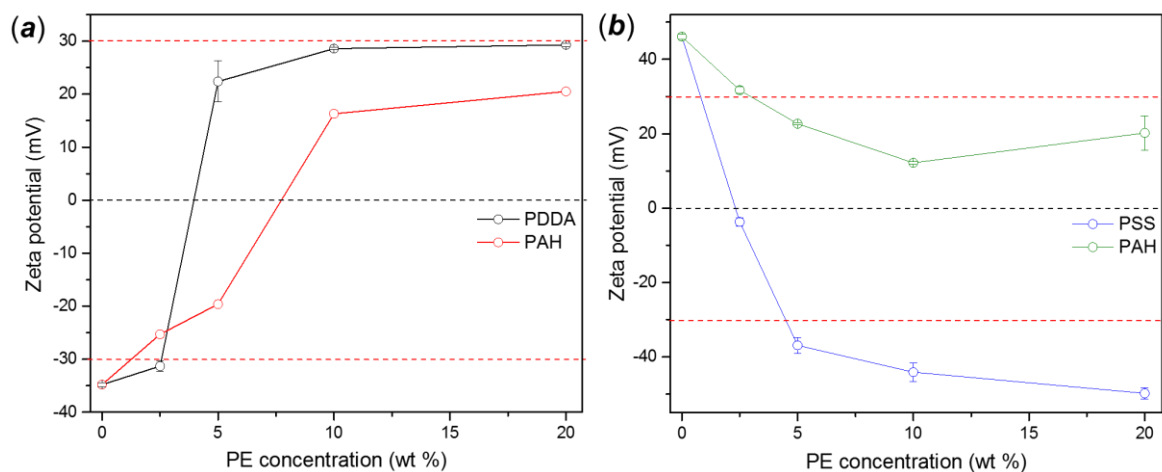


Figure 5.19: Zeta potential of the TiO_2 suspension (100 mg/L) with addition of (a) polycations and (b) polyanions.

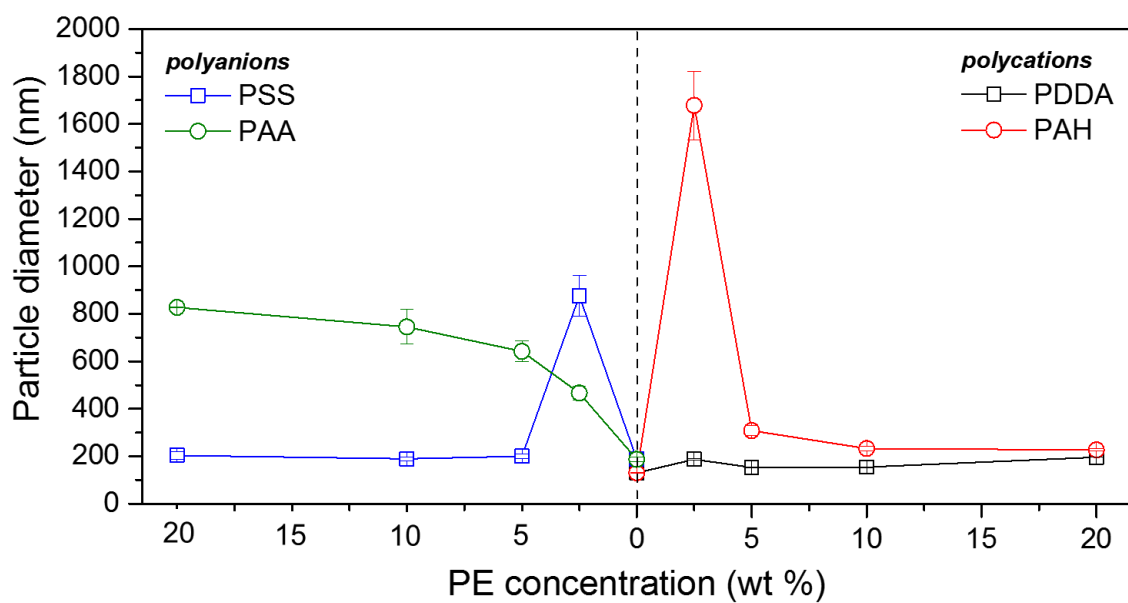


Figure 5.20: Hydrodynamic diameter of TiO_2 particles functionalised with using different concentrations of polyelectrolytes.

5.4 PEM-modified membranes

Several membranes were prepared combining different polyelectrolytes, selecting a series of specific deposition conditions. The multilayers were prepared by using the same technique described in section 5.2. The surface to be coated was immersed in the polyelectrolyte solution, then rinsed, then immersed again in the solution of an oppositely charged polyelectrolyte. The procedure was repeated until the sought number of layer was obtained. Among the options for the coating conditions, different combination of polyelectrolytes, the effect of the pH and the ionic strength, deposition time and rinsing conditions were tested and studied.

As a general consequence of the presence of the PEM coating on the membrane surface, a reduction of the permeate flux is expected, with the membrane active layer protected by a further barrier.^[32] This would alter the hydraulic performance of the membranes, requiring higher filtration pressure to retain the same permeability. Unlike other substrates, membranes require coating of the active surface only, avoiding the production of a second barrier on the back side of the membrane. For this reason, membranes were attached to a plastic surface (usually polypropylene) in order to protect the support layer of the membrane from the exposure to the polyelectrolyte solutions.

After deposition of the multilayer coating, the membranes were preserved using glycerol solution following the procedure reported by Ilyas *et al.*^[33]

5.4.1 Ultrafiltration (UF) membranes

Extensive characterisation of the commercial ultrafiltration (UF) membrane was performed before their modification *via* deposition of polyelectrolyte multilayers. The main analytical techniques were applied to assess the properties of the original membranes and to determine the differences in comparison with the PEM-modified surfaces. In this section, physical-morphological characterisation of the membrane surface and hydraulic performance are examined. Specifically, the analysis which proved not useful for the characterisation of the multilayer are briefly described for completeness.

The commercial membranes were provided by Sinder Filtration[®], selecting two main polymer used as active layer, polyethersulfone (PES) and polyacrylonitrile

(PAN). The characteristics and applications of the selected membranes are listed in Table 5.3.^[34]

Table 5.3: List of the commercial membranes used in the thesis project.

Commercial series	PY	PZ	LY (UE 50)	SM
Material	PAN	PAN	PES	PES
Feed	Wastewater	Wastewater	Industrial water	Industrial water, Wastewater
Application	Corn Wet Milling and Particle removal	Oil Removal, Enzyme Processing	Oil Removal and Enzyme processing	Beverage and Dairy Clarification
pH range (25 °C)	2-11	3-10	2-11	2-11
Flux (gfd/psi)	70-100 (15 psi)	NA	270-289 (50 psi)	147 (60 psi)
Flux (Lhm/bar)	120-170 (1.03 bar)	NA	460-490 (3.45 bar)	250 (4.14 bar)
Rejection size	100k Da	30k Da	100k Da	20k Da

5.4.2 Morphology

Commercial UF membranes are generally composed of a textile support providing mechanical stability and a thin porous layer (defined as the active layer) made of chemical resistant polymer such as PES, PAN or PTFE, deposited onto the support. Polyester woven or non-woven fabrics are generally employed as support material for these membranes.^[35]

At a first visual observation, no relevant changes were observed on the membrane surfaces after the Lbl deposition. The SEM analysis is unable to provide a clear image of the membrane surface. For this reason, the technique was not exploited for morphological characterisation. However, the SEM images of the cross-section of the membranes provides insight on its internal structure, with the woven polyacrylic textile support and the active layer produced by phase inversion casting.^[36]

Atomic Force Microscopy (AFM) was used to investigate the surface topography of the modified membranes. The analysis revealed a more complex topography for the samples coated with PEM compared to the original membranes. The superficial features, which were accounted of a maximum size scale of about 25 nm for the unmodified membrane (Figure 5.21), are now several times higher, which denotes increase of the surface roughness due to the coating process.

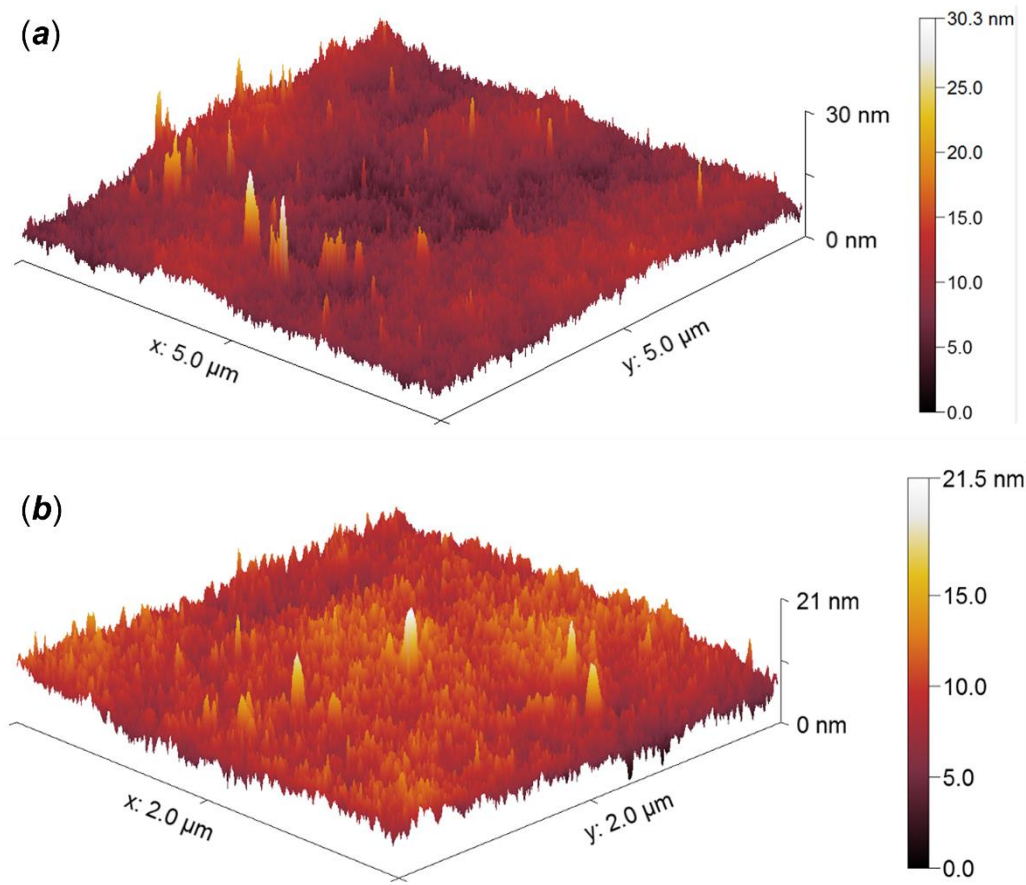


Figure 5.21: AFM image of the SM-UF membrane; top view of (a) $2 \mu\text{m}^2$ section and a (b) $5 \mu\text{m}^2$ section of the membrane surface, with relative chromatic scale bar for the profile depth.

A preliminary analysis was performed on the membrane surfaces coated with different combination of polyelectrolytes and under different conditions. In Figure 5.22 the effect of different combination of polyelectrolytes and deposition conditions is observed *via* the result of AFM analysis. From these preliminary observations, the deposition time is responsible for the increase of the surface roughness ((a) and (b)), whereas the increase of the ionic strength (c) and (d) modifies profoundly the surface topography. The surfaces of the SM membranes coated with (PAH-PAA) (e) and (PAH-PSS) multilayer (f) show a complete different morphology from the (PDDA-PSS) multilayer in Figure 5.22 a, despite the same number of polyelectrolyte layers. However, the resolution of the images is not high enough (especially Figure 5.22 c) to determine precisely the effect of the deposition conditions on the selected membranes. Example of plots of the surface texture are also available in Figure A.33 in the Appendix.

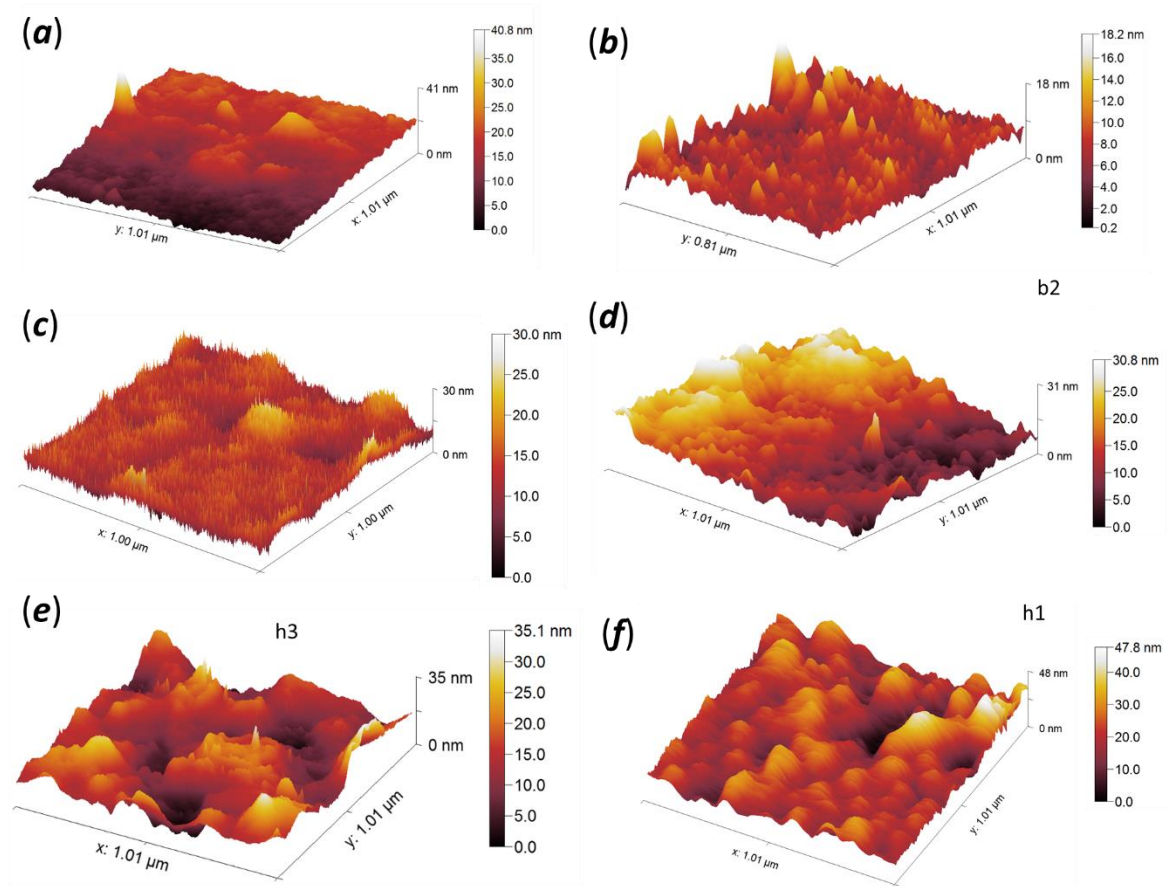


Figure 5.22: AFM images of portion of modified SM-UF membranes using different PEM systems under different conditions; (a) (PDDA-PSS)_{3.5}, 5 min deposition; (b) (PDDA-PSS)_{3.5}, 10 min deposition; (c) (PDDA-PSS)_{3.5}, 5 min deposition, 150 mM NaCl; (d) (PDDA-PSS)_{3.5}, 5 min deposition, 500 mM NaCl; (e) (PAH-PAA)_{4.5}, 5 min deposition (f) (PAH-PSS)_{4.5}, 5 min deposition.

The analysis was affected by the electrostatic nature of the coating, making difficult the selection of the optimal instrumental settings. An excess of charge can indeed alter the interactions between the probe tip and the surface features. An estimate of the surface roughness for the selected membranes is given in Table 5.4, with the roughness estimated sampling homogeneous 1 μm^2 areas. The results presented significant differences from the statistical point of view only in terms of number of layer and increase of the ionic strength compared with the untreated membranes (Figure A.34 in the Appendix).

Table 5.4: AFM roughness values calculated for the selected membranes. R_a indicates the average roughness, R_q indicates the root-mean squared roughness of the surface. Statistical analyses for the R_a and R_q of the different samples are reported in Figure A.34 a and b in the Appendix, respectively.

	R_a	R_q
SM (1 st)	0.84 ± 0.05	1.06 ± 0.07
SM (2 nd)	0.89 ± 0.08	1.12 ± 0.11
(PDDA-PSS) _{3.5} , ($I_s = 100$ mM)	1.10 ± 0.09	1.40 ± 0.13
(PDDA-PSS) _{3.5} , ($I_s = 500$ mM)	1.12 ± 0.10	1.39 ± 0.12
(PAH-PSS) _{4.5}	2.51 ± 0.63	3.24 ± 0.78
(PAH-PAA) _{4.5}	0.92 ± 0.11	1.16 ± 0.17
(PDDA-PSS) _{5.5}	1.23 ± 0.26	1.59 ± 0.35
(PDDA-PSS) _{3.5}	0.69 ± 0.05	0.87 ± 0.08
(PDDA-PSS) _{3.5} (10 min/ly)	0.75 ± 0.05	0.94 ± 0.06

5.4.3 Swelling and water content

The swelling of the membrane due to water adsorption was determined by measuring the mass change before and after immersion of small pieces of membrane (around 1 cm²) in deionized water; the membrane samples were dried and weighted. After immersion for 24 hours, the water on the surface was removed by simple mechanical agitation and the membranes weighed. The swelling was hence calculated using the expression: [37]

$$S(\%) = \frac{m_w - m_d}{m_w} \quad (\text{eq. 5.1})$$

where m_w is the mass of the swollen wet membrane and m_d the mass of the dried membrane respectively. As shown in

Figure 5.23, the water uptake for the commercial membrane is particularly high, with an absorption capacity over 50 % of the dry weight of the membrane. From these results it is apparently difficult to correlate the material and the selectivity active layer with the water uptake data. For instance, **SM** (MWCO 20 kDa) absorbs less water compared to **LY** (MWCO 100 kDa) even though the active layer is always PES. However, water uptake measurements are too inaccurate to ensure significant differences between the results. Statistical analysis assessed that only the values measured for the membranes **LY** and **MT** showed significant differences compared to the other membrane tested and the membrane support.

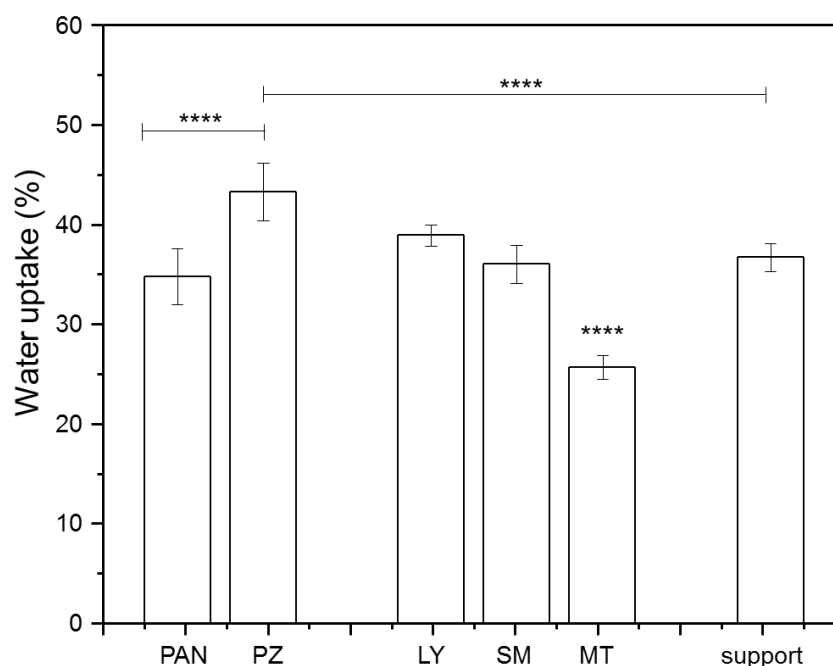


Figure 5.23: Water uptake measurement for the original untreated commercial membranes. Statistical analysis is reported for significant results: * $P \leq 0.05$, ** $P \leq 0.01$, * $P \leq 0.001$, **** $P \leq 0.0001$. P values were calculated using one-way analysis of variance (ANOVA).**

A series of SM-UF membranes modified using the three PEM systems was prepared and tested for water uptake (Figure A.35 in the Appendix), with statistically significant differences only for coating produced by a higher number of layer (ca. 5 bi-layers). As an example, the statistical comparison is reported for the (PAH-PAA) multilayer, for which the observed values showed more consistent changes compared to the original membrane and to the other multilayers tested. (Figure A.36 in the Appendix). However, the application of the polyelectrolytes caused relevant modification of the swelling behaviour after a certain number of deposited layers. Analysing the specific effect of the single systems, PDDA caused a general increase of the water uptake, whereas the system PAH-PAA in acidic conditions produced a relevant reduction of uptake after the third bi-layer. Water uptake measurement can be considered independent from the surface wettability, because of the methodology of the measurement (24 hours soaked in water).

5.4.4 Porosimetry

An estimation of the pore size was also tried by analysing nitrogen adsorption-desorption isotherm. Such measurements are using specific instruments. However, there was no record of use of Quadrasorb Evo, mainly designed surface area measurement of fine powder. Membrane pore size is usually measured by using capillary flow porosimetry which includes more specific and accurate methods, such as bubble point determination and liquid displacement porosimetry.^[38] Due to the different nature of the sample analysed, a correct interpretation of the isotherms requires particular attention.

Figure 5.24 shows the isotherms for PAN and PES commercial UF membranes. The shape of the isotherms is very similar, a type IV with the presence of hysteresis. The hysteresis is wider for PAN than for PES membranes. Comparing the membranes with different molecular weight cut-off (MWCO), 20-30 kDa membrane presents a slightly higher surface area compared to the 100 kDa membrane. However, the 5 kDa membrane (closer to nanofiltration purposes than the other UF membranes) has a lower N₂ volume uptake compared with the other PES membranes. (Figure 5.24 *b*). The comparison with the textile support was not possible, since no regular isotherm was produced during the analysis and even negative N₂ uptake volume. Analogous situation was observed for a sample of nanofiltration membranes (Dow Filmtec, Polyamide-TFC, MWCO *ca.* 200-400 Da), which active layer is thicker than UF membranes. The adsorbed volume is below the precision of the instrument, giving an irregular isotherm also in this case. Both cases are presented in Figure A.35 in the Appendix.

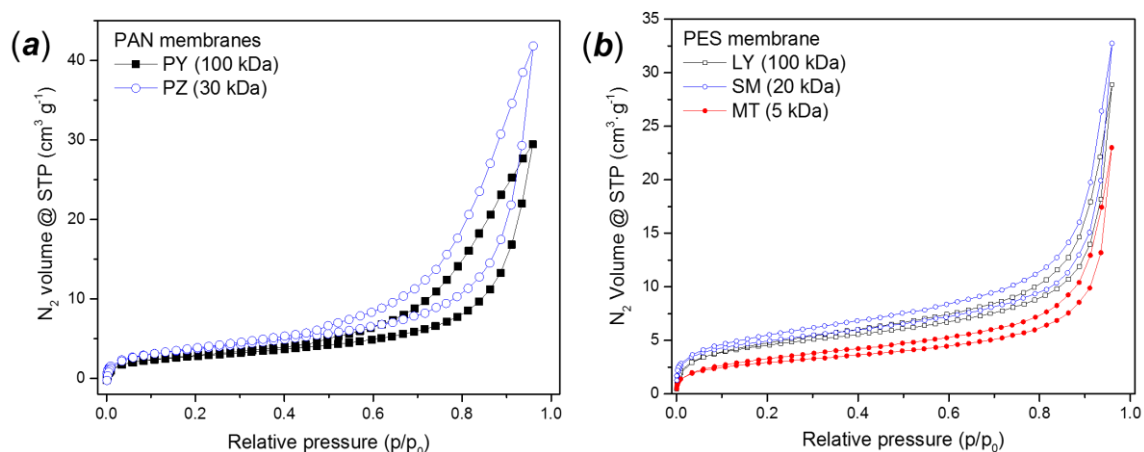


Figure 5.24: N₂ isotherm adsorption-desorption curves for UF membranes, with active layer made of (a) PAN and (b) PES. The rejection capacity of the membranes is indicated in the legend.

BET surface area calculations of the pore volume and size distribution for the commercial membranes are reported in Table 5.5. The measurement of the N₂ adsorption/desorption was also used in an attempt to determine eventual differences produced by the presence of the PEM coating. All the selected PEM-modified membranes showed decrease of the surface area and the pore volume, as expected by applying a polymeric coating on the active layer, as shown in Figure 5.25 *a*. Worth of notice is the reduction of the surface area caused by the use of PEI as priming layer, which has influence also on other important properties of the membrane, phenomenon detailed in the following sections of this chapter. However, no other information was obtained from this analysis. For instance, the attempt to calculate the pore size distribution using conventional BJH calculation on the commercial membrane gave no relevant data (Figure 5.25 *b*), confirming the limits of this technique applied to polymeric membranes. Therefore, no further investigation was performed on this method due to the unsupportive results.

Table 5.5: BET surface area and pore size distribution analysis for the commercial UF membranes (calculations based on 3 measurements on different portions of the same sample).

Membrane	MWCO (kDa)	BET surface area (m ² /g)	Pore Volume (cm ³ /g)	Pore diameter (Å)
PAN PY	100	10.00 ± 0.31	0.049 ± 0.01	19.55 ± 2.10
PAN PZ	30	13.44 ± 0.47	0.069 ± 0.05	43.24 ± 7.02
PES LY	100	16.71 ± 1.25	0.041 ± 0.06	14.89 ± 0.57
PES SM	20	17.11 ± 1.67	0.046 ± 0.08	23.41 ± 3.86
PES MT	5	10.72 ± 0.62	0.033 ± 0.04	19.58 ± 2.74

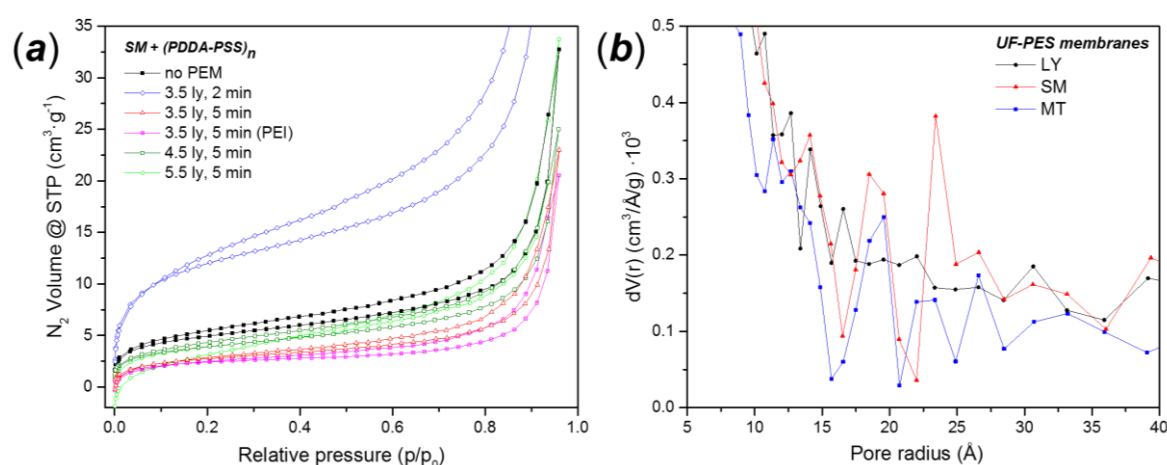


Figure 5.25: (a) N₂ isotherm adsorption-desorption curves for PEM-coated UF membranes and (b) pore size distribution of the commercial UF membranes.

Table 5.6: BET surface area and pore size distribution analysis for the PEM-coated SM ultrafiltration membranes (calculations based on 3 measurements on different portions of the same sample).

Membrane	PEM conditions	BET surface area (m ² /g)	Pore Volume (cm ³ /g)	Pore radius (Å)
SM	-	17.11 ± 1.67	0.046 ± 0.08	23.41 ± 3.86
SM-A5	3.5 ly, 2 min	9.34 ± 1.76	0.032 ± 0.03	19.57 ± 3.11
SM-K2	3.5 ly, 5 min	10.19 ± 0.53	0.034 ± 0.05	24.90 ± 5.24
SM-K7 *	3.5 ly, 5 min	8.97 ± 1.95	0.031 ± 0.01	21.97 ± 2.21
SM-T0	4.5 ly, 5 min	14.15 ± 0.82	0.035 ± 0.05	15.68 ± 0.46
SM-K1	5.5 ly, 5 min	14.44 ± 1.60	0.052 ± 0.07	19.56 ± 2.71

* PEI as priming layer

5.4.5 Spectroscopic characterisation

5.4.5.1 FT-IR and Raman characterisation

IR and Raman spectroscopy were used for the characterisation of the UF membranes surfaces. Figure 5.26 shows the different chemical composition of support, PAN and PES active layers. Specifically, the region between 1000-1800 cm^{-1} of the IR spectra was analysed in detail, since is considered as the fingerprint of a compound. Lower frequencies showed relevant signals only in case of PAN (strong peak around 2250 cm^{-1}), besides peaks attributed to surface hydroxylation at ca. 3200-3600 cm^{-1} (not showed in Figure 5.26).

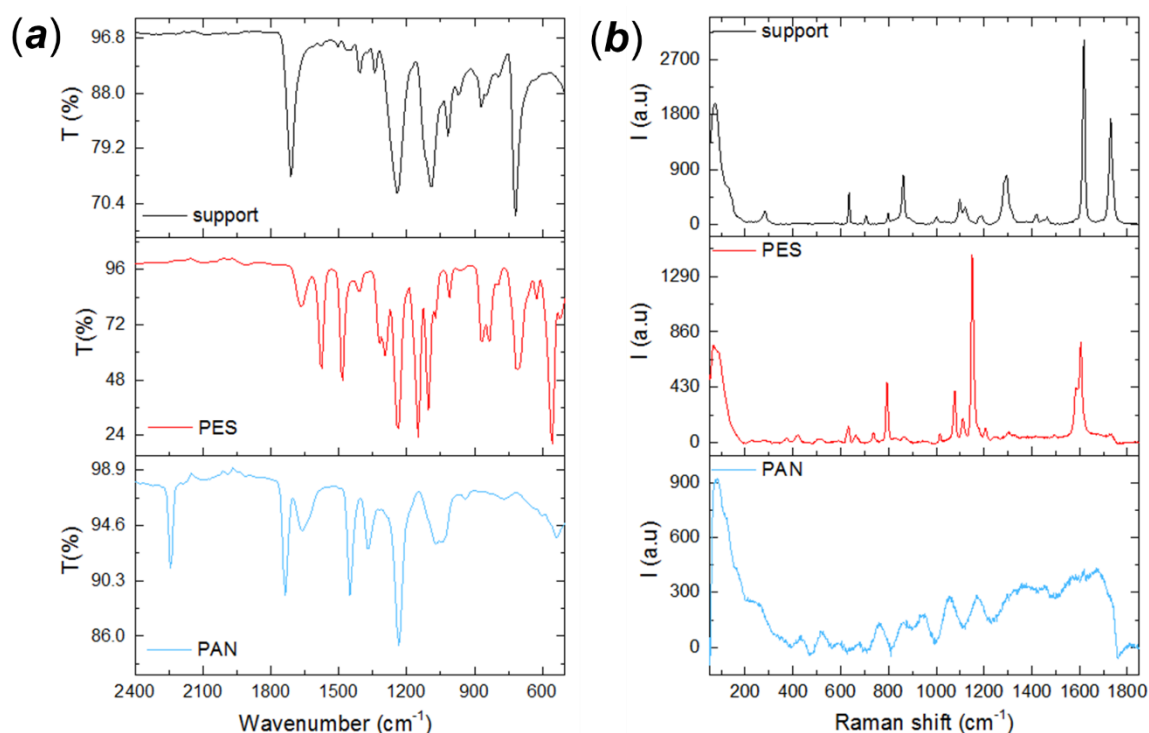


Figure 5.26: (a) FT-IR and (b) Raman spectra for the commercial UF membranes.

Despite the vast literature about the two polymers and the applications of the membranes, little details are available about the FT-IR and Raman characterisation. The IR and Raman spectra of PES are complex, and it is difficult to attribute all the bands to the respective vibration modes, with only one work in literature assigning most of the bands.^[39] Among the IR signals, it is easy to identify the typical structural vibration corresponding to the stretching of the benzene (1580 and 1486 cm^{-1}),^[40] aromatic ether (1244 cm^{-1}) and C-O bond (1106 cm^{-1}),^[41] together with the presence of sulfone (SO_2) with the strong peaks at

1148 and 1294 cm^{-1} and finally a peak at *ca.* 699 cm^{-1} attributed to phenyl groups. Considering the Raman spectrum, the strong signal at around 1600 cm^{-1} is the product of the convolution of two bands (1600 and 1581 cm^{-1}) attributed to ν C-C (in-planar benzene ring deformation), the strongest peak at 1146 cm^{-1} attributed to ν SO₂, followed by two medium intensity bands (1107 and 1073 cm^{-1}) assigned to in-plane δ C-H and finally the strong band at 790 cm^{-1} , unassigned but lying between the regions of signal attributed to ν C-S (*ca.* 700-740 cm^{-1}) and out-of-plane δ C-H (820-865 cm^{-1}). [39]

Because of its less complex molecular structure, the IR spectra of PAN present less and easily identifiable signals, such as the strong ν C-N (2237 cm^{-1}), δ C-H (1447 cm^{-1}), wagging of the C-H bond (1247 cm^{-1}) and the combination of the vibration modes of the C-CN group centred at 1047 cm^{-1} . [42] The band at 1730 cm^{-1} can be attributed to C-O or C=O bonds, resulting from the residual presence of methyl acrylate as co-monomer during the synthesis process. [43, 44] The Raman spectra of the PAN membrane is not particularly clear, with a huge shoulder and relatively weak signals.

The presence of the PEM on the membranes was not detected neither by FT-IR nor by Raman spectroscopy, as already observed for other surfaces. The very small thickness of the multilayers (few tenths of nanometer) is also in this case the probable cause, making useless these spectroscopic methods for the chemical characterisation of the multilayers.

5.4.5.2 UV-Vis spectroscopy

The characterisation via UV-Vis of the UF-membranes is shown in Figure 5.27. All membranes present no absorption at wavelength higher than 400 nm, with characteristic signals only in the UV-region. The absorbance spectrum of the textile support shows two characteristic peaks at 296.5 and 230.5 nm and a small peak in the IR region (1128 nm). The presence of the active skin layer can be observed by the change in absorption in the UV-region, with generally lower absorbance intensity compared to the support. Membranes with active layer made of PAN, with two evident peaks at around 270 and 195 nm. The active layer of PES membrane shows two absorption bands at around 292 nm and between 259-266 nm. The selectivity of the unmodified membranes depends on the thickness of the active layer. Lower cut-off values give lower absorption intensity. For PAN

membranes this effect is only visible for the peak at *ca.* 195 nm. Conversely, the UV-Vis spectra of the PES membrane is more sensitive to the thickness of the active layer, with evident differences among membranes with different MWCO values across the whole absorption region. The absorption intensity is lowered by 20-30% passing from the membrane with 20-30 kDa to those with 100kDa cut-off.

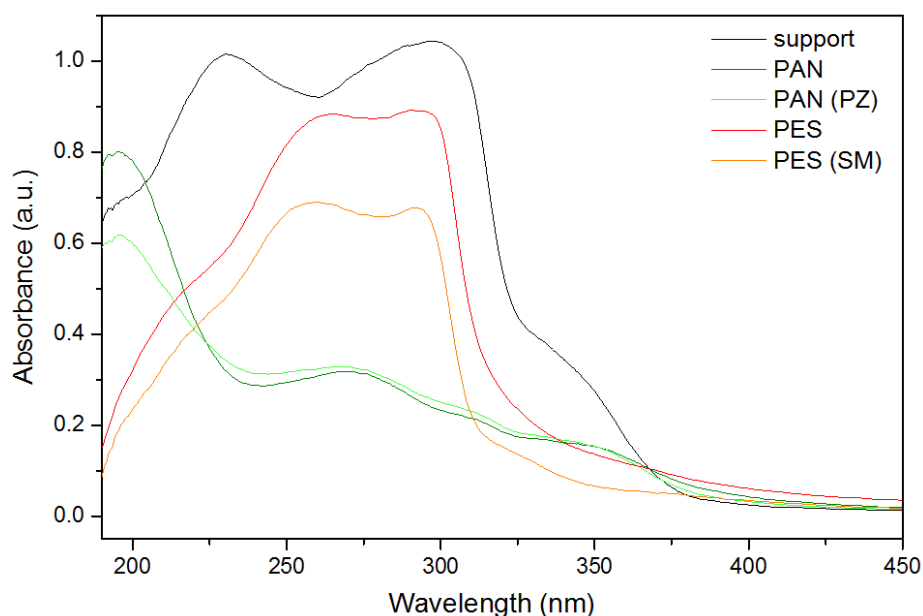


Figure 5.27: UV-Vis Absorbance spectra for the commercial membranes compared with the textile support

However, the same principle does not apply to the PEM coating. The presence of an organic layer should increase the absorbance. For example, the phenyl rings of PSS should present an absorption peak at 228 nm.^[83] On the contrary, the presence of the PEM cannot be distinguished from the original surface by the UV-Vis absorption spectra. As an example, the presence of the PSS/PDDA system on SM membrane showed the increase of the relative intensity of the band at 292 nm with respect to the other at lower wavelength. No alteration of the spectral features, such as peak shifts, was observed. Notably, the decrease of the absorption intensity is not related to the number of layer and regardless the type of exposed polyelectrolyte.

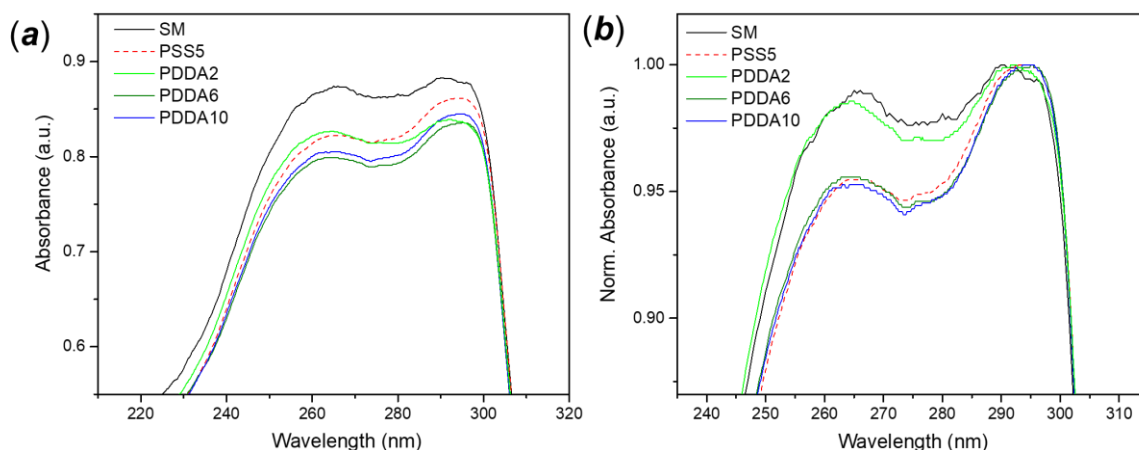


Figure 5.28: (a) UV-Vis absorption spectra of UF-SM membranes coated with different number of (PDDA-PSS) layers and (b) the same spectra normalised for the value of maximum intensity. The outermost polyelectrolyte and the number of layers are indicated in the legend.

5.4.5.3 Wide angle XRD

In another attempt to characterise the membranes surface, Wide Angle XRD (WAXD) was performed on the membrane sheets. This technique applies the same Bragg-Brentano geometry adopted for powder PXD. A small portion of membrane was mounted on a bracket sample holder (used for powder diffraction), with the X-ray beam incident on the flat polymeric surface.

The WAXD analysis revealed the presence of clear peaks for all the samples. Unfortunately, the strong peaks can only be associated with the cellulosic membrane support. In Figure 5.29 the compared patterns of the bare support, the membranes and the PEM-modified membranes are shown. The presence of the polymeric active layer is only decreasing the intensity of the original peaks of the support, in some cases hiding some peaks. Measurement of the samples using different orientations were also performed, with no change in the peak relative intensity, proving the isotropy of the crystalline fibre distribution. The presence of the PEM coating is likewise undetectable. For this reason, no further characterisation using this technique were performed.

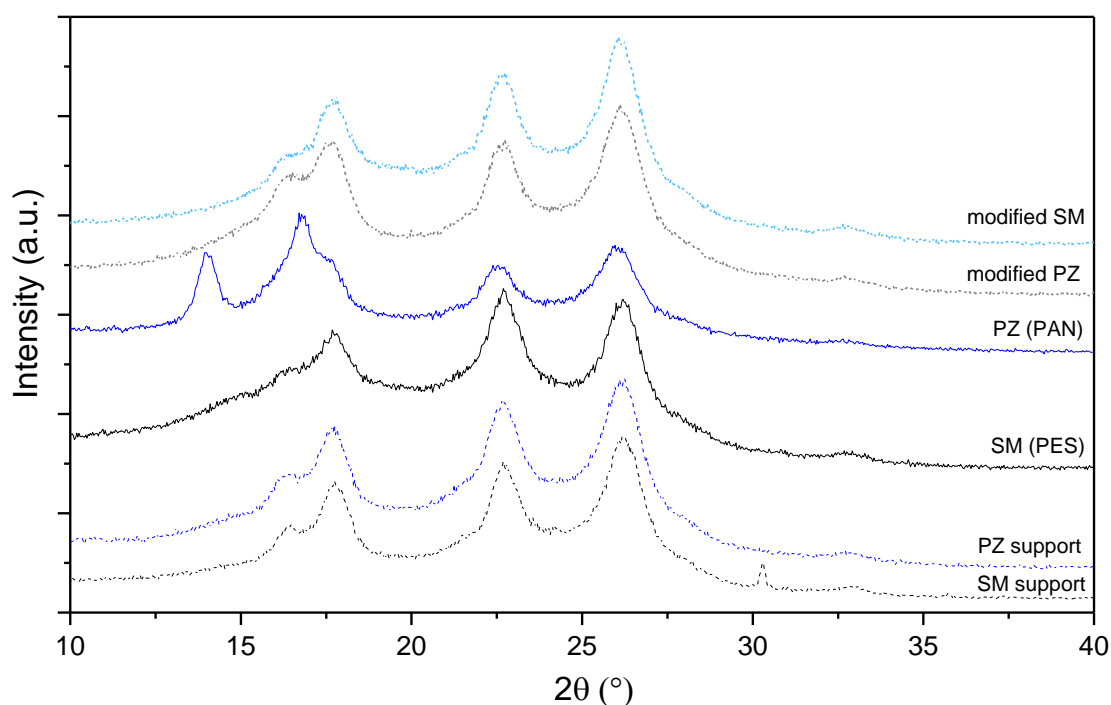


Figure 5.29: Wide angle XRD pattern for different UF membrane compared with their bare support and after modification with PEM coating.

Polyester fabric presents very distinct peaks at 17° , 23° and 26° .^[45] PAN active layer occasionally showed a different pattern (Figure 5.29), probably due to specific orientation of the membrane. PAN is reported to show only a definite peak at *ca.* 17° when the polymer is not undergoing further treatments (e.g. annealing).^[46] The peak at *ca.* 14° , present in the experimental pattern, has been observed in thermal degradation experiments as a consequence of the enhanced crystallisation of the polymer under vacuum.^[47]

5.4.6 Contact angle measurements

The analysis of the surface wettability shown in Figure 5.30 provides an accurate description of the effect of the different layer on the contact angle. In general, polyanion showed higher hydrophilicity whereas polycations presented the opposite trend. In the examples in Figure 5.30, PAH made the surface more hydrophobic in combination with PAA and even with PSS, which shows a strong reversibility effect, as observed from the contact angle trend between the third and fifth bi-layers for system (b). On the other hand, PDDA is not presenting the same effect, with mild reversibility effect. In the system (a) the surface is sharply more hydrophilic, even though the outermost layer is made of PDDA. Statistical

analysis revealed (Figure A.38 in the Appendix) that the oscillations of contact angle values are relevant only after a certain number of layers, where the difference between contact angle of a layer and the previous one are significantly different, as observed in the measurement of water uptake on the same kind of multilayer (Figure A.35 in the Appendix). The most significant differences were observed for the (PDDA-PSS) multilayer.

On the other hand, the effect of the polyelectrolytes on the modification of the wettability changes with the substrate. In Figure 5.31, the wettability of PES and PAN membranes coated with a (PDDA-PSS) multilayer is compared with the effect of the same multilayer on Mylar. The same oscillation between more hydrophilic or more hydrophobic tendencies is observed. The highest differences between the contact angle measured after deposition of the polyanion and the polycation occurred for Mylar, whereas for the two membranes the effect is weaker, at least for the first deposited layers. Statistical analyses were performed on the same multilayer measured on the three different surfaces. The measurements showed significant differences only for the first layers, indicating the importance of the first step of the coating deposition and the effect of the adhesive interactions between the substrate and the first layers on the overall properties of the multilayer structure (Figure A.39 in the Appendix).

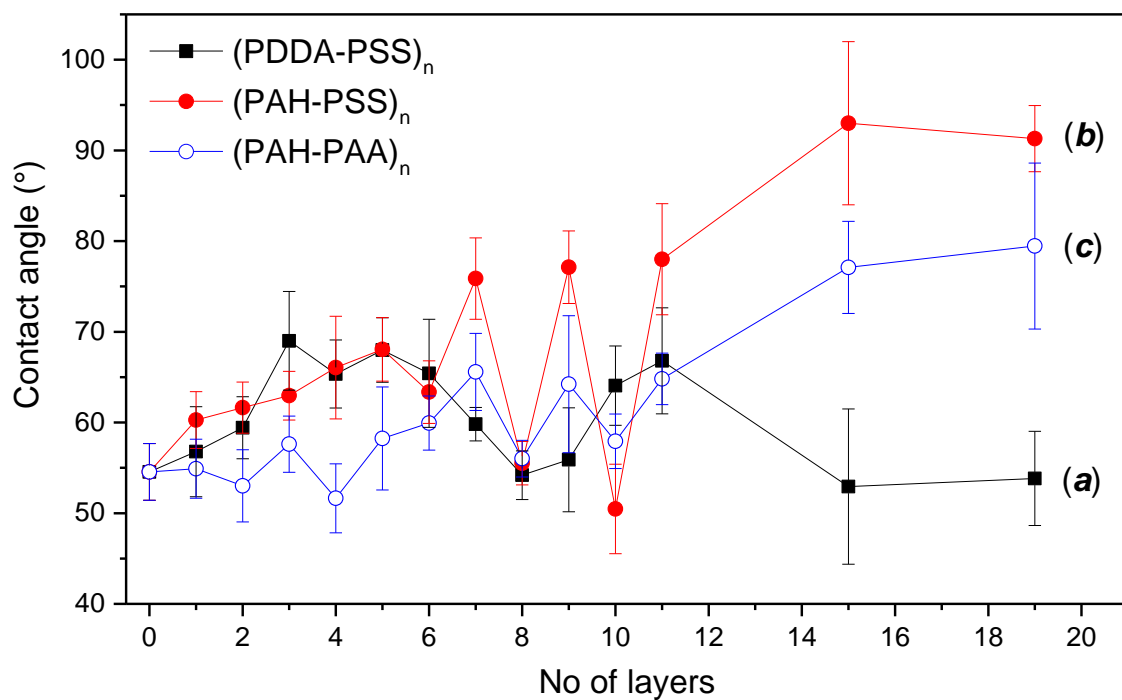


Figure 5.30: Contact angle variation on SM-UF membrane active surface after deposition of different polyelectrolyte multilayer systems: (a) (PDDA-PSS)_n; (b) (PAH-PSS)_n; (c) (PAH-PAA)_n. Statistical analysis is reported in Figure A.38 in the Appendix.

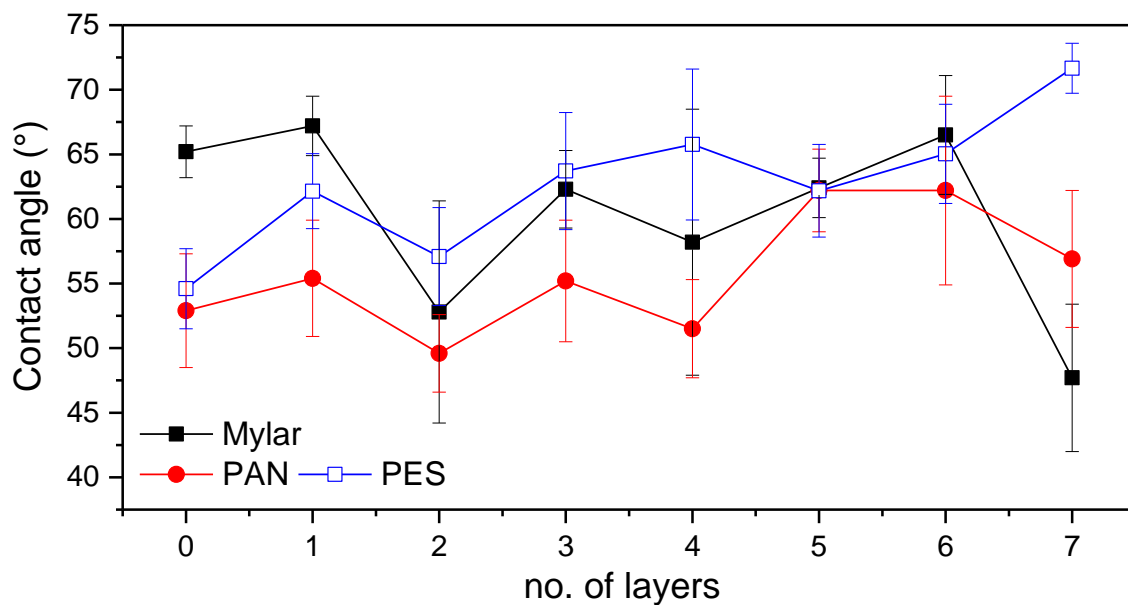


Figure 5.31: Contact angle of (PDDA-PSS)_{3.5} multilayer on different surfaces. Statistical analysis is reported in Figure A.39 in the Appendix.

An example on the effect of the priming layer on the contact angle is offered by the analysis of the (PAH-PAA) and (PAH-PSS) multilayers, modified with an initial PEI layer (

Figure 5.32). The contact angle values without the priming layer are in agreement with the observation reported in Figure 5.30, with marked hydrophobicity of the (PAH-PSS) system. For this multilayer, the PEI priming has no significant effect. On the other hand, the presence of PEI seems to have a pronounced effect of the wettability of the (PAH-PAA) multilayer, with a net increase of the hydrophobicity. Statistical analysis confirmed the significance of the increase of contact angle in these last two measurements.

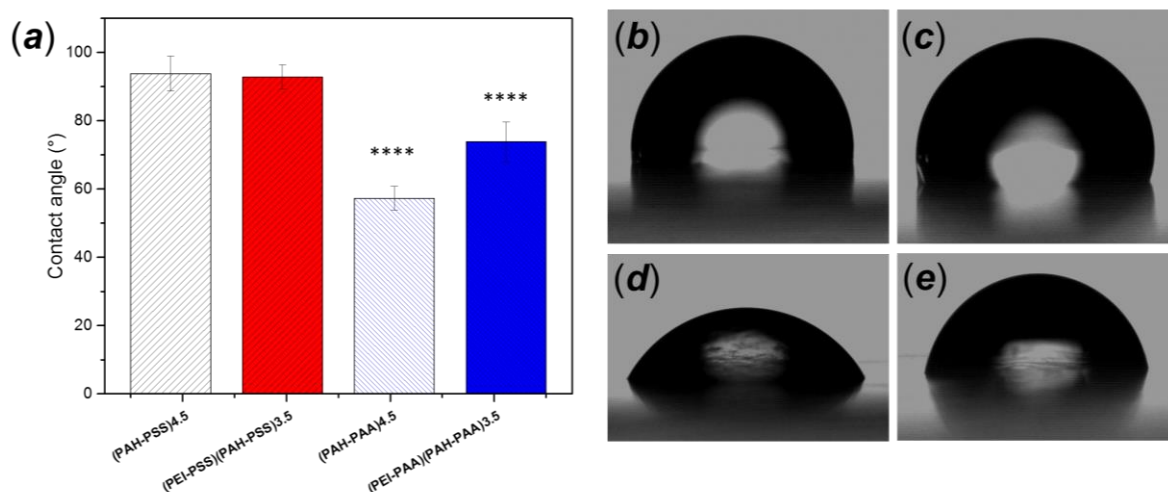


Figure 5.32: (a) effect of the PEI primer layer on the contact angle of different multilayers on SM-UF membranes; sessile drop images of (b) (PAH-PSS)_{4.5}, (c) (PEI-PSS)(PAH-PSS)_{3.5}, (d) (PAH-PAA)_{4.5}, (e) (PEI-PAA)(PAH-PAA)_{3.5} multilayers. Statistical analysis is reported for significant results: * $P \leq 0.05$, ** $P \leq 0.01$, * $P \leq 0.001$, **** $P \leq 0.0001$. P values were calculated using one-way analysis of variance (ANOVA).**

5.4.7 Permeability

5.4.7.2 Pure water permeability of UF membranes

Permeability of the commercial membranes (PES-SM) was tested in dead-end configuration. In most of the experiments, membrane complete compaction occurred in ca. 15-20 minutes. The initial pressure was set at 4 bars in order to accelerate the compaction phase. The SM membranes presented permeability values around 50-70 LMH/bar, in agreement with the supplier technical data (Table 5.3). Figure 5.33 shows a typical example of permeability curve for UF

membrane. If the membrane is not compacted, the permeate flux stabilises in longer time. The permeability of the membrane is assumed as the value of permeate flux after complete stabilisation. The dispersion of the points (collected every 30 s) is due to the accuracy of the recording system. Increasing the interval between the collection of two points would result in a lower dispersion of the measured values.

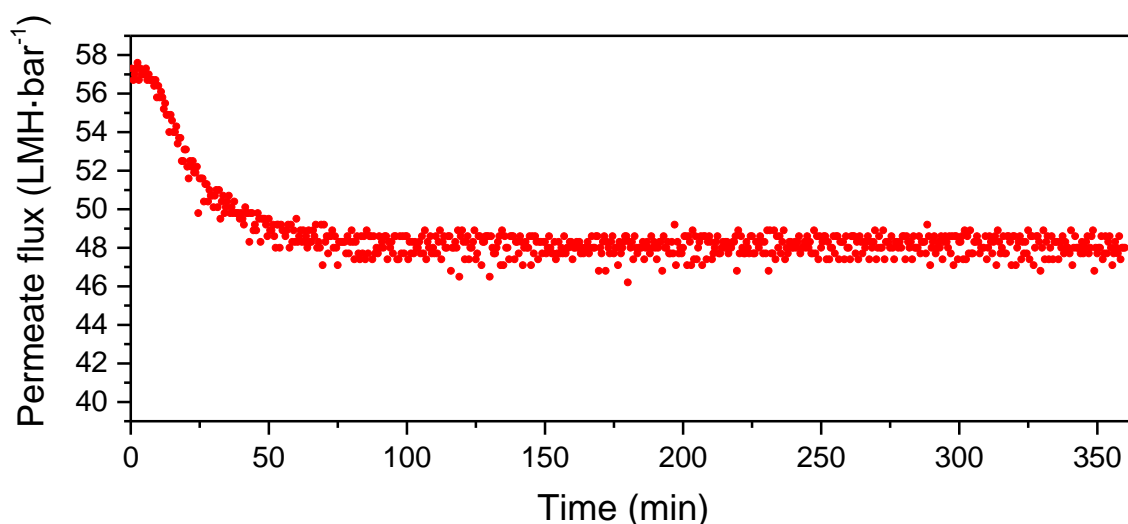


Figure 5.33: Permeability curve for an SM-UF PES membrane. The membrane was not previously compacted.

In some cases, much lower permeability was observed for other membranes. The reduction of permeability occurred for membranes which were extracted from the original package for several weeks, causing the ageing by drying of the polymeric active layer. The active layer becomes tougher, with the pores progressively closing. The dried membrane requires higher pressure to achieve the same permeability provided in the technical specifications by the commercial supplier. Moreover, the sieving properties are also altered, with increase of the selectivity due to the reduction of the pore volume.

The unwanted drying of the membrane can be imputed to an incorrect preservation (storage environment and temperature). The permeability measurements were thus performed almost immediately after the deposition of the multilayer. In case of measurement in the short-term period after the preparation, membranes were stored in a wet Petri dish, with a certain amount of deionised water preventing the drying of the modified active layer. In case of

long term storage, the membranes were soaked overnight in a solution of glycerol and then stored in a 4 °C fridge.

5.4.7.3 (PDDA/PSS)_n multilayer

The combination of PDDA-PSS was considered worth of more detailed investigation, due to the improved hydrophilicity of the multilayer surface, the stronger interaction due to the nature of the polyelectrolyte and the potential antibacterial properties related with the presence of exposed PDDA chains. Multiple membranes were prepared using the same conditions, varying only the number of layers and the deposition time. Membrane permeability was measured almost immediately after the preparation, using the dead-end filtration apparatus. Contact angle and water uptake were also measured on the dried membranes.

Table 5.7: General properties of the PSS/PDDA multilayer (K series) on SM membranes. Statistical analysis for the contact angle measurements is reported in Figure A.40 in the Appendix.

Membrane	n. of layer	Deposition time (min/layer)	Permeability (Lm ⁻² h ⁻¹ bar ⁻¹)	CA (°)
SM	0	0	58.4 ± 2.71	54.4 ± 3.6
SM-K1	2.5	5	28.32 ± 0.74	58.1 ± 6.4
SM-K2	3.5	5	36.74 ± 0.44	58.5 ± 7.0
SM-K3	5.5	5	43.38 ± 0.51	59.3 ± 5.4
SM-K7*	3.5	5	7.72 ± 0.19	49.8 ± 4.7
SM-K8	3.5	10	32.09 ± 0.65	66.3 ± 5.5
SM-K9	3.5	2	54.97 ± 1.65	57.4 ± 5.6

* use of PEI as primer layer, (PEI-PSS)(PDDA-PSS)_{2.5}

As expected, the number of layers and immersion time are strongly affecting the permeability of the membrane. The former parameter has a stronger effect, supposedly due to the increase in thickness of the coating. According to the adsorption kinetic studies on the *in-situ* deposition of polyelectrolyte adsorption by SPR, the deposition time affect both the thickness and stability of the multilayer. If the available time is not sufficient, the polymer chain arrived on the surface are not able to bind through multiple charged sites, being more prone to

desorption as a consequence of the rinsing step, which are aimed to improve the stability to the multilayer removing the loosely bound chains. As for the wettability, only increased deposition time (10 min) or presence of PEI (which is able to change the surface energy of the entire multilayer, as previously described) showed significant differences from the statistical point of view, as observed from the statistical analysis of the data (Figure A.40 in the Appendix). In Figure 5.34 is also compared the permeability of SM-UF membranes produced in the “K series”, coated both protecting the membrane textile support from the exposure to the polyelectrolyte solution and not. The two membranes showed the same permeability, which could mean that the multilayer adsorb on both side of the membranes regardless of the presence of the protection. This indicated that the protection strategy is not effective.

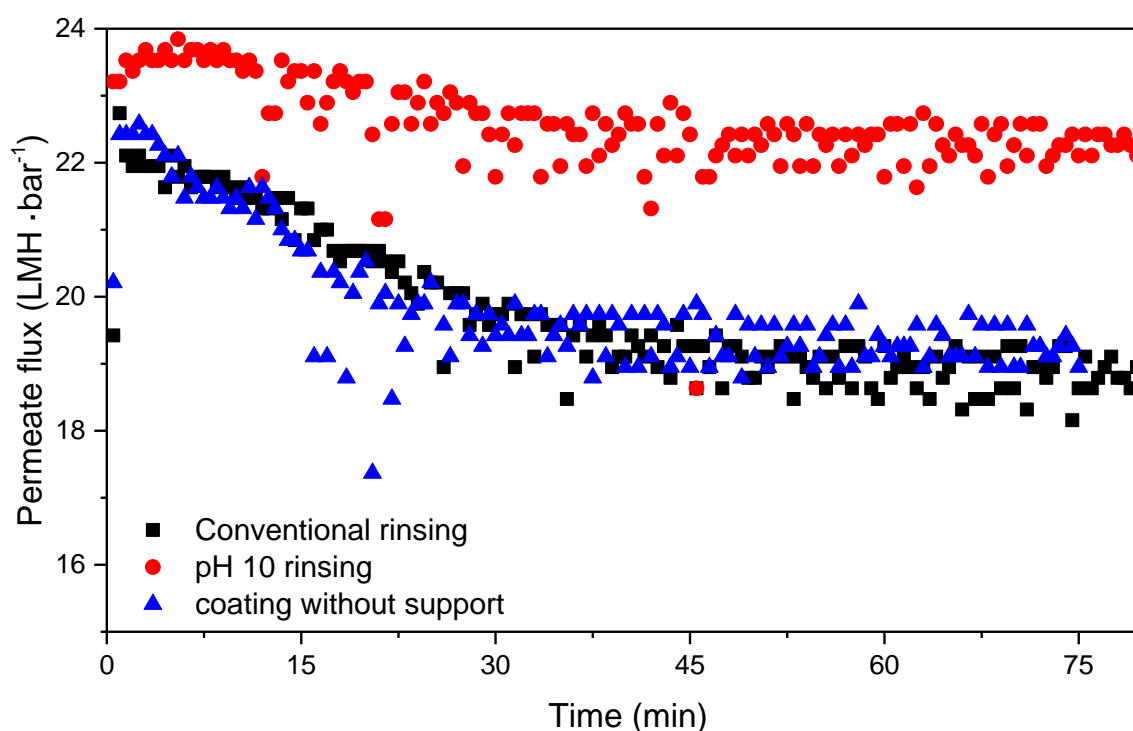


Figure 5.34: Effect of different rinsing conditions or presence of support on PEM-modified SM-UF membrane ((PDDA-PSS)_{2.5}, 2 min deposition).

5.4.7.4 Effect of the ionic strength and rinsing solution

The ionic strength is generally affecting the multilayer coating thickness. The permeability of the membrane decreases with the increase of electrolyte concentration, as it can be observed comparing membranes B1-B2 and B7-B8 in Table 5.8.

As observed in the SPR study, the structure of the multilayer changes with the conditions of the surrounding environment. Adapting the rinsing solution to the same pH or ionic strength used during deposition, the effect of the ionic strength on the permeability is different. The permeate flux is decreased, as expected by the thicker layers originated by the modified rinsing solution.

Table 5.8: SM-B membrane series, (PDDA-PSS)_n multilayer on SM-UF membranes, varying the ionic strength of the polyelectrolyte solution and the rinsing method. Statistical analyses for contact angle (CA) and water uptake measurements are reported in Figure A.41 a and b in the Appendix, respectively.

Membrane	n. of layer	Ionic strength (mM)	Permeability (L m ⁻² h ⁻¹ bar ⁻¹)	CA (°)	Water uptake (%)
SM	0	0	58.4 ± 2.71	54.4 ± 3.6	35.95 ± 1.9
SM-B1	3.5	150	10.21 ± 0.46	51.2 ± 4.6	30.5 ± 0.6
SM-B2	3.5	500	8.65 ± 0.31	58.0 ± 4.6	33.9 ± 0.6
SM-B3	3.5	150	1.35 ± 1.29	63.9 ± 2.7	34.9 ± 0.3
SM-B4	3.5	500	2.94 ± 0.14	62.7 ± 9.1	34.1 ± 0.9
SM-B5	3.5	150	6.71 ± 0.27	76.5 ± 2.7	31.0 ± 0.9
SM-B6	3.5	500	6.62 ± 0.35	61.7 ± 2.5	32.9 ± 0.9
SM-B7	3	150	12.13 ± 0.31	58.2 ± 2.5	31.0 ± 0.9
SM-B8	3	500	4.31 ± 0.10	78.1 ± 6.4	33.8 ± 0.7

B1-B2: washed with water

B3-B4: washed with DI water at pH 10

B5-B6: washed with DI water with the same Is of the PE solution

B7-B8: washed with water, starting with PSS

Membranes coated using higher ionic strength polyelectrolyte solutions presents higher values of water uptake, as expected by the higher hydration of the multilayer structure when built in presence of high concentrations of electrolytes. This effect was not observed only in the membrane B4 and B5, for which the rinsing solution had the same pH of the polyelectrolyte solutions.

The effect of the ionic strength can be also observed analysing the water affinity of the surface via contact angle measurement. As observed by the SPR analysis (Figure 5.5), the effect of the presence of the electrolyte causes a dramatic enhancement on the thickness of the polyelectrolyte on the surface. The statistical dispersion of the measurement is also remarkable, denoting irregularity of the surface. The water uptake results did not show any relevant difference compared to the original unmodified membrane, with substantially minor effects due to the deposition conditions. Statistical analysis of the results was performed

on the contact angle and water uptake measurements. Apart from the multilayer washed with water (B1 and B2), the use of different ionic strengths led to significant differences between the multilayers (Figure A.41 a in the Appendix). Similar results were observed for the water uptake measurements (Figure A.41 b in the Appendix), in which case only the multilayers prepared with DI water at the same pH of the polyelectrolyte solutions (pH 10) showed no statistically significant difference.

5.4.7.5 Effect of the priming layer

The use of an initial priming layer is detrimental for the permeability of the modified membrane, as shown in Figure 5.35. A single PEI-layer reduced the permeability of almost 50% compared with the membrane coated using the PDDA-PSS multilayer system. Increasing the concentration of PEI solution, the reduction of permeability can be even higher, up to 70-80% of the permeability of a membrane modified without PEI.

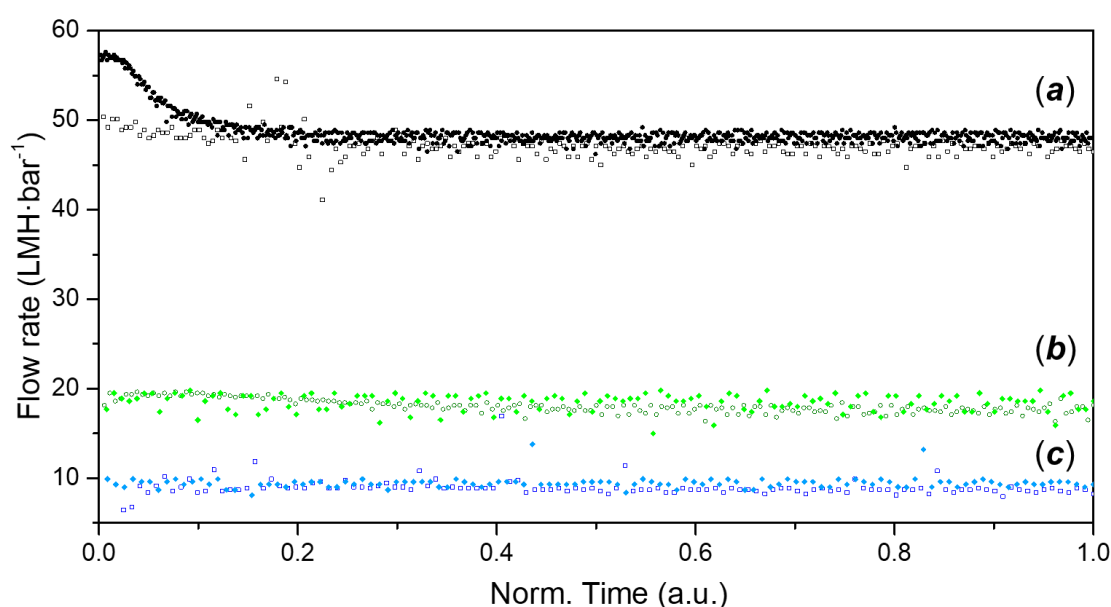


Figure 5.35: Permeation curve for the PES UF-membranes modified with PEM-coating under the same deposition conditions (2 min immersion, 5.5 bilayers): (a) unmodified PES; (b) (PDDA-PSS)_{5.5} modified PES; (c) (PEI-PSS)(PDDA-PSS)_{4.5} modified PES.

5.5 TiO₂-PEM composite membranes

According to the examples provided in literature and the results of the SPR *in situ* analysis, the optimal way to integrate TiO₂ into the PEM structure consists of intercalating the particles between polyelectrolyte layers. In Table 5.9, the characteristics of a series of membrane produced integrating TiO₂ nanoparticles by alternate immersion with polyelectrolyte solutions are reported. Membranes C2 and C3 differ from the following ones by the immersion time in the TiO₂ suspension, 5 min for the former and 10 min for the latter. The TiO₂ suspensions were adjusted at pH 9.75 by means of NaOH solution. The presence of a TiO₂ layer reduced the membrane permeability in all cases. The membranes exposed to the nanoparticle suspension for longer time presented higher permeability compared with the ones exposed for only 5 min. The contact angle of these membrane was not particularly affected by the presence of TiO₂, showing the same wettability as the reference modified membrane, in which the outermost layer of PDDA governs the surface behaviour. As for the water uptake measurements, it was not possible to correlate the results with the multilayer preparation conditions, as confirmed by the low significant differences between the measurements on different membranes, as observed by statistical analysis (Figure A.42 in the Appendix).

Table 5.9: Relevant properties of PES UF membranes (SM type) coated with a composite (PDDA/PSS) multilayer with integration of TiO₂ (Aeroxide P25, 1 g/L). PDDA composed the outermost layer in all membranes. Statistical analysis for water uptake measurements are reported in Figure A.42 in the Appendix.

Membrane	no. of layer	Immersion time (min/ly)	[TiO ₂] (mg/L)	Permeability (Lm ⁻² h ⁻¹ bar ⁻¹)	Water uptake (%)
SM	0	0	0	58.4 ± 2.71	35.95 ± 1.9
SM-C1	3.5	5	0	30.60 ± 0.45	32.7 ± 1.9
SM-C2	3.5	5	150	15.52 ± 0.33	32.3 ± 1.1
SM-C3	3.5	5	250	12.41 ± 0.16	36.3 ± 1.5
SM-C4	3.5	10*	150	22.68 ± 0.45	33.0 ± 1.1
SM-C5	3.5	10*	250	13.52 ± 0.37	37.2 ± 1.4

* only for TiO₂ layers, 5 min/ly for the polyelectrolyte layers

In another series of experiment, 2 bi-layers containing TiO₂ were deposited and protected by a further polyelectrolyte bi-layer, always letting PDDA as exposed layer. This structure (PDDA/PSS)₂(PDDA/TiO₂)₂(PDDA/PSS)_{1.5} was prepared by using different ionic strength for the polyelectrolyte solutions. Figure 5.37 **a** shows the effect of the presence of TiO₂ in these multilayers. The combination of TiO₂ and polyelectrolyte deposited under high ionic strength conditions reduces the uptake, likely due to the increased thickness of the coating. However, the results showed limited significance from the statistical point of view, as determined by the statistical analysis. Concerning the contact angle of the coated active layer (Figure 5.37 **b**), the presence of TiO₂ counteracts the increased hydrophobic behaviour conferred by the PEM, even though the hydrophilic behaviour of the coating decreases with the increase of the ionic strength (thus of the multilayer thickness). A thicker polymeric layer might shield the TiO₂ nanoparticles, reducing the affinity for water. Unlike what occurred for water uptake measurement, statistical analysis confirmed the presence of significant differences between the samples. In particular, the analysis evidenced significant differences between the multilayers produced using TiO₂ particles.

Some preliminary morphological analyses were performed via SEM imaging. The membranes of the series C did show only few aggregates of TiO₂ particles, even at higher concentration. Other membranes were prepared using more concentrated suspension. The SEM images of composite coating prepared with 250 mg/L, 500 mg/L and 1 g/L suspension are shown in Figure 5.36. The new membranes confirmed that 250 mg/L is not sufficient to provide a uniform coating. However, despite the increase of the number of particles on the surface, the coating does not appear uniform, with localised agglomeration of TiO₂.

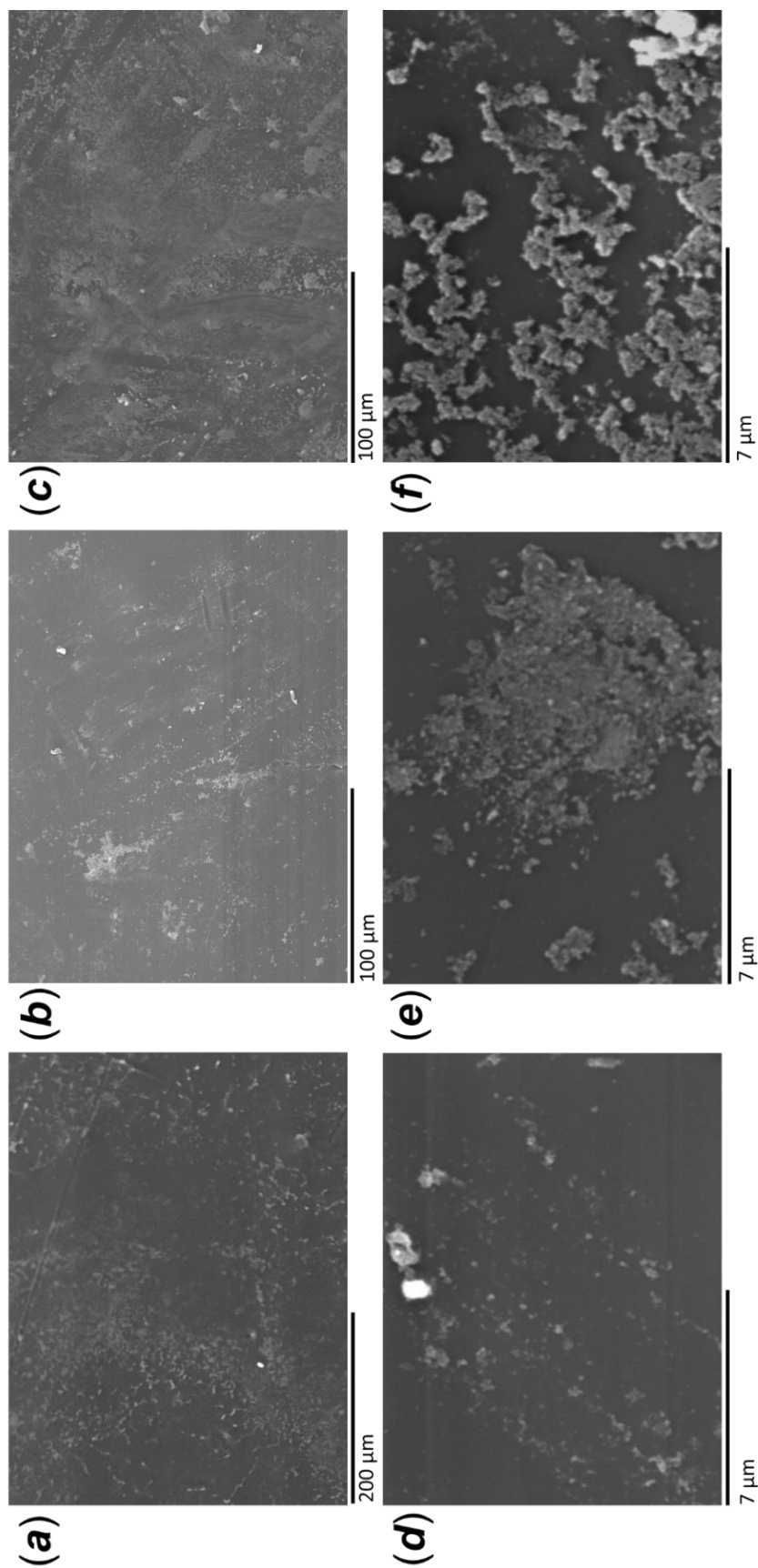


Figure 5.36: SEM images of TiO₂-PEM composite multilayer on SM membranes, prepared by immersion coating deposition. The composite multilayer consists of (PDDA-PSS)(PDDA-TiO₂)_{3.5}, prepared using different concentration of TiO₂ in suspension: (a) and (d) were prepared using a 250 mg/L suspension, (b) and (e) 500 mg/L and (c) and (f) 1 g/L.

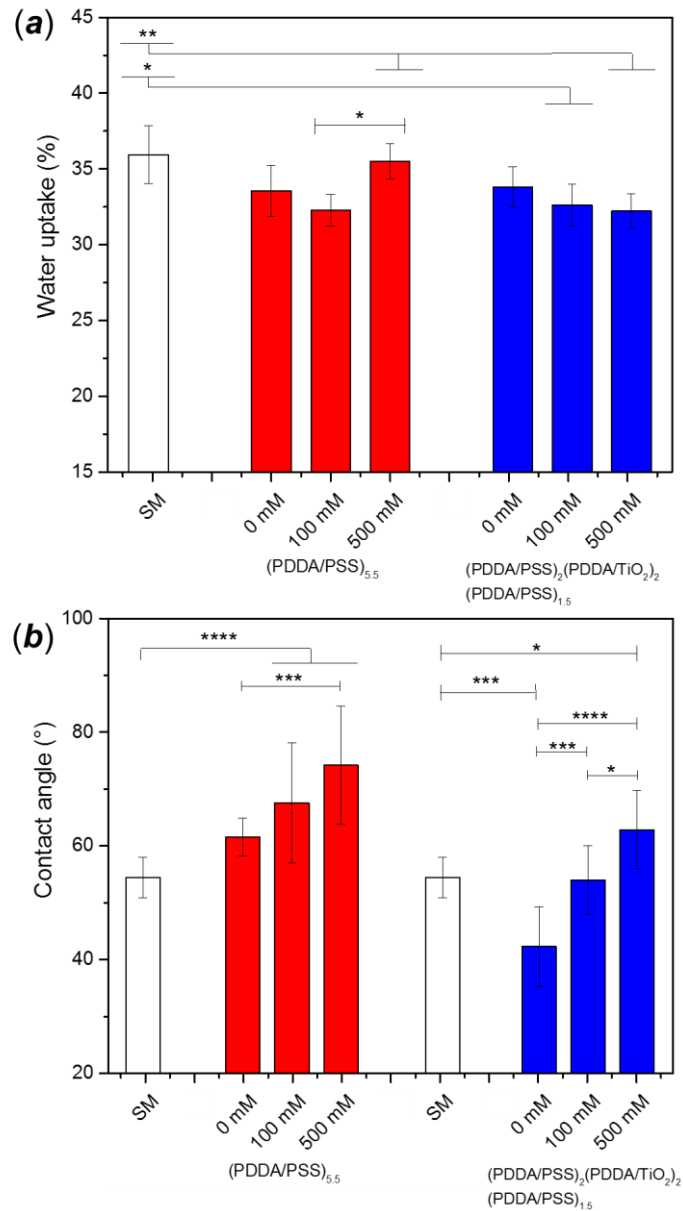


Figure 5.37: Effect of the insertion of TiO₂ nanoparticles in (PDDA-PSS) multilayer deposited on SM-UF membranes on (a) water uptake and (b) contact angle measurement. Statistical analyses. Statistical analysis is reported for significant results: * P ≤ 0.05, ** P ≤ 0.01, *** P ≤ 0.001, **** P ≤ 0.0001. P values were calculated using one-way analysis of variance (ANOVA).

As shown in Figure 5.38, the increase of the concentration of TiO_2 led to the reduction of the contact angle, due to the higher amount of inorganic particles on the surface. However, the increase of the concentration led also to a higher dispersion of the contact angle values (Figure 5.38 *b* observed most of all for the sample produced with a suspension of 500 mg/L TiO_2), as a further confirmation of the poor homogeneity and uniformity of the coating. The statistical analysis confirmed the statistically significant differences of the contact angle data.

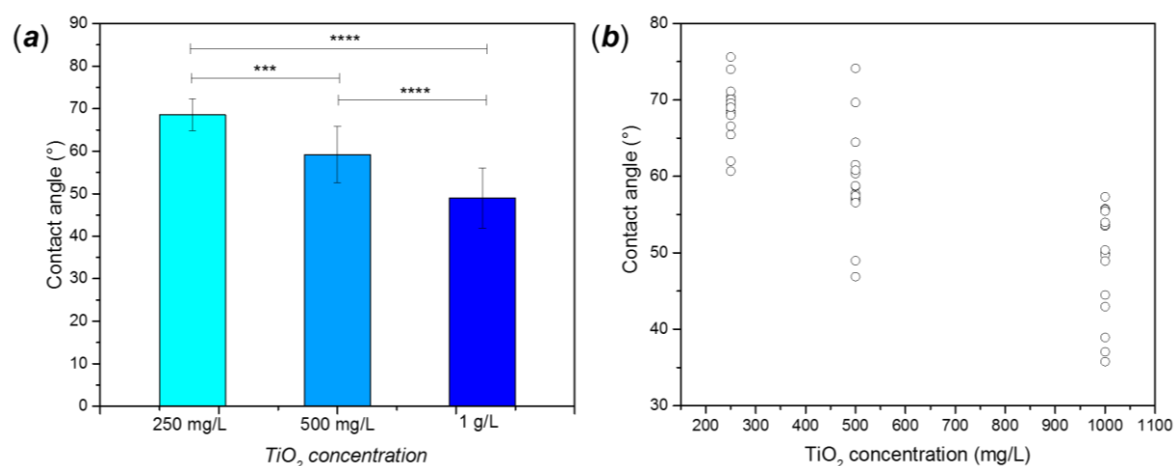


Figure 5.38: (a) contact angle of the TiO_2 -PEM composite multilayer ((PDDA-PSS)(PDDA- TiO_2)_{3.5}) on SM membranes with different concentration of TiO_2 and (b) dispersion of the contact angle values. Statistical analysis is reported for significant results: * $P \leq 0.05$, ** $P \leq 0.01$, *** $P \leq 0.001$, **** $P \leq 0.0001$. P values were calculated using one-way analysis of variance (ANOVA).

Another parameter influencing the contact angle is the time of immersion in the TiO_2 layer. This effect is related to the composition of the multilayer, being more effective if the polyelectrolyte established stronger interactions with the TiO_2 particles. The effect is shown in Figure 5.39 for a (PAH-PSS) multilayer, for which the different immersion time caused a drastic reduction of the contact angle. However, these data are not statistically relevant, as confirmed by the statistical analysis. However, the images in Figure 5.39 *b*, *c* and *d* are representative of localised change of the surface wettability, which reproducibility over the entire surface is affected by the inhomogeneity of the coating.

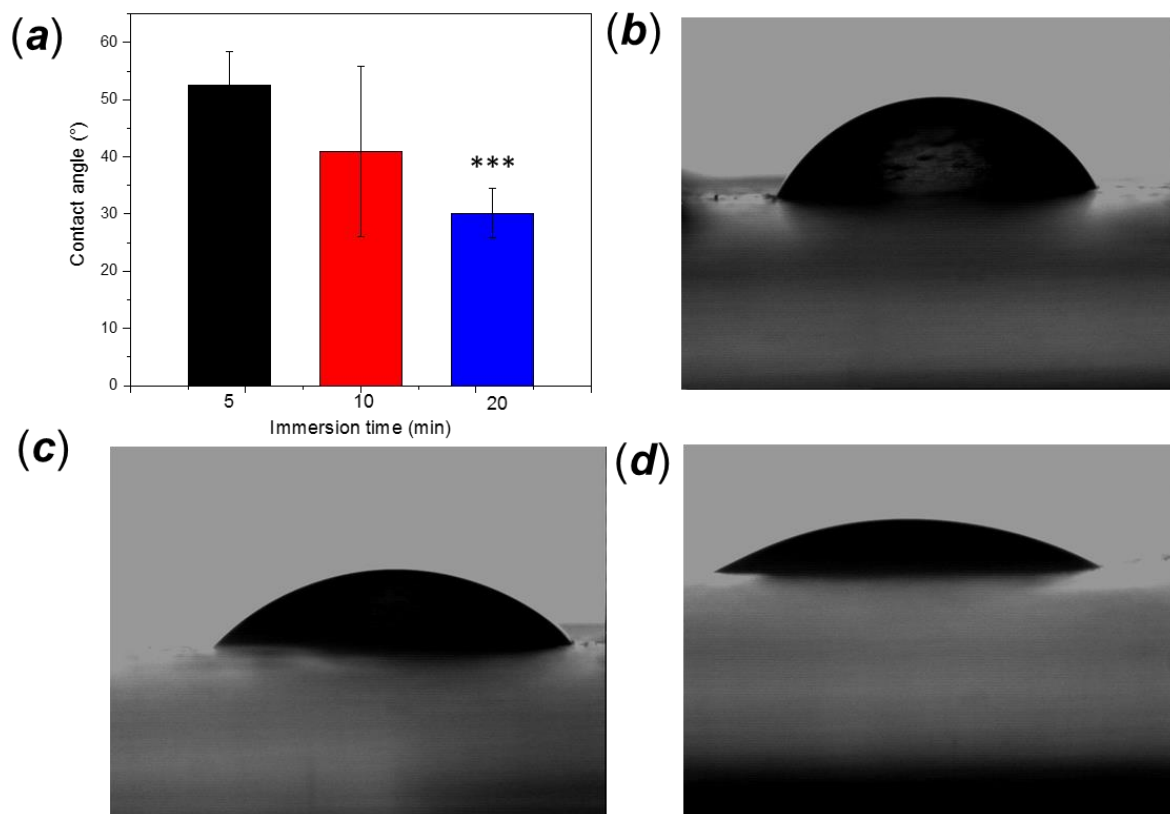


Figure 5.39: (a) contact angle values of $(\text{PAH-PSS})_2(\text{PAH-TiO}_2)_{3.5}$ multilayer with the surface immersed in TiO_2 suspension for 5, 10 and 20 min as shown in (b), (c) and (d) respectively, with increase of the hydrophilic behaviour. The contact angle values were compared in pair (with the 5 min immersion sample when not indicated). Statistical analysis is reported for significant results: * $P \leq 0.05$, ** $P \leq 0.01$, *** $P \leq 0.001$, **** $P \leq 0.0001$. P values were calculated using one-way analysis of variance (ANOVA).

Cross-contamination between the polyelectrolyte solutions and TiO_2 suspensions was often observed, with the TiO_2 particles previously deposited on the membrane previously immersed in the latter suspension, are released in the former solutions. Contamination can be perhaps attributed to the poor adhesion of TiO_2 particles on the multilayer surface. Eventually, the inorganic particles might preferentially desorb in the solution due to stronger interactions with the oppositely charged polyelectrolyte chains free in the solution. Cross-contamination can be observed by increase of the turbidity of the polyelectrolyte solution and/or acceleration of flocculation phenomena in the TiO_2 suspension, enhanced by the presence of the polyelectrolytes (with the same destabilisation phenomenon described in section 5.3.3).

5.6 Improvement of PEM deposition conditions

Dip or immersion coating of surfaces (membranes in particular) for the preparation of PEM coatings presented several inconveniences, among which contamination can be listed as one of the principal. The polyelectrolyte solutions were indeed cross-contaminated by the oppositely charged polyelectrolyte, external sources of contamination (e.g. dust) or in some cases from the membrane itself. The solutions are soon contaminated, requiring preparation of fresh batches or, in the less critical case, the pH needs to be constantly adjusted to the optimal values. Furthermore, deposition on membranes without using a support resulted in clouding the polyelectrolyte solutions, probably due to loosen polyelectrolyte chains with weak adhesion to the membrane textile support. This confirmed the necessity of protecting the textile support from the exposure to the polyelectrolyte solutions.

Moreover, the deposition process is not efficient, as witnessed by the same permeability of membranes coated using the Mylar support and not. The deposition is probably occurring on both sides in either case, due to the inefficacy of any prevention measures adopted to isolate the support side of the membrane. In order to reduce the risk of cross-contamination, an alternative method of deposition was conceived. A definite aliquot of polyelectrolyte solution was used for each step and not recycled. The surface was fixed to a polystyrene disposable vessel (Petri dishes or similar) and the solution poured into the container. The box was hence placed on an orbital shaker for the amount of time equivalent to that of immersion. The procedure facilitates also the washing and rinsing step, without removing the surface from its container. The apparently higher consumption of solution (which is not recycled for further deposition) corresponds approximately to the lifetime of a batch necessary for the deposition on a surface with equivalent area. Permeability and the contact angle of the membrane produced with the improved method are reported in Table 5.10. Compared to the membrane produced by immersion coating (Figure 5.11), the PEM coatings appear thicker, with less layers and deposition time dramatically decreasing the membrane permeability. Despite the statistical analysis showed some significant differences between the different samples (Figure A.43 in the Appendix), it was difficult to associate the contact angle values to the deposition conditions, for example the

total absence of a significant trend changing the immersion time in the (PDDA-PSS)_{5.5} multilayer.

Table 5.10: Characteristics of selected PEM-coated membrane produced using the improved deposition method. Statistical analysis is reported in Figure A.43 in the Appendix.

Multilayer	No of layers	Immersion time (min)	Permeability (LMH · bar ⁻¹)	Contact angle (°)
(PDDA-PSS)	2.5	1	29.67 ± 0.36	57.1 ± 4.5
	2.5	2	26.97 ± 0.36	44.7 ± 4.7
	5.5	1	18.79 ± 0.25	46.0 ± 6.3
	5.5	2	21.69 ± 0.26	42.7 ± 4.0
	5.5	5	15.39 ± 0.44	46.4 ± 4.5
(PAH-PSS)	5.5	5	9.02 ± 0.31	40.41 ± 4.3

5.6.1 TiO₂-PEM composite coating

From the microscopic analysis, the coating appeared more uniform compared to that produced by simple immersion. In Figure 5.41 four examples of composite coating with TiO₂ are reported in comparison with analogous conditions using the simple immersion coating. On Mylar foils, TiO₂ particles form a thick layer on the surface, as displayed in the SEM images in Figure 5.40. However, despite the resistance in water, also these composite coating presented poor mechanical stability, since a minimum friction can cause visible removal of the TiO₂ layer on the surface.

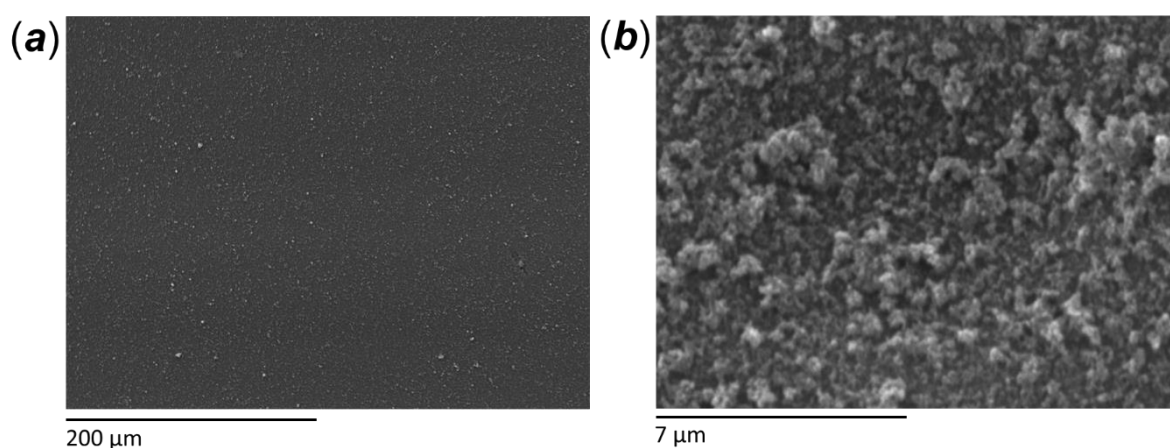


Figure 5.40: SEM images of TiO₂-PEM composite coating on Mylar foil; (a) low magnification (1000X) and (b) higher magnification (5000X) image.

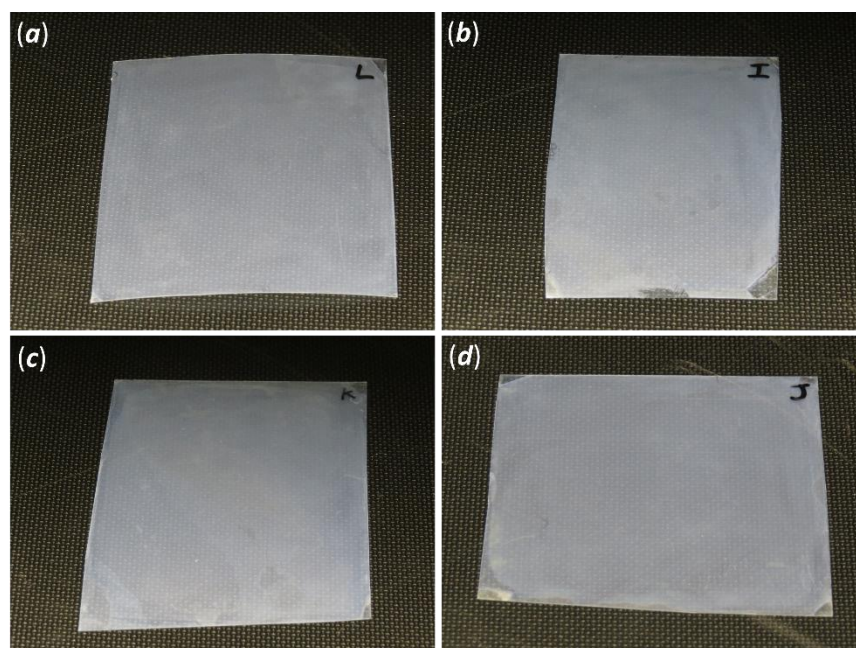


Figure 5.41: Pictures of Mylar samples coated with nanocomposite TiO_2 -PEMs $((\text{PDDA-PSS})_2(\text{PDDA-TiO}_2)_{3.5})$ under different conditions; (a) 5 min immersion for the polyelectrolytes, 10 min for TiO_2 ; (b) 10 min immersion for all layers; (c) 5 min immersion for the polyelectrolytes, 20 min for TiO_2 ; (d) 5 min immersion, application of a protective (PDDA-PSS) layer at the end of the deposition process.

Even though Mylar is an optimal substrate to test the adhesion of the composite coating on surfaces other than polymeric membranes, it offered a limited range of characterisation technique. Different deposition conditions and combinations were tested, with no relevant differences from the point of view of the morphology, examined *via* SEM analysis.

However, contact angle measurement revealed very different surface wettability depending on the combinations or conditions adopted. The characteristics of selected samples are reported in Table 5.11, with the contact angle plotted in Figure 5.42. In this case, the ionic strength of the polyelectrolyte solutions affects the most the surface wettability, with achievement of superhydrophilic conditions (contact angle below 15°). For the multilayer produced with the highest value of ionic strength (condition *H*, 500 mM of NaCl), the estimation of the contact angle was made difficult by the extremely fast spreading of water on the surface. An approximate value (less than 5°) was hence attributed to this surface.

Moreover, the multilayer composed only by PEI and TiO_2 showed a very hydrophilic behaviour as well. High ionic strength polyelectrolyte solution and strong interactions provided by PEI are probably the key for the stable adhesion of TiO_2 particles in the multilayer structure.

The conditions for the assembly of the multilayer reported in Table 5.11 are efficiently changing the multilayer properties. The statistical analysis confirmed the presence of significant differences between some of the conditions, such as the immersion time in the TiO₂ particle suspension (conditions *A*, *C* and *E*), leading to very different values of contact angle, which confirms the results previously reported in Figure 5.37.

Table 5.11: List of the sample of Mylar foil coated with the TiO₂- composite multilayer by using the improved deposition method. (Sample *H* arbitrary attributed because of the difficulty in estimation of a precise value below 5° of contact angle).

	Sample	Contact angle (°)
	(PDDA-PSS) ₂ (PDDA-TiO ₂) _{3.5}	
A	TiO ₂ conc. 1 g/L, 10 min/ly	73.9 ± 3.4
B	(PDDA-(TiO ₂ +PSS))	61.12 ± 3.5
C	TiO ₂ conc. 1 g/L, 20 min/ly	54.1 ± 5.2
D	TiO ₂ conc. 500 mg/L, 5 min/ly	52.73 ± 6.8
E	TiO ₂ conc. 1 g/L, 5 min/ly	36.15 ± 2.79
F	(PEI-TiO ₂) _{5.5}	15.5 ± 2.9
G	A, I _s = 100 mM	11.4 ± 3.8
H	A, I _s = 500 mM	< 5

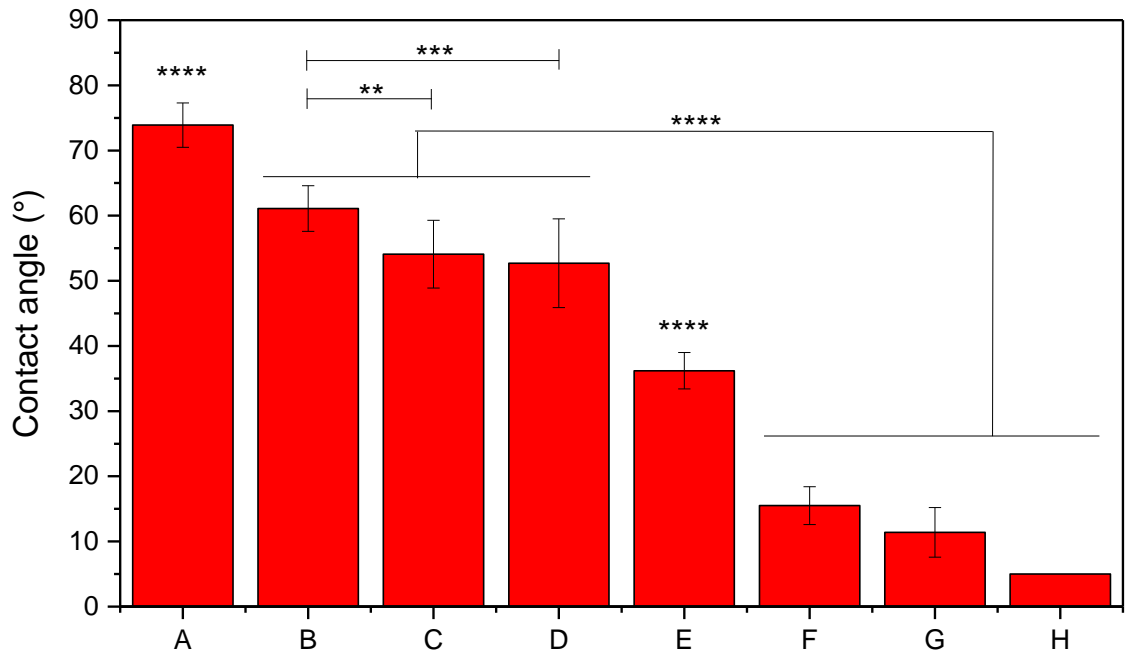


Figure 5.42: Contact angle for different sample of TiO₂-composite PEM coating on Mylar foils. The characteristics and the preparation conditions of the coating are listed in Table 5.11. (Sample H arbitrary attributed because of the difficulty in estimation of a precise value below 5° of contact angle). Statistical analysis is reported for significant results: * P ≤ 0.05, ** P ≤ 0.01, *** P ≤ 0.001, **** P ≤ 0.0001. P values were calculated using one-way analysis of variance (ANOVA).

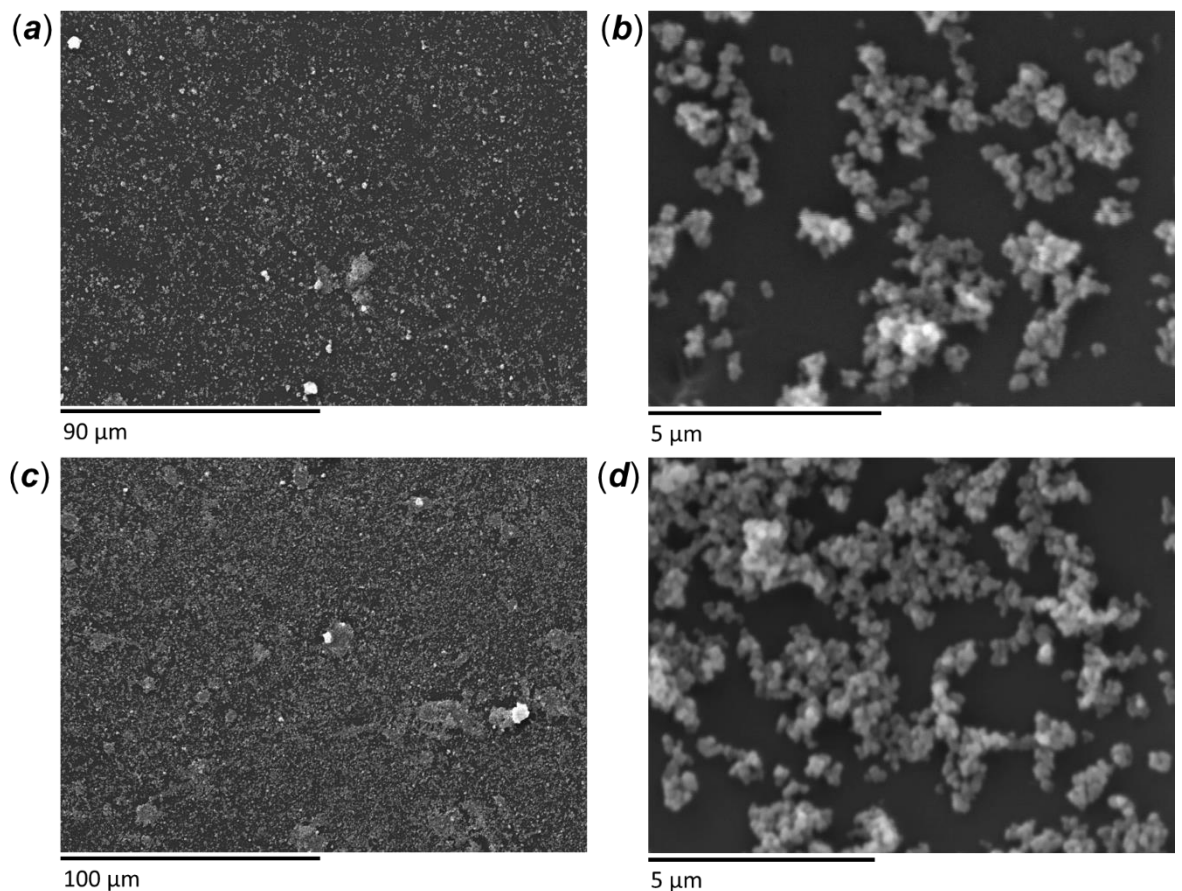


Figure 5.43: SEM images of SM membrane coated with a TiO₂-PEM composite multilayer by using the improved deposition method.

The same composite coatings were applied on the SM membranes, partly replicating the conditions observed for the C series. The morphological analysis of the coating revealed higher homogeneity of the distribution of TiO_2 particle onto the membrane surface, as shown in Figure 5.43. Also in this case, the deposition time of TiO_2 influences the amount of particles present onto the membrane surface. The resulting permeability and contact angle values for these membranes are listed on Table 5.12. In Figure 5.44 the permeability curves of the membranes modified using this improved method are reported. Also in this case, the insertion of a layer of TiO_2 replacing the anion slightly increased the membrane permeability in both systems. Among the contact angle measurements for this series of membranes, only two conditions (the multilayer produced using only branched PEI and TiO_2 particles and the coating with TiO_2 directly exposed in a (PDDA-PSS) multilayer) showed significant difference from the statistical point of view, as reported in Figure A.44 in the Appendix. It is hence difficult to reproduce the superhydrophilic behaviour obtained on Mylar using polymeric membrane, confirming the strong influence of the coating substrate on the final properties of the PEM.

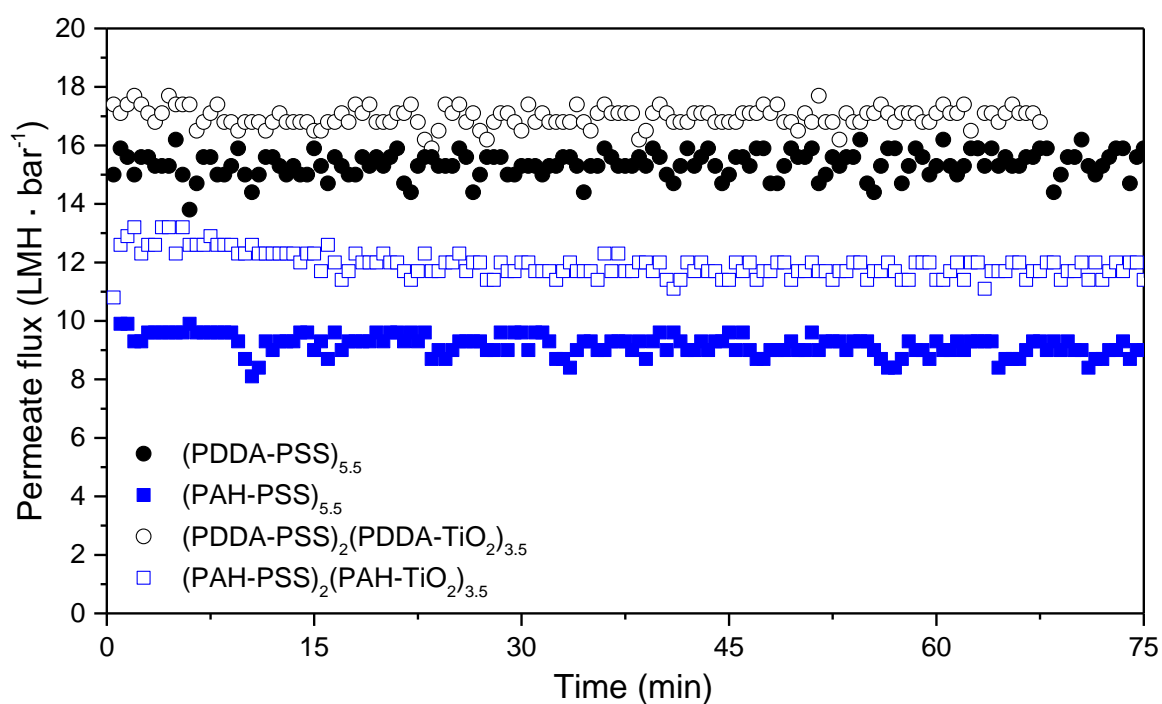


Figure 5.44: Permeability curves of SM-UF membranes coated with two different system of multilayers using the “oscillating box” method. The curves are compared with similar system with the presence of an alternate layer of TiO_2 replacing the polyanion in the multilayer coating.

Table 5.12: List of the membrane coated with TiO₂-composite PEMs and their properties. Statistical analysis for the contact angle measurements is reported in Figure A.44 in the Appendix.

	Immersion time (min)	Permeability (LMH · bar ⁻¹)	Contact angle (°)
(PDDA-PSS) ₂ (PDDA-TiO ₂) ₂ (PDDA-PSS) _{1.5} (TiO ₂ 1 g/L)	5	17.10 ± 0.46	53.5 ± 2.8
(PDDA-PSS) ₂ (PDDA-TiO ₂) _{3.5} (TiO ₂ 1 g/L)	5	16.92 ± 0.32	46.4 ± 4.5
(PDDA-PSS) ₂ (PDDA-TiO ₂) _{3.5} (TiO ₂ 500 mg/L)	5	16.25 ± 0.56	51.2 ± 5.7
(PEI-TiO ₂) _{5.5} (TiO ₂ 1 g/L)	5	11.97 ± 0.27	33.3 ± 6.7
(PDDA-PSS) ₂ (PDDA-TiO ₂) _{3.5} (Is 100 mM)	5	12.83 ± 0.26	49.3 ± 7.9
(PAH-PSS) ₂ (PAH-TiO ₂) _{3.5} (TiO ₂ 1 g/L)	5	11.80 ± 0.29	53.4 ± 3.0

5.7 Fouling test and coating resistance

5.7.1 Preliminary fouling test

In Figure 5.45 is shown a typical fouling test using alginate solution in dead-end configuration. The cell has a maximum volume of 300 mL. In the presence of alginate, the permeate flux declines asymptotically until the concentration polarisation occurs, reducing further the membrane permeability. For a correct analysis of the effect of the fouling on the membrane it is necessary to separate the two events. From Figure 5.45 *a*, the concentration polarisation affects relevantly the permeation regime when only 20% of the original volume is left in the filtration cell. In Figure 5.45 *b* the effect of a second cycle of fouling without backflush or membrane cleaning is reported, with the concentration polarisation occurring at the same remaining volume but after longer time compared with the first cycle, since the membrane is already partially fouled.

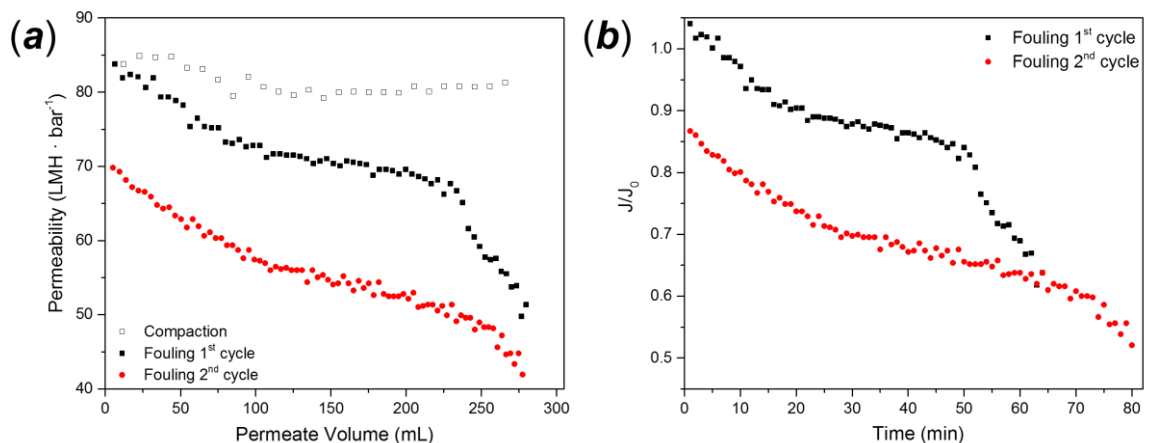


Figure 5.45: Fouling test using alginate solution (20 mg/L, 20 mM NaCl, pH 7.5) on PES UF membrane (SM-01) using the dead-end filtration cell.

5.7.2 Alginate fouling

Fouling tests were performed on previously compacted membranes. Filtration of the alginate solution was performed under a constant pressure of 1 bar (0.1 MPa), controlled by a digital pressure transmitter (Omega). The typical experimental procedure is shown in Figure 5.46. The membrane is first equilibrated, filtrating a solution with the same ionic strength of the foulant solution (in this case, 20 mM NaCl solution was used). Once the flux is stable, the foulant solution is inserted.

The permeate flux of the membrane dramatically decrease. Eventually, the flux stabilises at a constant value. In our experiment, the flux did not achieve stabilisation. After fouling, the membrane is removed from the filtration cell and cleaned. The membrane was rinsed with water, removing the gelatinous film of alginate from the active layer, and left soaked in deionised water for at least 30 min. After another rinsing step, the membrane was allocated in the cell and a final pure water filtration was performed. The permeate flux value allow the calculation of the flux recovery of the membrane and to establish the relative amount of reversible and irreversible fouling.

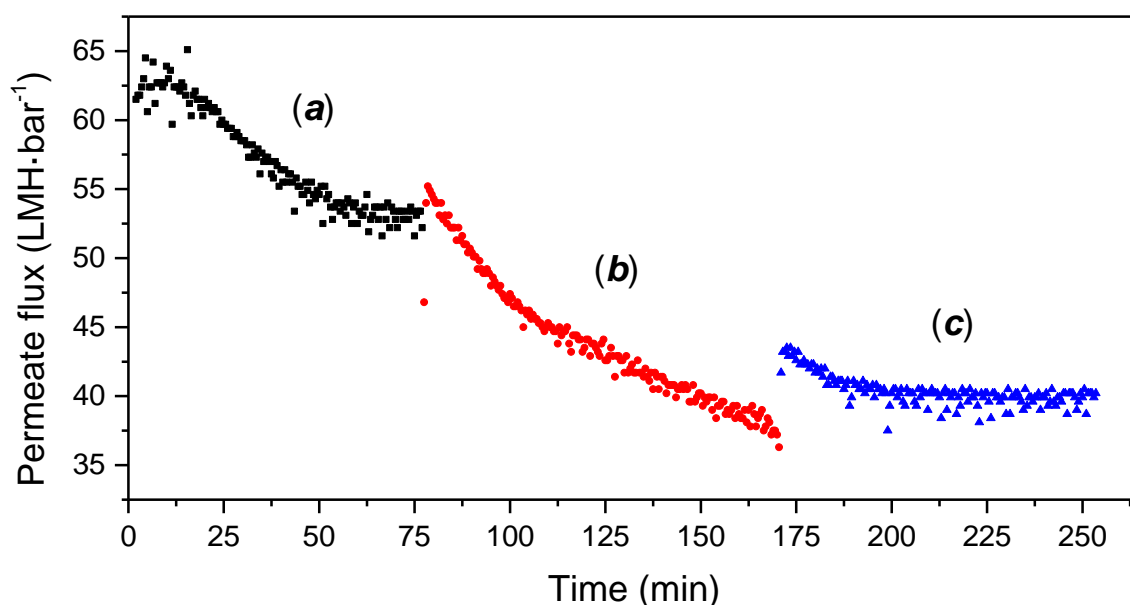


Figure 5.46: Fouling experiment of SM-UF membrane, performed at 1 bar (0.1 MPa) using a 50 mM alginate solution with 20 mM NaCl. (a) equilibration with salt solution only; (b) fouling with alginate; (c) pure water filtration after membrane physical cleaning.

The results of fouling experiment for different PEM-modified membranes are shown in Table 5.13 and Figure 5.47. The PEM-coated membranes presented an increase of the permeate flux during the equilibration phase and a higher flux recovery compared to the initial pure water permeability. The multilayer structure is supposed to swollen when in contact with solutions with a certain ionic strength, due to the intercalation of counterions in the structure, with the structure more open and hydrated. The same effect led to thicker multilayer during the PEM deposition, due to the fact that the increase of the ionic strength leads to thicker coating.

Table 5.13: Permeate flux during the different stage of the fouling experiment for TiO₂-PEM coating on SM membrane, applied by using immersion coating.

Membrane	Permeability (LMH · bar ⁻¹)	Equilibration (LMH · bar ⁻¹)	Fouling (LMH · bar ⁻¹)	After fouling (LMH · bar ⁻¹)
(PDDA-PSS)2.5 (10 min/ly)	17.71 ± 0.20	21.50 ± 0.27	18.78 ± 0.25	21.00 ± 0.34
(PDDA-PSS)3.5 (2 min/ly)	41.53 ± 0.54	*	35.53 ± 0.76	47.24 ± 0.46
(PDDA-PSS)5.5 (2 min/ly + rinse at pH 10)	15.37 ± 0.31	17.71 ± 1.48	16.28 ± 0.37	17.28 ± 0.80
(PEI-PSS) (PDDA-PSS)4.5	9.57 ± 1.34	8.49 ± 0.24	8.87 ± 0.28	8.86 ± 0.19

* Not measured/reported

On the other hand, the increase of the permeate flux after the membrane cleaning indicates the probable removal of part of the multilayer, partly restoring the original permeability. As a confirmation of this theory, the membrane showing this effect the most is coated with a 3.5 layer- PEM, using an immersion time of just 2 minutes. The pure water permeability of this membrane after fouling and cleaning is comparable with that of uncoated SM membranes. Only the membrane prepared using a PEI priming layer showed the same behaviour of the untreated membranes, with no swelling effect and “conventional” flux recovery (around 7.5 % of loss of permeability due to alginate adhesion after cleaning).

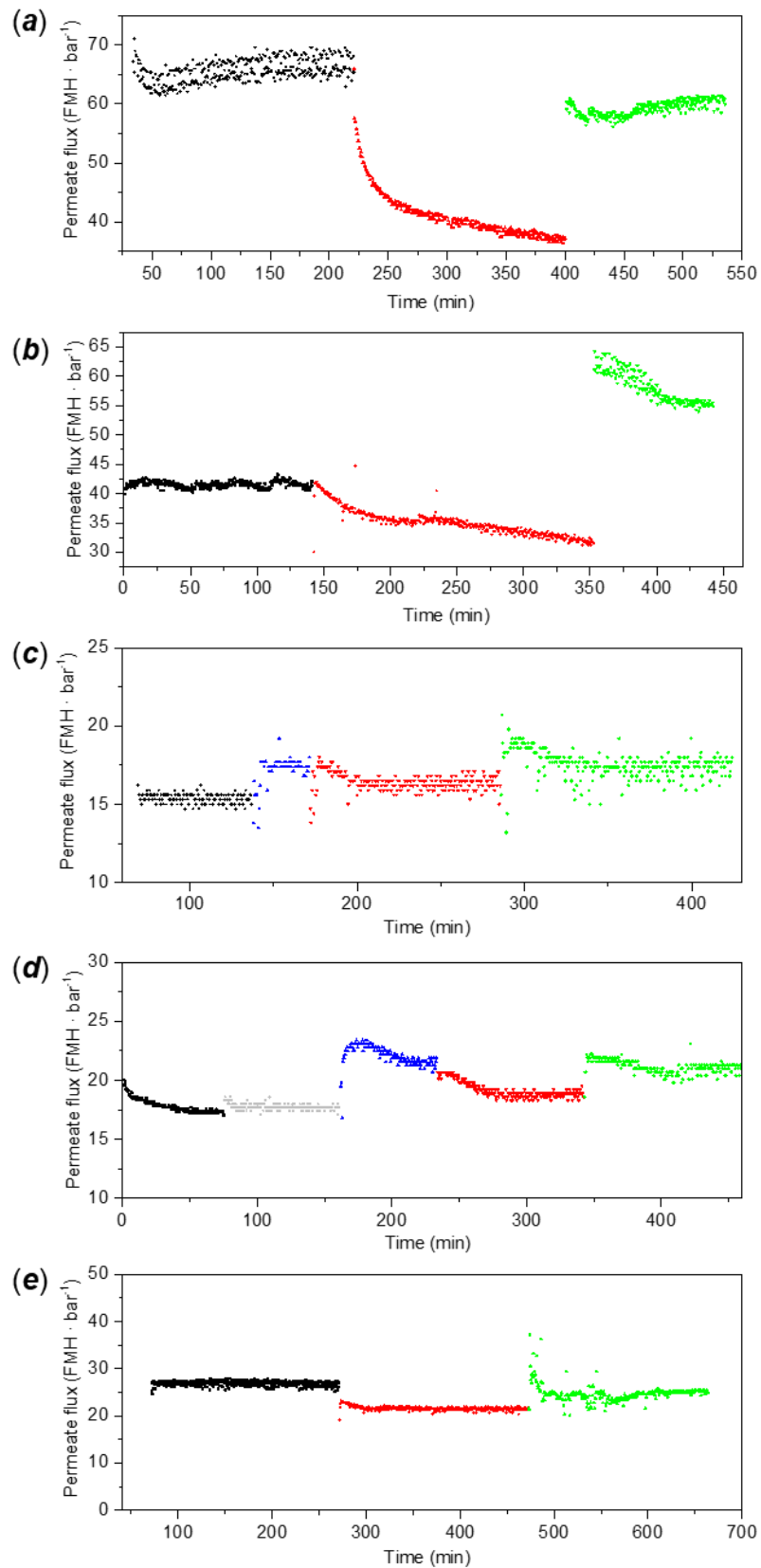


Figure 5.47: Fouling experiments on different UF membranes coated with a (PDDA-PSS) multilayer. Specifically, SM-UF membrane with (a) no coating. (b) (PDDA-PSS)_{3.5}, 2 min/ly, (c) (PDDA-PSS)_{2.5}, 10 min/ly, (d) (PDDA-PSS)_{5.5}, 2 min/ly, rinsed with deionise water at pH 10, (e) (PDDA-PSS)_{5.5}, 5 min/ly. The colours of the filtration curves correspond to black-grey: compaction; blue: equilibration; red: fouling; green: pure water permeation after cleaning.

Some of the new produced membranes were selected for fouling test in dead-end configuration. The permeate fluxes relative to all the stages of the fouling experiment are listed in Table 5.14. Compared to the experiments previously reported, the coating appeared more resistant compared to the previously described experiments.

Table 5.14: Permeate flux during the different stage of the fouling experiment for TiO₂-PEM coating on SM membrane, applied by using the “improved” deposition method.

Membrane	Permeability (LMH · bar ⁻¹)	Equilibration (LMH · bar ⁻¹)	Fouling (LMH · bar ⁻¹)	After fouling (LMH · bar ⁻¹)
(PAH-PSS) _{5.5}	9.02 ± 0.31	16.94 ± 0.39	9.15 ± 0.20	9.74 ± 0.27
(PAH-PSS) ₂ (PAH-TiO ₂) _{3.5}	11.80 ± 0.29	15.23 ± 0.22	8.22 ± 0.23	7.22 ± 2.48
(PDDA-PSS) ₂ (PDDA-TiO ₂) ₂ (PDDA-PSS) _{1.5}	17.10 ± 0.46	16.00 ± 0.76	16.96 ± 0.32	18.93 ± 0.85
(PDDA-PSS) ₂ (PDDA-TiO ₂) _{3.5} (Is 500 Mm)	16.58 ± 0.25	20.71 ± 0.41	15.70 ± 0.24	17.17 ± 0.73

Despite the presence of TiO₂ and the apparently thicker multilayer due to the modified coating procedure, also the membranes prepared using the improved deposition method are prone to lose part of the multilayer (as this is supposed as the most plausible explanation for the increase of permeability after fouling). In this case, only the multilayer prepared using PAH instead of PDDA show more resistance to the swelling-detachment effect.

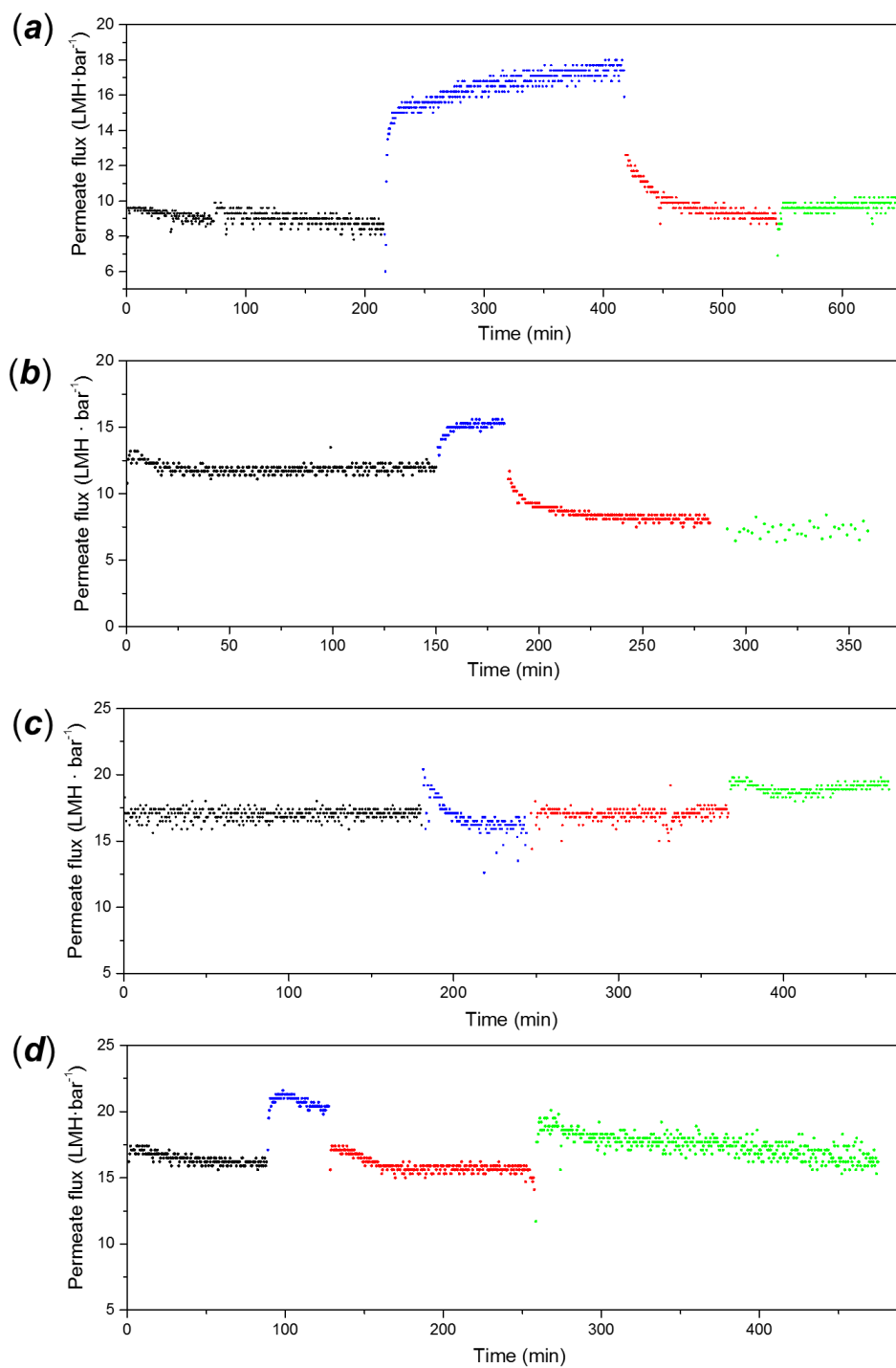


Figure 5.48: Fouling experiments on different UF membranes coated with a (PDDA-PSS) multilayer using the improved procedure. Specifically, SM-UF membrane with (a) (PAH-PSS)_{5.5}, 5 min/ly (b) (PAH-PSS)₂(PAH-TiO₂)_{3.5}, 5 min/ly, (c) (PDDA-PSS)₂(PDDA-TiO₂)₂(PDDA-PSS)_{1.5}, 5 min/ly, (d) (PDDA-PSS)₂(PDDA-TiO₂)_{3.5}, 5 min/ly, polyelectrolyte solution with 500 mM NaCl. The colours of the filtration curves indicates compaction (black), equilibration (blue), fouling (red) and pure water permeation after cleaning (green).

5.8 Discussion

5.8.1 PEM deposition

AFM preliminary analysis showed a change in the surface morphology and an increase of the surface roughness due to the presence of the multilayers. However, it was impossible to determine the effect of specific deposition conditions of multilayer on the surface topography. The presence of PEMs on polymer membranes has been reported to increase the surface roughness, such as in case of the application of a (PAH-PSS)₃ multilayer on PAN membranes, with a 2.5-fold increase of the roughness.^[48] Fery *et al.* showed that the abruptly change of ionic strength from the dipping to the washing cycle was able to cause increase of surface roughness from 1 to 17 nm in a 10-layer PAA/PAH multilayer.^[49] Conventional optical spectroscopic methods such as UV-Vis and FT-IR, were unable to characterise polyelectrolyte multilayers on surfaces such as membranes in the presence of a coating of few tenth of nanometers. The small thickness of the multilayer is indeed below the detection threshold of those techniques. The only change observed was in the signal intensity.

5.8.1.1 Effect of deposition conditions

SPR analysis results are compatible with the other two popular technique for the *in situ* analysis of polyelectrolyte deposition: quartz crystal microbalance with dissipation (QCM-D)^[50] and reflectometry.^[51] SPR allowed an indirect assessment of the assembly mechanism of the PEM. The analysis is generally performed on a gold coated substrate, which is not representative of the characteristics of other surfaces, such as the ones tested in this project. PEM assembly is strongly influenced by the substrate used, specifically influencing the adsorption of the first layers, which is crucial for the final properties of the entire multilayer.^[52] The results of the SPR analysis provided an indication about the effect of other assembly conditions, such as ionic strength and pH of the polyelectrolyte solutions or concentration and surface charges of the inorganic particles, on the growth of the multilayer. However, the effect of the substrate can have a stronger influence compared to the other parameters, as demonstrated by the different wettability of PEM coating applied onto different surfaces.

The multilayer thickness increases linearly with the number of layers. In systems like polystyrene sulfonate/poly allylamine hydrochloride (PSS/PAH), the thickness increases linearly with the number of deposited layers. The adsorption profile is characteristic for each multilayer. The compression of the new layer when exposed to the rinsing water appears to be constant apart from the first couple of bi-layers. For example, PSS is more prone to this compression phenomenon compared to PDDA.

The principal effect of pH modification is a change of the layer thickness, especially in case of weak polyelectrolyte, for which the pH alters the charge density on the polymer chains. When the weak polyelectrolyte is strongly protonated, the stronger interactions lead to a more compact structure; on the other hand, weaker interactions due to a lower charge density give a more swollen and open structure. In particular, the charge density of a polycation is high at low pH values, with low ionisation of the polyanions; at high pH the situation is reversed.^[53]

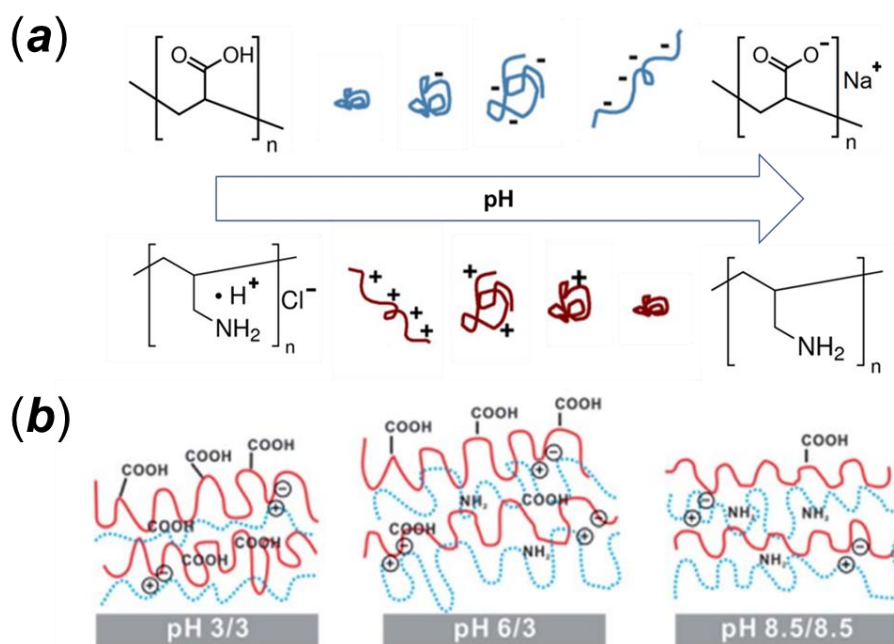


Figure 5.49: Schematic of (a) the effect of pH on polymer conformation of PAA (up) and PAH (down) (adapted from ref [54]) and (b) schematic representation of the internal structure of (PAH/PAA)_n multilayer assembled at different pH conditions. [55]

The change of pH during the self-assembly process also affects the mechanical properties and the compliance of the multilayers. Lichter *et al.* modulated the elastic moduli of the PAH/PAA multilayer between 1 and 100 MPa. The stiffness

of the coating increased raising the pH of the polymers above their pKa values.^[56] PAH/PAA films assembled at a relatively neutral pH are significantly thinner and about two orders of magnitude stiffer than those assembled in acidic conditions. The multilayer stiffness has been proven to be strictly dependant on the outer final layer, allowing the elastic modulus of the film to be tuned just by adding a single layer of a polyelectrolyte with a different pH.^[57] Apart from the mechanical properties of the coating, the film stiffness is reputed to have an important role for antibacterial and anti-adhesive properties.^[58]

The ionic strength has also been reported to affect the surface roughness. The presence of counterions generates lateral and superficial inhomogeneity. Salt-free assembly resulted in PEM with surface roughness of the order of 1 nm, regardless of the number of bi-layers adsorbed.^[59] Polyelectrolyte solutions with zero ionic strength lead to laterally homogeneous films with no distinct surface features, whereas the presence of NaCl could lead to a significant increase of the surface roughness, with strong thickness modulations and a distinct lateral periodicity.^[60] The concentration of the electrolytes added in solution is associated with thicker and more open layers, affecting the resulting properties of the PEM film, such as permeability and rigidity.^[61] The permeability of the B series of SM membranes are in agreement with results in the literature. For example, Qi *et al.* induced a permeability loss of 85% applying a single (PAH-PSS) bilayer with 500 mM NaCl of ionic strength.^[48]

In the case of strong polyelectrolytes, for which charge distribution and structural configuration are generally not affected by the variation of pH, the presence of counterions alters the charge compensation equilibrium with a screening effect on the intermolecular interactions between the polymer chains. Increasing the ionic strength leads to weaken interactions and intercalation of counterions between the layers. The overall structure tends to swell becoming more soften and smooth.^{[62],[63]} Type and concentration of counterions might also have a combined effect. For instance, depending on the hydration layer of the different ions, the increase of the ionic strength lead to the progressive detachment of the chains from each other, with increase of the free space and the degrees of freedom for chain movements.^[64]

The presence of uncompensated counterions in solution causes a configurational change of the polymer chains, producing a highly coiled structure when assembled; multilayers produced under high ionic strength conditions are usually

thick and highly hydrated because of the water molecules entrapped in the structure during the assembly process. The effect of the exposure to high ionic strength solution is not limited only to the outer layer and has been reported to affect the deep multilayer structure (up to 10 layers).^[65]

5.8.1.2 Immersion time, Priming layer and “odd-even” effect

The time of immersion is a relatively important parameter, although it affects the stability and the adhesion kinetics of the different layers to a lesser extent than charge distribution or ionic strength. Typical immersion times vary from a few seconds to around 1 hour. In most of the cases, the first layer requires more time to ensure a stable interface between the substrate and the multilayer. The only experimental study analysing the influence of the time on the multilayer thickness evidenced the saturation of the multilayer after a certain deposition time. The effect has been explained through the formation of a like-charged electrostatic barrier preventing the approach of additional polyelectrolyte,^[66] or alternatively by steric repulsion in the case of high ionic strength.^[67] Due to the influence of the diffusion regime and the polymer mass transfer, the deposition time necessary for a certain thickness is intimately related to other assembly parameters.

The deposition of the first layer is considered as fundamental for the growth of a film with a high lateral homogeneity and the consequent properties of the coating. According to Kniprath *et al.*, an initial immersion of 5 minutes for the first bi-layer is sufficient for the stability of the whole structure. Less than 1 minute is sufficient for the deposition of the following bi-layers because of the limited amount of potentially adsorbed material, with no relevant changes in the internal film structure applying longer immersion cycles.^[78] These findings are confirmed by the results reported by Qi *et al.*, in which a potentially thick multilayer (high ionic strength and 30 min of immersion per layer) reduced the permeability of 85 % with a single bi-layer, followed by a further reduction of 36% with the second and only less than 6% for the third.^[48]

Regardless of the composition of the multilayer, the most important steps in the assembly process are generally the initial and last layer deposition. The first layer (or layers) represents the interface between the substrate and the rest of the multilayer. A very recent study has shown how the first layer can affect the assembly process and the properties of the resulting multilayer, humorously

describing this behaviour as “the princess and the pea” effect.^[68] To ensure a stable interface with the substrate, PEM coatings are deposited on a preliminary layer of strong adhesive polyelectrolyte such as PEI,^[69, 70] or even using polydopamine^[71] in order to “prime” the surface. The last deposited layer could be determinant in changing the final properties of the surface. The phenomenon is referred to as the odd-even effect and it could involve at various extents, the surface charge, the swelling degree, the water mobility and the wettability of the surface.^[72] The effect of the priming layer has been observed only in the analysis of the surface wettability by contact angle measurement, with the increase of the hydrophobic behaviour. In this case, the effect of the priming layer counteracted that of the outermost PAA layer, generally conferring hydrophilicity to the surface.

5.8.2 TiO₂ stability and integration with polyelectrolytes

The surface of oxide compounds has the property to acquire charges when in solution at a pH different from their isoelectric point. The presence of charges is mainly due to the presence of surface defects on these surfaces, where the lattice network is abruptly interrupted, and the energy is higher compared to the bulk. The formation of hydroxyl groups and oxo-bridges compensate the situation of structural and energetic instability when the oxide is immersed in water. When the pH is lower than the pH at the isoelectric point ($\text{pH} < \text{pH}_{\text{iso}}$), the moieties of the hydroxylated surface are protonated, causing the formation of positive charges on the surface. On the other hand, a pH higher than pH_{iso} , the oxo- and hydroxyl groups undergo deprotonation, leaving negative charges on the surface. This principle is the basis for the stabilisation of oxide particle colloidal suspension and the particle integration in macromolecular structures, such as the polyelectrolyte multilayers (PEMs) establishing electrostatic interactions.

Colloidal suspension stabilisation is often required to enhance the dispersivity of nanoparticles, improving the quality of the wanted application. For instance, higher homogeneity of the nanoparticles in a multifunctional coating or into a matrix for the production of composite materials is reputed to increase the final performance. Charged molecules with long chains, such as surfactants, can adhere by electrostatic interaction to the surface of a particle in colloidal suspension. In case of oxide particles, the surface charge can be easily modified altering the pH

of the suspension. Since their nature of charged molecules, polyelectrolyte such as PAA, PAH and PEI have been reported in literature to be capable of stabilise TiO₂ nanoparticle suspension. In particular, the structure of the commercial surfactant Darvan is based on the modification of PAA and PMMA.

In the past decades, both association of negatively charged TiO₂ with polycations and positively charged TiO₂ with polyanions have been reported for different applications. The method has been mainly used for the production of surface with specific optical or electronic properties, such as antireflective coatings or photocathodes, for example combining PDDA with TiO₂ nanosheets [73] or PSS and PAA with TiO₂ nanoparticle colloidal solution.[74] Some attempts of TiO₂-PE composite multilayer have been proposed to improve the conversion efficiency of DSSC creating a blocking layer which would prevent recombination processes at the FTO surface.[75] The same authors reported the deposition of highly concentrated suspension of mesoporous TiO₂ sol (10 g/L) at pH 2 with negative polyions such as PSS, PAA and sulfonated lignin, with the production of a very dense and compact layer of TiO₂ NPs.[76] Another composite multilayer lignosulfate/TiO₂ has been reported, using 1 g/L particle suspension at pH 3.5 for the photocatalytic functionalisation of cellulose fibers for paper production.[77] Nanoporous TiO₂ particle coating for DSSC was the final purpose of Kniprath *et al.*[78] as well, which associated 2 g/L anatase nanoparticles (40 nm average size) with both PSS and PDDA (pH unadjusted, 10 mM concentration).

It has been reported the increase of thickness of composite multilayers formed by nanoparticles up to a certain particle size, above which it is much lower, indicating poor integration of the particles in the layered structure. The explanation for the limit of nanoparticles loading in the multilayer has been provided by Li *et al.*: considering the same nanoparticles concentration, the increase of the average size reduces the available surface for the adsorption of the polyelectrolyte.[79]

The steric-electrostatic stabilisation of TiO₂ particles is generally particularly efficient at limited concentration of polyelectrolyte. Ohtman *et al.* reported the apex of stabilising effect at 3 wt% in a TiO₂ nanoparticles suspension, which corresponds to 30 mg/L for a 1 g/L suspension, very low compared to the common concentration of polyelectrolytes used for the multilayer build-up (1 to 2 g/L).[80] PAH was also used in similar concentration (4.5%wt) with good performance in improving the dispersion of TiO₂ nanoparticle suspension, comparable with the

electrostatic repulsion provided by very low pH (2.5). Despite the efficacy of the dispersion is directly proportional to the concentration of polyelectrolyte, higher concentration values are supposed to have the opposite effect destabilising the suspension.^[81] An even better approach is represented by the functionalisation of the particles in suspension using the polyelectrolytes. Al-Awadi *et al.* functionalised TiO₂ nanoparticles using a double bi-layer of PSS/PAH just exploiting the electrostatic interactions on the nanoparticle surface.^[82]

5.8.3 Further improvement of PEM coating on particles and surfaces

5.8.3.1 Selective removal and regenerable multilayers

As for pH, high ionic strength could ultimately lead to complete deconstruction of the multilayer structure.^[83] The amount of salt required depends on the structure itself and hence on the assembly conditions (pH, type of polyelectrolyte). Disintegration of a PDDA/PAA multilayer system has been reported after exposure to a 0.6 M NaCl solution, whereas the same effect was observed in PDDA/PSS using a 3.5 M NaCl solution.^[84] The control of the deconstruction process has been proposed for the production of microporous structures, useful for example for antireflective coatings,^[85] or the selective removal of part of the PEM coating for surface micro-patterning.^[86] The use of ionic strength to remove or modify a PEM coating is commonly referred to as "salt etching".

As demonstrated by the fouling experiments, the examined PEM coatings are not stable when exposed to particular conditions of pH or ionic strength, which could modify the multilayer properties weakening the intermolecular bonding and progressively leading to the complete destabilisation of the structure. The selective destruction of the multilayer could be applied to regenerate the active surface in cases when original properties are deactivated because of fouling, biofilm establishment or depletion of active agents incorporated in the multilayer. Despite the development of efficient control strategies, the exposed surface undergoes progressive and unavoidable fouling throughout its operative lifetime, leading ultimately to irreversible damage and consequent replacement.^[87] Moreover, most strategies specifically target a certain type of fouling, being less effective towards others.^[88] The idea of a regenerable PEM layer in order to remove fouling and restore the active layer represents a cost-effective alternative

to extend the life of the membrane, with a theoretically infinite number of regeneration cycles. The concept of sacrificial/regenerable functional coatings has recently been proposed for filtration membranes.^[89] Pontie' *et al.* regenerated an antibiofouling PSS/PDDA on a Nafion cationic-exchange membrane using a 2 M NaCl solution, pointing out how a complete recovery of the original properties is strictly dependent on the original membrane surface, with the presence of macropores detrimental to restore the original properties.^[90] Mi *et al.* demonstrated the complete regeneration of a PEI/PAA coating on polysulfone FO membrane, removing the fouled surface with a concentrated solution of HCl (pH 1).^[91] The idea of a sacrificial coating layer has been applied in different technological fields,^[92] with the polyelectrolyte properties particularly suitable for this strategy, with complete and reversible restoration of the original surface conditions.^[93] Depending on the combination of polyelectrolytes employed for the multilayer assembly, the removal strategies are different. Surfactants are able to disrupt non-ionic interactions, whereas electrostatic interactions generally are weakened by pH change for weak polyelectrolytes or ionic strength for strong polyelectrolytes. The versatility of the multilayer structure might allow the controlled degradation of part of the multilayer, for example using stimuli-responsive polyelectrolytes or degradable multilayer combinations where integrity depends on weak interactions such as hydrogen bonding.^[94] The removal of part of the multilayer structure could expose a new functional surface or prepare the surface for further deposition steps to restore the previous conditions.^[95]

5.8.4 Development of an integrated system

The most common PEM deposition method is the dip or immersion coating technique, also reported as the “static assembly method” (SAM) to distinguish this technique from dynamic coating methods. Dynamic methods exploit the filtration configurations for an *in situ* self-assembly of the PEM on the membrane active layer, exposing the membrane surface to the polyelectrolyte solution in dead-end or cross-flow configuration. A comparative study performed on NF membranes showed an increase in salt rejection with lower number of layers and higher charge inversion after layer deposition adopting the dynamic approach.^[96] A preliminary study on the design of a dynamic deposition method, not reported in this thesis, involved a cross-flow filtration system integrating in-flow PEM deposition with

conventional filtration experiment. The PEM is applied to the membrane flowing polyelectrolyte solution by using a peristaltic pump. The same system can be applied for the selective removal of the polyelectrolyte coating, associating the introduction of high ionic strength solutions to the feed of the filtration apparatus, which would facilitate the removal operations. The preliminary design was successful in demonstrating the possibility of providing a PEM coating for the membrane and in proceeding with the hydraulic characterisation test using the same apparatus.

(a)



(b)

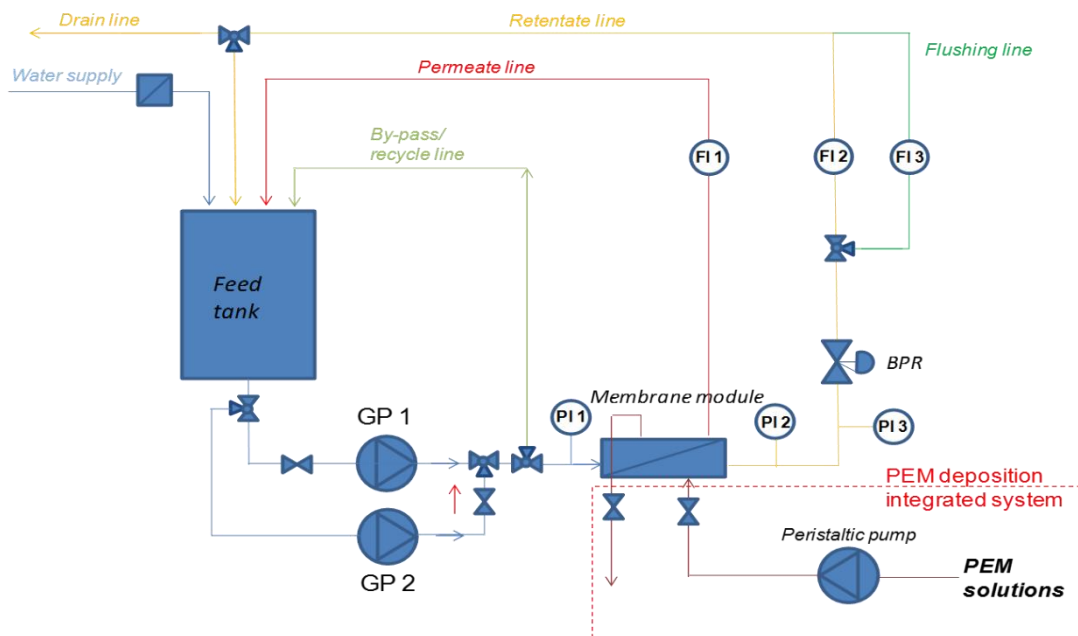


Figure 5.50: (a) image of the experimental setup (realized on August 2014 at Johns Hopkins University, Dept. of Geography). The main components are marked with numbers: (1) 20 liters feed tank; (2) main gear pump; (3) secondary gear micropump; (4) membrane module; (5) peristaltic pump (PEM deposition integrated system); (6) inlet module pressure gauge; (7) outlet module pressure gauge; (8) digital pressure gauge; (9) backpressure regulator (BPR); (10) permeate flowmeter; (11) retentate flowmeter; (12) flushing line flowmeter; (b) schematic diagram of the system.

5.9 Conclusions

In this chapter the possibility of production of a composite coating formed by PEM and TiO₂ particles was investigated. Commercial TiO₂ photocatalysts (polycrystalline anatase and Aeroxide P25) were applied as a proof of concept for the realisation of a multifunctional coating for water filtration. The principal findings are summarised as listed below:

- Identification of the adsorption mechanism of TiO₂ particles in polyelectrolyte multilayer by SPR measurement;
- Modification of the superficial properties through the TiO₂-PEM coating, with notably increase of hydrophilicity;
- Achievement of superhydrophilic conditions associating TiO₂ particles with high ionic strength polyelectrolyte solutions;
- Limited mechanical stability of the composite multilayer, potentially useful as sacrificial/regenerable active layer in antifouling application for filtration membranes;

The adsorption kinetics of polyelectrolyte and TiO₂ particles has been studied thanks to the SPR measurement, determining the effect of the interaction of synthetic polyelectrolyte and TiO₂ particles in suspension. The instrumental parameters used for the SPR can be potentially transferred to the conventional coating techniques adopted to produce PEM on surfaces. The tested polyelectrolytes follow a linear kinetics of growth, confirming the overcompensation mechanism allowing the build-up of the multilayer structure. TiO₂ particles were also deposited, with the thickness of the layer depending on the concentration. Due to the lower superficial charge of TiO₂ compared to the polyelectrolyte, the charge is not compensated, reducing the adsorption capacity of the multilayer, which thickness appear to stabilise after a certain number of layers. To mention an example, 150 mg/L suspension is not able to build up more than 3 multilayers, with negligible increase of thickness. Increasing the concentration of particles also the charge available increases. However, a more dense and thick layer of particle would negatively affect permeability of filtration membranes, as reported in Table 5.9.

Both PEM and TiO₂-PEM composite were able to efficiently modify the surface properties of the substrate onto which they were applied. The applications of PEM modified the original properties of the selected surfaces. Firstly, the optical properties, enhancing the transmittance of glass slides in the visible-light region, potentially useful for specific applications (e.g. anti-reflective coatings) not developed in this project. Moreover, the absorption capacity of TiO₂ is efficiently transferred to the substrate onto which the TiO₂-PEM composite has been deposited, with reduction of the transmittance up to 45% for the most efficient deposition conditions. Secondly, modification of surface property such as a general improvement of the surface roughness (estimated by AFM) and the surface affinity for water. Slightly hydrophobic membranes were converted into more hydrophilic, condition potentially enhancing the antifouling properties. However, increase of thickness led to loss of permeability for the UF membranes of 20-50% without increasing the ionic strength and 78-97% adding NaCl. Only limiting the deposition time per layer led to partial preservation of the original conditions. Efficient design of dip coating experiment, improving the simple immersion technique increasing the interaction between the substrate and the Pes solution and inorganic particle suspension. The use of non-recyclable smaller amount of solutions noticeably increased the uniformity of the coating, due also to the larger amount of adherent particles (Figure 5.40 and Figure 5.41).

Superhydrophilicity was achieved on some of the tested surfaces, in particular Mylar. These properties represent a proof for the efficacy of the improved deposition method, leading to increased uniformity of the multilayer and of the capacity of adhesion of the particles to the surface. The superhydrophilic condition was achieved using a particular combination of TiO₂ particles and a higher concentration of an external electrolyte (NaCl) to increase the ionic strength of the polyelectrolyte solutions. With no ionic strength, TiO₂ particles bestowed hydrophilicity displayed by water contact angle of 30-40°. The use of 100 mM and 500 mM of NaCl in the polyelectrolyte solutions reduced the angles to ca. 10° and less than 5, respectively.

On the other hand, the same effect was not observed on the polymer membrane surface, in some cases showing even increased hydrophobicity compared to the original surface. In those cases, the effect of hydrophobic polymer (such as PDDA) prevails on the presence of TiO₂. The results confirmed the strong influence of the substrate on the final structures and properties of the multilayer.

The possibility of regeneration of the active layer after fouling was also explored. Due to the poor mechanical stability to the cleaning procedure of some multilayers, the permeability of the membrane after cleaning increased to higher values compared with the values collected during pure water filtration. The most sensitive conditions to this phenomenon were observed in case of brief exposure time during PE deposition or limited number of layers (generally below 3.5 bilayers), previously chosen because reducing the permeability less with respect to the uncoated membranes.

5.10 References

- ¹ G. Decher, Fuzzy nanoassemblies: Toward layered polymeric multicomposites. *Science*, 1997, **277**, 1232–1237.
- ² A. Wu, D. Yoo, J.K. Lee, M.F. Rubner, Solid-state light-emitting devices based on the tris-chelated ruthenium(II) complex: 3. High efficiency devices via a layer-by-layer molecular-level blending approach, *J. Am. Chem. Soc.*, 1999, **121**, 4883-4891.
- ³ C. Holmes, J. Daoud, P.O. Bagnaninchi, M. Tabrizian, Polyelectrolyte multilayer coating of 3D scaffolds enhances tissue growth and gene delivery: non-invasive and label-free assessment, *Adv. Healthc. Mater.*, 2014, **3**, 572-580.
- ⁴ N. Joseph, P. Ahmadiannamini, R. Hoogenboom, Ivo. F. J. Vankelecom, Layer-by-layer preparation of polyelectrolyte multilayer membranes for separation, *Polym. Chem.*, 2014, **5**, 1817-1831.
- ⁵ P. Schaaf, J.-C. Voegel, L. Jierry, F. Boulmedais, Spray-assisted polyelectrolyte multilayer buildup: From step-by-step to single-step polyelectrolyte film constructions, *Adv. Mater.*, 2012, **24**, 1001–1016.
- ⁶ J. Cho, K. Char, J.D. Hong, K.B. Lee, Fabrication of Highly Ordered Multilayer Films Using a Spin Self-Assembly Method, *Adv. Mater.*, 2001, **13**, 1076-1078.
- ⁷ B. Su, T. Wang, Z. Wang, X. Gao, C. Gao, Preparation and performance of dynamic layer-by-layer PDADMAC/PSS nanofiltration membrane, *J. Membr. Sci.*, 2012, **423-424**, 324–331.
- ⁸ S. Mulyati, R. Takagi, A. Fujii, Y. Ohmukai, T. Maruyama, H. Matsuyama, Improvement of the antifouling potential of an anion exchange membrane by surface modification with a polyelectrolyte for an electro dialysis process, *J. Membr. Sci.*, 2012, **417-418**, 137-143.
- ⁹ H. Guo, Y. Ma, P. Sun, S. Cui, Z. Qinb Y. Liang, Self-cleaning and antifouling nanofiltration membranes-superhydrophilic multilayered polyelectrolyte/CSH composite films towards rejection of dyes, *RSC Adv.*, 2015, **5**, 63429-63438.
- ¹⁰ A. Fujishima, T.N. Rao, D.A. Tryk, Titanium dioxide photocatalysis, *J. Photochem. Photobiol. C: Photochem. Rev.*, 2000, **1**, 1-21.
- ¹¹ T. Kruka, K. Szczepanowicza, D. Kregielb, L. Szyk-Warszynskaa, P. Warszynskia, Nanostructured multilayer polyelectrolyte films with silver nanoparticles as antibacterial coatings, *Coll. Surf. B: Biointerfaces*, 2016, **137**, 158-166.
- ¹² Y. Liu, Y. Wang, R.O. Claus, Layer-by-layer ionic self-assembly of Au colloids into multilayer thin-films with bulk metal conductivity, *Chem. Phys. Lett.*, 1998, **298**, 315–319.
- ¹³ N. Hilal, O.O. Ogunbiyi, N.J. Miles, R. Nigmatullin, Methods employed for control of fouling in MF and UF membranes: a comprehensive review, *Sep. Sci. Technol.*, 2005, **40**, 1957–2000.
- ¹⁴ L. Zhang, N. Zhao, J. Xu, Fabrication and application of superhydrophilic surfaces: a review, *J. Adhes. Sci. Technol.*, 2014, **28**, 769–790.
- ¹⁵ J.D. Mendelsohn, S.Y. Yang, J. Hiller, A.I. Hochbaum, M.F. Rubner, Rational Design of Cytophilic and Cytophobic Polyelectrolyte Multilayer Thin Films, *Biomacromol.*, 2003, **4**, 96-106.
- ¹⁶ B.D. Monnery M. Wright, R. Cavill, R. Hoogenboom, S. Shaunak, J.H. Steinke, M. Thanou, Cytotoxicity of polycations: Relationship of molecular weight and the hydrolytic theory of the mechanism of toxicity, *Int. J. Pharm.*, 2017, **521**, 249-258.
- ¹⁷ B.P. Tripathi, N.C. Dubey, M. Stamm, Functional polyelectrolyte multilayer membranes for water purification applications, *J. Haz. Mat.*, 2013, **252–253**, 401–412.
- ¹⁸ D.B. Vieira, A.M. Carmona-Ribeiro, Cationic nanoparticles for delivery of amphotericin B: preparation, characterization and activity in vitro, *J. Nanobiotechnol.*, 2008, **6:6**.
- ¹⁹ C. Wandrey, J. Hernandez-Barajas, D. Hunkeler, Diallyldimethylammonium chloride and its polymers, *Adv. Polym. Sci.*, 1999, **145**, 123–182.
- ²⁰ AWWA standard for poly(diallyldimethylammonium chloride), AWWA B451- 87, AWWA, Denver, Colorado, 1998.
- ²¹ J.A. Lichter, M.F. Rubner, Polyelectrolyte multilayers with intrinsic antimicrobial functionality: The importance of mobile polycations. *Langmuir*, 2009, **25**, 7686–7694.

- ²² B. Gilbert, G.P. Lu, C.S. Kim, Stable cluster formation in aqueous suspensions of iron oxyhydroxide nanoparticles. *J. Coll. Interf. Sci.*, 2007, **313**, 152–159.
- ²³ K.A.D. Guzman, M.P. Finnegan, J.F. Banfield, Influence of surface potential on aggregation and transport of titania nanoparticles. *Environ. Sci. Technol.*, 2006, **40**, 7688–7693.
- ²⁴ M.K. Ridley, V.A. Hackley, M.L. Machesky, Characterization and surface-reactivity of nanocrystalline anatase in aqueous solutions. *Langmuir*, 2006, **22**, 10972–10982.
- ²⁵ H.J. Cleaves, Isoelectric Point. In: M. Gargaud *et al.* (eds) *Encyclopedia of Astrobiology*. Springer, 2011.
- ²⁶ E. Matijevic, M. Budnik, L. Meites, Preparation and mechanism of formation of titanium dioxide hydrosols of narrow size distribution, *J. Colloid Int. Sci.*, 1977, **61**, 302-311.
- ²⁷ M.D. Chadwick, J.W. Goodwin, E.J. Lawson, P.D.A. Mills, B. Vincent, Surface charge properties of colloidal titanium dioxide in ethylene glycol and water, *Colloids Surf. A*, 2002, **203**, 229-236.
- ²⁸ M. Larsson, A. Hill, J. Duffy, Suspension Stability; Why Particle Size, Zeta Potential and Rheology are Important, *Ann. Trans. Nord. Rheol. Soc.*, 2012, **20**, 209-214.
- ²⁹ I. Pastoriza-Santos, L.M. Liz-Marzan, Formation of PVP-protected metal nanoparticles in DMF, *Langmuir*, 2002, **18**, 2888-2894.
- ³⁰ A.R. Studart, E. Amstad, L.J. Gauckler, Colloidal Stabilization of Nanoparticles in Concentrated Suspensions, *Langmuir*, 2007, **23**, 1081-1090.
- ³¹ G. Li, L. Lv, H. Fan, J. Ma, Y. Li, Y. Wan, X.S. Zhao, Effect of the agglomeration of TiO₂ nanoparticles on their photocatalytic performance in the aqueous phase, *J. Colloid Interf. Sci.*, 2010, **348**, 342–347.
- ³² W. Ritcharoen, P. Supaphol, P. Pavasant, Development of polyelectrolyte multilayer-coated electrospun cellulose acetate fiber mat as composite membranes, *Eur. Polym. J.*, 2008, **44**, 3963-3968.
- ³³ S. Ilyas, J. de Groot, K. Nijmeijer, W.M. de Vos, Multifunctional polyelectrolyte multilayers as nanofiltration membranes and as sacrificial layers for easy membrane cleaning, *J. Colloid Interf. Sci.*, 2015, **446**, 386–393.
- ³⁴ <https://www.sterlitech.com/ultrafiltration-uf-membrane.html> (accessed December 2017).
- ³⁵ H.R. Lohokare, Y.S. Bhole, U.K. Kharul, Effect of Support Material on Ultrafiltration Membrane Performance, *J. App. Poly. Sci.*, 2006, **99**, 3389-3395.
- ³⁶ K. Nouzaki, M. Nagata, J. Arai, Y. Idemotb, N. Koura, H. Yanagishita, H. Negishi, D. Kitamoto, T. Ikegam, K. Haraya, Preparation of polyacrylonitrile ultrafiltration membranes for wastewater treatment, *Desalination*, 2002, **144**, 53-59.
- ³⁷ Y.S. Li, T.S. Zhao, W.W. Yang, Measurements of water uptake and transport properties in anion-exchange membranes, *Int. J. Hydrogen En.*, 2010, **35**, 5656 -5665.
- ³⁸ J.I. Calvo, A. Bottino, P. Pradanos, L. Palacio, A. Hernandez, Porosity, in: E.M.V. Hoek, V.V. Tarabara (Eds.), *Encyclopedia of Membrane Science and Technology*, John Wiley & Sons, 2013, pp. 1-15.
- ³⁹ G. Ellis, A Sanchez, P.J. Hendra, H.A. Willis, Fourier transform vibrational spectroscopy in the study of poly (aryl ether sulphone), poly (aryl ether sulphone) and their copolymers, *J. Mol. Struct.*, 1991, **241**, 385-395.
- ⁴⁰ S. Belfer, R. Fainchtain, Y. Purinson, O. Kedem, Surface characterization by FTIR-ATR spectroscopy of polyethersulfone membranes-unmodified, modified and protein fouled, *J. Membr. Sci.*, 2000, **172**, 113–124.
- ⁴¹ G. Zhang, S. Lu, L. Zhang, Q. Meng, C. Shen, J. Zhang, Novel polysulfone hybrid ultrafiltration membrane prepared with TiO₂-g-HEMA and its antifouling characteristics, *J. Membr. Sci.*, 2013, **436**, 163–173.
- ⁴² C.Y. Liang, S. Krimm, Infrared Spectra of High Polymers. VII. Polyacrylonitrile, *J. Polym. Sci.*, 1958, **31**, 513-522.
- ⁴³ I. Shimada, T. Takahagi, FT-IR Study of the Stabilization Reaction of Polyacrylonitrile in the Production of Carbon Fibers, *J. Polym. Sci. A: Polym. Chem.*, 1986, **24**, 1989-1995.
- ⁴⁴ P. Rajalingam, G. Radhakrishnan, Polyacrylonitrile Precursor for Carbon Fibers, *Macromol. Chem. Phys.*, 1991, **283**, 301-310.

- ⁴⁵ S.I. Abou-Elela, H.S. Ibrahim, M.M. Kamel, M. Gouda, Application of Nanometal Oxides In Situ in Nonwoven Polyester Fabric for the Removal of Bacterial Indicators of Pollution from Wastewater, *The Scientific World Journal*, 2014, **2014**, 950348.
- ⁴⁶ P. Bajai, D.C. Gupta, A.K. Gupta, Structure and properties of acrylonitrile-[(2-methacryloyloxy)alkoxy]trimethyl silane copolymers, *J. Appl. Polym. Sci.*, 1980, **25**, 1673-1684.
- ⁴⁷ N. Chatterjee, S. Basu, S.K. Palit, M.M. Maiti, An XRD Characterization of the Thermal Degradation of Polyacrylonitrile, *J. Polym. Sci. B, Polym. Phys.*, 1995, **33**, 1705-1712.
- ⁴⁸ S. Qi, C.Q. Qiu, Y. Zhao, C.Y. Tang, Double-skinned forward osmosis membranes based on layer-by-layer assembly-FO performance and fouling behaviour, *J. Memb. Sci.*, 2012, **405-406**, 20-29.
- ⁴⁹ A. Fery, B. Scholer, T. Cassagneau, F. Caruso, Nanoporous Thin Films Formed by Salt-Induced Structural Changes in Multilayers of Poly(acrylic acid) and Poly(allylamine), *Langmuir*, 2001, **17**, 3779-3783.
- ⁵⁰ T. Saarinen, M. Österberg, J. Laine, Adsorption of polyelectrolyte multilayers and complexes on silica and cellulose surfaces studied by QCM-D, *Coll. Surf. A*, 2008, **330**, 134-142.
- ⁵¹ J.C. Dijt, M.A. Cohen Stuart, G.J. Fleer, Reflectometry as a tool for adsorption studies, *Adv. Coll. Interf. Sci.*, 1994, **50**, 79-101.
- ⁵² C.C. Buron, C. Filiatre, F. Membrey, C. Bainier, D. Charrat, A. Foissy, Effect of substrate on the adsorption of polyelectrolyte multilayers: Study by optical fixed-angle reflectometry and AFM, *Colloids and Surfaces A: Physicochem. Eng. Aspects*, 2007, **305**, 105-111.
- ⁵³ J. Choi, M.F. Rubner, Influence of the degree of ionization on weak polyelectrolyte multilayer assembly, *Macromolecules*, 2005, **38**, 116-124.
- ⁵⁴ J.C. Grunlan, L. Liu, O. Regev, Weak polyelectrolyte control of carbon nanotube dispersion in water, *J. Coll. Interf. Sci.*, 2008, **317**, 346-349.
- ⁵⁵ M. Gu, J. Lee, Y. Kim, J.S. Kim, B.Y. Jang, K.T. Lee, B.-S. Kim, Inhibiting the shuttle effect in lithium-sulfur batteries using a layer-by-layer assembled ion-permselective separator, *RSC Adv.*, 2014, **4**, 46940-46946.
- ⁵⁶ M.T. Thompson, M.C. Berg, I.S. Tobias, M.F. Rubner, K.J. Van Vliet, Tuning compliance of nanoscale polyelectrolyte multilayers to modulate cell adhesion, *Biomaterials*, 2005, **26**, 6836-6845.
- ⁵⁷ J.A. Lichter, M.T. Thompson, M. Delgadillo, T. Nishikawa, M.F. Rubner, K.J. Van Vliet, Substrata mechanical stiffness can regulate adhesion of viable bacteria. *Biomacromolecules*, 2008, **9**, 1571-1578.
- ⁵⁸ L. Richert, P. Lavalley, E. Payan, X.Z. Shu, G.D. Prestwich, J.F. Stoltz, P. Schaaf, J.C. Voegel, C. Picart, Layer by layer buildup of polysaccharide films: Physical chemistry and cellular adhesion aspects. *Langmuir*, 2004, **20**, 448-458.
- ⁵⁹ A. Fery, B. Scholer, T. Cassagneau, F. Caruso, Nanoporous Thin Films Formed by Salt-Induced Structural Changes in Multilayers of Poly(acrylic acid) and Poly(allylamine), *Langmuir*, 2001, **17**, 3779-3783.
- ⁶⁰ J.D. Mendelsohn, C.J. Barrett, V.V. Chan, A.J. Pal, A.M. Mayes, M.F. Rubner, Fabrication of Microporous Thin Films from Polyelectrolyte Multilayers, *Langmuir*, 2000, **16**, 5017-5023.
- ⁶¹ J.B. Schlenoff, S.T. Dubas, Mechanism of polyelectrolyte multilayer growth: charge overcompensation and distribution, *Macromolecules*, 2001, **34**, 592-598.
- ⁶² S.T. Dubas, J.B. Schlenoff, Swelling and Smoothing of Polyelectrolyte Multilayers by Salt, *Langmuir*, 2001, **17**, 7725-7727.
- ⁶³ J. Heuvingh, M. Zappa, A. Fery, Salt Softening of Polyelectrolyte Multilayer Capsules, *Langmuir*, 2005, **21**, 3165-3171.
- ⁶⁴ S. Dadoo, R. Steitz, A. Laschewsky, R. von Klitzing, Effect of ionic strength and type of ions on the structure of water swollen polyelectrolyte multilayers, *Phys. Chem. Chem. Phys.*, 2011, **13**, 10318-10325.
- ⁶⁵ A.F. Xie, S. Granick, Local electrostatics within a polyelectrolyte multilayer with embedded weak polyelectrolyte, *Macromolecules*, 2002, **35**, 1805-1813.
- ⁶⁶ K. Lowack, C.A. Helm, Molecular Mechanisms Controlling the Self-Assembly Process of Polyelectrolyte Multilayers, *Macromolecules*, 1998, **31**, 823-833.

- ⁶⁷ S.T. Dubas, J.B. Schlenoff, Factors Controlling the Growth of Polyelectrolyte Multilayers, *Macromolecules*, 1999, **32**, 8153-8160.
- ⁶⁸ X. Lyu, A.M. Peterson, The Princess and the Pea Effect: Influence of the first layer on polyelectrolyte multilayer assembly and properties, *J. Coll. Interf. Sci.*, 2017, **502**, 165-171.
- ⁶⁹ M. Kolasinska, R. Krastev, P. Warszynski, Characteristics of polyelectrolyte multilayers: Effect of PEI anchoring layer and post-treatment after deposition, *J. Coll. Interf. Sci.*, 2007, **305**, 46-56.
- ⁷⁰ G. Decher, *Multilayer Thin Films* in G. Decher, J.B. Schlenhoff *Multilayer Thin Films: Sequential Assembly of Nanocomposite Materials*. 2nd Eds.; Wiley-VCH: Weinheim, 2003.
- ⁷¹ Y. Kang, S. Zheng, C. Finnerty, M.J. Lee, B. Mi, Regenerable Polyelectrolyte Membrane for Ultimate Fouling Control in Forward Osmosis, *Environ. Sci. Technol.*, 2017, **51**, 3242-3249.
- ⁷² J. de Grooth, R. Oborný, J. Potreck, K. Nijmeijer, W.M. de Vos, The role of ionic strength and odd-even effects on the properties of polyelectrolyte multilayer nanofiltration membranes, *J. Memb. Sci.*, 2015, **475**, 311-319.
- ⁷³ T. Sasaki, Y. Ebina, K. Fukuda, T. Tanaka, M. Harada, M. Watanabe, Titania Nanostructured Films Derived from a Titania Nanosheet/Polycation Multilayer Assembly via Heat Treatment and UV Irradiation, *Chem. Mater.*, 2002, **14**, 3524-3530.
- ⁷⁴ J.H. Kim, S. Shiratori, Characterisation of TiO₂/Polyelectrolyte Thin Film Fabricated by a Layer-by-Layer Self-Assembly Method, *Jap. Journ. App. Phys.*, 2005, **44**, 7588-7592.
- ⁷⁵ A.O.T. Patrocínio, L.G. Paterno, N.Y. Murakami Iha, Layer-by-layer TiO₂ films as efficient blocking layers in dye-sensitized solar cells, *J. Photochem. Photobiol. A: Chem.*, 2009, **205**, 23-27.
- ⁷⁶ A.O.T. Patrocínio, L.G. Paterno, N.Y. Murakami Iha, Role of Polyelectrolyte for Layer-by-Layer Compact TiO₂ Film in Efficiency Enhanced Dye-Sensitized Solar Cells, *J. Phys. Chem. C*, 2010, **114**, 17945-17959.
- ⁷⁷ H. Li, S. Fu, L. Peng, Surface Modification of Cellulose Fibers by Layer-by-Layer Self-assembly of Lignosulfonates and TiO₂ Nanoparticles: Effect on Photocatalytic Abilities and Paper Properties, *Fibers and Polymers*, 2013, **14**, 1794-1802.
- ⁷⁸ R. Kniprath, S. Duhm, H. Glowatzki, Internal Structure of Nanoporous TiO₂/Polyion Thin Films Prepared by Layer-by-Layer Deposition, *Langmuir*, 2007, **23**, 9860-9865.
- ⁷⁹ Q. Li, J. F. Quinn, Y. Wang, F. Caruso, Preparation of Nanoporous Polyelectrolyte Multilayer Films via Nanoparticle Templating, *Chem. Mater.*, 2006, **18**, 5480-5485.
- ⁸⁰ S.H. Othman, S.A. Rashid, T.I.M. Ghazi, N. Abdullah, Dispersion and Stabilization of Photocatalytic TiO₂ Nanoparticles in Aqueous Suspension for Coatings Applications, *J. Nanomat.*, 2012, **2012**, 718214.
- ⁸¹ G. Li, L. Lv, H. Fan, J. Ma, Y. Li, Y. Wan, X.S. Zhao, Effect of the agglomeration of TiO₂ nanoparticles on their photocatalytic performances in the aqueous phase, *J. Collid. Interf. Sci.*, 2010, **348**, 342-347.
- ⁸² M.J. Al-Awasy, G.M. Greenway, V.N. Paunov, Nanotoxicity of polyelectrolyte-functionalised titania nanoparticles towards microalgae and yeast: role of the particle concentration, size and surface charge, *RSC Adv.*, 2015, **5**, 37044.
- ⁸³ A.J. Nolte, N. Takane, Thin Film Thickness Gradients and Spatial Patterning via Salt Etching of Polyelectrolyte Multilayers, *Macromolecules*, 2007, **40**, 5479-5486.
- ⁸⁴ Z. Gui, B. Du, J. Qian, Q. An, Q. Zhao, Construction and deconstruction of multilayer films containing polycarboxybetaine: Effect of pH and ionic strength, *J. Coll. Interf. Sci.*, 2011, **353**, 98-106.
- ⁸⁵ S.D. Wang, F.H. Huang, Antireflection coatings formed from polyelectrolyte multilayers on PMMA substrate, *Surf. Eng.*, 2011, **27**, 279-285.
- ⁸⁶ S.Y. Yang, M. F. Rubner, Micropatterning of Polymer Thin Films with pH-Sensitive and Cross-linkable Hydrogen-Bonded Polyelectrolyte Multilayers, *J. Am. Chem. Soc.*, 2002, **124**, 2100-2101.
- ⁸⁷ W.S. Ang, N.Y. Yip, A. Tiraferri, M. Elimelech, Chemical cleaning of RO membranes fouled by wastewater effluent: Achieving higher efficiency with dual-step cleaning. *J. Membr. Sci.*, 2011, **382**, 100-106.
- ⁸⁸ Y. Liu, B. Mi, Combined fouling of forward osmosis membranes: Synergistic foulant interaction and direct observation of fouling layer formation. *J. Membr. Sci.*, 2012, **407**, 136-144.

- ⁸⁹ W. Shana, P. Bacchin, P. Aimar, M.L. Bruening, V.V. Tarabara, Polyelectrolyte multilayer films as backflushable nanofiltration membranes with tunable hydrophilicity and surface charge, *J. Membr. Sci.*, 2010, **349**, 268–278.
- ⁹⁰ M. Pontié, S. Ben Rejeb, J. Legrand, Anti-microbial approach onto cationic-exchange membranes, *Sep. Purif. Technol.*, 2012, **101**, 91–97.
- ⁹¹ Y. Kang, S. Zheng, C. Finnerty, M.J. Lee, B. Mi, Regenerable Polyelectrolyte Membrane for Ultimate Fouling Control in Forward Osmosis, *Env. Sci. Technol.*, 2017, **51**, 3242–3249.
- ⁹² W.M. de Vos, A. de Keizer, M. A. Cohen Stuart, J. M. Kleijn, Thin polymer films as sacrificial layers for easier cleaning, *Coll.Surf. A: Physicochem. Eng. Aspects*, 2010, **358**, 6-12.
- ⁹³ J. Hiller, J. D. Mendelsohn, M. F. Rubner, Reversibly erasable nanoporous anti-reflection coatings from polyelectrolyte multilayers, *Nature*, 2002, **1**, 59-63.
- ⁹⁴ S.S. Ono, G. Decher, Preparation of Ultrathin Self-Standing Polyelectrolyte Multilayer Membranes at Physiological Conditions Using pH-Responsive Film Segments as Sacrificial Layers, *Nano Lett.*, 2006, **6**, 592–598.
- ⁹⁵ J. Lichter, K. Van Vlietpa, M. Rubner, Design of antibacterial surfaces and interfaces: Polyelectrolyte multilayer as multifunctional platform, *Macromolecules*, 2009, **42**, 8573-8586.
- ⁹⁶ B. Su, T. Wangb, Z. Wangb, X. Gaoa, C. Gao, Preparation and performance of dynamic layer-by-layer PDADMAC/PSS nanofiltration membrane, *J. Membr. Sci.*, 2012, **423-424**, 324–331.

Chapter 6 Conclusion and future work

6.1 Conclusions

The work of this thesis describes very different but necessary aspects in the design of nanostructured inorganic photoactive materials for water treatment applications. The main accomplishment of this project can be summarised in three key points:

- The development of a very fast synthesis (Flash Microwave-assisted Hydrothermal/solvothermal synthesis or FMH) for nanostructured TiO₂ microspheres, with morphology and internal structure easily controllable through few synthesis parameters and without use of surfactant or other templating agents;
- The fulfilment of optimal photocatalytic performance under visible light irradiation for both as-synthesised TiO₂ particles and after annealing under vacuum post-synthetic treatment, outperforming in some cases commercial catalyst, notably Aeroxide® P25;
- The integration of TiO₂ particles into a composite coating designed for ultrafiltration membranes, producing multifunctional coatings with some promising application properties, such as hydrophilic/superhydrophilic behaviour by tuning the coating conditions;

Flash Microwave-assisted Hydrothermal/Solvothermal (FMH) synthesis proved to be an efficient, rapid and easy method for the rapid synthesis of nanostructured TiO₂ submicroparticles with hierarchical mesoporosity. The novelty of the approach consisted in the application of constant MW power inspired to acid digestion of inorganic materials to obtain a surfactant-free and template-free synthesis. The particles obtained by this MW-assisted technique proved a good balance of morphological and structural properties, with better morphological features (shape, size distribution) as a major improvement compared to other “explosive” synthesis methods that can be characterised by very fast particle formation kinetics. An almost perfect spherical structure was achieved with the additional advantages of the low toxicity of the reactants and the absence of templating molecules or surfactants.

The accurate selection of the experimental parameters provided a valuable control of the synthesis, despite the lack of direct control over conditions such as temperature and pressure. Synthetic and operational parameters can strongly influence crystalline phase, structure of the particles and their size distribution. For instance, the use of ethanol as a solvent is a key parameter in the formation of spherical particles, since it slows the fast hydrolysis of the precursors. Additional control of the particle characteristics was achieved by modification of other synthesis conditions such as the type and concentration of the acid and precursor. The concentration of this last plays a dominant role in controlling the size of the final secondary particles, with particle diameters as small as 200 nm for the minor concentration used (40 mM of precursor). The selection of the acid and its concentration is determinant for the control the resulting product characteristics. HNO_3 enhance the formation of smaller spherical particles and ensure the production of pure anatase. The internal structure of these spherical particles is composed of smaller crystallites of nanometric size, ranging from 2 to 15 nm. TEM images revealed a dense agglomeration of the crystallites composing the spheres. HCl led to higher probability of forming rutile and the formation of a completely different particle internal structure (acicular nanorods growing radially from the centre). Increasing the acidity also led to smaller particles, narrower size distribution and larger surface areas (200-400 m^2/g using 2 M HNO_3 in ethanol). The FMH- TiO_2 particles contain a wide range of porosity, formed by the intergranular void between crystallites conferring microporosity and the formation of larger mesopores (10-50 nm of diameter). The pore size distribution is controllable via the synthesis parameters. Calcination treatment significantly improved homogeneity, with modification of the internal structure of the microparticles and the reorganisation of the porosity in more regular and cylindrical shape at relatively low calcination temperature. At conventional calcination temperatures (673-773 K), the particles lost their mesoporous structure and, as a consequence, the surface area was drastically reduced. A very important characteristic of the FMH- TiO_2 particles is the influence of the nanostructure on the macroscopic properties. Besides the large surface area, increase (blue-shift) of the optical band gap and modification of the Raman modes denote that the secondary submicrometric particles are acting as a “container” for the smaller nanocrystallites, hence transferring their properties to the larger particles.

Annealing under vacuum was successfully employed to activate the FMH-TiO₂ in terms of absorption capacity of visible light, improving the generation of radicals potentially useful for Advanced Oxidation Processes (AOPs) in water purification. Other techniques such as selective calcination in air (aiming the optimal composition in terms of proportion between anatase and rutile) or ammonolysis (one of the simplest nitrogen-doping technique) failed in the achievement of the optimal photocatalytic performance principally because of the loss of surface area and the uncontrolled increase of structural disorder. On the other hand, vacuum activation partially preserved the adsorption capacity observed for the as-synthesised particles and allowed satisfying degradation results (towards rhodamine B, used as representative model of organic pollutant) due to the formation of Ti³⁺ superficial defects and oxygen vacancies. The introduction of these stoichiometric defects in the TiO₂ structure allowed efficient modification of the electronic properties, with reduction of the optical band gap in the range 1.9-2.8 eV, depending on the synthesis conditions, without compromising the migration process of the photogenerated charges from the bulk to the particle surface. More severe post-synthesis treatment, such as temperature higher than 773 K or heavily reducing atmosphere such as NH₃, led to generation of non-optimal concentration of recombination centres, quenching electrons and holes before they could reach the surface and hence compromising the overall photoactivity. Vacuum heating under low vacuum (2 to 5 Pa) at 773 K resulted to be the optimal conditions for the improvement of the photocatalytic properties. Remarkably, also the as-synthesised particles showed photoactivity under visible-light, with degradation rate partially higher than P25, the undisputed benchmark among TiO₂ photocatalysts. The two-stage process involves a first rapid de-ethylation of the rhodamine and a slower cleavage of the chromophore group. In particular, rhodamine is de-ethylated even four times faster by the FMH-TiO₂ particles than in presence of P25. In P25, vacuum heated FMH-TiO₂ particles and anatase in general, the two processes occur at the same time, with uniform decolouration of the initial purple colour of the rhodamine. The selective de-ethylation of the as-synthesised particles led to the rapid transformation of the solution colour in yellow, indicating achievement of the fully de-ethylated product (identified as rhodamine 110).

The surface properties of the FMH-TiO₂ particles are at the basis of their success in photocatalysis in the selective de-ethylation of rhodamine by the as-synthesised

particles and the good performance of the vacuum heated particles. In both cases, the initial adsorption capacity is exceptionally higher compared to P25, which surface adsorbed rhodamine for only 3% of the initial concentration, compared with an average of 10% (with peaks of 18%) in case of the untreated particles and up to 80% observed in some vacuum-activated sample. The initial adsorption capacity is directly correlated to the photocatalytic performances, with the higher degradation rate observed in case of strong adsorption capacity under dark, where the adsorption-desorption equilibrium between molecule and particle surface is achieved.

Concerning the integration of inorganic particles in order to create a multifunctional surface for AOPs, the deposition of TiO₂ nanoparticles (Aeroxide P25) and micron-sized particles (commercial anatase) was successfully performed on different surfaces (active layer of polymer membranes, Mylar, borosilicate glass slide) by means of electrostatic interactions with water-soluble charged polymer assembled in a composite multi-layered structure. Modification of the surface properties was observed, with an increase in surface roughness and change in wettability and optical properties. The stepwise adsorption of polyelectrolyte and inorganic particles was followed by SPR. Higher concentration of TiO₂ provided higher density of superficial charge, allowing the deposition of further layers through charge overcompensation mechanism. This phenomenon was successfully associated to the thicker multilayer produced increasing the ionic strength of the polyelectrolyte solution. The more opened structure of these multilayers play a determinant role in the interaction between particles and polymer chains, with enhancement of the TiO₂ properties transferred to the coating, such as hydrophilic behaviour. The presence of TiO₂ had the general effect to improve the hydrophilicity of the coated surfaces. In particular, the combination of TiO₂ particles with multilayer structures built with polyelectrolyte solution with high ionic strength resulted in superhydrophilic surfaces (Mylar foil) even without exposure to UV light, as it is usually reported for TiO₂.

The coating technique was significantly improved modifying the classic immersion coating with a design able to reduce the cross-contamination, due to release of particles in the polyelectrolyte solution, and to obtain more uniform and stable coatings. The multilayers assembled by using this method demonstrated higher homogeneity, providing a significant step forward towards integration in filtration systems.

The permeability of the original membranes was preserved reducing the immersion time during the deposition step, while it was extremely reduced using the conventional number of bi-layer reported in literature (up to 50% of the original permeability) and even further thickening the multilayer structure increasing the ionic strength of the polyelectrolyte solution (up to 95%). However, the mechanical stability of the multilayer affecting the less the permeability is not suitable for post-fouling operation (e.g. physical cleaning), with detachment of the coating. Despite this drawback, the principle of selective destabilisation of the multilayer can be successfully implemented in terms of sacrificial/regenerable active layer, replacing the part of the membrane exposed to fouling with a freshly-made new layer, extending the membrane life-time. Tuning the ionic strength proved to be an efficient way, with the stability of the multilayer challenged by the presence of electrolytes in the feed solution.

6.2 Future works

The results reported in this thesis revealed promising information about the application of microwave heating in the ultra-rapid synthesis of nanostructured inorganic particles and their applications as visible-light photocatalysts and in membrane functionalisation. However, several other research aspects are worth of further investigation. The main ones can be outlined as follows:

- Design improvement for the Flash Microwave-assisted Hydrothermal (FMH) synthesis for a better reproducibility/scalability of the process;
- Investigation on the “pulsed” synthetic approach;
- Elucidation of the eventual role of the impurities in structural and photocatalytic properties;
- Improvement of the stability of the TiO₂-PEM composite coating;
- Assessment of antifouling and antibacterial properties of the TiO₂ particles integrated on the membrane surface
- Detailed investigation about the selective removal of part of or of the entire multilayer in order to develop a sacrificial/regenerable approach for the active layer of filtration membranes;

The Flash Microwave-assisted Hydrothermal (FMH) technique benefits from very fast synthesis times, outclassing even the “conventional” MW-assisted synthesis, based on the control of temperature by tuning the MW power. However, the pressure values involved in the FMH synthesis require the improvement of the experimental design, with stricter control of the internal conditions of the reactor. The advances in microwave technology over the last decades have allowed the development of instruments with more precise control of reaction pressure and temperature. Single-mode cavity and larger multimode MW furnaces are evolving towards being able to reproduce optimal synthesis conditions, with reactors withstanding pressure comparable with those achieved in the autoclaves (80-100 bars) both in conventional and multimode microwave reactors. The success of such bespoke MW equipment should allow processes to be subsequently scaled up. Despite the commercialisation of dedicated device, MW cavity and reactor design still represents a challenge in terms of reproducibility and predictability of the synthesis, most of all in processes in which several parameters can affect the resulting product, such as in hydrothermal growth of inorganic particles. A better control of the synthesis condition would give easier access to the properties highlighted in this thesis, including better control of the photocatalytic properties.

Without resorting to a drastic change of design, the proposed setup (multimode reactor and MW-transparent autoclave) can be more efficiently used adopting a “pulsed” approach, with repetition of short MW treatment. The lack of control over internal conditions and the autogenous pressure build-up strongly limits the duration of the reactions at constant MW power. The “pulsed” approach was successfully tested during the thesis but not fully implemented, giving promising preliminary results in terms of higher control of porosity and crystallinity in the particles, for example the reduction of the surface area from 490 to 280 m²/g from the 1st to the 5th cycle of MW heating (section 3.6.2). The development of this reaction pathway would require further studies of kinetics and mechanisms of the particle formation, since the MW treatment is performed over an already pre-formed colloidal suspension rather than a uniform precursor solution, changing the type of hydrothermal approach (according to the classification mentioned in section 1.8.1).

Microparticles with nanocrystalline structure similar to the one of the FMH-TiO₂ particles have been successfully employed in photovoltaic and photochemical

technology such as dye sensitised solar cell (DSSC). Further test could be performed on the FMH-TiO₂ particles, exploring properties such as conductivity or electrochemical measurements, assessing the potential exploitation of this synthesis for other applications.

The role of the carbon and nitrogen impurities in the FMH-TiO₂ particles needs further investigation. The presence of NO/N₂O might have a role in the formation of the mesoporous structure of the particles synthesised using HNO₃ and ethanol. The presence of the impurities affected the electronic structure of the sample, introducing localised states observed by means of the Urbach tails in the absorption spectra of the as-synthesised particles. Calcination treatments removed the impurities and subsequently the localised states. It is not clear if the presence of these impurities can be advantageous in terms of non-metal doping method. As mentioned in chapter 4, examples of “carbon self-doping” exploiting the residual presence of the organic precursor have been reported in the past. The presence of carbon in the FMH-TiO₂ particles might be one of the reason of the selective de-ethylation of rhodamine B under visible light, with organic moieties in the surface providing further interaction sites for the molecule. More detailed investigation, such as XPS analysis with higher sensitivity towards carbon or X-ray absorption near edge structure (XANES) would be necessary to clarify the role of the impurities in the electronic structure of the particles.

From the point of view of the production of a multifunctional coating for environmental applications (in particular filtration membranes), the deposition of a nanocomposite TiO₂-PEM coating is a simple and versatile method to confer novel properties on every kind of surface. However, the mechanical stability of the assembled structure still represents a challenge. Use of different polyelectrolytes (*e.g.* branched PEI), tuning the assembly conditions could all potentially improve the stability of the multilayer. To provide an example, the effect of the ionic strength and the rinsing water on the final properties was briefly explored in section 5.4.7.4. In alternative, several post-deposition treatments can be also applied, such as chemical or thermal crosslinking, exposure of the multilayer to different pH or ionic strength solutions. However, the enhancement of the mechanical stability should correspond to an acceptable compromise with the filtration properties, in particular permeability and solute rejection (MWCO). The selectivity of the membrane can be dramatically affected by applying few polyelectrolyte layer. The application of more stable multilayer to membrane with

higher permeability or larger inner pore network, such as microfiltration, could represent a potential solution to produce membrane suitable for ultrafiltration process (e.g. removal of organic matter from water).

The same concerns can be considered about the stability of the adhesion of the TiO₂ particles in the multilayer structure. Further polyelectrolyte bi-layers can be applied reinforcing the multilayer and enhancing the cohesion of the particles, even though this solution would be detrimental for permeability and selectivity of the membranes. A more efficient stabilisation could be provided by functionalising the particles with appropriate chemical moieties. Polyelectrolytes can help also in this case, with the assembly of a PEM-based multifunctional shell. Several studies reported in the literature have demonstrated the possibility of producing a layer-by-layer shell using the same polyelectrolyte, improving the colloidal stabilisation of the particles in solution (as also described in section 5.3.3). The functionalised particles should experience enhanced interactions with the PEM coating, improving the adhesion of the particles and the resistance of the entire structure. The ultimate integration of the FMH-TiO₂ particles directly within the multilayer was not explored in this thesis, but it would be an interesting development for the demonstration of the full capability of these particles. From the theoretical point of view, the PEM structure should be able to sustain the incorporation of the submicroparticles up to a certain size, since the TiO₂ particles tested formed micrometric agglomerates in solution and hence onto the coated surface. Moreover, the high surface area of the microparticles can enhance the interaction with the multilayer.

The application of the improved hydrophilicity of the surfaces and the direct effect of the presence of TiO₂ onto the membrane surface should be assessed in terms of antifouling and antibacterial activity. For example, the same combination of TiO₂ particles/polyelectrolytes conferring superhydrophilicity to Mylar foil was not as effective on the membranes, confirming the relevance of the influence of the original substrate on the overall properties of the coating. The enhancement of the surface wettability and the exposure of cationic polyelectrolyte as the outermost layer of the coating are two of the potential solutions proposed against bacterial adhesion and resistance and to prevent the establishment of biofouling. The application of the TiO₂-PEM multifunctional coating in photocatalysis could be a simple and effective method to assess the

transfer of the TiO₂ properties to the coated surface, comparing the degradation power of the functionalised surface with that of the particles.

As a final point, another interesting aspect worthy of exploration is the production of a sacrificial layer. The destabilisation of PEM assemblies observed during fouling tests was caused by exposure of the structure to specific conditions such as pH or ionic strength. Selective destabilisation can lead to the removal of fouled outermost layers, providing a fresh and clean surface, which can be also renewed with a new deposition procedure. The design of an integrated system for PEM deposition and filtration purposes would extend the lifetime operation of a membrane avoiding its replacement. For instance, cross-flow filtration would provide a more representative condition with respect to the dead-end configuration adopted in this project. An effective way to recover the removed coating and particles and to provide *in situ* the active surface of the membrane with a new multifunctional coating should be the key points for a promising re-design of the experiment.

Appendices

Appendix A: Figures and tables for Chapter 3

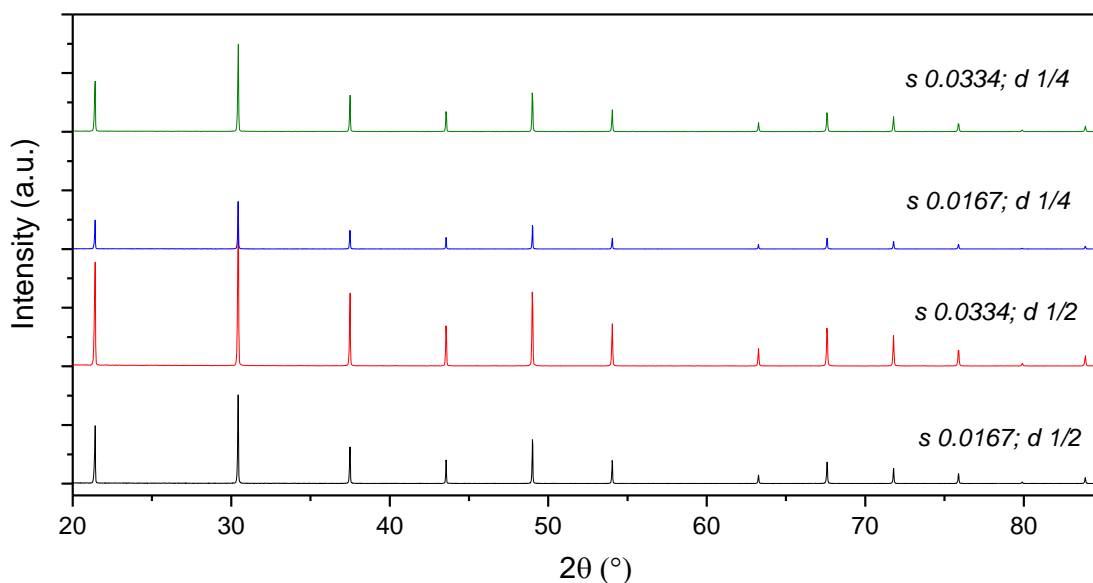


Figure A.1: PXD pattern of LaB₆ (Aldrich, 99%) using different instrumental conditions, specifically the step size (“s”) and the divergence slit (“d”), both in angular values.

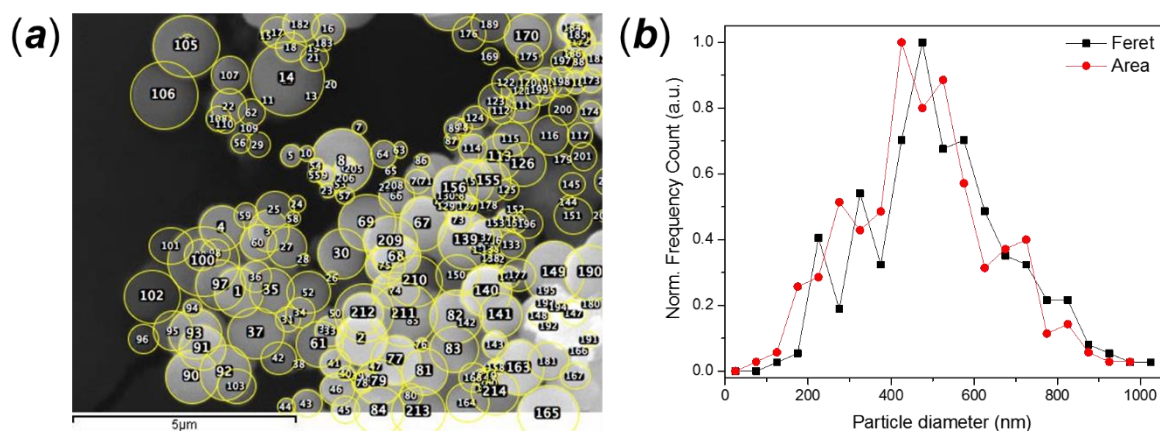


Figure A.2: (a) Particle size counting method by using the ImageJ software and (b) comparison between particle diameter distribution using the approximating the particle to perfect spheres compared with the Feret's diameter.

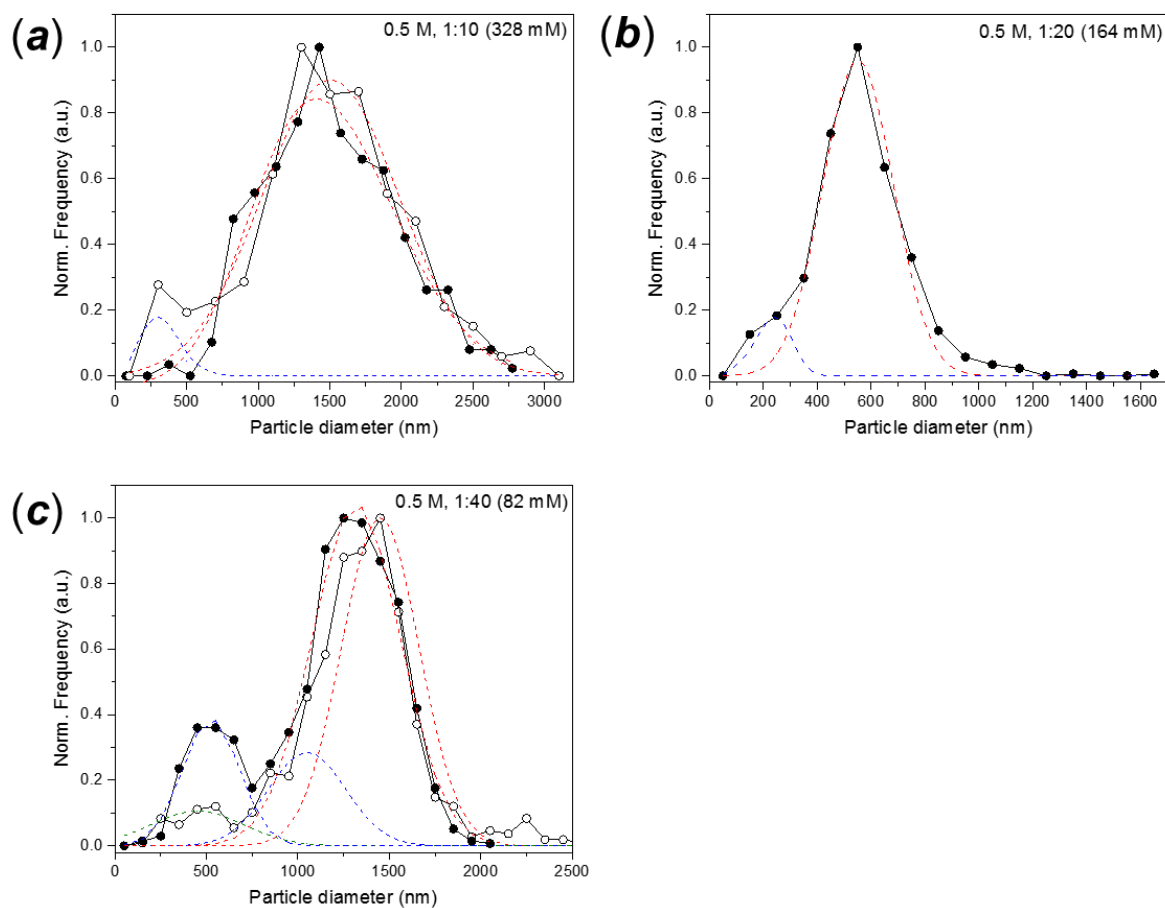


Figure A.3: Particle size distribution of FMH-TiO₂ particles, NE series produced using 0.5 M HNO₃ solution and a precursor concentration of (a) 328 mM, (b) 164 mM and (c) 80 mM. The dots indicate the centre of the frequency bin, connected by continuous lines. The dotted lines indicate the Gaussian distribution calculated using the Fityk software. Different colours were used in case of multiple size distributions.

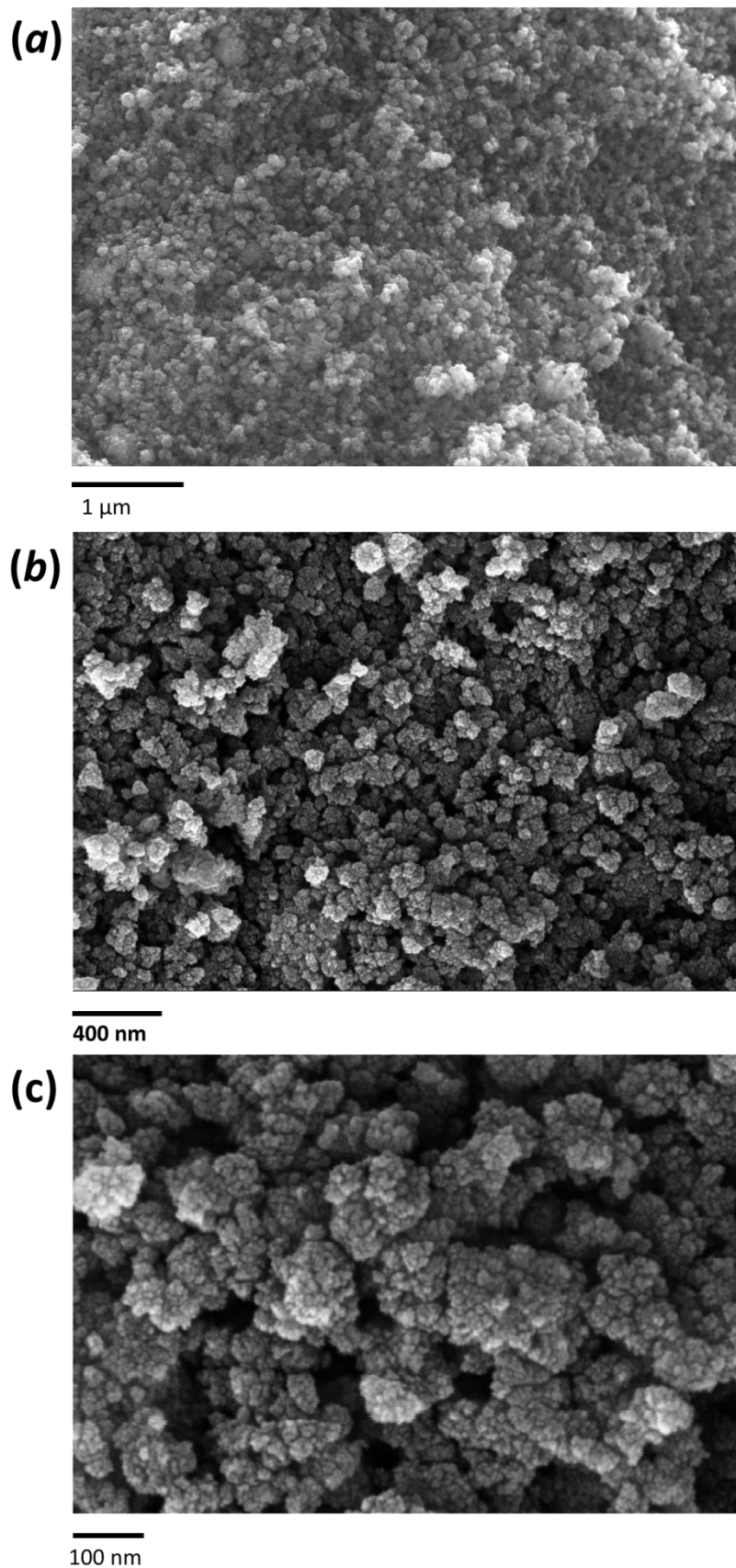


Figure A.4: SEM images of particles from the CW series (2 M HCl in water, 162 mM precursor concentration, 90 s MW treatment) at different magnification: (a) 50000X; (b) 100000X and (c) 300000X.

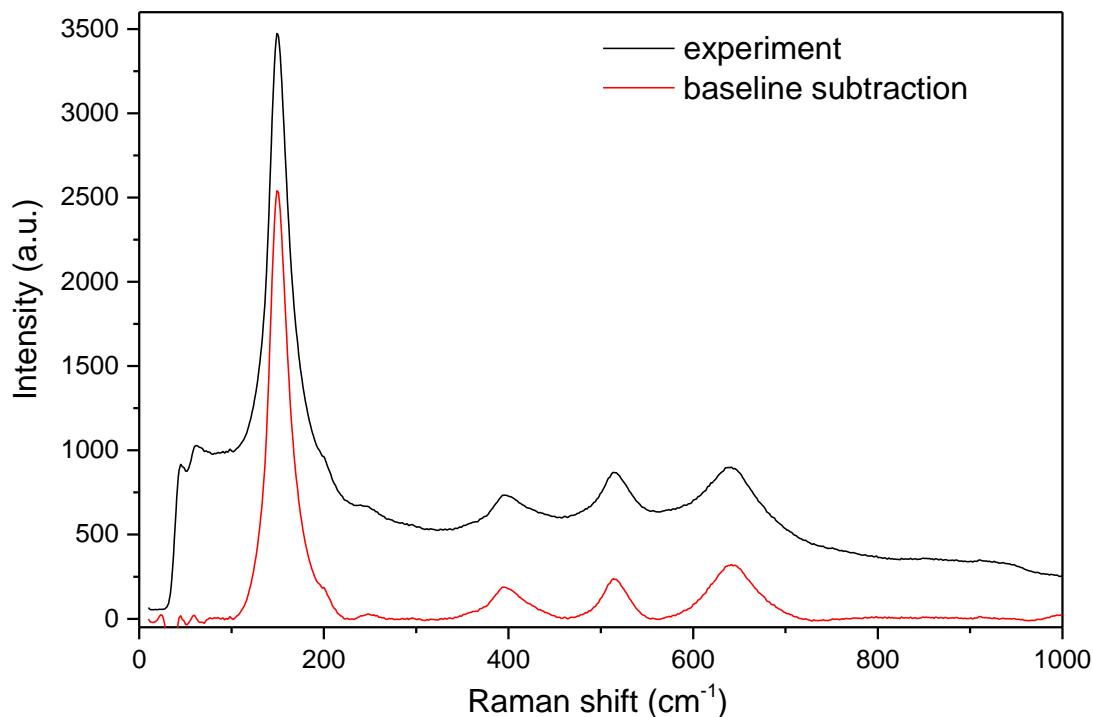


Figure A.5: Example of Raman spectra baseline subtraction using the 8-degree polynomial fit. (sample from the *NE* series, 1 M HNO_3 , 162 mM precursor, 1 min MW treatment).

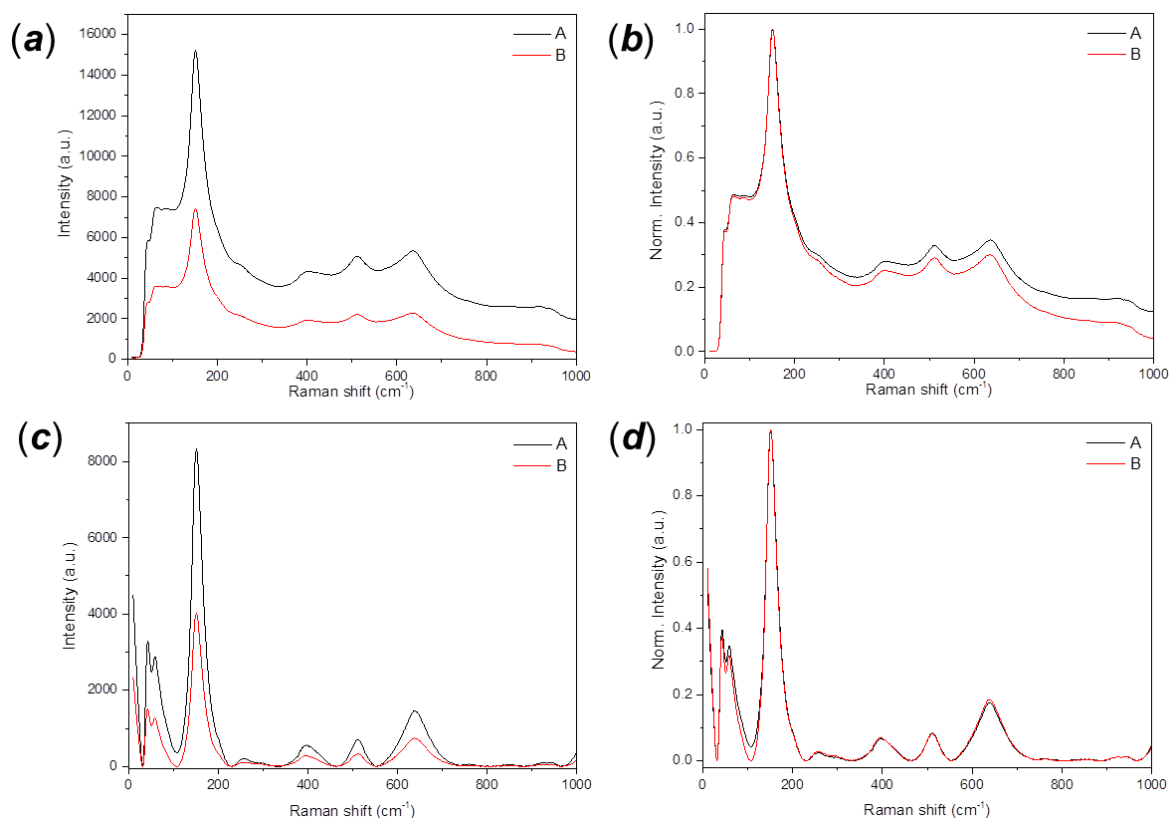


Figure A.6: Example of Raman spectra normalisation procedure. The sample (*NE* series, 1 M HNO_3 , 162 mM precursor, 1 min MW treatment) was collected using different acquisition time (A: 5 s; B: 10 s). (a) represents the spectra as they were collected; in (b) the spectra are normalised without baseline subtraction; in (c) baseline subtraction is applied to the two spectra and finally in (d) the spectra of (c) are normalised for the maximum of the most intense peak (E_{g_1} mode).

Table A.1: Error calculation estimated for the optical band gap measurement of commercial materials

	Intercept	(σ)	Slope	(σ)	Adj R ₂	E _g (eV)
Anatase	-40.264	0.49	12.411	0.141	0.9959	3.244
	-42.708	0.42	13.146	0.123	0.9975	3.248
	-42.020	0.45	12.951	0.131	0.9967	3.245
<i>average</i>						3.246
Rutile	-4083.13	65.5	1310.4	20.41	0.9961	3.116
	-4638.38	34.4	1485.7	10.78	0.9995	3.122
	-4187.26	38.2	1342.4	11.97	0.9990	3.119
<i>average</i>						3.119

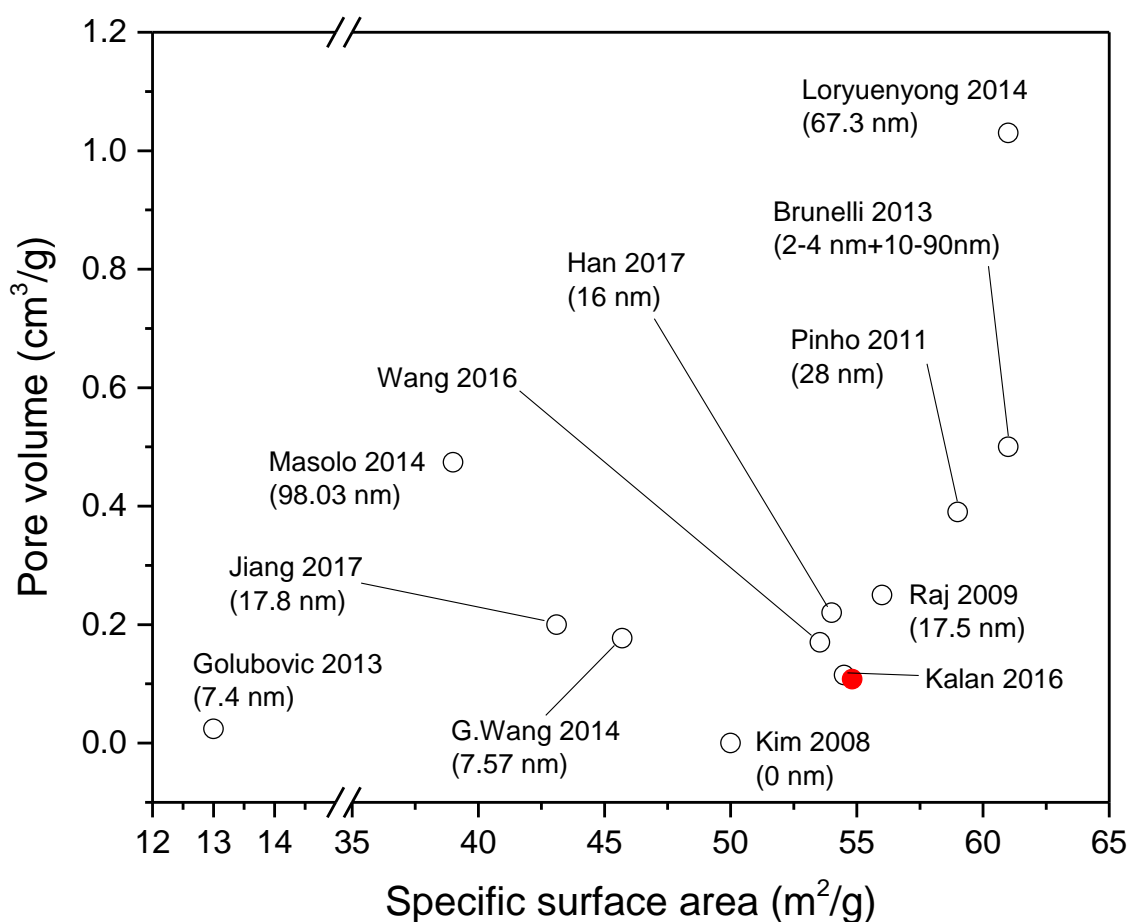


Figure A.7: Comparison among the different values reported for the surface area and the pore volume of Aerioxide® P25, with the estimated average pore size reported in brackets (when reported)

Table A.2: Comparison among the different values of surface area, pore volume and average pore size in the recent literature for Aeroxide® P25.

Work	Surface area (m ² /g)	Pore volume (cm ³ /g)	Pore size (nm)	Ref
Evonik	50 ± 15			[2]
Raj (2009)	56	0.25	17.5	[3]
Brunelli (2013)	61	0.5	2-4/10-90	[4]
Wang (2016)	53.54	0.17	n.r	[5]
Kim (2008)	50	n.obs	n.obs	[6]
Masolo (2014)	39	0.474	98.03	[7]
Loryuenyong (2014)	61	1.03	67.3	[8]
C.Wang (2014)	45.7	0.177	7.57	[9]
Pinho (2011)	59	0.39	28	[10]
Golubovic (2013)	13	0.024	7.4	[11]
Han (2017)	54	0.22	16	[12]
Kalan (2016)	54.5	0.115	n.r	[13]
Jiang (2017)	60.8	n.r.	17.8	[14]
Riaz (2012)	43.1	0.20	18.5	[15]
Pino (2012)	93.7	0.304	10.7	[16]
L.Wang (2008)	49.6	n.r.	n.r.	[17]
Zuccheri (2016)	43	n.r.	n.r.	[18]

² Evonik industries, AEROXIDE®, AERODISP® and AEROPERL® Titanium Dioxide as Photocatalyst, (Technical Information 1243)

³ K.J.A. Raj *et al.*, *Indian J. Chem.*, 2009, **48A**, 1378-1382.

⁴ A. Brunelli *et al.*, *J. Nanopart. Res.*, 2013, **15**, 1684-1688.

⁵ W. Wang *et al.*, *Bioresources*, 2016, **11**, 3084-3093

⁶ E. Kim *et al.*, *Bull. Korean Chem. Soc.*, 2009, **30**, 1

⁷ E. Masolo *et al.*, *Nanomaterials* 2014, **4**, 583-598

⁸ V. Loryuenyong *et al.*, *Adv. Mat. Sci. Eng.*, 2014, 348427.

⁹ C. Wang *et al.*, *App. Surf. Sci.*, 2014, **319**, 2–7.

¹⁰ L. Pinho *et al.*, *J. Phys. Chem. C*, 2011, **115**, 22851–22862.

¹¹ A. Golubovic *et al.*, *Mat. Res. Bullet.*, 2013, **48**, 1363–1371.

¹² E. Han *et al.*, *Catalysis Today* (Available online 30 August 2017)

¹³ E. Roghi *et al.*, *App. Cat. B: Environ.*, 2016, **187**, 249–258.

¹⁴ X. Jianga, *et al.*, *Catalysis Today* (Available online 20 June 2017)

¹⁵ N. Riaz, *et al.*, *Chem. Eng. J.*, 2012, **185–186**, 108–119.

¹⁶ E. Pino *et al.*, *J. Photochem. Photobiol. A: Chem.*, 2012, **242**, 20–27.

¹⁷ L. Wang *et al.*, *J. Haz. Mat.*, 2008, **152**, 93–99.

¹⁸ T. Zuccheri, *et al.*, *Materials*, 2013, **6**, 3270-3283

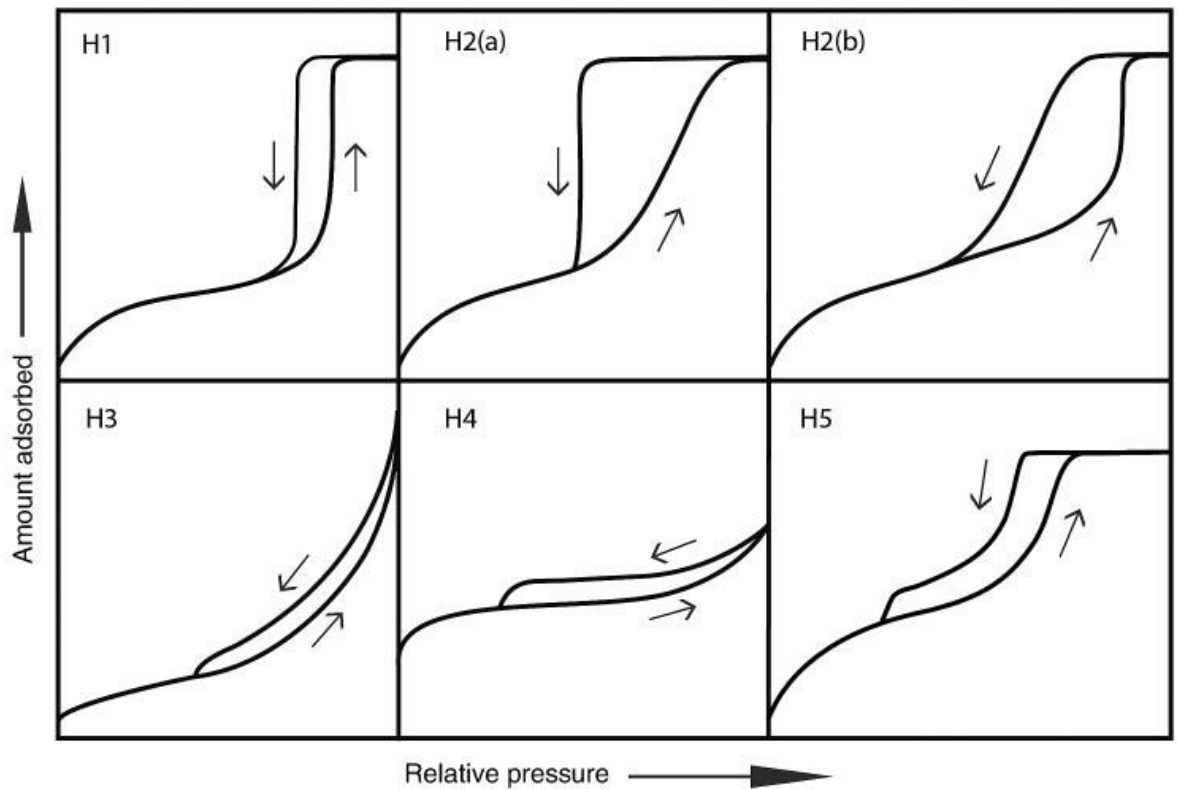


Figure A.8: Classification of the hysteresis loop in mesoporous material, in which capillary condensation occurs, according to Thommes *et al.* [19]

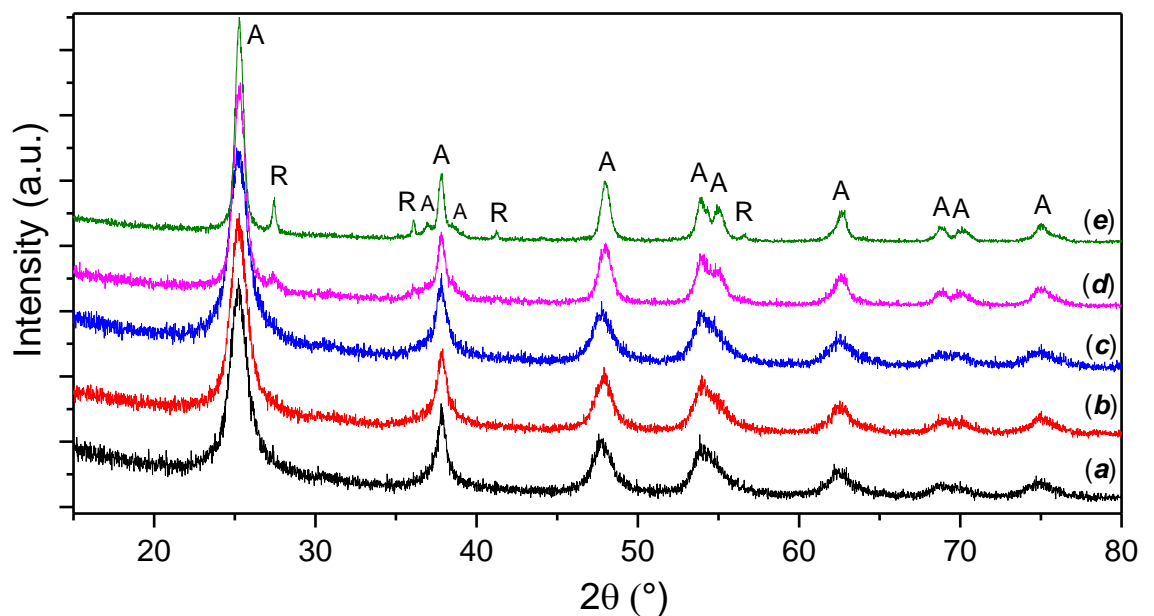


Figure A.9: PXD patterns for the CW series of FMH-TiO₂ particles (TTIP conc. 164 mM, HCl 2 M solution) as a function of the MW treatment time: (a) 30 s; (b) 60 s; (c) 90 s; (d) 120 s; (e) 150 s.

¹⁹ M. Thommes *et al.*, *Pure Appl. Chem.*, 2015, **87**, 1051–1069.

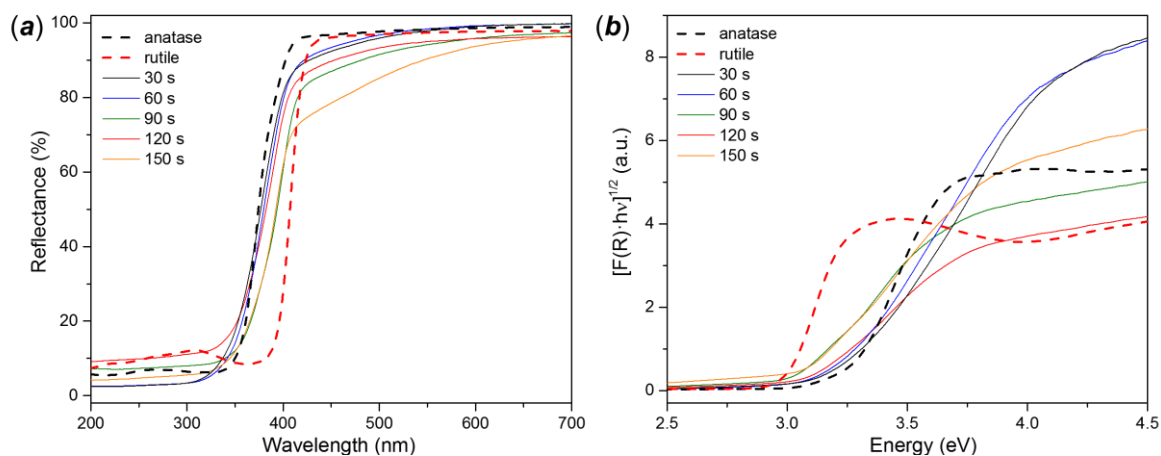


Figure A.10: (a) reflectance spectra and (b) Kubelka-Munk function for the calculation of the indirect band gap of FMH-TiO₂ particles (CE series, 2 M HCl in ethanol, 164 mM TTIP concentration) for different MW treatment time, compared with reflectance and Kubelka-Munk functions of bulk anatase and rutile. The calculated values of band gap are reported in Table 3.8.

Table A.3: Coefficient for the exciton quantum confinement equation for the Raman peak broadening and redshift.

	<i>Xue et al.</i>	<i>Zhu et al.</i>
A (cm ⁻¹)	128.7	127
B (cm ⁻¹)	226.1	270
Γ ₀ (cm ⁻¹)	8.99	7
γ	1.497	1.32
γ'	1.497	1.29

Table A.4: relative intensity of the mass spectrometer signal of the lighter molecules containing carbon and nitrogen atoms (from reference [20])

MW (g mol ⁻¹)	NO ₂	NO	N ₂ O	CO	CO ₂	N/N ₂	O/O ₂
12	-	-	-	3.54	8.62	-	-
14	7.32	9.52	12.82	-	-	13.15	-
15	2.20	-	0.01	-	-	-	-
16	1.30	22.24	4.90	0.51	9.52	-	21.8
28	-	-	10.72	100	9.72	100	-
29	-	-	0.01	0.01	0.01	0.01	-
30	100	100	31.06	-	-	-	-
31	0.20	-	0.01	-	-	-	-
32	0.10	-	-	-	-	-	100
44	-	-	100	-	100	-	-
45	-	-	0.60	-	1.1011	-	-
46	-	36.97067	-	-	0.3003	-	-

²⁰ NIST Chemistry WebBook (<http://webbook.nist.gov>, accessed on December 2017)

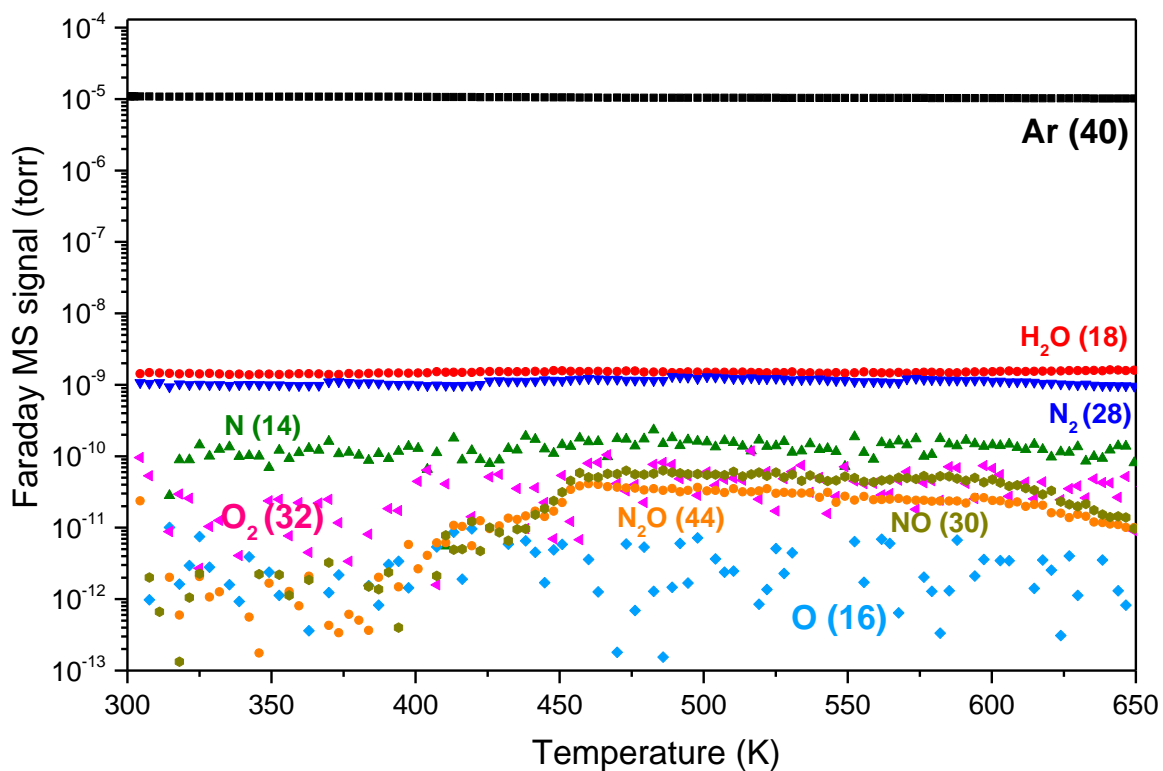


Figure A.11: Absolute values (in pressure) of the different signal detected during the MS analysis of the evolved gas by heating the FMH-TiO₂ particles

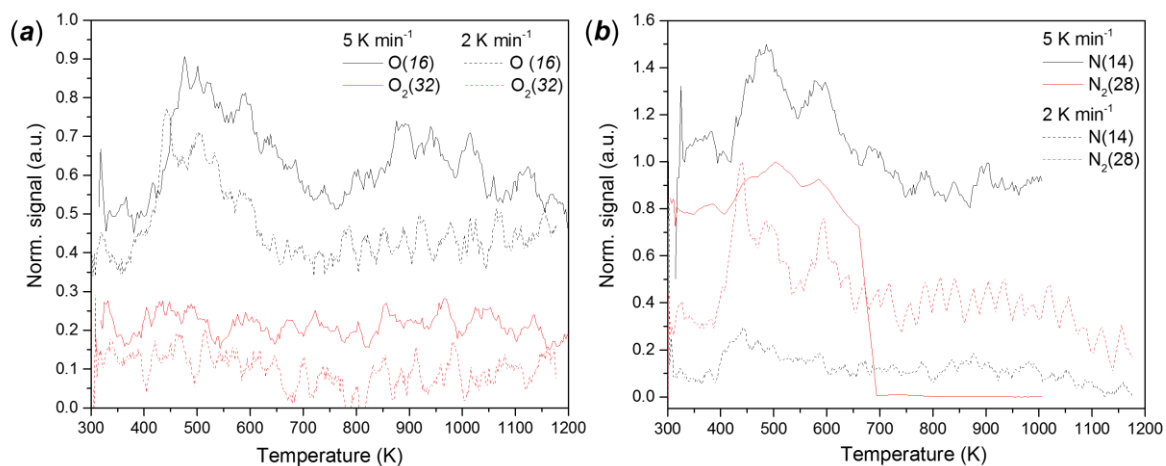


Figure A.12: Evolved gas MS for the signal relative to (a) N₂ and N and (b) to molecular O₂ and atomic O for the selected FMH-TiO₂ sample (NE series, 2 M, 324 mM).

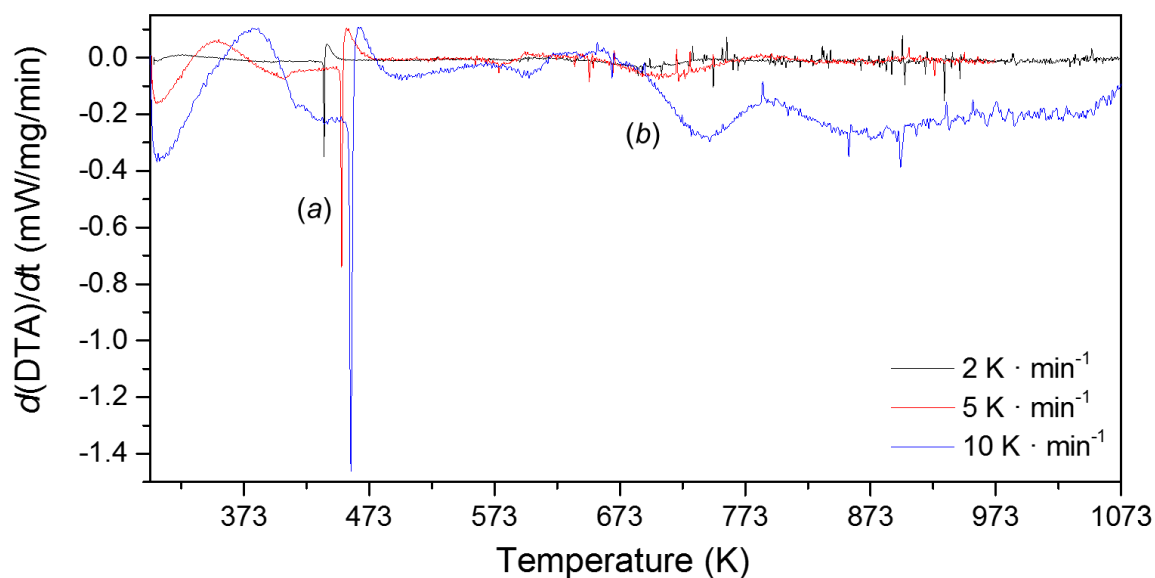


Figure A.13: Differential DTA of the sample *NE* series, 2 M, 324 mM (shown in Figure 3.51) with the peak (a) relative to the release of gaseous impurities and the peak (b) probably indicating the phase transition.

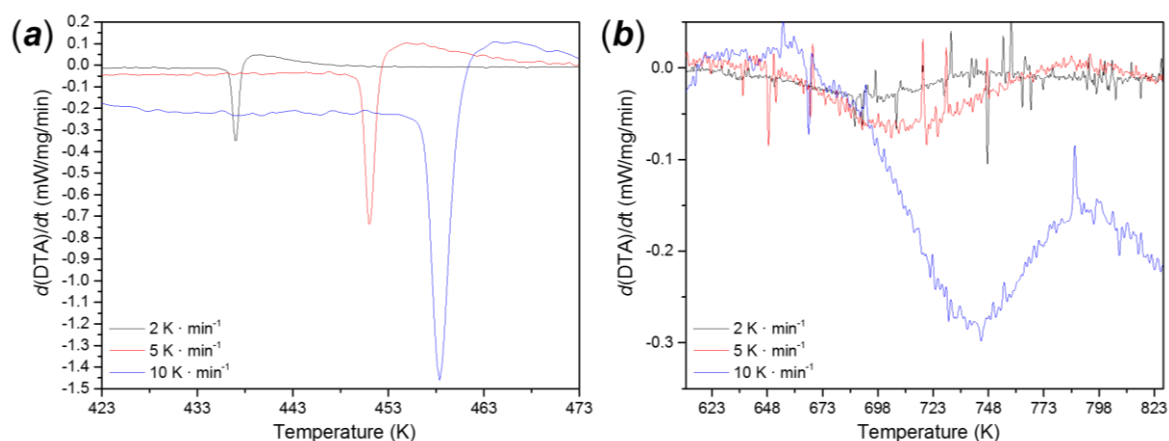


Figure A.14: Detail of (a) peak (a) and (b) peak (b) reported in Figure A.13

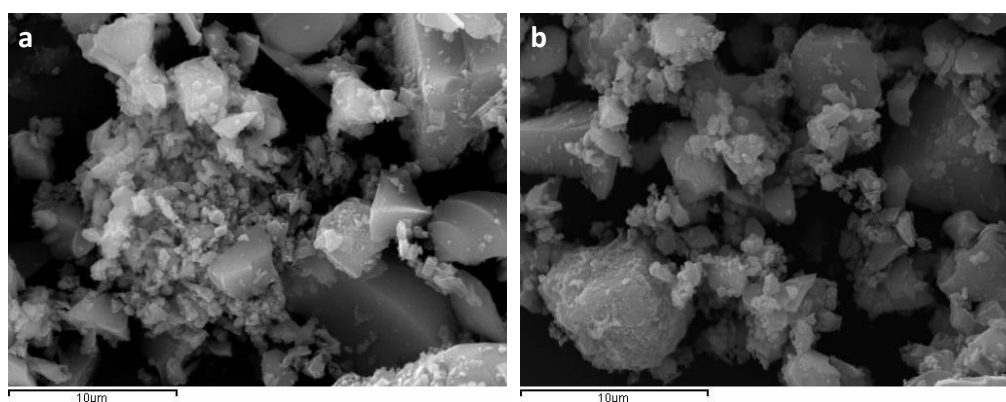


Figure A.15: SEM images of the products of the flash MW-assisted reactions performed using 50 mM (a) and 200 mM (b) of HCl in ethanol (164 mM precursor concentration, 90 s MW treatment at full power)

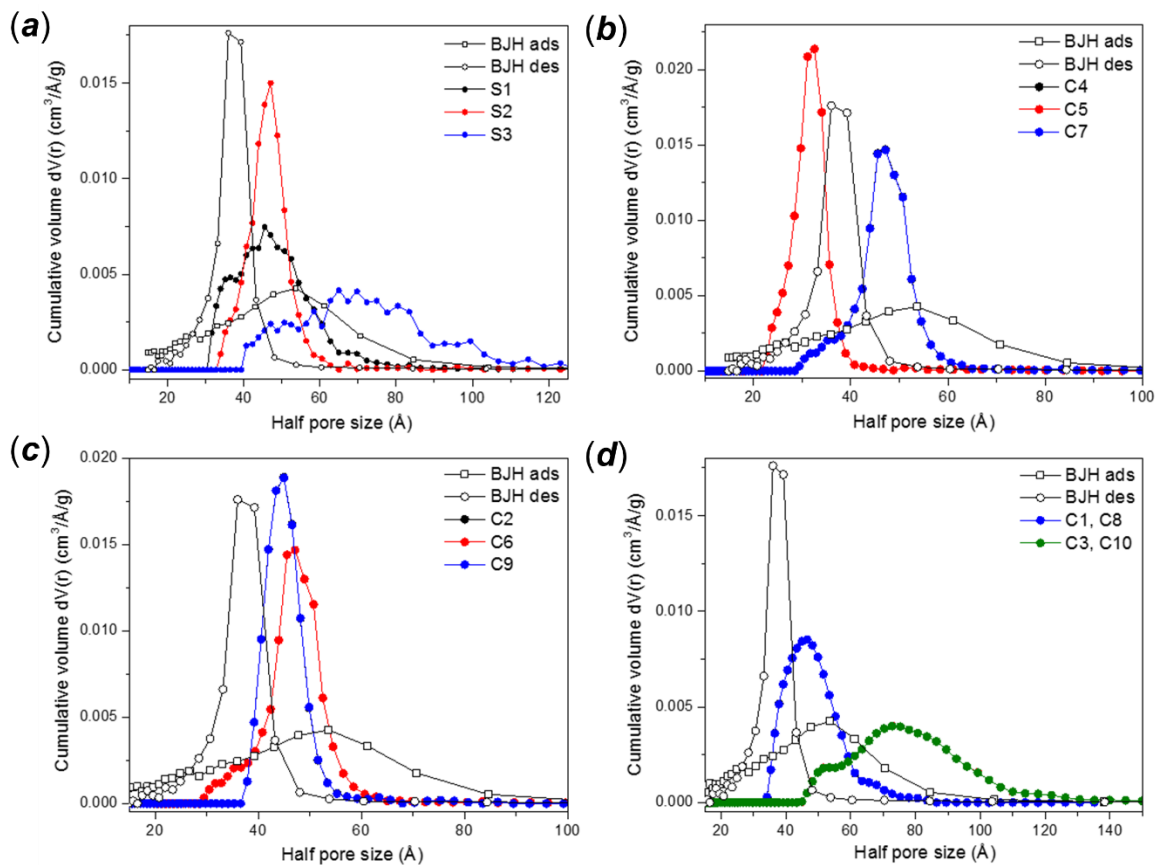


Figure A.16: Comparison between different DFT model with the BJH calculation (considering both the adsorption and the desorption branches of the isotherm)

Table A.5: Description and comparison of the DFT kernel for Carbon and SiO₂ for N₂ adsorption at 77 K of Aeroxide P25.

Method	type	Pore type	Pore volume (cm ³ /g)	Surface area (m ² /g)	Lower confidence limit (Å)	Fitting error (%)	Half pore width (mode) (Å)
C1	Qs ads	Cylindrical	0.163	68.775	6.55	4.453	46.544
C2	Qs eq	Cylindrical	0.162	71.798	6.55	5.066	44.971
C3	Qs ads	Cylindrical/sph	0.165	65.245	6.55	2.297	72.794
C4	NL eq	Cylindrical	0.168	71.899	5.65	2.356	47.160
C5	NL eq	Slit	0.163	52.012	4.92	2.505	32.555
C6	Qs eq	Slit	0.166	61.703	3.07	2.829	28.800
C7	NL eq	Slit/cylindrical	0.168	71.900	4.91	2.359	47.160
C8	Qs ads	Slit/cylindrical	0.163	68.776	4.630	4.453	46.544
C9	Qs eq	Slit/cylindrical	0.162	71.799	4.445	5.066	44.971
C10	Qs ads	Slit/cylindrical/	0.165	65.245	4.63	2.297	72.794
S1	NL ads	Cylindrical	0.167	71.641	6.1	3.375	45.490
S2	NL eq	Cylindrical	0.165	71.364	6.1	3.376	47.080
S3	NL ads	Cylindrical/sph	0.163	71.398	6.1	3.110	64.955
BJH	ads	-	0.174	76.805	-	-	53.656
BJH	Des	-	0.184	99.790	-	-	36.015

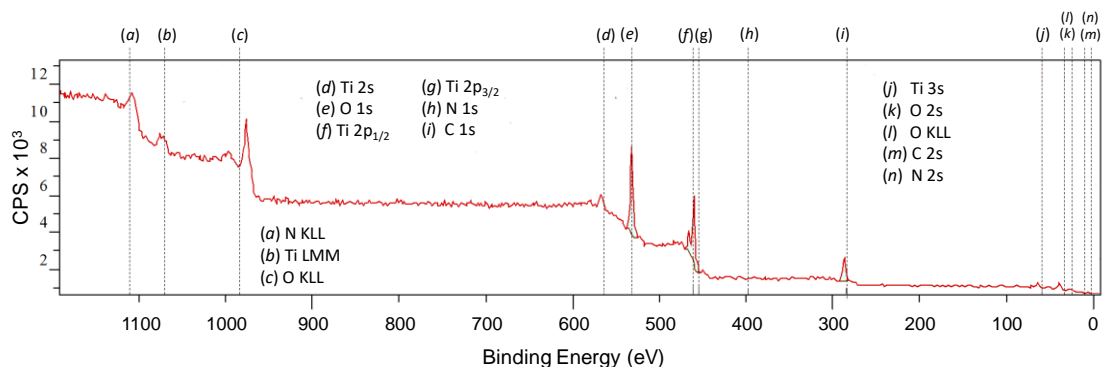


Figure A.17: Complete XPS spectrum for the untreated FMH-TiO₂ particles (series NE, precursor concentration 1:20, 2 M HNO₃, 1 min MW treatment at full power) with all the signals relative to Ti, O, C and N.

Table A.6: Thermodynamic parameters for the solvent used in this thesis.

Solvent	Water	Ethanol
Fusion temperature, T_f (K)	273.15	159.05
Boiling temperature, T_b (K)	373.15	351.80
Critical temperature, T_c (K)	647.14	513.92
Critical Pressure, P_c (bar)	220.64	61.48
Critical Volume, V_c (cm ³ /mol)	55.95	167.00
Acentric factor, ω	0.344	0.649
Tangential loss, δ	0.12	0.66

Table A.7: List of the characteristics of the acids used for the particle preparation. The acids were used without further purification.

	HCl	HNO ₃	H ₂ SO ₄	CH ₃ COOH
K_a [21]	$1 \cdot 10^6$	28	$1 \cdot 10^3$	$1,8 \cdot 10^{-5}$
pH (theoretical in H ₂ O)	-2.85	-0.57	-1.35	2.52
Water content (raw)	63%	30%	4%	0%
Water content (in precursor solution per 1M)	15.4 %	6.2 %	0.7 %	0%
Hydrolysis ratio (per 1M)	42.5	17.4	2.0	0

²¹ <http://chemed.chem.purdue.edu/genchem/topicreview/bp/3organic/acids.html>

Table A.8: pH measurement of the acidic solution used for the FMH synthesis.

	HCl in H ₂ O	HNO ₃ in H ₂ O	HCl in C ₂ H ₆ O	HNO ₃ in C ₂ H ₆ O
2 M	-0.26	-0.31	-0.76	-0.68
1 M	-0.09	-0.14	-0.59	-0.47
0.5 M	0.21	0.19	-0.47	-0.27
0.25 M	0.61	0.67	-0.30	-0.12
0.1 M	0.78	-	-0.12	-

Table A.9: Conductivity of the acidic solution used for the FMH synthesis.

	HCl in H ₂ O	HNO ₃ in H ₂ O	HCl in C ₂ H ₆ O	HNO ₃ in C ₂ H ₆ O
2 M	>400*	>400*	25.2	34.2
1 M	>400*	>400*	13.8	14.8
0.5 M	198.5	193.8	7.6	6.1
0.25 M	99.0	101.0	4.5	2.5
0.1 M	41.2	-	2.2	-

Table A.10: pH and conductivity of mixed solution of water and ethanol.

H ₂ O:C ₂ H ₆ O	0.5 M HNO ₃		1 M HNO ₃	
	pH	Conductivity (mS/cm)	pH	Conductivity (mS/cm)
100:0	0.19	193.8	-0.14	>400*
75:25	0.18	116.0	-0.13	222.0
50:50	0.29	72.1	-0.04	118.6
25:75	0.41	36.0	-0.27	62.6
0:100	-0.27	6.1	-0.59	14.8

*values out of instrumental range

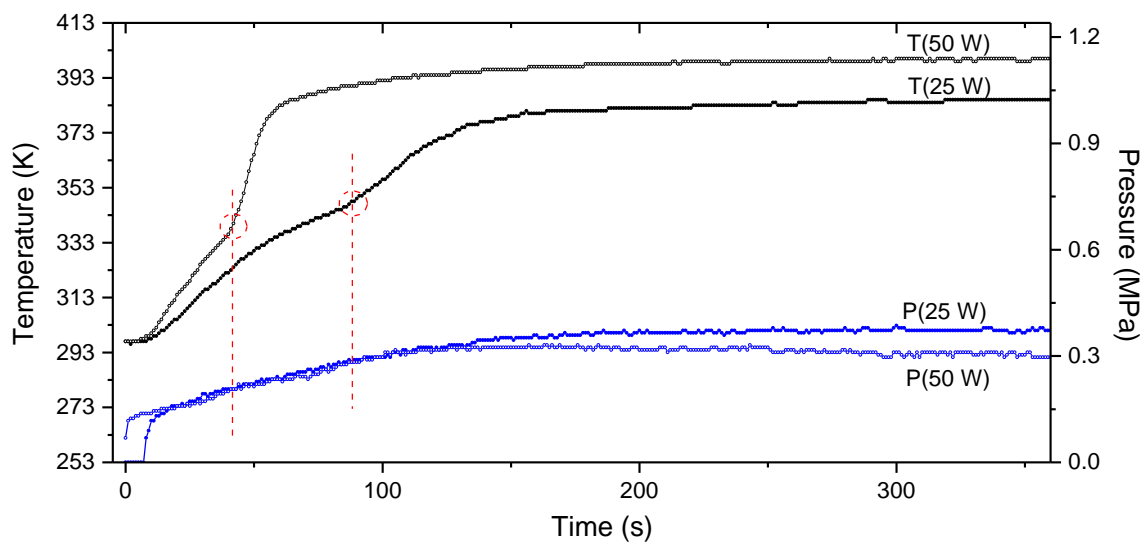


Figure A.18: Temperature-Pressure profile for water at low MW power, measured using a single-mode MW cavity (CEM Discovery®)

Appendix B: Figures and tables for Chapter 4

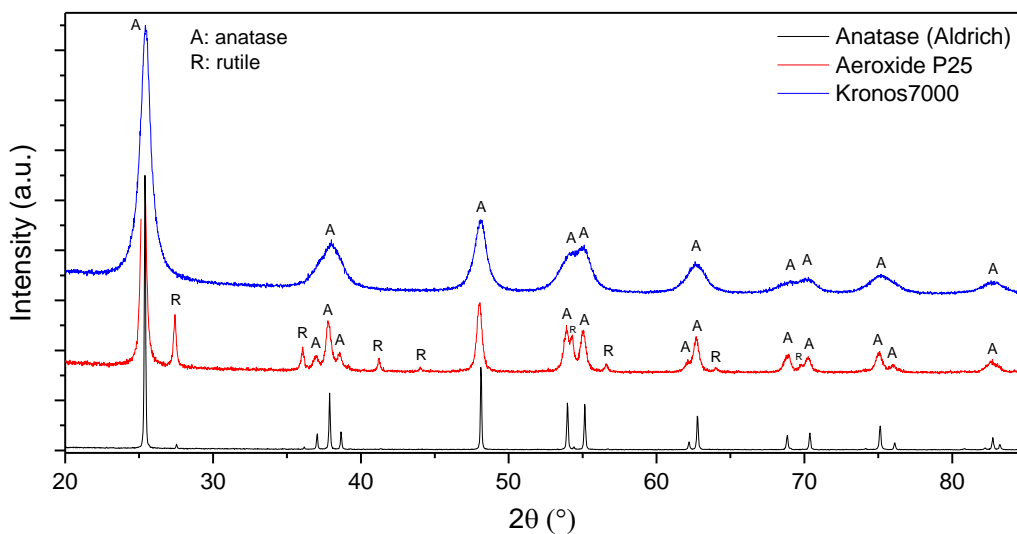


Figure A.19: PXD patterns of commercial anatase (Aldrich), Aeroxide® P25 and Krono7000. The patterns were normalised in intensity.

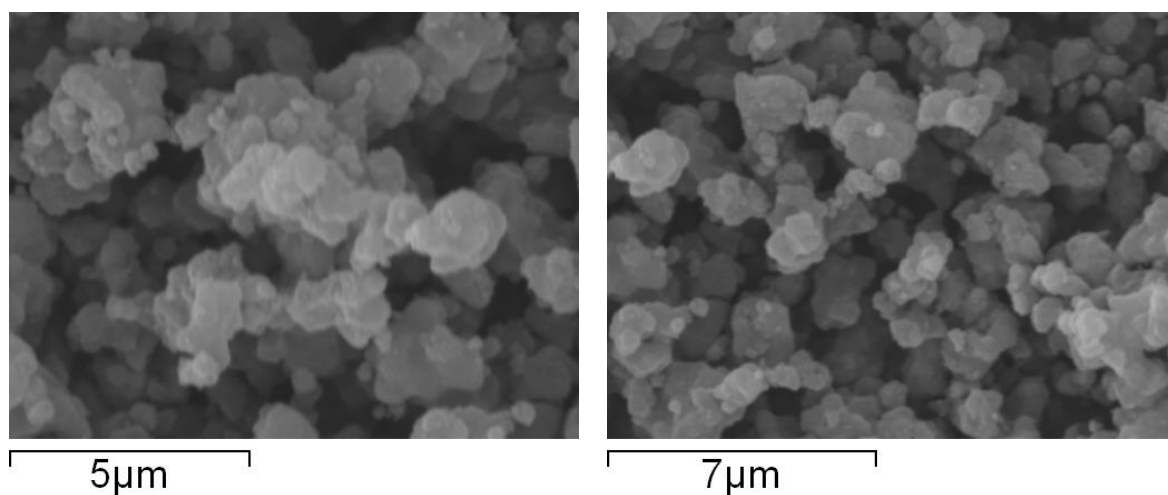


Figure A.20: SEM images of Kronos (Kronoclean 7000) sample.

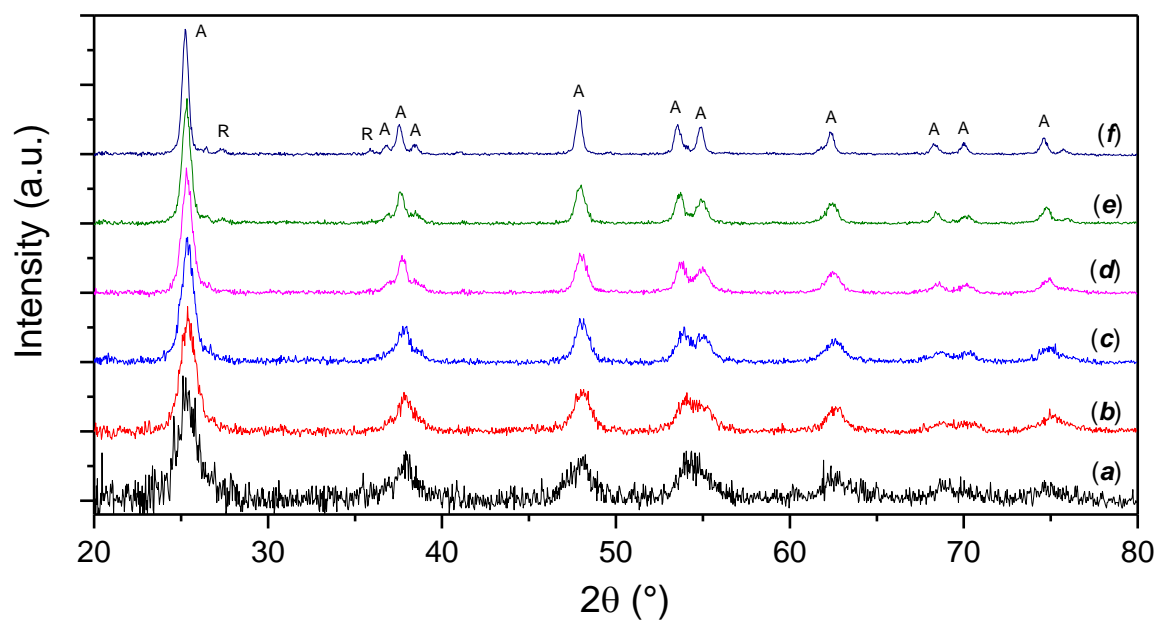


Figure A.21: In situ variable temperature measurement of the sample CE (1 M, 162 mM prec. concentration). PXD pattern collected at (a) 573 K, (b) 673 K, (c) 773 K, (d) 873 K and (e) 973 K.

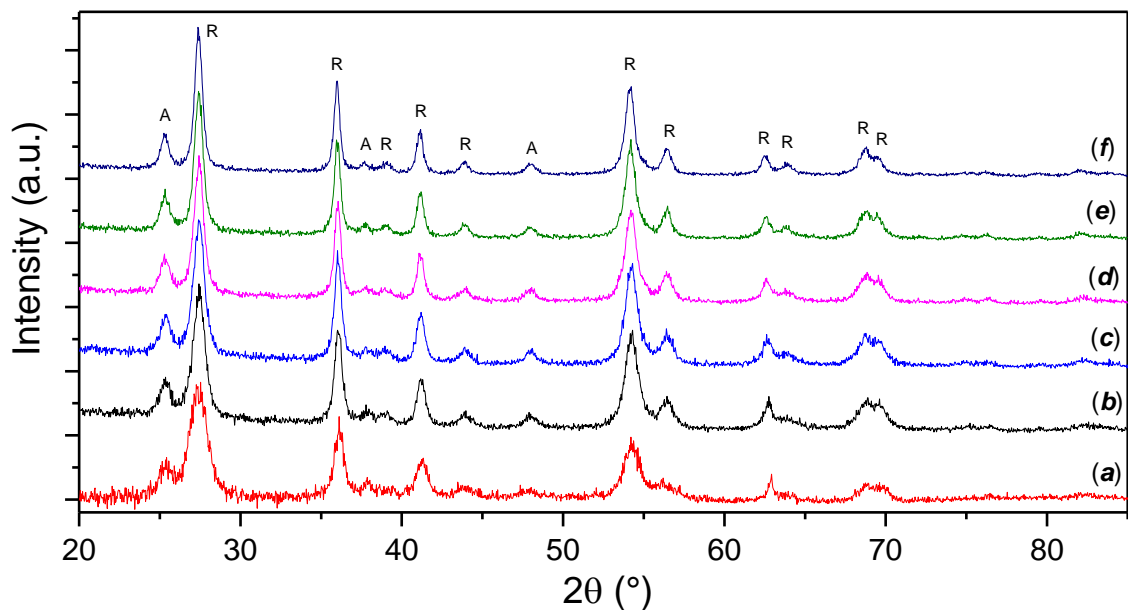


Figure A.22: In situ variable temperature measurement of the sample CE (2 M, 162 mM prec. concentration). PXD pattern collected at (a) 573 K, (b) 623 K, (c) 673 K, (d) 723 K and (e) 773 K.

Table A.11: CHN microanalysis of the FMH-TiO₂ particles after oxidative calcination (thermal annealing in air) at 773 K in function of the treatment time

Treatment time	C	H	N
1 h	0.13 ± 0.02	0.09 ± 0.01	0.16 ± 0.01
2 h	0.08 ± 0.01	0.08 ± 0.01	0.23 ± 0.01
3	0.11 ± 0.01	0.03 ± 0.01	0.28 ± 0.01

Table A.12: Optical properties, surface area and pore size analysis of the FMH-TiO₂ samples (NE, 2 M, 164 mM) calcined under N₂.

Temperature (K)	573	673	773	873
Indirect band gap (eV)	3.34	3.13	-	3.14
Direct band gap (eV)	3.64	3.58	-	3.41
Urbach energy (meV)	108	250	-	118
BET surface (m ² /g)	-	369 ± 25	148 ± 14	13 ± 3

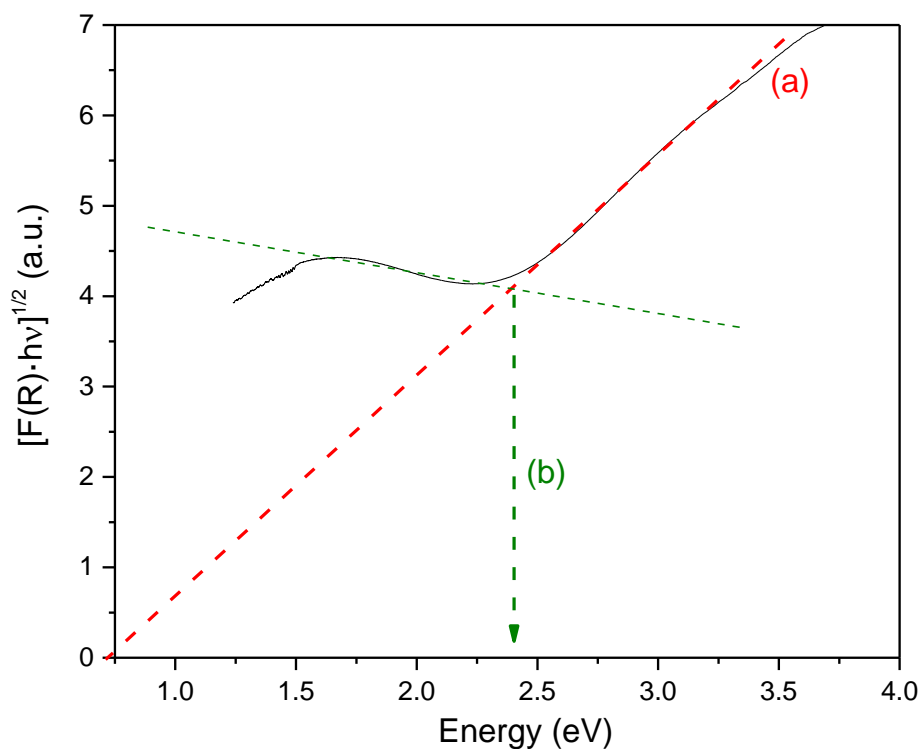


Figure A.23: Band gap calculation (indirect Kubelka-Munk function transformation) in case of non-zero absorption at wavelength higher than the optical band gap, due to reduction treatments (ammonolysis, vacuum heating, etc.).

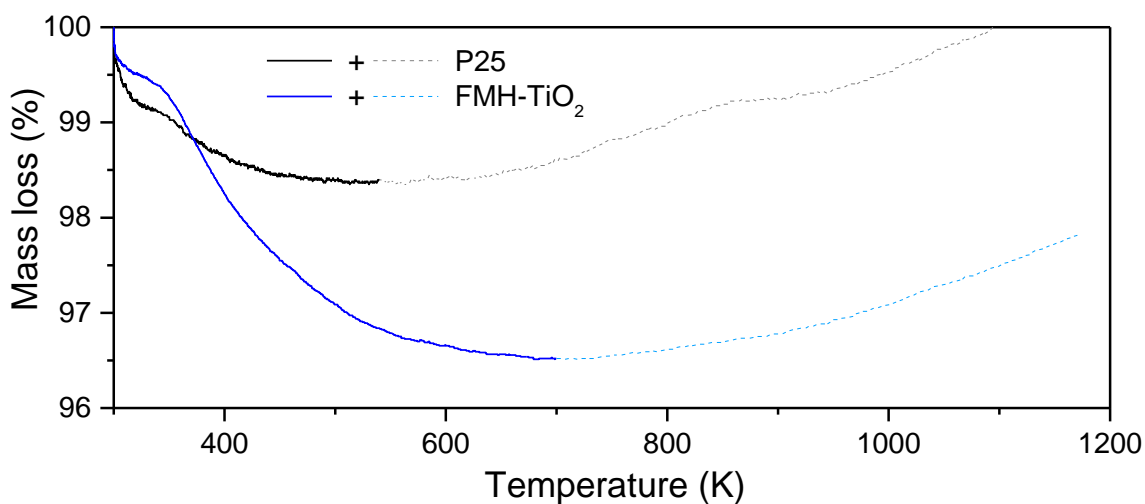


Figure A.24: TG of ammonolysed samples after STA. The mass increase was probably due to an error of the instrument correction file at high temperature or buoyancy effect of the balance. The effect was seldom observed in some other samples, but is totally unrelated with the sample properties.

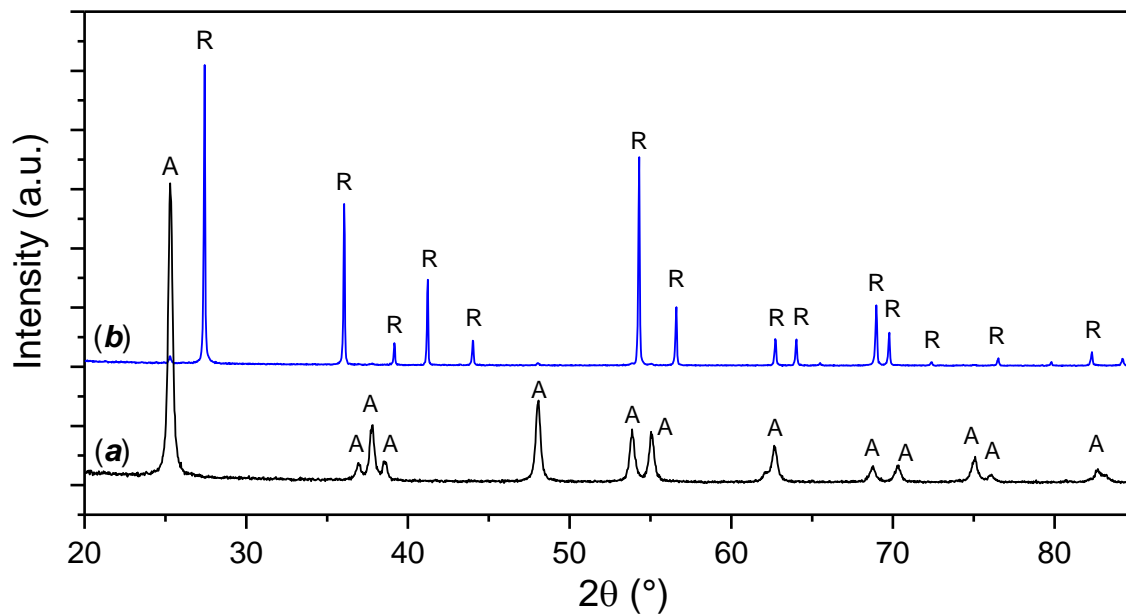
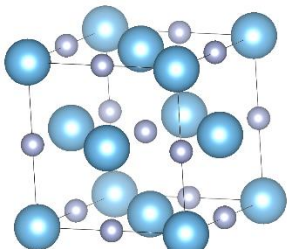
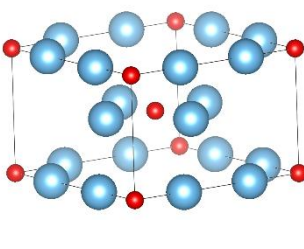
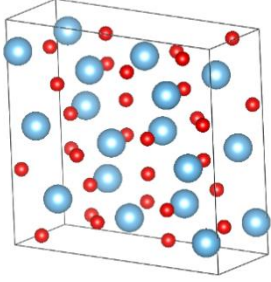


Figure A.25: PXD pattern of the selected ammonolysed FMH-TiO₂ sample (NE, 2 M, 648 mM) before and after the STA analysis

Table A.13: Crystallographic data for Ti/Ti-N phases observed after ammonolysis at high temperature (data from ICSD database).

	TiN	Ti ₄ O ₅	Ti ₃ O ₅
			
Symmetry	cubic	tetragonal	monoclinic
Space group	F m -3 m	I 4/m	C 2/m
Lattice parameters			
a	4.2442	6.632	9.7520
b	4.2442	6.632	3.8020
c	4.2442	4.156	9.4420
B (°)	90	90	91.920
Volume (Å ³)	76.45	182.80	349.89

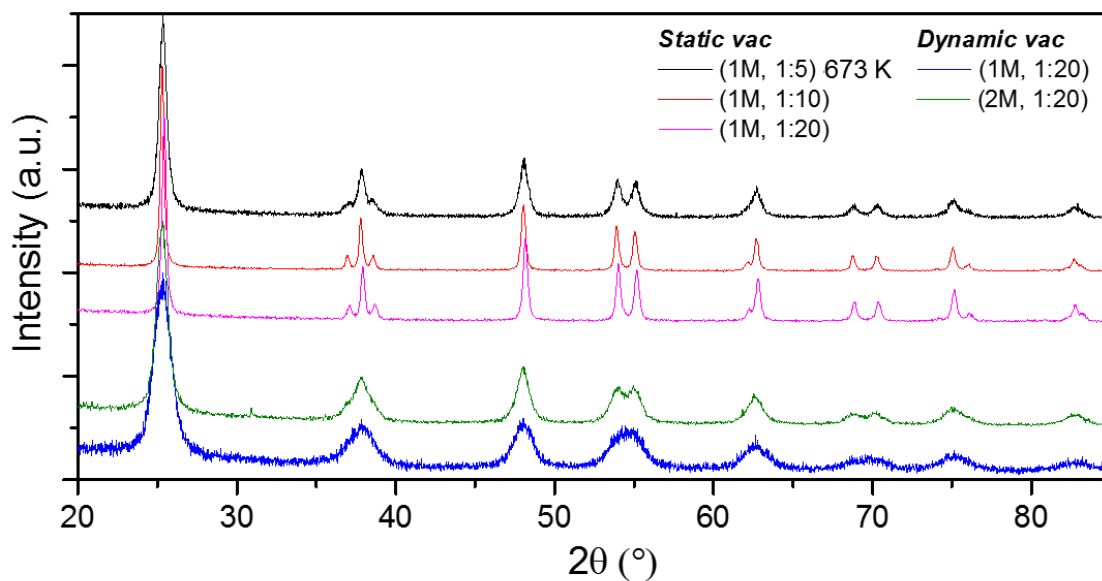


Figure A.26: PXD patterns of representative FMH-TiO₂ samples heated under static and dynamic vacuum (treatment temperature 773 K when not indicated)

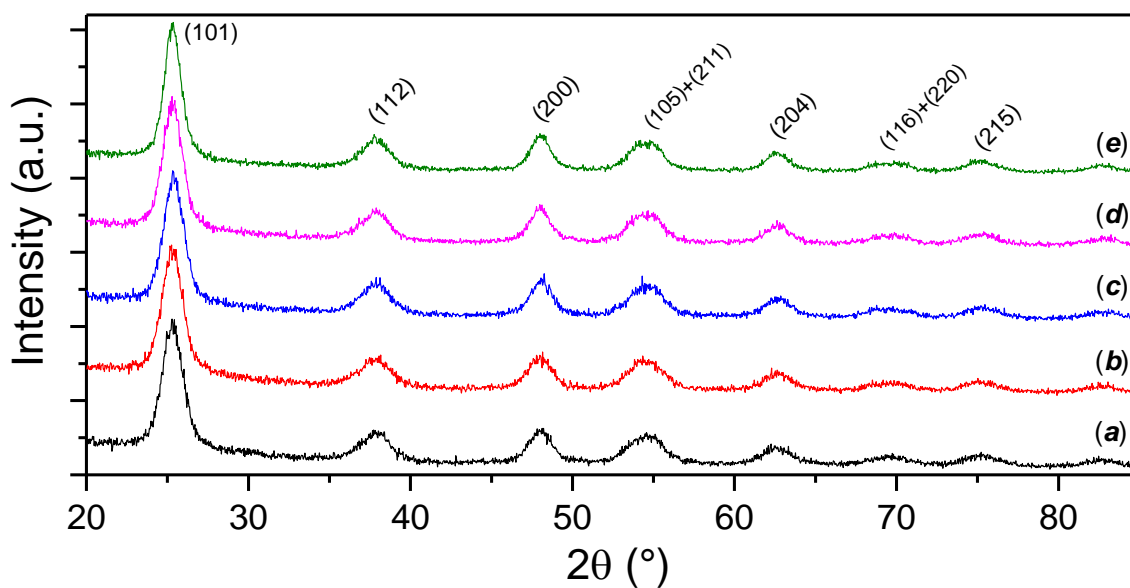


Figure A.27: PXD patterns of a representative FMH-TiO₂ sample (*NE* series, 2 M HNO₃, 648 mM precursor concentration, 1 min MW treatment) annealed under static vacuum at 673 K for different times: (a) 3 hrs, (b) 5 hrs, (c) 7 hrs, (d) 9 hrs. (e) PXD of the sample annealed under vacuum for 7 hrs and successively calcined in air for additional 3 hrs at 673 K.

Table A.14: XPS signal integration for the N-doped P25 and the N-doped FMH-TiO₂ representative sample, both treated by ammonolysis at 773 K (3 hrs).

	Position (eV)	FWMH	Area	At%
<i>N-doped P25</i>				
Ti 2p	458.77	2.509	23607.07	16.11
O 1s	530.77	2.877	27609.53	50.22
C 1s	284.77	2.929	6317.55	33.67
<i>N-doped FMH-TiO₂</i>				
Ti 2p	459.25	2.818	22357.42	19.24
O 1s	530.25	2.862	21980.18	50.41
C 1s	284.25	3.097	4516.99	30.35

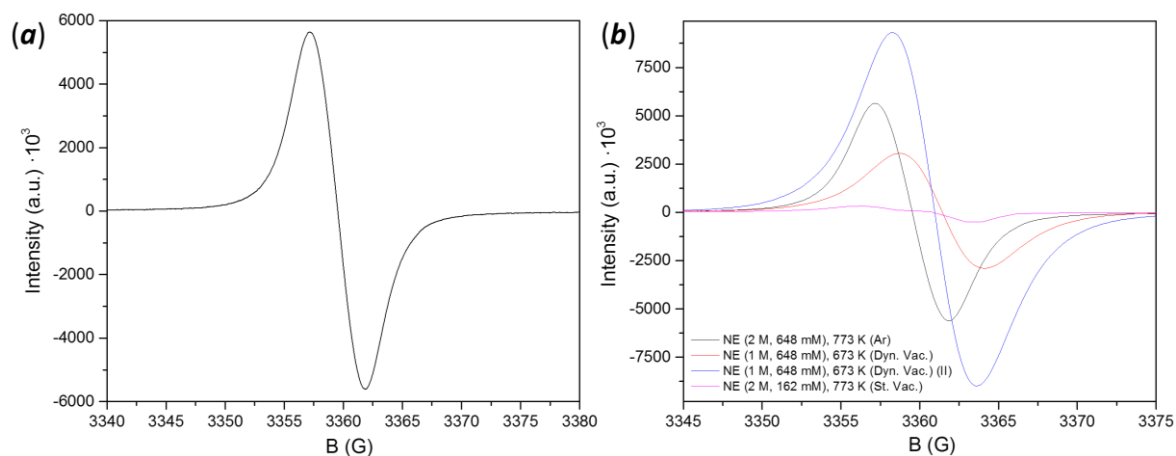


Figure A.28: (a) EPR spectra of FMH-TiO₂ sample calcined under argon constant flow at 673 K and (b) comparison of the EPR signal of all the selected samples.

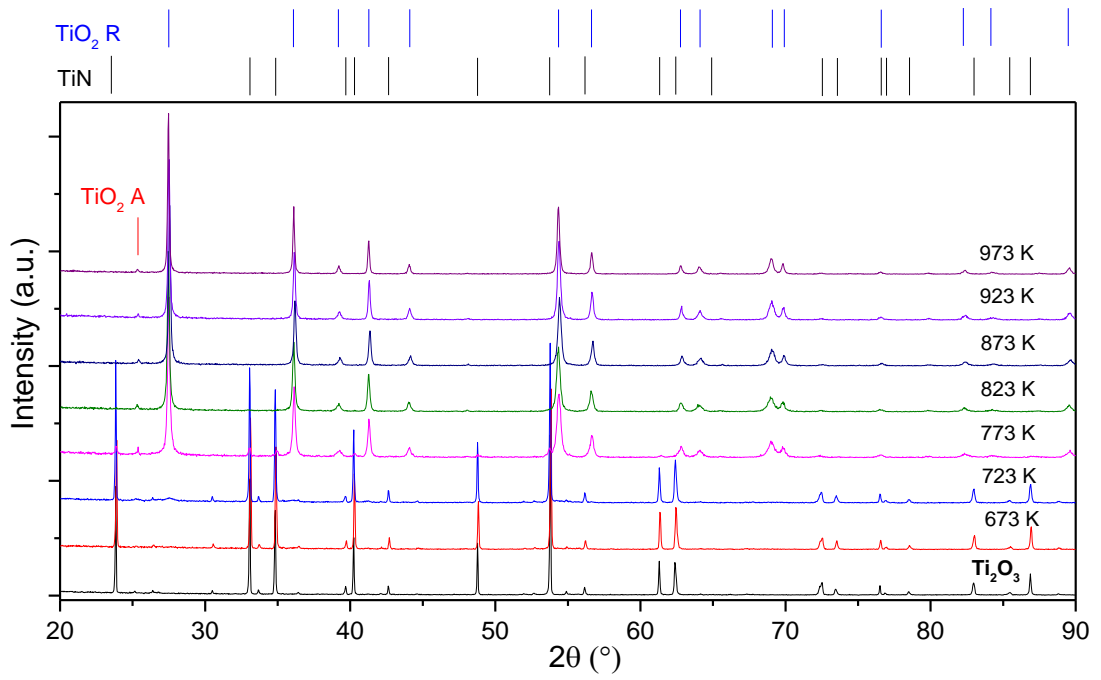


Figure A.29: PXD pattern relative to the thermal oxidation under air of Ti_2O_3 in function of the temperature (thermal treatment performed for 3 hrs, heating rate 10 K/min)

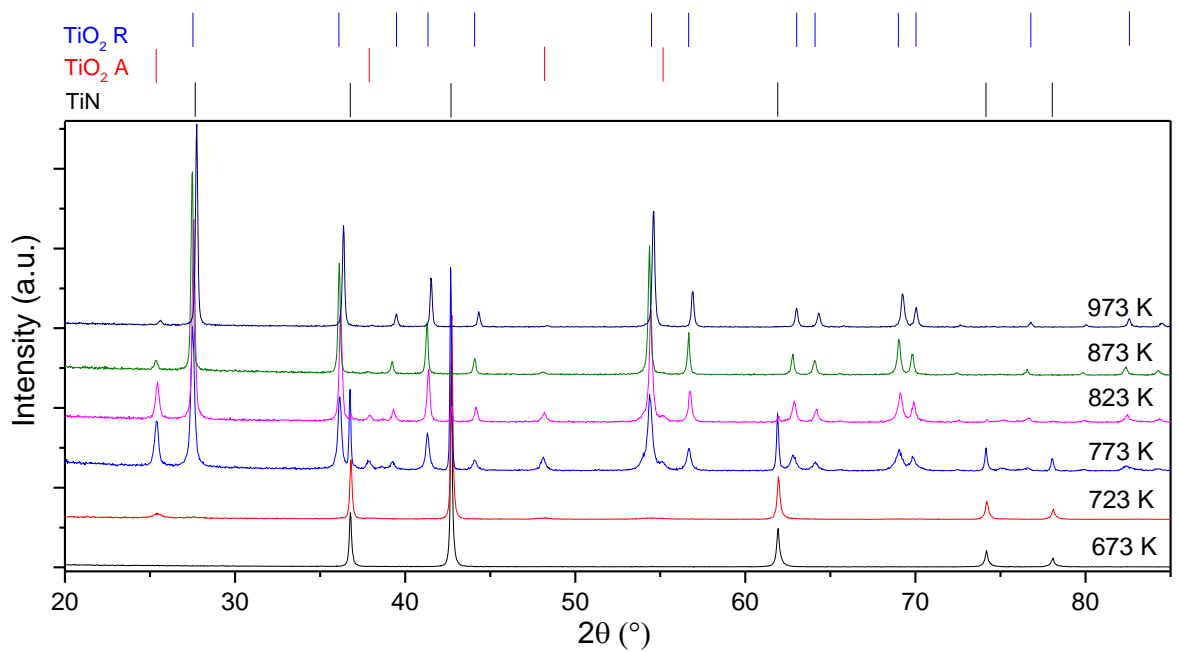


Figure A.30: PXD pattern relative to the thermal oxidation under air of TiN in function of the temperature (thermal treatment performed for 3 hrs, heating rate 10 K/min)

Table A.15: Band gap values and Urbach energies of the Ti₂O₃ sample calcined in air at different temperatures.

	Treatment temperature (K)	Indirect band gap (eV)	Direct band gap (eV)	Urbach energy (meV)
Ti ₂ O ₃	Untreated	1.46	1.85	254.4
	673 K	1.25	1.59	224.1
	773 K	2.61, 1.83	3.00, 2.41	277.7, 398.1
	823 K	2.74, 2.12	3.02, 2.48	186.1, 180.3
	873 K	2.84, 2.11	3.04, 2.48	123.3, 186.7
	923 K	2.91, 2.06	3.05	79.1, 228.6
	973 K	2.94, 1.85	3.06	56.3, 411.4

Table A.16: Band gap values and Urbach energies of the TiN sample calcined in air at different temperatures.

	Treatment temperature (K)	Indirect band gap (eV)	Direct band gap (eV)	Urbach energy (meV)
TiN	Untreated	1.85	2.43	421.4
	673 K	1.93	2.39	311.2
	773 K	0.64, 2.78	3.11	201.7
	823 K	1.83, 2.95	3.13	85.4
	873 K	1.87, 2.97	3.13	73.6
	973 K	1.63, 2.98	3.13	62.7

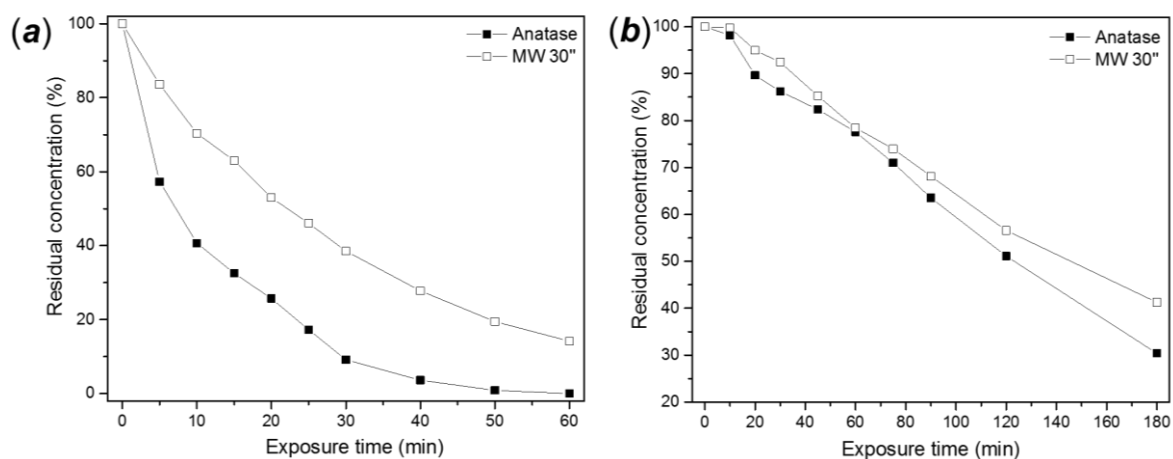


Figure A.31: Comparison of the photoactivity of MW heated anatase with untreated anatase under (a) UVA and (b) visible light irradiation.

Appendix C: Figures and tables for Chapter 5

Table A.17: Initial model used for the thickness determination from the SPR curves, provided by the instrument company (Bionavis)

	Thickness (nm)	n(1)	n(2)	ϵ
λ (nm)		690	785	690
Glass	0.00	1.52020	1.51600	0.00000
Cr	3.44	4.51088	3.34018	0.72178
Au	50.57	0.25558	0.25547	3.78758
Water	0.00	1.33100	1.32900	0.00000

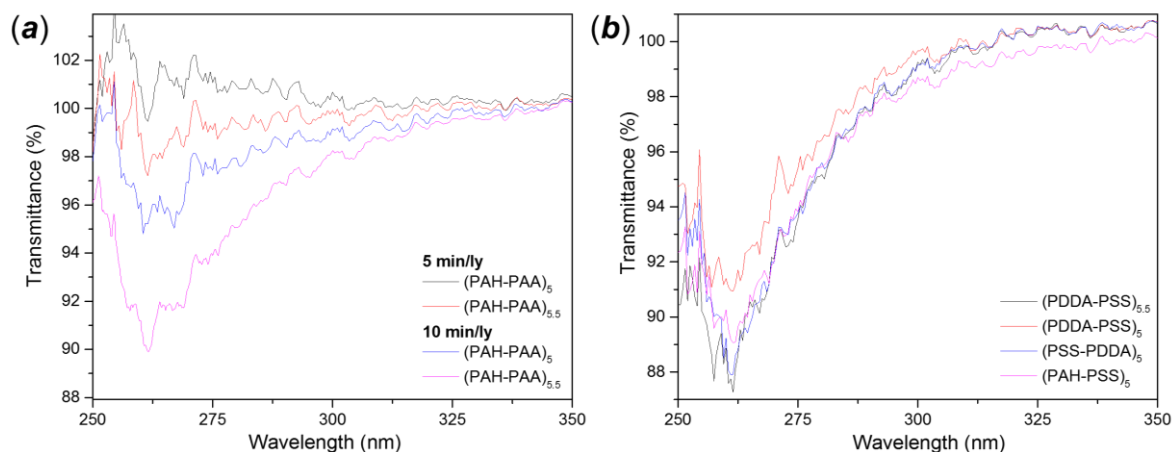


Figure A.32: DR-UV-Vis transmittance of microscope glass slides coated using different combination of (a) (PAH-PAA) and (b) (PDDA-PSS) multilayers.

Table A.18: Z-average, zeta potential and conductivity measurement relative to P25 basic system stabilised by the addition of polycations

	Z-avg. Size (nm)	Zeta potential (mV)	Zeta deviation (mV)	Conductivity ($\mu\text{S}/\text{cm}$)
<i>No polyelectrolyte</i>	130 \pm 1	-34.8 \pm 0.4	15.80 \pm 1.21	0.28
PDDA 2.5%	187 \pm 4	-31.3 \pm 1.00	4.88 \pm 0.11	0.30
PDDA 5%	153 \pm 1	22.4 \pm 3.9	4.0 \pm 0.4	0.32
PDDA 10 %	154 \pm 2	28.6 \pm 0.2	4.01 \pm 0.39	0.26
PDDA 20%	196 \pm 9	29.3 \pm 0.3	4.23 \pm 0.11	0.30
PAH 2.5 %	1678 \pm 144	-25.3 \pm 3.4	8.03 \pm 0.91	0.30
PAH 5 %	308 \pm 21	-19.6 \pm 1.7	6.41 \pm 0.54	0.28
PAH 10%	232 \pm 11	16.3 \pm 0.3	3.93 \pm 0.19	0.29
PAH 20%	227 \pm 5	20.5 \pm 0.4	3.69 \pm 0.65	0.25

Error for conductivity < 0.1%

Table A.19: Z-average, zeta potential and conductivity measurement relative to P25 acid system stabilised by the addition of polyanions.

	Z-avg.Size (nm)	Zeta potential (mV)	Zeta deviation (mV)	Conductivity ($\mu\text{S}/\text{cm}$)
<i>No polyelectrolyte</i>	187 \pm 10	46.1 \pm 0.7	18.6 \pm 3.3	3.28 \pm 0.17
PSS 2.5%	876 \pm 86	-3.7 \pm 1.1	14.60 \pm 4.86	3.52 \pm 0.20
PSS 5%	200 \pm 10	-36.9 \pm 2.1	8.61 \pm 1.56	3.54 \pm 0.17
PSS 10 %	189 \pm 7	-44.1 \pm 2.5	10.5 \pm 1.6	3.52 \pm 0.16
PSS 20%	203 \pm 15	-49.8 \pm 1.5	6.74 \pm 1.25	3.49 \pm 0.16
PAA 2.5 %	466 \pm 30	31.7 \pm 0.9	10.75 \pm 3.86	3.57 \pm 0.18
PAA 5 %	642 \pm 44	22.7 \pm 0.3	10.2 \pm 2.3	3.53 \pm 0.17
PAA 10%	745 \pm 73	12.2 \pm 0.4	11.0 \pm 4.1	3.47 \pm 0.17
PAA 20%	827 \pm 1	20.2 \pm 4.6	9.62 \pm 1.10	3.45 \pm 0.18

Error for conductivity < 0.1%

Table A.20: Zeta potential measurement for anatase, P25 and Kronos (100 mg/L suspension) at different pH values.

pH	Zeta potential (mV)		
	Anatase	P25	Kronos
2	36.9 ± 0.5	42.6 ± 0.2	30.3 ± 0.4
3	28.7 ± 3.0	37.7 ± 0.3	33.1 ± 0.7
4	-1.6 ± 1.1	37.6 ± 0.5	32.1 ± 0.3
5	-21.2 ± 0.4	30.6 ± 0.7	18.5 ± 0.5
6	-29.4 ± 0.7	26.2 ± 0.4	5.7 ± 1.1
7	-39.3 ± 0.9	8.1 ± 0.4	-6.1 ± 0.3
8	-47.2 ± 0.3	-6.0 ± 0.5	-12.9 ± 0.3
9	-46.7 ± 0.5	-15.0 ± 0.2	-18.1 ± 0.3
10	-53.7 ± 0.2	-28.4 ± 0.5	-32.3 ± 0.4
11	-52.3 ± 0.9	-38.1 ± 0.6	-33.3 ± 0.9
12	-60.3 ± 4.6	-44.2 ± 2.9	-31.8 ± 0.4

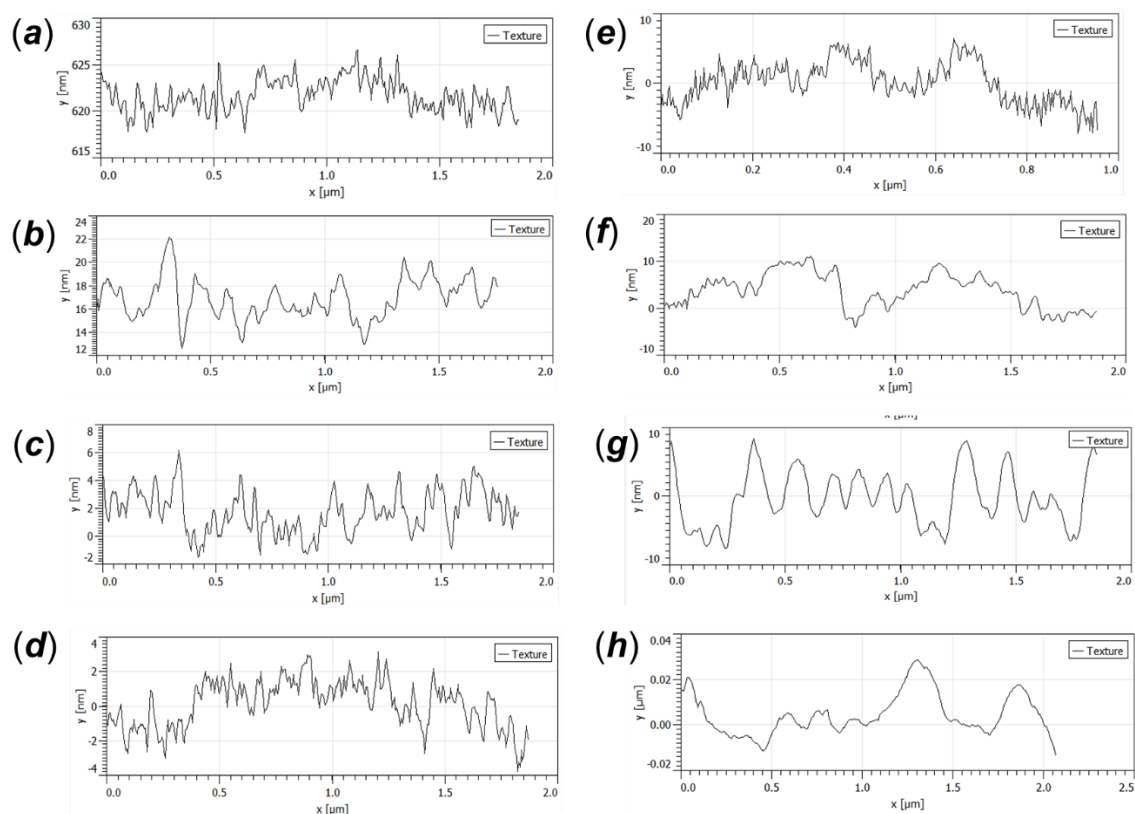


Figure A.33: Example of texture calculated from AFM images from selected PEM-modified UF membranes, measured using Gwyddion software. (a) untreated SM membrane; (b) (PDDA-PSS)_{5.5}; (c) (PDDA-PSS)_{3.5}; (d) (PDDA-PSS)_{3.5} (immersion time 10 min/ly); (e) (PDDA-PSS)_{3.5}, (ionic strength 100 mM); (f) (PDDA-PSS)_{3.5}, (ionic strength 500 mM); (g) (PAH-PSS)_{4.5}; (h) (PAH-PAA)_{4.5}.

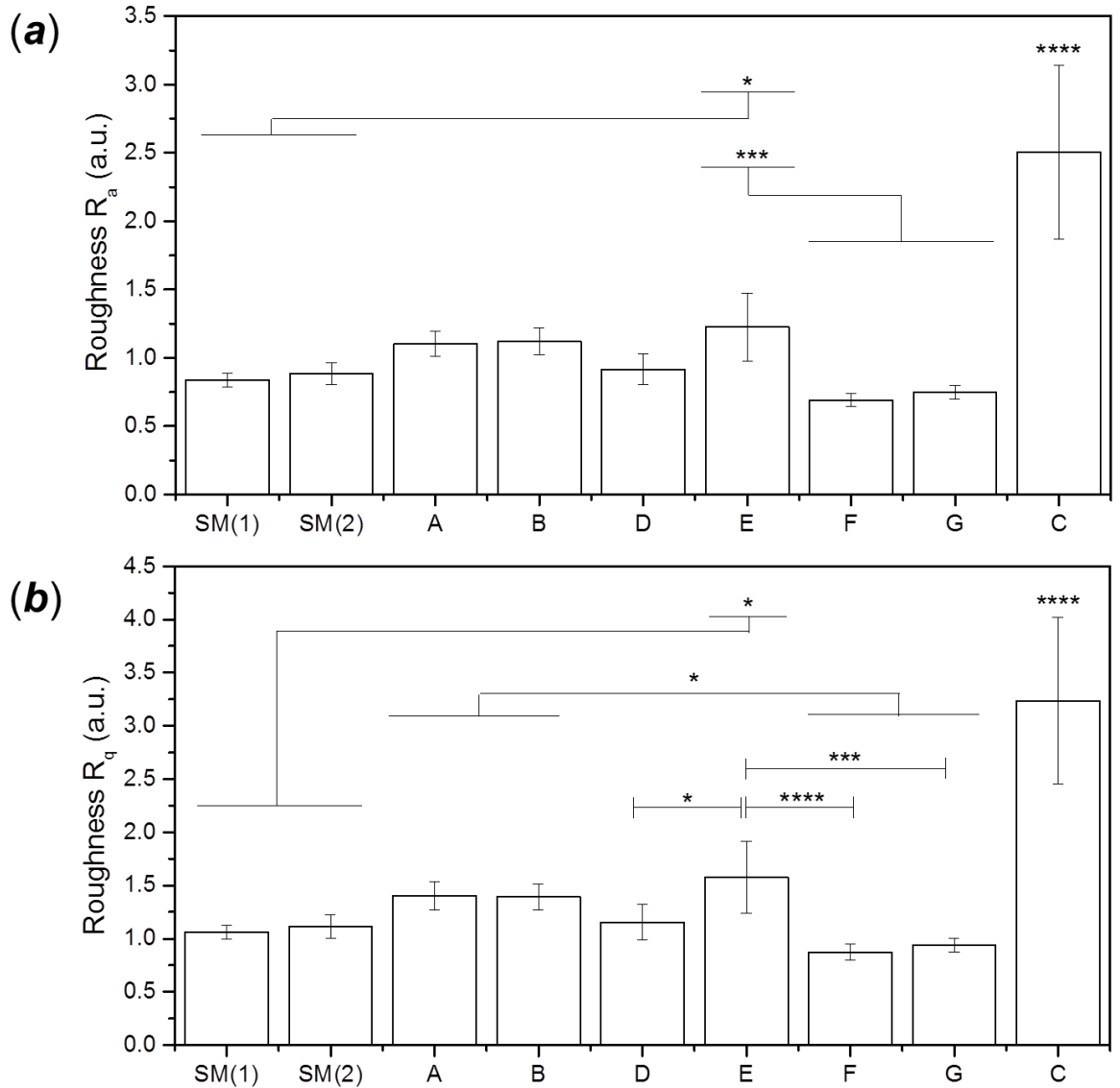


Figure A.34: Statistical analysis for the roughness calculated by AFM measurement on UF membranes. The full data are reported in Table 5.4. (a) R_a values, indicating the average roughness and (b) R_q values, indicating the root-mean squared roughness of the surface. The letters in the graph represent the same sample order reported in Table 5.4 (except for C, moved to simplify the visualisation). Following the alphabetical order, A: (PDDA-PSS)_{3.5} (I_s = 100 mM); B: (PDDA-PSS)_{3.5}, (I_s = 500 mM); C: (PAH-PSS)_{4.5}; D: (PAH-PAA)_{4.5}; E: (PDDA-PSS)_{5.5}; F: (PDDA-PSS)_{3.5}; G: (PDDA-PSS)_{3.5} (10 min/ly instead of 5 as for all the other samples) Statistical analysis is reported for significant results: * $P \leq 0.05$, ** $P \leq 0.01$, * $P \leq 0.001$, **** $P \leq 0.0001$. P values were calculated using one-way analysis of variance (ANOVA).**

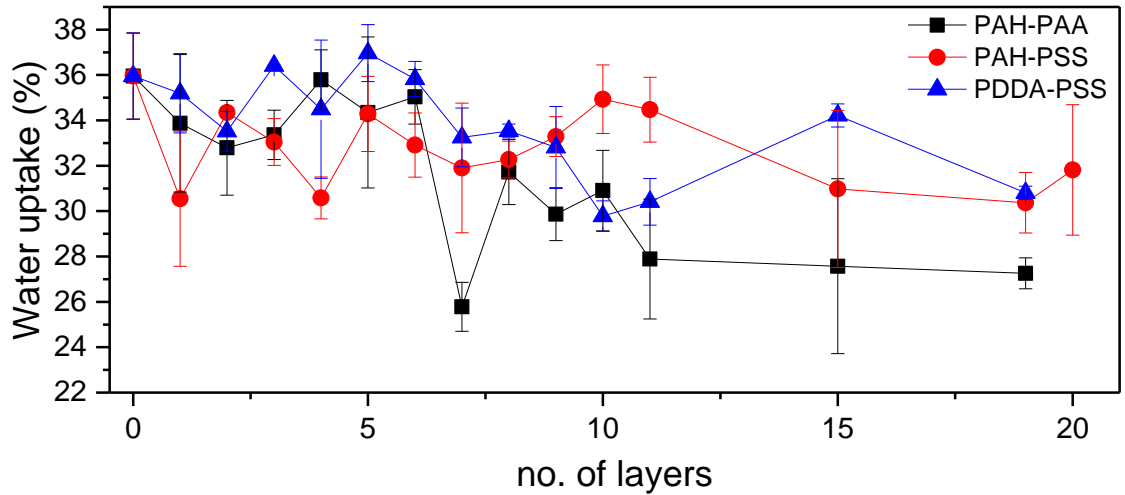


Figure A.35: Water uptake values for UF-SM membranes coated with different PEMs.

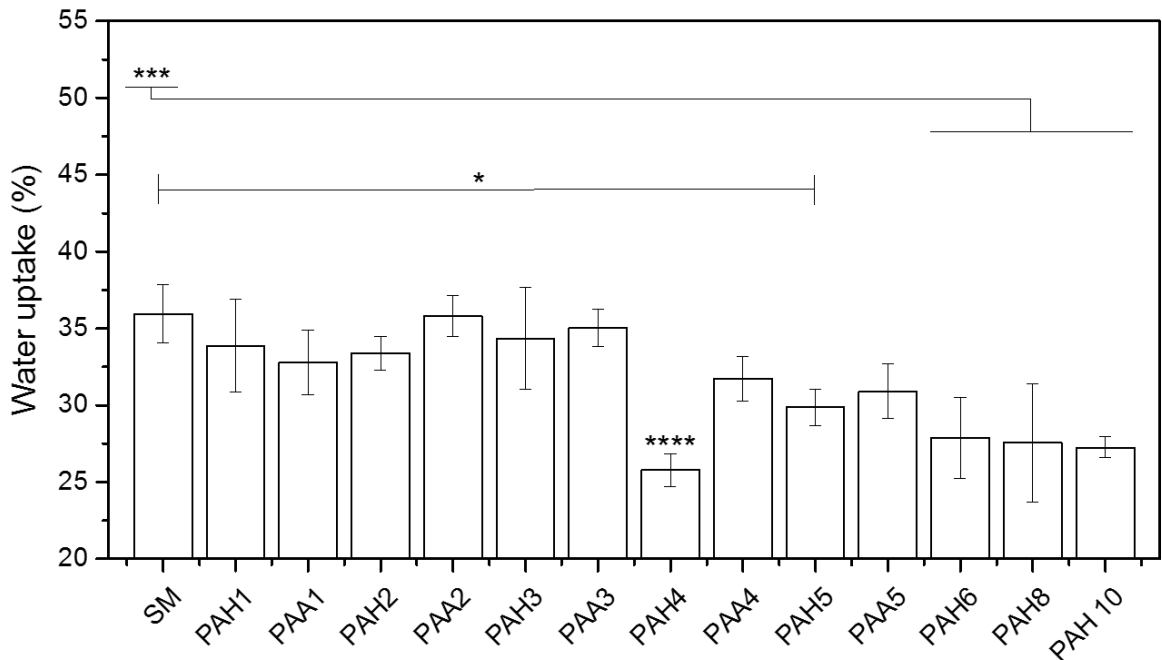


Figure A.36: Statistical analysis for the water uptake measurement on SM membrane coated with different number of layers of a (PAH-PAA) coating, reported in Figure A.35. Statistical analysis is reported for significant results: * $P \leq 0.05$, ** $P \leq 0.01$, *** $P \leq 0.001$, **** $P \leq 0.0001$. P values were calculated using one-way analysis of variance (ANOVA).

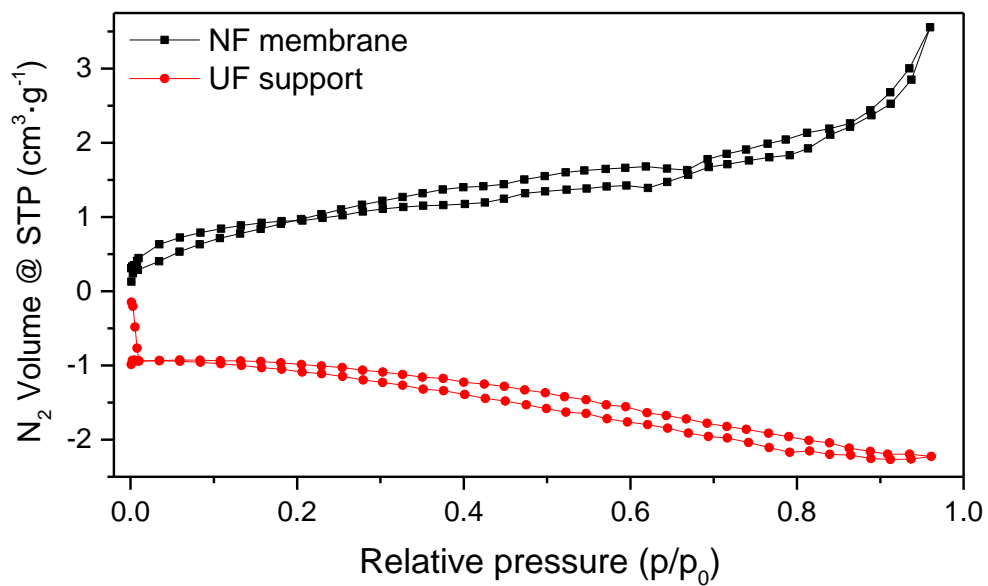


Figure A.37: N₂ adsorption-desorption isotherms for nanofiltration (NF) membranes and textile support of the commercial UF membranes analysed in chapter 5.

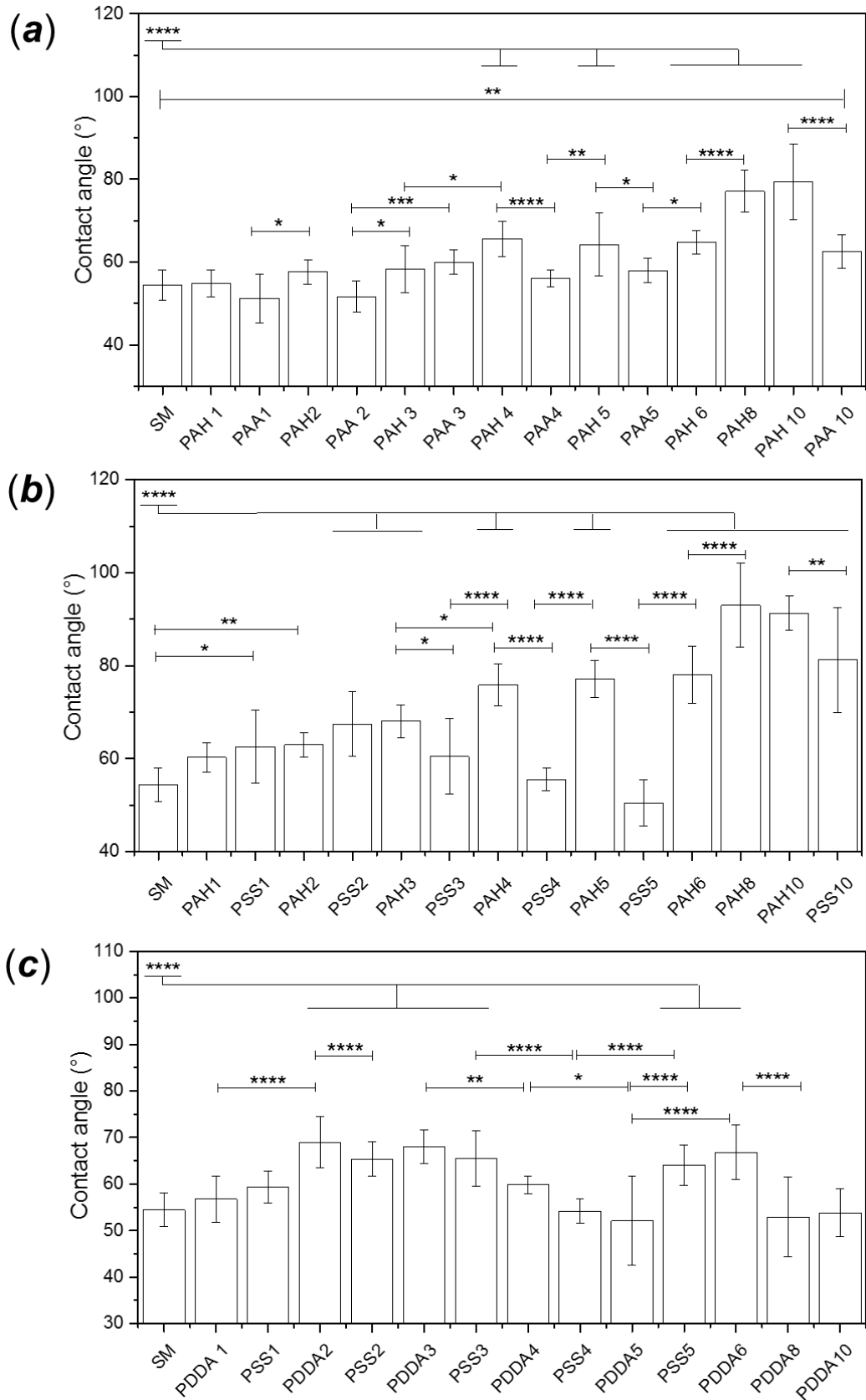


Figure A.38: Statistical analysis of the effect of different multilayers on contact angle measurement on SM membrane surface reported in Figure 5.30. Statistical analysis is reported for significant results: * $P \leq 0.05$, ** $P \leq 0.01$, * $P \leq 0.001$, **** $P \leq 0.0001$. P values were calculated using one-way analysis of variance (ANOVA).**

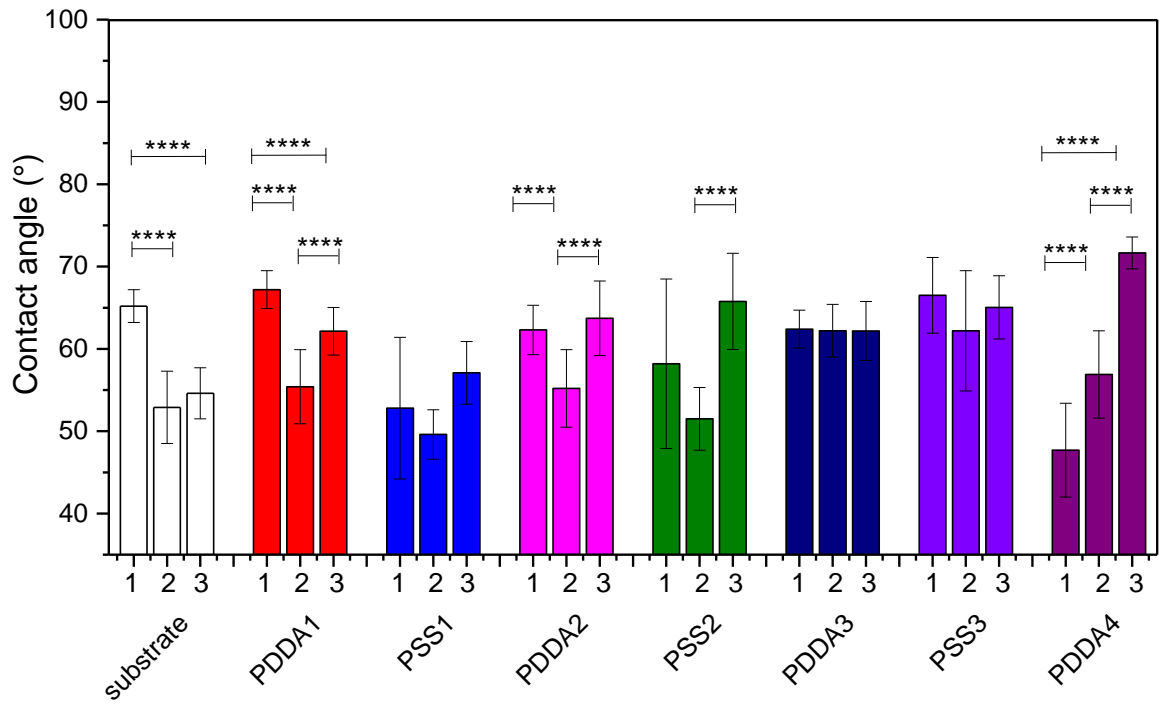


Figure A.39: Statistical analysis of contact angle measurements on (PDDA-PSS) multilayers on different surfaces (Mylar sheet, PAN and PES membranes) showed in Figure 5.31. The numbers in the graph indicate 1: Mylar foil; 2: PAN membrane and 3: PES membrane. Statistical analysis is reported for significant results: * $P \leq 0.05$, ** $P \leq 0.01$, * $P \leq 0.001$, **** $P \leq 0.0001$. P values were calculated using one-way analysis of variance (ANOVA).**

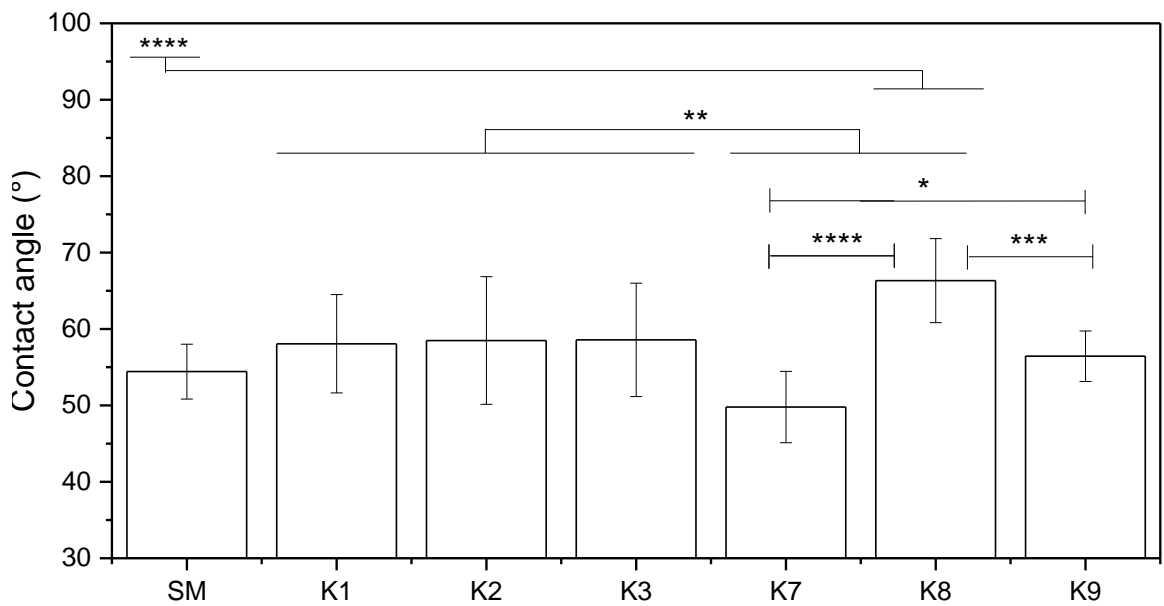


Figure A.40: Statistical analysis on the effect of different multilayers on contact angle measurements on SM membranes (Table 5.7). Statistical analysis is reported for significant results: * $P \leq 0.05$, ** $P \leq 0.01$, * $P \leq 0.001$, **** $P \leq 0.0001$. P values were calculated using one-way analysis of variance (ANOVA).**

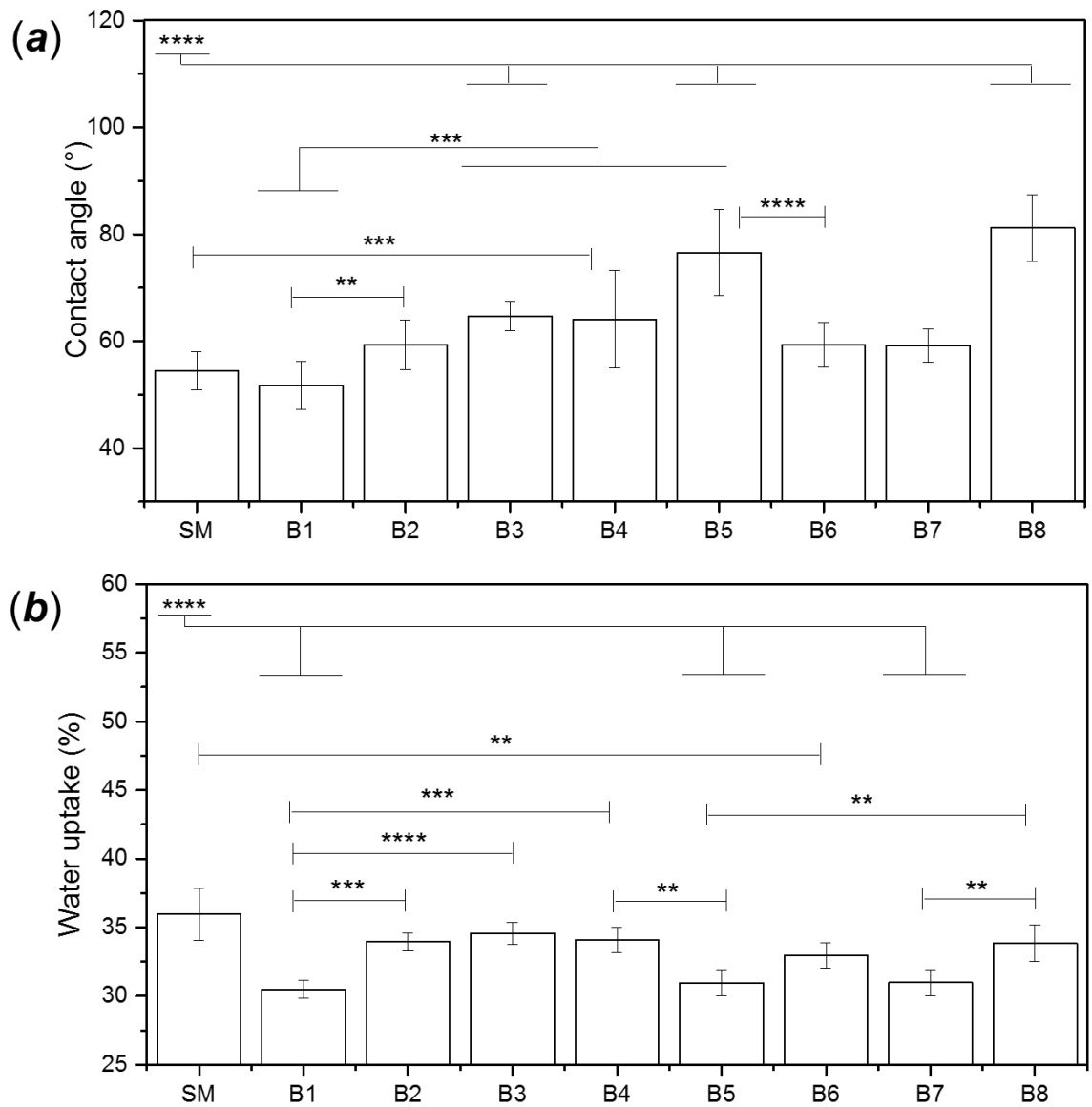


Figure A.41: Statistical analysis of (a) contact angle and (b) water uptake measurements on the SM-B membrane series, (PDDA-PSS)_n multilayer on SM-UF membranes, varying the ionic strength of the polyelectrolyte solution and the rinsing method (Table 5.8). Statistical analysis is reported for significant results: * $P \leq 0.05$, ** $P \leq 0.01$, * $P \leq 0.001$, **** $P \leq 0.0001$. P values were calculated using one-way analysis of variance (ANOVA).**

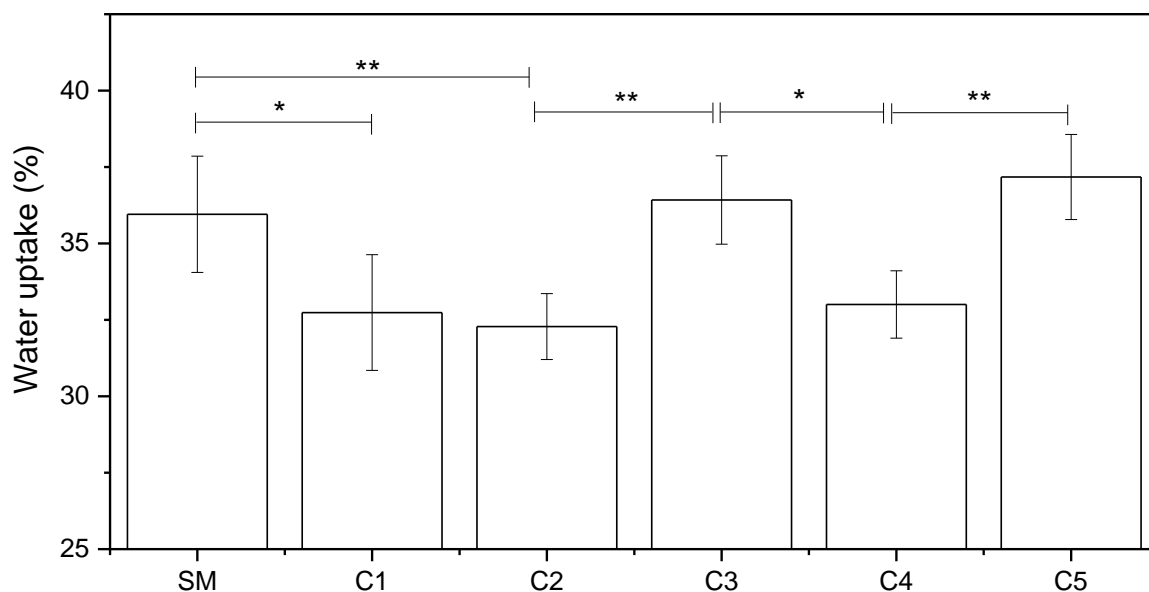


Figure A.42: Statistical analysis for the water uptake measurements on the SM membranes coated with a composite (PDDA/PSS) multilayer with integration of TiO₂ (Aeroxide P25, 1 g/L), reported in Table 5.9. The significance of the measurements is reported in comparison with the unmodified membrane (SM). Statistical analysis is reported for significant results: * P ≤ 0.05, ** P ≤ 0.01, * P ≤ 0.001, **** P ≤ 0.0001. P values were calculated using one-way analysis of variance (ANOVA).**

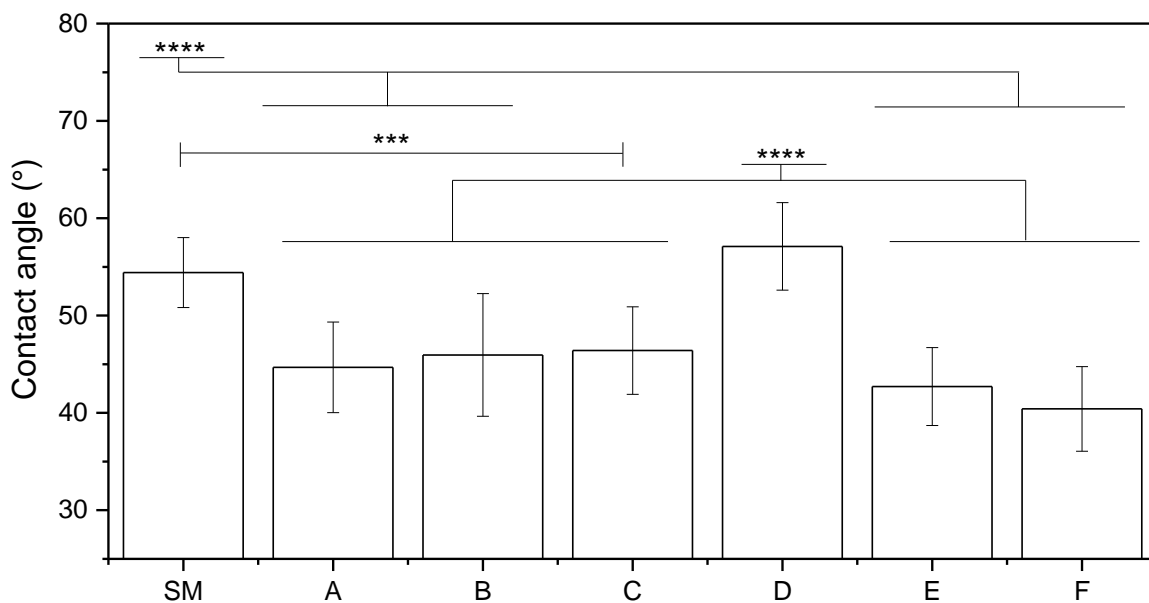


Figure A.43: Statistical analysis of the contact angle measurement results reported in Table 5.10. The letters in the graph indicate A: (PDDA-PSS)_{2.5}, 2 min immersion; B: (PDDA-PSS)_{5.5}, 1 min immersion; C: (PDDA-PSS)_{5.5}, 5 min immersion; D: (PDDA-PSS)_{5.5}, 2 min immersion; E: (PDDA-PSS)_{2.5}, 1 min immersion; F: (PAH-PSS)_{5.5}, 5 min immersion. Statistical analysis is reported for significant results: * P ≤ 0.05, ** P ≤ 0.01, * P ≤ 0.001, **** P ≤ 0.0001. P values were calculated using one-way analysis of variance (ANOVA).**

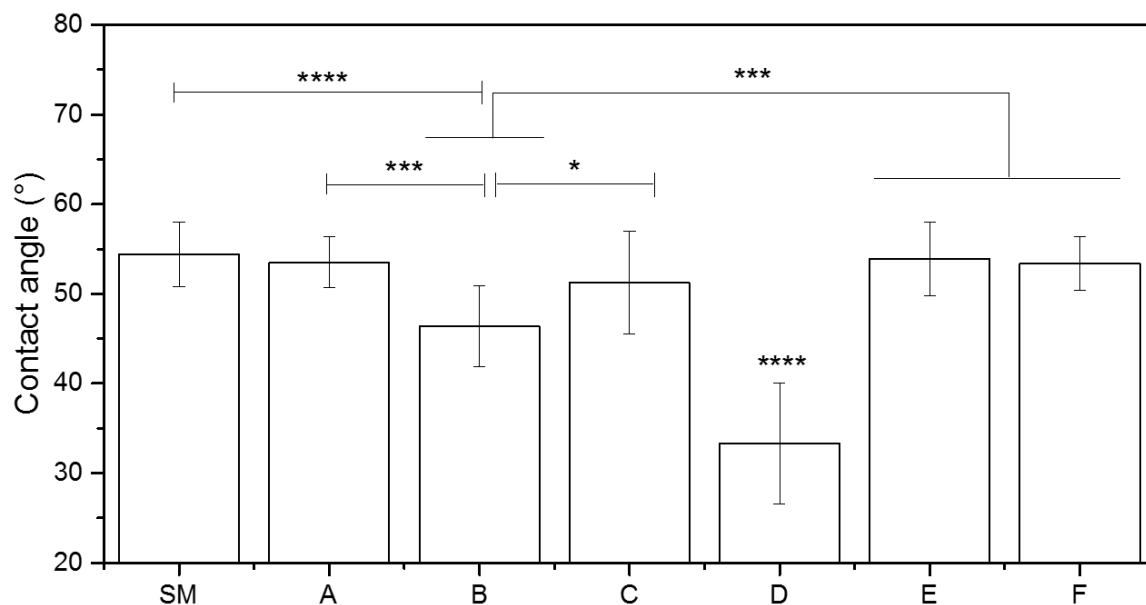


Figure A.44: Statistical analysis of the contact angle measurements reported in Table 5.12. The letters in the graph indicate A: (PDDA-PSS)₂(PDDA-TiO₂)₂(PDDA-PSS)_{1.5}; B: (PDDA-PSS)₂(PDDA-TiO₂)_{3.5} with TiO₂ concentration of 1 g/L; C: same as B using TiO₂ concentration of 500 mg/L; D: same as B using an ionic strength of 100 mM (NaCl) for the deposition process; E: (PEI-TiO₂)_{5.5}; F: (PAH-PSS)₂(PAH-TiO₂)_{3.5}. Statistical analysis is reported for significant results: * P ≤ 0.05, ** P ≤ 0.01, * P ≤ 0.001, **** P ≤ 0.0001. P values were calculated using one-way analysis of variance (ANOVA).**